RECEIVED
LAWRENCE
BERKELEY LABORATORY

MAR 13 1989

LIBRARY AND
DOCUMENTS SECTION

PUB-5172 Rev.

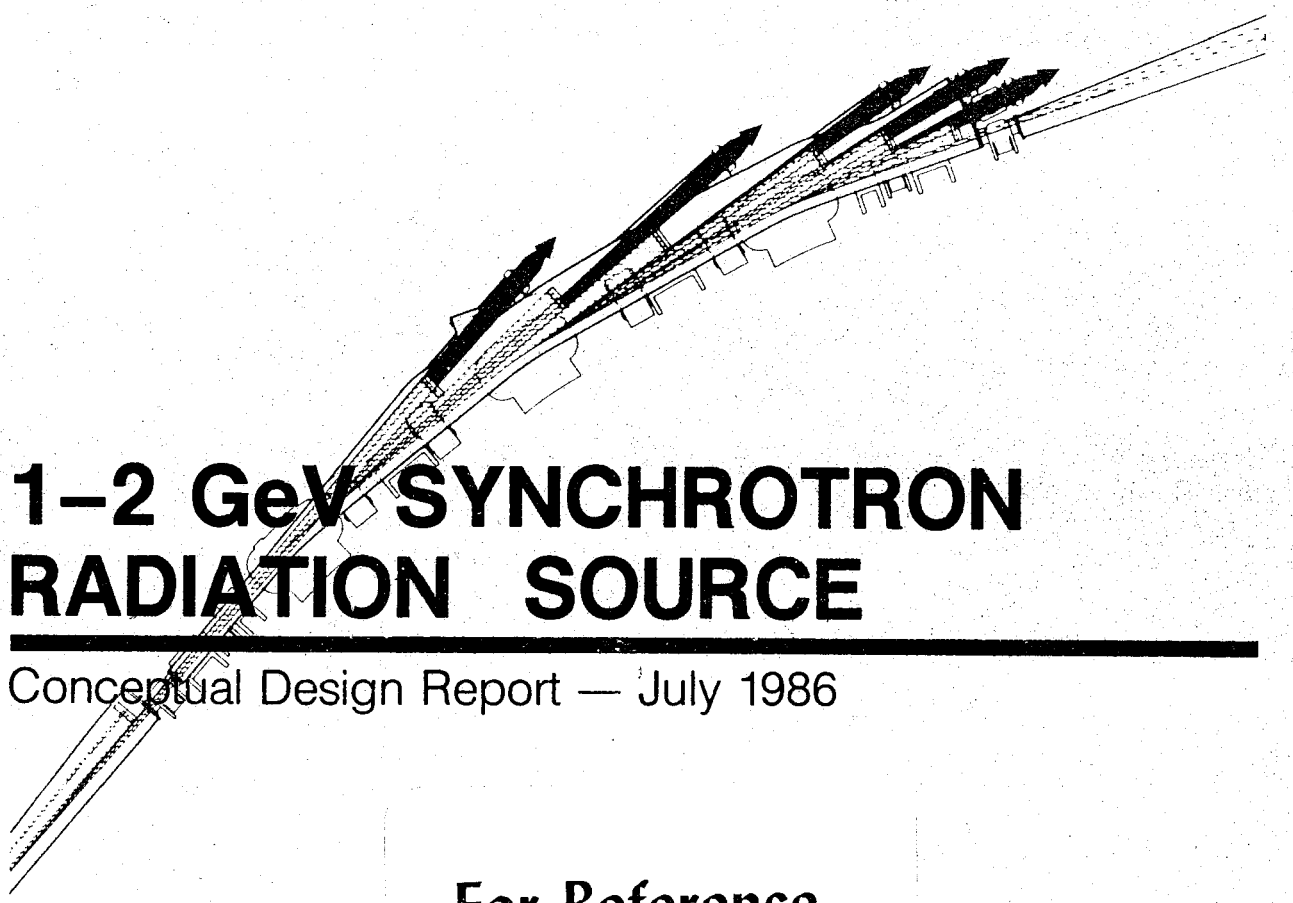

# 1–2 GeV SYNCHROTRON RADIATION SOURCE

Conceptual Design Report — July 1986

For Reference

Not to be taken from this room

Lawrence Berkeley Labortory
University of California
Berkeley, California 94720

Prepared for U.S. Department of Energy under Contract No. DE-AC03-76SF00098

PUB 5172

## DISCLAIMER

This document was prepared as an account of work sponsored by the United States Government. Neither the United States Government nor any agency thereof, nor The Regents of the University of California, nor any of their employees, makes any warranty, express or implied, or assumes any legal liability or responsibility for the accuracy, completeness, or usefulness of any information, apparatus, product, or process disclosed, or represents that its use would not infringe privately owned rights. Reference herein to any specific commercial products process, or service by its trade name, trademark, manufacturer, or otherwise, does not necessarily constitute or imply its endorsement, recommendation, or favoring by the United States Government or any agency thereof, or The Regents of the University of California. The views and opinions of authors expressed herein do not necessarily state or reflect those of the United States Government or any agency thereof or The Regents of the University of California and shall not be used for advertising or product endorsement purposes.

Lawrence Berkeley Laboratory is an equal opportunity employer.

PUB-5172 Rev.

# 1–2 GeV SYNCHROTRON RADIATION SOURCE

Conceptual Design Report — July 1986

Lawrence Berkeley Labortory
University of California
Berkeley, California 94720

Prepared for U.S. Department of Energy under Contract No. DE-AC03-76SF00098

# CONTENTS


**1 Overview** **1**

**2 Introduction** **5**

2.1 Synchrotron Radiation Characteristics of Insertion Devices 8
2.2 Research Opportunities 10
2.3 Design Considerations 14

2.3.1 Storage Ring 15
2.3.2 Insertion Devices and Beam Lines 17

**3 Storage Ring** **19**

3.1 Operating Modes and Performance Goals 21
3.2 Magnet Lattice 22

3.2.1 Description 22
3.2.2 Tunability 24
3.2.3 Chromaticity Correction and Dynamic Aperture 25
3.2.4 Injection and Accumulation 26

3.3 Accelerator Physics Issues 30

3.3.1 Magnetic Imperfections and Misalignments 30
3.3.2 Collective Effects and Beam Lifetime 36
3.3.3 Ion Trapping 49
3.3.4 Effects of Insertion Devices 56
3.3.5 Detuned Version of the Lattice 60
3.3.6 Summary 61

3.4 Storage Ring Magnets and Supports 62

3.4.1 Bending Magnets 63
3.4.2 Quadrupole Magnets 63
3.4.3 Sextupole Magnets 68
3.4.4 Skew Quadrupoles 71

3.4.5 Steering 71
3.4.6 Injection Magnets 73
3.4.7 Magnetic Field Measurements 75
3.4.8 Support and Alignment 76

3.5 Vacuum System 79

3.5.1 Principle of Operation 81
3.5.2 Vacuum Pumps 85
3.5.3 Vacuum Chamber Construction 85
3.5.4 Sector Valves and Bellows 86
3.5.5 Bake-out 86
3.5.6 Other Considerations 88

3.6 Survey and Alignment 88

3.7 Magnet Power Supply Systems 89

3.7.1 Bending Magnet Power Supplies 90
3.7.2 Quadrupole Magnet Power Supplies 92
3.7.3 Sextupole Magnet Power Supplies 92
3.7.4 Correction Magnet Power Supplies 93
3.7.5 Injection Magnet Power Supplies 93

3.8 Radio-Frequency System 95

3.8.1 Cavity 95
3.8.2 Power Source and Distribution 96
3.8.3 General 100

3.9 Instrumentation and Low-Level Electronics 100

3.9.1 Beam-Position Measurement (BPM) 101
3.9.2 Traveling-Wave Electrodes 103
3.9.3 Optical Monitoring 103
3.9.4. DC Current Transformer (DCCT) 105
3.9.5 Scintillators (Flags) 107
3.9.6 Beam Damping 107
3.9.7 Control-Room Instrumentation 109
3.9.8 Communications 109
3.9.9 Timing 111
3.9.10 Beam Line Steering Control 111
3.9.11 Vacuum Monitoring 112

3.10 Safety System 113

3.10.1 Design Philosophy 113
3.10.2 Tone Loop 114
3.10.3 Controlled Access Zone 114

3.10.4 Area Monitoring 116
3.10.5 Safety Shutters 116
3.10.6 Reset/Crash-off Boxes 116

3.11 Control System 117

3.11.1 System Architecture 118
3.11.2 Operator Interface 124
3.11.3 Subsystems 125

**4 Injection System** **129**

4.1 Injection Process and System Parameters 131

4.1.1 Multibunch Mode 131
4.1.2 Few-Bunch Mode 131
4.1.3 System Parameters 132

4.2 Linac System 134

4.2.1 Electron Gun 136
4.2.2 Buncher and Chopper 136
4.2.3 Linac 136
4.2.4 Transverse Focusing 138
4.2.5 Linac Instrumentation 138

4.3 Linac-to-Booster (LTB) Transfer Line 139

4.4 Booster Synchrotron 141

4.4.1 Magnet Lattice 141
4.4.2 Accelerator Physics Issues 145
4.4.3 Booster Magnets and Supports 149
4.4.4 Other Components and Auxiliary Systems 157

4.5 Booster-to-Storage-Ring (BTS) Transfer Line 164

**5 Insertion Devices and Beam Lines** **167**

5.1 Insertion Devices 167

5.1.1 Light Source Insertion Devices and Their Performance 167
5.1.2 Mechanical Description 176
5.1.3 Special Undulators for Polarization Control 181

5.2 Insertion Device Beam Lines 181

5.2.1 Introduction 181
5.2.2 History 182
5.2.3 Theory 183
5.2.4 User Requirements 187

5.2.5 Optical Systems 187
5.2.6 Beam Line Component Engineering 199

5.3 Bending Magnet Beam Lines 205

**6 Conventional Facilities 207**

6.1 Site Preparation 212

6.1.1 Demolitions and Shielding Block Removals 212
6.1.2 Utilities Removals and Relocations 212

6.2 Equipment Removals 212
6.3 Construction 214

6.3.1 Site Improvements 214
6.3.2 Building 6 Addition 214

6.4 Building Modifications 215

6.4.1 Building 7 215
6.4.2 Building 80 215
6.4.3 Building 10 215

**7 Schedule and Cost Estimate 217**

7.1 Schedule 217
7.2 Cost Estimate 233

**Appendix A: Parameter List 247**

**Appendix B: Accelerator Theory 257**

**Appendix C: Multipole Components in the Lattice Magnets 261**

C.1 Dipole Magnets 262
C.2 Quadrupoles 263
C.3 Conclusions 265

**Appendix D: Positron Injection 267**

D.1 Description of System 267
D.2 Injection Process 271

D.2.1 Multibunch Mode 271
D.2.2 Few-Bunch Mode 271

D.3 System Parameters 272
D.4 Cost Estimate 275

**Appendix E: Source Characteristics of Synchrotron Radiation 277**

E.1 Source Characterization 277

E.2 Radiation Characteristics of Undulators 278
E.3 Radiation Characteristics of Wigglers and Bending Magnets 280

**Appendix F: Special Undulators for Polarization Control** **283**

F.1 Helical Undulator 283
F.2 Crossed Undulator 283
F.3 Other Devices 284

**References** **285**

# 1. Overview

The utilization of electromagnetic radiation in the visible light portion of the spectrum has been of fundamental importance in the advancement of science and technology, especially since the relatively recent invention of the laser. During the past several decades, synchrotron radiation sources (which make use of the intense beams of ultraviolet and x-ray radiation emitted by relativistic electron beams circulating in a magnetic field) have extended the uses of electromagnetic radiation in the study of many physical, chemical, and biological processes.

The field has grown dramatically through three generations of facilities. Whenever a synchrotron light facility offering an increase in brightness, typically by a factor of from 10 to 10,000, became available, new types of research became possible. The first generation was based largely on the parasitic use of synchrotron light from the bending magnets of electron synchrotrons and storage rings built for high-energy physics. In the U.S., the second generation formally began with a 1976 National Academy of Sciences report that recommended the construction of dedicated new facilities specifically designed to produce synchrotron light. This led to construction of the National Synchrotron Light Source at Brookhaven National Laboratory and the Aladdin facility at the University of Wisconsin.

The second generation of light sources has been improved by retrofitting existing storage rings with special magnetic structures called wigglers and undulators, which enhance the intensity of synchrotron light. The Lawrence Berkeley Laboratory has played a key role in the development and improvement of these devices. However, the design and construction of the present generation of storage rings came too early to optimize the use of these devices.

The third generation of synchrotron radiation facilities requires the construction of new machines specifically designed to maximize the brightness of the radiation from wigglers and undulators. The result will be light 50 to more than 100 times as bright as that available from the best synchrotron radiation sources we have today—or might expect by adding new insertion devices to existing facilities. The 1–2 GeV Synchrotron Radiation Source described in this report will be one of two third-generation U.S. synchrotron radiation facilities designed to exploit the superior properties of the electromagnetic radiation emitted from wigglers and undulators. The facility will produce beams of very high intensity, extreme brightness, very short pulses, and laserlike coherence. Because of its broad range of capabilities, the 1–2 GeV Synchrotron Radiation Source will serve the needs of a wide

segment of the scientific community, including

- Materials, interface, and surface science
- Biology and medicine
- Chemical dynamics
- Atomic and molecular physics

The facility will also provide unexcelled opportunities for industrial research and technology development and will undoubtedly lead to new research possibilities not presently envisioned.

The 1–2 GeV Synchrotron Radiation Source project (see Fig. 1-1) consists of

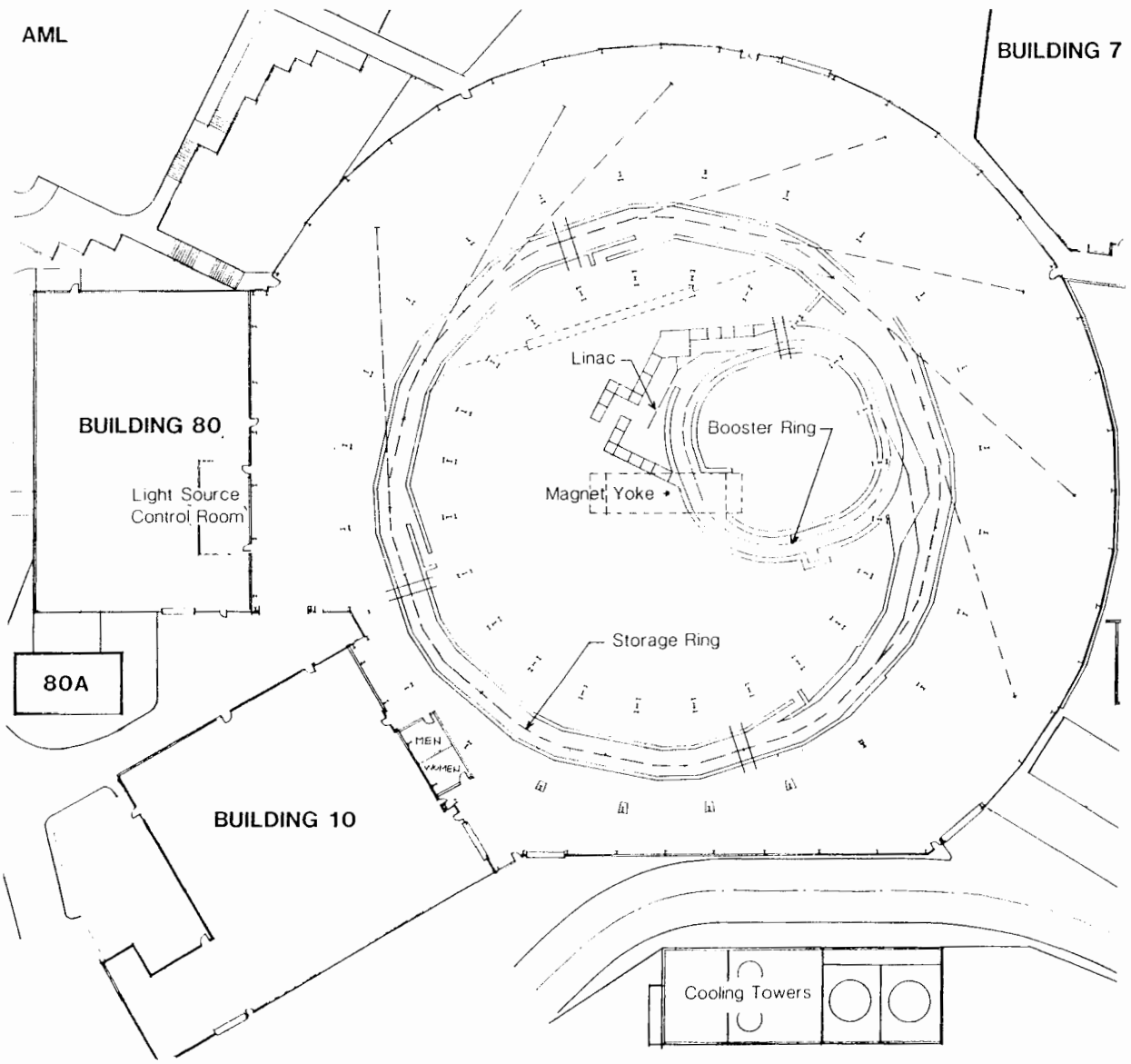


**Fig. 1-1.** A plan view of the 1–2 GeV Synchrotron Radiation Source (above) and a more detailed schematic of the special research facilities (facing page), showing the injection system, storage ring lattice, insertion devices, and location of seven beam lines.

- A low-emittance electron storage ring optimized at 1.5 GeV.
- An initial complement of five insertion devices (four undulators and one wiggler), located in the storage ring straight sections, and a total of seven photon beam lines.
- An injection system (50-MeV linac plus 1.5-GeV booster synchrotron).

This new facility will be constructed in an existing building, which will be substantially expanded and upgraded to fulfill its new purpose. By including the initial complement of insertion devices and photon beam lines, the proposed project will become a powerful research facility immediately after its commissioning period.

The design of the facility is aimed at achieving two principal goals:

- To provide high-brightness photon beams (primarily from insertion devices) in the nominal energy range from 0.5 to 1000 eV.
- To produce very short pulses (tens of picoseconds) that will allow time-resolved experiments in this time regime.

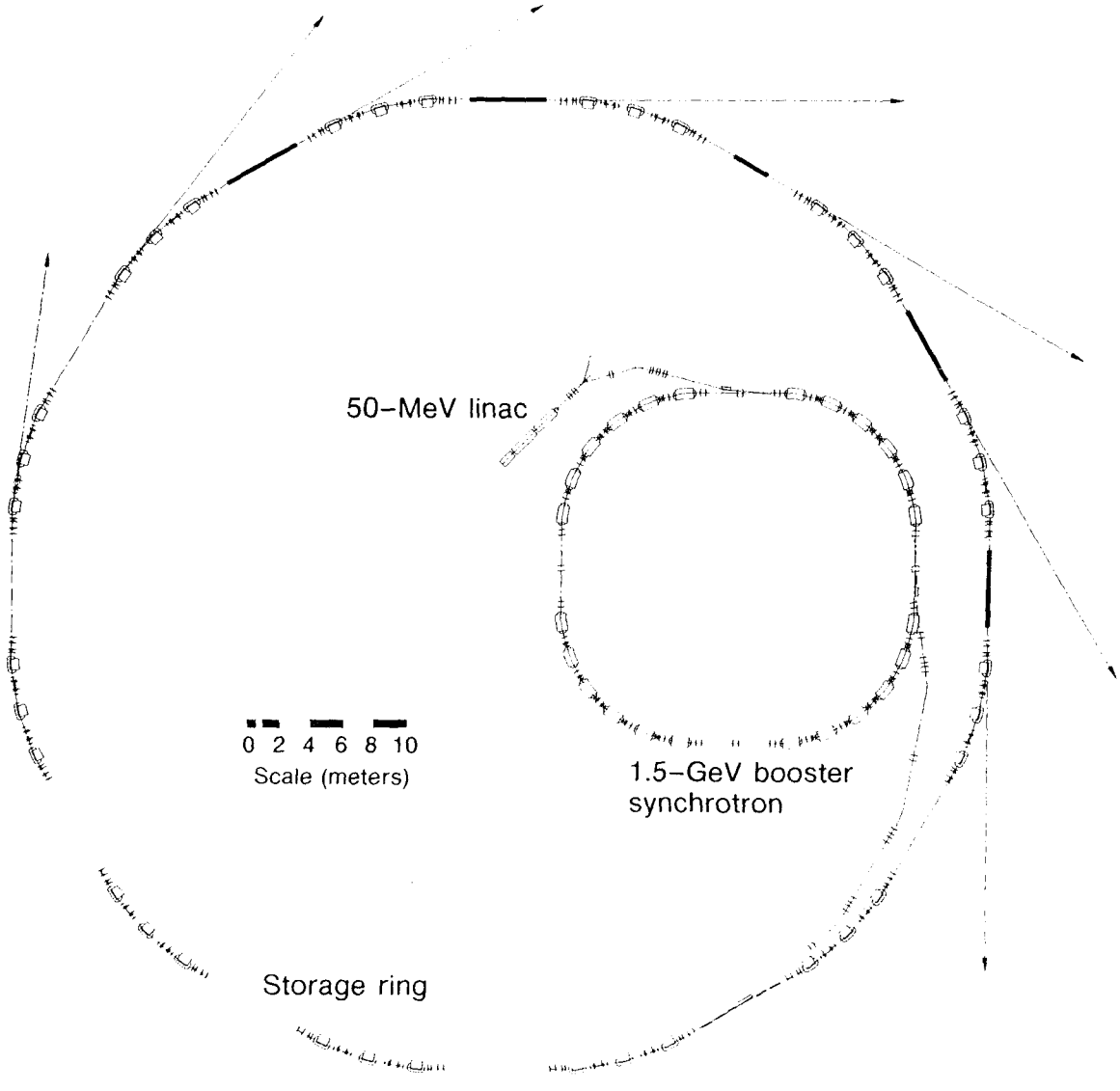

To accomplish these goals, the storage ring incorporates 12 long straight sections; 11 of these will be available for the placement of insertion devices. Of the initial seven beam lines, five will be from insertion devices; however, as many as 60 beam lines could ultimately be part of the facility if all the bending magnets were to be developed. The design is based primarily on well-proven technology, which will minimize the commissioning period and maximize reliability. In a few selected areas, such as the storage-ring vacuum chamber, innovative new designs have been developed that promise very substantial performance gains over more traditional techniques.

In view of the unique scientific opportunities that will be available at the new light source, it will be operated as a national facility. The intention is to integrate the user community into the design and operation of the research facilities as closely as possible. In particular, this will be accomplished by

- Assigning a portion of the overall project budget to the creation of insertion devices and beam lines to be available as a community resource.
- Creating a cadre of in-house scientists who can provide liaison and technical help for outside groups.

The Lawrence Berkeley Laboratory has a long and distinguished history in the field of accelerator design and construction and is also a leader in the design and utilization of magnetic insertion devices and photon beam lines. Indeed, the design of permanent-magnet insertion devices has been pioneered at LBL. Thus, the expertise required to design and construct a next-generation synchrotron radiation source is already in place.

The total estimated cost of the 1–2 GeV Synchrotron Radiation Source is $98.7 million for a six-year construction schedule (FY 1987 through FY 1992). Completion of the injection system and storage ring is anticipated at the end of FY 1991, at which time machine commissioning will begin. The entire project will be completed with the finishing of the photon beam lines at the end of FY 1992.

# 2. Introduction

The ability to harness electromagnetic radiation has played a significant role in the development of science and its subsequent benefit to society. Galileo's telescope and Leeuwenhoek's microscope extended the range of human observation to much larger and much smaller objects than had previously been seen. Pasteur used the microscope to peer into the world of microorganisms and then to link bacteria to the cause of disease. Towne's invention of the visible-light laser has created many new opportunities for our society in the fields of science, medicine, and technology. These examples all involve the utilization of visible light—that portion of the electromagnetic spectrum to which our eyes respond (see Fig. 2-1). (Recent papers by Townes [1984], Lamb [1984], Bloembergen [1984], Schawlow [1984], and Patel [1984] expand on the development of lasers and related techniques in the visible and near-visible spectral regions.) Equally interesting opportunities await us as we master the generation and utilization of shorter-wavelength radiation, at ultraviolet and x-ray wavelengths.

Over the past several decades, the construction of particle accelerators and storage rings dedicated to high-energy physics research has led, by serendipity, to a new class of facilities—synchrotron light sources—that will enable these new opportunities to become reality. When a circulating electron beam is deflected by the bending magnets in a storage ring, an intense flux of electromagnetic radiation, called synchrotron radiation, is produced. Relativistic effects cause this synchrotron radiation to be emitted in a narrow cone centered about the electron-beam direction. For electron energies of the order of 1 GeV, the half-angle of this cone is typically a fraction of a milliradian.

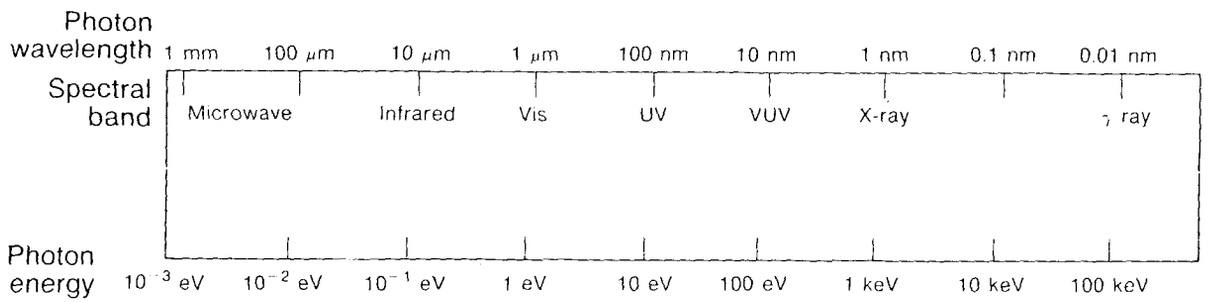


**Fig. 2-1.** Electromagnetic spectrum.

Originally, synchrotron radiation was viewed primarily as an annoyance because of the need to compensate for the electron-beam energy loss by using a powerful radio-frequency accelerating system. However, it was soon recognized that synchrotron radiation is useful for a wide range of physical, chemical, and biological experiments, quite unrelated to the original purpose of these electron storage rings. Although the scientific community has taken great advantage of the synchrotron radiation produced by these first-generation light sources (originally constructed for high-energy physics), the properties of the accelerators were not at all optimized for this purpose.

More recently, electron storage rings specifically dedicated to producing synchrotron radiation have been designed and constructed. Most storage rings in this so-called second generation of synchrotron radiation sources have become operational in the relatively recent past, both in the United States (the National Synchrotron Light Source at Brookhaven National Laboratory, Aladdin at the University of Wisconsin) and abroad (England, Germany, Japan). These second-generation facilities, while built expressly for the production of synchrotron radiation, were designed primarily for photon beam lines from the storage ring bending magnets (which serve to keep the electron beam in its approximately circular orbit). Thus, their figure of merit was primarily the integrated flux of photons.

In the third generation of synchrotron light sources, of which the proposed LBL 1–2 GeV Synchrotron Radiation Source is a prime example, the spectral properties of the photon beams will be considerably enhanced by utilizing special magnetic devices (described below) called "wigglers" and "undulators" that are placed in the straight sections (insertions) of the storage ring. Compared with bending magnet sources, these insertion devices can produce far more intense photon beams with greater flexibility in terms of their characteristics. Wigglers and undulators are magnetic structures in which electrons experience periodic reversals in the static transverse magnetic field as they traverse the length of the device. This is illustrated schematically in Fig. 2-2. A storage ring designed for optimum utilization of photon beams from insertion devices must include a suitable number of long straight sections to accommodate the wigglers or undulators, and must provide an electron beam with very small transverse dimensions in order to yield photon beams with the highest possible density. Both of these features are integral to the design of the 1–2 GeV Synchrotron Radiation Source proposed here. The design consists of an injection system (linac plus booster synchrotron), a low-emittance storage ring optimized at 1.5 GeV, several insertion devices located in the storage ring straight sections, and beam lines from the insertion devices and bending magnets. The layout of the facility is shown in Fig. 1-1; in the remainder of this document we often refer to it as the "Light Source."

In recent years, several national advisory panels [Eisenberger-Knotek, 1984; Seitz-Eastman, 1984; Stehli, 1985; Brinkman, 1986] have identified as high-priority projects the construction of two third-generation dedicated synchrotron radiation sources, one having a 6-GeV electron-beam energy and the other having a 1–2 GeV beam. The latter project, to which this proposal is responsive, is intended to provide a facility optimized for the production of ultraviolet and soft x-ray photons from magnetic insertion devices.

Photon energies in the ultraviolet–x-ray region span the range from several electron volts (eV) to several thousand electron volts (keV). This energy range is well-matched to the primary atomic resonances of the light elements (C, N, O, Na); resonances from many

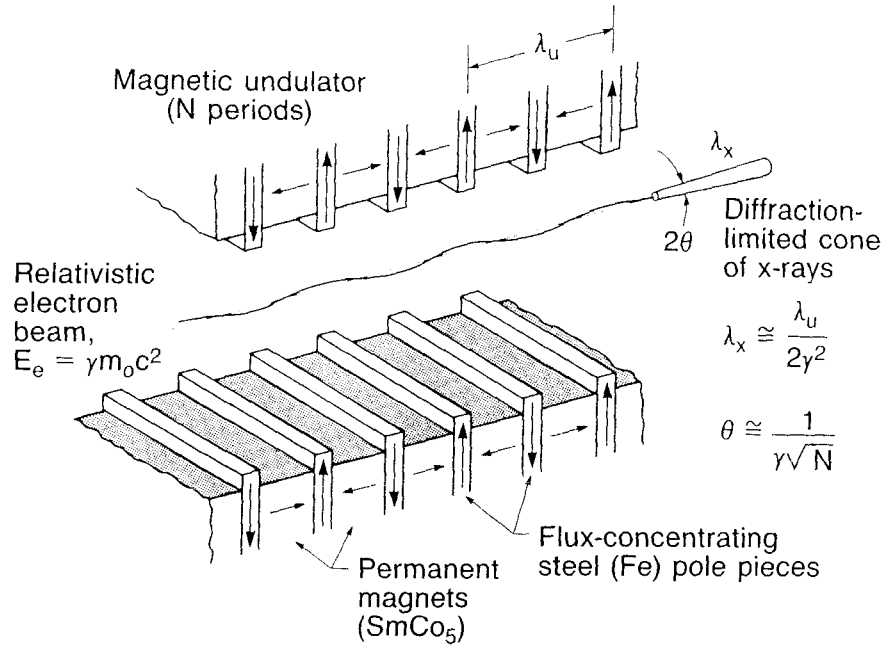


**Fig. 2-2.** Schematic of a periodic magnet structure (an undulator) of period $\lambda_u$ and with a number of periods, $N$. The oscillations of the electron beam (of energy $\gamma m_0 c^2$) passing through the structure produce ultraviolet and soft x-ray radiation (photons) of high spectral brightness and high coherent power. The radiation occurs at a wavelength $\lambda_x$ in a narrow spectral width $(\lambda_x/\Delta\lambda_x) \simeq N$, and is propagated forward in a narrow cone of half-angle $\theta \simeq (\gamma\sqrt{N})^{-1}$.

molecular transitions also appear in this regime. In addition, the wavelengths in this energy range are comparable to important spatial scales, e.g., the pitch and diameter of biochemical helices, the microstructural features of materials, and the feature sizes of next-generation electronic microcircuits. Although this wavelength region offers tremendous scientific promise, shorter-wavelength radiation is more difficult to generate than visible light, it is more easily absorbed, and it is more difficult to manipulate and transport efficiently, via optical elements such as mirrors, lenses, and filters. Such radiation has been particularly difficult to generate at high brightness and with laserlike coherence. It is in this particular area that third-generation synchrotron radiation facilities will be especially valuable. The emitted radiation of undulators will be very well controlled in spectral width and will have focusing and collimating properties that are close to being diffraction-limited. Undulator radiation will thus be well-suited to microprobe and scattering techniques designed to track the dynamics of elemental species.

This elemental sensitivity gives an important additional dimension to existing techniques. For example, it will permit the identification and tracking of specific critical elements, such as calcium or iron, in biological samples. Furthermore, it will permit us to obtain clearer insights into the structural features of new materials and the dynamics of surfaces and interfaces.

At shorter wavelengths, other important advantages will also accrue, especially the capability both to "see" and to "write" smaller features. It will be possible to construct x-ray microscopes that can penetrate functioning biological assemblies and resolve features

far smaller than can be seen with optical microscopes, again with elemental sensitivity. It will also be possible to write electronic microcircuit (chip) patterns with yet smaller feature sizes, forming the basis for next-generation computers that are more compact and more economical than today's.

## 2.1 Synchrotron Radiation Characteristics of Insertion Devices

The properties of synchrotron radiation that make these new opportunities possible with next-generation facilities can be understood by considering Fig. 2-2. The oscillation of relativistic electrons as they pass through a periodic magnet structure (an undulator) causes radiation to be generated in narrow spectral lines and with minimal divergence, approaching limits set by the small but finite wavelength of the radiation (the so-called diffraction limit). It is important that the very thin, pencillike beam of fast electrons be tightly controlled in phase space, i.e., that the emittance be as small as possible. If it is not, the small divergence and the spatial coherence of the synchrotron radiation will be compromised.

The extent of the resulting electron deflection in a wiggler or undulator is characterized by the dimensionless parameter

$$K = 0.934\, B_0 \lambda_u \ ,$$

where $B_0$ is the peak magnetic field (in T) and $\lambda_u$ is the spatial period (in cm) of the magnetic field.

An undulator is characterized by a low value of $K$ ($\simeq 1$). Because of the interference of radiation from different periods, undulator radiation is spectrally compressed into a series of narrow peaks (see Fig. 2-3) at harmonics of the fundamental energy, given by

$$\epsilon_1\,[\mathrm{keV}] = \frac{0.95\, E^2[\mathrm{GeV}]}{\lambda_u[\mathrm{cm}]\,(1 + K^2/2)} \ ,$$

where $E$ is the electron energy. If the electron-beam emittance is small, the radiation appears to emanate from an area of almost diffraction-limited size, with an almost diffraction-limited angular divergence. Undulators can thus provide radiation of unparalleled spectral brightness.

For wigglers, which are characterized by large $K$, higher harmonics become increasingly important. However, spectral peaks at very high harmonics tend to smooth out owing to the blurring effects of the electron-beam emittance and energy spread, thus producing a smooth spectrum. Wigglers can therefore be regarded simply as a sequence of bending magnets of alternating polarity. The radiation from the alternating bending sections adds incoherently, giving rise to a $2N$-fold increase in the radiation intensity (compared with a single bending magnet), where $N$ is the number of magnet periods. Note that, although a magnetic device with large $K$, say, $K > 10$, is usually said to be a wiggler, it will, in general, produce prominent undulator peaks at lower harmonics and, therefore, is an undulator in the energy region covered by the lower harmonics.

In discussing the propagation properties of electromagnetic radiation, the density of the

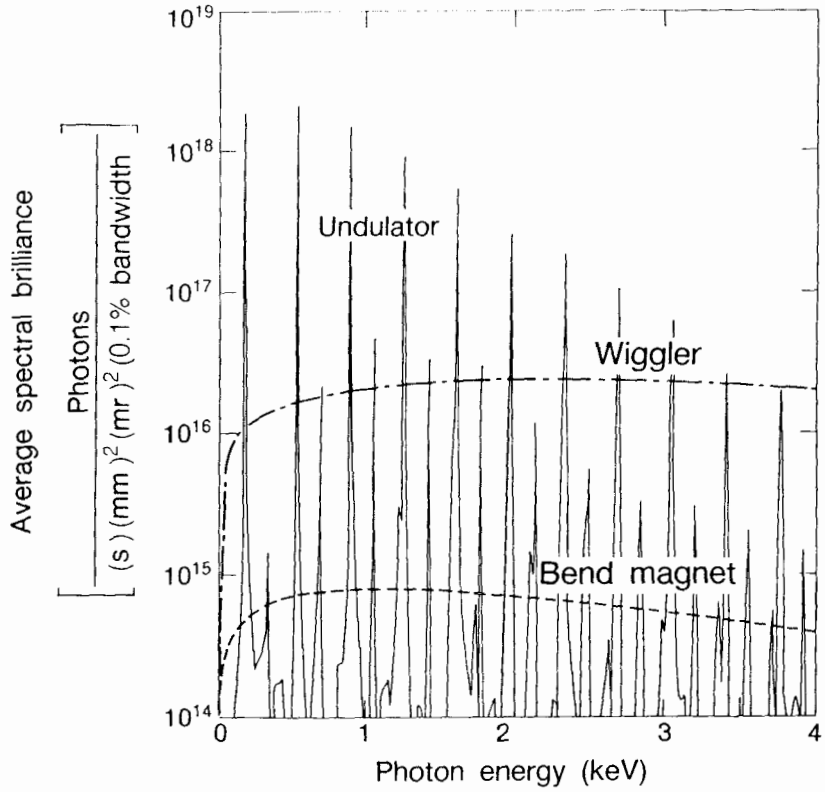


**Fig. 2-3.** Harmonic content of undulator radiation arising from interference of radiation from different periods.

photon flux in phase space plays a fundamental role and is generally referred to as the brightness. In this report, we reserve the term *brightness* for the phase-space density of the photon flux, evaluated in the forward direction and at the center of the source, i.e., at the origin of the phase space:

$$\mathscr{B} = \left. \frac{d^4\mathscr{F}}{d\theta d\psi dx dy} \right|_0 . \tag{1}$$

Here, $\theta$ and $\psi$ are the horizontal and vertical angles, and $x$ and $y$ are the horizontal and vertical coordinates, respectively. (Note that this quantity is sometimes called the brilliance.) The brightness uniquely characterizes the strength of a radiation source, as it is invariant under propagation through linear optical elements, such as lenses or free space.

Integrating the phase-space density over the angles (or the position coordinates) gives the spatial (or angular) density of flux:

$$\frac{d^2\mathscr{F}}{dx dy} = \int \frac{d^4\mathscr{F}}{d\theta d\psi dx dy} d\theta d\psi , \tag{2}$$

$$\frac{d^2\mathscr{F}}{d\theta d\psi} = \int \frac{d^4\mathscr{F}}{d\theta d\psi dx dy} dx dy . \tag{3}$$

For synchrotron radiation, the *angular* density of flux [Eq. (3)] is the more familiar quantity, as it can be calculated from standard textbook formulas; it is sometimes mistakenly called brightness. However, it is *not* an invariant measure of the source strength, because its magnitude depends on the nature of the beam line focusing elements. Finally, the flux can be obtained by further integration:

$$\mathscr{F} = \int \frac{d^2\mathscr{F}}{d\theta d\psi}\, d\theta d\psi = \int \frac{d^2\mathscr{F}}{dxdy}\, dxdy \,. \tag{4}$$

The flux is another invariant that characterizes the source strength.

It is generally convenient to consider the various differential fluxes introduced above in a small bandwidth around a given energy. In this case, we use the adjective *spectral*. Thus, we speak of the spectral brightness, spectral flux, the angular density of spectral flux, and so on.

The quantity called spectral flux is defined as

$$\text{spectral flux} = \frac{\text{No. of photons}}{\text{s} \times (0.1\% \text{ bandwidth})} \,.$$

As mentioned, the spectral flux is a global characteristic of a radiation source. For sources with narrow angular and spatial features, another quantity of merit is the so-called spectral brightness, which is measured in the following units:

$$\text{spectral brightness} = \frac{\text{No. of photons}}{\text{s} \times \text{mm}^2 \times \text{mrad}^2 \times (0.1\% \text{ bandwidth})} \,.$$

The spectral brightness is the density of spectral flux in the transverse phase space defined by the angle and position of the emitted radiation.

Another property of the photon beam from an undulator is "coherence." In the limited sense used here, coherence refers to the ability to form interference patterns when wave fronts are separated and then recombined. Although the photon beams from the Light Source undulators are only partially coherent [Attwood, 1985], they will nonetheless be satisfactory for many experiments that utilize phase-sensitive techniques, e.g., x-ray interferometry and x-ray microholography.

The narrowness of the spectral emission line is set by the number of undulator periods, $N$. Again, this will be significantly increased in this new ring, the first specifically optimized for undulator radiation. Narrow spectral lines allow most of the generated photons to be concentrated in the most desired regions—at or near resonances of the atoms and molecules of interest.

## 2.2 Research Opportunities

For a storage ring operating at 1.5 GeV, the radiation covers the spectrum of photon energies from a few eV to several keV. For many advanced experiments, especially those aimed at studying the fast processes of chemical reactions, surface dynamics, and interface formation, short pulses are also required to time-freeze the action. For this reason, the Light

Source is designed for very short electron bunch lengths, resulting in radiation pulses in the 20- to 50-ps regime. This will be particularly valuable in conjunction with pump-probe experiments, such as might be used for studying phase transitions with synchronous visible laser and shorter-wavelength undulator radiation pulses. It is important that the radiation be broadly tunable, a feature not available with any other high-brightness technology. Tunability permits many elements to be tracked, as variables such as the concentrations of perturbing neighbors are increased in a given experiment.

Examples of the types of experiments possible with a modern 1- to 2-GeV synchrotron light source can be found in the recent *Report of the Workshop on an Advanced Soft X-Ray and Ultraviolet Synchrotron Source: Applications to Science and Technology* [1985]. The applications cover diverse areas, including atomic and molecular physics; biology and medicine; chemical dynamics; materials, interface, and surface science; industrial research and technology; and special new techniques, such as pump-probe dynamical response studies involving synchronized picosecond/femtosecond lasers and x-ray or ultraviolet synchrotron radiation. Several examples follow.

In *atomic and molecular physics*, the brightness of the new source will permit spectroscopists to measure effects in very dilute gas sources. Relativistic, quantum-electrodynamics, and correlation effects will be readily measurable. Also, the properties of open-shell atoms, atoms in excited states, and highly stripped ions can be studied. These are systems that occur in astrophysical and plasma environments and that may someday serve in x-ray laser schemes. Some of these experiments will involve combinations of the synchrotron source with tunable lasers and with heavy-ion beams, storage rings, or traps. The vibrational structure of molecules will become resolvable, even for core levels. It will become possible to study the dynamics of energetic processes in atomic inner shells, including resonances that occur on a uniquely fast time scale. The high intensity of the light from the new source will allow experimenters to measure spin polarization of the photoelectrons—the third crucial quantity in the photoelectric effect (in addition to energy and angle). Thus, the degeneracy in the continuum between the two spin components will be lifted, permitting the complete determination of all transition amplitudes and leading to direct measurements of relativistic interactions in atoms. The brilliance of the source will permit measurements on tiny samples of rare materials, such as the radioactive actinides, whose properties have largely eluded determination in the past because the available quantities were insufficient for study by traditional means.

In *biology and medicine*, one of the most attractive potential capabilities of the Light Source lies in the area of imaging small biological specimens—perhaps even macromolecules. The high brightness and considerable coherence of the radiation from undulators offer promise for the success of new techniques for imaging wet, unstained biological samples through x-ray microscopy and holography, contact microscopy, and soft-x-ray diffraction, with sufficiently short exposure times to permit dynamical studies. Utilizing another potential capability of the Light Source—crossed undulators [Kim, 1984]—biophysicists could switch rapidly between right- and left-circularly polarized light to measure, through circular intensity differential scattering, the higher-order structure of polymers in biological systems.

Interesting applications of the new source are anticipated in the area of *chemical dynamics*, which encompasses all phenomena in which molecules undergo energetic or

chemical transformations. As a photo-analysis source, the Light Source can produce macroscopic yields of vacuum ultraviolet photoproducts. If operated in conjunction with an infrared free-electron laser, it would additionally be a powerful tool for the study of chemical processes induced by infrared multiphoton absorption. The time structure of the synchrotron light will permit the study of ultrafast processes. For example, the cleavage of the chemical bonds of photoexcited molecules can occur in picoseconds; such processes could be followed through special techniques, utilizing the fast pulses and high repetition rate of the new source. Bond-selective photochemistry will be possible, using a new technique through which specific bonds in large molecules can be cut selectively with tunable ultraviolet radiation, "as with a scalpel." Cluster chemistry is an exciting new field, in which aggregates of atoms or molecules that exhibit the transition between the properties of isolated atoms and those of the solid state are studied. Here, the Light Source is ideally suited for measurements of such phenomena as the variation of ionization energies with cluster size, which yield data on the onset of bulk properties as the size of the aggregates increases. Finally, photoionization mass spectroscopy and photoelectron spectroscopy can provide valuable thermochemical data that serve to characterize the structure and energetics of reactive intermediates in chemical reactions. The high ultraviolet output of the new source will make it possible to conduct such studies with unprecedented sensitivity and resolution.

Several of the most exciting applications of the Light Source lie in the field of *materials, interface, and surface science.* An outstanding challenge in experimental studies of solid surfaces is the performance of real-time measurements on dynamically changing systems. The high flux and brightness of the radiation from the proposed storage ring and its sharp time structure will make it possible to study chemical reactions, phase transitions, and the time evolution of excited states, giving new insight into intermediate states and reaction dynamics. For example, time-resolved NEXAFS can be used to observe a phase transition, a chemical reaction of molecules on a surface triggered by the admission of a gas pulse onto it, or a temperature-induced change of an adsorbed species.

Enhanced spatial resolution is another beneficial consequence of the high brightness of the Light Source; this will make possible a new class of surface analytic measurements, namely, the combination of microscopic imaging and photoelectron spectroscopy. A photoelectron spectromicroscope will provide images in which the contrast is due to differences in molecular species and chemical environment, as reflected in the binding-energy spectrum. The approach encompasses virtually all of materials science: analysis of individual grains of polycrystalline samples; correlation of surface chemistry and contrast due to magnetic domains; studies of chemically active small particles on substrates, as in supported metal catalysts; the morphology and surface chemistry of thin-film growth; and finally, studies of surface chemisorption, which could be applied to surface modification processes in device fabrication.

Every technical advance in the utilization of synchrotron radiation has given rise to new opportunities in materials and surface science. One dimension that has yet to be exploited in the U.S. is electron-spin resolution. Spin polarization of photoemitted electrons is due to the exchange interaction in magnetic materials and to the spin-orbit interaction in nonmagnetic materials. For magnetic materials, the opportunities range from very basic questions concerning theories of finite-temperature itinerant magnetism and surface

critical phenomena, to applications-oriented areas associated with film growth and the properties of magnetic memory and recording devices.

The Light Source will allow significant advances in core-level spectroscopy, which today represents the mainstream of applied research with synchrotron radiation. Core-level spectroscopy can be applied to understanding many complex materials and interfaces that have technological applications. Highlights include the use of core-level shift and intensity measurements in characterizing metal-semiconductor interfaces and the application of EXAFS and photoelectron diffraction to determine the bonding geometries of a variety of surface and interface systems. A consequence of such studies will be predictive capabilities as to interface formation and materials engineering, both of which are crucial for many areas of high technology, including current developments in microelectronics.

The Light Source furthermore has significant potential for defect spectroscopy of semiconductor interfaces and surfaces, for which no suitable probe now exists. Soft x-ray photoabsorption studies may be extended to determine the local structure around atoms present in very dilute concentrations in a host system, and this will be an extremely important achievement in surface studies of precursor states, oxidation, poisoning, and chemical reactions on transition-metal catalysts.

Finally, materials science will benefit from the soft x-ray and vacuum ultraviolet scattering capabilities of the new facility. Scattering at these wavelengths is uniquely suited for studying structures that have feature sizes larger than atomic dimensions, but this possibility has not yet been exploited. One possible application is scattering from ultrathin polymer films on solid substrates; these structures are of both scientific and technological interest.

The Light Source will also offer important opportunities for advances in *industrial research and technology.* Foremost among these is cutting-edge research in advanced lithography, addressing issues related to lithography for 256-Mbit chips and beyond. Central to this aim will be the development of advanced imaging techniques, probably by means of projection optics (rather than proximity printing). Other industrial applications include micromachining, surface scanning, contact transmission microscopy, holography, and polymer characterization and optimization.

Considerable attention has also been given to *new techniques* that may become possible with the proposed source, such as laser-synchrotron picosecond-pulse experiments, dynamical diffraction from crystals with glancing-incidence x-rays, as well as the possibility of developing a synchronous free-electron laser.

At the conclusion of the workshop cited above, working-group leaders met to determine the optimal parameters for a new facility that would permit the exciting new research and development that had been proposed to go forward. A consensus was reached on parameters that appear to be thoroughly feasible; they are summarized in Table 2-1. Undulator fundamentals should range between 4 and 900 eV, with tuning possible during operation; position and angular stability of the beam should be a fraction of the nominal values of these quantities. In addition, the ring design should be flexible, so as to permit operation up to 1.9 GeV, and perhaps as low as 0.75 GeV. The facility described in this report successfully addresses these requirements.

The photon flux and brightness anticipated with nominal designs of undulators and wigglers are shown in Figs. 2-4 and 2-5, respectively. The chosen storage ring energy range

**Table 2-1.** Performance goals established by potential Light Source users.

| | |
|---|---|
| Beam energy, nominal (GeV) | 1.5 |
| Energy range (GeV) | 0.75–1.9 |
| Average current (mA) | 400 |
| Horizontal emittance, rms (m-rad) | $<10^{-8}$ |
| Number of straight sections | 12 |
| Straight section length for insertion devices (m) | 6 |
| Bunch length, $2\sigma$ (ps) | 20–50 |
| Beam lifetime (hr) | $>6$ |
| High position and angular stability | |
| Minimum longitudinal jitter | |

provides the highest spectral brightness and coherent power in the ultraviolet and soft x-ray regions. The ultraviolet region is particularly interesting for chemistry and surface science and the soft x-ray region, containing the primary ($K$-shell) resonances of the lower-$Z$ elements and the $L$-shell resonances of intermediate-$Z$ elements, is of special interest for industrial lithography, interface studies, atomic physics studies, and studies of living biological systems within the so-called "water window." In addition to the four undulators, a wiggler is also planned. Wigglers do not generate photon beams of high spectral brightness; however, their radiation does extend to considerably higher photon energies than does the radiation from undulators. As seen in Fig. 2-4, the wiggler will generate a high flux of photons out to about 10 keV. The wiggler will thus be of particular interest to the atomic physics and biological research groups.

## 2.3 Design Considerations

The design of the Light Source has been optimized to achieve two major goals:

- To provide intense photon beams (especially in terms of spectral brightness) in the nominal energy range from 0.5 to 1000 eV.
- To produce very short pulses (tens of picoseconds long) for the many time-resolved experiments planned in this range.

To achieve these goals, the storage ring incorporates 12 long straight sections in which wigglers and undulators produce intense beams of synchrotron light. Altogether, there will be 7 beam lines provided as part of the initial facility. Since each wiggler can service several photon beam lines, about a dozen insertion device beam lines can eventually be constructed, together with up to 48 beam lines from the bending magnets.

LBL scientists and engineers have been studying the possibilities for a facility of this type for several years now and have had the opportunity to review and refine all facets of

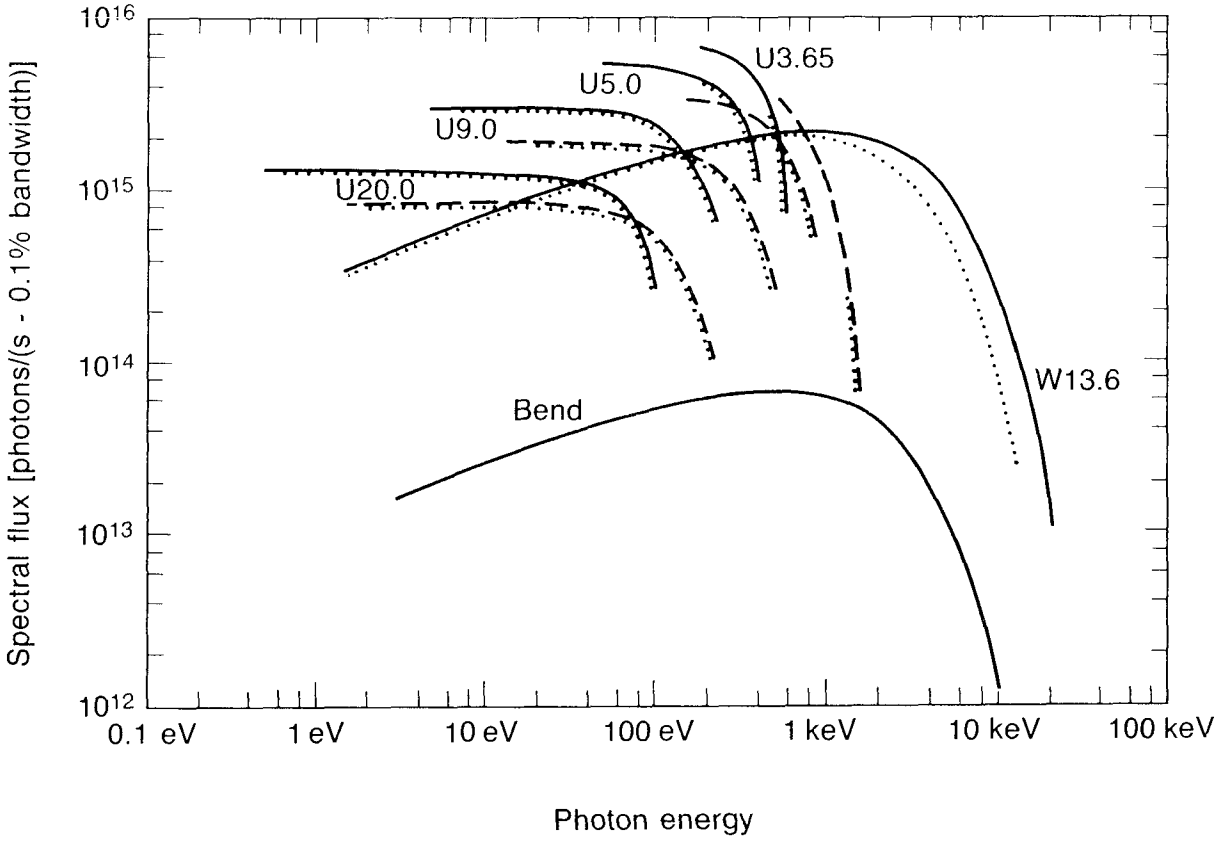


**Fig. 2-4.** Photon flux of radiation generated at the 1–2 GeV Synchrotron Radiation Source. This figure is discussed in detail in Section 5.1.

the design of the Light Source in light of both recent insights into machine design [A. Jackson, 1986; A. Wrulich, 1986] and detailed specifications based upon user requirements.

The basic parameters of the machine we propose are compatible with those of Table 2-1. These parameters, while presenting a challenge to accelerator designers, are within reach of the existing state of technology.

### 2.3.1 Storage Ring

The design of a storage ring to achieve the goals outlined in Table 2-1 is a sophisticated task, requiring a careful analysis of conflicting requirements. One of the most important aspects of the storage ring is the lattice, i.e., the optical arrangement of bending magnets and focusing quadrupoles. As discussed earlier, a high photon brightness requires a high-intensity electron beam of very small emittance. The minimum horizontal emittance achievable in an electron storage ring depends on the detailed design of the lattice. To achieve a small horizontal emittance, a small horizontal beam size is required at the bending magnets. To obtain this, the beam must be strongly focused by quadrupoles. Unfortunately, the side effects of the strong focusing are a worsening of the chromatic properties of the lattice and a reduction of its dynamic aperture, which lead, ultimately, to a short lifetime of the stored beam.

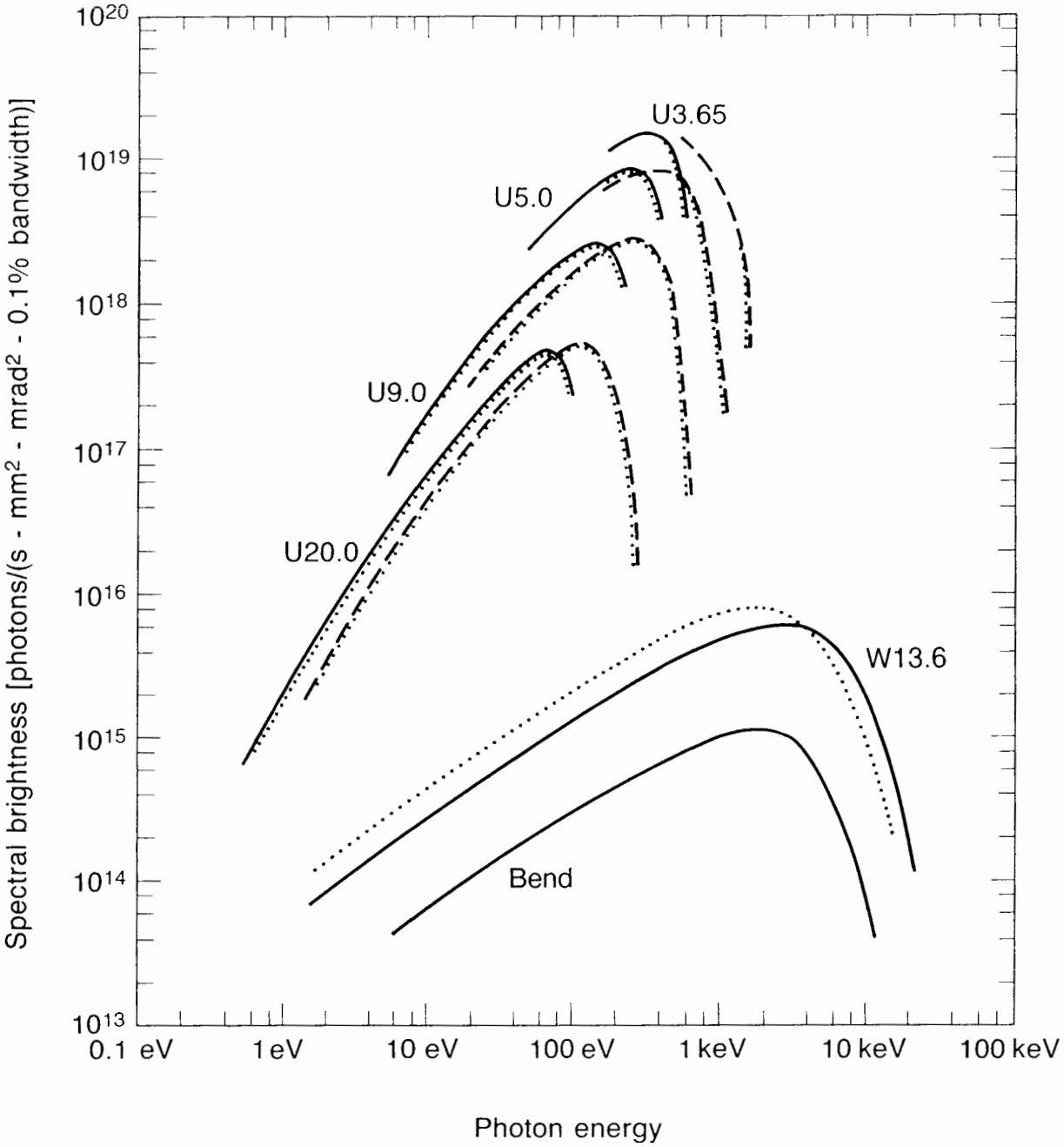


**Fig. 2-5.** Spectral brightness of radiation generated at the 1–2 GeV Synchrotron Radiation Source. This figure is discussed in detail in Section 5.1.

In the course of a reevaluation of possible lattices for the Light Source, several options were examined. In January 1986, a review was held at LBL to discuss lattice candidates for a 1–2 GeV Synchrotron Radiation Source [Krinsky et al., 1986]. The reviewing panel found three of the candidates "potentially equally interesting." These were the triple-bend achromat (TBA), the separated-function FODO, and the expanded Chasman-Green structures. The panel concluded that "a final decision on the lattice must be based on the

demonstrated flexibility of a set of parameters," namely, emittance, beta functions in the insertion regions, tunability, and sensitivity to field and alignment errors.

Since the January review, we have developed a deeper understanding of the characteristics of these three lattices [Jackson, 1986; Wrulich, 1986; Cornacchia et al., 1986], especially the flexibility of the TBA structure. Ultimately, the TBA lattice was chosen for the Light Source because of its capability for flexible operation and its high tolerance to magnetic imperfections and misalignments. This structure, incorporating three bending dipoles per achromat (thus its name), was first proposed by Vignola [1985] for a 6-GeV light source.

As optimized for the Light Source, the TBA lattice achieves a very small natural emittance ($4.1 \times 10^{-9}$ m-rad, rms value) with moderate focusing. Each of its 12 superperiods consists of a dispersive region, where the bending occurs, matched to a straight section, 6.75 meters long, reserved for undulators, wigglers, injection devices, radio-frequency cavities, and additional quadrupoles for insertion device matching. The straight sections are dispersion free, and the optics functions are optimized for photon-beam brightness. A detailed description of the storage ring and its ancillary equipment can be found in Section 3; the injection system for the Light Source is discussed in Section 4.

### 2.3.2 Insertion Devices and Beam Lines

The first insertion device routinely used for the production of synchrotron radiation was an electromagnetic wiggler implemented at SSRL in 1979. However, the capabilities of electromagnetic devices are limited because the magnetic period cannot be made small (owing to problems of coil cooling combined with the saturation properties of soft iron). A more versatile design, developed at LBL in 1979, uses permanent-magnet materials such as samarium-cobalt. The first undulator based on this innovation was one of thirty 6.1-cm periods, which was built at LBL in collaboration with SSRL and which began operation at SSRL in late 1980.

The design of permanent-magnet insertion devices was further refined in 1981 by the development at LBL of a hybrid structure [Halbach, 1983] that combines the magnetic properties of samarium-cobalt with the flux-concentrating properties of iron, thus achieving a higher magnetic field with less sensitivity to material properties. Figure 2-6 shows the design of a 27-period wiggler with a 7-cm period length, based on this concept and constructed at LBL. This wiggler began producing high-power synchrotron radiation for Beamline VI at SSRL in late 1983.

In the Light Source design, there are 12 straight sections, 11 of which are available for insertion devices. Four undulators and one wiggler are planned for initial machine operation. Their performance is shown in Figs. 2-4 and 2-5, which depict the large photon flux and high spectral brightness achievable with the Light Source, covering a photon spectrum from 0.5 eV to about 1 keV. Note especially the dramatic increase in photon flux of the wigglers, as compared with that achievable from the bending magnets.

Eleven beam ports will ultimately be served by undulators and wigglers, and an additional 48 could be served by bending magnets. Most of these can be subdivided into at least two branch lines.

Details on the initial complement of insertion devices and beam lines can be found in Section 5.

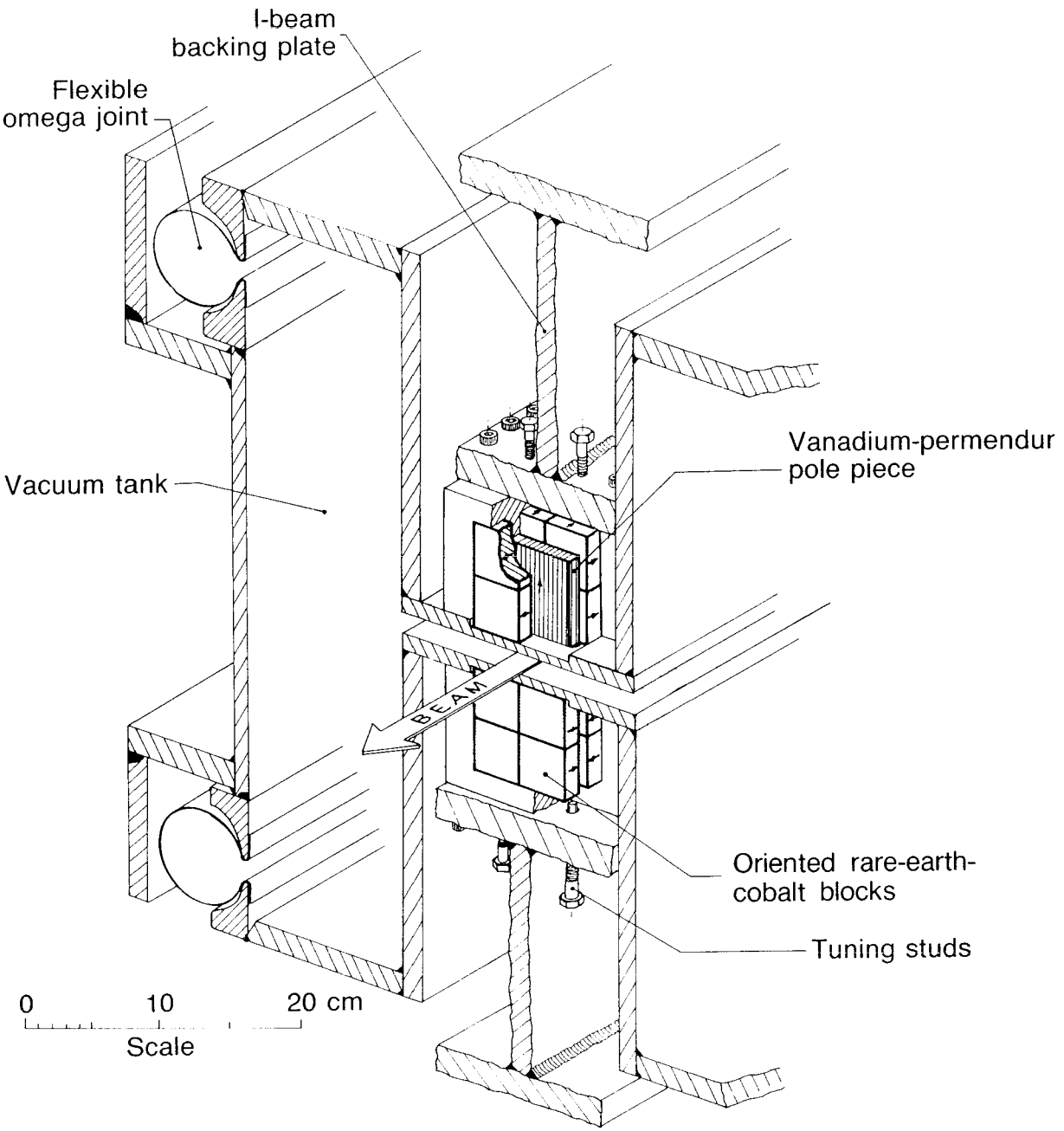


**Fig. 2-6.** Schematic of a 27-period permanent-magnet wiggler designed and built at LBL for Beamline VI at SSRL.

# 3. Storage Ring

In this section we describe in detail the storage ring that is the principal component of the 1–2 GeV Synchrotron Radiation Source. Its major parameters are summarized in Table 3-1, and a detailed parameter list can be found in Appendix A. Section 3.1 describes the operating modes and performance goals of the Light Source. In Section 3.2, we discuss the triple-bend achromat (TBA) lattice on which the storage ring design is based. This lattice was selected for the Light Source after detailed comparisons with other possible lattice designs, as discussed in Section 2.

The effects of collective instabilities (both coherent and incoherent) have been studied and are discussed in Section 3.3. These instabilities have adverse effects on the lifetime of the beam, the maximum electron intensity that can be stored, and the possibility of achieving very short bunches. Based on realistic assumptions regarding impedances and other relevant parameters, we conclude that the performance goals of the Light Source are achievable.

We have devoted particular attention in Section 3.3 to the issue of ion trapping by the potential well of the electrons. Although this phenomenon has caused problems in some storage rings, our studies indicate that the problem is manageable in our design. Because of the small electron-beam emittance, the electromagnetic field associated with the beam drives the ions out of the potential well of the electrons more effectively than is the case in existing storage rings. Moreover, a study of the stability of ions in the presence of the focusing field of the electrons has shown that introducing a controllable gap in the train of bunches helps in suppressing the ions. (The proposed injection system has the flexibility of filling the ring with any desired bunch pattern.)

The Light Source will be the first storage ring where wigglers and undulators occupy a sizable part of the circumference. Because the magnetic fields of wigglers and undulators contain intrinsic linear and nonlinear terms, we have undertaken theoretical and computational studies of the effects of these fields on the beam dynamics. Preliminary results, described in Section 3.3, indicate that the linear effects can be compensated and that the nonlinear perturbations caused by the proposed wigglers and undulators are acceptable and should not compromise the stability of the beam.

Finally, in the remainder of this section, we describe the designs of the various ancillary systems (magnets, power supplies, rf, controls, etc.) that are required for the storage ring.

**Table 3-1.** Summary of major storage ring parameters.[a]

| | |
|---|---|
| Nominal energy (GeV) | 1.5 |
| Maximum circulating current, multibunch (mA) | 400 |
| Number of stored electrons, multibunch | $1.64 \times 10^{12}$ |
| Maximum circulating current, single bunch (mA) | 7.6 |
| Number of stored electrons, single bunch | $3.12 \times 10^{10}$ |
| Natural emittance (m-rad) | $4.08 \times 10^{-9}$ |
| Natural energy spread, rms | $7.1 \times 10^{-4}$ |
| Energy spread, rms, at max. current | |
| Multibunch | $0.8 \times 10^{-3}$ |
| Single bunch | $1.48 \times 10^{-3}$ |
| Bunch length, rms, natural (mm) | 3.7 |
| Bunch length, ($2\sigma$), natural | 24 |
| Bunch length, ($2\sigma$), maximum current | |
| Multibunch (ps) | 28 |
| Single bunch (ps) | 47 |
| Peak energy (GeV) | 1.9 |
| Beam lifetime, half-life | |
| Gas scattering[b] (hr) | 30 |
| Touschek, maximum current | |
| Multibunch (hr) | 18.5 |
| Single bunch (hr) | 8.4 |
| Filling time | |
| Multibunch, to 400 mA (min) | 2.1 |
| Single bunch, to 7.6 mA per bunch (s) | 16 |
| Circumference (m) | 196.8 |
| Orbital period (ns) | 656.4 |
| Harmonic number | 328 |
| Radio frequency (MHz) | 499.654 |
| Peak effective rf voltage (MV) | 1.5 |
| Number of superperiods | 12 |
| Insertion straight section length (m) | 6.75 |
| Length available for insertion device (m) | 5.0 |
| Mean radius (m) | 31.32 |
| Bending field (T) | 1.248 |
| Bending radius (m) | 4.01 |
| Injection energy (GeV) | 1.5 |
| Injection field (T) | 1.248 |
| Number of dipoles per superperiod | 3 |
| Number of quadrupoles per superperiod | 6 |
| Betatron tunes | |
| Horizontal | 14.28 |
| Vertical | 8.18 |
| Synchrotron tune | 0.0082 |
| Natural chromaticities | |
| Horizontal | −24.1 |

| | |
|---|---|
| Vertical | −28.5 |
| Beta functions at insertion symmetry points | |
| Horizontal (m) | 11.0 |
| Vertical (m) | 4.0 |
| Beam size at insertion symmetry point, rms | |
| Horizontal ($\mu$m) | 201 |
| Vertical, 10% emittance ratio ($\mu$m) | 38 |
| Momentum compaction | $1.43 \times 10^{-3}$ |
| Damping times | |
| Horizontal (ms) | 13.1 |
| Vertical (ms) | 17.6 |
| Longitudinal (ms) | 10.7 |
| Number of sextupole families | 2 |

[a]All parameters at nominal energy unless otherwise noted.
[b]20-mm vertical gap, 1 nTorr $N_2$.

## 3.1 Operating Modes and Performance Goals

The major parameters of the Light Source can best be understood by comparing them with those of existing electron storage rings dedicated to synchrotron radiation production. This is done in Table 3-2. The most prominent feature of the present design is the provision of 11 straight sections for wigglers and undulators. As discussed in Section 2, these special devices provide greatly enhanced photon-beam performance, as compared with bending

**Table 3-2.** A comparison of Light Source parameters with those of Aladdin (University of Wisconsin), two rings at Brookhaven's National Synchrotron Light Source, and the SPEAR ring at the Stanford Synchrotron Radiation Laboratory.

| | Light Source | Aladdin | NSLS (VUV) | NSLS (XRAY) | SSRL (SPEAR) |
|---|---|---|---|---|---|
| Electron energy (GeV) | 1.5 | 1 | 0.75 | 2.5 | 3 |
| Electron current (mA) | 400 | 100[a] | 800[b] | 125[b] | 100[c] |
| Circumference (m) | 196.8 | 88 | 51 | 170 | 234 |
| Horizontal emittance ($10^{-8}$ m-rad) | 0.41 | 32 | 14.5 | 8 | 40 |
| Bunch length, $2\sigma$ (ps) | 28 | 850 | 400 | —[d] | 130 |

[a]For 15 bunches.
[b]For six bunches.
[c]For 16 bunches.
[d]Not available.

magnets; the required straight sections account for the relatively large circumference of the storage ring. The second noteworthy feature of the storage ring is the very small design value of the horizontal emittance of the electron beam. This emittance has been carefully minimized in our design to maximize the spectral brightness of the undulator photon beams. The use of high-performance wigglers and undulators permits the selection of modest values for the electron energy and electron current, while maintaining outstanding photon-beam performance.

To meet the needs of several categories of users, the Light Source design can accommodate various combinations of insertion-region optics and electron bunch structures. Short bunches are required by some users—in biology and medicine, chemical dynamics, materials and surface science, for instance—to permit short exposure times for dynamical studies. The Light Source can circulate bunches as short as 28 ps for such users. Both multibunch (250 bunches) and few- or single-bunch modes are possible. The projected average circulating beam current for 250 bunches is 400 mA. For those experiments requiring long dead times between successive pulses, the storage ring will be operated with a few electron bunches, at a lower average electron current of 7.6 mA per bunch.

During operation, high positional and angular stability of the beam at the undulator and wiggler positions are very important. As an example, a positional stability of the order of 10% of the horizontal beam size is a performance goal. Sophisticated instrumentation and feedback systems will guarantee this stability. Excellent reproducibility from fill to fill is also required.

The following sections embark on a detailed discussion of the storage-ring lattice and the accelerator physics issues encountered in its design. As an introduction, Appendix B defines a few elementary accelerator physics concepts.

## 3.2 Magnet Lattice

The performance of the Light Source is determined primarily by the design of the storage ring "lattice" (the periodic arrangement of the bending and focusing magnets in the ring). For this reason, a great deal of emphasis has been placed on selecting the proper lattice. The criteria we have stressed are:

- low horizontal emittance
- flexibility (in the sense of being easily tuned to other operating conditions)
- insensitivity to magnetic-field and/or magnet-misalignment errors.

As discussed in Section 2.3, and demonstrated in what follows, the Triple-Bend Achromat (TBA) structure meets all these criteria, and we have chosen it for the Light Source design.

### 3.2.1 Description

The storage ring lattice includes 12 dispersion-free straight sections, each 6.75 meters long, to accommodate insertion devices and machine utilities (injection elements and accelerating rf cavities). The insertion straights are connected by achromatic arcs, with matching between straights and arcs performed by quadrupole doublets. Figure 3-1 shows a schematic layout of one unit cell (i.e., one-twelfth) of the storage ring. The ring circumference is 196.8 meters. Jackson [1986] showed how the layout of the achromat is determined

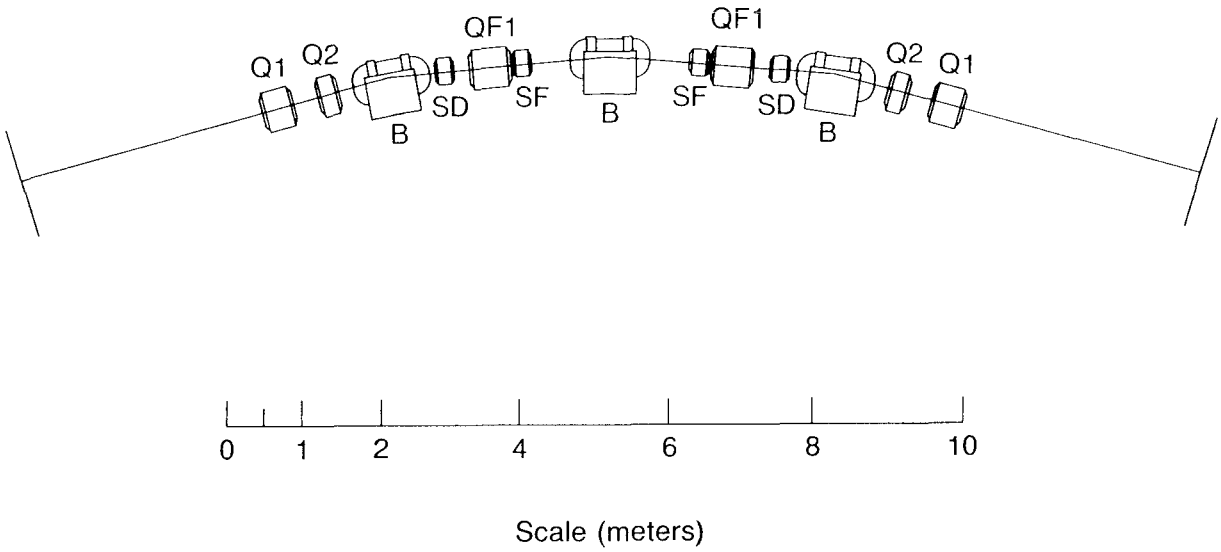


**Fig. 3-1.** One unit cell of the TBA structure.

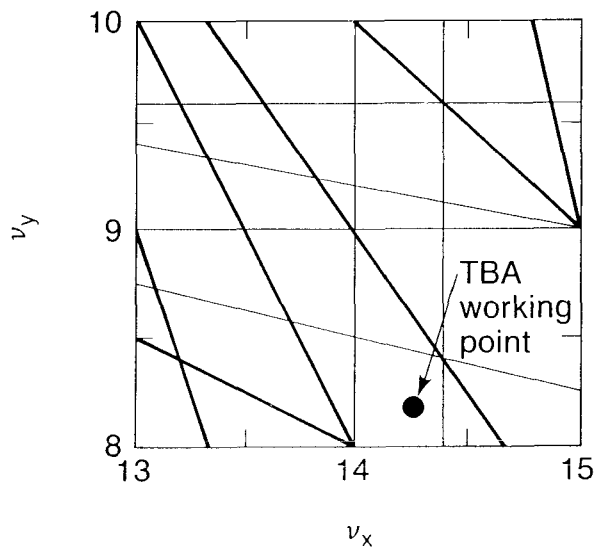


**Fig. 3-2.** Tune diagram, showing resonances of the type $n\nu_x + m\nu_y = 12p$, up to order six.

by the choice of the radial beta function in the insertion region and by the desired radial betatron tune. Here, we chose $\beta_x^* = 11.0$ meters, $\nu_x = 14.28$. In the vertical plane, the tune was chosen close to 8.0 to avoid systematic resonances of the type $2\nu_y + \nu_x = 12p$. The choice of $\nu_y = 8.18$ results in $\beta_y^* = 4.0$ meters and the working point shown in Fig. 3-2. The resulting structure has a natural emittance of $\epsilon_0 = 4.1 \times 10^{-9}$ m-rad and the lattice functions shown in Fig. 3-3.

A novel feature of the design, compared with existing triple-bend lattice structures [Einfeld and Mülhaupt, 1980; Rowe, 1981], is the use of combined dipole and quadrupole fields in the bending magnets. This feature is included primarily to keep the vertical beta func-

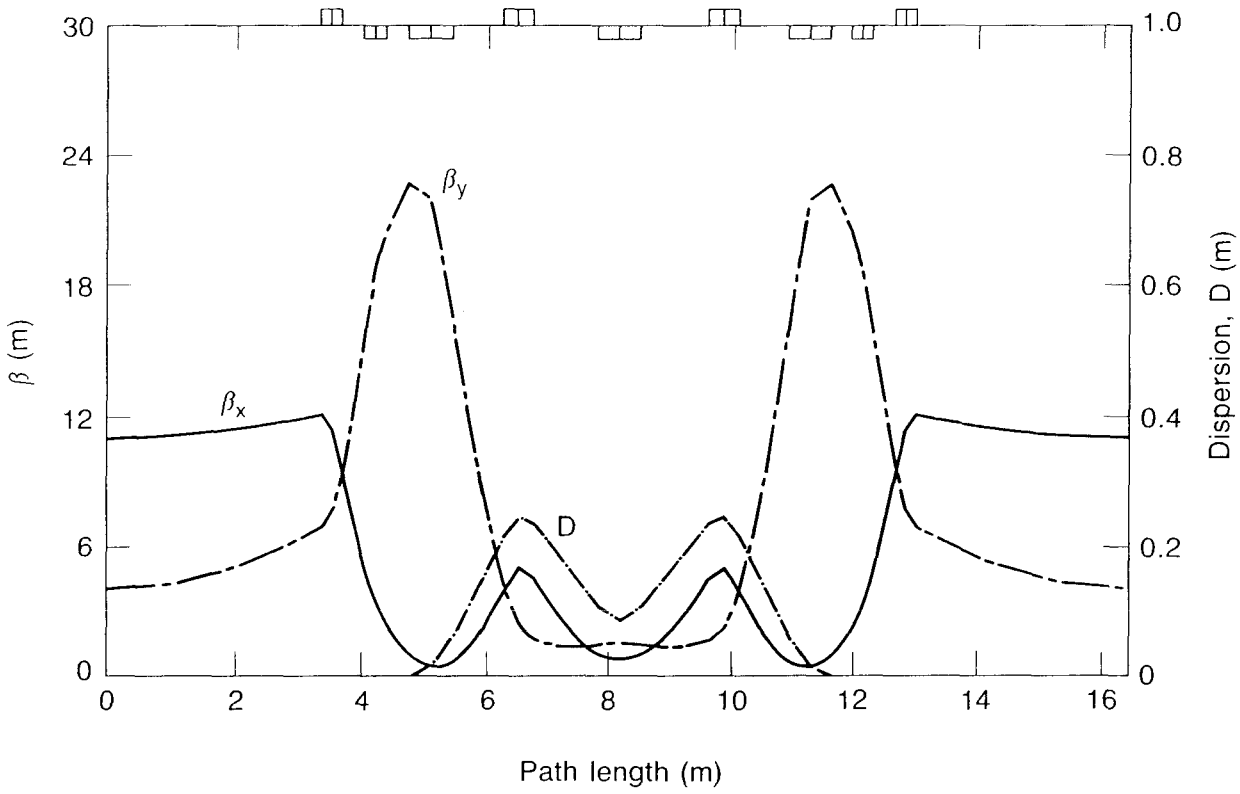


**Fig. 3-3.** Lattice functions through one unit cell of the TBA structure.

tion under control in the bending magnets, where the vertical beam size is greatest. However, it also has secondary benefits in that it changes the damping partition numbers in such a way as to reduce the emittance, and it produces beneficial separation of the beta functions in the region where the chromatic sextupoles are placed. Also, in contrast to the other lattices investigated for the January lattice review, it was found that chromatic correction with only two families of sextupoles (the minimum number) produced excellent dynamic behavior in the TBA structure (see Section 3.2.3, below).

Magnet multipole errors and misalignments result in closed-orbit distortions in both transverse planes (which must be corrected), vertical dispersion, and a degradation of the dynamic aperture. An analysis of the effects of magnets built to standard tolerances and aligned using conventional techniques is discussed in Section 3.3.1.

### 3.2.2 Tunability

Since quadrupole QF1 is used to match the dispersion in the arcs, the only quadrupoles available for tuning the lattice are Q1 and Q2 in the insertion region. Because there are only two tuning variables, we can independently adjust only two parameters, e.g., $\nu_x$ and $\nu_y$; all associated parameters, $\beta_x$, $\beta_y$, and the emittance, are then dependent parameters. As noted above, the nominal tunes for the lattice are $\nu_x/\nu_y$ = 14.28/8.18, with beta values at the symmetry point in the insertion region of $\beta_x^*/\beta_y^*$ = 11.0 meters/4.0 meters and a natural emittance of $\epsilon_0 = 4.1 \times 10^{-9}$ m-rad. The nominal tune of the lattice has been carefully

chosen to be as far as possible from systematic third-order resonances, thus the tuning range of interest is $14.0 < \nu_x < 14.5$ and $8.0 < \nu_y < 8.5$. The lattice is actually tunable over a significantly wider range, and within these limits, the changes to the dependent parameters are small. For example, over the whole of the half-integer tune square, the emittance changes by only 4%. In changing the radial tune from 14.0 to 14.5, $\beta_x$ varies from 13.0 to 10.0 meters, and in the vertical plane $\beta_y$ only ranges from 3.5 to 4.5 meters over the tune square. We expect changes of this magnitude to have no significant impact on machine tuning.

### 3.2.3 Chromaticity Correction and Dynamic Aperture

Chromaticity, defined as $\xi_{x,y} = d\nu_{x,y}/(dp/p)$, is the tune shift experienced by an electron with momentum deviation $dp/p$. To combat an effect known as the head-tail instability, $\xi_{x,y}$ must be adjusted to be zero, or slightly positive, from their naturally negative values. This is normally achieved with sextupole magnets placed in regions of the lattice where the dispersion is finite, i.e., in the achromatic arcs. Chromatic correction in the TBA structure is carried out with just two families of sextupoles, SF and SD, the minimum number that allows compensation in both transverse planes. These sextupoles are situated in the achromatic arcs, as shown in Fig. 3-1.

The difficulty associated with inserting these nonlinear elements in the lattice is that they induce nonlinear motion into the electron trajectories, resulting in amplitude-dependent tune variations and, ultimately, unstable motion at an oscillation amplitude that defines the dynamic aperture. The dynamic aperture is determined by tracking test electron trajectories through a computer model of the magnet lattice and observing whether or not the motion is bounded. In electron machines, it is customary to track for a period corresponding approximately to the synchrotron radiation damping time, which for this machine is about 23,000 turns. Such an approach would be extremely expensive (in terms of computer time) and time consuming. For the lattice considered here, we found that tracking for 400 turns produced only a 0.5-mm overestimate of the dynamic aperture, as compared with tracking for 23,000 turns.

Figure 3-4 shows the radial phase-space trajectories of two electrons, one with an amplitude well within the dynamic aperture and a second near the limit of the dynamic aperture. The distortion of the trajectories from their linear elliptical shape, caused by the sextupole fields, is clear. The dynamic aperture of the machine, shown in Fig. 3-5, was used to specify the beam-stay-clear region and, in turn, the magnet apertures. In Section 3.3.1, we show that the dynamic aperture is reduced by other nonlinear effects in the storage ring, namely, those arising from unwanted residual magnet multipole components and misalignments.

In analyzing the expected performance of the storage ring, there are two other parameters that are useful: the amplitude-dependent betatron tune shift and the momentum-dependent tune shift, shown in Figs. 3-6 and 3-7, respectively. Cornacchia et al. [1986] have shown that, in terms of these functions, the TBA lattice compares favorably with the other candidate lattices for the Light Source.

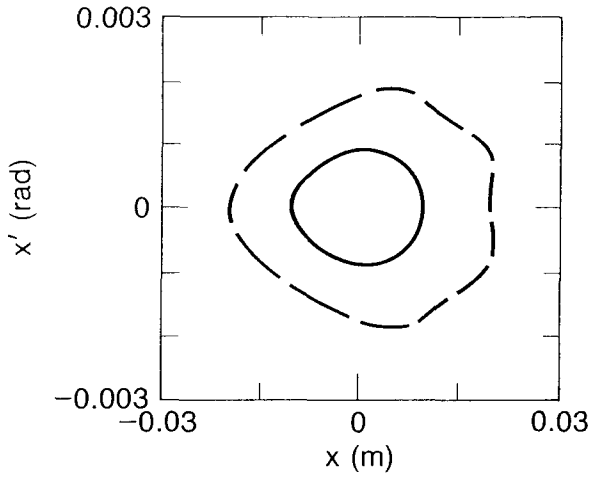


**Fig. 3-4.** Radial phase-space trajectories of electrons with amplitudes well within the stability limit (solid line) and close to the stability limit (dashed line).

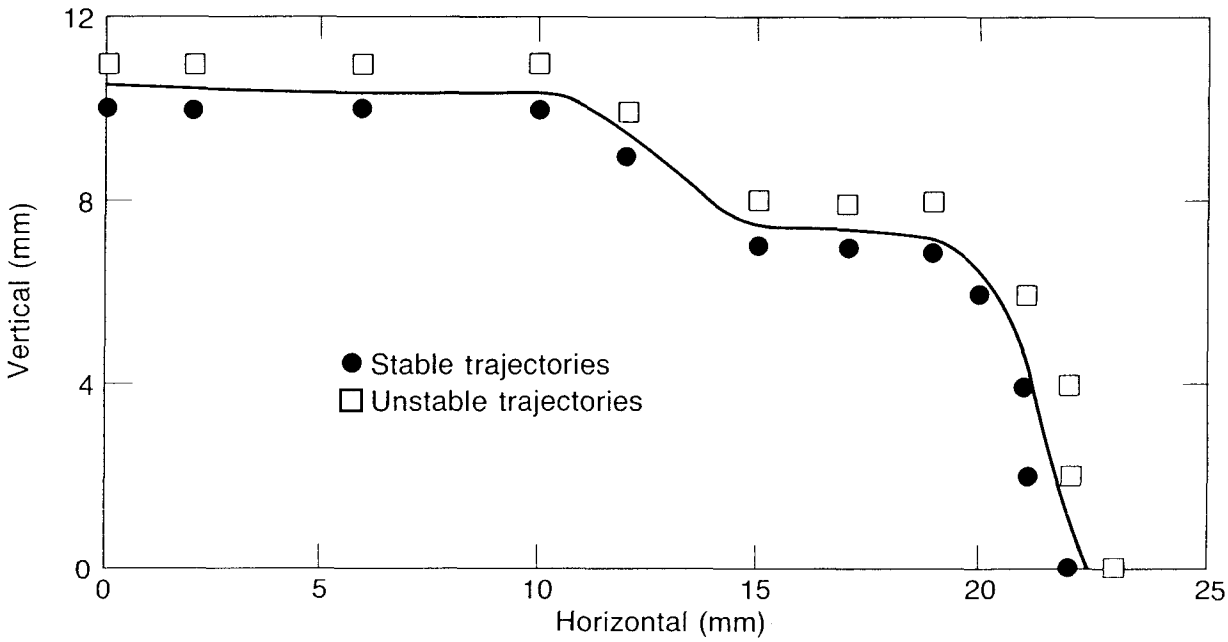


**Fig. 3-5.** Dynamic aperture of the TBA structure.

### 3.2.4 Injection and Accumulation

Accumulation of electrons in the storage ring is by the well-proven technique of stacking in radial phase space, injection taking place in a long straight section from inside the circumference of the machine.

Prior to injection, the storage ring closed orbit is deflected close to the end of the injection septum by four bump magnets, as shown schematically in Fig. 3-8. (The magnets are powered in series and are capable of displacing the orbit by up to 15 mm.) A pulse of electrons is then ejected from the booster synchrotron and transported through the injection septa into the storage ring. The injection septa produce deflections of 8.0° (thick) and 2.5°

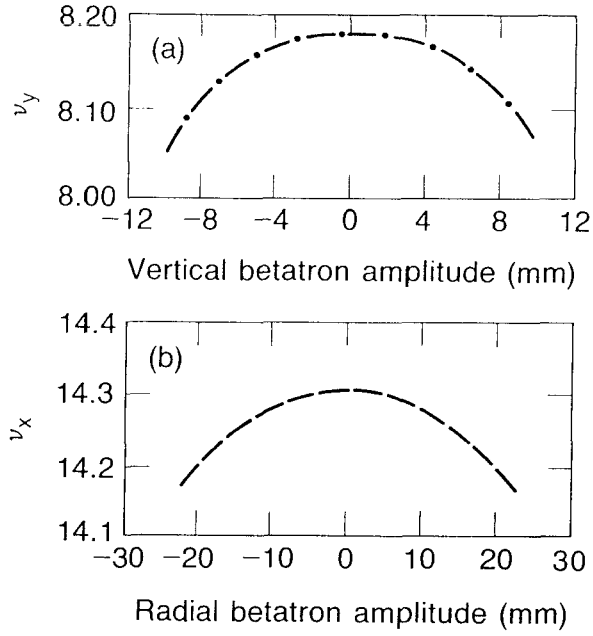


**Fig. 3-6.** Betatron-amplitude-dependent tune shifts: (a) vertical and (b) radial.

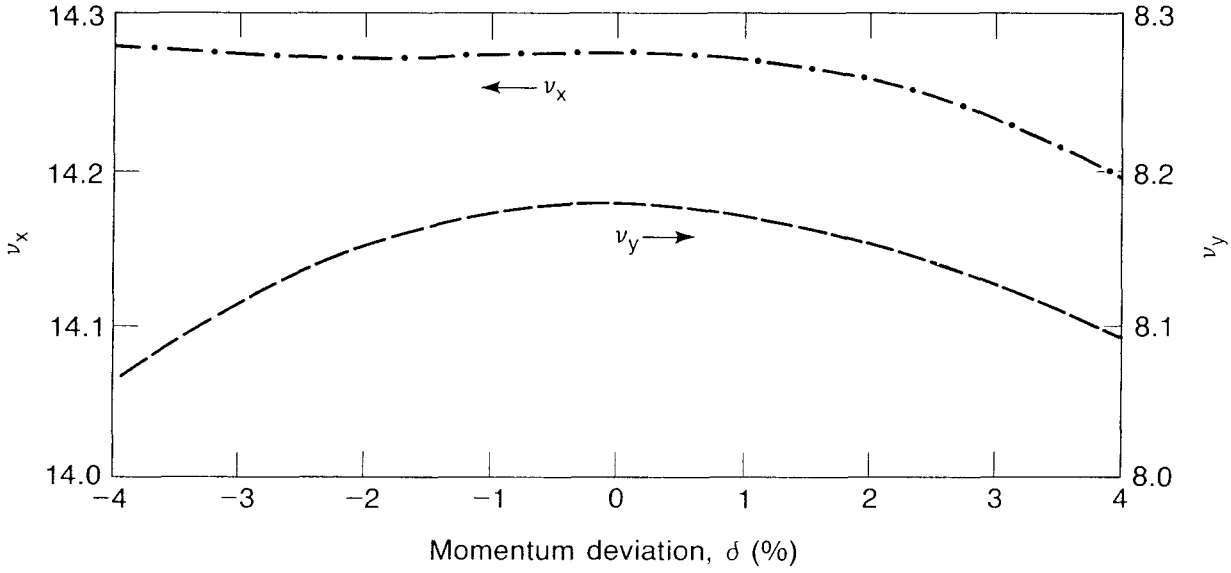


**Fig. 3-7.** Momentum-dependent tune shifts.

(thin). The radial position of the thin injection septum is adjustable in order to produce the best match to the dynamic aperture. Figure 3-9 shows the juxtaposition of the closed orbit and the injected beam, in radial phase space, at the end of the septum magnet. It can be seen that the injected beam fits well within the acceptance of the ring. (In the vertical plane the beam is matched to the acceptance.) The bump magnets are then turned off in a time corresponding to about three orbits of the ring to prevent the new beam from colliding with the septum (see Fig. 3-10). The newly injected beam then undergoes coherent betatron motion about the closed orbit—motion that is rapidly damped by means of synchrotron

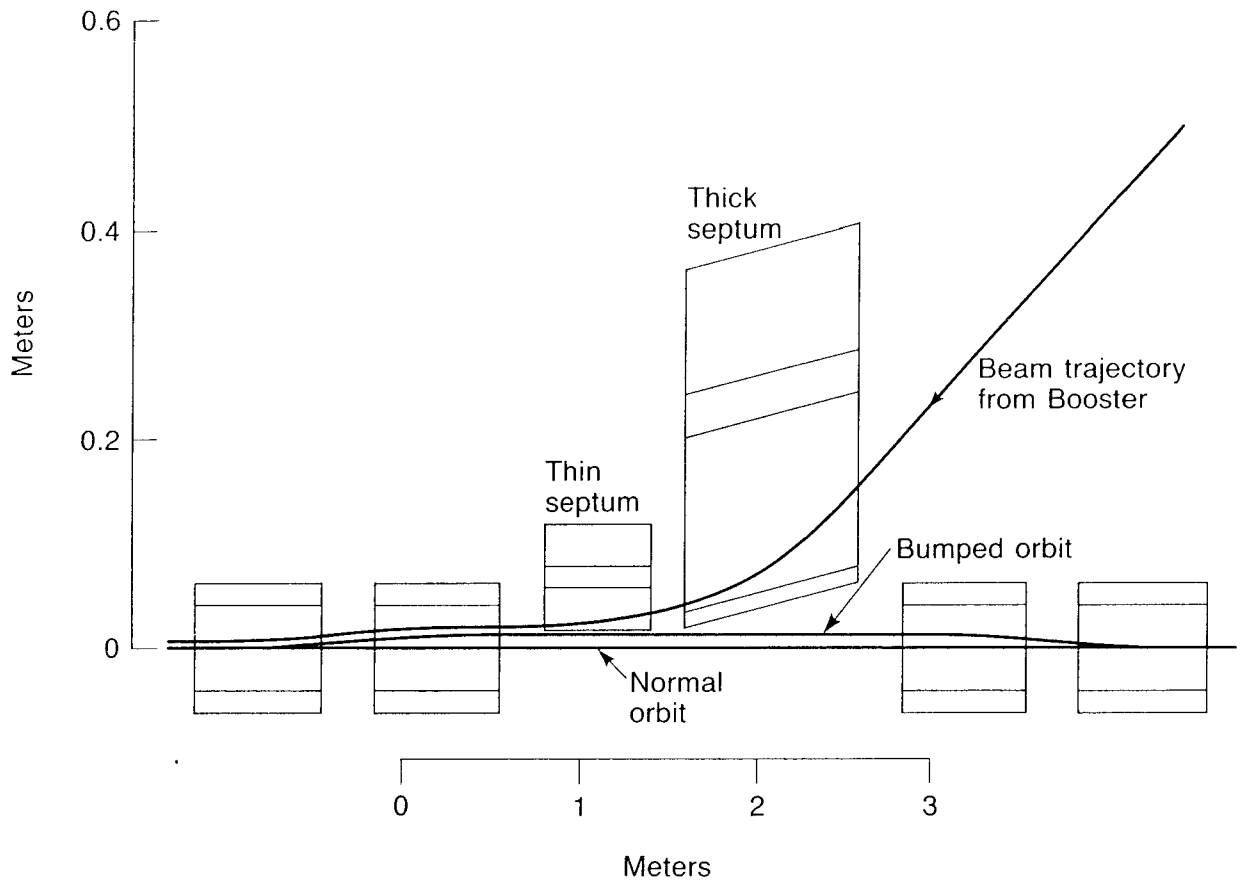


**Fig. 3-8.** Anamorphic diagram of the storage-ring injection process.

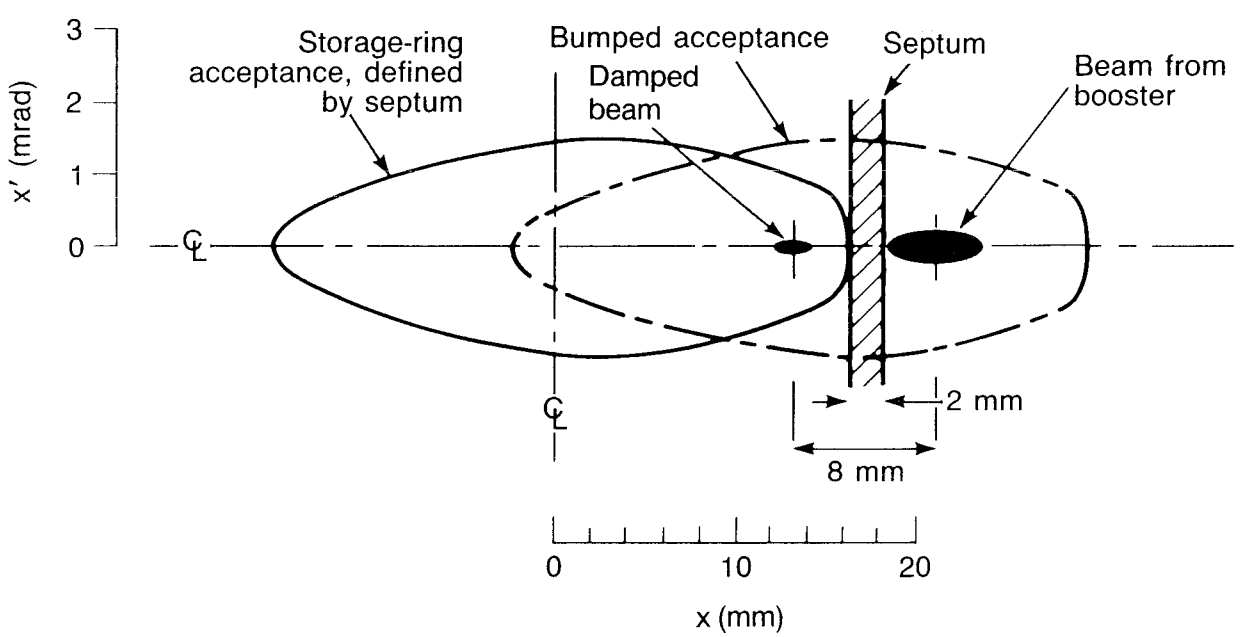


**Fig. 3-9.** Normal storage-ring acceptance, bumped acceptance, and the injected beam, in radial phase space, at the end of the septum magnet. The center lines shown are for the vacuum vessel.

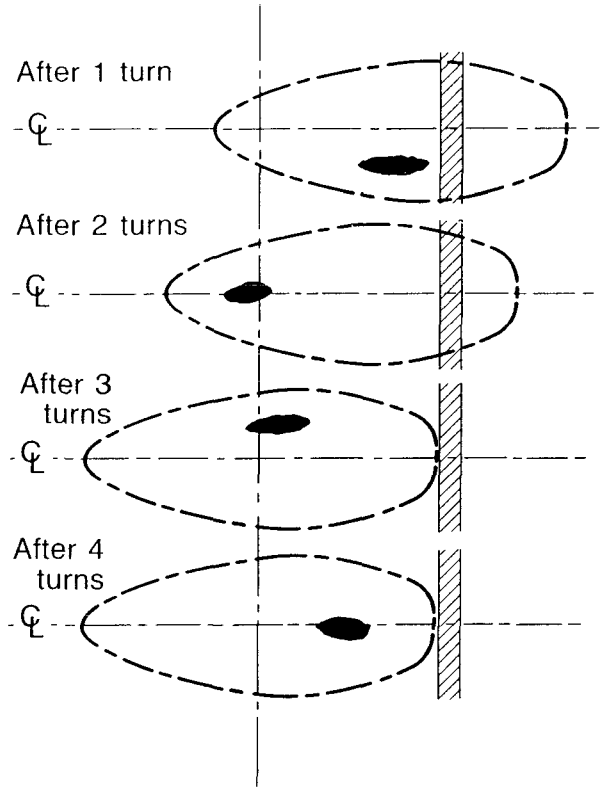


**Fig. 3-10.** Evolution of the bumped acceptance and the injected beam, in radial phase space.

**Table 3-3.** Parameter summary for storage-ring injection magnets.

| | Length (m) | Bend angle (deg) | Maximum field (T) | Rise/Fall time | Amplitude stability (%) | Trigger jitter (ns) |
|---|---|---|---|---|---|---|
| Thick injection septum | 1.0 | 8 | 0.698 | half sine 100 $\mu$s | 0.1 | $\pm 100$ |
| Thin injection septum | 0.6 | 2.5 | 0.364 | half sine 20 $\mu$s | 0.2 | $\pm 100$ |
| Bump magnets | 0.7 | 0.86 | 0.104 | half sine 4 $\mu$s | 0.5 | $\pm$ 20 |

radiation damping. (The radial betatron damping time is 13.0 ms.) This process is repeated at the cycle rate of the booster (1 Hz) until the desired beam current is reached.

The bump magnets and injection septa are described in Section 3.4; major parameters are summarized in Table 3-3.

## 3.3 Accelerator Physics Issues

### 3.3.1 Magnetic Imperfections and Misalignments

An analysis of the effects of magnet multipole errors (systematic and random) and of magnet misalignments is currently under way. We present here the philosophy of our analysis and the results we have obtained to date.

To separate the impact of the different "magnet errors," we analyze each separately, then lump all errors together. First, we look at the effects of multipole errors on an otherwise unperturbed machine. In this case, the closed orbit passes through the center of each element, and the predominant effect is a reduction of the dynamic aperture. (There are also small changes in the amplitude-dependent tune shifts and a small amount of coupling introduced between betatron motion in the two transverse planes.) Next, we investigate the effects of magnet misalignments on the unperturbed machine. These errors produce a closed-orbit distortion that must be corrected; however, even after correction, a residual distortion remains that causes the closed orbit to pass off-center through the lattice magnets. This residual orbit error gives rise to a random quadrupole component when the electrons pass through the sextupole magnets. This could lead to a reduction in dynamic aperture. As mentioned, associated with the residual orbit distortion are the introduction of vertical dispersion and a coupling of betatron motion between the transverse planes. The result is a vertical equilibrium beam size significantly larger than its "natural" damped value.

In the final simulation, we include all these effects: random and systematic magnet multipole errors, random magnet misplacements, and errors in orbit correction (including random misalignments of position monitors and uncertainty in the setting accuracy of the correctors).

**3.3.1.1 Magnet Multipole Errors.** Multipole components in iron-dominated magnets arise because the poles have finite dimensions to accommodate the excitation windings and are constructed using finite tolerances. The first constraint leads to systematic multipole components (the same in all magnets of the same type), the second to both normal and skew components with random amplitudes.

In tracking codes, the multipole components are incorporated using a field expansion, such as

$$B_y(x,\phi) = B\rho \sum_n \frac{k_n x^n}{n!} \cos[(n+1)\phi + \delta],$$

where $k_n$ is the multipole amplitude, $\phi$ is the angle about the beam axis, and $\delta$ is a measure of the skew with respect to the normal orientation. In practice, field-quality data on existing dipole magnets (PEP, SPS, etc.) are given in the form of a field error $\Delta B/B$ at a given distance from the axis, from which the expansion above is deduced. In the case of quadrupole magnets, the data from existing machines are much clearer, since these are often measured using a rotating coil device that gives the multipole components and their relative orientations directly.

In our case, the data used for input to the simulation code were extrapolated from information from PEP (Stanford), SPS and LEP (CERN), and SRS (Daresbury). The details are given in Appendix C. Briefly, we took data from existing magnets and scaled the multipole components according to magnet aperture, while maintaining standard mechanical tolerances on the magnet pole profiles and on assembly. All values used in the simulation are conservative when compared with those for existing magnets. Table 3-4 shows the input values used for the simulation code.

The results of tracking simulations are shown in Fig. 3-11, where we present the dynamic aperture in the presence of these multipole errors. For comparison, we also show the aperture determined by the sextupole nonlinearities only, as described above. It is seen that the main effect of the errors is felt in the radial plane, where the aperture is reduced from 22 mm to between 16 and 20 mm. This variation reflects the different distributions of "random" multipole components in the simulations.

It is possible to test the sensitivity of the dynamic aperture to a particular multipole component (say, the random octupole field in the quadrupole magnets) simply by switching that component off. In this way, we are able to determine that the single most harmful component listed in Table 3-4 is the random gradient error in the dipole magnet. By reducing this error from $10^{-3}$ to $10^{-4}$ (an achievable, though difficult, goal), the radial region of dynamic aperture variation contracts to between 18 and 20 mm. However, it is not clear whether such action is necessary, since a radial aperture of 16 mm is quite sufficient both for injection and for an acceptable beam lifetime.

**3.3.1.2 Closed-Orbit Distortions and Corrections.** Closed-orbit distortions are generated mainly by quadrupole displacement errors, dipole field errors, and errors in the rotation angle of dipole magnets. An analysis of orbit distortions produced by such errors, and their correction using the bump method, has been carried out.

In estimating the closed-orbit distortion, we have taken alignment tolerances and field errors which are typical of operating accelerators, namely, quadrupole displacement errors of 0.15 mm (rms), dipole field errors ($\Delta B/B$) of $1 \times 10^{-3}$ (rms), and magnet rotation errors of 0.5 mrad (rms).

Orbit distortions have been simulated by using the computer code RACETRACK to generate an ensemble of 20 storage ring models, each with a different set of random errors. We then calculated the closed orbit, and "measured" its amplitude at 96 monitor stations, whose positions around the machine are shown in Fig. 3-12. Distributions of the rms values of the orbit distortions, as measured at the monitoring stations, are shown in Fig. 3-13. The larger values in the vertical plane reflect the facts that, compared with the corresponding horizontal values, the vertical beta values are larger and the vertical tune is closer to an integer.

The storage ring has 48 orbit-correction dipole modules, each of which contains one vertical and one horizontal dipole. In addition, there are dipole windings in sextupoles, such that there are a total of 96 correctors in the horizontal plane and 72 correctors in the vertical plane. Some of these correctors will be reserved for fine-tuning the orbit at the insertion devices, leaving 72 horizontal and 48 vertical correctors to be used for general orbit correction purposes. These latter correctors are arranged around the circumference as shown in Fig. 3-12. In the bump method, three consecutive corrector elements, with a

**Table 3-4.** Input parameters, and their values, for multipole error simulations.

$$B(x) = B\rho \sum_n \frac{k_n x^n}{n!}$$

| | $k_1\ell$ | $k_2\ell$ | $k_3\ell$ | $k_4\ell$ | $k_5\ell$ | $k_9\ell$ |
|---|---|---|---|---|---|---|
| **Systematic** | | | | | | |
| Dipoles | 0.0 | 0.05 | 0.0 | 1000.0[a] | 0.0 | 0.0 |
| Quadrupoles | 0.0 | 0.0 | 0.0 | 0.0 | $1.5 \times 10^5$ | $1.5 \times 10^{12}$ |
| **Random/normal**[b] | | | | | | |
| Dipoles | $0.7 \times 10^{-3}$ | 0.1 | 15.0 | 100.0 | 0.0 | 0.0 |
| Quadrupoles | $10^{-3}$ | 0.1[c] | 15.0 | 300.0 | $3 \times 10^4$ | $5 \times 10^{11}$ |

**Skew**
Quadrupoles: rotated about axis with rms skew = 0.5 mrad
Sextupoles: rotated about axis with rms skew = 1.0 mrad

[a]Estimated from radial field profile of Daresbury dipoles
[b]Assumed Gaussian distribution, truncated at $2\sigma$; values are for $1\sigma$.
[c]Random component from sextupoles included.

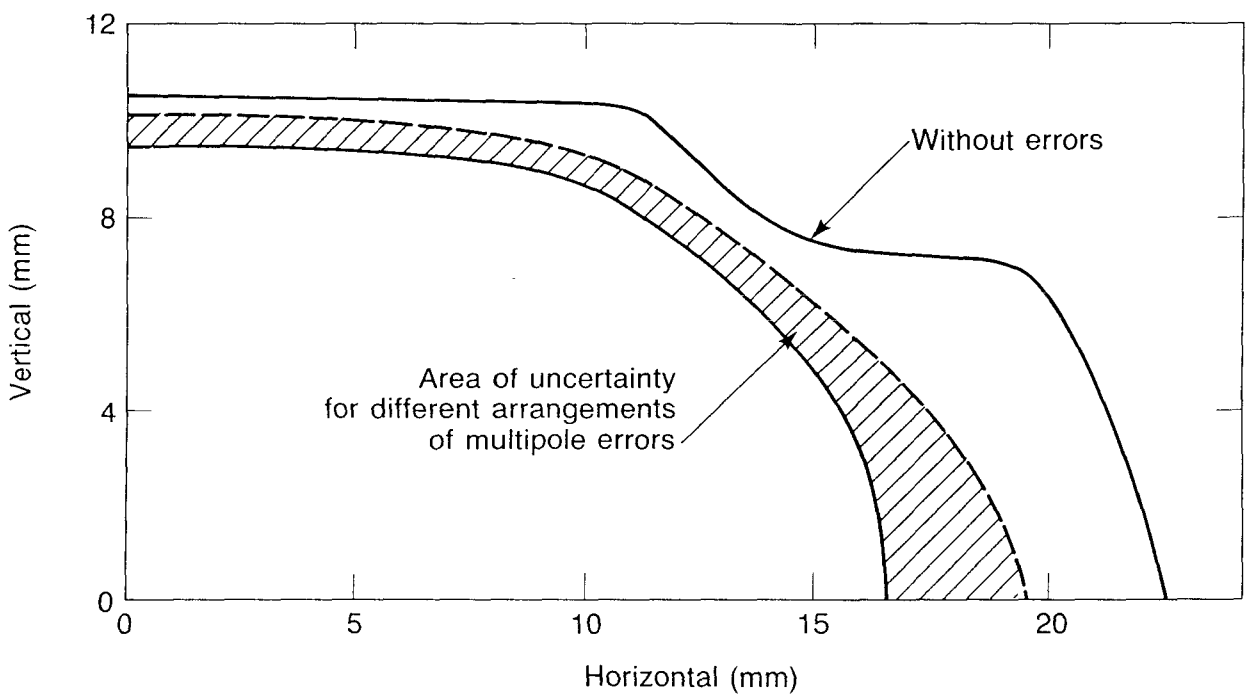


**Fig. 3-11.** Dynamic aperture in the presence of multipole errors.

favorable phase relationship, are chosen and adjusted to minimize the rms distortion locally within the bump. Each corrector is limited in strength according to the hardware specification to 2 mrad. Bumps are created around the circumference and the calculation iterated until a convergence in the residual distortion is achieved. The distribution of the rms orbit distortions after correction is shown in Fig. 3-14. Figure 3-15 shows, for one set of errors, the orbit distortion before and after correction.

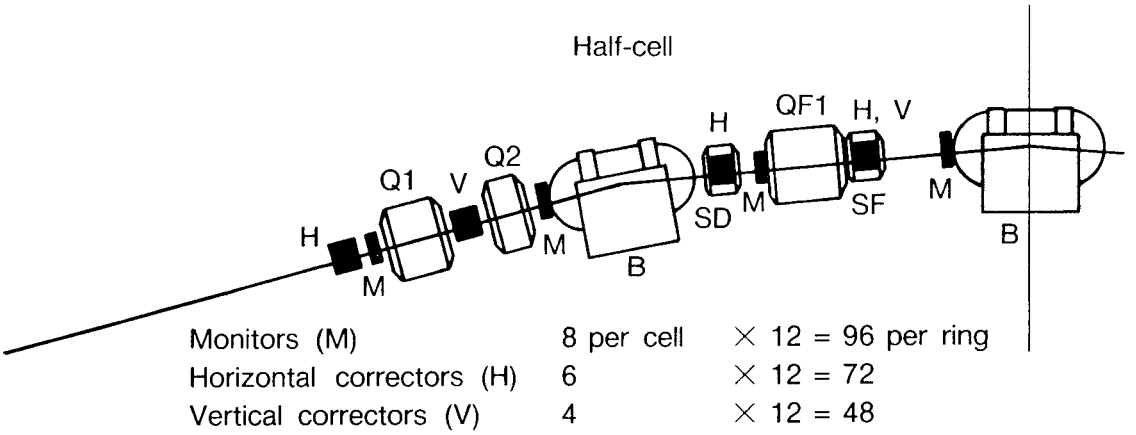


**Fig. 3-12.** Schematic of the storage-ring half-cell, showing the positions of monitors and correctors.

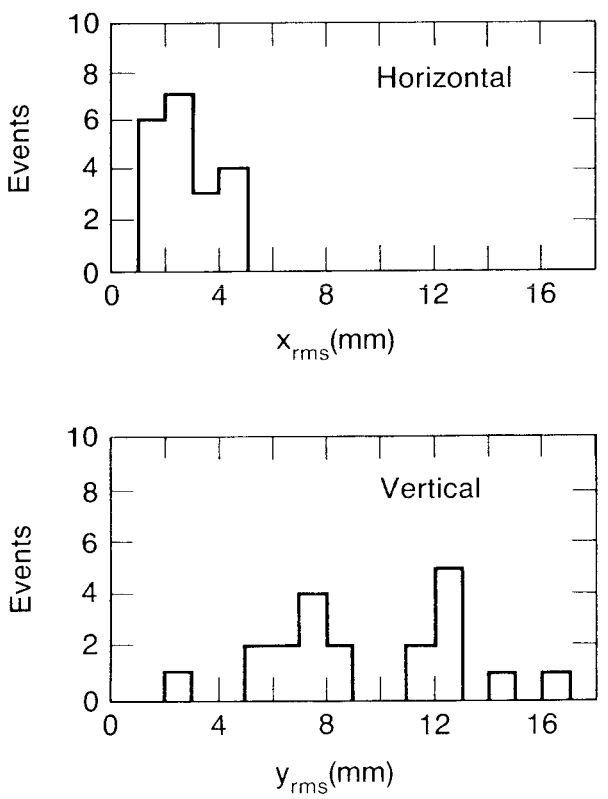


**Fig. 3-13.** Calculated rms orbit distortions produced by 20 sets of random errors, before correction.

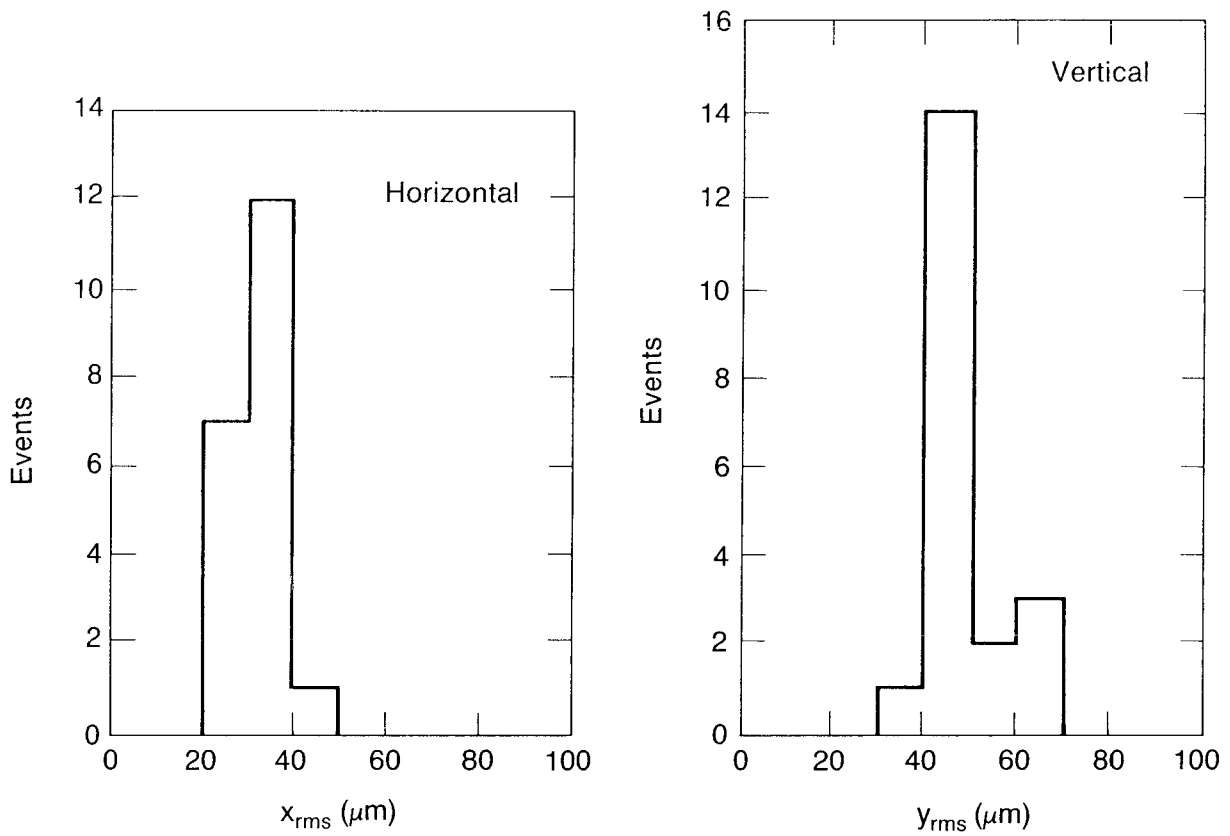


**Fig. 3-14.** Calculated rms orbit distortions produced by 20 sets of random errors, after correction.

If displacement errors are introduced into the transverse positions of the monitors, the effectiveness of the correction procedure decreases, and the residual distortion is larger. The corrected orbit, under the assumption of a 0.15-mm rms monitor displacement error, is also shown in Fig. 3-15.

The residual dispersion introduced by magnet errors, although very large before correction, is reduced to less than 5 mm (horizontal and vertical) at the insertion symmetry point after orbit correction. Since the rms momentum spread in the beam is of the order of $10^{-3}$, the resulting increase in beam size is only about 5 $\mu$m. This is negligible when compared with the natural rms beam size of 202 $\mu$m horizontal $\times$ 38 $\mu$m vertical (assuming a 10% vertical-horizontal emittance ratio).

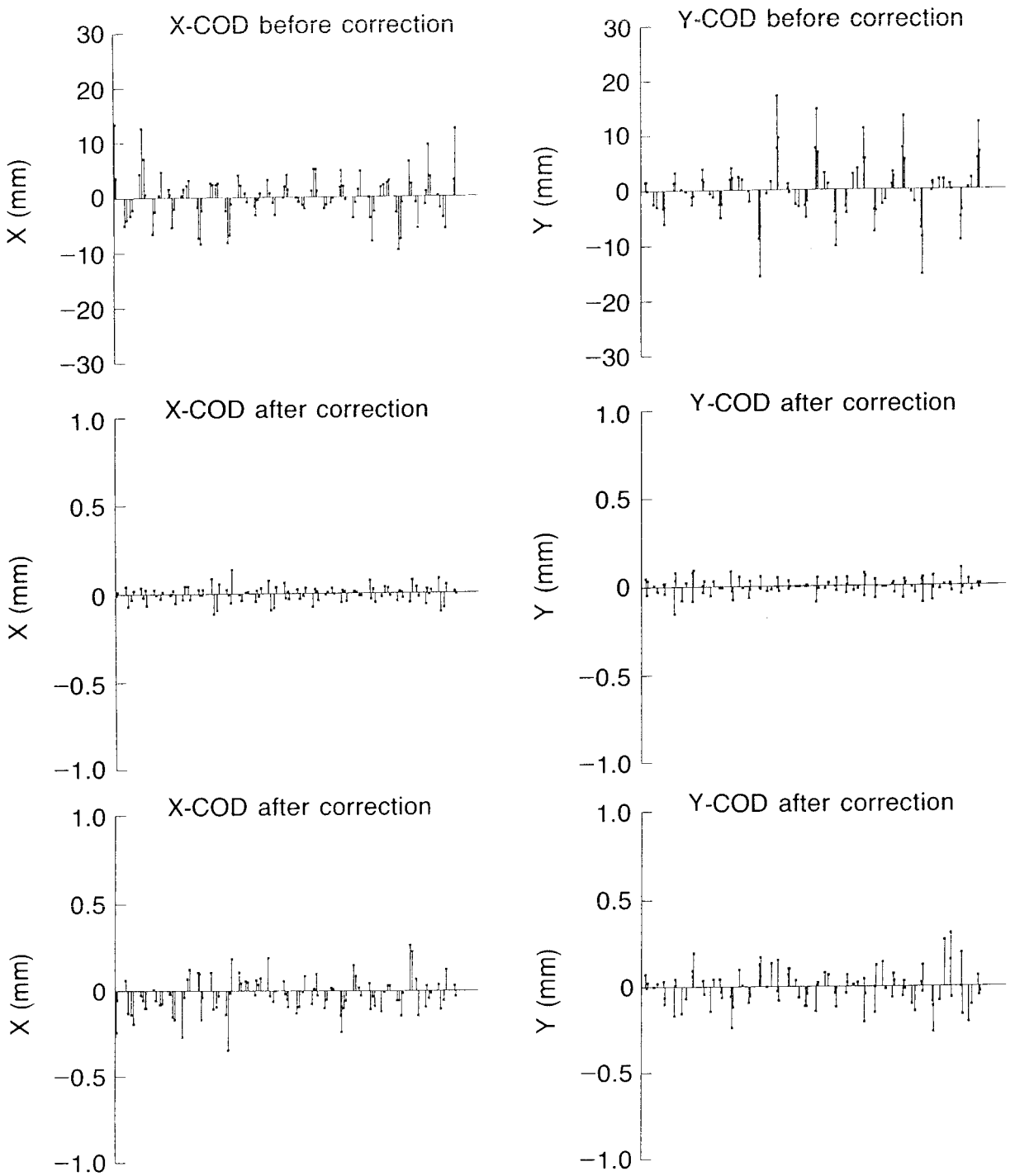


**Fig. 3-15.** Orbit distortions at 96 locations for one set of errors before correction (top), after correction (middle), and after correction but assuming random monitor displacements (bottom).

### 3.3.2 Collective Effects and Beam Lifetime

The beam specifications for the LBL 1–2 GeV Synchrotron Radiation Source, based on user requirements [*Report of the Workshop,* 1985], are summarized in Table 2-1. In this section, we examine the lattice that was selected to meet these requirements in terms of collective effects that can influence machine performance. Before describing our findings, however, we discuss, in Section 3.3.2.1, the various coupling impedances that drive these instabilities. In Section 3.3.2.2, we deal with the issue of bunch length; the expected bunch length obtainable from the lattice is calculated under several assumptions. Next, in Section 3.3.2.3, we look at the effects of coupled-bunch instabilities. Calculations of coupled-bunch growth rates are then used to specify the requirements for the longitudinal and transverse feedback systems described in Section 3.9. An estimate of possible growth in beam emittance due to intrabeam scattering is made in Section 3.3.2.4. Although this phenomenon is generally expected to be unimportant at high energies, the dense beam bunches specified for the Light Source make it necessary to confirm this expectation for the particular lattice under consideration. Finally, in Section 3.3.2.5 we deal with beam lifetime, taking into account the combined effects of Touschek and gas scattering.

All of the calculations reported here were performed with the LBL accelerator physics code ZAP [Zisman et al., 1986].

**3.3.2.1 Beam–Storage-Ring Coupling Impedances.** Many elements in the Light Source storage ring contribute to the longitudinal and transverse beam-coupling impedances, which are potentially capable of driving various single-bunch and multibunch coherent instabilities. The impedances fall into two distinct categories: the long-wake-field, high-$Q$, narrow-band impedances, which induce coupled-bunch modes, and the short-wake-field, low-$Q$, broadband impedances, which induce coherence and instability within a single bunch.

The narrow-band, high-$Q$ impedances arise primarily from the rf cavities, through their higher-order parasitic longitudinal and transverse modes. The shunt impedances, resonant frequencies, and quality factors for the higher electromagnetic modes of the 500-MHz cavity are taken from experimental observations and calculations for the similar KEK rf cavity with undamped modes [Yamazaki et al., 1981].

The broadband, low-$Q$ impedance arises from the vacuum chamber itself, together with other elements, such as diagnostic instruments, bellows, etc., and the equivalent broadband impedance arising from the many rf cavity modes spanning a wide frequency range. The rf-equivalent broadband impedance is taken to be 0.25 Ω per rf cell, as obtained from the higher-order modes of our reference rf design (taken from the KEK cavity). A detailed impedance inventory has not yet been performed; however, based on preliminary laboratory measurements of the prototype Light Source vacuum chamber, we expect the broadband impedance contributed by the vacuum chamber itself to be much smaller than $(Z_{\parallel}/n) \simeq 2\ \Omega$.

For the Light Source storage ring, we chose a beam-tube cross section with an antechamber because of vacuum considerations (see Section 3.5). There are pumps, photon stops, and ports in the antechamber, together with interruptions at the two rf stations, but otherwise the beam tube is largely continuous and smooth, with gentle transitions at the insertion devices. The structure can thus be visualized as a smooth cylinder with partial

reflections at rf sections, etc. Accordingly, measurements using both wire and antenna methods were carried out on sections of the chamber, with and without the antechamber. To validate our methods, we compared experimental results with results of a numerical simulation for a stepped-radius pipe.

The wire results can be accepted with a reasonable level of confidence at low frequencies (i.e., below the cutoff of the beam tube), the uncertainty limits being

$$\left.\begin{aligned} \Delta Z_{\parallel} &\simeq 0.1\ \Omega \\ (\Delta Z_{\parallel}/n) &\simeq 10^{-4}\ \Omega \text{ at } 2 \text{ GHz} \end{aligned}\right\} \text{ up to } 4.5 \text{ GHz}$$

$$\Delta Z_{\perp} \simeq 2000\ \Omega/\text{m} \qquad \text{up to } 2.4 \text{ GHz}$$

for the longitudinal and transverse cases, respectively. Wire results show no effect from the antechamber. Resonances below cutoff should appear directly in the wire measurements. If high-frequency impedances are present, they should also show up as reactive components at low frequency.

Impedance measurements above cutoff are less direct and were done by measuring a section of the chamber with closed ends, using an antenna. This corresponds to the extreme case of total reflection. This closed-tube case shows $Z_{\parallel} \simeq 0.1\ \Omega$.

In conclusion our studies indicate that

- The narrow slot effectively hides from the beam any antechamber responses below 10 GHz.
- The antechamber contributes only above the TE cutoff for the slot; there the waves propagate freely in the beam tube.
- Not only are responses above 10 GHz weak in the beam tube, but they also contribute negligibly to impedances because of propagation along the beam tube.
- Impedances important to the beam are determined by structures and variations on the beam tube side and, at high frequency, by coherent synchrotron radiation and the curvature effect ("free space" impedance).

With the narrow-gap insertion devices envisaged for the Light Source, there may be cavitylike resonances of the whole beam-tube volume, bounded by the narrow restrictions imposed by the undulator gap. For undulators with 2-cm gaps, microwaves at frequencies above 8 GHz will propagate through the aperture. However, between 4.5 and 8 GHz, there will be many resonances ($\sim$750–1000), with complete overlap at the low-frequency end and isolated at the high-frequency end, within the volume of the beam tube between two insertion devices. For ten such devices, the real part of $Z_{\parallel}$, averaged over the frequency range, starts at about 40 $\Omega$ at 4.5 GHz, falling off to 4 $\Omega$ at 8 GHz, with a total low-frequency reactive component $(Z_{\parallel}/n)$ of about 0.3 $\Omega$. This is entirely consistent with our estimate of total impedance ($Z_{\parallel}/n \simeq 2\ \Omega$) and is not expected to cause beam disruption.

For a 1-cm-gap undulator, this impedance pattern extends to 16 GHz, which is also the approximate bunch cutoff frequency. Effects on the single-bunch instability begin to become significant at this stage.

**3.3.2.2 Bunch Length.** In the 1–2 GeV Synchrotron Radiation Source, we are striving for short bunch lengths. These short bunches will sample primarily the high-frequency components of the ring broadband impedance. Specifically, high frequencies beyond the bunch cutoff frequency are dominant in the turbulent-bunch-lengthening process. A knowledge of the beam–storage ring broadband coupling impedence that is effective in this frequency regime is thus crucial in estimating the attainable bunch lengths. Experience with other electron storage rings suggests that, for bunch lengths much smaller than the transverse dimensions of the vacuum chamber, the electromagnetic interaction of the beam with its environment is significantly attenuated. These experimental observations seem to suggest that, for bunches with an rms bunch length smaller than the beam-pipe radius ($\sigma_\ell < b$), the effective longitudinal broadband impedance $|Z_{\|}/n|_{\text{eff}}$ seen by the beam at frequencies beyond the pipe cutoff ($\omega > \omega_c$) is reduced substantially from what one might expect at low frequencies, say, $|Z_{\|}/n|_0$. Observations [Chao, 1983] of the bunch-lengthening phenomenon at the SPEAR storage ring, as a function of bunch current, suggest the following phenomenological power law for the longitudinal broadband impedance at high frequencies:

$$
\begin{aligned}
|Z_{\|}/n|_{\text{eff}} &= |Z_{\|}/n|_0 && \omega \leqslant \omega_c \,, \\
&= |Z_{\|}/n|_0 \left(\frac{\omega}{\omega_c}\right)^{-1.68} && \omega > \omega_c \,.
\end{aligned}
$$

This "law" has come to be called the SPEAR scaling law.

Since perturbations affecting the single-bunch instability and turbulent bunch lengthening must have a wavelength comparable to or less than the rms bunch length, the frequencies relevant to this scaling law are $\omega \geqslant c/\sigma_\ell$. To be conservative (in the sense of assuming the highest possible impedance value), we take $\omega = c/\sigma_\ell$ in this scaled impedance relation. For $\sigma_\ell < b$, the effective impedance is then reduced to the SPEAR-scaled value:

$$
|Z_{\|}/n|_{\text{eff}} = |Z_{\|}/n|_0 \left(\frac{\sigma_\ell}{b}\right)^{1.68}
$$

While there may be a question as to the precise frequency dependence of the broadband impedance implied by SPEAR scaling, there is no doubt that the effective impedance felt by the beam is significantly reduced for short bunches. We therefore illustrate the range of possibilities by performing two separate sets of calculations, one assuming no reduction in the impedance from nominal values (no SPEAR scaling) and a second assuming a reduction as given by SPEAR scaling. Computations of coupled-bunch instabilities in Section 3.2.3.3 were also performed by assuming bunch lengths corresponding to these two assumptions.

The bunch length in the Light Source must be very short: $2\sigma_t \simeq 20$–$50$ ps. In practice, the attainable bunch length for a given lattice is determined by two things, the rf parameters and the constraints imposed by the longitudinal microwave instability. With regard to the rf parameters, we take as our nominal case a 500-MHz system operating at 1.5 MV. The choice of these parameters establishes a lower limit to the bunch length.

The influence of the longitudinal microwave instability is determined by the effective broadband impedance assumed for the ring. In particular, the magnitude of the turbulent bunch lengthening is very sensitive to whether or not we assume the validity of SPEAR scaling [Chao and Gareyte, 1976] in obtaining the effective impedance. The microwave threshold is given by

$$I_{\text{thresh}} = \frac{\sqrt{2\pi}\,|\eta|(E/e)\sigma_p^2\sigma_\ell}{R\;|Z_{\|}/n|_{\text{eff}}} ,$$

where $\eta$ is the phase-slip factor, $\sigma_p$ is the rms relative momentum spread, and $R$ is the machine radius.

The broadband impedance is made up of contributions from the vacuum chamber and the rf cavities:

$$|Z_{\|}/n|_0 = |Z_{\|}/n|_{\text{chamber}} + n_{\text{cell}}|Z_{\|}/n|_{\text{rf}} ,$$

where we take $n_{\text{cell}}$, the number of rf cells, from the rf voltage (assuming 750 kV per cell). As discussed above, SPEAR scaling considerably reduces bunch lengthening in the regime where $\sigma_\ell < b$. Although SPEAR scaling can lead to very low impedance values, we follow our past practice [Bisognano et al., 1985] of not allowing the effective impedance to become smaller than the free-space value of

$$(Z_{\|}/n)_{\text{fs}} = 300(b/R)\ [\Omega]$$

For the lattice considered here, this limit is about 0.3 Ω.

We take a value of 2 Ω for the vacuum chamber broadband impedance. The rf cavity is calculated to have an impedance (per cell) of 0.25 Ω, a value obtained from the higher-order modes of our reference cavity design. Thus, at a voltage of 1.5 MV, i.e., $n_{\text{cell}} = 2$, the effective impedance is 2.5 Ω prior to applying SPEAR scaling. As mentioned, applying SPEAR scaling reduces this value to roughly 0.3 Ω.

In Fig. 3-16, we show the bunch length as a function of average current. As can be seen, the SPEAR scaling assumption leads to very short bunch lengths in the 250-bunch case and to slightly longer bunches in the single-bunch scenario. At the higher currents, the effect of SPEAR scaling is to reduce the bunch length by about a factor of two or three. If there were no impedance reduction from SPEAR scaling, it would be difficult to achieve a bunch length of 20 ps at a reasonable single-bunch current.

Based on the above results, we can draw several conclusions. If the SPEAR scaling assumption is applicable to the LBL Light Source, there should be no problem reaching bunch lengths of about 20 ps. If not, we would expect to give up as much as a factor of two or three in bunch length. In the latter case, it does not appear practical to regain the lost bunch length by any reasonable variation of rf parameters [Zisman, 1986].

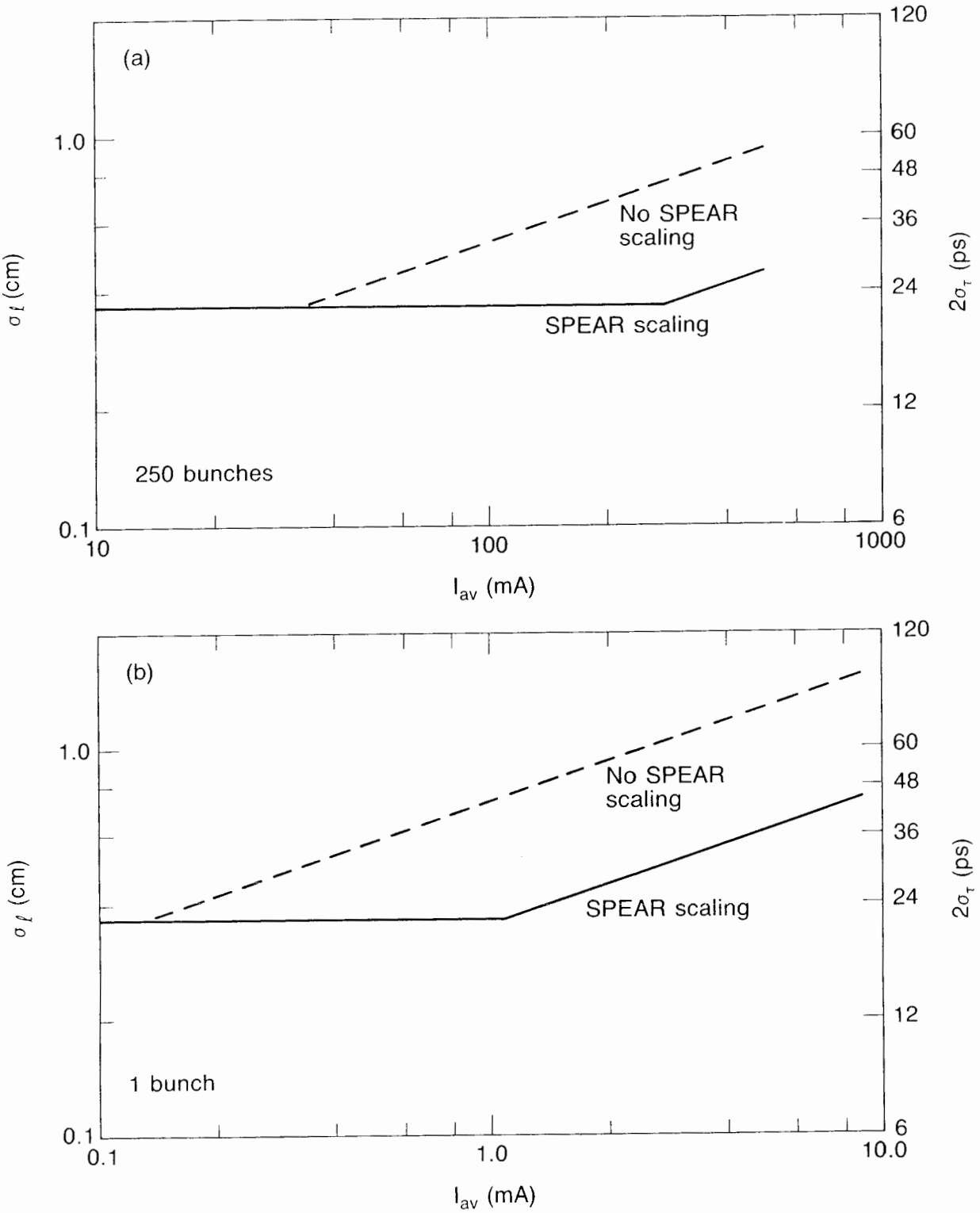


**Fig. 3-16.** Bunch length vs. current at 1.5 GeV, with and without the SPEAR scaling law, for (a) the 250-bunch case and (b) the single-bunch case.

**3.3.2.3 Coupled-Bunch Instabilities.** Narrow-band impedances from, for example, higher-order parasitic modes of the rf cavities can produce long-range wake fields that couple succeeding bunches and cause longitudinal and transverse multibunch instabilities. Care in the design of the rf system (e.g., suppressing higher-order modes by using antennas or holes in an outgoing port, which reduce the $Q$ of certain cavity modes) and feedback dampers, if necessary, are fundamental ways of eliminating this coherent effect.

Two mode numbers are needed to describe a longitudinal coupled-bunch mode. For a beam consisting of $B$ equal bunches, there are $B$ coupled-bunch modes with mode number $m = 0,1,...(B - 1)$. In addition, an index $a$ is required to describe the motion of individual bunches in synchrotron phase space. For example, $a = 1$ means a dipole mode in which bunches move rigidly as they execute the longitudinal oscillations; $a = 2$ means a quadrupole mode in which bunch head and bunch tail oscillate longitudinally out of phase, etc. In the case of transverse coupled-bunch modes, a similar notation is used. One difference in the transverse case, however, is that the index $a$ can assume the value $a = 0$, meaning that the bunches move rigidly as they execute transverse oscillations; $a = 1$ means the bunch head and tail oscillate transversely out of phase, etc.

We have calculated the complex coherent frequency shifts (i.e., the real coherent-oscillation frequency shifts and growth rates) for the first few fastest-growing coupled-bunch modes in the Light Source. Consistent with our standard multibunch operating mode, we used a current of 1.6 mA per bunch in our calculations; however, we assumed a completely filled, 328-bunch configuration, since our calculations are valid only for a symmetric coupled-bunch configuration. This approach yields a conservative estimate of the coupled-bunch instabilities.

The resonance parameters for the higher-order modes of the Light Source rf cavity were taken from the undamped values of these parameters for the similar KEK 500-MHz rf cavity. The broadband impedance for the ring was taken as $|Z_{\parallel}/n|_{\text{chamber}} = 2\ \Omega$, and, to obtain a measure of the resistivity, we assumed the vacuum chamber wall to be constructed of aluminum. All calculations were done with the LBL accelerator physics computer code ZAP [Zisman et al., 1986], using Gaussian bunch shapes.

Table 3-5 summarizes the input values of bunch lengths and momentum spreads, at energies of 1, 1.5, and 2 GeV (with and without the assumption of SPEAR scaling for the ring broadband impedance), used in the coupled-bunch calculations. The SPEAR scaling assumption and its consequences are discussed at length in Section 3.3.2.2.

**Table 3-5.** Bunch lengths $\sigma_\ell$ and momentum spreads $\sigma_p$ for energies of 1, 1.5, and 2 GeV, with and without the SPEAR scaling assumption. The average bunch current was 1.6 mA ($N_b = 6.56 \times 10^9$). These values were used as inputs for the coupled-bunch calculations summarized in Tables 3-6 and 3-7.

| | With SPEAR scaling | | Without SPEAR scaling | |
|---|---|---|---|---|
| $E$ (GeV) | $\sigma_p$ ($10^{-4}$) | $\sigma_\ell$ (cm) | $\sigma_p$ ($10^{-4}$) | $\sigma_\ell$ (cm) |
| 1.0 | 9.8 | 0.42 | 20.2 | 0.86 |
| 1.5 | 8.0 | 0.42 | 16.5 | 0.86 |
| 2.0 | 9.4 | 0.57 | 14.2 | 0.86 |

A summary of the results of the Light Source coupled-bunch calculations is given in Tables 3-6 and 3-7 for the first few fastest-growing longitudinal and transverse modes, respectively. Calculations were done for all the higher-order modes of a single rf cell, with the resonant shunt impedances enhanced by a factor of two because of the presence of two cells. We also assumed no effective spread of the resonance frequencies (i.e., no "de-Q-ing") arising from the use of more than one rf cell. If we assume a modest de-Q-ing factor of two due to the multicell rf structure, the growth rates decrease roughly twofold.

It is obvious from the tables that, of all unstable modes, the longitudinal dipole coupled-bunch synchrotron mode is the fastest-growing one in all cases and imposes the most severe limits on rf and feedback system design. Longitudinally, both the dipole and quadrupole synchrotron mode oscillations are unstable and not Landau damped by the small synchrotron frequency spread of the bunch. The coherent tune shift comes mainly

**Table 3-6.** Growth rates and tune shifts for the fastest-growing longitudinal coupled-bunch modes.

| Energy, $E$ (GeV) | Synchrotron mode number, $a$ | Coherent growth time, $\tau$ (ms) | Tune shift, $\lvert\Delta\nu\rvert_{coh}$ | Landau damping[a] |
|---|---|---|---|---|
| **Without SPEAR scaling** | | | | |
| | 1 | 0.13 | $2.76 \times 10^{-3}$ | U |
| 1.0 | 2 | 4.12 | $1.92 \times 10^{-4}$ | U |
| | 3,4,... | | | D |
| | 1 | 0.14 | $2.35 \times 10^{-3}$ | U |
| 1.5 | 2 | 4.38 | $1.63 \times 10^{-4}$ | U |
| | 3,4,... | | | D |
| | 1 | 0.15 | $2.12 \times 10^{-3}$ | U |
| 2.0 | 2 | 4.44 | $1.48 \times 10^{-4}$ | U |
| | 3,4,... | | | D |
| **With SPEAR scaling** | | | | |
| | 1 | 0.12 | $3.32 \times 10^{-3}$ | U |
| 1.0 | 2 | 16.2 | $1.62 \times 10^{-4}$ | U |
| | 3 | | | Border of stability |
| | 1 | 0.13 | $2.82 \times 10^{-3}$ | U |
| 1.5 | 2 | 17.2 | $1.33 \times 10^{-4}$ | U |
| | 3 | | | Border of stability |
| | 1 | 0.14 | $2.37 \times 10^{-3}$ | U |
| 2.0 | 2 | 9.6 | $1.34 \times 10^{-4}$ | U |
| | 3 | | | Border of stability |

[a]D = damped, U = undamped.

**Table 3-7.** Growth rates and tune shifts for the fastest-growing transverse coupled-bunch modes.

| Energy, $E$ (GeV) | Synchrotron mode number, $a$ | Coherent growth time, $\tau$ (ms) | Tune shift, $\lvert\Delta\nu\rvert_{coh}$ | Landau damping[a] |
|---|---|---|---|---|
| **Without SPEAR scaling** | | | | |
| | 0 | 1.18 | $2.5 \times 10^{-4}$ | U |
| 1.0 | 1 | 112 | $1.215 \times 10^{-5}$ | U |
| | 2,3,... | | | D |
| | 0 | 1.76 | $1.67 \times 10^{-4}$ | U |
| 1.5 | 1 | 147 | $8.1 \times 10^{-6}$ | U |
| | 2,3,... | | | D |
| | 0 | 2.35 | $1.25 \times 10^{-4}$ | U |
| 2.0 | 1 | 176 | $5.98 \times 10^{-6}$ | U |
| | 2,3,... | | | D |
| **With SPEAR scaling** | | | | |
| | 0 | 1.18 | $2.12 \times 10^{-4}$ | U |
| 1.0 | 1 | 420 | $1.03 \times 10^{-5}$ | U |
| | 2,3,... | | | D |
| | 0 | 1.76 | $1.42 \times 10^{-4}$ | U |
| 1.5 | 1 | 551 | $6.83 \times 10^{-6}$ | U |
| | 2,3,... | | | D |
| | 0 | 2.35 | $1.14 \times 10^{-4}$ | U |
| 2.0 | 1 | 370 | $6.35 \times 10^{-6}$ | U |
| | 2,3,... | | | D |

[a]D = damped, U = undamped.

from the rf modes, with a small component from the broadband impedance. Consequently, reducing the storage ring broadband impedance will not help stabilize the beam via Landau damping.

Transversely, both the rigid dipole (stationary $a = 0$ in synchrotron space) and the first nonrigid dipole (dipole $a = 1$ in synchrotron space) mode oscillations are unstable and not Landau damped by the synchrotron frequency spread. For the rigid dipole mode, it is only the transverse betatron tune spread that is effective in Landau damping. We have not included such a spread in our calculations. The nonlinear betatron tune spread required to stabilize the rigid dipole mode can be estimated from the corresponding coherent tune shift. Again, a lower ring broadband impedance is of little help, since the coherent tune shift comes mainly from the rf modes themselves. Modes with synchrotron mode numbers higher than $a = 2$ longitudinally and higher than $a = 1$ transversely are all effectively Landau damped by the synchrotron frequency spread in the beam.

The calculated growth rates are high, especially the longitudinal ones. Synchrotron radiation damping is of little help, except for the first nonrigid transverse dipole mode ($a = 1$), since the radiation damping times are of the order of 10–20 ms—much longer than the instability growth times. Consequently, the storage ring design includes both higher-order mode-suppression schemes for the rf and feedback systems.

For the feedback system, described in Section 3.9, we have used the following conservative estimates for the worst growth rates, assuming all rf buckets occupied and undamped rf parasitic modes (de-Q-ed by a factor of two due to the presence of two rf cells):

Longitudinal: $\tau_{gr} \simeq 0.3$ ms

Transverse: $\tau_{gr} \simeq 2$ ms .

A bandwidth of $W = 250$ MHz is sufficient for the feedback damper, but the actual bandwidth necessary may be much smaller than this. The required feedback voltages at the kicker are 1 kV and 50 V for the longitudinal and transverse dampers, respectively.

Coupled-bunch instabilities are not expected to limit the performance of the Light Source. In addition to higher-order mode-suppression and feedback systems, a second small rf system of a higher harmonic could be installed to provide either a bunch-to-bunch or an intrabunch spread in synchrotron frequency, sufficient to Landau damp the modes and to achieve the design current of 400 mA without any residual oscillation. Past experience has always been favorable for multibunch operation. For example, at the KEK Photon Factory, which has a comparable instability threshold, the longitudinal coupled-bunch instability has not been a limiting factor in attaining more than 200 mA of stored beam.

**3.3.2.4 Emittance Growth.** In this section, we use ZAP to estimate the equilibrium emittance of the machine based on the theory of intrabeam scattering (IBS) of Bjorken and Mtingwa [1983]. On the basis of comparisons between ZAP predictions and experimental results at low energies from Aladdin [Chattopadhyay et al., 1985] and MAX-lab [Eriksson, 1986], we are confident that the results of the code are in reasonable agreement with experiment.

In general, the severe effects of IBS diminish rapidly as the beam energy increases. However, in the case of the Light Source lattice, the values for the natural emittance ($\epsilon_0 = 4.1 \times 10^{-9}$ m-rad) and the natural bunch length ($\sigma_{\ell 0} = 0.37$ cm) are very small; hence, we have a very high bunch density. Thus, even at rather high energies, we might expect to see some beam emittance blowup from IBS. Because the IBS phenomenon is a single-bunch effect, the most severe problems occur in the (high-current) single-bunch scenario.

In Fig. 3-17a, we show the emittance growth at a 10:1 horizontal-vertical emittance ratio. A beam current of 7.6 mA in a single bunch has been assumed. The emittance growth is negligible at high energies and leads to only about a twofold increase over the natural emittance at 1 GeV. Because of the higher beam density, the SPEAR scaling case leads to more growth than does the case of no SPEAR scaling at the same average beam current. As shown in Fig. 3-17b, the standard multibunch scenario, i.e., 400 mA in 250 bunches, leads to an even smaller growth.

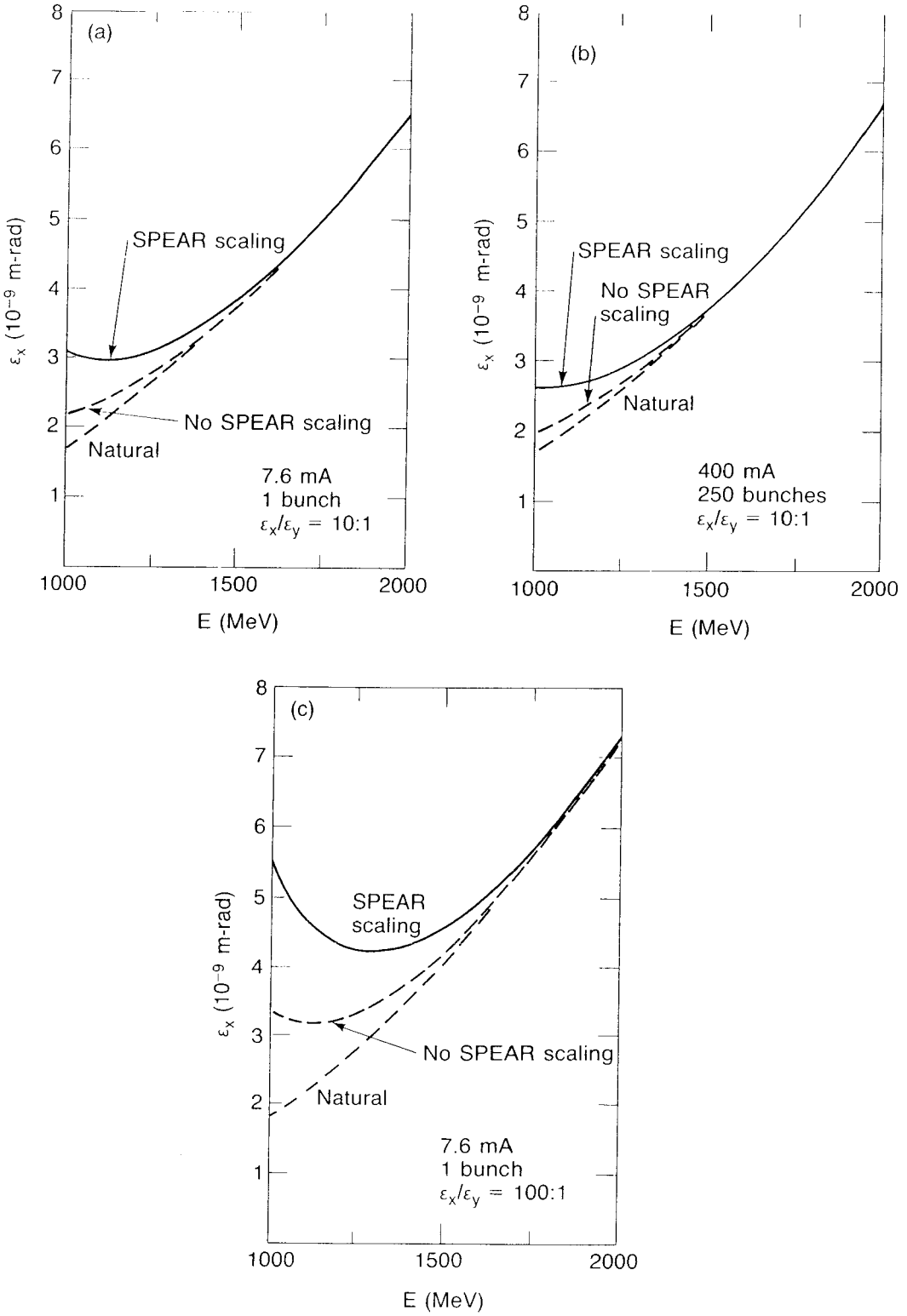


**Fig. 3-17.** Predicted emittance growth from IBS for three cases: (a) 7.6 mA in a single bunch, emittance ratio of 10:1; (b) 400 mA in 250 bunches, emittance ratio of 10:1, and (c) 7.6 mA in a single bunch, emittance ratio of 100:1.

If we take a case with a larger emittance ratio of 100:1, the beam density is higher, hence the emittance growth is larger; this is shown in Fig. 3-17c. Nonetheless, the expected emittance growth at the lower energies does not compromise the operating specifications outlined in Table 2-1.

To summarize, we conclude that there is a noticeable emittance growth at the lower end of the energy range (near 1000 MeV), but it is not severe enough to limit the performance of the machine.

**3.3.2.5 Beam Lifetime.** Beam lifetime is limited by a combination of two effects, Touschek scattering and gas scattering. In this section, we first discuss the former phenomenon and then briefly report on the results of our gas-scattering lifetime estimates.

*Touschek Scattering.* Touschek scattering, which is large-angle intrabeam scattering, is most severe for short, high-current bunches with low emittance and a large coupling ratio—precisely the properties we are striving for in the Light Source. In addition, the Touschek lifetime is strongly influenced by the momentum acceptance of the lattice.

The momentum acceptance limit of the lattice can be either longitudinal, i.e., the rf bucket height, or transverse, i.e., the physical or dynamic aperture. In the code ZAP, the transverse limits can be used in several ways. In this case, we specified a pair of values that give the maximum momentum acceptance in the dispersive and nondispersive regions of the lattice. (The distinction arises because, in the dispersive region, a scattering event gives rise to a betatron oscillation amplitude proportional to the momentum change of the scattered electron, whereas in the nondispersive region, it does not. The available aperture is thus lower in the dispersive region, owing to the need to accommodate both the closed-orbit deviation and the betatron oscillation.) The values for the transverse momentum aperture used in this study—based on tracking results—are 4.0% in the dispersive region and 5.0% in the nondispersive region. In practice, however, the rf (longitudinal) aperture (3.5% at 1.5 GeV) is the limiting one at energies above about 1.2 GeV.

Touschek lifetimes have been calculated for the cases of 400 mA in 250 bunches and 7.6 mA in one bunch, both with and without the SPEAR scaling assumption. Figure 3-18 shows the Touschek half-life for both operating modes, with SPEAR scaling; on the average, the single-bunch lifetime is about half that for the multibunch case. Not using the SPEAR scaling assumption (Fig. 3-19) leads to longer bunches (by a factor of about two or three) and to longer lifetimes (by a similar factor).

The Touschek lifetime can also be affected by the rf parameters. This is demonstrated in Table 3-8, which compares the calculated Touschek lifetimes at 1.5 GeV (for both single- and multibunch scenarios) for the standard case of 1.5 MV with those for a 3-MV rf system. At this energy, the lifetime for the higher voltage increases almost twofold, despite the increased bunch density. At low energies, on the other hand, where the transverse limit is dominant, the increased rf voltage would actually affect the beam lifetime adversely [Zisman, 1986].

Increasing the emittance ratio from 10:1 to 100:1 reduces the Touschek lifetimes by about a factor of three; this is demonstrated in Fig. 3-20 for the single-bunch case.

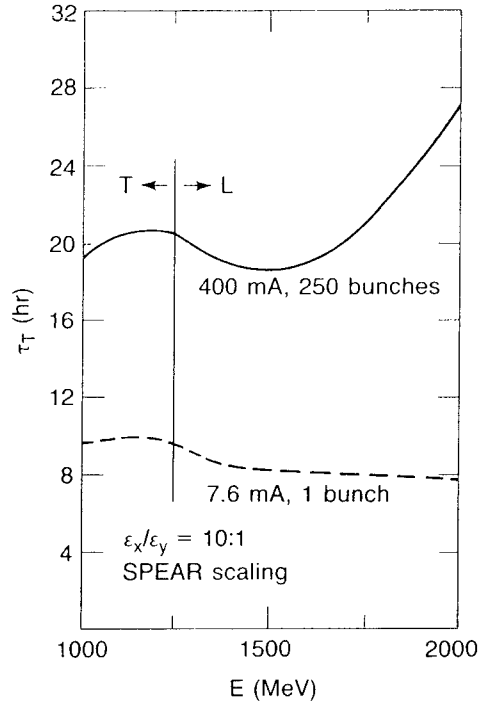


**Fig. 3-18.** Touschek lifetime with 10:1 emittance ratio, assuming SPEAR scaling, for the cases of 400 mA in 250 bunches and 7.6 mA in 1 bunch. Below about 1200 MeV, the aperture limit is transverse (T); above this energy, the aperture limit is longitudinal (L).

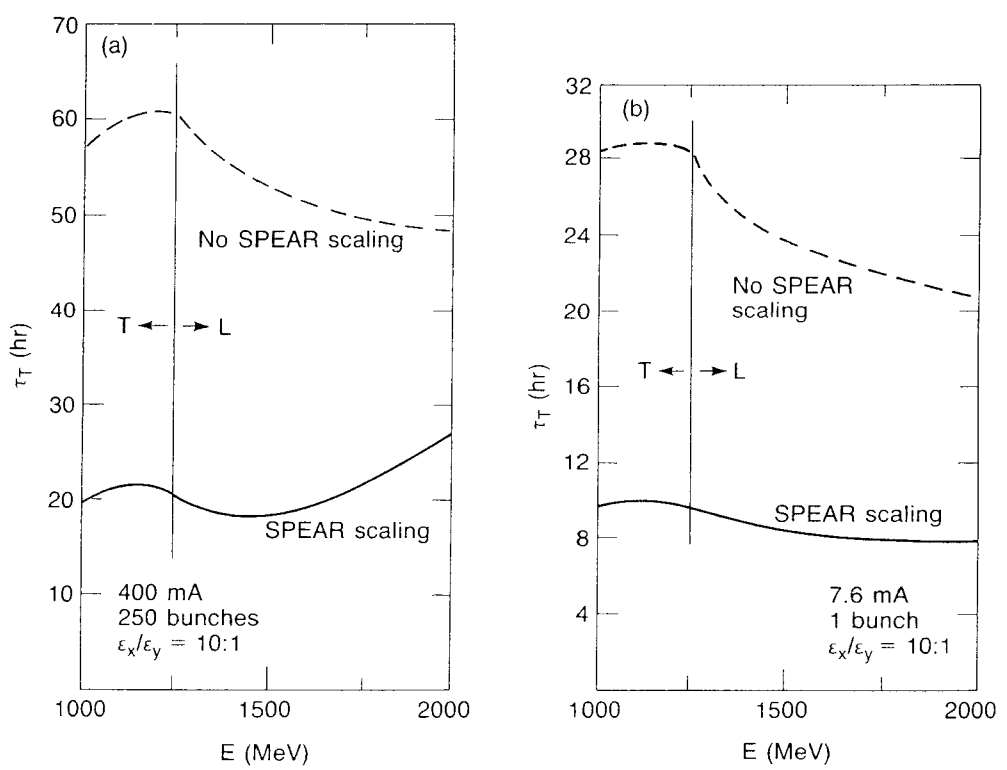


**Fig. 3-19.** Touschek lifetime (10:1 emittance ratio) for (a) the multibunch and (b) the single-bunch modes, showing the effect of the SPEAR scaling assumption.

**Table 3-8.** Effect of rf voltage on Touschek lifetimes at 1.5 GeV. An emittance ratio of 10:1 is assumed.

| $V_{rf}$ (MV) | $\sigma_p$ ($10^{-4}$) | $\sigma_\ell$ (cm) | $\epsilon_x$ ($10^{-9}$ m-rad) | $\tau_T$ (hr) |
|---|---|---|---|---|
| **400 mA in 250 bunches** | | | | |
| 1.5 | 8.0 | 0.42 | 3.8 | 18.5 |
| 3.0 | 9.0 | 0.33 | 3.8 | 30.6 |
| **7.6 mA in 1 bunch** | | | | |
| 1.5 | 13.5 | 0.70 | 3.8 | 8.4 |
| 3.0 | 15.1 | 0.56 | 3.9 | 14.8 |

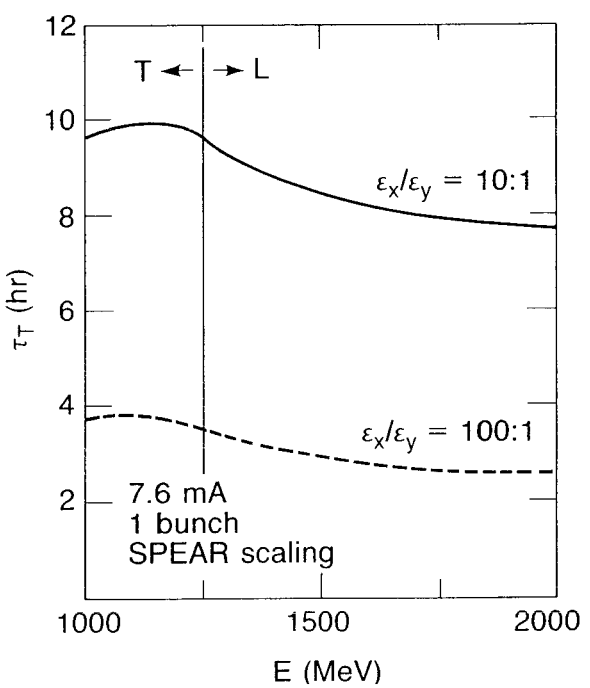


**Fig. 3-20.** Effect of the emittance ratio on Touschek lifetime; the 7.6-mA, single-bunch case with SPEAR scaling is shown.

*Gas Scattering.* Gas scattering lifetimes were calculated on the basis of formulas given by Le Duff [1985]. The calculations assume a pressure of 1 nTorr of nitrogen gas and a ring acceptance limited by undulator vacuum chambers with full apertures of 2 cm. The resultant lifetimes (Fig. 3-21), which include contributions from both elastic and inelastic (bremsstrahlung) scattering, lie in the range of about 20–35 hours. Also shown in Fig. 3-21 is the effect of reducing the apertures to 1 cm. The lifetime degradation is substantial.

*Overall Lifetime.* Overall beam lifetimes (at an aperture of 2 cm) are shown in Fig. 3-22 for the various beam scenarios. Lifetimes in excess of 6 hours should be achieved even in the single-bunch mode. The effect of reducing the undulator aperture to 1 cm is shown in Fig. 3-23. Multibunch lifetimes remain in excess of 6 hours, although the single-bunch case yields lifetimes of only about 4–5 hours. Given the ability to fill the storage ring rapidly, this should still lead to acceptable experimental conditions. In Fig. 3-24, we show the effect of changing the emittance ratio from 10:1 to 100:1; this would reduce the beam lifetime to about 3 hours in the case of a 2-cm undulator gap. It turns out that these rather short 100:1-emittance-ratio lifetimes are dominated by the Touschek lifetime, so reducing the undulator gap to 1 cm would cause only about a 20% further reduction in overall lifetime.

### 3.3.3 Ion Trapping

The electron beam circulating in the storage ring ionizes the molecules of any residual gas, leading, under certain conditions, to an accumulation of the ions. This in turn leads to an increase in the local gas pressure within the beam volume (with adverse effects on beam lifetime and emittance) and to space-charge effects.

In this section, we explore the conditions that must exist to start ion accumulation and describe means to avoid this phenomenon in our design. A linear approximation [Baconnier and Brianti, 1980] has been used for the interaction of the ions with the beam. A more accurate study, which includes all nonlinear effects, is under way.

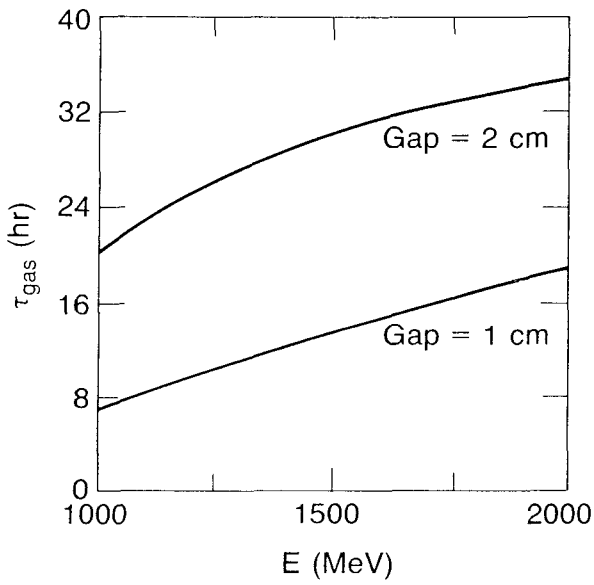


**Fig. 3-21.** Predicted gas scattering half-lives for two different assumptions regarding the limiting vertical aperture. Calculations assume 1 nTorr of nitrogen gas.

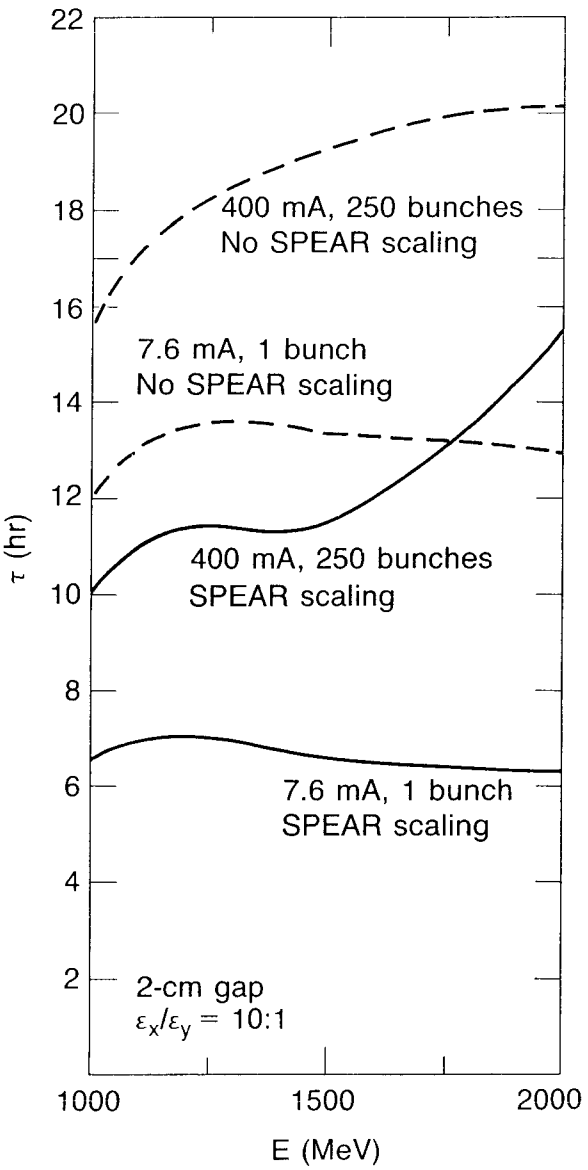


**Fig. 3-22.** Predicted overall beam lifetimes for single-bunch and multibunch scenarios. Calculations assume a limiting gap of 2 cm.

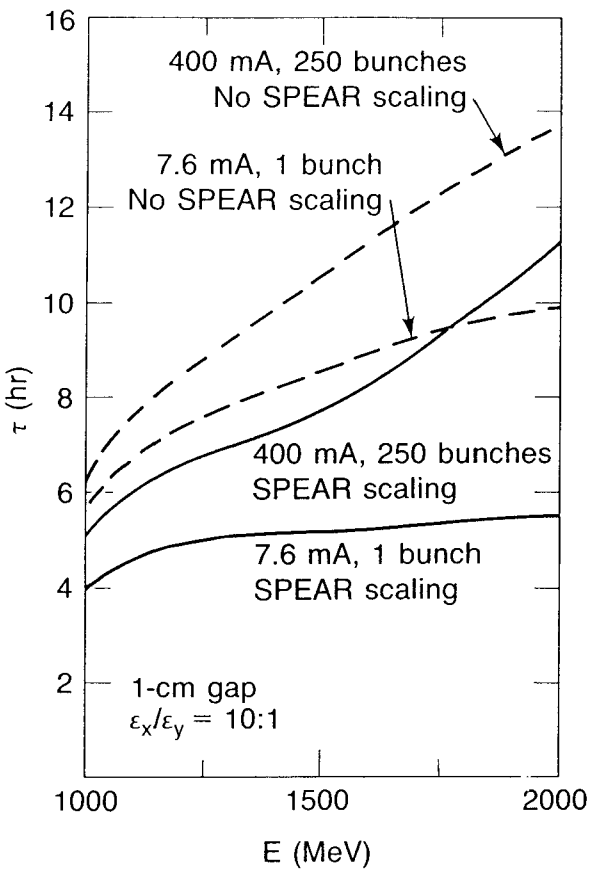


**Fig. 3-23.** Predicted overall beam lifetimes for single-bunch and multibunch scenarios, assuming a limiting gap of 1 cm.

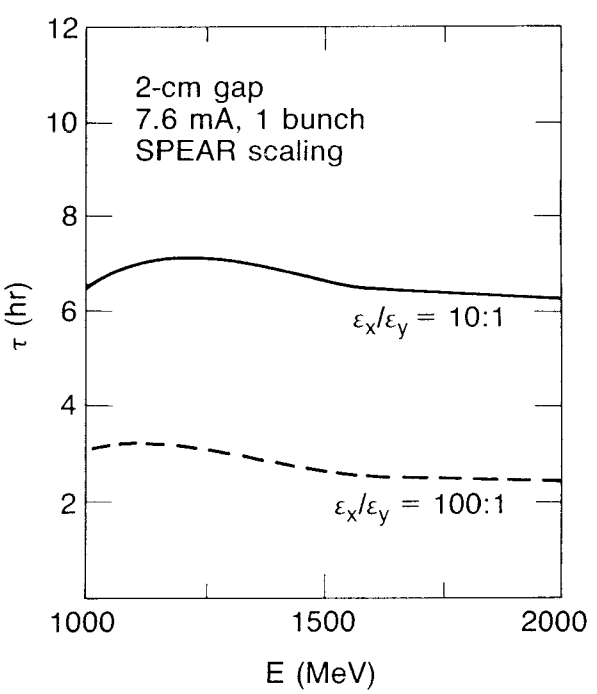


**Fig. 3-24.** Overall beam lifetime for the single-bunch case with SPEAR scaling, assuming a limiting gap of 2 cm. The effect of changing the emittance ratio from 10:1 to 100:1 is to increase the bunch density and thus to decrease the lifetime significantly.

**3.3.3.1 Stability.** The change in transverse velocity for an ion created within a beam having an elliptical cross section and a uniform particle distribution is given for a small displacement in the horizontal (vertical) plane by

$$\frac{dx}{dt} = -a_x x \qquad \left(\frac{dy}{dt} = -a_y y\right) , \tag{1}$$

where $x(y)$ is the horizontal (vertical) coordinate measured from the beam axis and the parameter $a$ is given by

$$a_{x,y} = \frac{2r_0 c N_b}{A\sigma_{x,y}(\sigma_x + \sigma_y)} . \tag{2}$$

Here, $c$ is the velocity of light, $r_0$ is the classical proton radius, $N_b$ is the number of particles per bunch, $A$ is the ion mass number, $\sigma_x$ is the rms horizontal beam size, and $\sigma_y$ is the rms vertical beam size. Because $\sigma_y < \sigma_x$ usually, an electron beam generally has an $a$ value that is larger in the vertical plane.

For a beam with equally spaced bunches having identical particle populations, one "period" of the forces acting on the ions is given by the "kick" given in Eq. (1), followed by a drift equal to the bunch separation, i.e.,

$$\mathbf{M} = \begin{pmatrix} 1 & t_B \\ 0 & 1 \end{pmatrix} \begin{pmatrix} 1 & 0 \\ -a & 1 \end{pmatrix} , \tag{3}$$

where $t_B$ is the time interval between the bunches. The motion is stable, i.e., ions are trapped, if

$$-2 < \mathrm{Tr}(\mathbf{M}) = 2 - at_B < 2 . \tag{4}$$

Using Eq. (2), the limit given by Eq. (4) is reached for the critical ion mass

$$A_c = \frac{r_0 C N_b}{2B\sigma_y(\sigma_x + \sigma_y)} , \tag{5}$$

where $C$ is the circumference of the ring and $B$ is the number of bunches.

To calculate the critical masses for the Light Source, we evaluated the geometry factor given by

$$g(x,y) = \max\left[\frac{1}{\sigma_x(\sigma_x + \sigma_y)} , \frac{1}{\sigma_y(\sigma_x + \sigma_y)}\right] \tag{6}$$

at various locations around the lattice. (We use $g(x,y)$ to obtain the $A_c$ value, because the ions in the plane with lower $A_c$ are expected to be lost in the other transverse dimension.) Two different cases were considered, corresponding to the design lattice (case 1) and the

detuned lattice of Section 3.3.5 (case 2). The results of this evaluation are given in Table 3-9. In our calculations, we took the minimum value of $g(x,y)$ in the lattice, and we assumed the following storage ring parameters: maximum number of bunches, 328; maximum average current, 400 mA; maximum single-bunch current, 7.6 mA; and ring circumference, 196.8 meters. Our results for the critical masses in various scenarios are given below.

**Table 3-9.** Parameter values for two ion-trapping cases.

| Parameter | Case 1 | Case 2 |
|---|---|---|
| Emittance, $\epsilon_x$ (m-rad) | $4 \times 10^{-9}$ | $1 \times 10^{-8}$ |
| $k = \epsilon_y/\epsilon_x$ | 0.1 | 0.3 |
| $g(x,z)$ ($m^{-2}$) | | |
| minimum | $0.703 \times 10^8$ | $0.142 \times 10^8$ |
| average | $0.179 \times 10^9$ | $0.348 \times 10^8$ |

**3.3.3.2 Single-Bunch Mode.** For the single-bunch mode, with a current of 7.6 mA, the critical masses for cases 1 and 2 are above the carbon dioxide mass of 44:

case 1: $A_c = 331$

case 2: $A_c = 67$ .

Thus, no ion trapping difficulties are expected in this mode.

**3.3.3.3 Multibunch Mode with Equidistant Bunches.** For a complete filling of the 328 bunches to 400 mA, the critical masses are lower than one mass unit:

case 1: $A_c = 0.16$

case 2: $A_c = 0.03$ .

For the maximum current per bunch of 7.6 mA, even two equidistant circulating bunches show ion accumulation for case 2. For case 1, eight such bunches are just at the limit where ions become unstable.

**3.3.3.4 Multibunch Filling with a Gap.** If a gap is introduced in the beam, the periodicity of the forces is reduced, and resonances are created that generate unstable bands within the range of ion masses (analogous to the half-integer resonance in an accelerator if quadrupole distortions are introduced).

Figure 3-25 shows, for case 1, the stability of ion masses for a multibunch mode without a gap ($B = 328$) and with two different gap sizes. If there is no gap, all ion masses are stable and may be trapped by the beam. A gap of 56 bunches (33.6 meters), on the

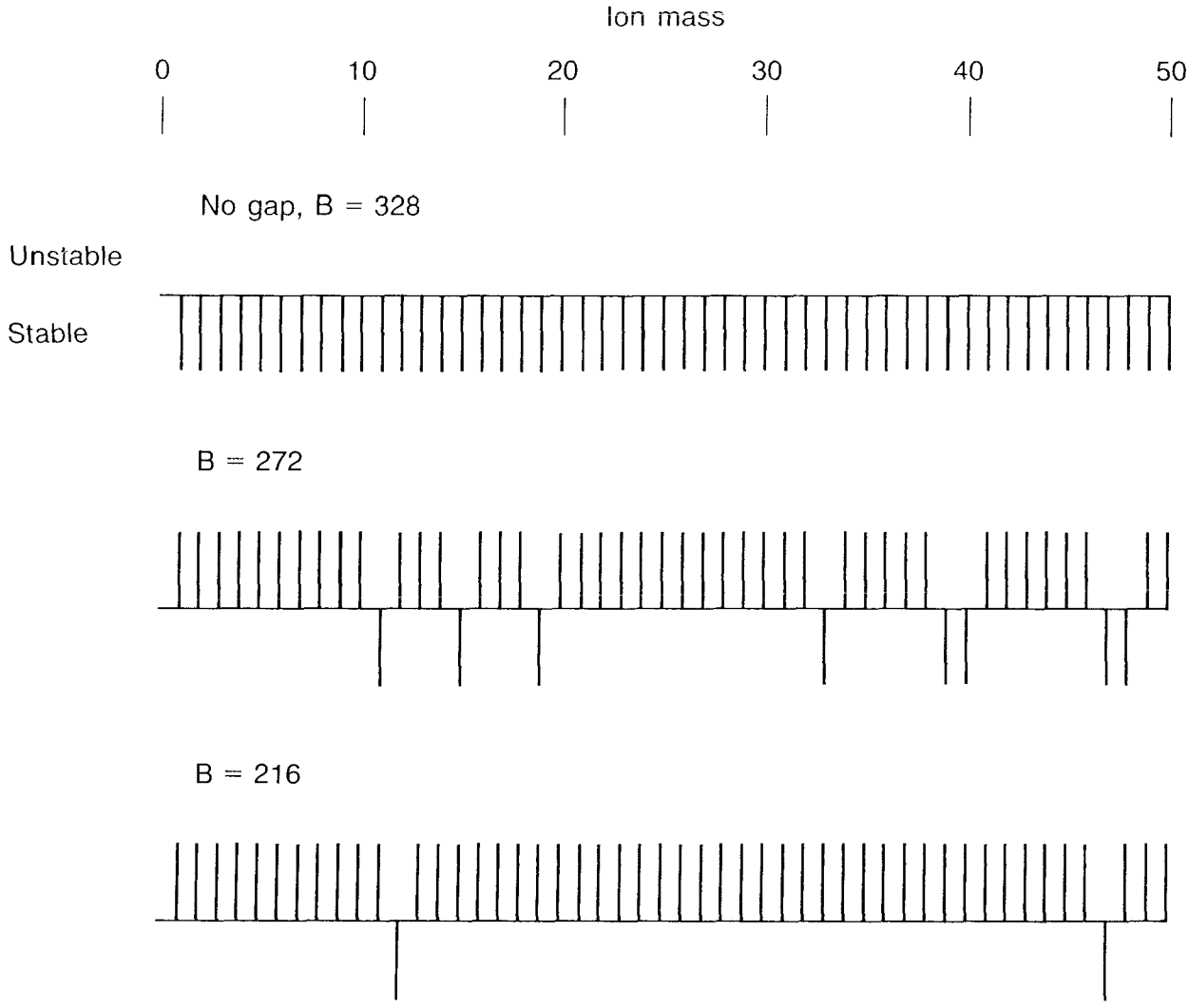


**Fig. 3-25.** Plots showing stable and unstable ion masses for three filling scenarios, assuming the parameters of case 1 in Table 3-9. In each scenario, the current is 1.22 mA/bunch.

other hand, leaves only a few mass numbers stable. The stability is further reduced to only two mass numbers if the gap is increased to 112 bunches (67 meters, or approximately one-third of the ring). Similar plots are shown in Fig. 3-26, for case 2. The increased beam size leads to greater ion stability, i.e., a less favorable situation.

These results (for a linear theory) indicate that most ions are not trapped if a gap is introduced. If an ion mass falls within a stable band, ions accumulate only until neutralization reduces the forces to the point where the ion is shifted into an unstable region. Thus, no "ion ladder" can be built up. Our findings are in qualitative agreement with the experimental observations and the theoretical studies [Barton, 1986] carried out at the VUV ring at the National Synchrotron Light Source.

This linear theory has also been successful in the past in predicting degradation of beam quality (and performance of the ring as a whole) due to trapped ions in the Aladdin storage ring at Stoughton, Wisconsin [Chattopadhyay, 1985]. The clearing electrode voltages

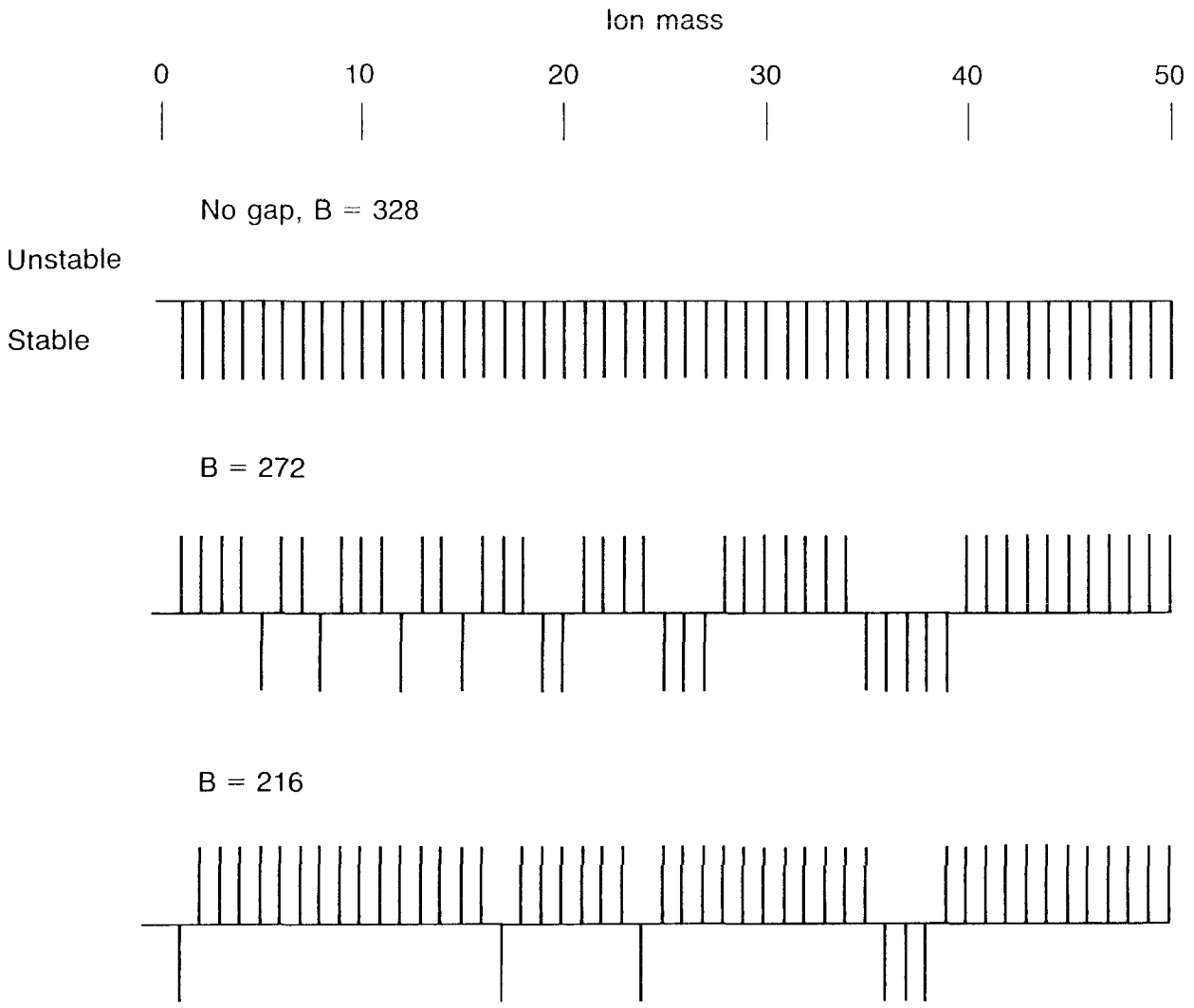


**Fig. 3-26.** Plots showing stable and unstable ion masses for case 2 in Table 3-9.

and their characteristic frequencies (dc plus a small amount of ac voltage) that were necessary at Aladdin in order to upgrade its performance to 150 mA of stored beam at 800 MeV are also in reasonable agreement with predictions (for characteristic beam sizes) of this linear model. Our theory thus seems to be consistent with experience with ion trapping.

**3.3.3.5 Oscillation Amplitude and Frequency of Ion Motion.** The oscillation frequency and the maximum excursion of the ion motion can be derived (as for particle motion in a focusing structure) by calculating the beta function and the frequency in the usual way. If no gap is introduced in the beam, the beta function varies regularly and has constant values for the bunch passing times. If a gap is introduced, the beta function beats with twice the oscillation frequency. The two scenarios are sketched in Figs. 3-27 and 3-28, which show the beta variation for stable ion motion without and with a gap, respectively. With a gap in the electron beam, an ion created during the bunch passing time with a small beta function increases its amplitude above the initial value as it follows the beta function modulation driven by the gap.

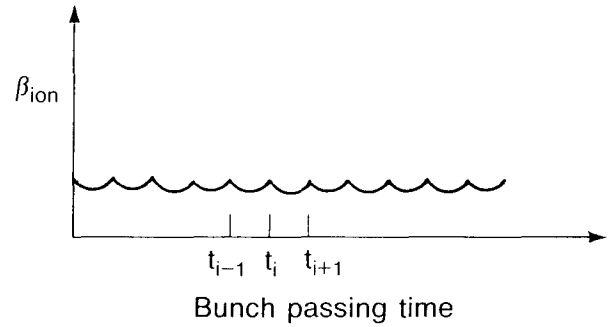


**Fig. 3-27.** Schematic illustration of the variation in $\beta_i$ for uniform ring filling.

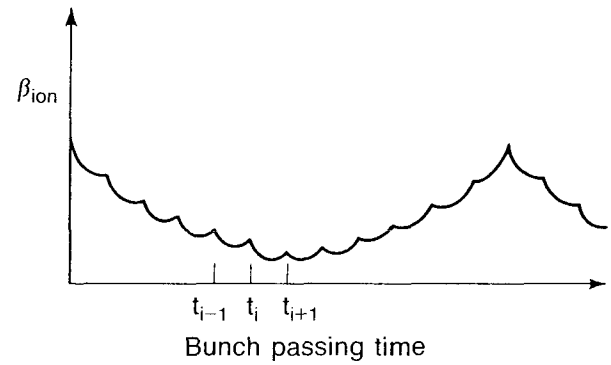


**Fig. 3-28.** Schematic illustration of the variation in $\beta_i$ for a bunch train with a gap.

If we define the stability limit for the ion amplitude to be $A_0$, where $A_0$ is the amplitude at which the space-charge force starts to become strongly nonlinear (the precise evaluation of this criterion is one of the goals of further studies), then ions created at $\beta_i$ are stable if their amplitude $A_i$ satisfies the relation

$$A_i \leqslant \sqrt{\frac{\beta_i}{\hat{\beta}}}\, A_0 \ ,$$

where $\hat{\beta}$ is the maximum beta value. Thus, the ion cloud "throbs" with the revolution frequency, and each bunch sees its characteristic trapped ion cloud of transverse dimensions proportional to $\sqrt{\beta_i}$, which is, in some cases, only a fraction of the beam size.

Beta functions and oscillation frequencies were calculated for both cases 1 and 2. Without a gap, all masses between 1 and 50 are stable for both cases, and the beta function shows the behavior described by Fig. 3-27. At the time of the bunch passing, we find $\beta$ = 2.4 meters for $A$ = 1, increasing to $\beta$ = 11.7 meters for $A$ = 50. If a gap of 78 bunches is introduced (which leaves 250 bunches in the ring), only three masses remain stable for case 1. These masses do not correspond to any species of concern. Their beta values and frequencies are shown in Table 3-10.

For the same bunch structure, 14 masses would be stable in case 2. Beta values and oscillation frequencies for the smallest and largest of these mass values are included in Table 3-10. A scenario with fewer circulating bunches will be required in this case.

**Table 3-10.** Beta values and oscillation frequencies for stable ions when 250 bunches are filled. For case 2, the results shown are for the highest and lowest of 14 stable mass numbers.

| Ion mass | Maximum $\beta$ (m) | Minimum $\beta$ (m) | Oscillation frequency (MHz) |
|---|---|---|---|
| **Case 1** | | | |
| 21 | 47.6 | 0.25 | 11.07 |
| 34 | 51.2 | 0.37 | 8.67 |
| 41 | 48.8 | 0.59 | 7.94 |
| **Case 2** | | | |
| 13 | 74 | 0.53 | 6.26[a] |
| 48 | 47 | 2.7 | 3.47 |

[a]By comparison, the oscillation frequency for mass 13 is 4.15 MHz when all 328 bunches are filled.

**3.3.3.6 Summary.** On the basis of the studies carried out so far, we conclude that ion trapping can be considerably alleviated by the introduction of a controllable gap in the bunch train. Only a few ion species remain stable in the presence of a 78-bunch gap (which corresponds to our standard multibunch configuration) and no "ion-ladder" can be built up. A more detailed study that includes the effects of nonlinear trapping fields is under way. In addition, we are studying the effectiveness of resonance excitation by oscillating clearing fields.

### 3.3.4 Effects of Insertion Devices

The magnetic fields of insertion devices can cause distortions of particle motion in the storage ring. An analytical approach to such effects by the use of a Hamiltonian averaged over the insertion device period has been developed by Smith [1986].

The magnetic fields used for the derivation of the equations of motion were as follows:

$$B_x = (k_x/k_y)B_0\sinh(k_x x)\sinh(k_y y)\cos(k_w z) ,$$

$$B_y = B_0\cosh(k_x x)\cosh(k_y y)\cos(k_w z) ,$$

$$B_z = -(k_w/k_y)B_0\cosh(k_x x)\sinh(k_y y)\sin(k_w z) ,$$

with

$$k_x^2 + k_y^2 = k_w^2 = (2\pi/\lambda_w)^2 ,$$

where $\lambda_w$ is the period length of the insertion device and $B_0$ is its magnetic field strength.

We have investigated the effects of periodic magnetic structures (specifically, a wiggler) on beam dynamics for the Light Source, using the tracking code RACETRACK. To solve the equations of motion within the wiggler, it was subdivided into slices, and each slice was treated with a thin-magnet approximation. The reference orbit was assumed to deviate from the design orbit (i.e., the orbit with zero wiggler field) only locally within the wiggler. This can be ensured by adding a unit of one-quarter period length at each end of the wiggler. The reference orbit thus oscillates within the wiggler, but no closed-orbit distortions are produced outside.

To be conservative, we have considered a worst-case scenario that assumes a superconducting wiggler with the following parameters: maximum field, 5 T; period length, 14 cm; and number of periods, 14. It should be noted that the actual wiggler fields foreseen for the Light Source are considerably lower than 5 T.

**3.3.4.1 Linear Optics Distortion.** The linear optics distortions generated from the assumed wiggler parameters are summarized in Table 3-11. Two types of wigglers were investigated, one with poles shaped to give equal focusing in both planes ($k_x = k_y$) and a second

**Table 3-11.** Linear optics distortions generated by a hypothetical 5-T wiggler. Beta values are given in meters, and $\Delta\nu$ is the fractional tune above an integer.

| | | $k_x = k_y$ | | $k_x = 0$ | |
|---|---|---|---|---|---|
| Wiggler status | | $\Delta\nu_x$ | $\Delta\nu_y$ | $\Delta\nu_x$ | $\Delta\nu_y$ |
| Off | | 0.10 | 0.10 | 0.10 | 0.10 |
| On | | 0.38 | 0.21 | 0.10 | 0.45 |
| | Position | $\beta_x$ | $\beta_y$ | $\beta_x$ | $\beta_y$ |
| Off | 1–7 | 11.0 | 4.0 | 11.0 | 4.0 |
| On | 1 | 1.6 | 1.9 | 11.2 | 1.3 |
| | 2 | 8.6 | 8.0 | 11.8 | 10.1 |
| | 3 | 57.8 | 6.7 | 11.6 | 9.2 |
| | 4 | 37.3 | 3.9 | 11.3 | 3.5 |
| | 5 | 79.2 | 8.5 | 11.9 | 12.2 |
| | 6 | 94.2 | 13.7 | 11.4 | 19.5 |
| | 7 | 9.8 | 2.6 | 12.0 | 2.4 |

without focusing in the horizontal plane ($k_x = 0$). The beta function distortions are given for the midpoints of the other insertion regions around the ring. (There is a symmetry in the distortion around points 1 and 7 for the remaining insertion points 8 through 12.) Beta function distortions are larger for the case of the wiggler with horizontal focusing in this lattice; changes of nearly a factor of 10 appear in the horizontal plane.

It is evident that the beta function distortions would require local compensation to reduce the half-integer stop band. This was simulated in our calculations by adjusting the adjacent quadrupole doublets of the regular insertion optics. Two quadrupole doublets in the wiggler insertion allow us only to compensate the beta values outside the wiggler insertion; those within the wiggler insertion cannot be controlled. After readjusting the beta values, the tunes still deviate from their original values; therefore, in a second rematching step, the cell quadrupoles of all achromats were used to recover the original tune values.

The rematching procedure utilizing the adjacent quadrupole doublets requires a change in quadrupole strengths of less than 10%. The resulting beta values at the wiggler are given in Table 3-12.

**Table 3-12.** Beta values, in meters, after correction and rematching.

| Wiggler | $\beta_x$ | $\beta_y$ |
|---|---|---|
| $k_x = k_y$ | 0.85 | 2.65 |
| $k_x = 0$ | 12.0 | 4.45 |

Because of its focusing property, a wiggler displacement error will cause an orbit distortion around the ring. For the worst case with $k_x = 0$, the integrated quadrupole strength in the vertical plane is approximately 1 $m^{-1}$, which is comparable to the strength of the lattice quadrupoles. It follows that the orbit-displacement errors produced by a single displaced wiggler are comparable to the orbit distortion produced by one misaligned quadrupole. To avoid the need to readjust the orbit after the wiggler field has been changed, it would be advantageous to center the wiggler by using its effect on the orbit as an indication of misalignment, analogous to the manner in which quadrupoles are sometimes physically aligned in an accelerator.

**3.3.4.2 Nonlinear Tune Shifts.** The reduction in dynamic aperture caused by the wiggler was examined by tracking an ensemble of particles (with different initial conditions) over 200 turns. The emittance coupling between horizontal and vertical motion was assumed to be 100%.

The nonlinear behavior is shown in Figs. 3-29 and 3-30, which give the variation of tune with amplitude for the cases of a wiggler with and without horizontal focusing, respectively. The values were found by Fourier analyzing the particle motion. The limits at higher amplitudes indicate the dynamical acceptance, i.e., the amplitude at which the motion becomes unstable. These values must be compared with the limit given by

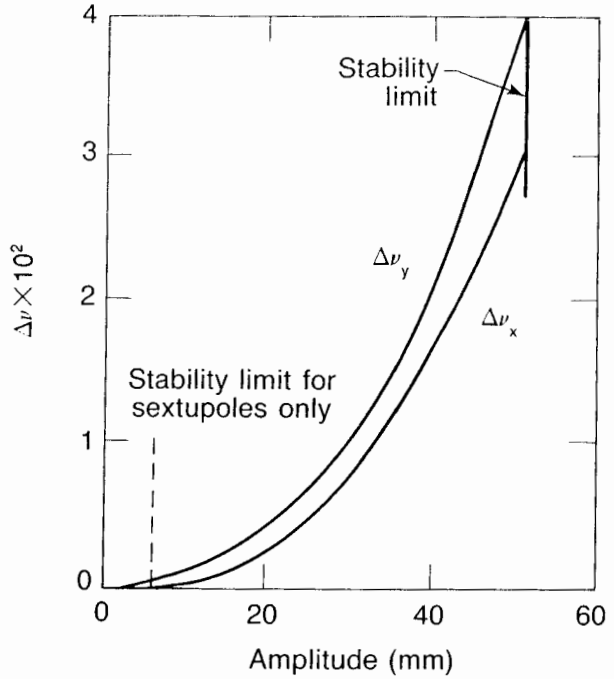


**Fig. 3-29.** Tunes as functions of amplitude (normalized to $\beta_x = 1$ meter), in the presence of a wiggler with $k_x = k_y$.

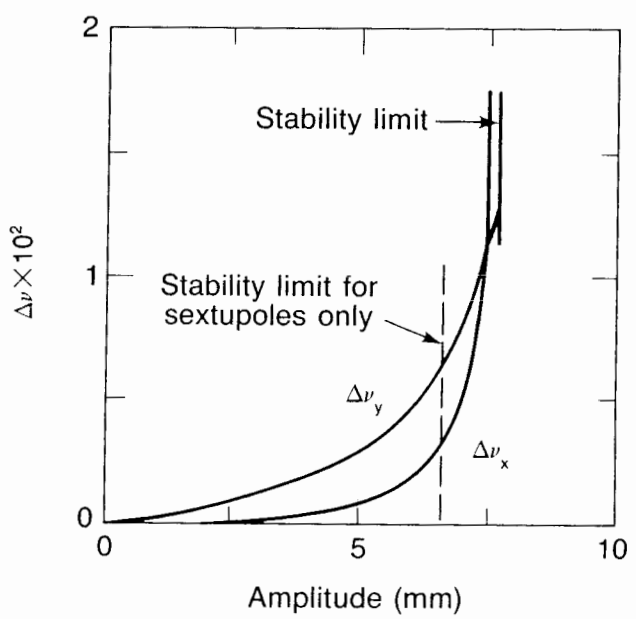


**Fig. 3-30.** Tunes as functions of amplitude (normalized to $\beta_x = 1$ meter), in the presence of a wiggler with $k_x = 0$.

chromaticity-correcting sextupoles only, which is 7.5 mm (for $\beta = 1$ meter). The amplitude-dependent tune shifts at the stability limit, produced by sextupoles only, are in the range of 0.1. Although the wiggler-produced tune shifts are smaller, they are not negligible. In the case of a wiggler with horizontal focusing (Fig. 3-29), $\beta_x$ is 0.85 meters after rematching, and the influence of the wiggler is greatly reduced. The stability limit is far above that given by chromaticity-correcting sextupoles only.

Figure 3-30 shows the results for $k_x = 0$, where the horizontal beta value after rematching is 12 meters. In this example, the nonlinear influence of the wiggler leads to a strong reduction in stable amplitude, which is comparable to the dynamic acceptance given by sextupoles.

The results emphasize that the beta values at the wiggler positions must be small after rematching to keep the nonlinear effects small. Then, apart from some narrow fourth-integer resonances, the dynamic limitations are determined entirely by chromaticity-correcting sextupoles. The results indicate that even a superconducting wiggler with a 5-T field is acceptable. As mentioned earlier, all insertion devices proposed for the Light Source have much weaker fields.

### 3.3.5 Detuned Version of the Lattice

Although we foresee no unusual problems associated with operating the storage ring with the parameters described above, it is prudent, with highly tuned machines, to consider a less sensitive lattice option—a so-called detuned version. With most lattice designs, the detuned version is formed by reducing the overall tune of the structure (by weakening the focusing of the quadrupole magnets). This in turn reduces the chromaticity and the strengths of the sextupoles required for correction. The aim is a structure with a larger natural emittance, a larger dynamic aperture, and reduced sensitivity to magnet errors and misalignments.

The problem with this procedure is that considerable time must be invested at each "detuned" tune point to establish good injection conditions, and they will only be found close to specific fractional tune values, i.e., close to 0.25. Since moving from the high-emittance configuration to one of low emittance usually means crossing an integer resonance, the experience gained in one regime is not always applicable to the next. In the case of the TBA structure, however, it is possible to detune the lattice *while maintaining exactly the same tune.* Thus, it is possible to inject into the less sensitive structure, make corrections, and then work continuously towards the low-emittance configuration, all with the same stored beam.

There is, however, a price to pay. The detuned optics obtained in this manner have dispersion in the insertion straight sections, as shown in Fig. 3-31. Any wiggler will then have a noticeable effect on the emittance, and synchro-betatron coupling may be introduced in the accelerating cavities. However, for machine start-up, we do not expect either of these aspects to be troublesome.

The dynamic aperture of the detuned lattice is shown in Fig. 3-32.

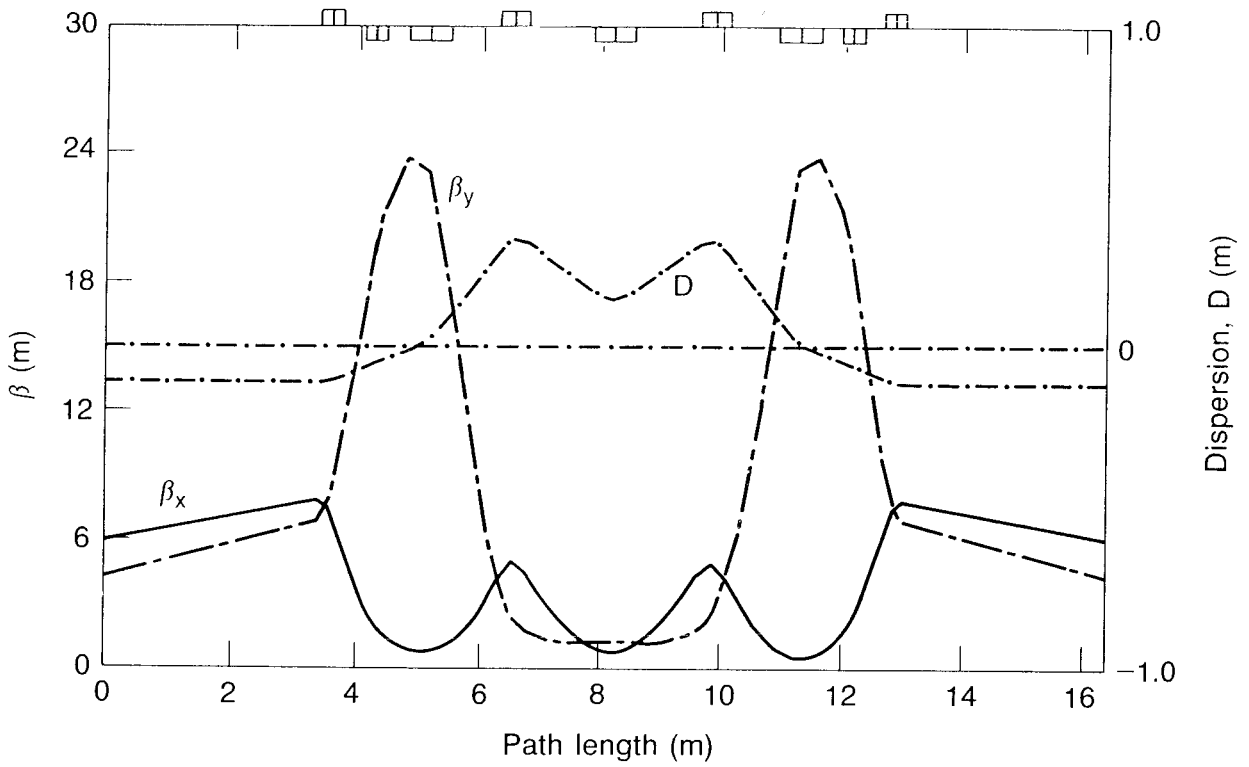


**Fig. 3-31.** Lattice functions through one unit cell of the detuned lattice.

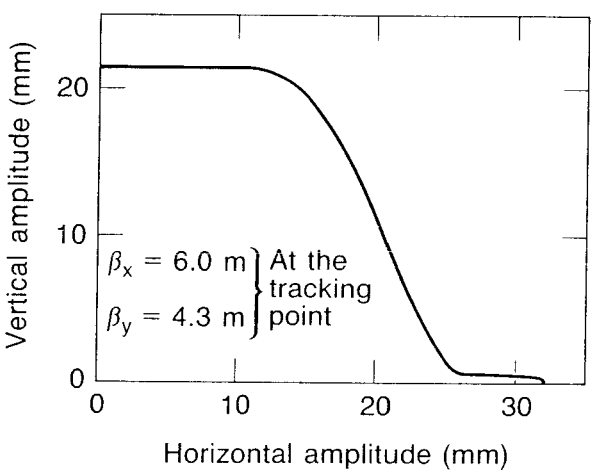


**Fig. 3-32.** Dynamic aperture of the detuned lattice.

### 3.3.6 Summary

We have simulated the effects of random magnetic field and magnet alignment errors and have demonstrated that the resultant orbit errors are correctable with the monitors and correctors in the lattice. The residual dispersion in the insertion regions (after orbit correction) is less than 5 mm and has a negligible influence on beam size.

With regard to bunch length, we find that if the SPEAR scaling assumption applies we can achieve very short bunches (about 20 ps) at a reasonable beam intensity. If the SPEAR scaling assumption is not valid, it will still be possible to achieve the beam intensity and emittance goals of the Light Source, but the bunches will be two or three times as long. Coupled-bunch results indicate that the longitudinal dipole synchrotron mode poses the most severe limit on beam stability. Growth rates are much faster than the radiation damping rate. However, we expect higher-order-mode suppression of the rf, feedback dampers, and special bunch configurations to limit the effect of coupled-bunch instabilities on beam quality. We find that emittance growth is not a serious issue for the machine. The growth can be a factor of two at low energies (about 1 GeV), but it is never enough to compromise performance. Without the SPEAR scaling assumption, the growth is even smaller. Both the single- and multibunch lifetimes are in excess of 6 hours for an undulator gap of 2 cm; the single-bunch lifetime would decrease somewhat below 6 hours if a 1-cm undulator gap were used but the multibunch lifetime remains in excess of 6 hours. Should it be necessary or desirable to run with a larger horizontal-vertical emittance ratio (e.g., 100:1 rather than 10:1), the lifetimes would drop significantly.

Our studies of ion trapping indicate that the introduction of a gap in the bunch train will eliminate the trapping of most ion species and that an "ion ladder" cannot be built up. We have also investigated the linear and nonlinear effects on beam dynamics due to the introduction of a very strong wiggler into the lattice. We find that the linear optics distortions can easily be compenstated by rematching lattice quadrupoles. Proper alignment of the wiggler will be important, however, to avoid the need for orbit readjustments each time the wiggler gap is adjusted.

We conclude that our storage ring design (based on the TBA lattice structure) does meet the demanding requirements for a next-generation synchrotron radiation source.

## 3.4 Storage Ring Magnets and Supports

The accurate construction and alignment of storage ring magnets are crucial to the proper operation of the Light Source; existing storage ring technology, with some adaptations, can meet the challenge. The ring magnets are of six types:

- Gradient bending magnets, which have the combined function of bending and focusing the beam.
- Quadrupole magnets to focus the beam.
- Sextupole magnets for chromaticity correction.
- Skew quadrupoles to control vertical beam size.
- Small dipole magnets for vertical and horizontal steering.
- Special septum and bump magnets for injecting beam from the booster into the storage ring.

This section describes the engineering details of these magnets, their stands and supports, and the procedures for installing them.

### 3.4.1 Bending Magnets

The storage ring bending magnets are of a C configuration, as shown in Fig. 3-33, to permit the easy extraction of synchrotron radiation and to accommodate the vacuum chamber (described in more detail in Section 3.5). The magnet pole tips have a hyperbolic contour so that they provide a combined dipole and quadrupole magnetic field. Many combined-function magnets of this general configuration have been built in past years, so the technology is well-proven. The corners of the poles are computer optimized to minimize the pole width, consistent with preserving field quality and avoiding magnetic saturation. The magnet return yoke is also proportioned to avoid saturation up to the 1.9-GeV excitation level.

We chose to construct the magnet from 1.5-mm-thick laminations of decarburized, annealed, low-carbon steel sheet (Armco special magnet steel) because of its high saturation induction and modest coercive force. This type of steel has been used for many accelerator magnets, including those at PEP and Fermilab. The laminations are punched to a precision of $\pm 13$ $\mu$m (0.0005 in.) along the critical profiles. Die clearance is kept to a minimum to reduce burr size along the edges of the laminations. Production of the laminations will be carried out under commercial contract.

Construction of the magnet cores will be carried out at LBL so that assembly techniques and tolerances can be closely monitored. Prior to stacking, the laminations are shuffled to provide uniformity of magnetic characteristics and half are flipped about their horizontal center line to minimize top-bottom symmetry errors. To form the magnet core, the laminations are stacked on an arc, as shown in Fig. 3-34, so that the pole center line follows the arc of the electron beam trajectory. End plates are constructed from a packet of 15 laminations glued together with epoxy resin. These laminations are shaped to form a smoothly increasing gap in order to avoid saturation at the ends of the magnet. Side bars are then welded to the laminations and end plates.

These construction techniques should easily keep the systematic and random sextupole error below the values of 0.05 $m^{-3}$ and 0.10 $m^{-3}$ rms assumed in Appendix C. Indeed, dipole magnets at existing storage rings (PEP, Daresbury) have demonstrated significantly lower values. The specified magnetic strength ($B \times \ell$) random error from magnet to magnet of $1 \times 10^{-3}$ corresponds to a magnet gap deviation of 50 $\mu$m or a length deviation of 0.7 mm, i.e., half the thickness of a lamination. It is unrealistic to expect all of the bending magnets to meet this criterion, so it is planned that small shunt resistors will be added. During magnetic measurements, the dipoles will be trimmed so that all magnets will satisfy the $1 \times 10^{-3}$ random field strength criterion.

The coils for the bending magnets are constructed as flat pancakes of 0.64-in.-square copper conductor with a 0.32-in.-diameter cooling channel, wrapped with insulation tape and impregnated with epoxy resin. It is anticipated that the coils will be fabricated commercially, as there are many firms in the San Francisco Bay area with proven capability in this type of work. The major parameters for the storage ring bending magnets at 1.9 GeV are given in Table 3-13.

### 3.4.2 Quadrupole Magnets

The storage ring quadrupole magnets have computer-optimized pole-tip contours, similar to those of the PEP insertion quadrupoles that were built at LBL [Avery et al., 1979]. The magnets are of two-piece construction (as shown in Figs. 3-35 and 3-36), which gives mag-

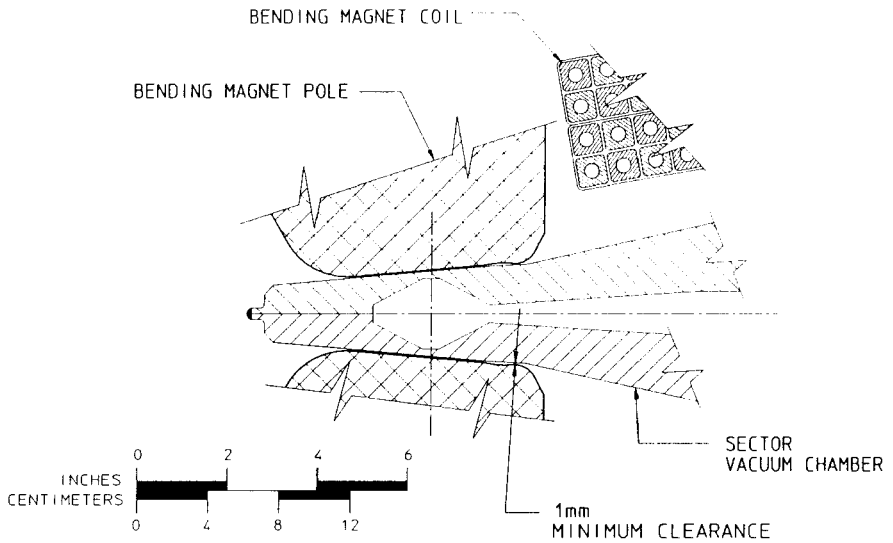


POLE AREA DETAIL

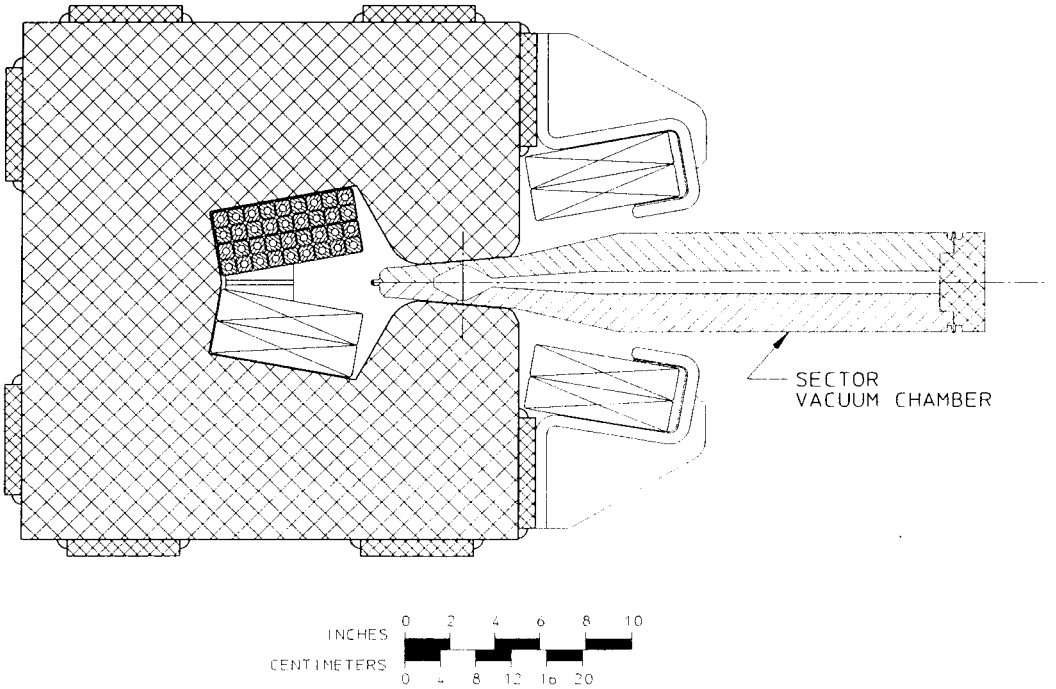


**Fig. 3-33.** Storage ring bending magnet cross section, including a close-up view of the pole area.

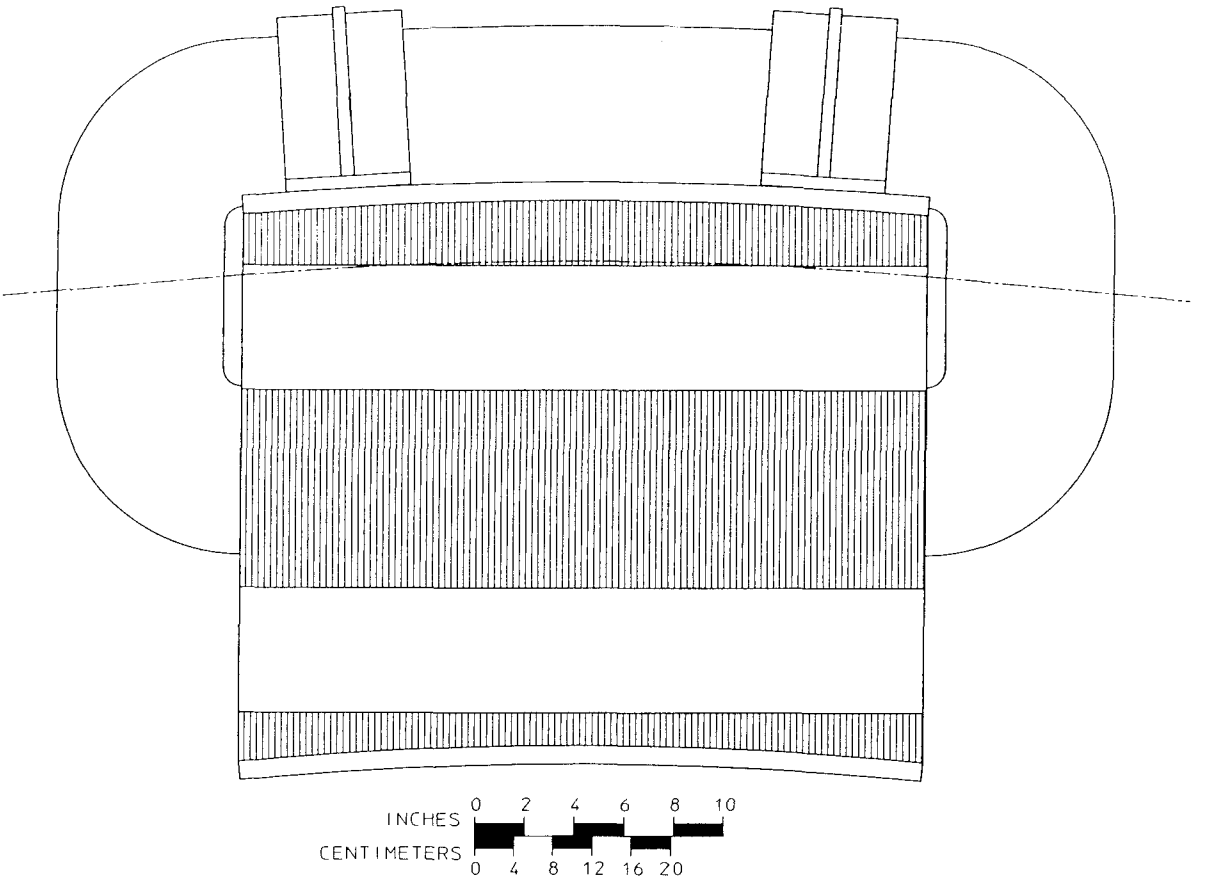


**Fig. 3-34.** Storage ring bending magnet plan view.

**Table 3-13.** Storage ring bending magnet parameters at 1.9 GeV.

| | |
|---|---|
| Number of magnets | 36 |
| Bend angle (deg) | 10 |
| Magnetic flux density on orbit (T) | 1.580 |
| Gradient parameter, $k$ ($m^{-2}$) | −1.0 |
| Magnetic length (m) | 0.70 |
| Magnet gap on orbit (mm) | 50 |
| Good field width (mm) | ±12.5 |
| Good field height (mm) | ±20.0 |
| Steel weight per magnet (lb) | 3700 |
| Conductor copper weight (lb) | 760 |
| Total magnet weight (lb) | 4600 |
| Number of turns, total | 72 |
| Current (A) | 919 |
| Conductor area ($mm^2$) | 214 |

**Table 3-13.** continued.

| | |
|---|---|
| Voltage drop (V) | |
| per magnet | 14.1 |
| 36 magnets, excluding leads | 508 |
| Power (kW) | |
| per magnet | 13.0 |
| 36 magnets, excluding leads | 468 |
| Inductance per magnet (mH) | 16 |
| Water circuits per magnet | 2 |
| Water flow per magnet (U.S. gpm) | 2.5 |
| Water pressure drop (psi) | 70 |

netic symmetry about both vertical and horizontal axes. The upper and lower halves are of a C configuration so that there is no joint in the magnetic circuit which could contribute magnetic field errors. The return leg of the C provides rigidity and proper alignment of the two poles relative to one another. The magnet cores are built up from laminations punched from the same type of steel sheet as used for the bending magnets, with the same precise tolerances on the critical profiles. Again, shuffling and flipping are carried out before assembly. For the quadrupoles, a packet of laminations is cut back to form a chamfer at the ends of the magnet in order to minimize the 12-pole and 20-pole magnetic field com-

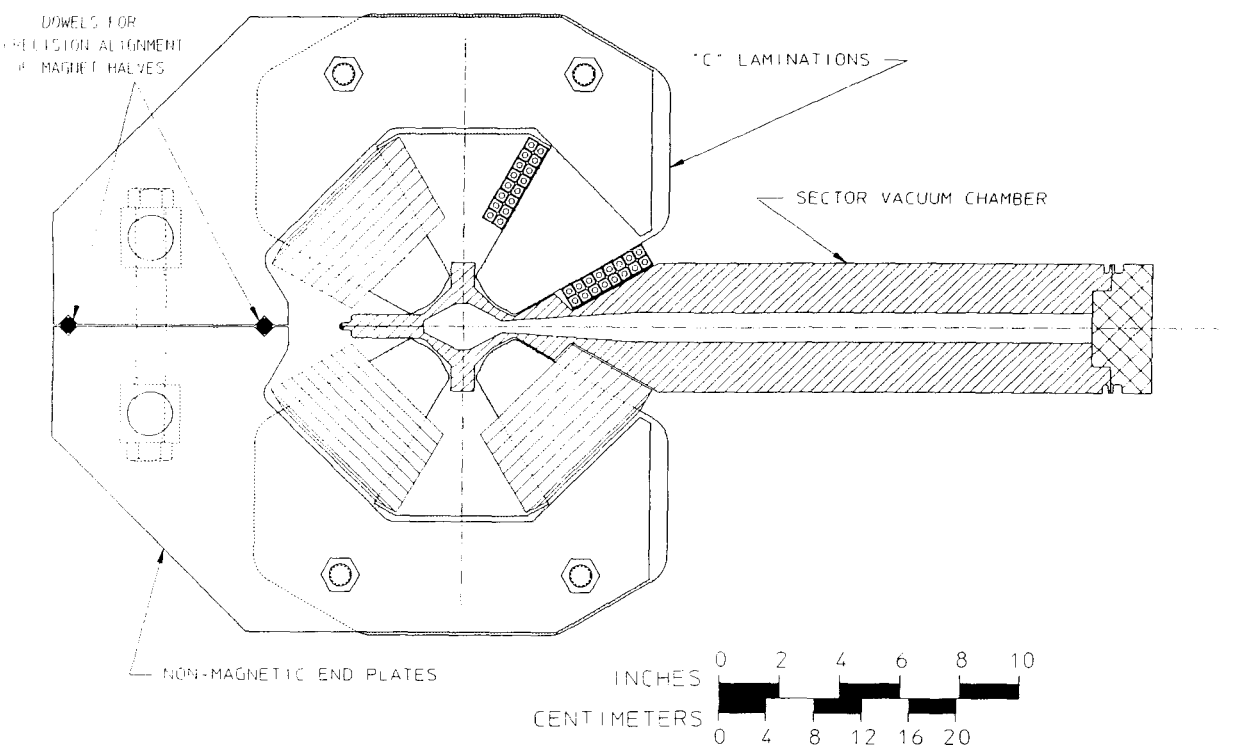


**Fig. 3-35.** Storage ring quadrupole magnet cross section.

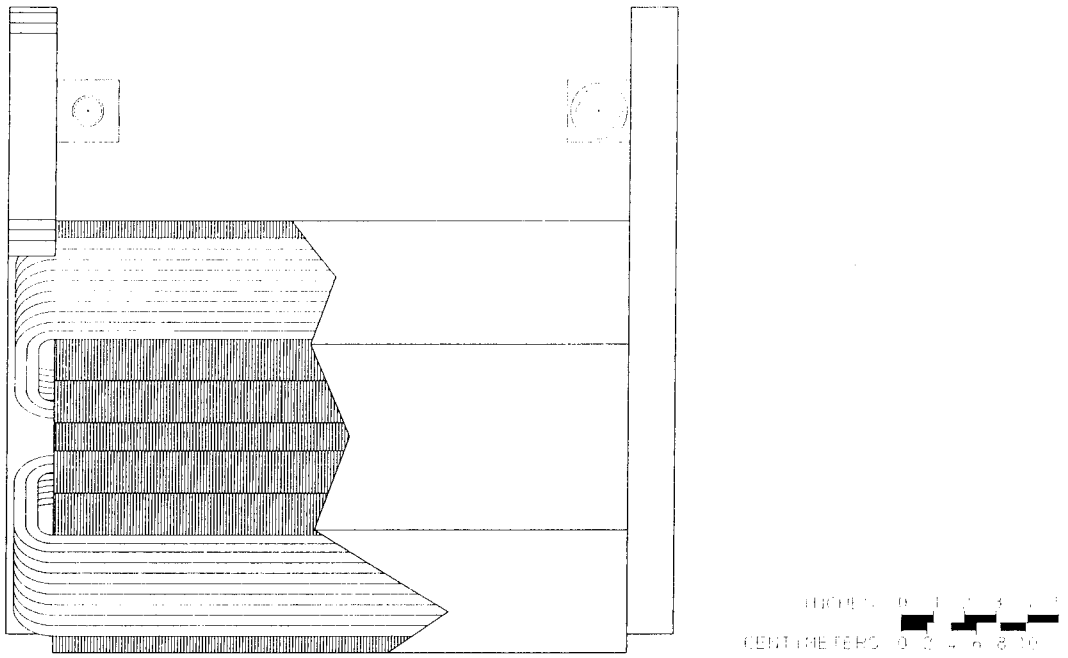

**Fig. 3-36.** Storage ring quadrupole magnet plan view.

ponents. To assemble the cores, the laminations are stacked on a precision granite surface plate with straight granite bars for alignment.

The end plates of the magnet halves are nonmagnetic and extend to the median plane on the inner side of the ring. After stacking, tie rods are used to pull the end plates together, then weld beads are run along the block edges to prevent any further movement of the laminations. The magnetic lengths of the Q1, Q2, and QF1 magnets are 0.35, 0.20, and 0.50 meters, respectively, but otherwise, the magnet yokes are identical. The coils for the quadrupoles are wound with hollow, square copper conductor, with a 0.18-in.-diameter cooling channel, tape insulated, and epoxy impregnated. The Q1 and Q2 magnets are individually powered, so their coils are wound with 66 turns per pole of 0.162-in.-square hollow conductor to reduce the current required from the power supplies. In contrast, the QF1 magnets are powered as a series string of 24 magnets, so their coils are wound with 16 turns per pole of 0.34-in.-square, hollow conductor to reduce the voltage required from the power supply. The conductor sizes were selected so that both coil types fit within the same exterior dimensions and thus can be potted in the same coil mold.

To assemble the complete magnet, the coils are first installed on the yoke halves. The two halves are then aligned relative to each other by means of precision dowel pins in the V grooves. This technique was refined for the highly sensitive PEP insertion quadrupoles that were built at LBL. During magnetic field measurements, the pins can be changed in increments as small as 2.5 $\mu$m (0.0001 in.) to achieve proper alignment of the upper and lower halves of the magnet. Experience with the PEP insertion quadrupoles demonstrated that magnets built with this technique can be split and reassembled with no significant loss in magnetic field quality. The foregoing fabrication techniques should keep the systematic and random multipole field errors at or below the values assumed in Appendix C. Those assumed values are already considerably relaxed compared with the values actually

achieved for the PEP insertion quadrupole magnets. As described for the bending magnets, small shunt resistors will be added during magnetic measurements so that the gradient × length product satisfies the specified $1 \times 10^{-3}$ random magnet-to-magnet error.

As with the bending magnets, it is envisaged that the laminations and the potted coils will be produced commercially, with the remaining assembly carried out at LBL. The major parameters of these magnets are presented in Table 3-14.

### 3.4.3 Sextupole Magnets

The configuration of the storage ring sextupole magnets is shown in Figs. 3-37 and 3-38. The laminated magnet yoke is made in three sections, each incorporating two poles, to facilitate installation around the vacuum chamber. These magnets also include the capability to provide horizontal and vertical steering, and skew quadrupole fields, as will be described below.

The magnet yokes are constructed from 0.64-mm (0.025 in.) M36 silicon steel laminations, coated with a C5 insulating film, to give a fast response capability to the dipole steer-

**Table 3-14.** Storage ring quadrupole magnet parameters at 1.9 GeV.

| | Q1 | Q2 | QF1 |
|---|---|---|---|
| Number of magnets | 24 | 24 | 24 |
| Magnetic length (m) | 0.35 | 0.20 | 0.50 |
| Magnet aperture radius (mm) | 32.5 | 32.5 | 32.5 |
| Good field radius (mm) | 30.0 | 30.0 | 30.0 |
| Gradient, maximum (T/m) | 17.0 | 17.0 | 17.0 |
| Flux density at pole apex (T) | 0.55 | 0.55 | 0.55 |
| Steel weight per magnet (lb) | 680 | 400 | 980 |
| Conductor copper weight (lb) | 64 | 44 | 84 |
| Total magnet weight (lb) | 900 | 600 | 1210 |
| Number of turns per pole | 66 | 66 | 16 |
| Current (A) | 110 | 110 | 456 |
| Conductor area ($mm^2$) | 12.5 | 12.5 | 57 |
| Voltage drop (V) | | | |
| per magnet | 38.2 | 25.5 | 11.2 |
| 24 magnets, excluding leads | — | — | 269 |
| Power (kW) | | | |
| per magnet | 4.20 | 2.81 | 5.13 |
| 24 magnets, excluding leads | — | — | 123 |
| Inductance (mH) | 70 | 40 | 5.8 |
| Water circuits per magnet | 2 | 2 | 2 |

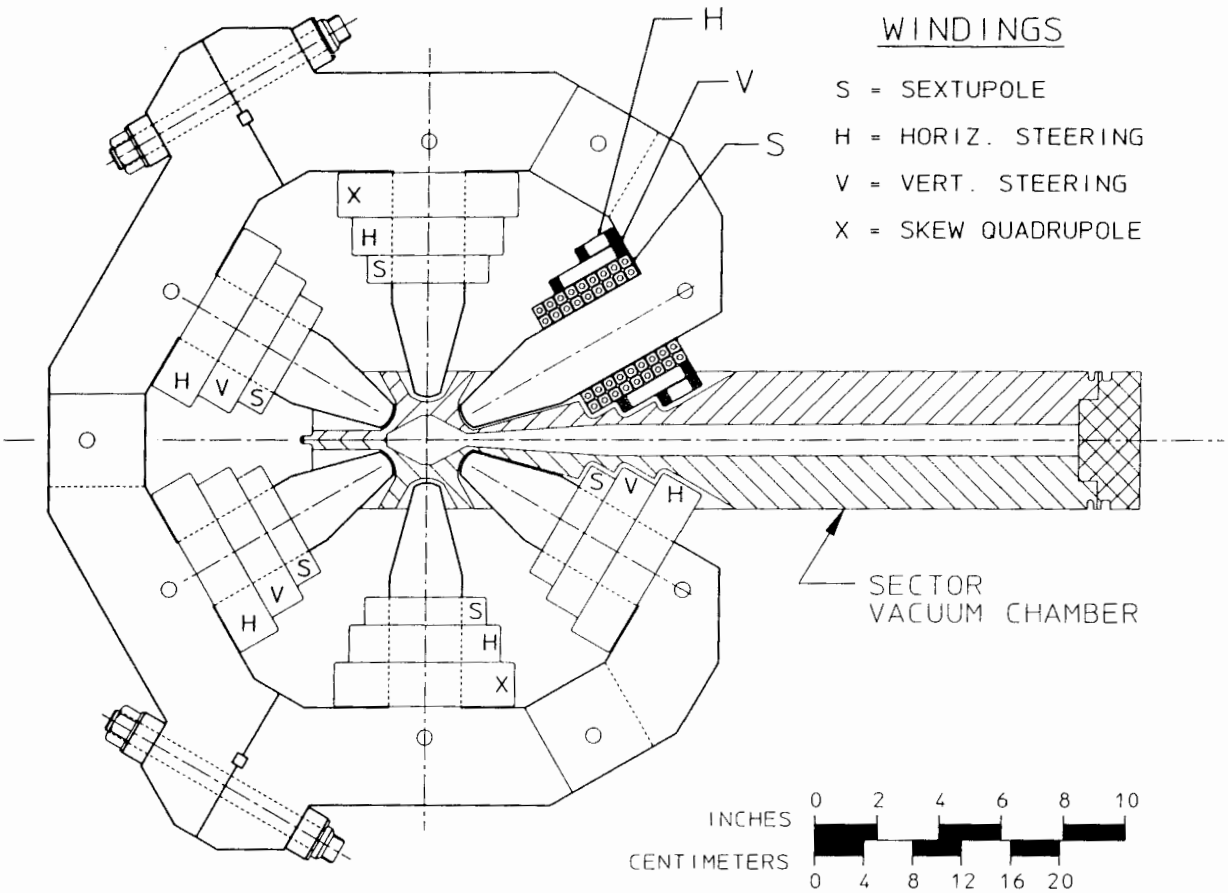


**Fig. 3-37.** Storage ring sextupole magnet cross section.

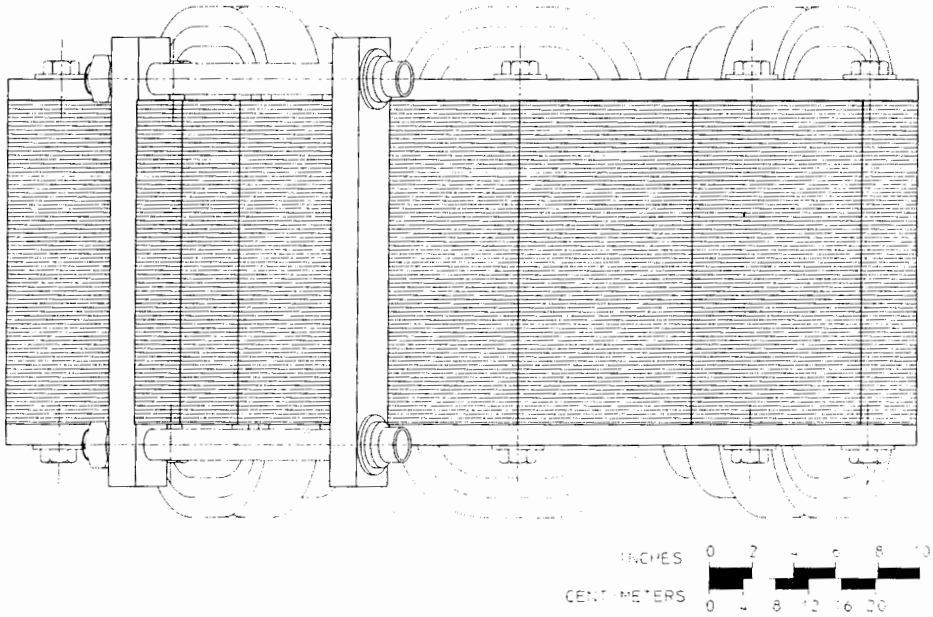

**Fig. 3-38.** Storage ring sextupole magnet plan view.

ing component. Each of the three sections is made up of two individual cores, one pole per core, stacked individually. After the coils are fitted to the pole, two core subassemblies are brought together, with the laminations interdigitated at the joint. (This type of joint is used successfully in almost all ac transformer construction.) Nonmagnetic end plates with tie bolts hold each pole pair assembly together.

Each pole of the sextupole magnet has a coil assembly containing three separate windings:

- 18 turns, LBL standard 0.34-in.-square hollow copper conductor, tape insulated, for sextupole excitation.
- 90 turns, #10 AWG heavy epoxy-coated magnet wire, for steering capability.
- 45 turns, #10 AWG heavy epoxy-coated magnet wire, used either for steering or for skew quadrupole field excitation.

Each coil assembly is epoxy impregnated to form a single coil unit. The magnet wire windings are cooled by conduction to the water-cooled sextupole windings. The function of each winding is shown in Fig. 3-37.

Table 3-15 gives the principal parameters for the sextupole magnets.

**Table 3-15.** Storage ring sextupole magnet parameters at 1.9 GeV.

| | |
|---|---|
| Number of magnets (24 SD + 24 SF) | 48 |
| Magnetic length (m) | 0.20 |
| Magnet aperture radius (mm) | 35.0 |
| Good field radius (mm) | 30.0 |
| Sextupole parameter, $S = B/r^2$, max (T/m$^2$) | 500 |
| Flux density at pole apex (T) | 0.61 |
| Steel weight per magnet (lb) | 650 |
| Copper weight per magnet, all coils (lb) | 125 |
| Total magnet weight (lb) | 850 |
| Number of turns per pole | 18 |
| Current (A) | 329 |
| Conductor area (mm$^2$) | 57 |
| Voltage drop (V) | |
| per magnet | 6.9 |
| 24 magnets, excluding leads | 165 |
| Power (kW) | |
| per magnet | 2.26 |
| 24 magnets, excluding leads | 54 |
| Inductance per magnet (mH) | 6.3 |

### 3.4.4 Skew Quadrupoles

Skew quadrupole magnets provide coupling of horizontal betatron oscillations into the vertical plane to provide control of the vertical size of the electron beam. If the poles of the sextupole magnets that are located at 6 and 12 o'clock are energized with the same polarity, they produce a significant skew quadrupole field. Special windings of magnet wire are incorporated into the ring sextupole coils, as described above, to provide this skew quadrupole excitation. These windings are cooled by the adjacent water-cooled conductors of the sextupole coils. The 6 and 12 o'clock poles of four adjacent sextupole magnets are connected in series to form one skew quadrupole circuit, each requiring a maximum current of 5A. The storage ring includes four such circuits. The principal parameters of the skew quadrupole circuits are given in Table 3-16.

**Table 3-16.** Storage ring skew quadrupole magnet parameters. Each circuit consists of two windings on four adjacent quadrupole magnets.

| | |
|---|---|
| Number of circuits | 4 |
| Gradient × length, max/circuit (T) | 0.6 |
| Current (A) | 8.1 |
| Voltage per circuit (V) | 8.1 |
| Power per circuit (kW) | 0.066 |

### 3.4.5 Steering

Horizontal and vertical steering is provided for closed-orbit correction, as described in Section 3.3.1.2. In addition to the steering capability included in the sextupole magnets, there are 48 steering magnets of the design shown in Figs. 3-39 and 3-40, situated at the ends of the insertion straight sections (four per straight).

The magnet yoke is of a C configuration to permit installation around the vacuum chamber. It consists of laminations punched from 0.64-mm-thick M36 silicon steel sheet, with C5 insulation coating, held together with tie bolts. Each magnet has a pair of coils, one per pole, to produce a vertical field for horizontal steering. The coils consist of 112 turns of #10 AWG heavy epoxy-coated magnet wire, wound onto a water-cooled form and epoxy impregnated.

Vertical steering is provided by windings of 0.255-in.-square hollow copper conductor, wound in four layers along the pole faces of the magnet. The coil is epoxy impregnated for rigidity and for additional electrical insulation.

To provide additional steering, magnet wire windings are incorporated into the coils of the 48 ring sextupole magnets. Excitation of the poles at 2 and 4 o'clock with one polarity and those at 8 and 10 o'clock with the opposite polarity provides vertical steering. Excitation of the poles at 10, 12, and 2 o'clock with one polarity (those at 10 and 2 at about half intensity) and the poles at 4, 6, and 8 o'clock with the opposite polarity provides horizontal steering. The storage ring thus includes 96 horizontal and vertical steering elements; the principal parameters of both types of steering elements are given in Table 3-17. (Since the

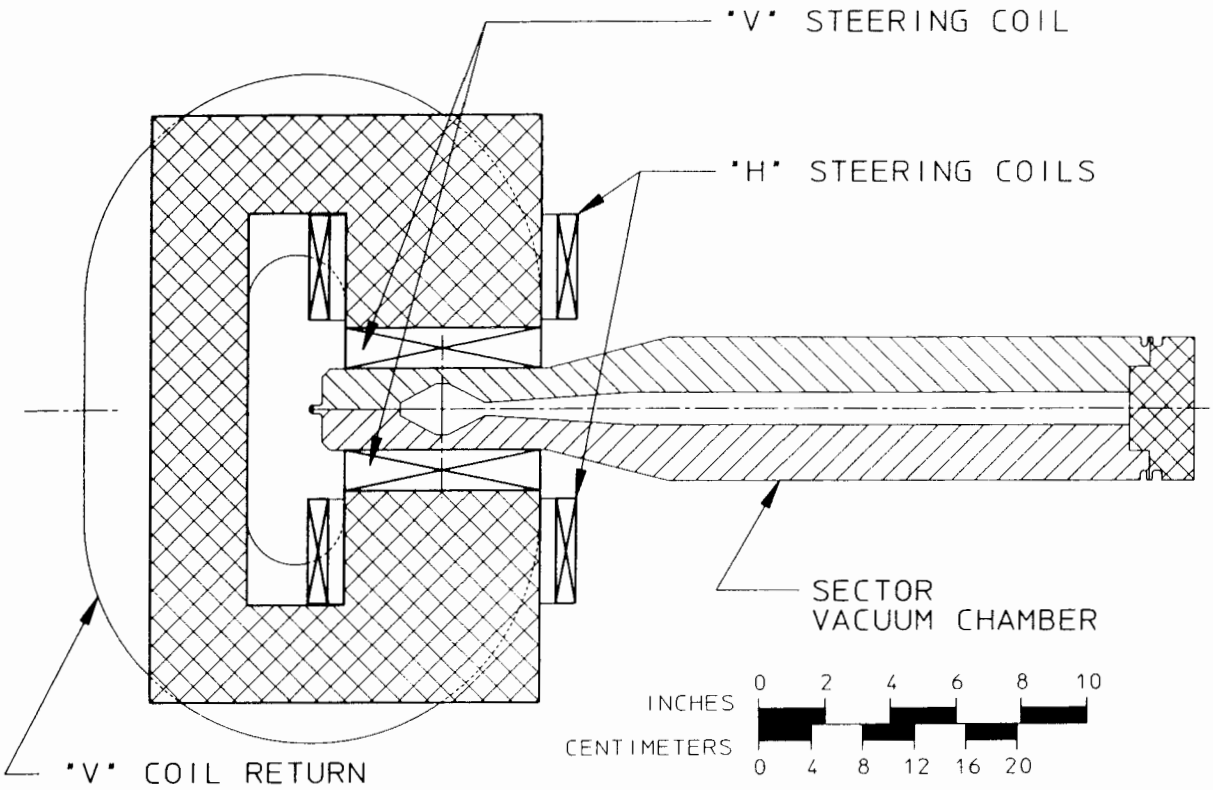


**Fig. 3-39.** Storage ring steering magnet cross section.

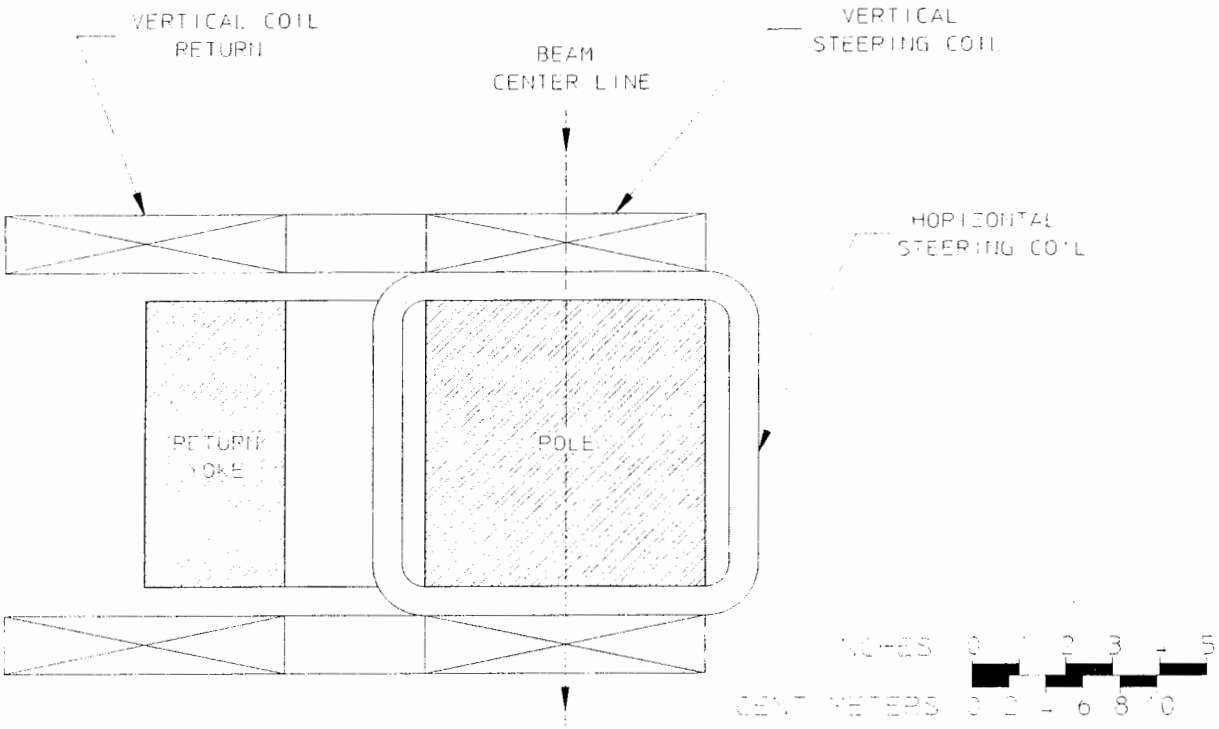


**Fig. 3-40.** Storage ring steering magnet plan view.

vertical tune in the storage ring is significantly smaller than the radial tune, we envisage utilizing only 24 out of the possible 48 vertical steering elements available in the sextupole magnets. This decision is supported by the excellent closed-orbit correction achieved in simulations with this reduced number of correctors.)

**Table 3-17.** Storage ring steering magnet parameters. Sextupole steering elements consist of special windings in the ring sextupole magnets that produce horizontal and vertical steering dipole fields.

| | "C" Steering magnets | | Sextupole steering elements | |
|---|---|---|---|---|
| | H | V | H | V |
| Number of elements installed | 48 | 48 | 48 | 48 |
| Number of circuits installed | 48 | 48 | 48 | 24 |
| Magnetic flux density (T) | 0.07 | 0.07 | 0.07 | 0.07 |
| Magnetic length (m) | 0.20 | | 0.20 | |
| Magnet aperture radius (mm) | 63 | | 35 | |
| Steel weight per magnet (lb) | 265 | | — | |
| Conductor copper weight (lb) | 20 | 130 | — | |
| Total magnet weight (lb) | 500 | | — | |
| Current (A) | 33 | 116 | 23 | 23 |
| Voltage, excluding leads (V) | 21 | 12.2 | 23 | 23 |
| Power, excluding leads (kW) | 0.69 | 1.41 | 0.53 | 0.53 |

### 3.4.6 Injection Magnets

Injection into the storage ring is achieved by a combination of a thick septum magnet and a thin septum magnet, which the incoming electrons traverse, and a set of four fast bump magnets that move the circulating beam orbit close to the septum. Both septum magnets are located inside the ultrahigh-vacuum environment of the storage ring, while the bump magnets are located outside of ceramic sections of the ring vacuum chamber. The septum magnets and their vacuum enclosure can be baked *in situ* to achieve the desired vacuum. The components all utilize well-proven technology used at several laboratories, including Brookhaven, Fermilab, Daresbury, and CERN.

The thick septum magnet is shown in Fig. 3-41. It is constructed of 0.36-mm-thick (0.014 in.) silicon steel laminations, with an insulation coating. These laminations are stacked so that the magnet follows the curved trajectory of the incoming electrons. This minimizes the magnet pole width and allows the use of the same magnet design for booster extraction. The principal parameters of this magnet are given in Table 3-18.

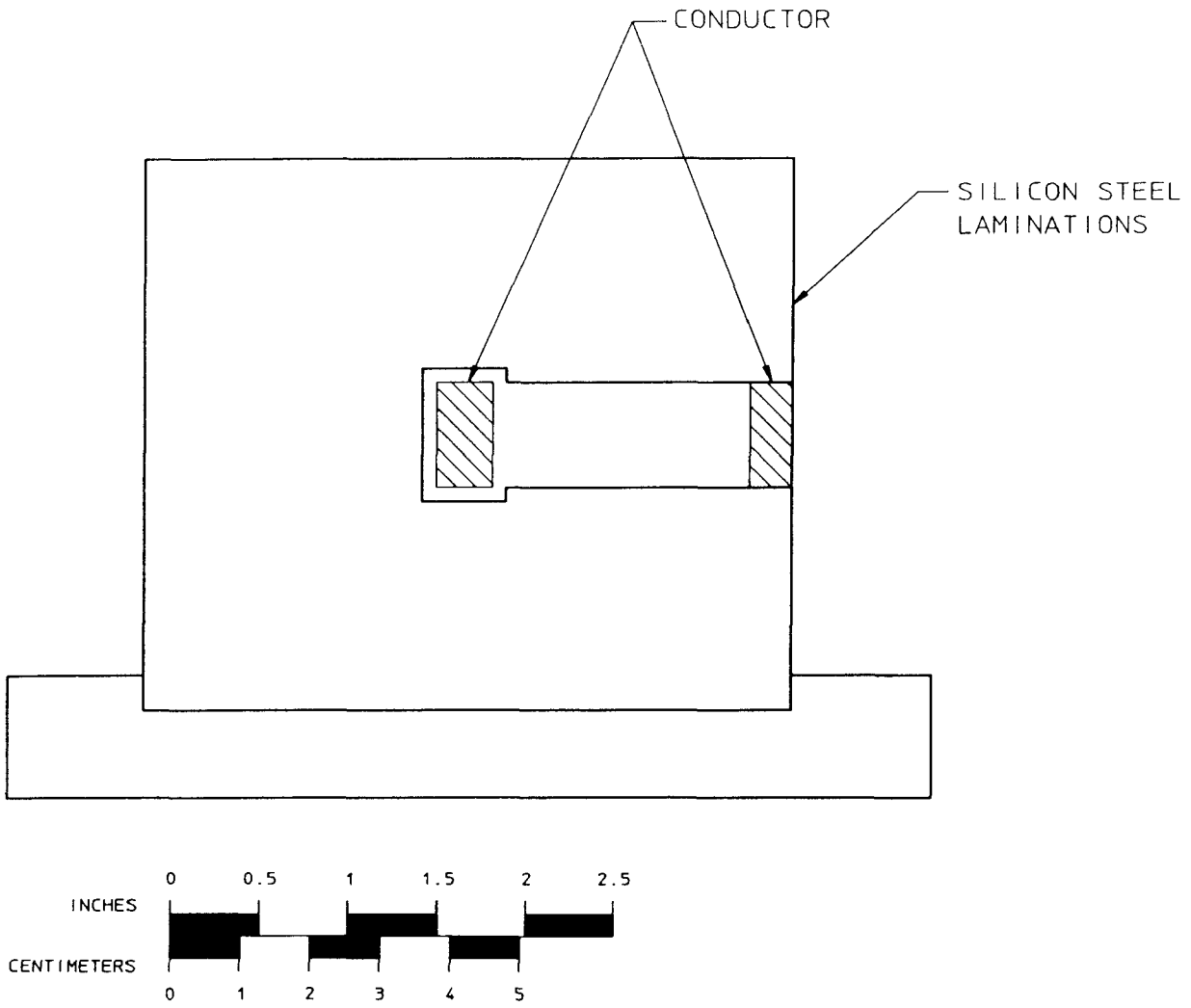


**Fig. 3-41.** Thick septum magnet cross section.

The thin septum magnet is shown in Fig. 3-42. The magnet is constructed of a manganese-zinc ferrite, surrounded by copper except for an entrance and exit port. Eddy currents in the copper capture the magnetic field within the thin septum magnet, so there is almost no leakage field to reach the circulating electron beam orbit. The magnet is energized by a single-turn copper winding around the back leg of the magnet. This type of "passive" septum has been used successfully at Daresbury and other laboratories. The principal parameters are given in Table 3-19.

Four bump magnets are connected in series to generate a local beam displacement toward the thin septum. These magnets are constructed of nickel-zinc ferrite in a window-frame geometry and are energized by a single-turn copper conductor, as shown in Fig. 3-43. A high-alumina ceramic vacuum chamber is located inside the magnet aperture. The inside of the ceramic chamber receives a slightly conductive coating to present a low impedance to the circulating electron bunches, yet it has enough resistance to permit the pulsed magnetic fields to penetrate. Table 3-20 gives the principal parameters of the bump magnets.

**Table 3-18.** Storage ring thick septum magnet parameters at 1.5 GeV.

| | |
|---|---|
| Core material | Silicon steel laminations, 0.356-mm Armco Di-Max M22-C5 |
| Length (m) | 1.0 |
| Septum thickness (mm) | 6.0 |
| Bend angle (deg) | 8.0 |
| Beam aperture (mm) | |
| Vertical | 15 |
| Horizontal | 16 |
| Magnet aperture (mm) | |
| Vertical | 15 |
| Horizontal | 37 |
| Magnetic field (T) | 0.698 |
| Number of coil turns | 1 |
| Current (A) | |
| Peak | 8330 |
| Rms | 58.9 |
| Repetition rate (Hz) | 1 |
| Current waveform | Half sine-wave |
| Current duration ($\mu$s) | 100 |
| Inductance ($\mu$H) | |
| Magnet | 3.15 |
| Total | 3.65 |
| Total ac resistance (m$\Omega$) | 3.12 |
| Voltage, peak, total (V) | 954 |

### 3.4.7 Magnetic Field Measurements

An area will be set up and equipped specifically for magnetic field mapping of the Light Source magnets. Available measuring devices will include: NMR for accurate calibration, curved search coils to determine the integrated fields through the bending magnets, "Halbach" search coil arrays for multipole component measurements in the quadrupole and sextupole magnets [Main et al., 1979], and line integral coils to measure the integrated field through the pulsed injection magnets.

All magnets will be standardized by carrying out a specific set of field excursions. Their magnetic performance will then be measured over the full range of excitation that they will experience in service. Included in this last set of measurements will be the perturbations due to adjacent magnets in the lattice. In the case of the quadrupole and sextupole magnets, checks on field reproducibility after breakdown and reassembly of the magnets will also be made. All data will be retained for the life the Light Source, should questions arise regarding the performance of individual magnets.

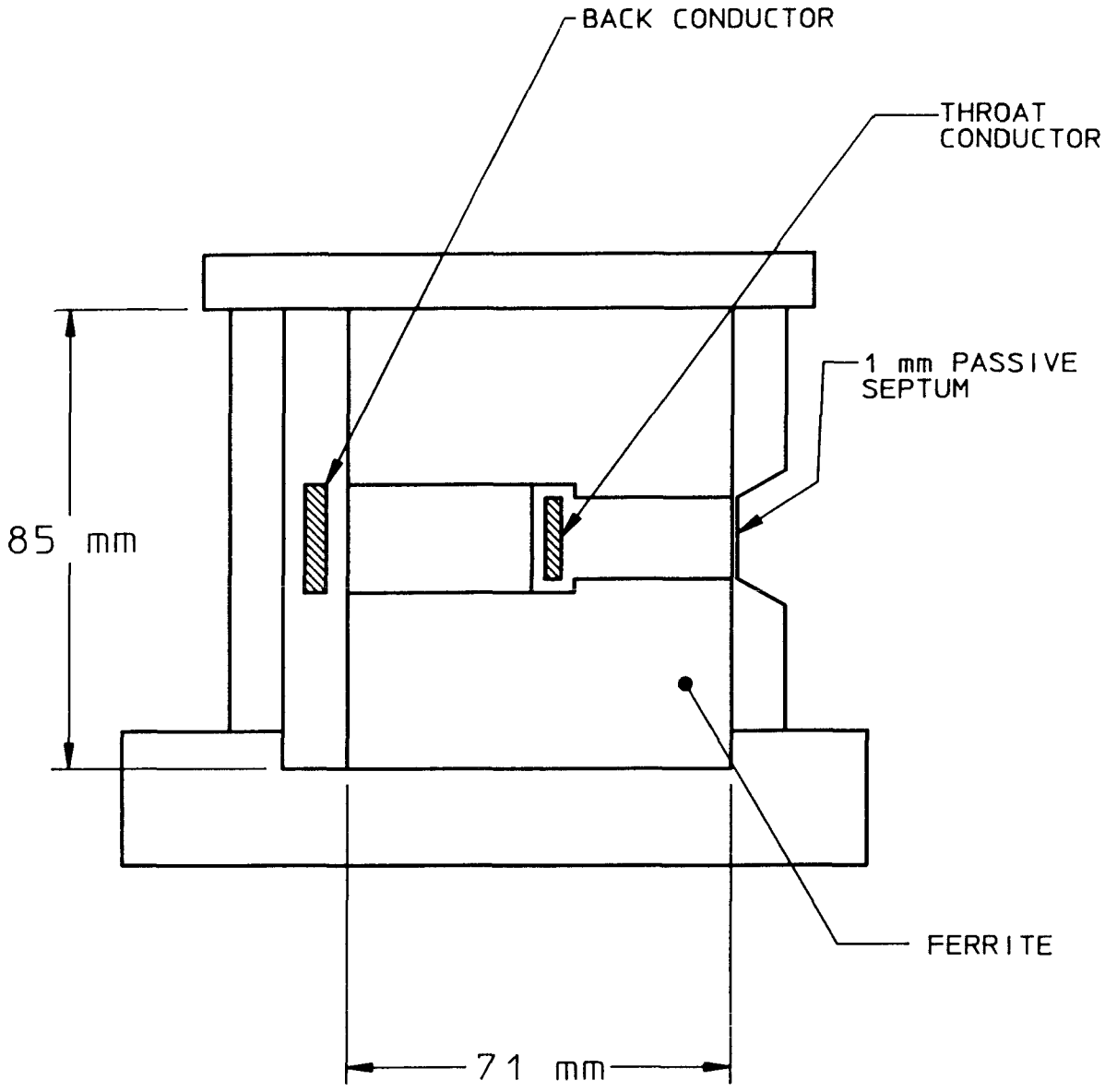


**Fig. 3-42.** Thin septum magnet cross section.

### 3.4.8 Support and Alignment

The proper support and alignment of the storage ring magnets are essential to the performance of the Light Source. All of the magnets (three dipoles, six quadrupoles, four sextupoles, and four steering dipoles) in each sector (one-twelfth) of the storage ring are mounted onto a single stress-relieved structural-steel box girder, as shown in Fig. 3-44. The steel girder was selected in preference to reinforced concrete because of its greater stability against slow creep and hairline cracking, as experienced at SLAC. The calculated static deflections of the steel girder due to the weight of the superposed load is a fraction of a millimeter, and the reproducibility of these deflections is a small fraction of that value. In the assembly shop, all of the magnets and the vacuum chamber for one sector are assembled on

**Table 3-19.** Storage ring thin septum magnet parameters at 1.5 GeV.

| | |
|---|---|
| Core material | Manganese-zinc ferrite<br>Ceramic Magnetics MN 67 |
| Length (m) | 0.6 |
| Septum thickness (mm) | 1.0 |
| Bend angle (deg) | 2.5 |
| Beam aperture (mm) | |
| Vertical | 15 |
| Horizontal | 16 |
| Magnet aperture (mm) | |
| Vertical | 15 |
| Horizontal | 33 |
| Magnetic field (T) | 0.364 |
| Number of coil turns | 1 |
| Current (A) | |
| Peak | 4350 |
| rms | 13.8 |
| Repetition rate (Hz) | 1 |
| Current waveform | Half sine-wave |
| Current duration ($\mu$s) | 20 |
| Inductance ($\mu$H) | |
| Magnet | 1.7 |
| Total | 2.2 |
| Total ac resistance (m$\Omega$) | 5.26 |
| Voltage, peak, total (V) | 1503 |

the girder, then precision aligned to an accuracy of better than 0.15 mm, using shim stacks under each magnet. Water-cooling manifolds are assembled to the girder at this stage, as are hoses to the components to be cooled. Electrical circuits are connected and brought to connectors. With all of this work being done in a shop rather than in the Light Source building, the work can be performed more efficiently, with higher quality and more reliable inspection. This approach also permits each assembled girder to be installed and connected in about one week, thereby speeding up the storage ring installation program.

The assembled girder is supported and aligned in the storage ring, using the same types of struts that were successfully used for the PEP magnets. There are six such struts (three vertical, two lateral, and one longitudinal), one each for the six degrees of freedom of a rigid body. Since all of these struts are in axial compression or tension, they provide very rigid support of the elements on the girder. The support struts are strong enough to support the maximum credible seismic event at this site. The assembled girder is aligned so that the magnets are all within 0.15 mm of their intended position. If there should be any settlement, only the girder struts need to be adjusted, not every magnet.

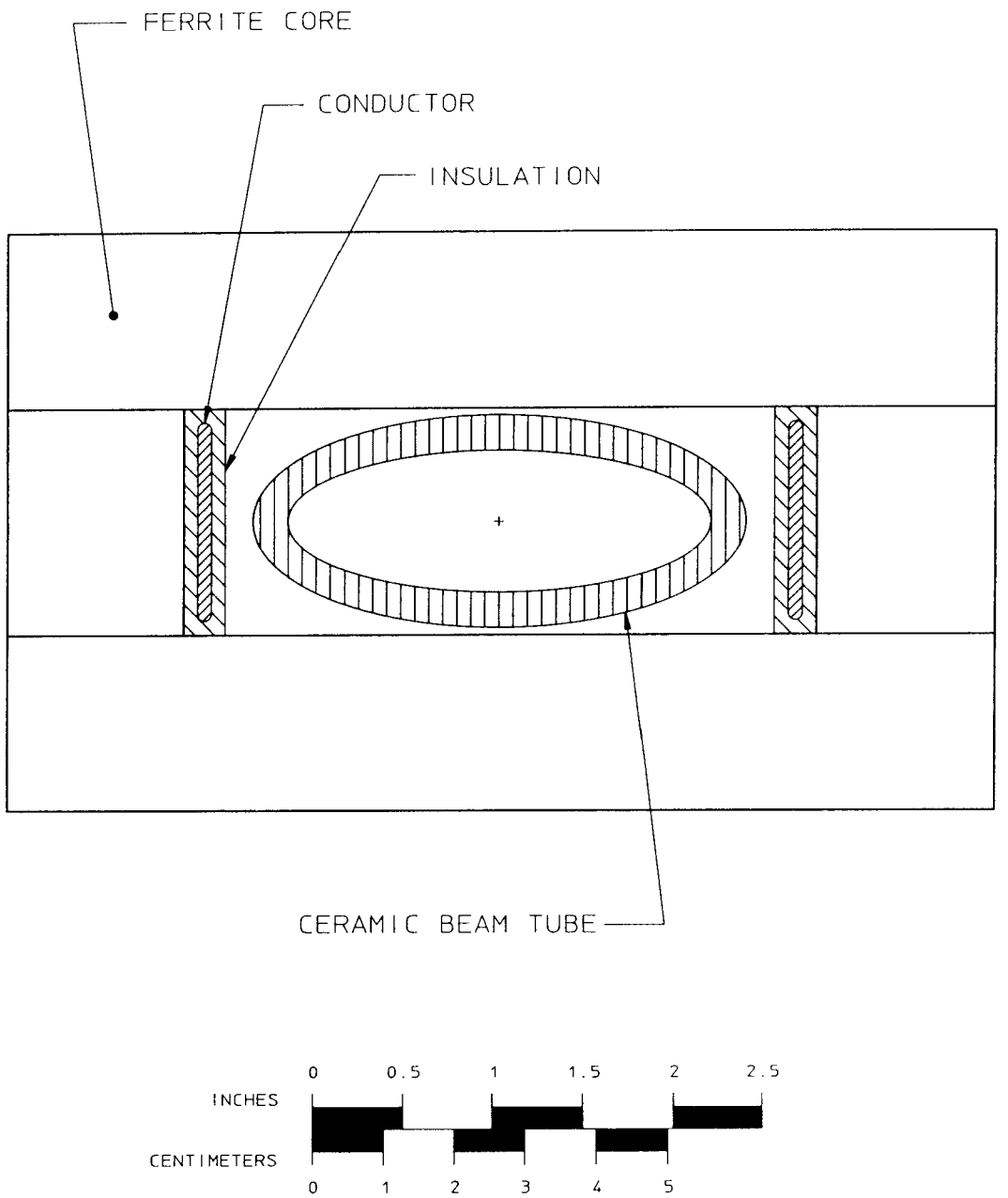


**Fig. 3-43.** Storage ring bump magnet cross section.

**Table 3-20.** Storage ring bump magnet parameters at 1.5 GeV.

| | |
|---|---|
| Core material | Nickel-zinc ferrite<br>Ceramic Magnetics CMD 5005 |
| Length (m) | 0.7 |
| Bend angle (mrad) | 15 |
| Beam aperture (mm) | |
| Vertical | 20 |
| Horizontal | 60 |
| Magnet aperture (mm) | |
| Vertical | 32 |
| Horizontal | 78 |
| Magnetic field (T) | 0.104 |
| Number of coil turns | 1 |
| Current (A) | |
| Peak | 2650 |
| rms | 3.7 |
| Repetition rate (Hz) | 1 |
| Current waveform | Half sine-wave |
| Current duration ($\mu$s) | 4 |
| Inductance ($\mu$H) | |
| Magnet | 2.36 |
| Total, four-magnet string | 10.1 |
| Total ac resistance, four-magnet string (m$\Omega$) | 17 |
| Voltage, peak, total (kV) | 21 |

Extensive ground motion measurements have been performed at the Light Source site and have been compared to ones at SLAC. We conclude that steady-state ground motion noise at the Light Source is comparable to or less than that at the SPEAR ring at SLAC—particularly in the range of 5–15 Hz. The reported results indicate that the motion of Light Source magnets due to background steady-ground motions should be less than 0.1 $\mu$m, which is clearly acceptable. Nearby transient sources of noise, such as operating cranes in the Light Source building, can produce magnet motions exceeding 1 $\mu$m and may need to be controlled by operational restrictions during Light Source operation.

## 3.5 Vacuum System

A vacuum of 1 nTorr or less is required in the storage ring to obtain adequate electron-beam storage times. Achieving this pressure is relatively straightforward in the absence of stored electrons. However, the stored beam produces a significant gas load by means of the following two-step process: The synchrotron-radiation photons generated in the bending

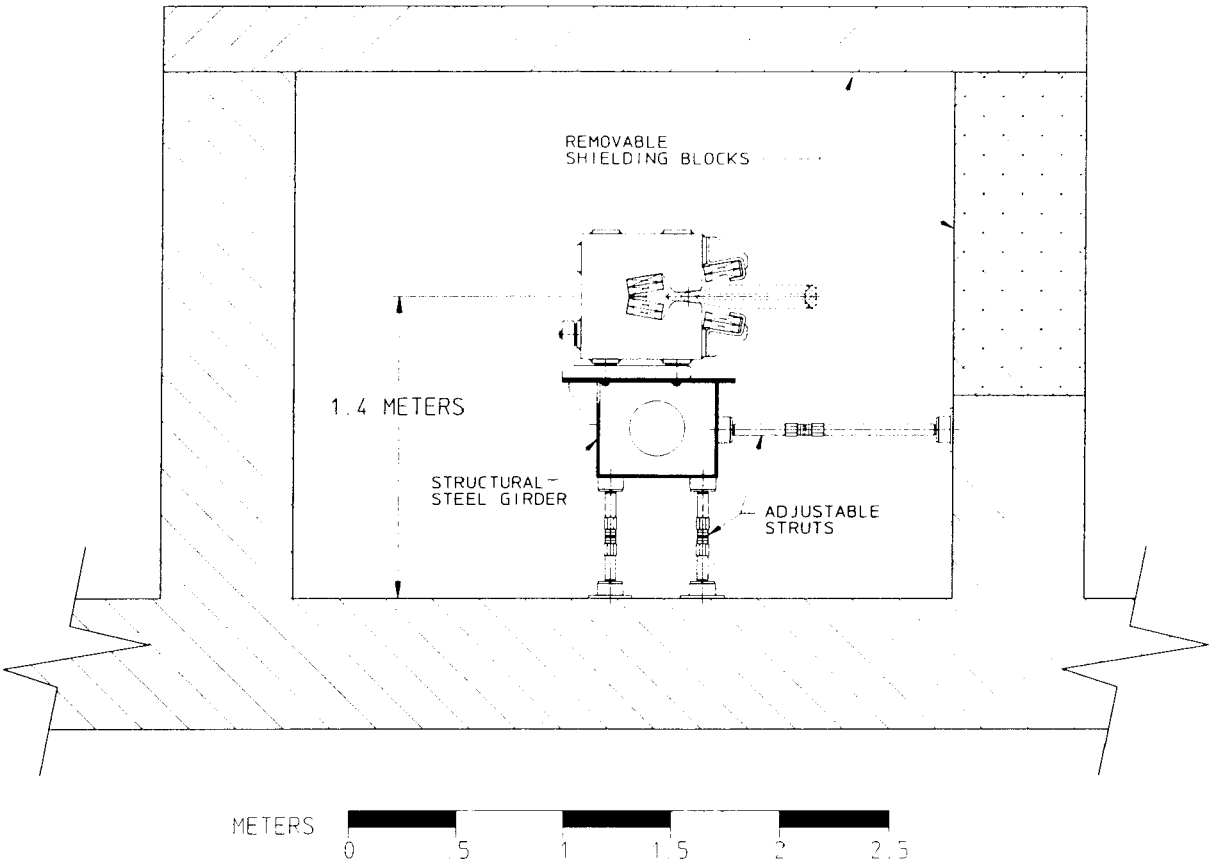


**Fig. 3-44.** Storage ring magnet supports.

magnets produce photoelectrons when they strike the surface of the vacuum-chamber wall. These electrons in turn cause the desorption of gas molecules, the most significant of which are $CO_2$, CO, $CH_4$, and $H_2$.

This photon-induced desorption process has produced copious amounts of gas during initial operation of existing electron storage rings, raising pressures up to 1000 nTorr at full electron current. Typically, electron storage rings have dealt with this gas load by means of a combination of distributed and lumped vacuum pumping equal to about 100 liters/s of circumference. Distributed ion pumps in the dipole magnet chambers have been a convenient method of delivering this pumping to the source of gas. However, the Light Source has only 13% of its circumference made up of dipoles (compared with 35% in SPEAR, for example), making this type of pumping inefficient. Also, the Light Source vacuum chamber aperture is small, having a conductance of only 15 liters/s per meter. Thus, to use conventional lumped pumping would require over 600 pumps, spaced every 30 cm; this is not a practical approach.

Instead, the solution we have adopted is to divide the vacuum chamber into two regions, one in which the electrons circulate, and a so-called antechamber in which the gas load from the synchrotron radiation is dealt with. The features of this novel solution are described below.

### 3.5.1 Principle of Operation

The precursor of the gas load, the synchrotron radiation produced in the bending magnets, is in the form of a fan in the median plane, with most of the power concentrated within a few milliradians of the horizontal. Figure 3-45 shows how the Light Source vacuum chamber has been designed to allow this radiation to pass through a slot in the beam chamber into the antechamber, where it is intercepted by a photon stop that is located directly above a titanium sublimation pump. Because gases desorbed from the photon stop are produced at the large throat of the vacuum pump, there is a high probability that the molecules will be trapped rather than finding their way into the beam chamber.

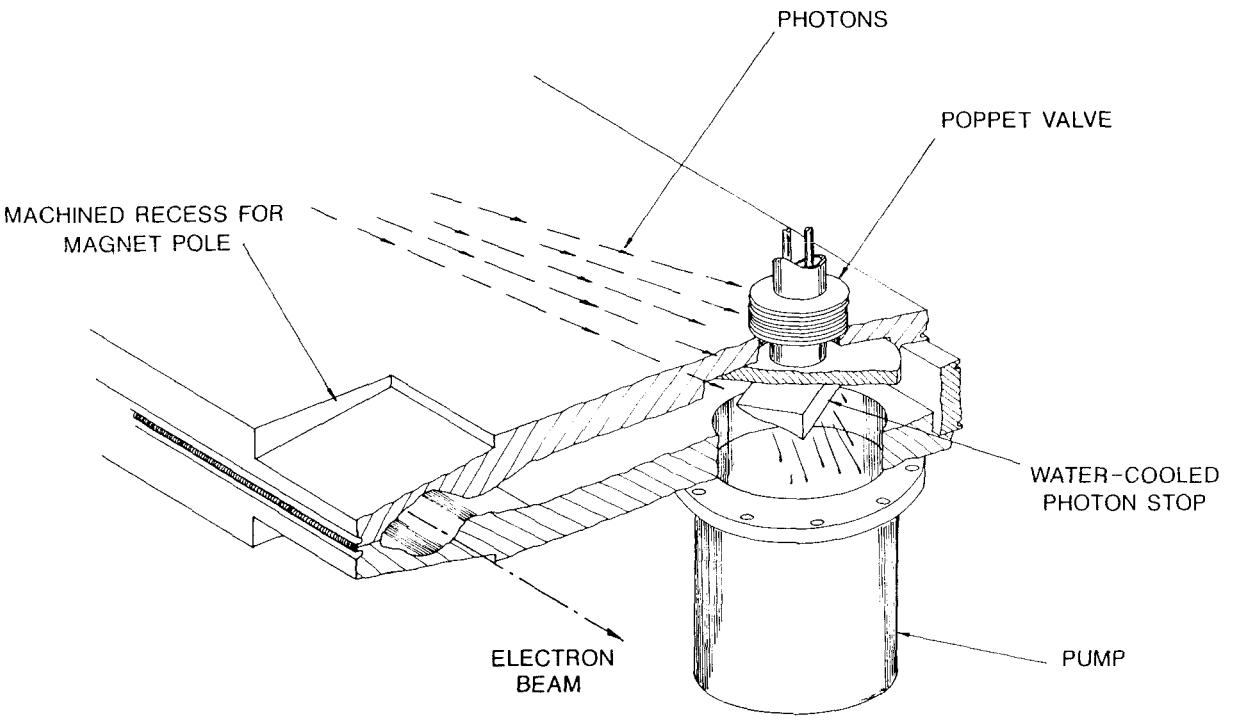


**Fig. 3-45.** Cutaway view of the Light Source vacuum chamber, showing a photon stop and titanium sublimation pump.

The effectiveness of this vacuum strategy depends on optimizing five steps:

(1) Minimizing the amount of synchrotron radiation power that lands on the beam-chamber walls.
(2) Intercepting the photons at the photon stop at an optimum angle.
(3) Minimizing the adverse effect of the photoelectrons.
(4) Delivering titanium vapor to the surfaces where the photon-desorbed gas first strikes.
(5) Arranging the titanium-coated pumping surfaces so that photon-desorbed gas molecules must undergo multiple bounces in order to escape the pump.

These issues will now be addressed in turn:

(1) The vacuum chamber has a 1-cm-high slot that separates the beam chamber from the antechamber. This dimension is a compromise between the need for rf isolation of the

two chambers, which favors a small slot (see the discussion in Section 3.3.2) and the need for a high escape probability for the synchrotron radiation fan, which favors a large slot.

The expression for the vertical angular distribution of synchrotron radiation power is:

$$P(\psi) = \frac{1}{(1 + \gamma^2\psi^2)^{2.5}} \left[ \frac{1 + 5\gamma^2\psi}{7(1 + \gamma^2\psi^2)} \right],$$

where $\psi$ is the vertical angle and $\gamma$ is the electron energy in units of its rest mass, $\gamma = (E/m_0c^2)$. The angle $\psi$ defined by the slot is determined by the distance from the synchrotron radiation source point to the place where the radiation exits the beam chamber; the variation in this distance for different portions of the radiation fan is depicted in Fig. 3-46. For our 1-cm slot, the angle subtended varies between 0.5 and 8.7 mrad, and we calculate that 99.3% of the photon power escapes the beam chamber.

(2) All the photons that exit the beam chamber are either directed to experimental stations or intercepted by a photon stop. For an effective design, the gases desorbed at the stop should have the highest probability of entering the pump. This is achieved by sloping the face of the stop to a shallow angle with respect to the radiation fan, thereby directing the desorbed molecules into the throat of the pump (see Fig. 3-45). Since 95% of the photon power lies within 0.5 mrad of the horizontal, the face of the stop can be shaped with a grazing angle in the center, with the outer edges shaped to intercept the lower-energy photons. However, care must be taken in the design to allow for the fact that the radiation fan will not always fall on the stop at the same height (due to beam-orbit changes, for example).

(3) Photoelectrons are the direct source of the gas load, since they desorb gas molecules when they leave their production site and then again when they are intercepted by a second surface. Since the photo-production cross section decreases as the grazing incidence angle of the photons increases, the efficiency of the pumping process described in (2) above is offset somewhat by the small photon incidence angle in our design. The gas desorption rate is also influenced by the condition of the surface, and synchrotron radiation cleaning ("scrubbing") has been shown to be one of the most effective ways of improving the surface. Thus, we expect the primary source of the gas load to diminish very quickly. If we can bend the photoelectrons (which have relatively low energy) back into the photon stop, we might expect the cleaning process to proceed even more rapidly. Either magnetic or electric confinement of the photoelectrons could be employed. For example, permanent magnets could be embedded in the stop. (The stray magnetic field introduced at the circulating electron-beam orbit would be negligible.) However, these magnets would effectively shield the stop against glow-discharge cleaning. Alternatively, electric confinement (i.e., biasing the stop) could be used; this would permit glow-discharge cleaning but would require that the cooling circuit embedded in the stop be electrically isolated. The choice between these methods will be made as part of our R&D program.

(4) Effective titanium sublimation pumping requires that both the titanium vapor from the sublimation source and the gas to be pumped have about the same distribution at the pumping surfaces. Filamentary titanium near the photon stops (see Fig. 3-47) has a distribution much like the gas coming from the photon stop. The proximity of the titanium sublimator to the photon stop will lead to the stop being coated with titanium. Burying the gas precursors on the surface of the photon stop with titanium may cause the gas precursors

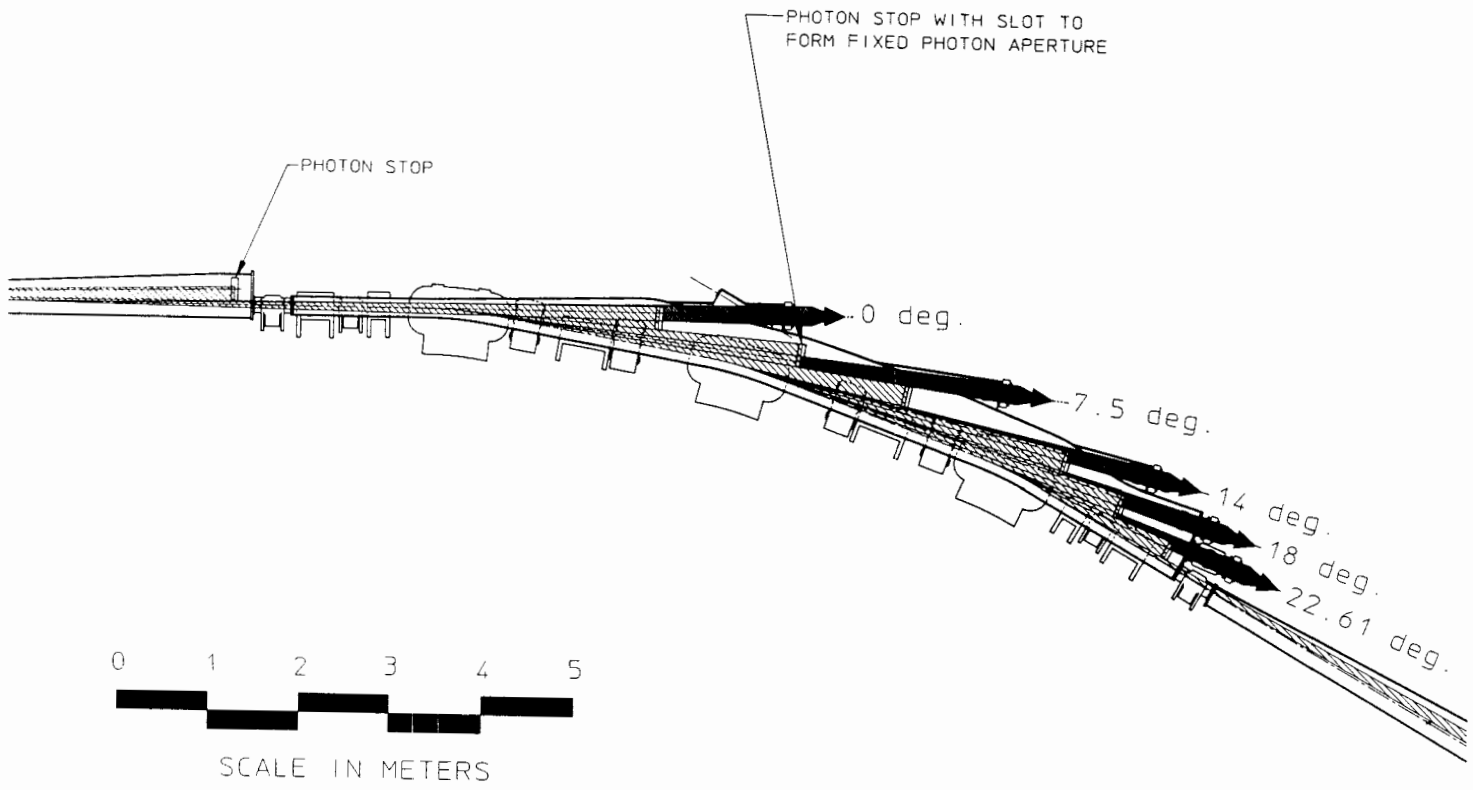


**Fig. 3-46.** Plan view of one sector of the storage ring, showing radiation transmitted to the beam lines (dark arrows) and intercepted by photon stops (crosshatching).

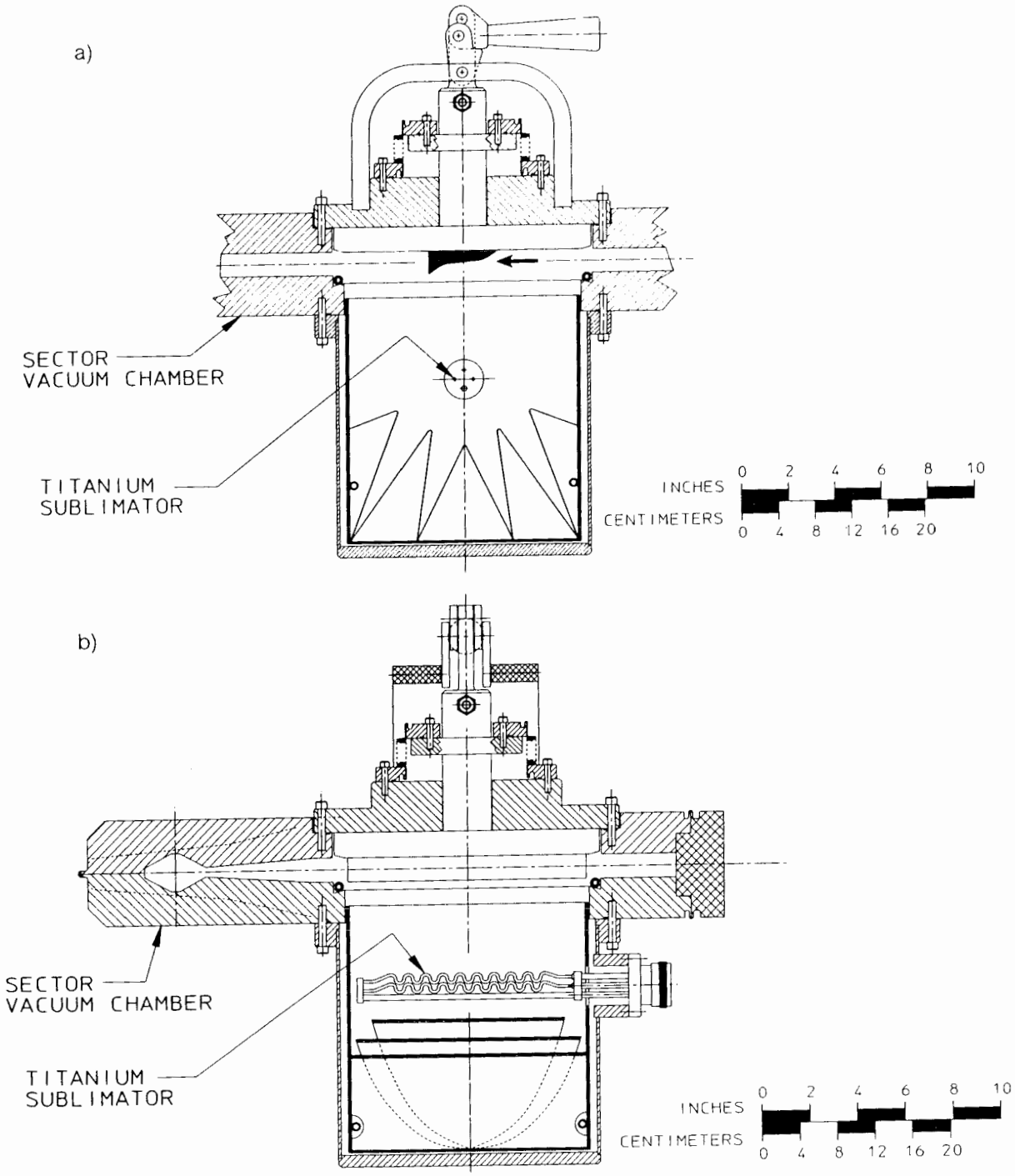


**Fig. 3.-47** Cross sections of a beam stop and sublimation pump: (a) along the beam axis and (b) perpendicular to the beam axis.

to react with titanium before they can become gaseous. If experiments should indicate that titanium-coated photon stops may be a problem, a shield will be used to protect the photon stop during sublimation.

(5) Freshly deposited titanium has a sticking factor for reactive gases that approaches unity; however, long before the titanium surface is saturated with gas, the sticking factor is halved. Arranging the titanium-coated surfaces such that gas molecules must make multiple bounces, as shown in Fig. 3-47, helps make up for the loss of sticking factor. The linear nature of both the source of the gas from the photon stops and the titanium from the sublimator makes it possible for the gas and the titanium to strike the condensation surfaces at a low grazing angle. This arrangement permits the titanium to be spread out over an extended surface and to direct the gas molecules deep into trapping pockets.

### 3.5.2 Vacuum Pumps

The major vacuum pumping for the storage ring comes from the 84 titanium sublimation pumps (TSPs) associated with the photon stops. While the primary function of these pumps is to trap the gas from the photon stops, each offers 1200 liters/s per meter of pumping to the ring or a total of 100,000 liters/s for the entire ring. Titanium sublimation does not pump methane or argon, so 108 StarCell sputter ion pumps are also distributed around the ring. These pumps each have 60 liters/s of pumping, and they are also designed for pressure measurement; thus, they constitute 108 vacuum-measurement stations. Since the ion pumps operate independently of the sublimation pumps, they can maintain a storage ring pressure, without beam, of 50 nTorr.

The TSPs can be isolated from the ring vacuum system (for regeneration and filament change) by a poppet valve. The photon stops are mounted on the poppet valve so that, when the valve is closed, the body of the pump, along with the photon stop, can be removed without venting the storage ring to air. The valve is sealed by a metal Helicoflex gasket that has been demonstrated to remain leak tight after 100 closures [Ishimaru, 1983]. In the case where the photon beam exits into a beam line, the "photon stop" is shaped to be a fixed photon aperture. Thus, it is also possible to tailor the aperture, after installation of the beam line, without breaking vacuum.

### 3.5.3 Vacuum Chamber Construction

The very wide unsupported vacuum chamber would be very difficult to build using sheet metal or extrusion techniques. A machined-aluminum alternative was investigated and found to have the following advantages:

- The precise tolerances obtainable by machining permit the accurate location of components, such as beam-position monitors.
- Complex shapes, such as a gently changing beam-chamber cross section, can be readily formed.
- Flange surfaces can be machined directly into the outside surface, making penetrations convenient.
- Selected areas of chamber wall can be made very thin while maintaining strength by having thick metal nearby, as, for example, in the quadrupole recesses shown in Fig. 3-35.

- The very thick aluminum provides excellent heat distribution during bake-out.
- Shaping aluminum by machining, rather than extrusion, avoids the formation of porous aluminum oxide–hydride. [Ishimaru, 1983].
- Machining avoids complex cutting, fitting, and welding with its attendant distortion.
- The existence of vendors with numerically controlled milling machines that can machine three parts (each 10 meters in length) at the same time allows the chamber costs to be accurately predicted.

The selection of aluminum alloy is based on economy of machining, yield strength, and ease of welding. The 2219 T87 alloy of aluminum has a good balance of these qualities: It is the least expensive to machine of all high-strength aluminum alloys, has a yield strength of over 55,000 psi (which is higher than annealed 304 stainless steel), and is not difficult to weld (though, as with all aluminum, due care must be taken).

All the welds on the sector chamber are designed to have low stress and are thermally isolated from the mass of the chamber by "weld preps." The welds on the outer radius are all non-load-carrying. The inner-radius welds are in tension at the cutout for the magnets, but these welds are far enough from the fulcrum to keep the stress low. The "weld preps" are made particularly deep, in case some repairs have to be made. The welds are autogenous and are made by an automatic ac tungsten–inert gas technique, guided by the "weld prep."

A plan view of the vacuum chamber for one sector of the ring is shown in Fig. 3-48.

### 3.5.4 Sector Valves and Bellows

At the end of the sector chamber and straight section chamber, where there are no major magnetic elements, the photon stops are placed very close to the electron beam. This reduces the width of the photon fan downstream of the stop to the point where a standard VAT gate valve with rf shielding can be used. Seven such sector valves are installed; they divide the storage ring into four separate vacuum areas for maintenance and provide isolation for the injection section and rf cavities.

Bellows are located between all vacuum chambers, for reasons of both thermal expansion and alignment. The narrow photon fan at these locations makes possible the use of relatively small bellows. The shape of the electron-beam chamber changes between the curved and straight sections to accommodate the insertion devices. This transition is incorporated in the rf shield for the bellows. Because the bellows are also the sites for some of the steering magnets, elliptical-cross-section bellows are used to reduce magnet aperture requirements.

### 3.5.5 Bake-out

The aluminum vacuum chamber has 150°C bakeout capability. The high thermal conductivity and large cross section of the aluminum vacuum chambers make it possible to heat them with a single line of strip heater clamped to the bottom. There are 200 strip heaters with a total power of 260 kW. Each strip heater has its own thermostat controller. Surface temperature monitors, located near each heater, will shut down a section in case of thermostat failure. The magnet pole tips are insulated from the vacuum chamber by multiple layers of thin Kapton.

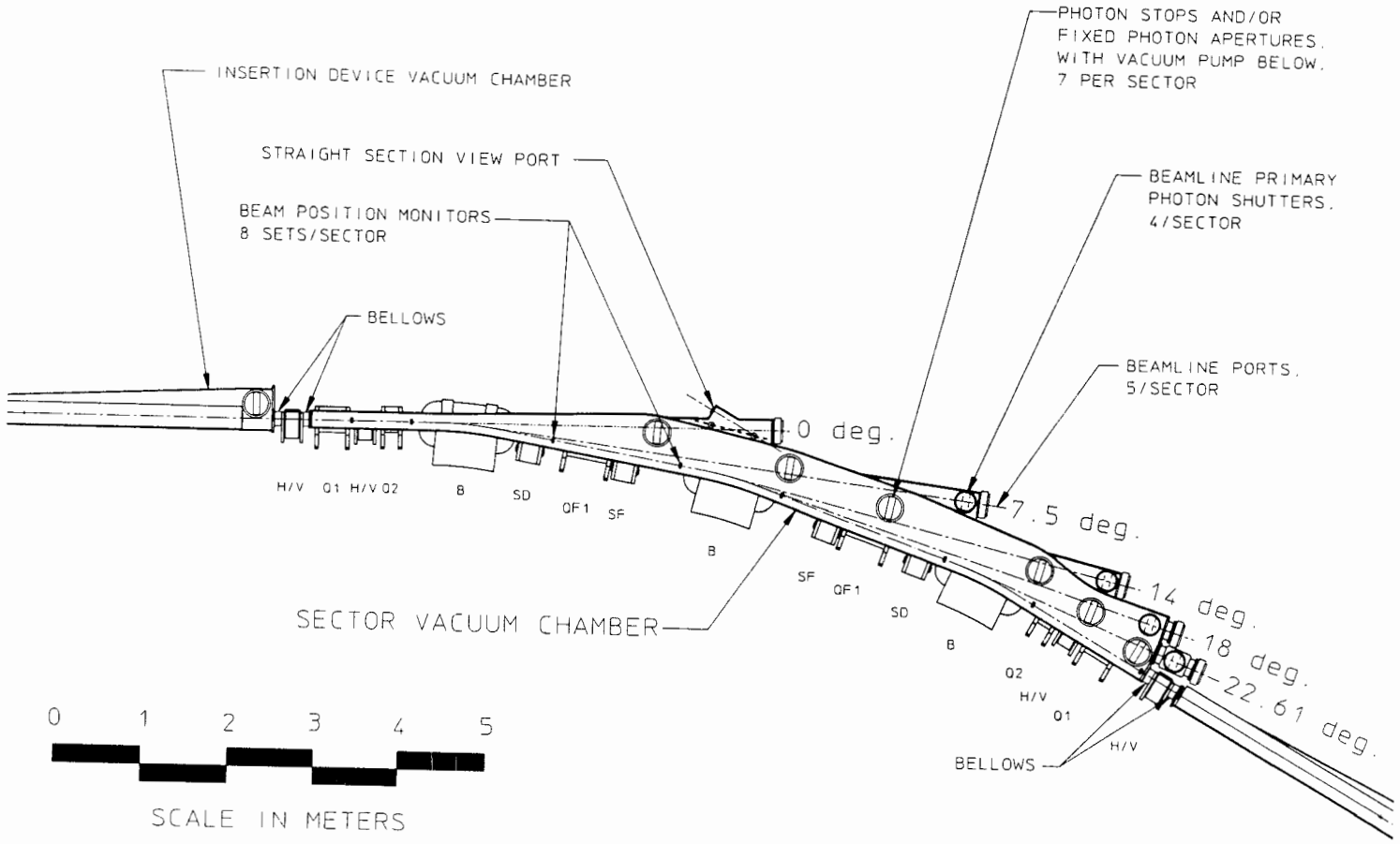


**Fig. 3-48.** Plan view of the vacuum chamber for one sector of the storage ring.

The injection chamber has laminated iron magnets in the vacuum, which create special vacuum problems. The outgassing load from the laminated iron can be reduced to acceptable levels only by *in situ* bake-out above 200°C. This high-temperature bake-out requires stainless-steel construction with many heaters, along with thick insulation. During baking of the injection chamber, the sector valves will be closed to prevent contamination of the remainder of the vacuum chamber.

### 3.5.6 Other Considerations

Vacuum measurements are made by 24 ionization gauges, one in each vacuum chamber. There is a residual gas analyzer in every chamber that incorporates a photon line. As mentioned, the 108 ion pumps will also monitor the vacuum.

The vacuum chambers are supported from the same girder that supports the magnets, but they are mechanically isolated from the magnets. Roughing is done by oil-free turbomolecular pumps backed by cryosorption pumps.

The demountable aluminum joints are sealed by Mott gaskets [F. Middleton 1981], and tooling balls are machined into the aluminum chambers near all beam-position monitors for survey and alignment.

## 3.6 Survey and Alignment

Survey and alignment for the Light Source will be accomplished with conventional optical tooling techniques using instruments such as theodolites, jig transits, and precision optical levels. The selected procedures are identical to those which were used by LBL staff in aligning PEP several years ago; even the existing computer programs can be used with minimal modification.

The most severe alignment requirements for the 1–2 GeV Synchrotron Radiation Source come from the transverse alignment of the storage ring bending and quadrupole magnets. These magnets must be located horizontally and vertically to an accuracy of $\pm 0.15$ mm, where this alignment must be maintained for modest distances along the storage ring, say, 5 to 10 meters. Over longer distances along the ring, say, 50 meters, less stringent alignment tolerances are required. Our experience at PEP shows that optical tooling methods are more than adequate for achieving these requirements.

The following general procedure will be used to align the Light Source:

- Existing survey monuments at the site provide initial reference positions and elevations.
- A network of survey monuments is then installed and surveyed relative to the reference positions. A liquid level system, identical to that used at PEP, provides reference elevations. (Figure 3-49 shows a read-out unit for this liquid level.)
- The Light Source components are installed on long girders in the shop and are accurately aligned relative to one another.
- The girder is installed in the accelerator housing.
- Fiducial fixtures are installed on the magnets and other accelerator components. These components are then surveyed relative to nearby reference points, and the girder is accurately aligned.

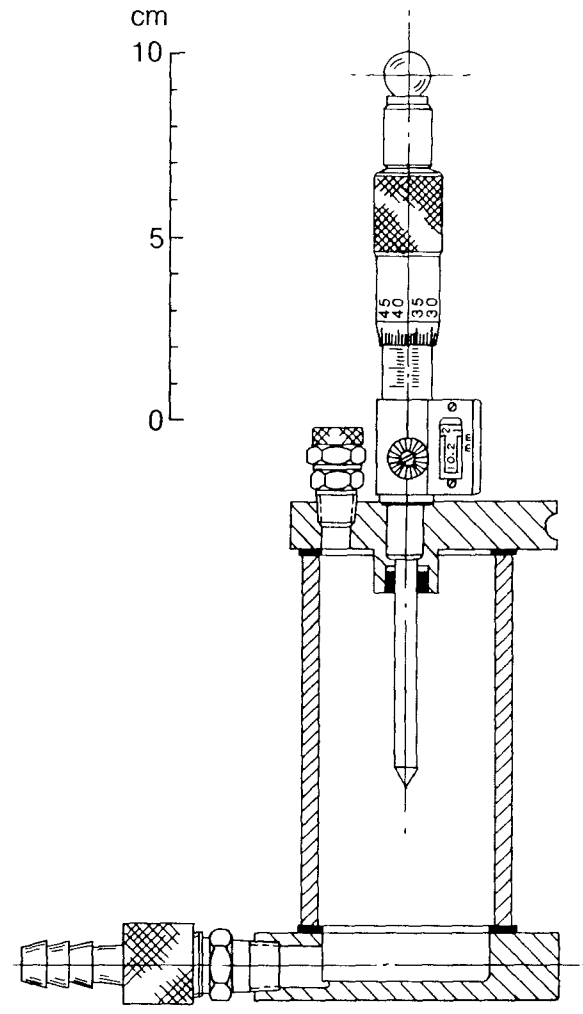


**Fig. 3-49** Liquid-level read-out unit. The probe is used to measure the water level in the partially filled vial.

- A final resurvey checks the location of the components.

The use of optical tooling techniques is fairly labor intensive, but this is not a serious problem for a modest-size project such as the Light Source. The use of computer programs to perform all data analysis greatly reduces the risk of human error in the survey and alignment procedure. Providing adequate redundancy by performing resurveys has been shown by experience to provide excellent reliability.

## 3.7 Magnet Power Supply Systems

The storage ring magnet power systems are all designed to operate stably over the full energy range of the ring. Power supply stability specifications (see Table 3-21) are based on the allowable tune shifts for the ring and the requirements for beam-position stability; dc stability and ripple will be carefully held to these specifications. A separate transformer bank is used to supply ac power for the ring supplies to minimize interactions with other Light Source operations. Ramping of the ring energy, when required, will be done with

**Table 3-21.** Storage ring magnet power supplies.

| Magnet circuit | No. | Current (A) | Voltage (V) | Power (kW) | Stability $\Delta I/I_{max}$ | Type of regulated power supply |
|---|---|---|---|---|---|---|
| Bending magnet | 1 | 919 | 540 | 500 | $\pm 5 \times 10^{-5}$ | Custom transistor |
| Quadrupole QF1 | 1 | 500 | 330 | 165 | $\pm 1 \times 10^{-4}$ | Custom transistor |
| Quadrupole Q1 | 24 | 110 | 42 | 4.6 | $\pm 1 \times 10^{-4}$ | Commercial chopper |
| Quadrupole Q2 | 24 | 110 | 30 | 3.3 | $\pm 1 \times 10^{-4}$ | Commercial chopper |
| Sextupole SF | 1 | 329 | 180 | 60 | $\pm 1 \times 10^{-3}$ | Custom SCR |
| Sextupole SD | 1 | 329 | 180 | 60 | $\pm 1 \times 10^{-3}$ | Custom SCR |
| Skew quadrupole | 4 | 10 | 10 | 0.1 | $\pm 1 \times 10^{-3}$ | Commercial transistor |
| Dipole, horizontal correction | 48 | 33 | 21 | 0.7 | $\pm 5 \times 10^{-4}$ | Bipolar transistor |
| Dipole, vertical correction | 48 | 116 | 12.2 | 1.4 | $\pm 5 \times 10^{-4}$ | Bipolar transistor |
| Sextupole, horizontal correction | 48 | 23 | 23 | 0.53 | $\pm 5 \times 10^{-4}$ | Bipolar transistor |
| Sextupole, vertical correction | 24 | 23 | 23 | 0.53 | $\pm 5 \times 10^{-4}$ | Bipolar transistor |

simultaneously stepped inputs to the power supplies; this avoids potential tune shifts caused by sequentially stepping the input digital-to-analog converters (DACs) of the control computer.

Power supply reference inputs and associated analog monitoring functions are done with 16-bit DACs and analog-to-digital converters (ADCs). These functions, as well as on/off control and status information, are controlled by the local microcomputers provided as part of the Light Source control system (see Section 3.11).

The major parameters of all of the storage ring magnet power supply systems are summarized in Table 3-21.

### 3.7.1 Bending Magnet Power Supplies

The 36 gradient bending magnets in the storage ring are electrically connected in series and powered by a single power supply consisting of a 12-pulse rectifier with an *LC* filter and a series transistor bank (operating in the linear mode). The basic circuit is shown in Fig. 3-50. The required degree of regulation is achieved by three feedback loops:

- A voltage loop that regulates the rectified voltage ahead of the *LC* filter to compensate for changes in line voltage.
- A voltage loop that regulates the voltage drop across the transistor bank.
- A current loop that regulates the output current.

A block diagram of the regulator is shown in Fig. 3-51. The two voltage loops control the firing signals to the silicon-controlled rectifiers (SCRs) and the current loop controls the drive signal to the series transistor bank. The main *LC* filter is designed both to attenuate the 720-Hz rectifier voltage ripple sufficiently for the transistor regulator and to compensate for the limited bandwidth of the SCR voltage regulator. The transistor bank is used for precision control; it also eliminates any power-supply-ripple contributions that remain after passive filtering. The dc current in the magnets is monitored and controlled by a feedback signal from a precision dc current transductor. The power supply is grounded at the center of the two series-connected rectifiers to keep the magnet voltages symmetrical with respect to ground. Power supplies of this type and having a suitable degree of regulation are available commercially and have been successfully used by others in similar applications [McCarthy and Wolf, 1985].

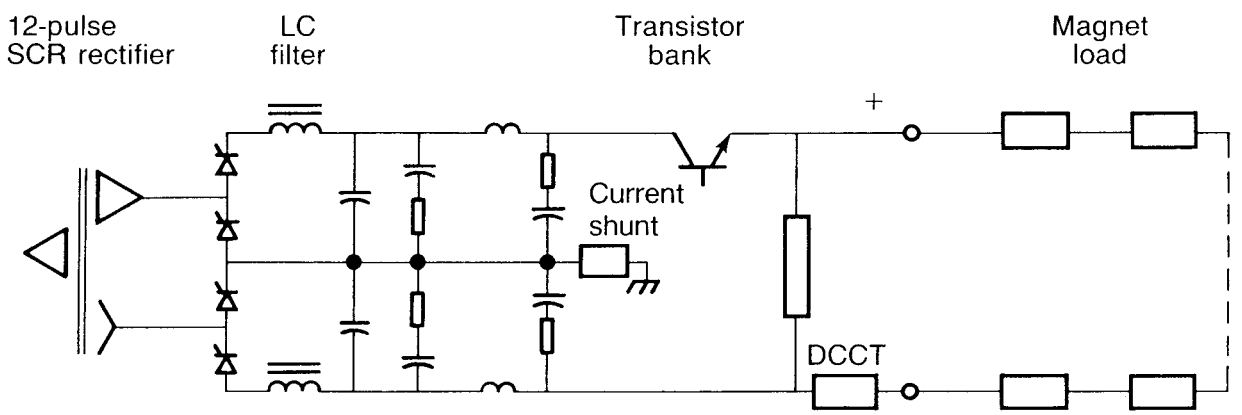


**Fig. 3-50.** Basic circuit for the bending magnet power supplies.

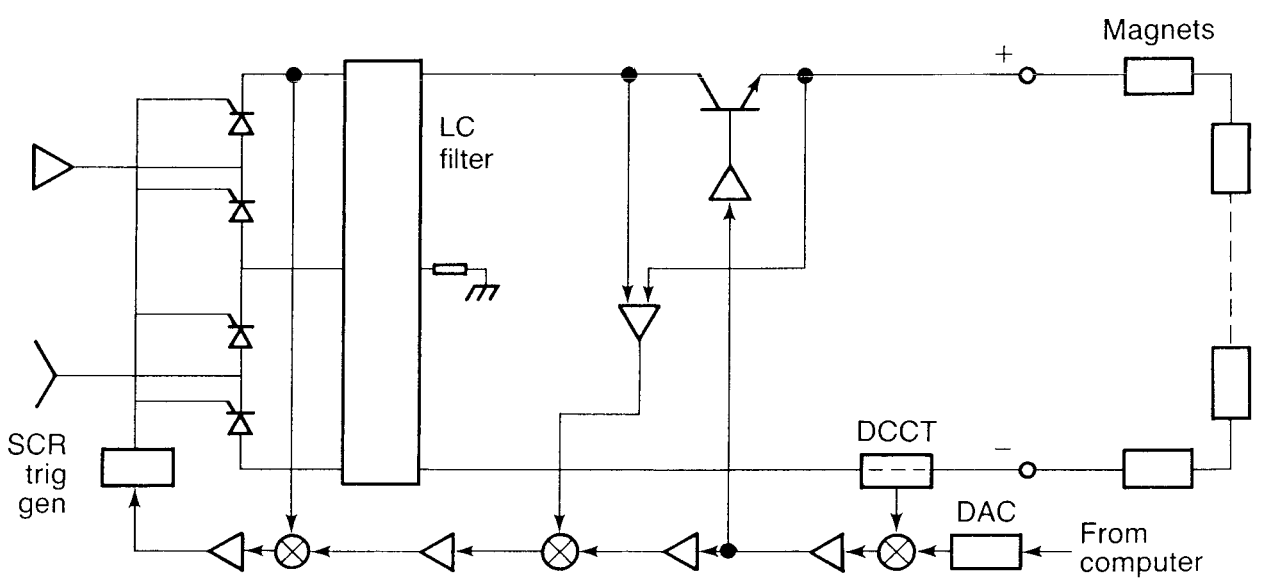


**Fig. 3-51.** Block diagram for the bending magnet power supply regulator.

### 3.7.2 Quadrupole Magnet Power Supplies

The 24 QF1 quadrupole magnets are electrically connected in series (i.e., they form one family) and are connected to a single power supply (of the same type as the bending-magnet supply). The remaining 48 quadrupole magnets (Q1 and Q2) are individually powered by separate power supplies. These magnets utilize a commercially available power supply of the chopper type that switches at a 20-kHz repetition rate.

### 3.7.3 Sextupole Magnet Power Supplies

The 48 sextupole magnets are divided into two families (SF and SD) with 24 magnets in each. Each family is electrically connected in series and powered by a separate SCR power supply, shown in Fig. 3-52. The sextupole magnets also have 48 horizontal and 24 vertical steering windings, rated at 23 V and 23 A. These are powered individually with bipolar transistor actuators that derive their power from common power supplies, as shown in Fig. 3-53. Twenty-four 30-V, 275-A commercial power supplies are installed around the storage ring to supply dc power to the transistor actuators.

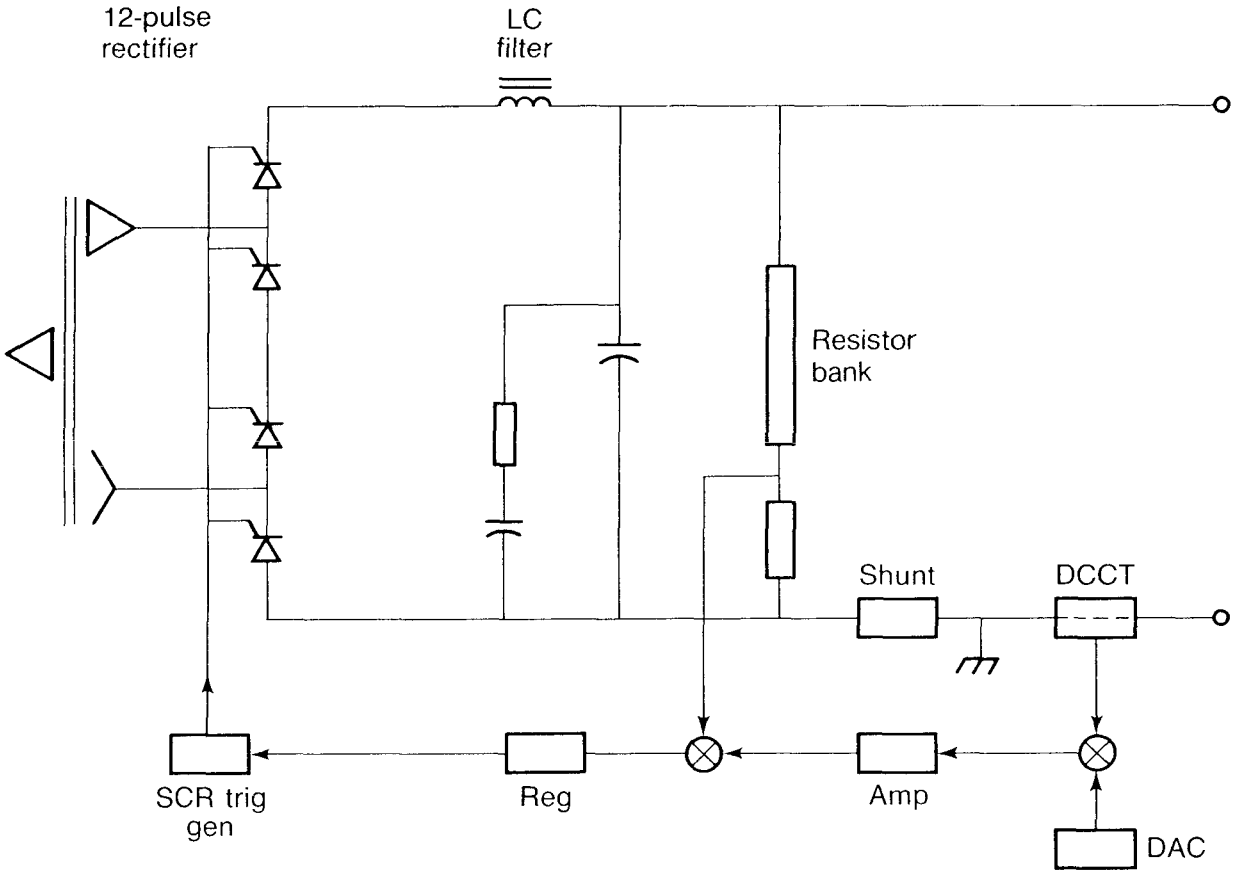


**Fig. 3-52.** SCR power supply for a family of sextupole magnets.

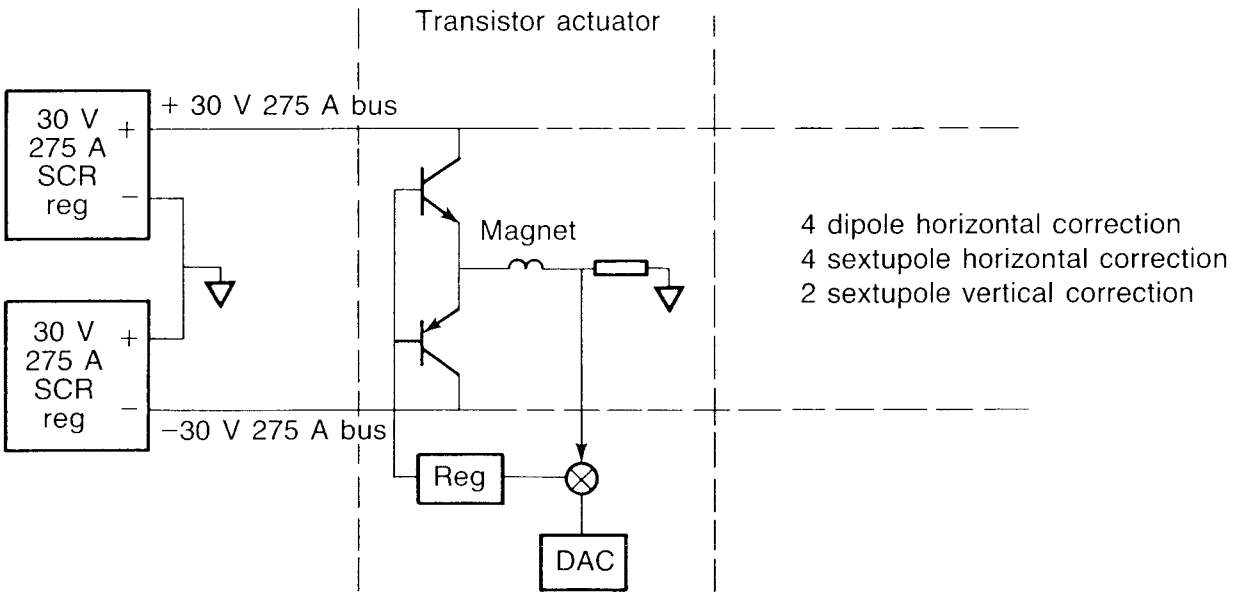


**Fig. 3-53.** Bipolar power supply for the correction magnets of one sector.

### 3.7.4 Correction Magnet Power Supplies

The 48 correction dipole magnets have separate windings for horizontal correction and vertical correction. Each of the 48 horizontal correction windings is powered by a bipolar transistor actuator connected to ±30-V busses. The busses are fed by the same commercial 275-A voltage-regulated power supplies used to power the sextupole steering windings. Each of the 48 vertical correction windings is also powered by a bipolar transistor actuator connected to ±20-V busses fed by 24 commercial voltage-regulated power supplies.

### 3.7.5 Injection Magnet Power Supplies

The storage ring injection process requires three pulsed power supplies that each create a half sine-wave of current in the three injection magnet families. Mechanical details of these magnets can be found in Section 3.4. The bump-magnet system, Fig. 3-54, has four magnets connected in series that move the storage ring beam close to the thin septum for injection. The thin septum magnet is an eddy-current septum and requires a medium-speed current pulse with sufficient flat-top for injection; its power supply is shown in Fig 3-55. The thick septum is a current-sheet septum that can use a longer current pulse, so it is less time critical. In each case, energy is stored in a suitable capacitor that is discharged (with an electronic switch) into the appropriate magnet at injection. Energy recovery is utilized to minimize capacitor-charging-supply requirements. Specifications for the magnets are shown in Tables 3-18 through 3-20 in Section 3.4.6. The power supply parameters are repeated here in Table 3-22 for completeness.

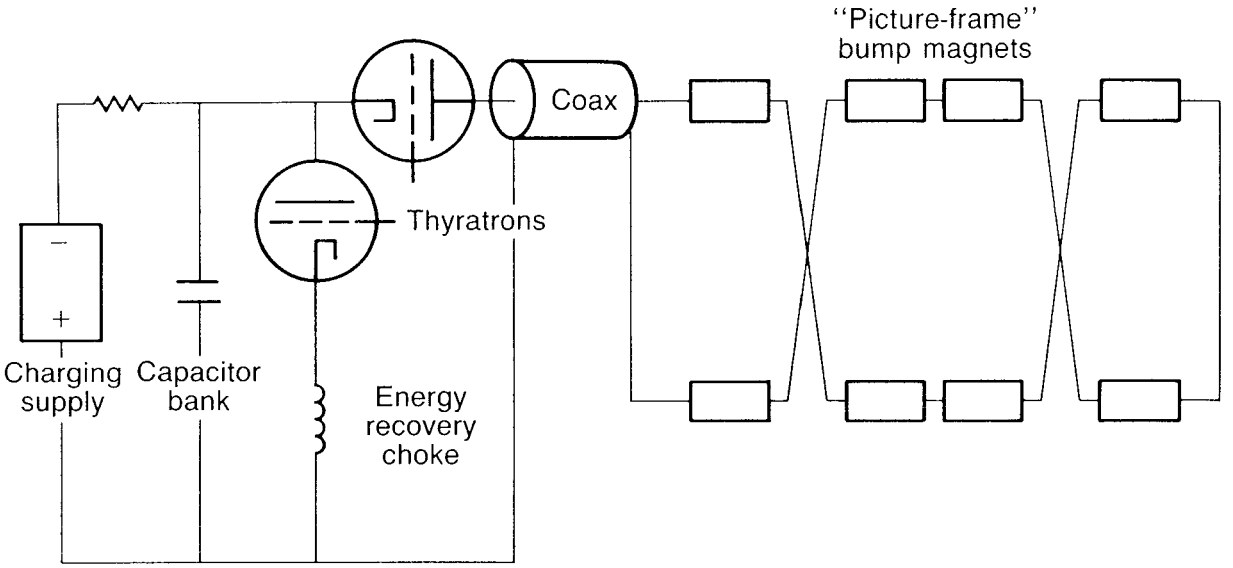


**Fig. 3-54.** Bump magnet power supply.

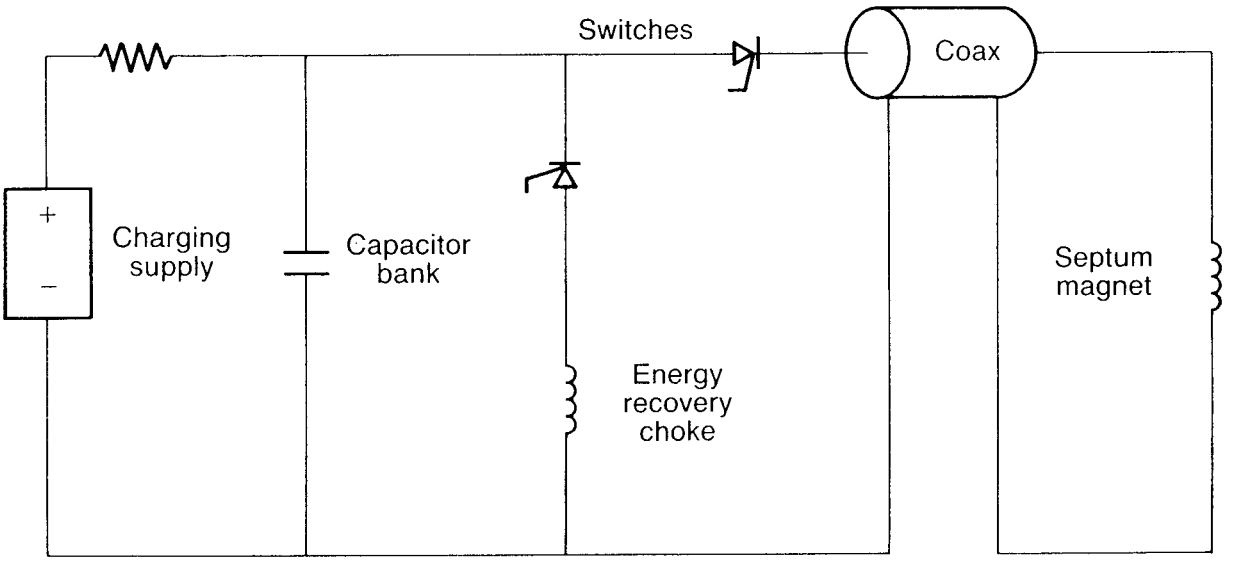


**Fig. 3-55.** Power supply for thick and thin septum magnets.

**Table 3-22.** Storage ring injection magnet power supply parameters.

| Magnet | Time ($\mu$s) | $L$ ($\mu$H) | $I$ (A) | $V$ (kV) |
|---|---|---|---|---|
| Bump | 4 | 10.1 | 2650 | 21 |
| Thin septum | 20 | 2.2 | 4350 | 1.5 |
| Thick septum | 100 | 3.7 | 8330 | 0.95 |

## 3.8 Radio-Frequency System

The purpose of the rf system is to provide sufficient accelerating voltage to make up beam energy losses to synchrotron radiation and to structures in the vacuum chamber, and to provide for an adequate beam lifetime. The rf system parameters are also the major factor in determining the length of the electron bunches.

The main source of energy loss is through the emission of synchrotron radiation in the bending magnets, amounting to 112 keV per turn at 1.5 GeV (228 keV at 1.9 GeV). To replace this energy, and to provide for a momentum acceptance of $\pm 3.5\%$ $\Delta p/p$ (which is necessary to maintain sufficient Touschek lifetime, see Section 3.3), the peak accelerating voltage required is 1.5 MV.

Electrons in the storage ring are confined within discrete bunches by the action of the accelerating voltage. The length of these bunches is determined by properties of the lattice (which are now fixed) and by the frequency and voltage of the accelerating cavities. In the limit of small current, where the effects of the interactions between the beam and its environment can be ignored, the bunch length varies as the inverse square root of the frequency. Therefore, to achieve the small bunch lengths required by the users (see Section 2), we require as high a frequency as possible. In view of the availability of sources of cw rf power in the hundreds-of-kilowatts range required to produce 1.5 MV (see below) we have chosen the frequency of 500 MHz. Systems using this frequency in various light sources, e.g., SRS (England), DESY and BESSY (Germany), and the Photon Factory (Japan), have proven the reliability and durability of the necessary components.

### 3.8.1 Cavity

The number of cavities required to support the design voltage is a trade-off among many factors, including construction/operating costs, voltage holding/power limits, and beam stability requirements. Choosing the smallest number of cavities minimizes the construction costs and beam stability problems, for example, but translates into the highest fundamental-mode gradient and power consumption. Since a primary consideration in this low-emittance light source is to minimize the broadband impedance seen by the beam, we have chosen the minimum number of cavities necessary to support the required voltage, i.e., two.

The cavity design, shown in Fig. 3-56, is based on the accelerating structures employed at the SRS (U.K.) [SRS Design Study, 1975] and the Photon Factory (KEK, Japan) [Batchelor and Kamiya, 1979]. They are made of electrodeposited copper to ensure no water-to-vacuum joints, with a water jacket (electron-beam welded to the cavity) to provide cooling. A constant-temperature water circuit, controlled by a local-station computer, minimizes the frequency drift during running periods. Tuning plungers similar to those developed at SRS are automatically adjusted to compensate for reactive beam loading. In addition, a separate control loop on each tuner is used to provide a constant detune offset to counter the Robinson instability and to compensate for any dissimilarities between the cavities. Initial detuning of the cavities is also necessary to control the transient beam loading caused by the shock excitation from an individual injected pulse, which is too fast for the automatic tuning control loop to follow. Power is fed into the cavity via a coupling loop similar to the system used at the Photon Factory. The vacuum feedthrough is a

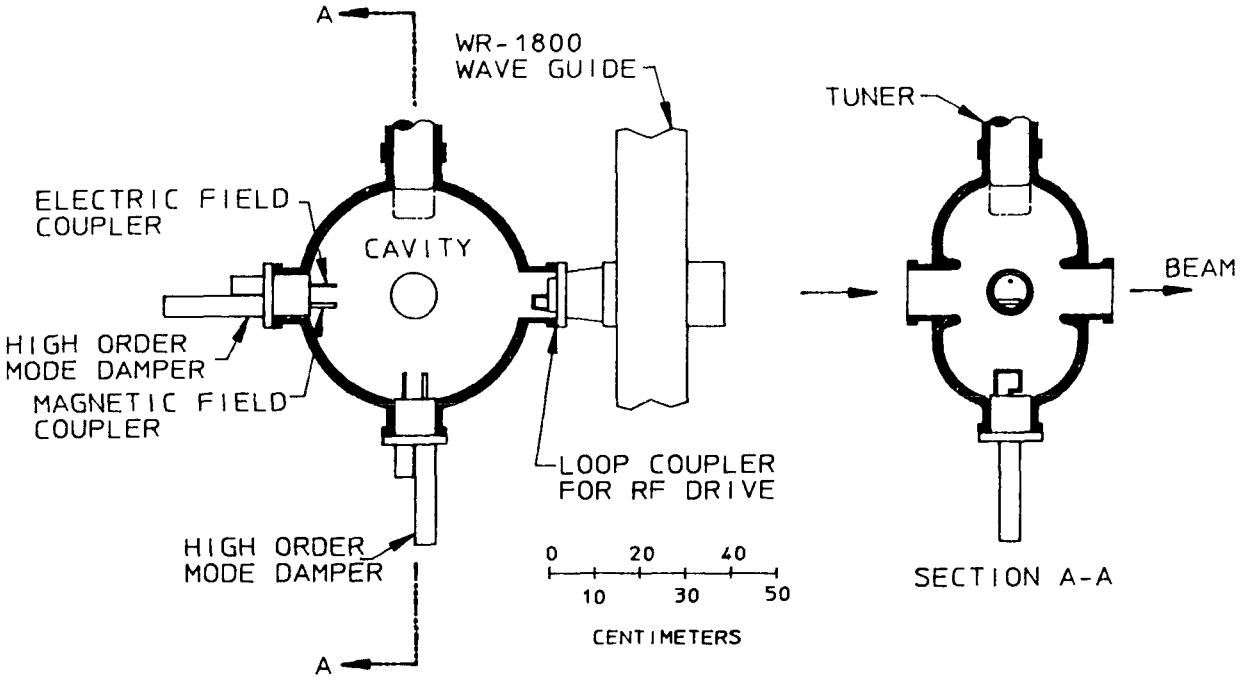


**Fig. 3-56.** Transverse and longitudinal sections of the Light Source rf cavity.

cylindrical alumina window, situated in the waveguide section, and is air cooled. Two higher-order-mode-damping antennas are mounted in the cavity ports, each having electric and magnetic field couplers. Similar devices in the KEK cavities have been successfully used to "de-Q" their parasitic modes [Yamazaki et al., 1981]. Table 3-23 shows the $Q$ values of the KEK cavity modes, before and after damping.

The cavities are located at the downstream end of an insertion straight section, where their internal surfaces can best be protected from synchrotron radiation from the upstream bending magnet. They are mounted on a common support girder and separated by one rf wavelength, center to center. Alignment of the cavities to the beam axis is not critical, since a misalignment has only a second-order steering effect on the beam.

Vacuum pumping is provided by a single 100-liter/s ion pump on each cavity. Monitoring is via an ion gauge, which forms part of the safety interlock system and turns off the rf drive in the event of a vacuum accident. The major parameters and power requirements for the rf system are given in Table 3-24.

### 3.8.2 Power Source and Distribution

RF power for the system is provided by a Varian VKP-8259 klystron amplifier, which delivers up to 300 kW cw at 500 MHz. The dc beam power required is 15 A at 45 kV and is provided by a standard pad-mounted power supply with a crowbar protection unit. Only 50 W of drive is required for fully saturated output; this is readily obtained from a standard communications-type solid-state amplifier. The power distribution system connecting the klystron to the cavities, shown in Fig. 3-57, is composed of commercially available components of WR-1800 aluminum waveguide. The physical layout of the waveguide system is shown in Fig. 3-58.

**Table 3-23.** KEK cavity modes with and without damping.

| Mode | Frequency (MHz) | Undamped $Q$ | Damped $Q$ |
|---|---|---|---|
| TM | 500 | 44000 | 44000 |
| | 758 | 37000 | < 50 |
| | 1052 | 34000 | 600 |
| | 1300 | 112000 | 1000 |
| HEM | 689 | 45000 | < 50 |
| | 829 | 56000 | 300 |
| | 1070 | 40000 | 300 |
| | 1138 | 45000 | 900 |
| | 1245 | 95000 | < 50 |

**Table 3-24.** Storage ring rf system parameters.

| | |
|---|---|
| Frequency (MHz) | 499.654 |
| Harmonic number | 328 |
| Peak effective voltage, VT (MV) | 1.50 |
| Transit time factor, $T$ | 0.683 |
| Total effective shunt impedance, $ZT^2L$ (MΩ) | 16.0 |
| Beam current, multibunch mode (mA) | 400 |
| Power loss (kW) | |
| Synchrotron radiation, dipoles | 45 |
| Synchrotron radiation, insertion devices | 20 |
| Fundamental-mode dissipation | 140 |
| Parasitic modes | 2 |
| Waveguide and other losses[a] | 20 |
| Total rf power installed (kW) | 300 |

[a]Assuming 10% loss.

The Magic Tee divides the power equally between the two cavities and is arranged to divert power that is reflected from the cavities into its termination load. Any mismatched power from the cavities that is directed from the Magic Tee towards the klystron is captured in the circulator load. This arrangement not only protects the klystron, but ensures that it sees a constant load for all beam-loading conditions. Two high-power phase shifters are included to enable the relative phases between the cavities, and between the cavities and the klystron, to be varied. Filters are placed in each cavity feed arm to block a potential feedback mechanism at frequencies in the beam-power spectrum that are capable of driving beam instabilities. This solution has been implemented at the SRS in Daresbury, where problems of beam stability related to this mechanism were first observed.

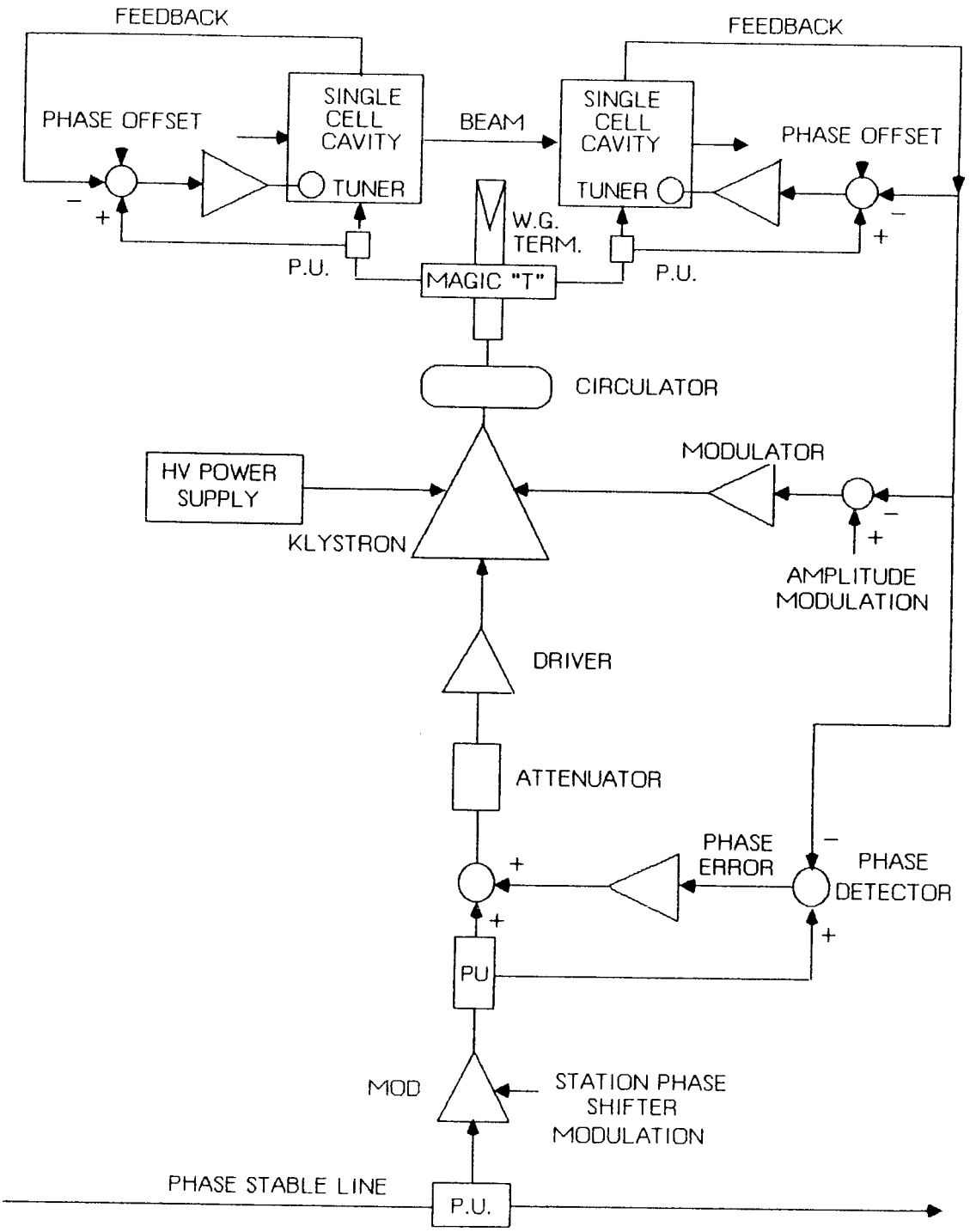


**Fig. 3-57.** RF power distribution system.

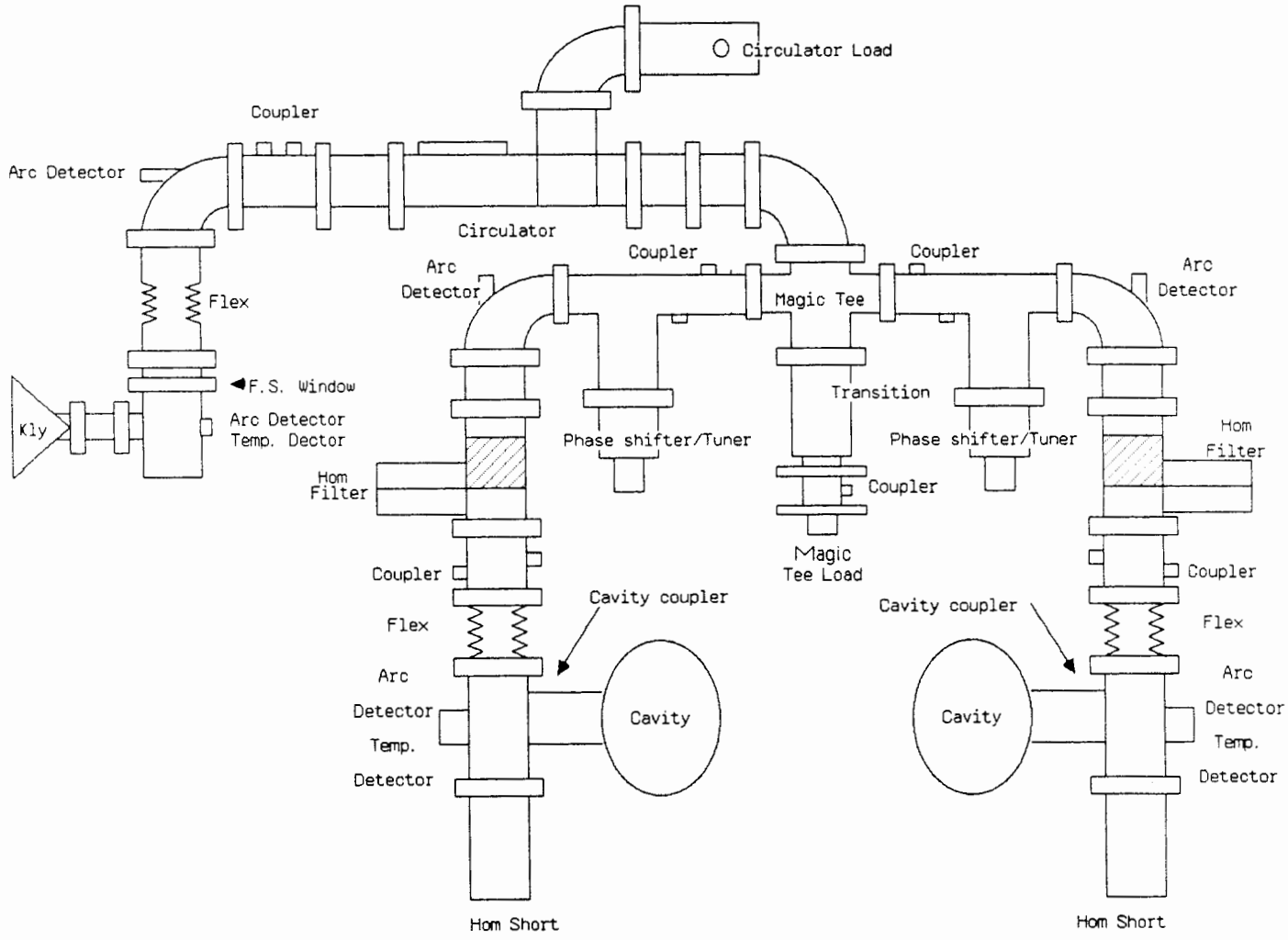


**Fig. 3-58.** Physical layout of the rf waveguide.

### 3.8.3 General

Proper operation of the facility requires accurate control of the relative phases of the rf in the storage ring and booster. A controller chassis similar to that developed for the LBL Uranium Beams Project [Fugitt et al., 1981] controls the relative phases to an accuracy of $\pm 1°$ and the amplitude to $\pm 1\%$. The bandwidths of the control loops are adjusted to be less than the synchrotron oscillation frequency of the beam in the storage ring.

Those parameters that involve personnel safety (e.g., high-voltage barriers) are controlled with a hard-wired interlock chain. All other system information is collected and processed by a local controller, the Input Output Micro Module (IOMM) described in Section 3.11. In addition, there is a fast crowbar controller (to detect klystron window sparks and gun arcs) that is capable of removing all power from the klystron within microseconds of fault detection. The status of the crowbar controller is monitored by the IOMM to ensure that it is in constant readiness.

All accelerator and experimental areas are served by a phase stable reference system, comprising a stable master oscillator at 499.654 MHz followed by a 100-W amplifier. Each drop-off from the stable reference cable is via a 30-dB coupler, which prevents any one user from causing system errors in the event of an equipment malfunction. Other timing signals, e.g., to allow the user to identify a particular rf bucket, are also distributed.

## 3.9 Instrumentation and Low-Level Electronics

In view of the stringent beam requirements for a synchrotron light source of advanced design and performance, strong emphasis is placed on accelerator diagnostics and instrumentation. A variety of techniques will be employed:

- The storage ring electron beam position is monitored with a system featuring rapid measurement and high accuracy.
- High-frequency monitoring of the electron beam is achieved with wide-band, traveling-wave electrodes.
- The average beam current is measured with a transformer featuring dc response.
- Beam instabilities are reduced with transverse and longitudinal damping systems.
- Synchrotron light from one of the bending magnets is directed to an optical monitoring station having instruments for measurement of beam cross section, bunch length, intensity, and stability.
- Fluorescent screens are installed for measurement of first-turn beam position during commissioning and trouble-shooting.
- The photon beam from insertion devices is stabilized with a beam-steering system.
- The low storage ring pressure, so essential for long beam lifetime, is monitored with ultrahigh-vacuum gauges and gas analyzers.

Diagnostic instruments to enable efficient loading of the storage ring are installed in the booster, beam transfer lines, and linac. A timing system, which synchronizes the pulsed magnets, gun, and linac, enables filling of specified buckets in the storage ring.

Commercial instruments are installed in the control room for measurement of various beam parameters throughout the entire facility, from the linac to the storage ring. Communications systems are provided for general public address, private contact with experi-

menters, and point-to-point communication via headsets. Each of the systems is described below.

### 3.9.1 Beam-Position Measurement (BPM)

Beam position in a storage ring is generally measured with a system of button-type electrodes capacitively coupled to the electron beam. The electrode signals are multiplexed to one or a few tuned rf receivers via a system of coaxial cables and relays. The button electrodes are attached to coaxial vacuum feedthroughs welded into the beam chamber. These systems are typically capable of 0.1- to 0.5-mm accuracy and resolution [Pellegrin, 1980]. In practice, however, signal multiplexing causes the systems to be relatively slow, and the relays limit accuracy and reliability.

The BPM requirements for the Light Source storage ring are 0.02-mm resolution and 0.03-mm accuracy. In addition, high-speed measurement is required for correction of beam-orbit distortions introduced, for example, by gap adjustments of insertion devices. The BPM system described below [Nakamura and Hinkson, 1985] provides the required resolution and speed. The required accuracy of a beam-position measurement is achieved with a systematic approach using error reduction and comparison techniques.

Storage ring beam position is measured at 72 locations close to the ring quadrupole magnets and at 24 sites near the entrance and exit of insertion devices. Nominally, seven measurement sites per horizontal betatron wavelength are provided. The beam is sensed by button electrodes flush-mounted to the vacuum chamber and capacitively coupled to the beam (Fig. 3-59). The sensitivity of the electrodes to beam position in a prototype beam chamber has been determined by the use of an antenna moved relative to the buttons with a precision micropositioner stage; the results are shown in Fig. 3-60. Because the vacuum chamber is machined out of solid aluminum, holes for the button electrodes and their insulators are precisely positioned with numerically-controlled tooling. Buttons are then accurately positioned by their insulators, which are held against shoulders machined in the chamber. The vacuum feedthroughs connect to the buttons but do not determine their position.

Single- and $n$th-turn position measurements of a single electron bunch and high-speed measurements of multiple bunches are made possible by each button having its own processing electronics (Fig. 3-61). The accuracy and resolution of a single-turn measurement are a few percent. More accurate beam-position measurements of a stored beam are made by averaging position data from many turns. Systematic offsets in the parallel amplifier chains are measured by introducing a calibration signal into the amplifiers. The small computer dedicated to each set of monitoring electronics measures amplifier response to the calibration signal and removes any gain errors from the beam-position data. This computer, known as the Intelligent Local Controller (ILC, see Section 3.11), also corrects for the nonlinearity of button sensitivity and controls the amplifier gain over a range of 40 dB. Absolute beam position relative to the magnetic center of the adjacent quadrupole magnet is determined by moving the orbit in that quadrupole with a localized beam bump, then varying the quadrupole current. When the beam is centered in the quadrupole, there will be no residual orbit changes when the quadrupole current is varied [Rice et al., 1983]. Offsets in the measured beam position are removed by the computer and the absolute position established.

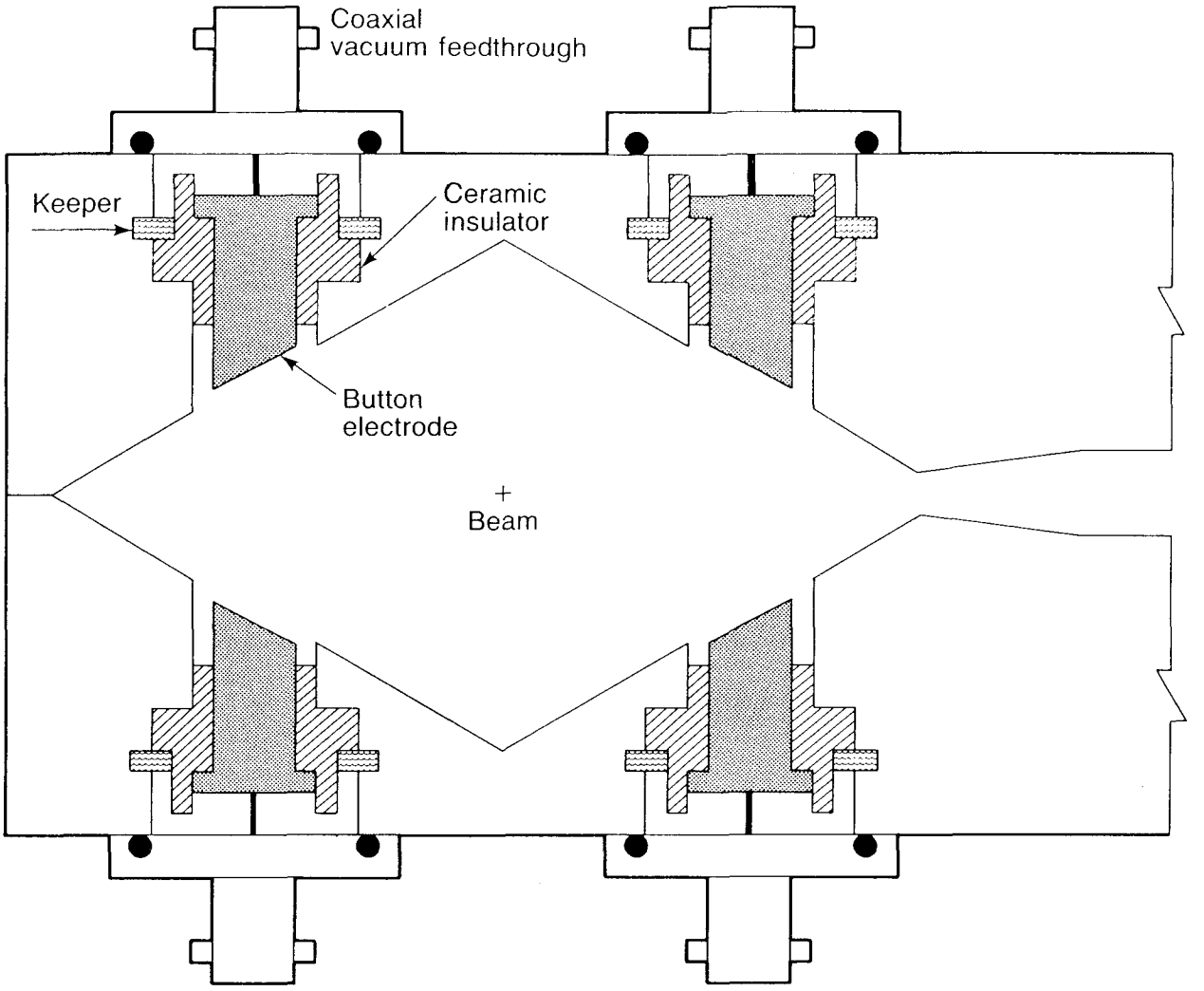


**Fig. 3-59.** Schematic cross section of beam-position measurement buttons.

The BPM amplifiers are the narrow-band type used in most storage rings. Bandpass filters tuned to the 500-MHz component of the bunch convert the very short bunch signal into rf, which is heterodyned down to an intermediate frequency (IF) of 60 MHz; commercial IF amplifiers boost and detect the signal. A track-and-hold amplifier captures the peak of the detected signal and holds it for digitization in the ILC. Position measurement of a single bunch on a selected turn is accomplished with the use of a fast solid-state switch. The switch is closed prior to the arrival of the bunch signal and opened after its passage. The selected bunch signal then drives the bandpass filter. The filter output, a burst of rf, is processed and delivered as a pulse to the track-and-hold amplifier for peak detection. Closed-orbit measurement of a stored beam is made with the switch left constantly closed. In this situation, the output of the IF amplifier detector is nearly dc. The track-and-hold amplifier can either be placed in the "track" mode to pass the dc or made to "hold" at some particular time.

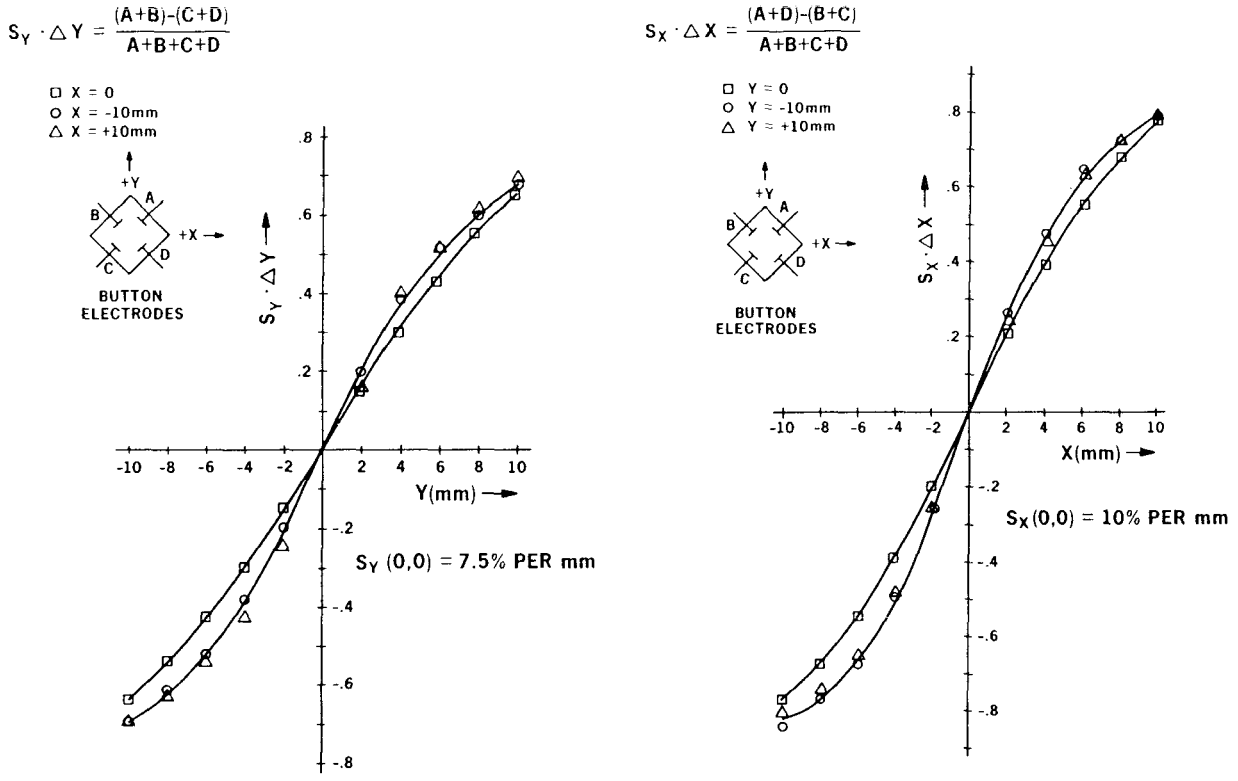


**Fig. 3-60.** Results of tests of beam-position-measurement sensitivity in the Light Source vacuum chamber: $y$ direction (at left) and $x$ direction.

### 3.9.2 Traveling-Wave Electrodes

Wide-band traveling-wave electrodes at two locations in the ring permit excitation and monitoring of the beam along two axes. The electrodes are positioned an odd number of betatron wavelengths apart. Electrode construction (Fig. 3-62) is based on a CERN SPS design [Linnecar, 1979]. The electrode width and spacing from the vacuum chamber wall are decreased exponentially over the electrode length, giving a smooth frequency response rather than the response characteristic of untapered electrodes (see Fig. 3-63). A system of high-quality coaxial cable, relays, and signal combiners allows the electrodes to be used for a variety of beam stimulus and response measurements. For example, the network analyzer described in Section 3.9.7 is used with these electrodes in determining the fractional betatron tune.

### 3.9.3 Optical Monitoring

In 1983 a study was commissioned to define the diagnostic requirements for the Light Source [Sabersky, 1983]. The resulting report includes a detailed description of a set of optical diagnostics that are compatible with our current design.

Synchrotron light from one of the bending magnets is directed by mirrors to an enclosed optical bench supporting the diagnostic instruments. Transverse beam dimensions, averaged over many turns, are measured with a lens system focusing the synchrotron

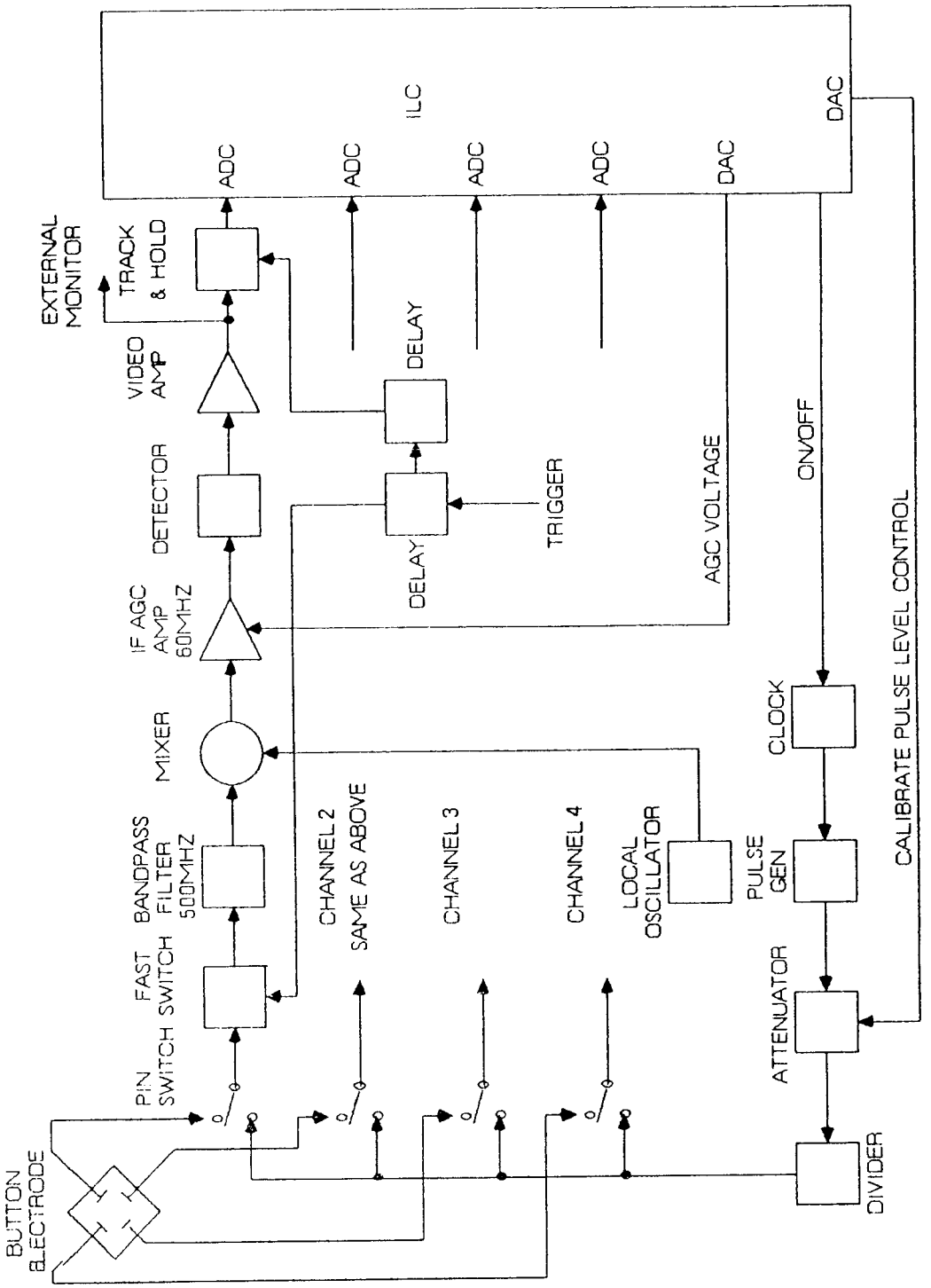


**Fig. 3-61.** Processing electronics for beam-position monitors.

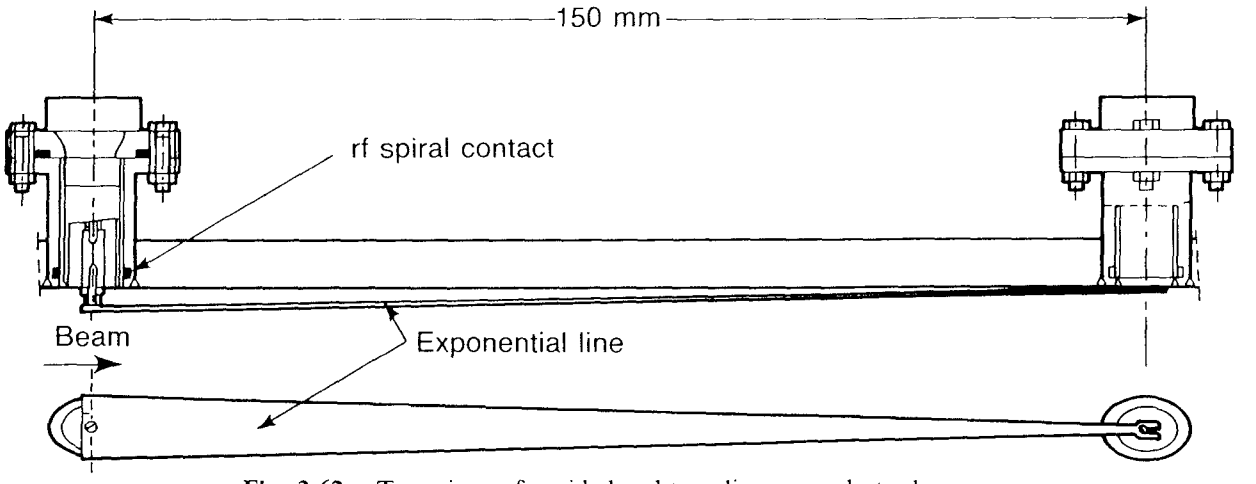


**Fig. 3-62.** Two views of a wide-band traveling-wave electrode.

light onto solid-state scanned photodiode arrays, such as EG&G Reticons. Slow, transverse beam blowup can also be observed with these arrays. Longitudinal beam dimension is measured with a streak camera having 2-ps resolution, such as a Hamamatsu Model C-1370 Temporal Disperser. The streak camera is the only instrument capable of measuring the 28-ps bunch in a single pass. Average bunch length is measured with a fast vacuum photodiode whose output voltage is observed on a sampling oscilloscope. TV cameras viewing the synchrotron light image against a reference graticule provide a reliable beam position and transverse size diagnostic. A fast photomultiplier tube equipped with a shutter measures the light over a wide intensity range. This device is useful as a diagnostic in commissioning and in determining the relative charge in individual beam pulses. The technique for relative charge measurement is similar to that in use at the Daresbury SRS [Brown and Jackson, 1983].

### 3.9.4 DC Current Transformer (DCCT)

A DCCT (Fig. 3-64) is installed over a metallized ceramic gap in one of the straight-section beam pipes. The DCCT provides an absolute measure of the average beam current and is used to determine beam lifetime. A typical design [Unser, 1981] has a 0- to 500-mA current range, 0.001% linearity, a 5-$\mu$A noise limit, and a frequency response of dc to 50 kHz.

The thin metal coating on the ceramic gap protects the transformer from the high-frequency, high-power components of the beam bunch, while passing the low-frequency components for measurement. The ceramic gap presents a longitudinal impedance to the beam, but this is reduced by the metal coating. The transformer consists of two magnetic cores having an equal number of oppositely-wound excitation turns. A low-frequency oscillator drives the cores in opposite senses. A sense winding wrapped around both cores measures no net flux unless the beam is present. The beam magnetic field causes a second harmonic of the core excitation frequency to be developed in the sense winding. This second-harmonic voltage is detected by a synchronous demodulator operating at twice the excitation frequency; the voltage is then amplified and applied to a feedback winding on both cores, thus canceling the beam-induced core flux. The amplifier output voltage, which is a measure of the beam current, is digitized and processed for control-room display.

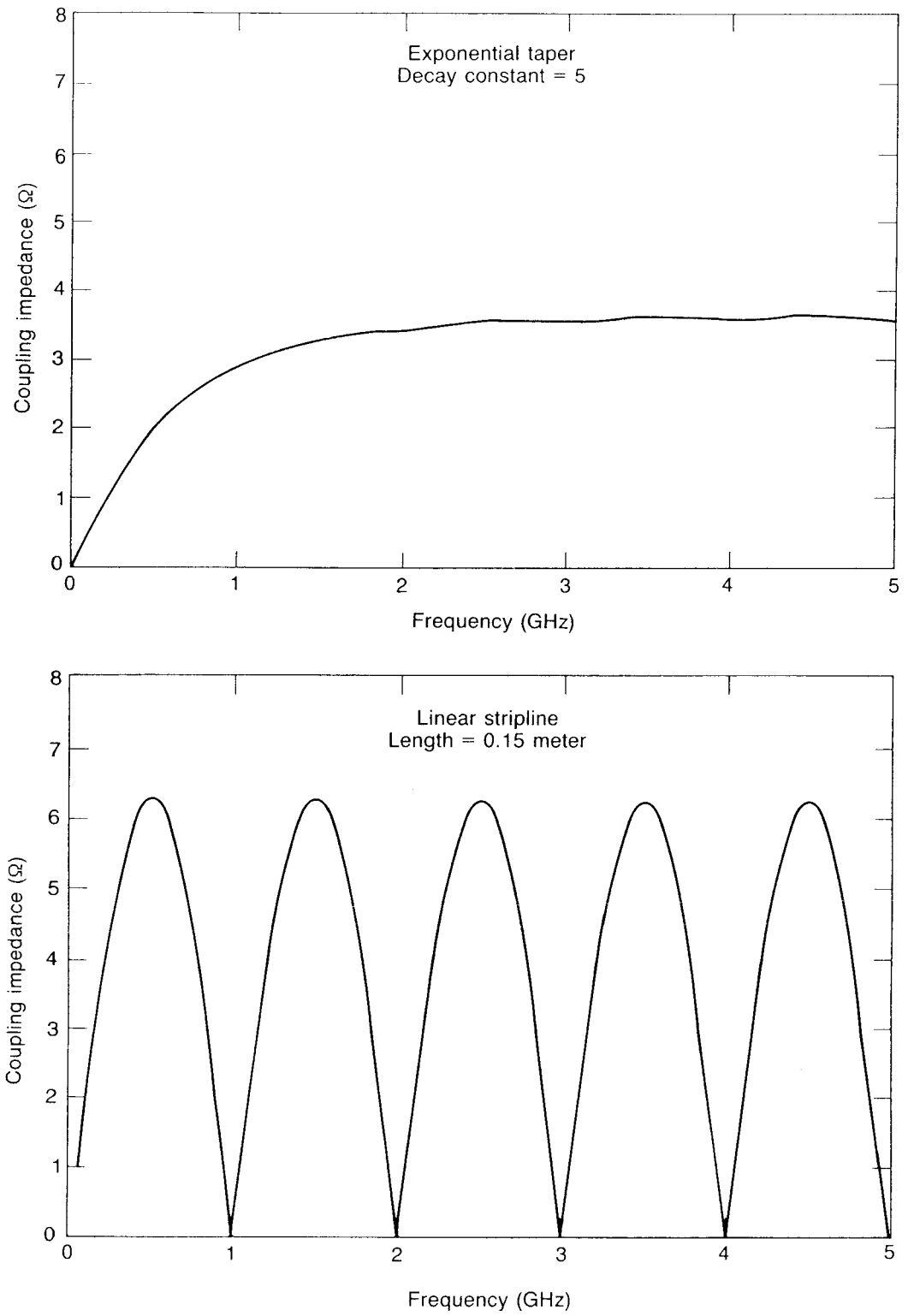


**Fig. 3-63.** Coupling impedance as a function of frequency for tapered (top) and untapered couplers.

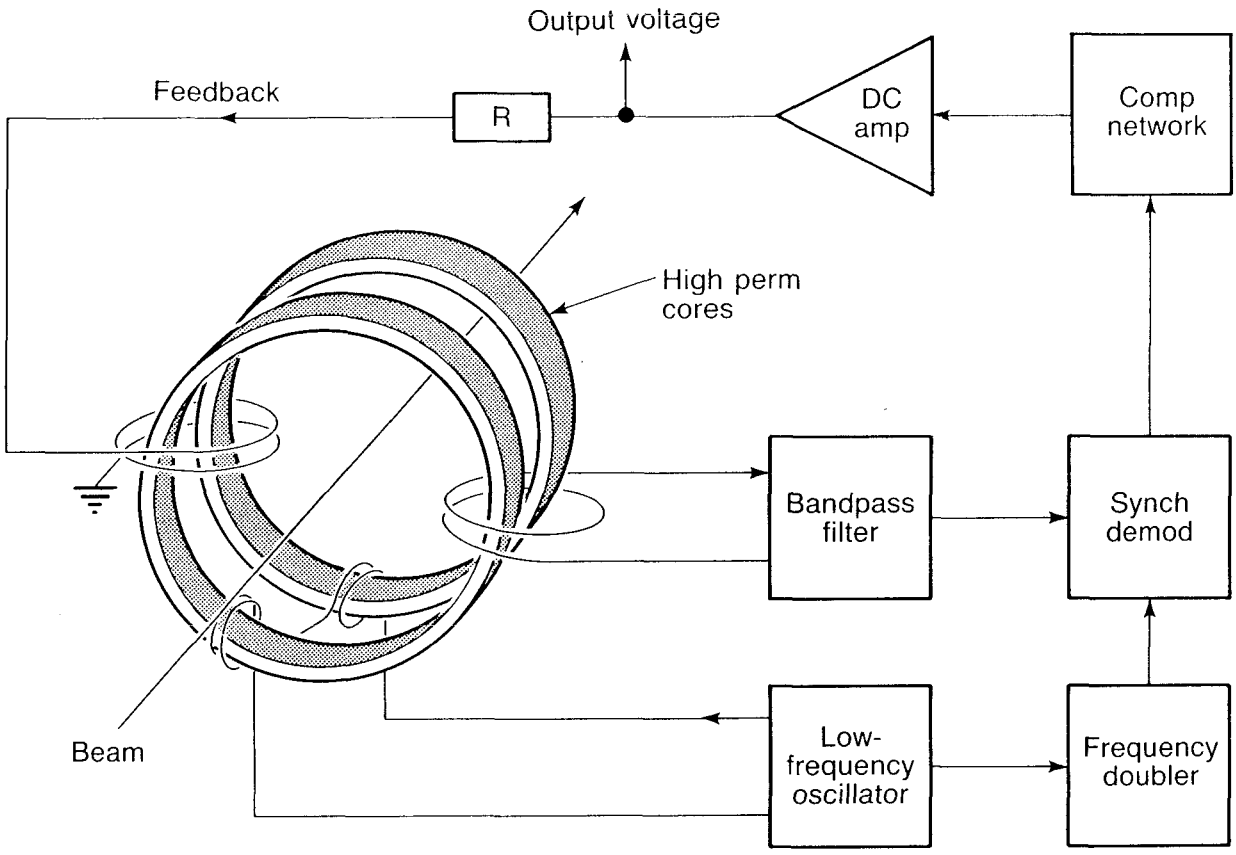


**Fig. 3-64.** Schematic of a dc current transformer (DCCT).

### 3.9.5 Scintillators (Flags)

Retractable scintillators and TV cameras are installed at six locations in the storage ring. These are the simplest and most reliable beam diagnostic tools in the ring for first-turn measurements. Flags are of greatest use during commissioning and trouble-shooting of the storage ring. TV monitors in the control room display the beam image formed on the scintillator against a reference graticule.

### 3.9.6 Beam Damping

Transverse and longitudinal instabilities in the beam are driven primarily by higher-order modes in the storage ring rf accelerating cavity, as discussed in detail in Section 3.3.2. Damping systems are installed to inhibit the growth of these synchrotron and betatron oscillations. If cavity higher-order modes are not attenuated, the beam-damping systems will have to provide damping for 164 possible modes in a bandwidth of 250 MHz. The growth rate of the longitudinal instabilities would require about 1 kV of damping voltage from the longitudinal kicker. Approximately 50 V would be required from the transverse kickers. The influence of the rf cavity higher-order modes on the beam is reduced by coupling their energy to dummy loads via antennas in the cavity, a procedure known as "mode damping." The longitudinal damping system is therefore designed to damp 100 modes with a kicker voltage of 700 V. It is modeled after the system used at the CERN PS booster

[Pedersen and Sacherer, 1977]. The transverse dampers are based on the NSLS booster system design [Galayda, 1985].

To provide the required longitudinal and transverse beam damping, three sets of pickup electrodes, filters, amplifiers, and kicker electrodes are installed. The pickup electrode voltages represent a pulse train occurring at the storage ring revolution frequency. The pulses are modulated by coherent betatron and synchrotron oscillations, which give rise to sidebands at specific frequencies in the beam power spectrum. Filters and tuned amplifiers in each system select only those frequency components related to a particular oscillation mode; the strong components at the revolution frequency are rejected. The radial oscillation signals are amplified in power amplifiers and applied to the beam via the kickers as a negative feedback voltage.

To damp the synchrotron oscillations, the antidamped synchrotron sidebands on the harmonics of the revolution frequency are selected, amplified, and applied to the beam as negative feedback. The synchrotron sidebands representing damped synchrotron modes are rejected. This is accomplished with a system of 100 narrow-band amplifiers (Fig. 3-65). The amplitude content of the pickup signal is removed in a saturating amplifier, while the phase information is preserved. A phase detector translates the pickup signal from 1 GHz down to low frequencies. The desired synchrotron modes up to 150 MHz are amplified and mixed back up to the 1-GHz level. The signals are combined and boosted in a 1-GHz power amplifier having a 250-MHz bandwidth. A phase shifter at the power amplifier input permits the rf phase to be adjusted for optimum damping. The high-power rf is applied to the longitudinal kickers via an in-phase power splitter. Should future accelerator

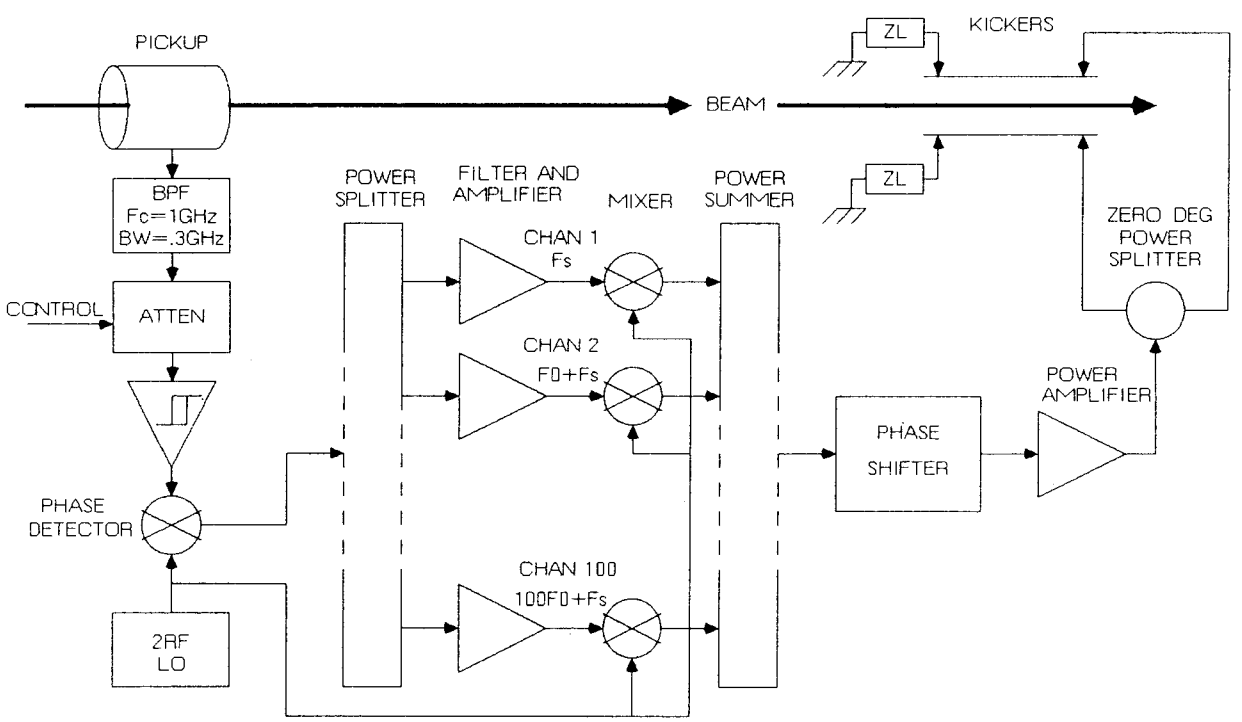


**Fig. 3-65.** Schematic of a system for longitudinal beam damping.

physics studies demonstrate the need for a wider bandwidth, more narrow-band amplifiers can be added.

Two filter and amplifier systems are required for horizontal and vertical transverse damping (Fig. 3-66). The amplitude of the pickup electrode pulses is dependent on beam current. Because it is desired to detect the pulse modulation representing betatron oscillations in a manner insensitive to beam current, automatic-gain-controlled (AGC) amplifiers are installed to stabilize the electrode signals over a 40-dB range before detection occurs. Removal of the rotation harmonics and selection of the betatron sidebands is accomplished with a correlator filter [Galayada, 1985]. This filter is composed of hybrid junctions and two lengths of coaxial cable. One cable has a time delay of 10 ns. The other cable has a time delay of 10 ns plus the 656-ns ring orbital period. These cables are connected to the hybrids with proper phasing to form a filter that rejects the orbital harmonics while passing the betatron sidebands. Power amplifiers with a bandwidth of 1 MHz to 250 MHz amplify the betatron sidebands and provide a transverse damping voltage of 50 V via 180° power splitters.

### 3.9.7 Control-Room Instrumentation

Two custom consoles arranged horseshoe fashion contain computer interface equipment for operator control of the accelerator. In addition, television monitors, oscilloscopes, a spectrum analyzer, and a network analyzer are installed in these consoles. The TV monitors are used for observation of the synchrotron light image, the response of scintillators to the electron beam, and the accelerator access gates. The control-room oscilloscopes include a Tektronix 7104 1-GHz real-time scope, two Tektronix 7834 400-MHz analog storage scopes, and two 10-MHz digitizing instruments, such as the Tektronix Model 5223. The oscilloscopes are synchronized to the accelerator timing system and are used to measure signals from beam diagnostics and pulsed magnets. A spectrum analyzer, such as an HP Model 8566B, is used to study storage ring beam harmonics and the performance of the rf accelerating cavity. The network analyzer, e.g., an HP Model 8753, in conjunction with the storage ring traveling-wave electrodes, is used to make fractional betatron tune measurements on the beam. Because phase is measured with the network analyzer, the complex impedance seen by the beam is determined. Measurements at frequencies above a few gigahertz are conducted as near to the signal source as possible; long coaxial cables going from the storage ring to the control room attenuate high-frequency signals sufficiently to make local measurements necessary. Standard racks installed around the perimeter of the control room will contain the remainder of the equipment necessary for remote operation of the accelerator complex.

### 3.9.8 Communications

A headset system enabling hands-free, multichannel communications between many sites in the accelerator is installed. These are commercial headsets, such as those manufactured by David Clark Corp., with microphones and long coiled cords. This system is especially useful during the installation and debug phase of the accelerator construction project. An intercom system providing private communications between an experimenter and the control room is provided, along with a general project public-address system.

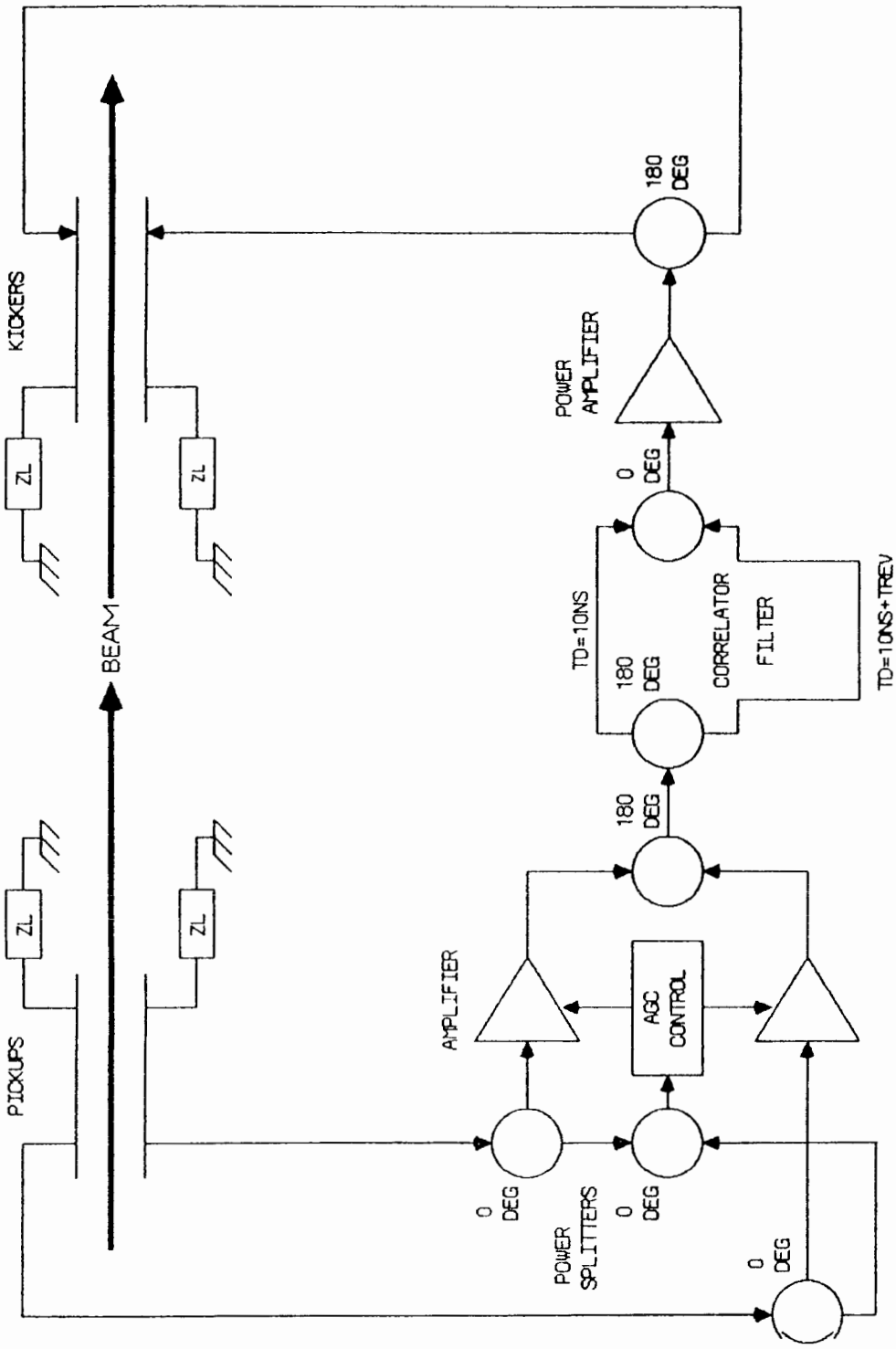


**Fig. 3-66.** Schematic of a system for transverse beam damping.

### 3.9.9 Timing

The timing system supplies synchronization pulses to the gun, linac, booster pulsed magnets, storage ring pulsed magnets, beam-position-monitoring system, and control-room instruments; it also provides pulses for use by the experimenters. Magnetic-field-derived pulses from the booster trigger the linac rf system and electron gun to fill a selected booster bucket. Single-bunch loading and transfer are accomplished with a system functionally similar to the NSLS single-bunch transfer system [Sheehan et al., 1983], but operated at 500 MHz rather than 50 MHz. A system of frequency counters (Fig. 3-67) provides rf/328 (the storage ring rotation frequency), rf/125 (the booster rotation frequency), and rf/41,000 (the frequency—12.2 kHz—at which selected booster and storage ring buckets are in coincidence). When a coincidence occurs, a pulse is generated that triggers the booster and storage ring pulsed magnets, causing the booster bunch(es) to be transferred to the appropriate storage ring bucket(s). Programmable time-delay instruments, synchronized by the bucket-counting system, deliver timing pulses to the BPM electronics to enable first- or $n$th-turn beam-position measurement.

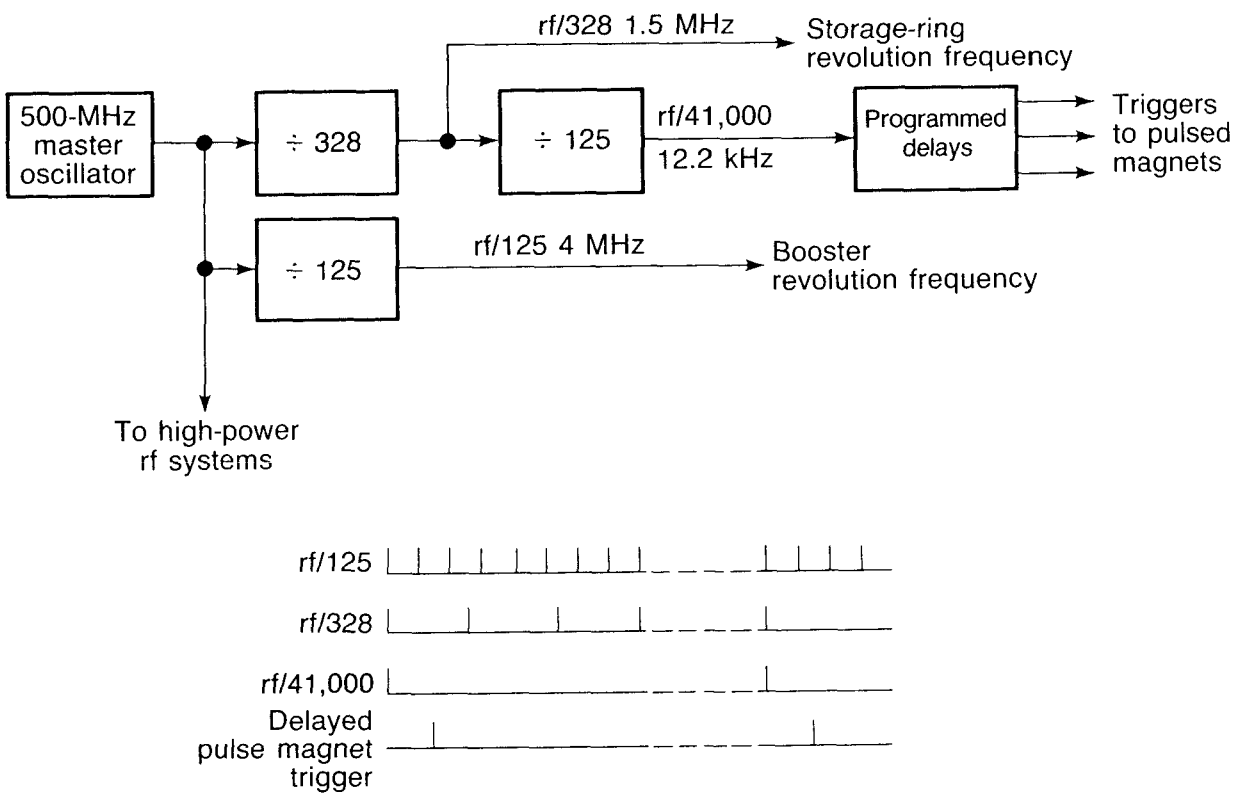


**Fig. 3-67.** Frequency counters for single-bunch transfer.

### 3.9.10 Beam Line Steering Control

To provide the high degree of photon beam position stability required by the experimenters, a beam line steering-control system similar to that in use at the SPEAR ring [Hettel, 1983] is installed (Fig. 3-68). Two steering magnets, each capable of deflecting the beam

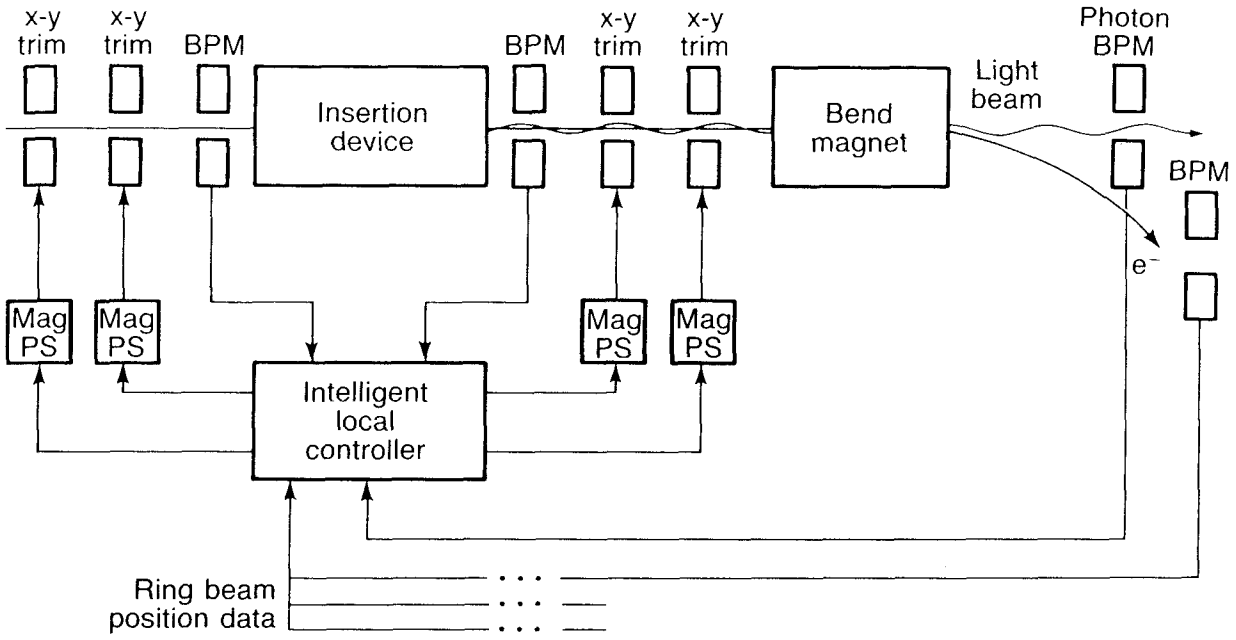


**Fig. 3-68.** Steering control system based on feedback from the photon beam line.

horizontally and vertically (see Section 3.4), are installed at each end of the insertion straight sections. Any (small) residual dipole fields introduced by an insertion device (wiggler or undulator) can be compensated by one or more of these local magnets. Variation of both beam position and angle through a device is provided in a completely compensated fashion. That is, small changes can be made locally that are transparent to the remainder of the machine. This latter capability will be used in a feedback loop with a bandwidth from dc to 10 Hz, with feedback signals taken from the photon beam itself.

### 3.9.11 Vacuum Monitoring

Very low pressure is required in the storage ring for good beam lifetime. Computer-controlled instrumentation is provided for measurement and analysis of the gases present in the vacuum chamber. An approximate indication of total pressure, and a measure of ion-pump performance, can be obtained from the ion-pump current. This current is monitored in each of the 108 ion pumps in the storage ring. Ultrahigh-vacuum ion gauges, such as the Varian UHV-24, are installed in the ring in 48 places. Ion gauge controllers are connected to 12 of the gauges; these are continuously monitored by the control system. One of the ion gauge controllers is interlocked to the high-power rf system and will shut down the rf in the event of a significant pressure rise. Residual gas analysis detectors are installed at 12 locations in the ring (Fig. 3-69). They are multiplexed to two nearby controllers that are monitored by the control system. An analyzer such as the Dataquad DAQ200 (with multiplexer) is capable of measuring better than $1 \times 10^{-12}$ Torr partial pressure and $1 \times 10^{-10}$ Torr total pressure. These analyzers are useful in measuring total pumping system performance and for analysis of gas loads from photon beam lines. The beam chamber is fitted with heaters for bake-out. A system of temperature controllers and scanners (with readouts) is provided for control and monitoring of the bake-out procedure. The vacuum measurement

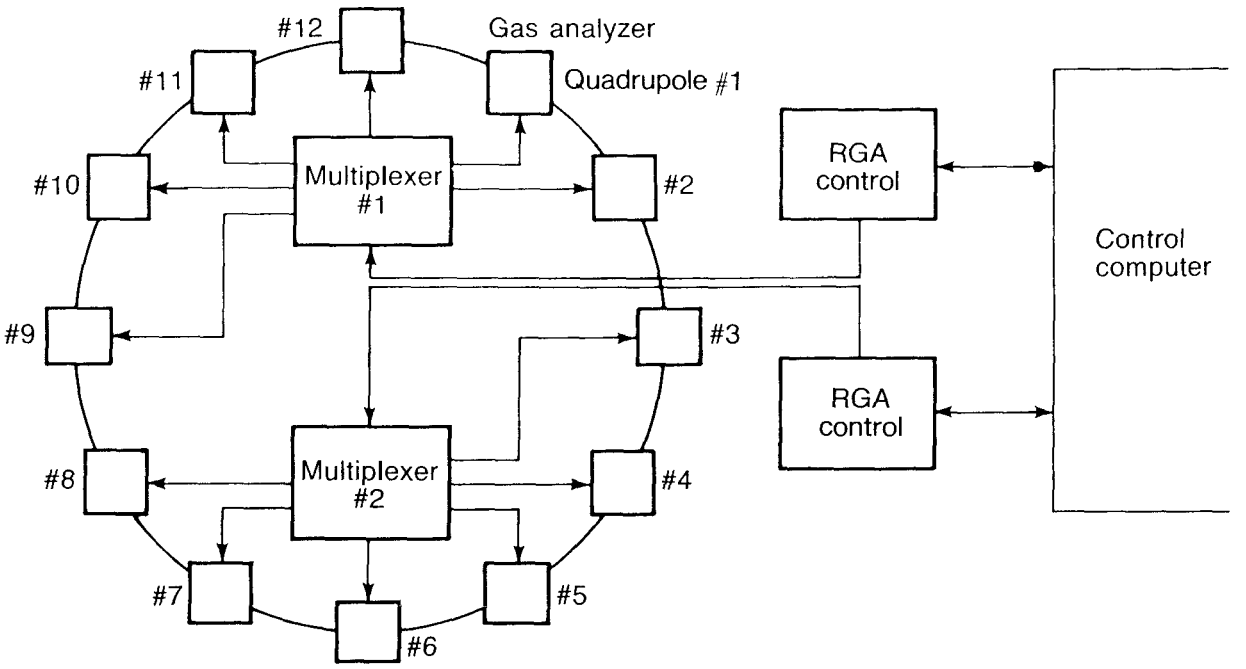


**Fig. 3-69.** Schematic of residual-gas analysis system.

requirements for the remainder of the accelerator system are less stringent than for the storage ring. Computers monitor the performance of all ion pumps and store measurement data from ion gauge controllers.

## 3.10 Safety System

### 3.10.1 Design Philosophy

The design philosophy behind the safety system described here is that it must protect personnel from all plausible hazards related to the operation of the injector, booster, and storage ring. The primary hazards addressed are those associated with radiation, high voltage, high-stored-energy devices, and moving mechanical parts or assemblies. To achieve its aim, such a system must be fail-safe, implying that it must be redundant, self-checking, reliable, and simple.

Redundancy requires more than one level of checking and protection. The question then becomes, how many levels? If one examines the operating philosophy of other accelerators, such as those at SLAC and Fermilab, one finds two levels of redundancy, whereas the Shiva laser facility at the Lawrence Livermore National Laboratory relies on three levels. The long history of safe operation at facilities using two levels led us to adopt the same number at the Light Source.

By self-checking, we mean that any single system error or failure must be detected before other errors or failures occur that might produce a hazardous situation. This requires that all individual circuits and chains be checked to determine whether they are reporting the same status. Clearly, the failure of a single device, such as an actuator, that operates two safety switches defeats the whole system.

On the basis of the above criteria, a simple hard-wired electromechanical system was selected. Switches of the Microswitch type are used to sense position (open or closed), while semiconductor tone transmitters are used to transfer status information over long distances. No semiconductors are used in applications where a failure would render the system inoperative or result in a hazardous situation.

### 3.10.2 Tone Loop

The system that ties together all safety subsystems and forms the status links among them is the "tone loop" shown in Fig. 3-70. Only if this tone loop is intact, i.e., only if a tone is being transmitted along each link, can potentially hazardous equipment be operated. If the loop is interrupted for any reason—say, if a gate interlock is violated—all such equipment is immediately shut down.

Each tone transmitter is, in fact, two transmitters, one of which operates at about 4 kHz, the other at about 5 kHz. Likewise, each receiver is actually a pair, again operating at about 4 and 5 kHz. These receivers have very narrow bandwidths, so that neither harmonics of the fundamental frequencies nor spurious signals are detected as "true" signals. A tone transmitter produces an output signal only if its companion tone receiver receives an input. If a true signal is present at the input of the receiver, an electromechanical relay in the receiver output is energized. The relays of both channels must be energized, i.e., both tone loops must be complete, before any equipment in the controlled access zone (see below) can be energized.

A tone interrupt unit (TIU) is interposed between the output of each tone transmitter and the input of the next tone receiver in the tone loop. Its purpose is to break the transmitted tones both by opening the tone wire pairs and by shorting the wire pairs which continue on to the tone receiver. The TIU receives its inputs from door interlocks, "crash-off" boxes, and other safety-related devices. If a TIU receives a fault signal, it breaks the tone loop. In this way, all tone transmitters and receivers are set in a "safe" condition, as this loss of signal is propagated around the ring. As shown in Fig. 3-70, the main computer monitoring system looks at the status of all these devices and displays the fault conditions.

We therefore have two systems (the two tone loops), in either of which a failure renders the area safe. This same type of system is in use at SLAC, and with slight modifications was installed at PEP. Fermilab also uses a loop system, but it relies on a dc level instead of a tone. An advantage of the tone loop is that it remains functional even in the event of an unwanted applied voltage.

### 3.10.3 Controlled Access Zone

"Controlled access" designates a system of physical barriers to prevent personnel from entering hazardous areas. If these barriers are violated, all hazardous equipment is turned off, and all sources of radiation are secured. Controlled access is achieved by locked gates at the following locations:

- Entrances to the area inside the storage ring.
- Entrances to each storage ring labyrinth.

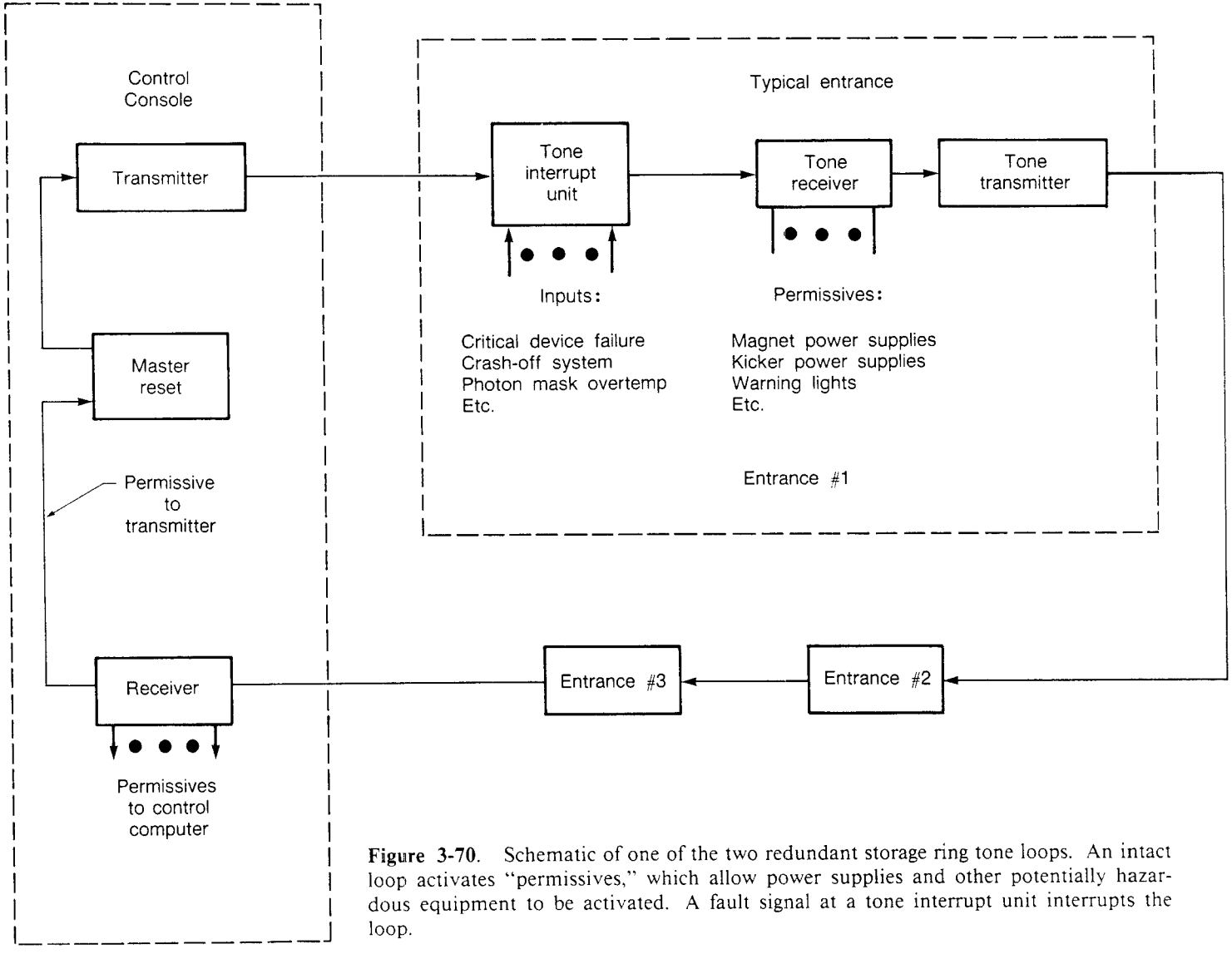


**Figure 3-70.** Schematic of one of the two redundant storage ring tone loops. An intact loop activates "permissives," which allow power supplies and other potentially hazardous equipment to be activated. A fault signal at a tone interrupt unit interrupts the loop.

- Each side of the rf cavity.
- Each side of the booster-to-storage-ring transfer line.

All gates are provided with two switches to indicate whether they are closed and latched. Each gate also has a lighted status sign, indicating machine status.

Only the main gate to the area inside the storage ring is keyed. Also located at this gate are a panel containing a badge reader, a TV camera, a key tree, a microphone, and a loudspeaker. Except in emergencies, access can only be gained when a key from the control room is inserted in the key tree. This releases a key to unlock the mechanical gate latch. In addition, the employee's badge must be inserted in the card reader to log in the employee. The control room operator, using a TV monitor to determine the number of people entering and to confirm that they have been logged in, can release the electromechanical gate latch. The opening of any gate in this area causes the shutdown of appropriate equipment.

### 3.10.4 Area Monitoring

Area monitoring is required if personnel are to be allowed to work inside the storage ring enclosure when the booster is on, or inside the booster enclosure with the linac operational. Excessive radiation or monitoring equipment failure must turn off all sources of radiation under these circumstances.

For the Light Source, area monitoring consists of a Panofsky Long Ion Chamber (PLIC), subdivided into 12 sections that are distributed around the ring. A small source is attached at the far end of each PLIC, and a bias supply and event counter are also connected to each. The event counters are interlocked to ensure that the count rate is above background—as it must be when the system is working, owing to the presence of the auxiliary source—and below a hazardous level. The faulting of either of these interlocks shuts down the booster and injector. These interlocks can be by-passed during normal operation, at which time the PLICs are available to monitor the amount and location of excess beam loss during filling of the storage ring.

### 3.10.5 Safety Shutters

The storage ring safety shutters protect personnel in the experimental areas during the filling of the storage ring. The system is designed so that the safety shutters cannot be closed unless the photon shutters are closed and the storage ring cannot be filled unless both are closed. The relay circuits are redundant at two levels, and self-checking ensures detection of a failure in a single circuit. A failure will not shut down the machine, but it will prevent further filling of the storage ring. (The safety shutter and the photon shutter are discussed further in Section 5.2.)

### 3.10.6 Reset/Crash-off Boxes

The reset/crash-off boxes are dual-function devices. The "crash-off" portion of each box interfaces with the TIU located at the entrance to the area inside the storage ring. If any of these boxes is activated, all hazardous locations are rendered safe by appropriate equipment shutdowns. In addition, the operators are alerted via an audible alarm. Manual activation

of a crash-off box is thus meant to indicate a serious problem—a fire, medical emergency, or radiation hazard. The "reset" portion of each box is part of a search-and-clear chain, which demands that a search be made of the area in a prescribed manner (and the boxes reset in a prescribed sequence) within a predetermined period before hazardous equipment can be made operational once again.

## 3.11 Control System

The computer control system provides a means for accessing all machine components, so that their values can be set and monitored remotely. This is done, by the operator, through a console consisting of a number of TV displays and appropriate data input devices. To allow flexible control, a number of computer programs are provided to the operator. The status of machine devices is displayed, with graphics where appropriate, and software is provided for archival saving (and subsequent retrieval) of machine parameters. A typical start to machine operation will be to recall a set of machine parameters from the archives, make a few corrections to it (either by direct operator input or under program control), and send it to the hardware devices.

The console displays and controls (also known as the operator interface) are structured to permit efficient operation. This requires that a number of different operational scenarios be accommodated. The experienced operator will require instant access, with a minimum of advice from the programs; for the beginning operator, a programmed path will be provided to ease the process of learning machine operation. A number of programs are available that will provide computer models of the machine (for example, a program that calculates the behavior of a beam through a series of steering and focusing magnets). These make it possible to exercise computer tuning, i.e., tuning under program control, to make measured beam parameters more closely approach those required by an idealized model. Normal day-to-day operation will require that a set of machine settings be given to the control system as a reference and that a set of tolerances be established on these data. The control system will then advise the operator of any values out of tolerance. Finally, the consoles will permit the parallel, independent activity of two or more operators when this is desirable.

The control system uses a highly distributed, microprocessor-based architecture. This approach was pioneered at LBL on the Uranium Beams Project [Lancaster et al., 1979; Magyary et al., 1981a; Magyary et al., 1981b], and many of its underlying ideas (parallel processing, all microprocessor based, distributed data base, bus-based system, etc.) are now widely used, for example by the LEP control system [LEP Design Report, 1984]. The major benefits of such decentralized systems are

- An improvement in system response.
- A substantial simplification in programming effort.
- A lower maintenance cost over the life of the accelerator.
- An ability to adapt to future developments both in hardware (processors, etc.) and in network topologies (Ethernet, MAP, etc.).

The design philosophy for the control system is to have a reliable, fast, and user-friendly system, from initial commissioning until achieving day-to-day operation, with complete

capability for reporting all operating parameters. All aspects of the linac, linac-to-booster (LTB) transfer line, booster, booster-to-storage ring (BTS) transfer line, storage ring, and parts of the photon beam lines are controlled through a distributed system based upon many high-performance microcomputers (Intel 80188, 80286, and 80386) operating in parallel. With this very flexible architecture, we can make careful trade-offs between hardware and software, thereby using technology effectively and holding software costs down. In addition, using a compatible family of processors simplifies the interface among the many parts of the system, further reducing software cost and complexity.

To facilitate the development of specialized auto-tuning or modeling applications software, workstations (MicroVAX, IBM PC/AT, and others familiar to accelerator physicists and operators) can be connected to the control system. This is accomplished by providing an industry-standard network interface with high-speed access to the accelerator data base. Since these programs will be written mostly in high-level languages (Basic, Fortran, PLM, C, Pascal, and ADA), they will be easy to integrate into the main part of the control system should even faster access and higher performance be desired. This transition is particularly simple if the workstations utilize Intel-based processors, as does the IBM PC family, since the processor used in the main part of the control system will be an Intel 80386. This microprocessor has the hardware-supported capability to run multiple operating systems simultaneously [MS/PC DOS, UNIX (XENIX), or RMX, a real-time operating system]. Additional features carried forward from the Uranium Beams Project control system include the following:

- Local debugging capability.
- High-level programming languages.
- Homogeneous processor architecture throughout the system.
- Ease of maintenance and repair.
- Use of workstations.
- Data-driven software capability.
- Built-in help functions.

Furthermore, it will be possible to utilize a substantial amount of existing software to minimize software development costs. Our understanding of the processors involved, the architectural features, and the computer languages used will lead to considerable cost savings and rapid commissioning.

### 3.11.1 System Architecture

The overall system architecture is shown in Fig. 3-71. The control system consists of

- A set of chassis that use parallel microcomputers and that serve as the interface units (Input-Output Micro Modules, or IOMMs, Fig. 3-72).
- A large number of single-processor units (Intelligent Local Controllers, or ILCs, Fig. 3-73).
- A central data base storage/collector (Collector Micro Module, or CMM, Fig. 3-74).
- The operator display driver (Display Micro Module, or DMM, Fig. 3-75).

These are described below.

The IOMMs or ILCs [Lancaster et al., 1983] provide an interface to the accelerator

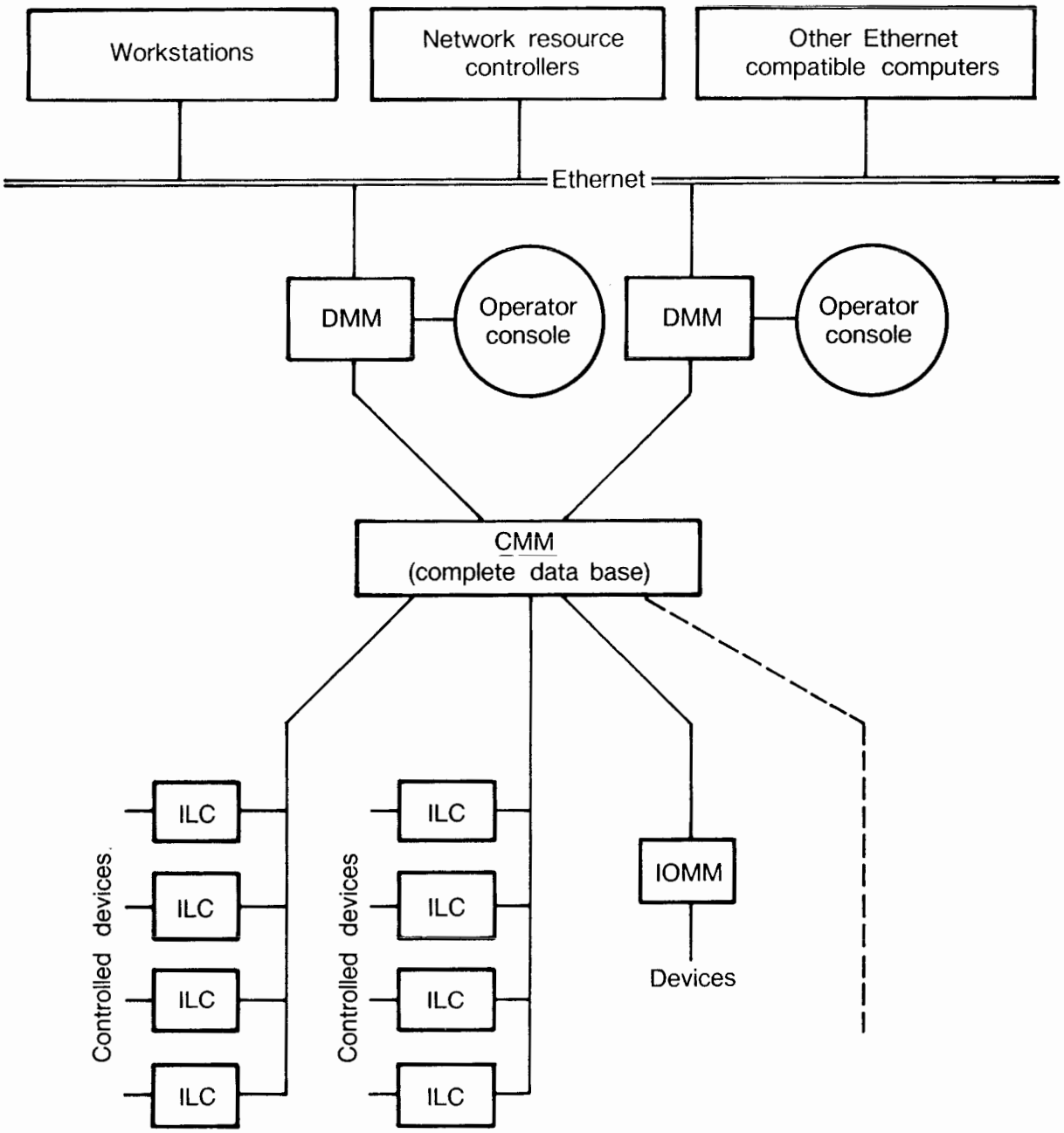


**Fig. 3-71.** Block diagram of the overall control system architecture.

equipment by collecting data and transmitting control instructions. They contain a local data base and reside near the accelerator hardware. A primary function of these units is to continually refresh the data stored in the central data base at the CMM.

The CMM collects the data from all the IOMMs and ILCs. Data are sent to and from the CMM over fiber-optics serial links at a 500-kilobaud rate. These data are stored in dual-ported memory, so that a fresh copy of the local data bases resides at all times in the CMM.

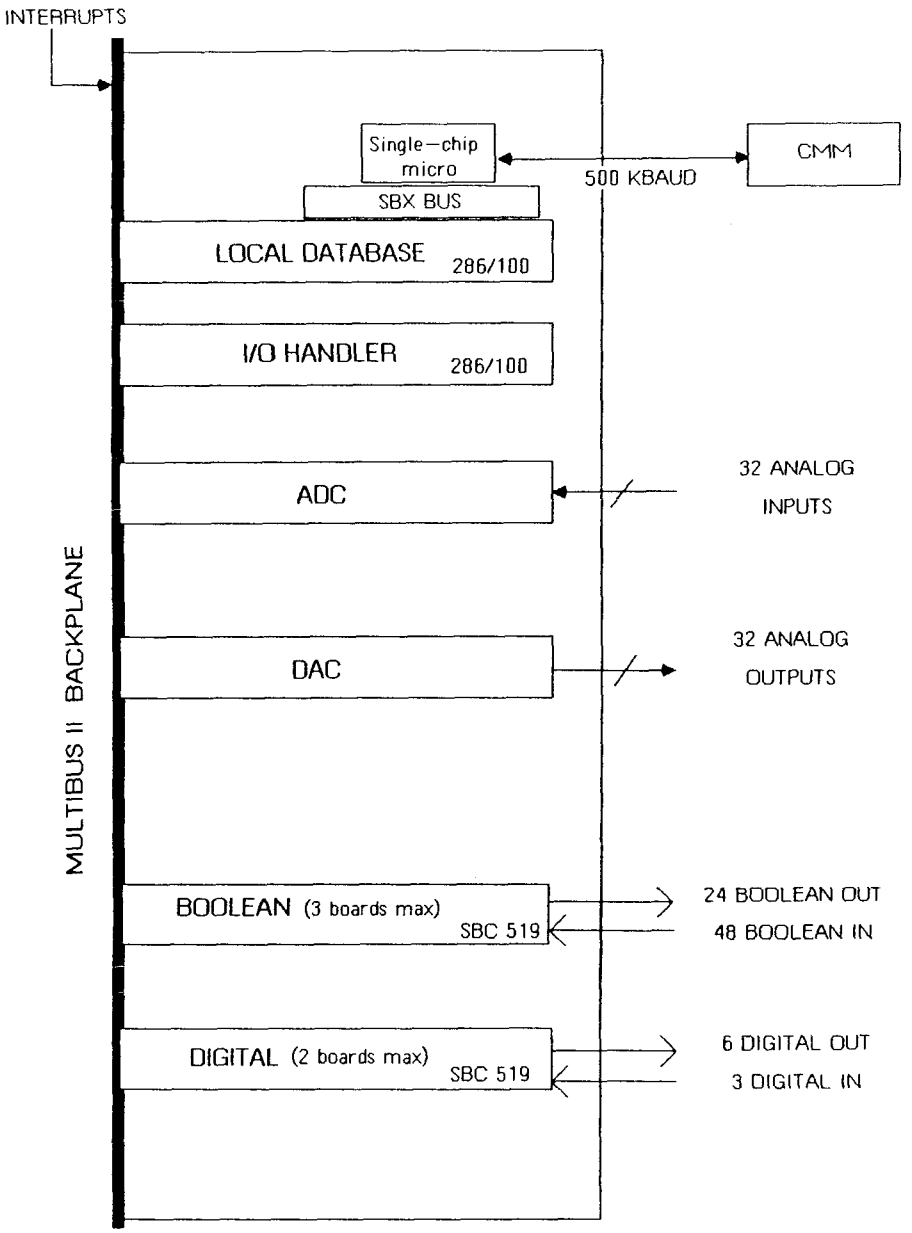


**Fig. 3-72.** Input-Output Micro Module (IOMM).

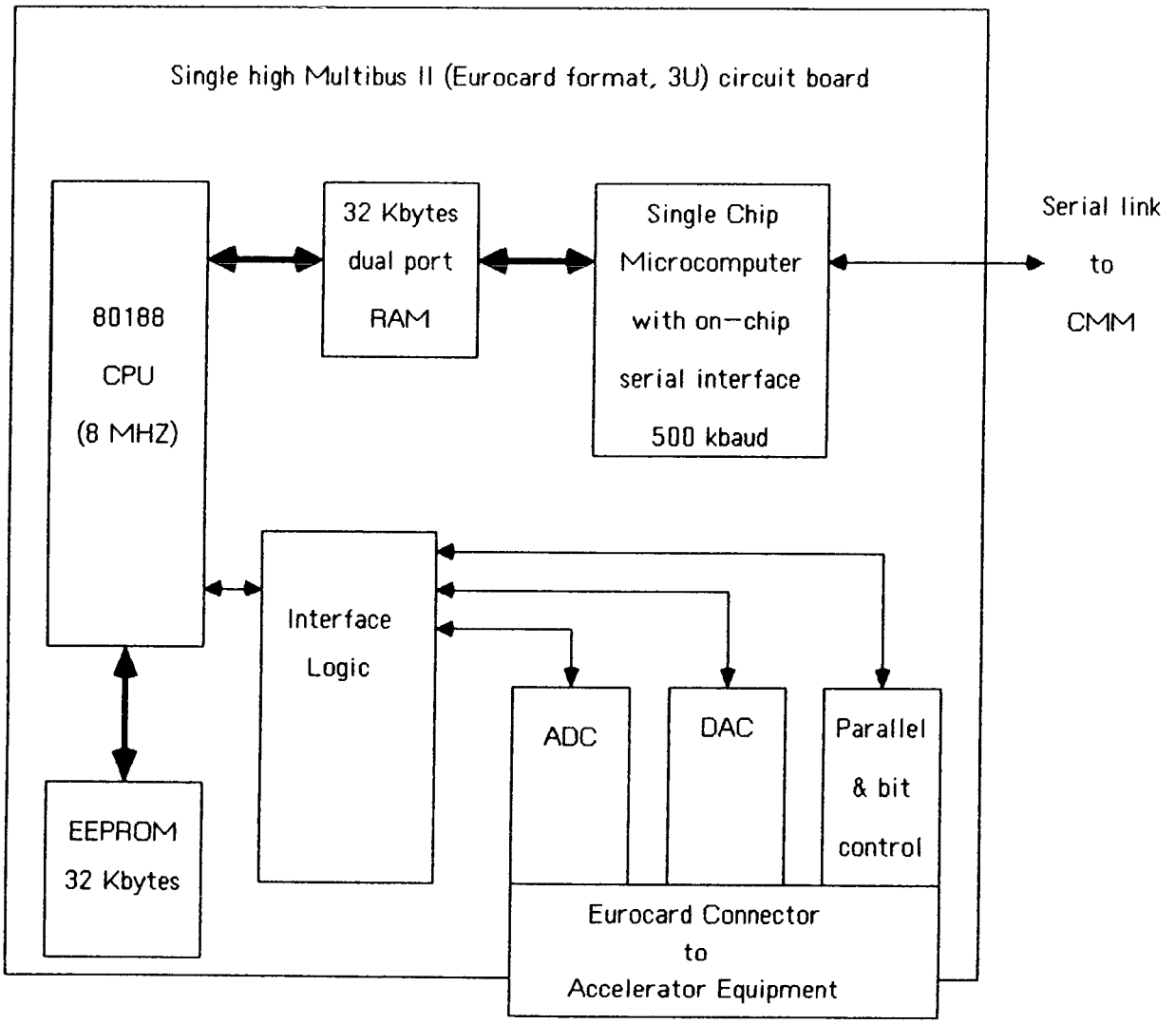


**Fig. 3-73.** Intelligent Local Controller (ILC).

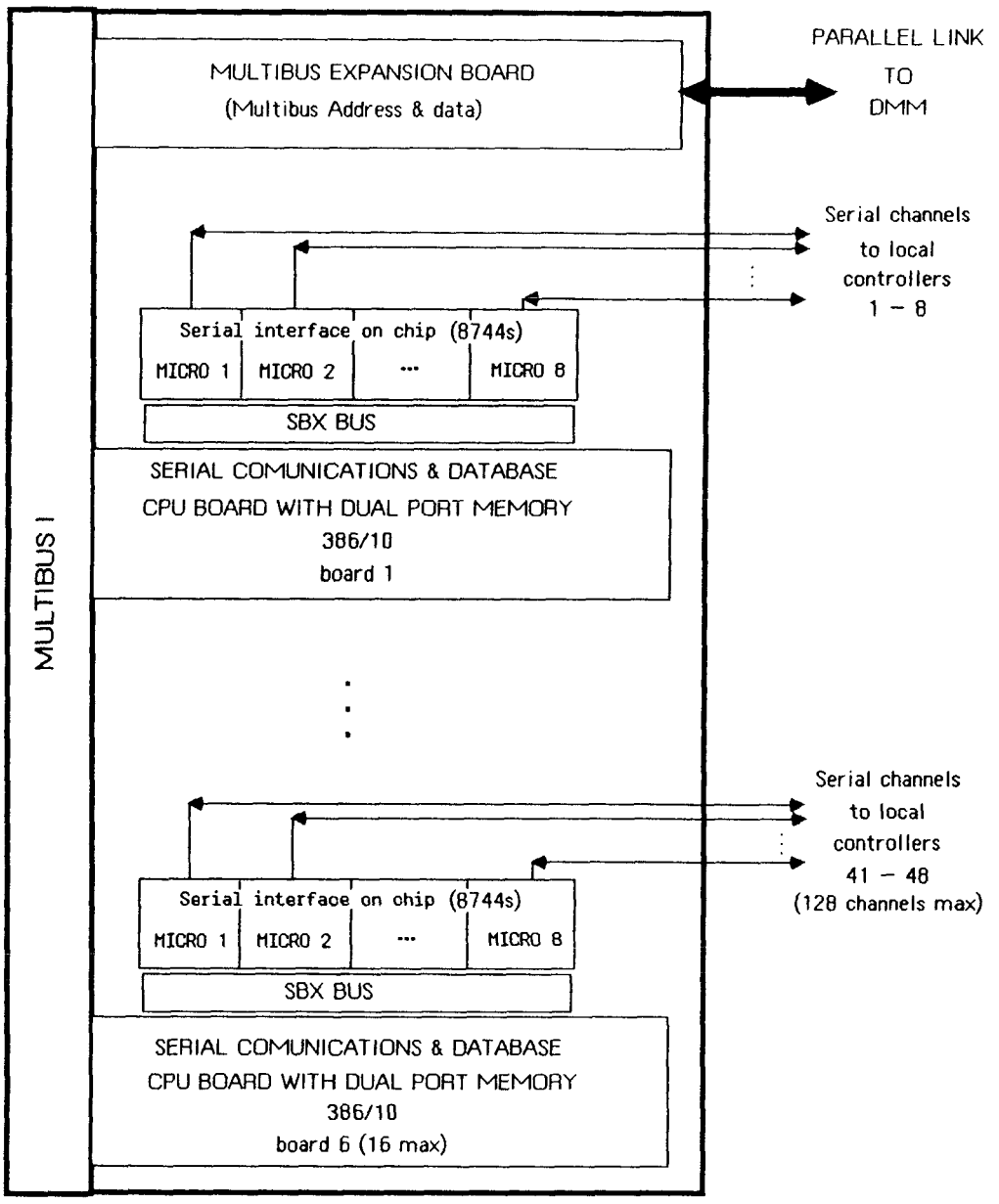


**Fig. 3-74.** Collector Micro Module (CMM).

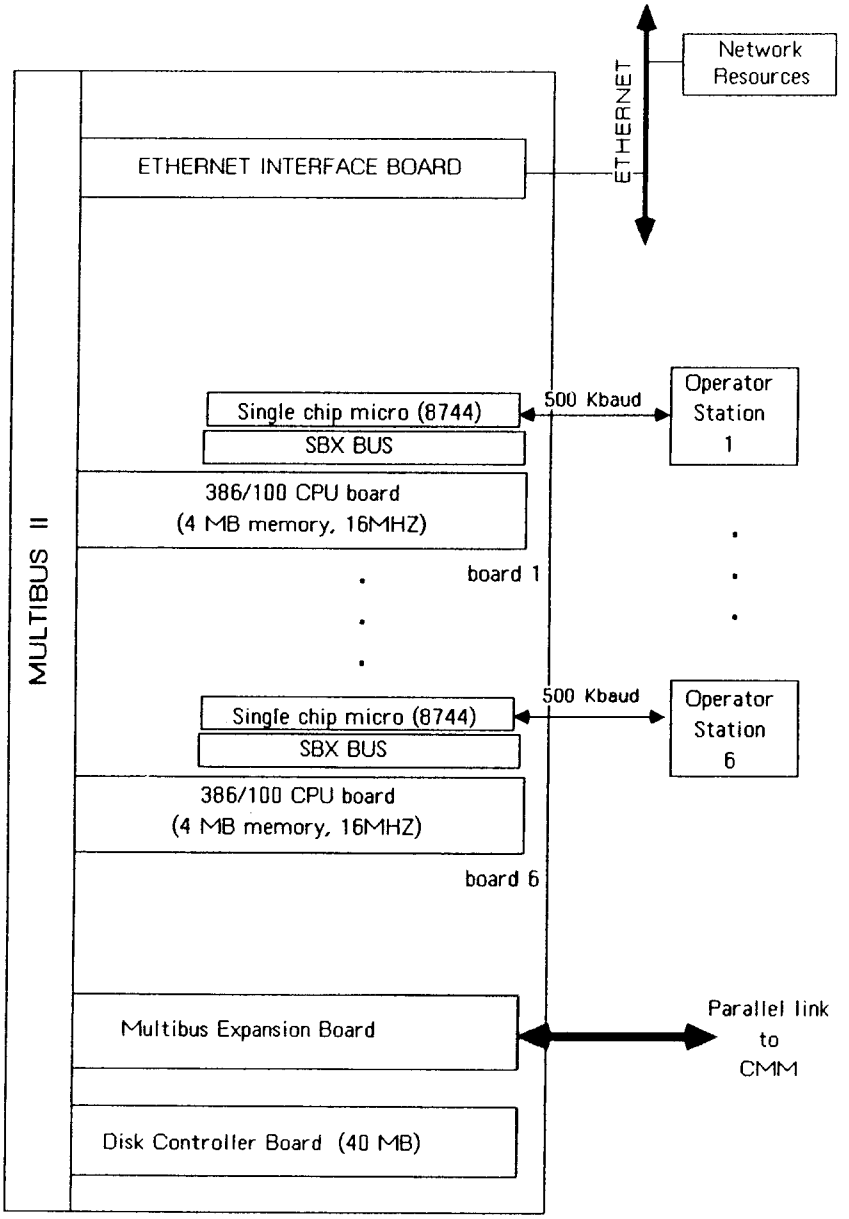


**Fig. 3-75.** Display Micro Module (DMM).

The DMM services the operator console. Access to the accelerator data base that resides in the CMM is provided via a commercial Multibus-II to Multibus-I extension board. A word of data can be fetched in less than 1 $\mu$s. There is one DMM per operator console; each console consists of six operator stations.

An Ethernet or MAP link connects the workstations, network resource manager, and the DMMs. Commercial hardware is used to provide communications to and from a file server/spooler, as well as data base entry and retrieval between the accelerator and the various workstations and personal computers. The file server/spooler is used to record accelerator data, to log errors, to hold output data, to store applications software and the appropriate tools to aid in its development, and in general, to perform system file management. The workstations and personal computers are used for program development and problem diagnosis. The philosophy is to develop and test programs such as auto-tuning and modeling [Pines, 1983; Timossi et al., 1985], with full access to the accelerator data base. Completed and debugged programs can then be installed for use by the operator.

It is crucial to minimize down time by providing spare hardware for all elements of the control system. The board-level computers in the control system are very powerful and can easily be augmented by board-level array processors for special functions (such as fast Fourier transforms). The Ethernet or MAP network also provides controlled access by the experimenters to appropriate control system parameters (such as undulator gap control) or beam-status information.

### 3.11.2 Operator Interface

Operator stations (see Fig. 3-76) provide the human interface to the control system. Each operator station contains a high-resolution (1280 $\times$ 1024) 19-inch color monitor. For input there will be overlaid touch panels, knob panels, keypads, and trackballs. The knob panel has an LED display for each of the knobs (for labeling or display of values), and these displays can be updated under program control when scrolling or using the touch panel. Efficient machine operation requires two independent consoles, each with its own DMM. Each console, made up of six operator stations, also has space for oscilloscopes, network analyzers, and other instruments.

Operator stations are connected to the DMM by high-speed (500 kilobaud) serial lines; this unique feature of the system allows the placement of such stations almost anywhere in the vicinity of the machine (for instance, as a local control station for any of the major subsystems of the accelerator). The DMM incorporates one high-performance single-board computer (SBC, Intel-80386-based) per station, thereby providing extremely fast (less than 0.1 s) response to operator input. The six SBCs (per DMM) share data and communicate via a commercial Multibus-II-based chassis. These microprocessors, operating in parallel, provide performance exceeding that of many superminicomputers (at a very modest price). Each operator station contains a video board, and an SBC; the latter does the serial communication with the DMM, drives the video board and translates operator inputs into higher-level commands for the DMM. The knob panel and touch panel electronics (both shown in Fig. 3-77) also contain single-chip microcomputers, so they, in turn, present only relatively high-level information to the operator station SBC.

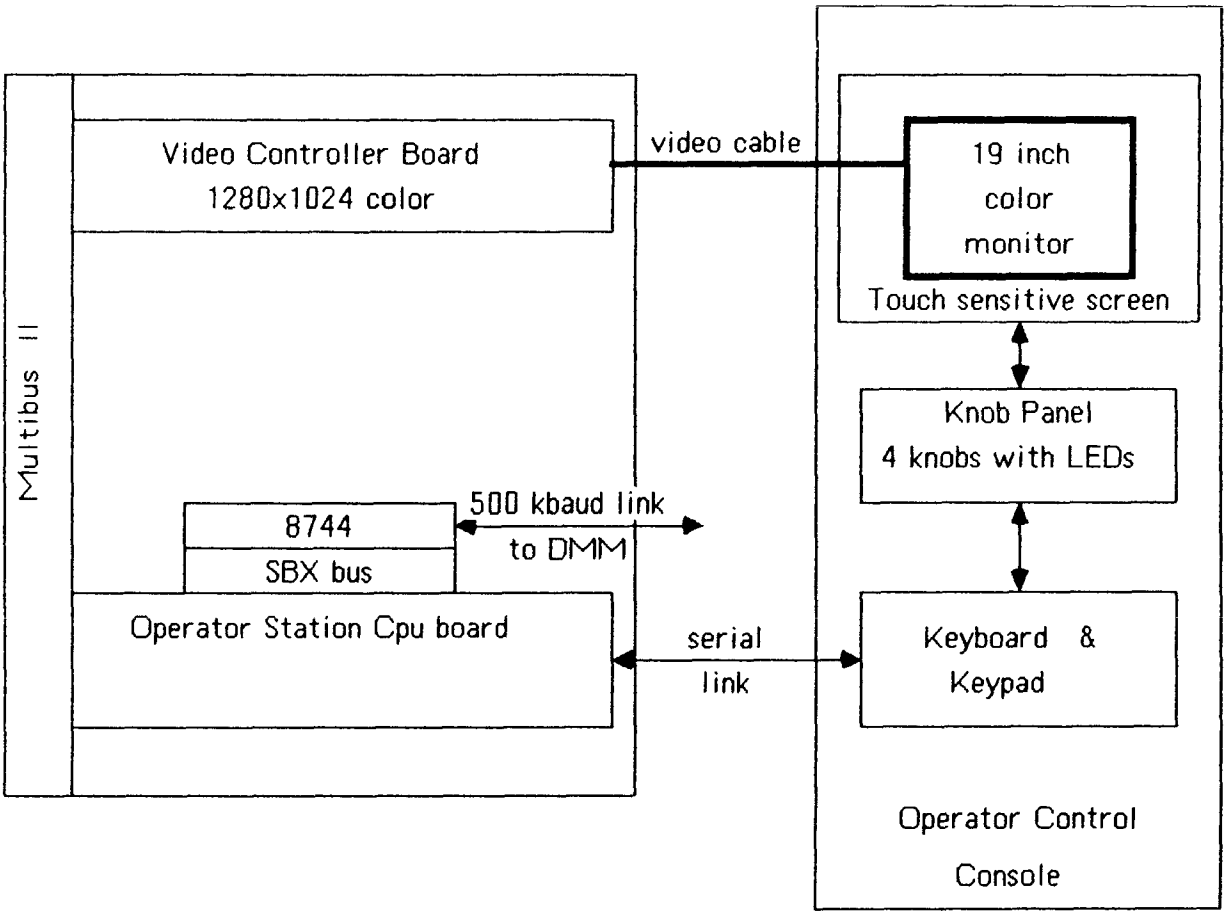


**Fig. 3-76.** Block diagram of an operator control station.

### 3.11.3 Subsystems

The DMM has access to the data that describe the status of the machine via a Multibus-II to Multibus-I extension into the CMM. The CMM collects data from the various IOMMs and the ILCs and stores them in memory accessible to the DMM. The CMM sends messages (new setpoints, etc.) generated by the DMM to the IOMMs and ILCs.

The ILCs and IOMMs monitor and control the operation of the machine. They are directly interfaced to the various components, and because they possess the computing power of a 16-bit minicomputer, they are capable of many control functions, such as monitoring interlocks, data acquisition, closed-loop control, data analysis, and error checking. Only data processed by the SBC in these chassis are sent to the CMM. The DMM, therefore, is not burdened with low-level signal-processing tasks. The ILCs control a single, or at the most a few, devices. The IOMMs contain up to 16 slots and can control a number of devices or an entire subsystem. The more powerful IOMMs can accommodate multiple SBCs for parallel processing or can include array processors. A modified operator station or portable console can interface directly to the ILC/IOMM links, thereby providing local control and testing. This is particularly useful during machine commissioning and for failure diagnosis (to isolate chassis from one another).

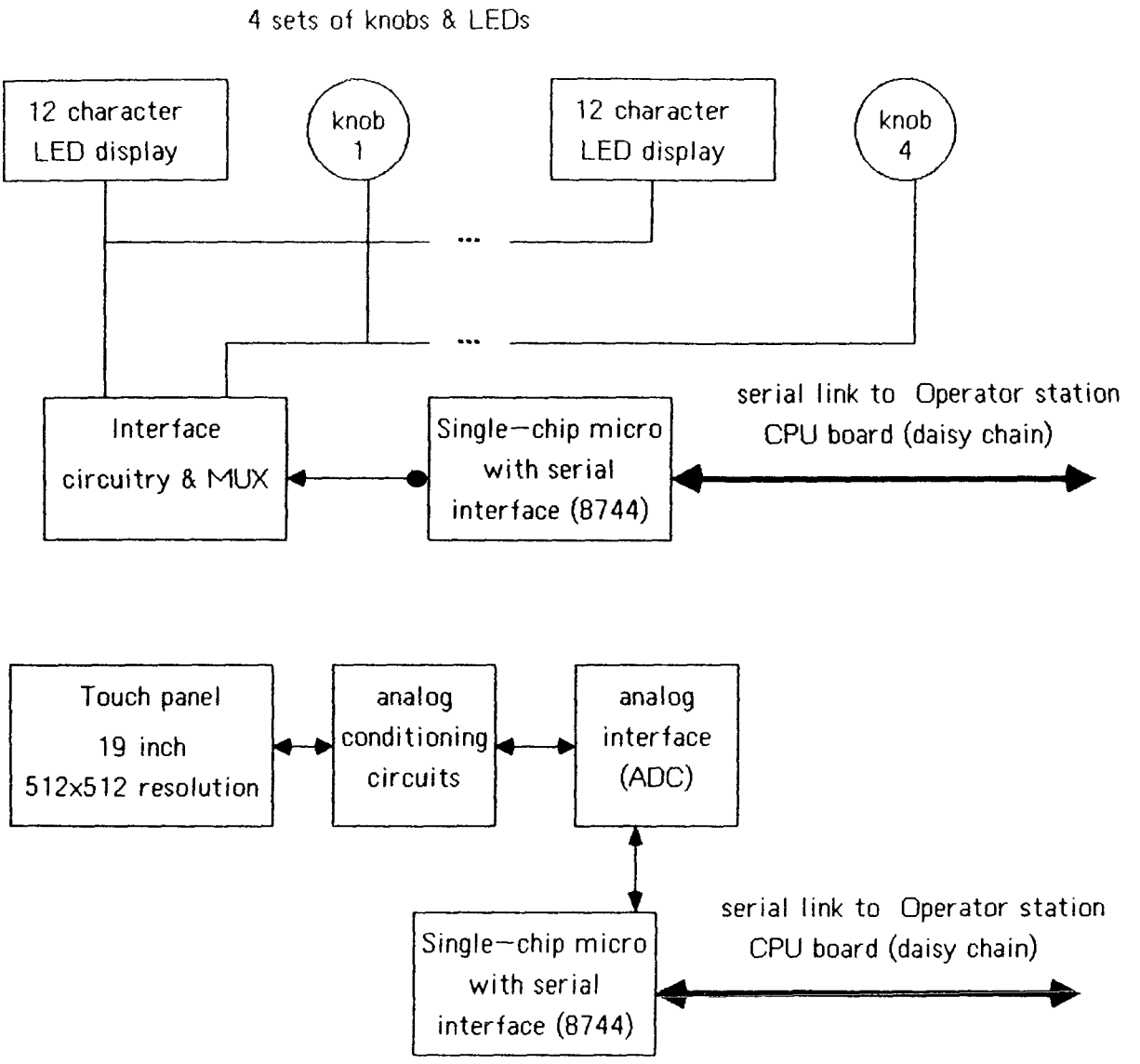


**Fig. 3-77.** Block diagram of an intelligent knob panel (top) and an intelligent touch panel system (bottom).

The justification for using many ILCs, as opposed to a few IOMMs, lies primarily with the complexity of the system. Each ILC deals mainly with one device (or one type of device), making it easy to provide additional computing and network capacity. This kind of power may be desirable during simultaneous ramping of a number of elements in the booster or storage ring. Furthermore, it simplifies the programming task and can shift the software (for example, floating-point conversion, error checking, or ADC/DAC processing) from the DMM to the ILC. The results are a reduction of DMM software, improved response to the operator, and simplified hardware maintenance.

The simplified system design provided by ILCs will be especially important during routine machine operation, when experts who built the control system may become less available. The use of ILCs also provides considerable flexibility for future expansion. If

the data refresh rate needs to be increased, the number of ILCs that are on a link can be decreased to accomplish this improvement. Use of the ILC means that only relatively simple boards must be added to provide control functions, and only a modest amount of software development effort would be required for such expansion.

# 4. Injection System

In specifying the injection system for the 1–2 GeV Synchrotron Radiation Source, we have assumed the following requirements:

- The system must provide a beam to the storage ring at its nominal operating energy of 1.5 GeV.
- The filling time should be short—not more than 5 minutes to reach the full current of 400 mA (in the multibunch operating mode).
- The design should allow essentially unrestricted access to user beam lines during the filling procedure.

In addition, of course, it is of paramount importance that the system be reliable.

To achieve these goals, we have adopted the injection system illustrated schematically in Fig. 4-1. The system consists of a high-intensity electron gun, a 50-MeV traveling-wave linac (similar to the SLAC design), and a 1-Hz, 1.5-GeV booster synchrotron. The injection system is capable of filling the storage ring to its full (multibunch) current of 400 mA in 2.1 minutes. In the few-bunch operating mode, the filling time is 16 seconds per bunch.

The linac and booster have been located inside the storage ring to avoid interference with user beam lines, to minimize shielding requirements, and to make best use of the layout of the existing building. The off-center arrangement shown in Fig. 4-1 has the advantage of minimizing the length of the transfer line between the booster synchrotron and the storage ring. In addition, sufficient floor area is left inside the ring for the eventual inclusion of a positron injector, should this option appear desirable at some future date (see Appendix D).

In Section 4.1, we describe the overall injection process and summarize the major parameters of the injection system. The next four sections cover in detail the electron gun and linac; the transfer line between the linac and the booster; the booster synchrotron—including its lattice design, accelerator physics issues, performance estimates, and injection/extraction details; and the transfer line from the booster to the storage ring. Section 4.4, covering the booster synchrotron, also describes such ancillary components as the booster vacuum system, power supplies, magnets, rf system, etc.

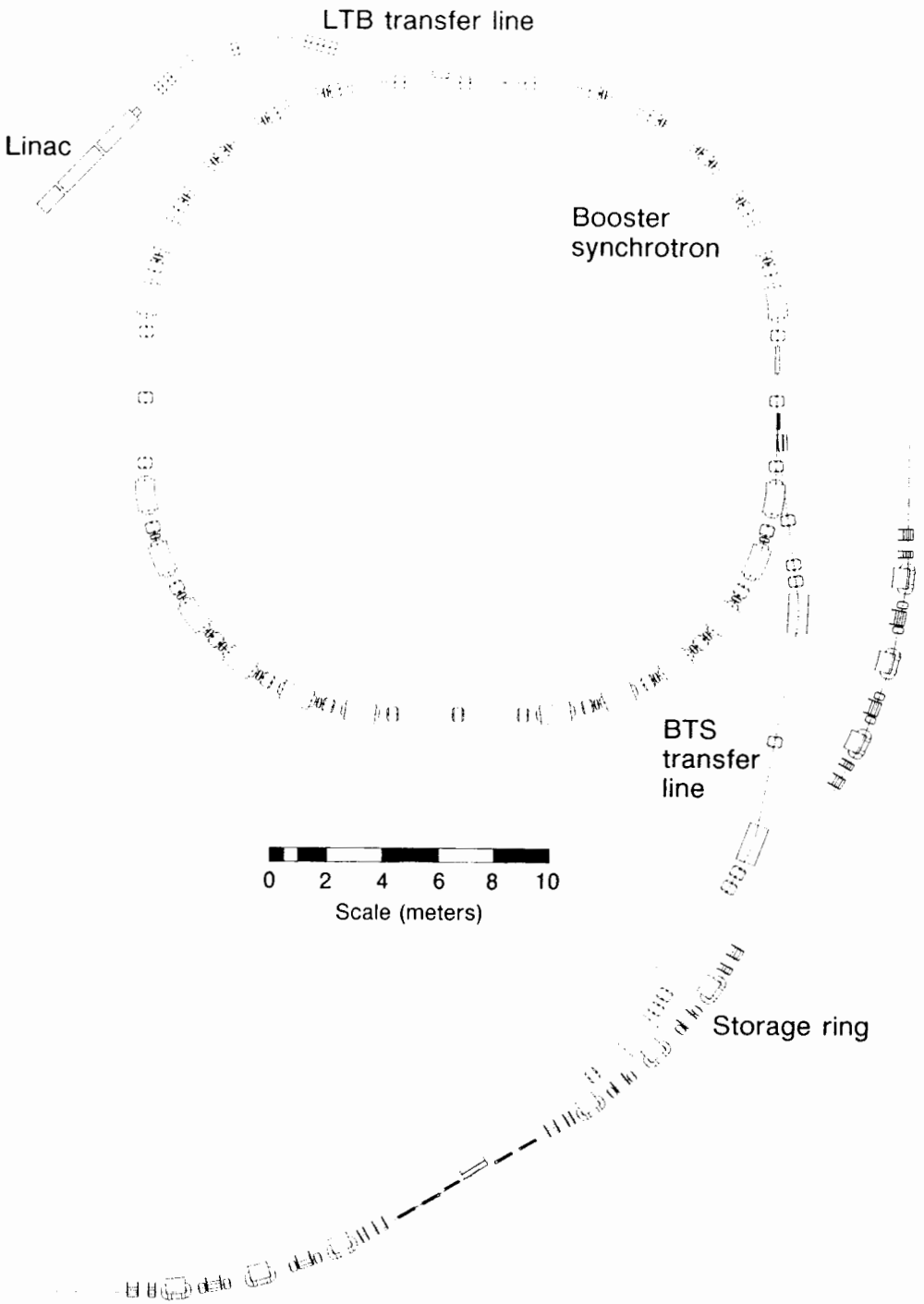


**Fig. 4-1.** Schematic diagram of the injection system layout.

## 4.1 Injection Process and System Parameters

There are basically two different operating modes of the storage ring, each requiring a somewhat different injection scenario. The multibunch operating mode requires that the storage ring be filled to a current of 400 mA in approximately 250 consecutive bunches (out of a total possible of 328). For the few-bunch operating mode, we assume a current of 7.6 mA per bunch. In this mode, the bunches are essentially filled one at a time, so the total filling time scales linearly with the required number of filled bunches. Filling procedures for the two modes are described below.

In an attempt to keep the system as straightforward and easy to operate as possible, beam transfers into and out of the booster are done in a single turn, using a full-aperture fast kicker. Such transfers require only a single kicker pulse per cycle. This choice should greatly simplify the initial commissioning of the injection system, as well as adding to the overall reliability by keeping the kicker requirements relatively modest and by minimizing booster aperture demands. A similar technique has been successfully employed in the SLC Damping Rings.

### 4.1.1 Multibunch Mode

In the multibunch mode, the electron gun is run with a long pulse, about 100 ns in duration. Prior to entering the linac, the beam from the gun is chopped at 500 MHz to minimize subsequent beam losses at higher energies. The linac beam is then injected into the booster synchrotron at 50 MeV in a single turn by means of a septum magnet and a full-aperture kicker. The injected beam fills 50 (out of 125) 500-MHz booster rf buckets, leaving a gap of about 150 ns for the kicker field to decay before the bunch train returns to the injection point. The 50 contiguous bunches are then accelerated to 1.5 GeV in the booster and extracted, again in a single turn, by means of a slow beam bump, a fast kicker, and a pair (thin and thick) of septum magnets. Transfer to the storage ring, which has an identical 500-MHz rf system, is boxcar fashion. By proper timing, the storage ring can be repetitively filled in the required 250-bunch pattern.

In Table 4-1, values of the beam intensity at various locations in the injection chain are indicated. In obtaining these values, we assumed an initial gun pulse of 1 A for 100 ns, i.e., a pulse of $6.2 \times 10^{11}$ electrons. The efficiencies assumed at various points are also included in Table 4-1. Based on the intensities given, it takes 126 booster cycles, or 2.1 minutes, to fill the storage ring to 400 mA.

### 4.1.2 Few-Bunch Mode

In the few-bunch mode, the electron gun and linac are run in such a way as to produce a single, short (about 0.5 ns), high-intensity pulse that is injected at 50 MeV into a single booster rf bucket. The single pulse is then accelerated in the booster to 1.5 GeV and extracted, as described above. The single booster bunch is subsequently transferred to a single rf bucket in the storage-ring. The control system monitors the timing such that the same storage ring bucket can be filled repetitively, once each booster cycle, until the desired current is reached.

**Table 4-1.** Intensities and transmission for electrons in the multibunch mode. Current values given are peak values for the gun and linac, and average values for the booster and storage ring.

| | $I$ (mA) | Number of electrons ($10^{10}$) | Efficiency | Transmission |
|---|---|---|---|---|
| Gun current[a] | 1000 | 62 | | 1.0 |
| | | | 0.25[b] | |
| Chopper exit | 250 | 16 | | 0.25 |
| | | | 0.75 | |
| S-band buncher exit | 188 | 12 | | 0.19 |
| | | | 0.67 | |
| Linac exit | 125 | 8 | | 0.13 |
| | | | 0.40 | |
| Accepted into booster | 20[c] | 3.2 | | 0.05 |
| | | | 0.80 | |
| Extracted from booster | 16[c] | 2.6 | | 0.04 |
| | | | 0.50 | |
| Accepted by storage ring | 3[d] | 1.3 | | 0.02 |

[a]Gun pulse length is 100 ns.

[b]Chopper transmits 90° of phase at 500 MHz, i.e., a 0.5-ns pulse every 2 ns.

[c]In 50 (out of 125) contiguous rf buckets.

[d]In 50 (out of 328) contiguous rf buckets.

The expected beam intensities at various locations in the injector chain are summarized in Table 4-2. Because the injection and extraction processes at all points are essentially identical for the multibunch and single-bunch operating scenarios, the efficiencies used in Table 4-2 are the same as those used for the multibunch case. To fill a single storage ring bunch to the nominal current of 7.6 mA takes 16 booster cycles, or 16 seconds.

### 4.1.3 System Parameters

The main parameters for the various components that make up the injection system are given in Tables 4-3 through 4-5. Details of the key components are given in Sections 4.2 and 4.4. It is useful here, however, to comment briefly on a few of the parameter choices that were made.

To optimize the injection efficiency, it is important to phase lock the linac and booster rf frequencies, as well as the booster and storage ring frequencies. Since a 500-MHz rf system was chosen for the storage ring, it was decided to adopt the identical rf system for the booster synchrotron. Such a choice greatly simplifies beam transfer between the two rings, allowing a straightforward boxcar filling of rf buckets in the storage ring. These frequency choices, however, mean that the 50-MeV S-band linac, which we modeled after the very successful SLAC design, cannot have the 2.856-GHz frequency used at SLAC. Instead, we

**Table 4-2.** Intensities and transmission for electrons in the few-bunch mode. Current values given are peak values for the gun and linac, and average values for the booster and storage ring.

| | $I$ (mA) | Number of electrons ($10^{10}$) | Efficiency | Transmission |
|---|---|---|---|---|
| Gun current[a] | 8000 | 10 | | 1.0 |
| | | | 0.25[b] | |
| Chopper exit | 2000 | 2.5 | | 0.25 |
| | | | 0.75 | |
| S-band buncher exit | 1500 | 1.9 | | 0.19 |
| | | | 0.67 | |
| Linac exit | 1000 | 1.25 | | 0.13 |
| | | | 0.40 | |
| Accepted into booster[c] | 3.2 | 0.50 | | 0.05 |
| | | | 0.80 | |
| Extracted from booster[c] | 2.6 | 0.40 | | 0.04 |
| | | | 0.50 | |
| Accepted by storage ring[c] | 0.5 | 0.20 | | 0.02 |

[a]Gun pulse length is 2 ns.

[b]Chopper transmits 90° of phase at 500 MHz, i.e., a 0.5-ns pulse every 2-ns gun pulse.

[c]In a single rf bucket.

**Table 4-3.** Electron gun parameters.

| | |
|---|---|
| Multibunch mode | |
| Voltage (kV) | 120 |
| Current (A) | 1 |
| Pulse length (ns) | 100 |
| Single-bunch mode | |
| Voltage (kV) | 120 |
| Peak current (A) | 8 |
| Pulse length (ns) | 2 |

adopted a somewhat higher frequency of 3 GHz, i.e., six times the booster synchrotron rf frequency. Fortunately, this choice coincides with the design for the LEP Injection Linacs (LIL) and the Daresbury SRS linac, so suitable klystrons are readily available.

Experience at Daresbury (12-MeV linac) confirms that the choice of 50 MeV for the linac energy is sufficient for good capture into the booster, and the booster injection field of 400 G is high enough to avoid any problems with remanent fields.

It is also important to note that the design is flexible enough to accommodate future upgrades—either in the maximum booster energy (to 1.9 GeV) or repetition rate—should

they become desirable. The higher energy could be reached simply by upgrading the power supplies and reconfiguring the cooling circuits. Similarly, the booster cycle rate could be raised to as much as 4 Hz by suitably modifying the power supplies.

## 4.2 Linac System

As a reference for our design, and for estimating beam properties (and costs), we rely heavily on SLAC experience. The recent work there that is most applicable to our needs involves the 35-MeV Nuclear Physics Injector (NPI), which has been running for about two years, and the 35- to 50-MeV SLC injector. The latter device, which was just recently completed, is especially useful as a model, because good beam measurements have been made for it [James and Miller, 1981; James et al., 1983]. As mentioned, the principal departure from the SLAC design is our use of 3 GHz as the linac rf frequency to allow us to phase lock the linac to the 500-MHz booster. For the linac structure, we expect to contract with someone already possessing the proper tools for fabrication. This could be done at SLAC, for example, and there are also commercial firms with this capability. The structure dimensions for a SLAC-type disk-loaded waveguide can be readily scaled from 2.856 to 3 GHz. At present, we envision purchasing the components to our specifications, then installing and testing them ourselves.

Figure 4-2 shows the principal components of the linac system; some of the major parameters are listed in Tables 4-3 and 4-4. We describe each of the main components below.

**Table 4-4.** Linac parameters.

| | |
|---|---|
| Energy (MeV) | 50 |
| Repetition rate (Hz) | |
| Maximum | 10 |
| Nominal | 1 |
| Frequency (MHz) | 2997.9 |
| Length, two sections (m) | 4 |
| S-band buncher length (m) | 0.105 |
| Peak rf power (MW) | 49 (= 25 + 24) |
| Multibunch mode | |
| Average current (mA) | 125 |
| Pulse length (ns) | 100 |
| Single-bunch mode | |
| Intensity | $1.25 \times 10^{10}$ |
| Pulse length (ns) | 0.5 |
| Emittance, rms ($10^{-6}$ m-rad) | 1.1 |
| Momentum spread, rms (%) | 0.3 |

**Table 4-5.** Booster parameters.

| | |
|---|---|
| Cycle rate (Hz) | 1 |
| Circumference (m) | 75.0 |
| Maximum energy (GeV) | 1.5 |
| Injection energy (GeV) | 0.05 |
| No. of superperiods | 4 |
| RF frequency (MHz) | 499.65 |
| Harmonic number | 125 |
| Revolution period (ns) | 250 |
| Magnets | |
| No. of dipoles | 24 |
| Dipole field at 1.5 GeV (T) | 1.2 |
| No. of quadrupoles (2 families) | 32 |
| Maximum gradient (T/m) | 15.0 |
| No. of sextupoles (2 families) | 24 |
| Maximum gradient (T/m$^2$) | 50 |
| No. of steering dipoles | 28 |

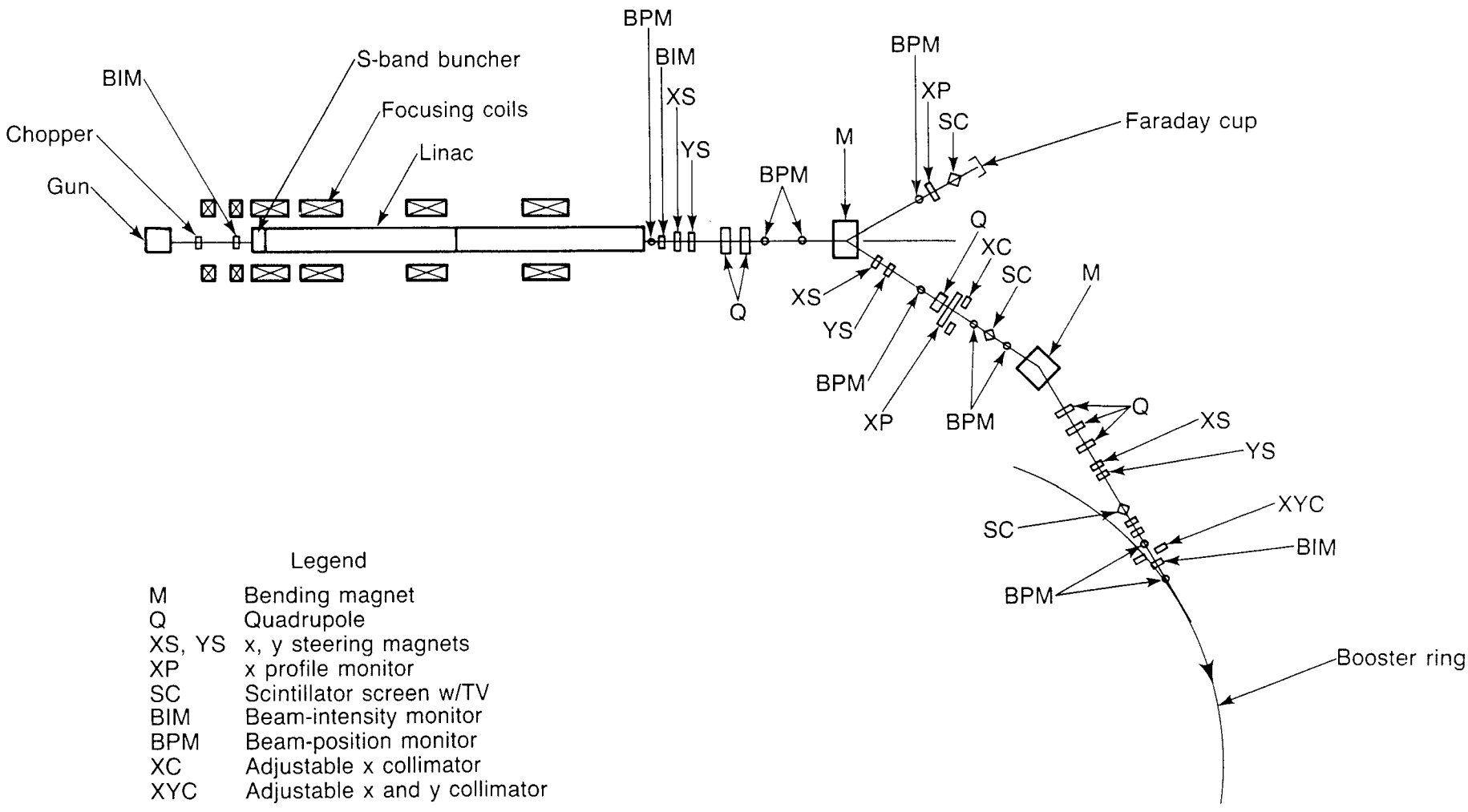


**Fig. 4-2.** Principal components of the injection linac system.

### 4.2.1 Electron Gun

Two guns have been developed recently at SLAC. One, known as the Model 7-1 gun, rated at 1.5 A [Koontz et al., 1984], is installed on the NPI; the other was developed for the SLC injector and is rated at 10 A [Koontz, 1981]. The two designs have many parts in common and differ mainly in the cathode size and in the shaping of the electrodes. Because of the high currents required for single-bunch operation, we have chosen to use the large 10-A gun; this choice circumvents the need for a subharmonic buncher.

Experience with the smaller gun at SLAC suggests that, at 1.5 A, cathodes last for a year or more before replacement is necessary. Although the large gun has seen less service, it was designed for much heavier use than we will require, so it is reasonable to expect a similar long cathode life. The gun is designed for easy cathode replacement, which should take about one day. In addition to spare cathodes, a spare ceramic envelope should be kept on hand.

Both of the guns described above, together with the necessary electronics (such as triggering circuits, isolation transformer, digitizing and data transmission through fiber optics, etc.), are available commercially.

### 4.2.2 Buncher and Chopper

To ensure efficient capture, we plan to inject only two S-band linac bunches (out of a possible six) into a 500-MHz booster rf bucket. Sufficient intensity is ensured by the choice of the bigger gun.

Bunching of the dc beam from the electron gun can be efficiently performed by a short section of S-band disk-loaded waveguide designed for a phase velocity of $0.75c$ [Miller et al., 1965]. Following the SLAC design, this S-band buncher is placed immediately in front of the linac. It must have independent phase control but can take power from the klystron that supplies the linac. Acting together with the first part of the linac, this buncher causes electrons entering it in 180° of S-band phase to be tightly bunched in the linac, riding the peak of the rf field [Helm and Miller, 1970]. A chopper is used to exclude from the linac (to the extent possible) beam that cannot be accelerated to full energy and successfully captured in the booster. This unwanted beam, if it were not eliminated at low energy, would be lost at higher energies, thus contributing to the radiation background. The chopper is to be installed between the gun and the S-band buncher.

For the single-bunch mode, we accelerate two S-band linac bunches for injection into a single 500-MHz booster bucket. Allowing for buncher acceptance, this corresponds to only a 0.5-ns beam pulse. This is too short for a gun pulse. For the multibunch mode, a 100-ns beam pulse is needed, but only one-third of the S-band buckets need to be filled. To accommodate both of these requirements, we employ a 500-MHz chopper, which permits a 2-ns gun pulse for the single-bunch mode, while rejecting unwanted beam.

### 4.2.3 Linac

As mentioned above, the entrance section of the linac aids in bunching the electrons. Electrons enter the linac at a velocity of $0.6c$, and the bunch is centered 90° ahead of the peak field, i.e., where $E_z = 0$. Because the phase velocity of the rf in the linac is $c$, the electrons

slip in phase and become tightly bunched at the peak of the rf field. The theory of this process has been treated by Helms and Miller [1970]. To take this effect into account in estimating the length of linac required to reach 50 MeV, we assume here that in the first 1 meter of linac the average accelerating field seen by the electrons is only half the peak rf field.

The linac consists of 4 meters of S-band waveguide, divided into two equal segments, each with input coupler and load. The structures are similar to the SLAC disk-loaded waveguide, except that, for reasons of fabrication economy, our design has all disk apertures equal (i.e., our structure has constant impedance rather than constant gradient). Each of the linac sections is driven by a separate klystron. The klystron driving the first section also supplies power to the S-band buncher. When beam loading and transmission losses are taken into account, the total peak power required is 49 MW. (Since the maximum duty cycle is only about $1 \times 10^{-5}$, the average power required is only 500 W.) Experience has shown that enhanced reliability and longer life can be expected when rf drivers are derated; hence, the total rated capacity of the klystrons should be considerably greater than 49 MW—say, at least 30 MW for each.

For estimating parameters of the linac structure, constants will be scaled from the SLAC waveguide. Strictly speaking, scaling from the SLAC design would require that each waveguide section and disk aperture be a different dimension. For simpler and less expensive fabrication, however, we plan to keep the waveguide diameter and the disk aperture size constant. In this case, the accelerating gradient decreases exponentially along the linac section. To obtain the same acceleration from a given length will thus require a higher initial gradient than that of the SLAC constant-gradient structure. This will not be a problem for the gradients under consideration here.

Beam loading acts to increase the energy spread. However, there are some means available to remedy this. In the case of the single-bunch mode, it is possible to shift the phase of the second linac section with respect to the first, which allows the beam bunch to see a sloping voltage gradient, in a sense that offsets the energy spread due to beam loading. This technique should reduce the energy spread to within the desired $\pm 1\%$. For the multibunch mode, the field induced by the leading bunches will cause trailing bunches to see less gradient. To offset this, the klystron power output must increase with time during the beam pulse. This can be accomplished by using fast-acting components such as solid-state pin-diode attenuators.

To evaluate the performance of our structure, we need to calculate the unloaded beam energy $V$, the beam loading $\Delta V$, the maximum accelerating gradient $\hat{E}_z$, the klystron power input $P_0$, the stored energy $W$, and the filling time $t_f$. Appropriate formulas can be obtained from the work of Helm and Miller [1970], Borghi et al. [1968], Leiss [1970], and Loew and Neal [1970]. Results [Selph, 1986] based on the structure constants for the SLAC waveguide are summarized in Table 4-6.

As an estimate of the linac emittance, we can use the measurements made on the SLC injector [James et al., 1983], which gave a normalized emittance of $7 \times 10^{-5}\ I^{1/2}$ m-rad, where $I$ is in units of $10^{10}$ electrons per linac bunch. If we take the linac current of $I = 5$, already achieved at SLAC (in a single bunch), and assume it to be in two linac buckets for our design, then at 50 MeV, letting $I = 2.5$ gives an expected emittance of $1.1 \times 10^{-6}$ m-rad.

**Table 4-6.** Performance parameters based on SLAC waveguide structure constants ($r$ = 53 MΩ/m; $Q$ = 13,000; $\tau$ = 0.57).

| | |
|---|---|
| Filling time (ns) | 790 |
| Beam loading per section (MV) | −10.1 |
| Unloaded energy gain per section (MV) | 38.7 |
| Power requirement per section (MW) | 21.3 |
| Stored energy per section (J) | 10.0 |

The momentum spread depends rather critically on the linac rf tuning. Therefore, to facilitate tuning, it is important to have instrumentation to measure momentum spread quickly. This feature will be incorporated into the linac-to-booster transfer line (described in Section 4.3). For the SLC injector, with an intensity of $5 \times 10^{10}$ electrons/pulse, the measured momentum spread was 0.5% FWHM and ±1.0% for 90% of the beam. To be conservative, we have specified an rms momentum spread of 0.3%, despite the lower current per bunch we envision.

### 4.2.4 Transverse Focusing

While the electrons are moving at nonrelativistic velocities, solenoid focusing is used to keep the beam size small and to oppose space-charge forces tending to blow up the beam. A number of separately powered coils are used, as the field strength must be adjusted to match conditions along the injection channel. A small beam cross section is needed in the buncher to minimize nonlinear effects. As the beam is compressed in the S-band buncher, the focusing fields must increase to counteract the increasing charge density. Taking the SLC injector as a guide [James and Miller, 1981], $B_z$ fields of 100–200 G are required up to the S-band buncher; thereafter, increasing fields up to about 2 kG are needed in the entrance section of the linac. The fields then decrease as the velocity approaches $c$.

### 4.2.5 Linac Instrumentation

Diagnostics are provided for measurement of linac beam position, intensity, and total charge. Three nondestructive beam-position monitors are provided. Beam position is sensed at each location by four electrodes resonant to the 3-GHz linac rf. The processing electronics are functionally identical to those in the storage-ring BPM system (Section 3.9.1). Beam intensity is measured at the input and output of the linac rf section with resistively loaded gap monitors [Koontz, 1976]. These monitors are composed of a low-capacitance ceramic gap in the beam pipe. The gap is shunted with four 50-Ω resistors and a high-quality 50-Ω coaxial cable giving a 10-Ω impedance to the beam and a 10-V/A sensitivity. Peak detectors and pulse integrators process the intensity signal for computer input. Integration of the intensity signal provides a measure of the total charge in the beam. Low-loss coaxial cables carry these signals to the control room for observation on a wide-band oscilloscope.

## 4.3 Linac-to-Booster (LTB) Transfer Line

The function of the LTB transfer line is to transport the 50-MeV electron beam from the end of the linac to the injection point of the booster synchrotron. In addition, the line serves to provide momentum analysis and transverse phase-space matching of the linac beam to the acceptance of the booster synchrotron. The LTB transfer line includes a dispersive section that is used both to characterize the injection energy and to define the full momentum spread presented to the booster. This ensures that the booster is injected with a beam whose energy spread is small enough that no significant distributed beam losses occur, thus minimizing the requirement for booster shielding. The major beam losses occur at a moderate beam energy of 50 MeV and are confined spatially to a region convenient for local shielding.

Figure 4-3 shows a schematic layout of the LTB transfer line. The first dipole magnet acts as a dispersing element; momentum selection and analysis are carried out downstream

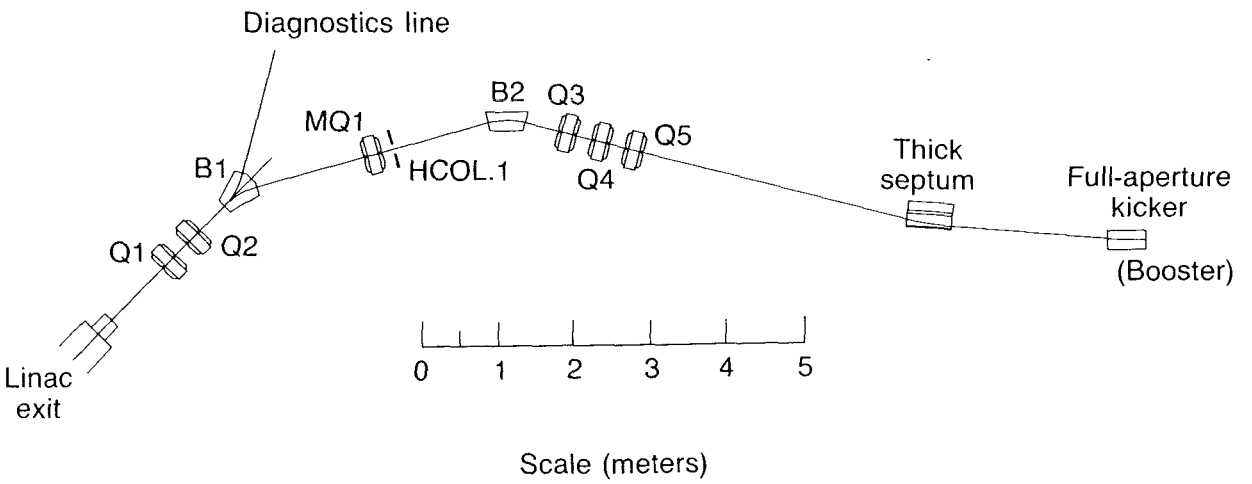


**Fig. 4-3.** Layout of the linac-to-booster (LTB) transfer line.

via a variable horizontal collimator (HCOL.1). The use of a quadrupole doublet immediately following the linac ensures that a suitable focus can be achieved at HCOL.1, more or less independently of the properties of the linac beam. The bend is made achromatic by the second dipole and the momentum matching quadrupole (MQ1). Phase-space matching to the booster acceptance is provided by the quadrupole triplet in the final part of the line. Small adjustments to the beam direction, both in the LTB line and for final alignment into the booster synchrotron, are made with three sets of low-power horizontal and vertical steering dipoles.

The calculated beam profiles ($2\sigma$) and momentum dispersion through the LTB transfer line are shown in Fig. 4-4. Should it be necessary to attenuate the beam to the booster (for protracted injection studies, for example), a set of fully adjustable jaws has been provided in the final dispersion-free section.

Injection into the booster is via a thick septum magnet and a fast full-aperture kicker magnet. Details of these devices are given in Section 4.4. Bending and quadrupole magnets for the LTB transfer line are commercially available devices. Power supplies are described in the section on the booster-to-storage-ring transfer line (Section 4.5).

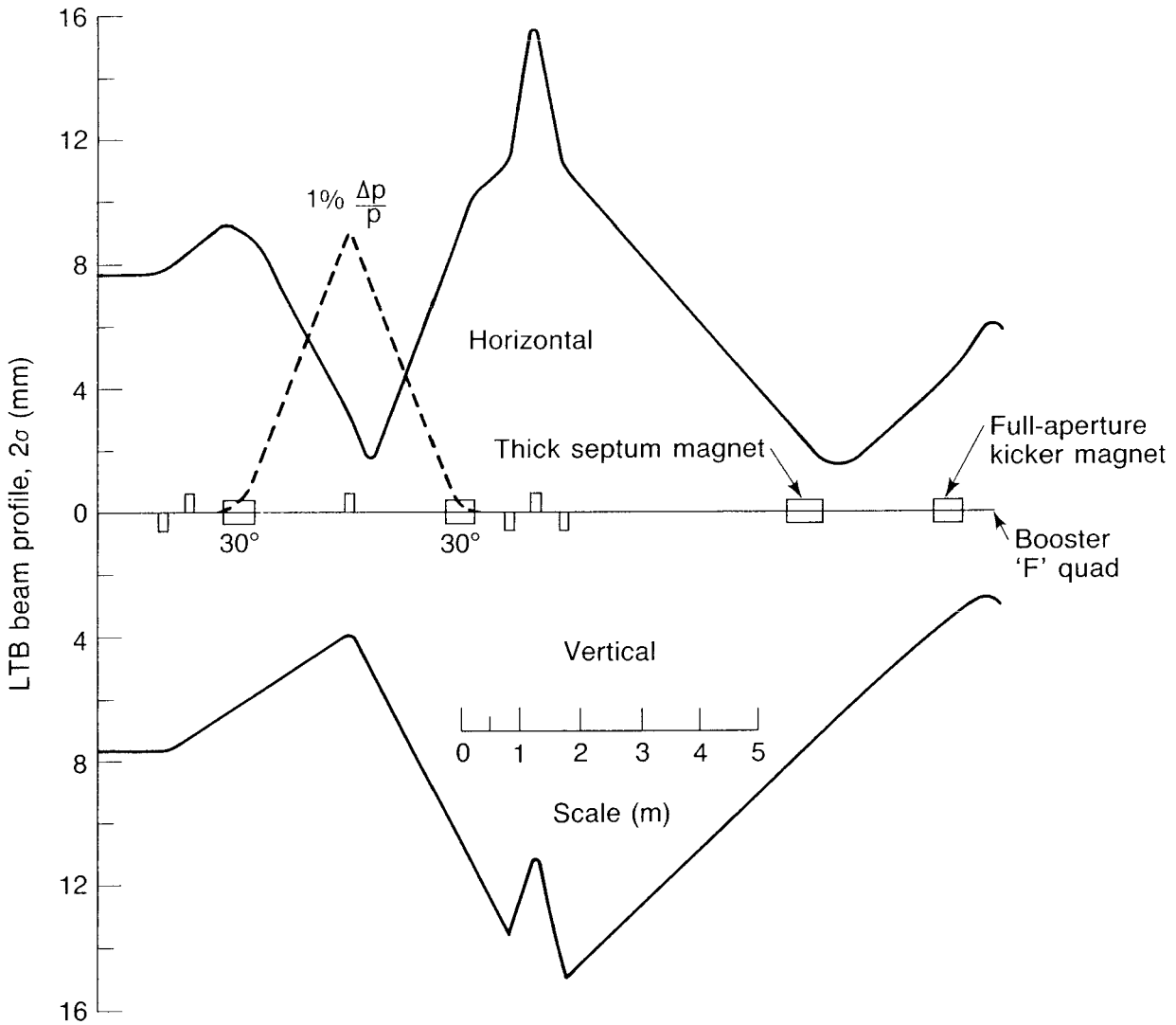


**Fig. 4-4.** Optics of the LTB transfer line.

For diagnostic purposes, a reverse-angle beam line is provided from the first dipole magnet after the linac; this feature permits analysis of the beam from the linac, even if the booster ring is not available for injection, e.g., during booster maintenance. The diagnostic line is a mirror image of the first part of the LTB line and is instrumented with a scintillation screen and a Faraday cup that sits inside a heavily shielded enclosure.

Retractable scintillators and TV cameras are located downstream of the LTB transfer line bending magnets. The scintillator image, viewed on a control-room monitor, helps the operator steer the beam through the transport line. There are four scintillators installed, two in the LTB transport line itself, one in the linac straight-ahead position, and one in the beam diagnostics line. Five nondestructive beam-position monitors are located in the LTB transfer line, and one is in the beam diagnostics line. These systems are identical to the linac beam-position monitors. The beam horizontal profile is measured with a retractable wire-grid assembly. One of these monitors is installed in the LTB transfer line downstream from the first quadrupole magnet, and one is installed in the beam diagnostics line. Ad-

justable beam collimators are installed in a zero-dispersion region in the LTB transfer line for beam attenuation. One beam-intensity monitor is installed near the booster injection area; it is identical to the gap monitors in the linac. The beam dump includes a Faraday cup and is instrumented with beam-charge-measurement electronics, such as a Keithley electrometer.

## 4.4 Booster Synchrotron

The booster synchrotron is used to accelerate the 50-MeV beam from the linac to the nominal 1.5-GeV operating energy of the storage ring—i.e., it is a "full-energy" booster. The cycle rate of the booster is 1 Hz. The natural (uncoupled) rms emittance of the booster is about $1.5 \times 10^{-7}$ m-rad at 1.5 GeV, which is quite satisfactory for subsequent injection into the storage ring. As shown in Section 4.4.2, the beam should maintain the natural emittance at energies above about 0.9 GeV. Major parameters of the booster synchrotron are summarized in Table 4-5.

### 4.4.1 Magnet Lattice

The booster lattice is a FODO structure with missing dipoles to provide utility straight sections for injection, extraction, and rf cavities. One quadrant of the lattice is shown in Fig. 4-5. The choice of this structure over several other possibilities was dictated by its flexibility and simplicity. For example, this design requires the minimum number of power supplies (in a separated-function design) that must track accurately through the acceleration cycle. Figure 4-6 shows the usual lattice functions for one particular tune, $\nu_x/\nu_y = 6.26/2.79$; these parameters correspond to a natural emittance of $\epsilon_0 = 1.5 \times 10^{-7}$ m-rad.

As discussed in Section 4.4.2, the rise time of the head-tail instability in a 1-Hz synchrotron is sufficiently short that chromatic correction must be maintained throughout the acceleration cycle. In this design, the correction is achieved by means of two families of sextupoles, denoted SF and SD; there are two SF magnets and four SD magnets per quadrant. The resulting dynamic aperture of the lattice (see Fig. 4-7) is significantly larger than the vacuum chamber aperture. This desirable feature is one of the reasons we adopted

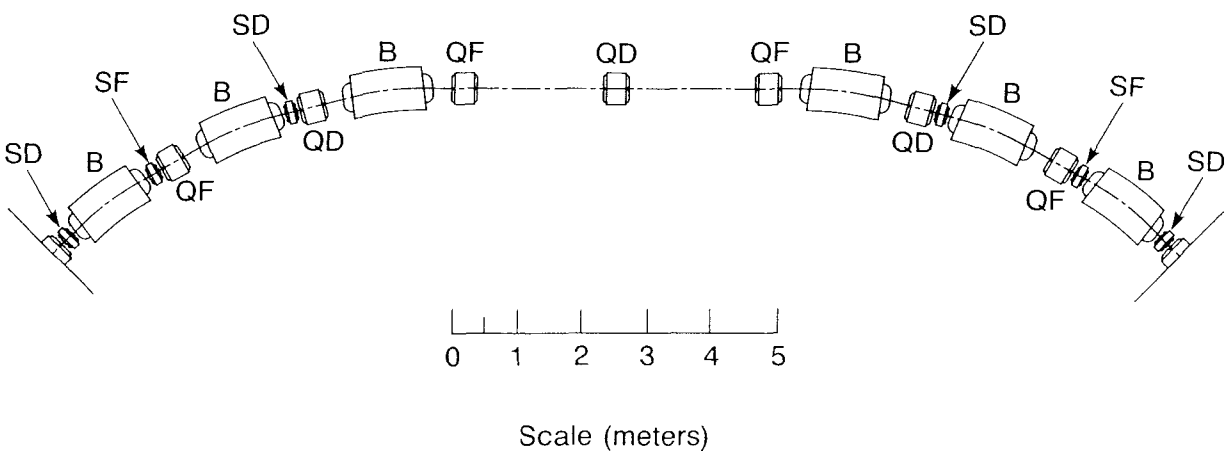


**Fig. 4-5.** One quadrant of the booster synchrotron lattice.

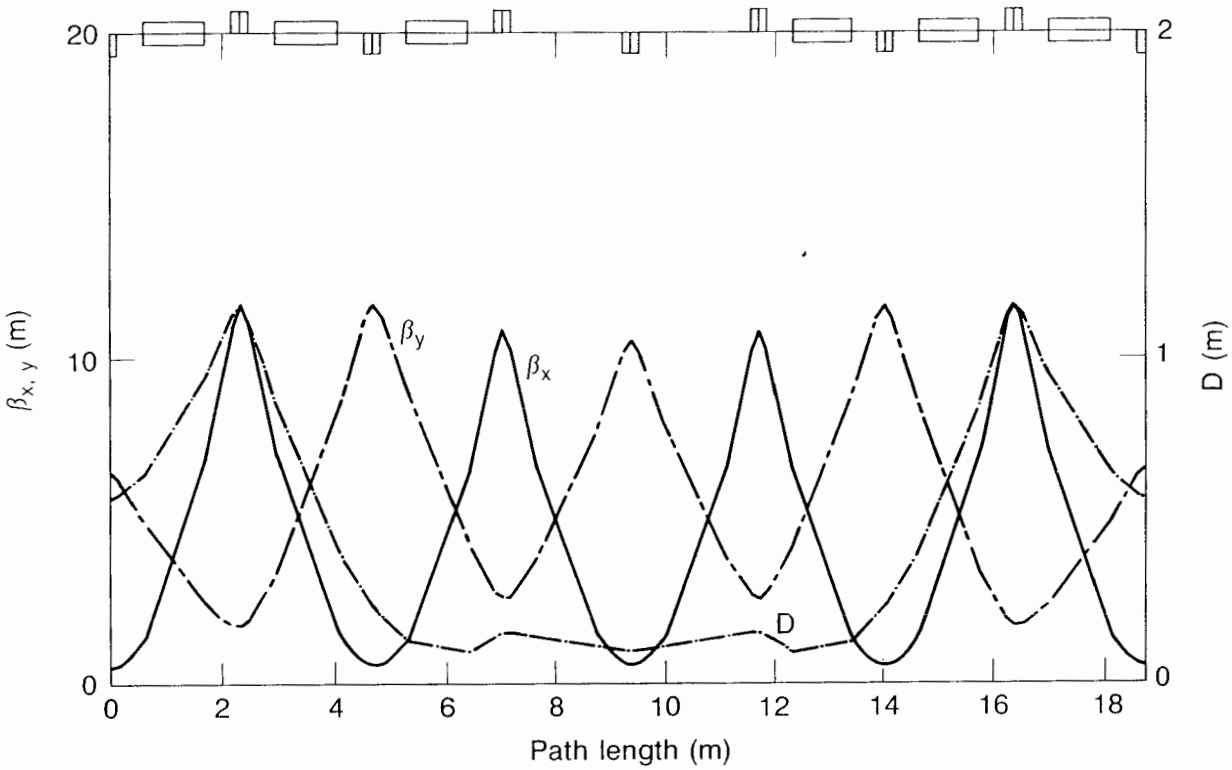


**Fig. 4-6.** Lattice functions for the booster.

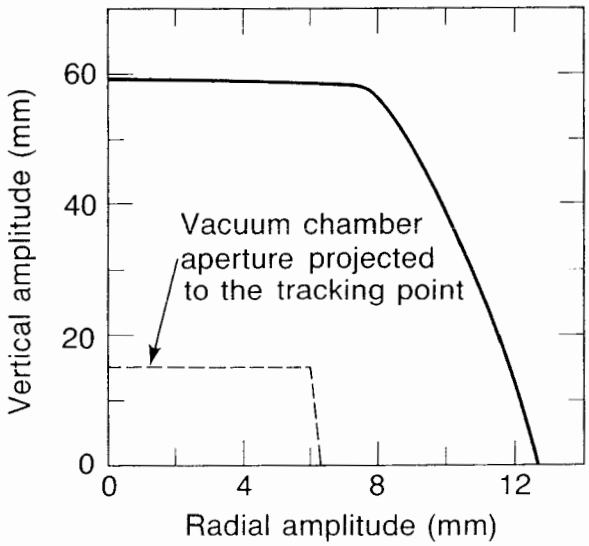


**Fig. 4-7.** Dynamic aperture of the booster synchrotron, compared with the projected size of the vacuum chamber.

this structure for the booster. As can be seen in Fig. 4-8, the tune variations with betatron amplitude and with momentum are quite acceptable.

As mentioned, injection into the booster makes use of a single-turn, on-axis technique. At the end of the LTB transfer line, the 50-MeV beam from the linac is deflected to a shallow angle (4.5°) with respect to the booster straight section by a thick septum bending mag-

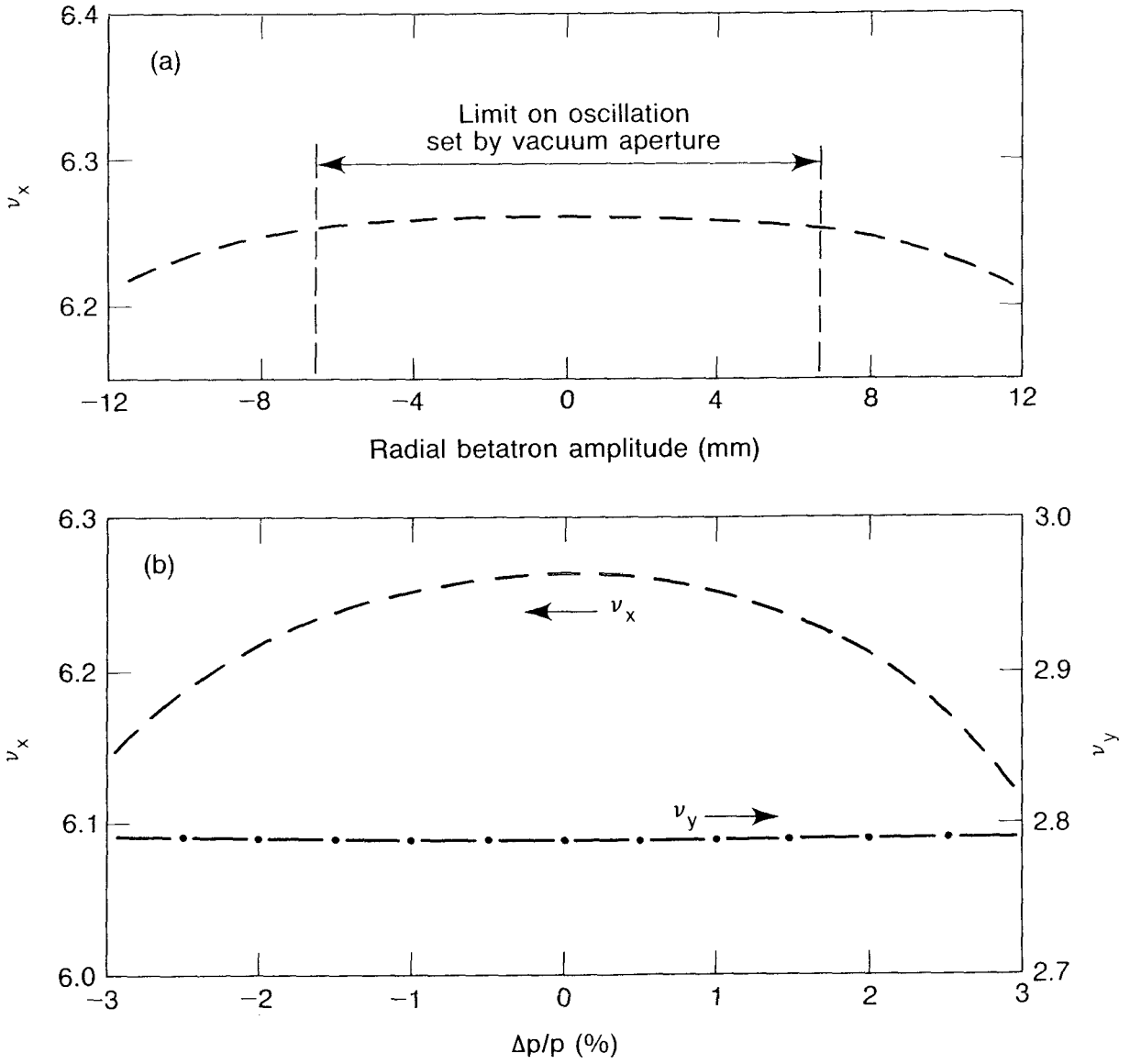


**Fig. 4-8.** (a) Radial amplitude-dependent tune variation and (b) momentum-dependent tune variation for the booster.

net that bends through an angle of 10°. When the beam crosses the booster axis, it is kicked 4.5° onto axis by a full-aperture kicker magnet. This kicker must maintain a steady field during the passage of the injected beam pulse (~100 ns) and be switched off in a time ($\lesssim$ 150 ns) much shorter than the orbit time of the booster. These requirements are not difficult with present technology. The beam-stay-clear region in the booster quadrupoles is ±3 cm horizontally and ±2 cm vertically; this aperture will accommodate the linac beam with a (full) momentum spread of 1% and an emittance of $1.1 \times 10^{-6}$ m-rad, allowing for 5 mm of closed-orbit deviations and a kicker jitter of 0.7%. A diagram of the injection trajectory is shown in Fig. 4-9.

After the injection process, the beam is ramped to 1.5 GeV. The dipole field ramp profile, which determines the energy, is shown in Fig. 4-10. During the ramp, the beam size is

reduced by adiabatic and radiation damping processes. At 1.5 GeV, the equilibrium emittances, both longitudinal and transverse, will have settled to their natural values; this is discussed in Section 4.4.2.

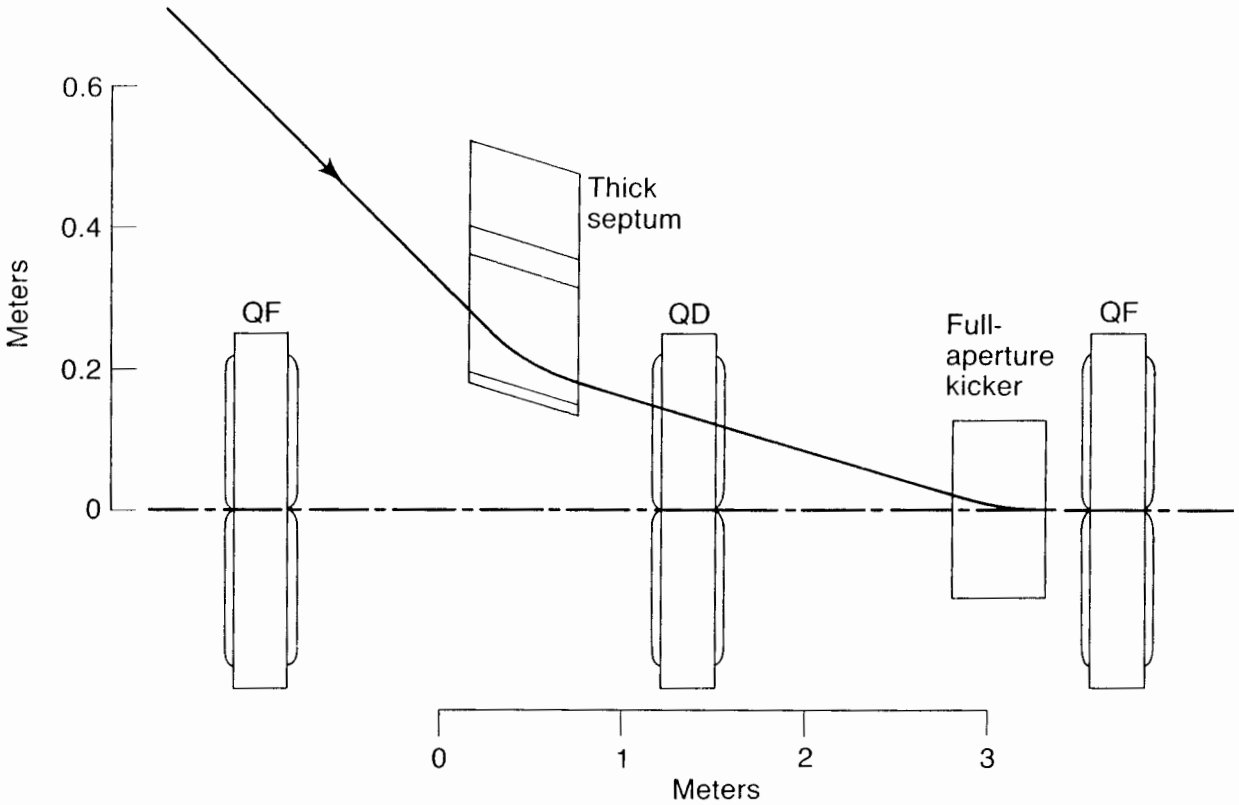


**Fig. 4-9.** Anamorphic diagram of the booster injection process.

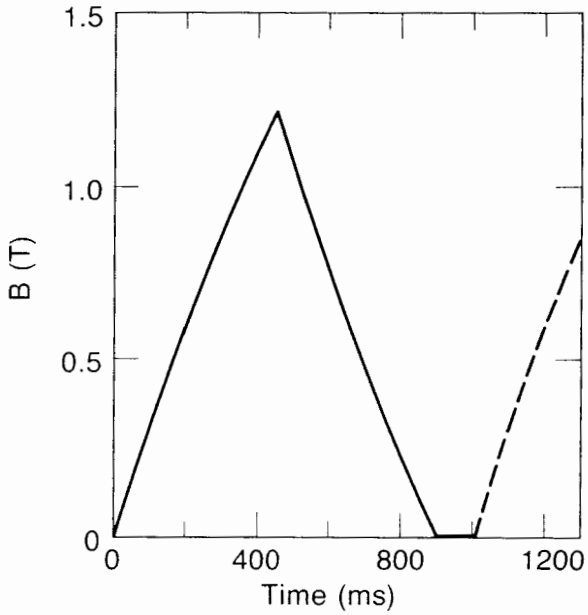


**Fig. 4-10.** Booster dipole ramping cycle.

Extraction from the booster utilizes a slow, localized orbit bump (to bring the beam close to a thin septum magnet), and a fast, full-aperture kicker magnet (capable of producing a deflection of 10 mrad) to move the beam into the thin septum magnet. This septum deflects the beam through 2.5° into a thick septum magnet that directs the beam (4.0°) away from the booster into the booster-to-storage-ring (BTS) transfer line.

Details of the injection and extraction elements and their power supplies are given, respectively, in Sections 4.4.3 and 4.4.4.3. A summary of specifications for the injection and extraction elements is provided in Table 4-7.

**Table 4-7.** Summary of booster injection and extraction magnet parameters.

| | Length (m) | Bend angle (deg) | Maximum field (mT) | Rise/fall time | Amplitude stability (%) | Trigger jitter (ns) |
|---|---|---|---|---|---|---|
| Thick injection septum | 0.35 | 10 | 83.5 | dc | 0.2 | — |
| Full-aperture injection kicker | 0.5 | 4.5 | 26.2 | 100 ns | <0.5 | ± 5 |
| Extraction kicker | 1.0 | 0.57 (10.0 mrad) | 50.0 | 100 ns | <0.5 | ± 5 |
| Thin extraction septum | 0.6 | 2.5 | 364 | half sine 20 μs | 0.2 | ± 100 |
| Thick extraction septum | 0.6 | 4.0 | 582 | half sine 100 μs | 0.1 | ± 100 |

### 4.4.2 Accelerator Physics Issues

In general, the performance requirements for a booster synchrotron are much less stringent than those for the storage ring. The main reason for this is that the beam spends only a relatively short time in the booster (less than 1 second), compared with the many hours during which it circulates in the storage ring. On the other hand, the beam is injected into the booster at a relatively low energy (50 MeV), where there is essentially no radiation damping and where the effects of any instabilities tend to be most pronounced. In this section, we look primarily at beam stability in light of collective effects at the injection energy of 50 MeV. We also examine the ramping process to see how the beam emittance (both longitudinal and transverse) evolves during the ramp. At the extraction energy, we do not expect any problems to arise from collective effects; thus, we merely examine the single-bunch thresholds to determine the bunch length of the extracted beam and to ascertain that it is compatible with the injection requirements of the storage ring.

**4.4.2.1 Behavior at 50 MeV.** The 50-MeV beam from the linac is expected to have an rms emittance of about $1 \times 10^{-6}$ m-rad in both transverse planes and an rms momentum spread of about $3 \times 10^{-3}$. Because of the large momentum spread, the threshold for onset of the longitudinal microwave instability (turbulent bunch lengthening) is quite high.

It is assumed here that the vacuum chamber impedance of the booster is higher than that of the storage ring: There are more "disruptive" beam-line elements (e.g., kickers and septa) in the booster, and generally speaking, the care taken in minimizing chamber discontinuities is likely to be less than is the case for the storage ring. Therefore, we have used the conservative value of $|Z_{\parallel}/n|_{\text{chamber}} = 10\ \Omega$ for the booster calculations, compared with an assumed value of $2\ \Omega$ for the storage ring. (This higher value has commonly been achieved, or bettered, in existing machines, and it is likely that the booster impedance will be lower than this.) Based on this assumed value, the single-bunch current that can be accommodated at 50 MeV was calculated by ZAP [Zisman et al., 1986] to be about 13 mA (i.e., about $2 \times 10^{10}$ electrons). In the most severe case, when the booster accelerates a single bunch for the few-bunch injection mode, the maximum required current is only 3 mA. Thus, we do not expect any turbulent bunch lengthening at injection. The transverse threshold is about twice as high as the longitudinal at 50 MeV and so will not be of any concern.

The natural uncorrected chromaticities of the booster ring are $\xi_x \simeq -10$ and $\xi_y \simeq -5$. The transverse broadband impedance,

$$|Z_{\perp}| = \frac{2R}{\beta b^2} |Z_{\parallel}/n|_{\text{eff}} \lesssim 1\ \text{M}\Omega/\text{m}\ ,$$

with short wake fields, will drive the chromaticity-dependent transverse head-tail modes. The growth rate is highest at the injection energy of 50 MeV, and it scales inversely with energy as we ramp. If uncorrected, the natural negative chromaticity of the booster would give rise to head-tail modes with growth rates as fast as 20 ms at 50 MeV [Chattopadhyay, 1986]. For a 1-Hz booster, this instability is fast enough to cause beam disruption. Hence, it is necessary to correct the chromaticity in the booster by means of chromaticity sextupoles.

We have also investigated the response of the booster beam to coupled-bunch instabilities. To do so, we took a worst-case scenario of all booster rf buckets filled and an undamped rf cavity. Although most of the unstable modes are predicted to be Landau damped, it is not clear that all will be. At 50 MeV, the growth rates predicted by ZAP (both longitudinal and transverse) are of the order of milliseconds for an undamped rf cavity. Thus, even for a 1-Hz booster, it may be necessary to provide higher-order mode damping for the rf cavity. Fortunately, the booster rf cavity is identical to those for the storage ring (for which some form of mode damping is already anticipated), so this will not require any additional effort to implement.

The last question we wish to investigate concerns the transverse beam emittance. At very low energies, where radiation damping is ineffective, it is well-known [Zisman, 1985; Chattopadhyay et al., 1985] that the beam dimensions can increase drastically owing to the influence of intrabeam scattering (IBS). To see how severe this growth might be for the booster, we used ZAP to obtain the equilibrium emittance value, based on the balance between IBS, quantum fluctuations, and radiation damping. At the beam current levels we require, the equilibrium value for the emittance was found to be about $1 \times 10^{-6}$ m-rad; this is just what the linac provides, so the growth rates from IBS must be very small at the booster injection energy of 50 MeV. The effects of IBS diminish very rapidly as the energy is raised, so this effect is of no concern during the 0.45-second acceleration ramp of the booster.

**4.4.2.2 Ramping Behavior.** For completeness, we have investigated dynamically the behavior of the longitudinal and transverse emittance during the booster ramping cycle. The 1-Hz cycle taken for these calculations is illustrated in Fig. 4-10; the beam is injected into the booster "on the fly" about 12 ms into the cycle and is extracted at 450 ms. Based on this cycle, the transverse emittance changes with energy during the ramp as shown in Fig. 4-11. Because the radiation damping is unimportant near the booster injection energy, the low-energy behavior of the emittance is determined mainly by adiabatic damping. At high energies, the emittance is determined, as expected, by the effects of quantum fluctuations. The behavior at intermediate energies (500–1000 MeV) corresponds to the transition between these two regimes. It can be seen that the transverse emittance drops below $2 \times 10^{-7}$ m-rad at about 250 MeV, i.e., about 60 ms into the cycle, and remains there until extraction.

The behavior of the longitudinal bunch area is illustrated in Fig. 4-12 for an rf voltage of 250 kV. In these calculations, we have taken a somewhat larger value ($4 \times 10^{-3}$) for the rms momentum spread to account for the longitudinal mismatch in the injection process. For a 1-Hz ramp, the required acceleration voltage is only about 1 kV/turn, so the specifications on the rf voltage come exclusively from the synchrotron radiation energy loss. At 1.5 GeV, the energy loss is 107 keV/turn, so a cavity voltage of about 150–250 kV is required.

In Fig. 4-12a, we show the longitudinal bunch area in units of eV-s. Expressed in this way, the bunch area is seen to be constant at low energies; there is no adiabatic damping effect. At high energies, the bunch area increases under the influence of the quantum fluctuations. Here again, intermediate energies correspond to the transition between the two situations. In Fig. 4-12b, we show the same data, plotted now in terms of the ratio of the rf bucket area to that of the bunch. At injection energy, the ratio is about 8; at extraction energy, it is about 4.

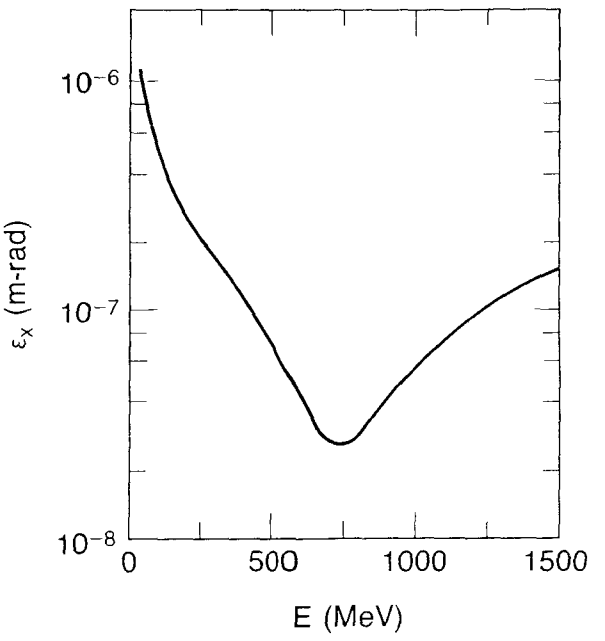


**Fig. 4-11.** Evolution of the booster transverse emittance during the ramp.

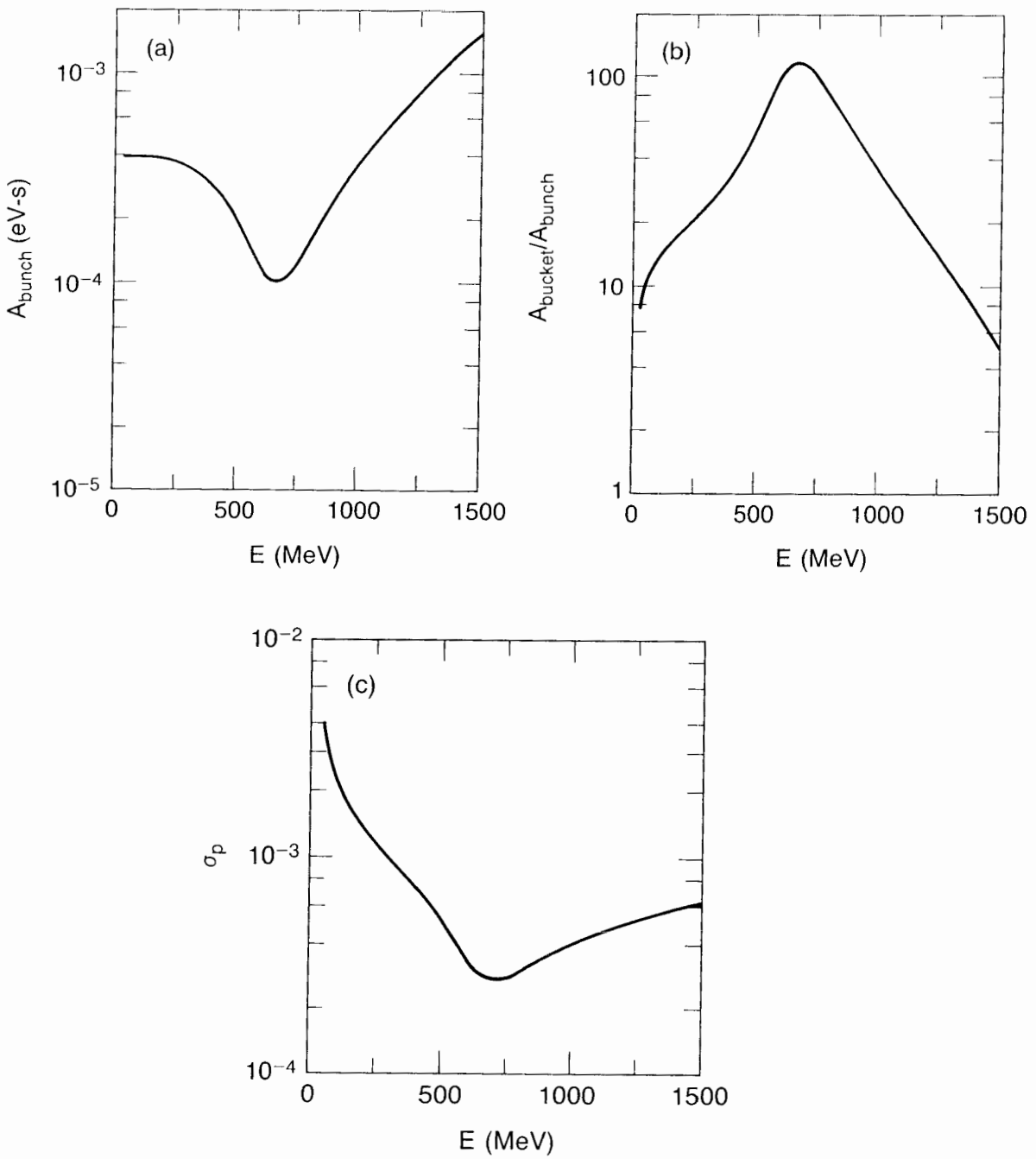


**Fig. 4-12.** Evolution of booster parameters during the ramp: (a) longitudinal bunch area; (b) ratio of rf bucket area to bunch area (the rf voltage is fixed at 250 kV); and (c) relative momentum spread.

The relative rms momentum spread is plotted as a function of booster energy in Fig. 4-12c. It can be seen that the relative momentum spread damps rapidly as the energy increases, falling by nearly a factor of two in the first 50 MeV of acceleration. At high energies, the momentum spread again rises slightly because of the influence of quantum fluctuations.

**4.4.2.3 Behavior at High Energies.** At the extraction energy of 1.5 GeV, the single-bunch longitudinal threshold current is about 15 mA/bunch at a momentum spread corresponding to the natural value for the booster, namely, $6.3 \times 10^{-4}$. As this current is well in excess of what we require, the beam is expected to be at its natural bunch length at extraction. For a voltage of 250 kV, the rms bunch length is about 0.1 ns; this will fit comfortably into the 500-MHz rf bucket of the storage ring.

### 4.4.3 Booster Magnets and Supports

The booster magnet system includes 24 dipoles, 32 quadrupoles, 24 sextupoles, 28 combined horizontal/vertical steering elements, and special magnets for injection and extraction. These magnets have many features in common with those in the storage ring, described in Section 3.4. To avoid repetition, this section concentrates on the features of the booster system that differ from those of the storage ring magnets.

The laminations for the booster dipole, quadrupole, sextupole, and steering magnets are all punched from 0.025-in.-thick M36 silicon steel sheet, with C5 insulation coating. This choice not only gives excellent performance at the nominal cycling rate of 1 Hz, but would also permit booster operation at repetition rates up to 10 Hz, should this be desirable in the future.

**4.4.3.1 Dipoles.** The booster dipole magnets are H-type with flat pancake coils, as shown in Fig. 4-13. They are curved to follow the electron-beam trajectory, which serves to minim-

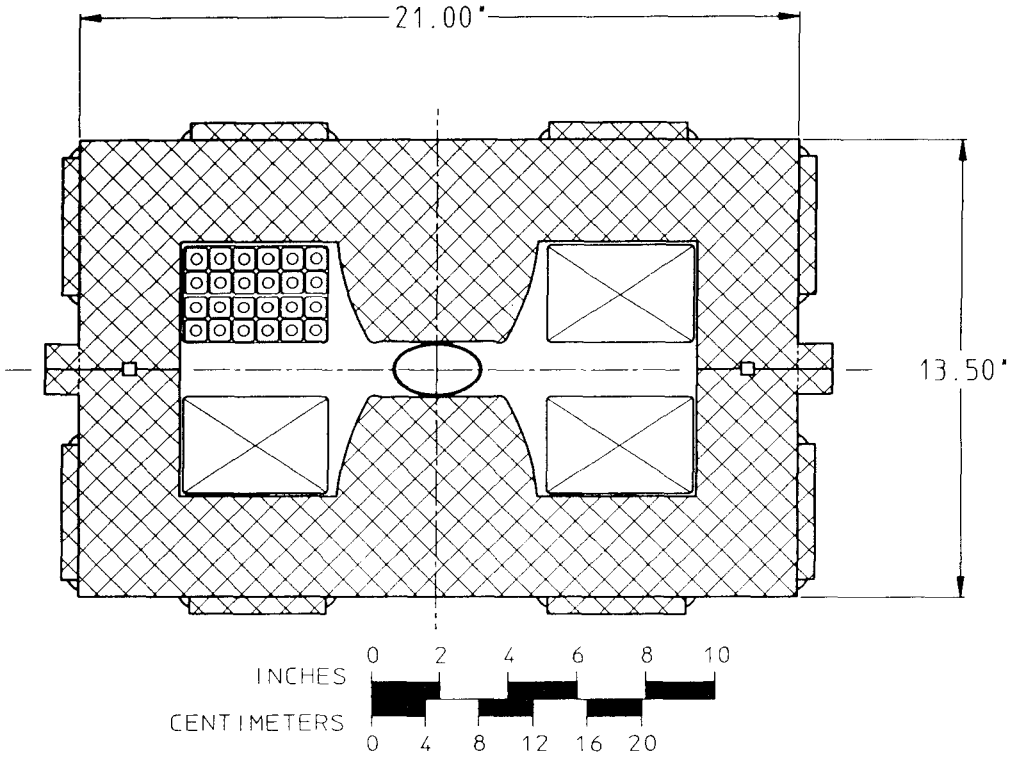


**Fig. 4-13.** Booster bending magnet cross section.

ize pole width (and thereby the stored energy and power requirements). Assembly of the magnet yoke halves follows a procedure similar to that used for the storage ring bending magnets. The coils are wound from the same material used for the storage ring bending magnet coils, with the same insulation and construction techniques. Principal parameters of the booster dipole magnets are given in Table 4-8.

**Table 4-8.** Booster bending magnet parameters at 1.5 GeV.

| | |
|---|---|
| Number of magnets | 24 |
| Bend angle (deg) | 15 |
| Cycle rate, nominal (Hz) | 1 |
| Magnetic flux density on orbit (T) | 1.198 |
| Magnetic length (m) | 1.094 |
| Magnet gap (mm/in.) | 42.0 / 1.654 |
| Good-field width (mm) | ±30.0 |
| Good-field height (mm) | ±17.6 |
| Steel weight per magnet (lb) | 2600 |
| Conductor copper weight (lb) | 610 |
| Total magnet weight (lb) | 3300 |
| Number of turns, total | 48 |
| Current (A) | 851 |
| Conductor area ($mm^2$) | 214 |
| DC resistance per magnet (mΩ) | 12.3 |
| DC voltage per magnet, at 851 A (V) | 10.5 |
| 24 magnets, excl. leads (V) | 251 |
| DC power per magnet, at 851 A (kW) | 8.9 |
| 24 magnets, excl. leads (kW) | 214 |
| Inductance per magnet (mH) | 12 |

**4.4.3.2 Quadrupoles.** The design of the booster quadrupole magnets, shown in Fig. 4-14, is based on the PEP insertion quadrupoles, which were designed and built at LBL. The yoke halves have a C configuration, with no joint in the magnetic circuit. Precision dowels are used to align the top and bottom halves. Coil construction follows the procedure described in Section 3.4.2, using 0.34-in.-square hollow copper conductor. Principal parameters of the booster quadrupole magnets are given in Table 4-9.

**4.4.3.3 Sextupoles.** The booster sextupole magnets, shown in Fig. 4-15, are constructed from the same laminations as the storage-ring sextupoles. However, the field strengths required are much smaller than those for the storage-ring sextupoles, so the coils can be built from 12 AWG magnet wire (120 turns per pole), and air-convection cooling is adequate. Principal parameters of the booster sextupole magnets are given in Table 4-10.

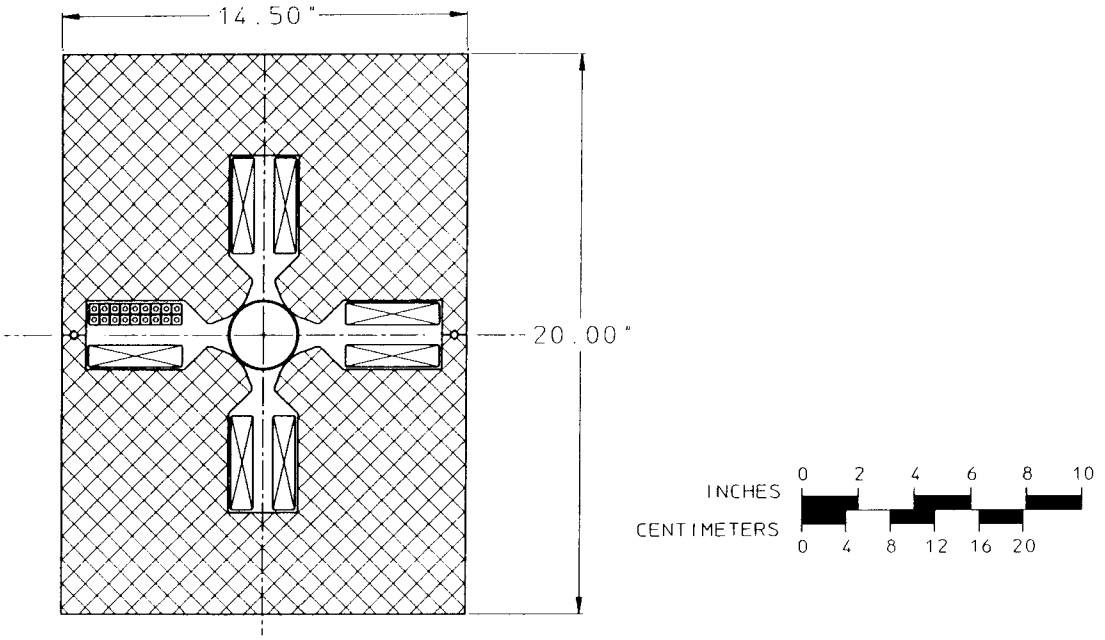


**Fig. 4-14.** Booster quadrupole magnet cross section.

**Table 4-9.** Booster quadrupole magnet parameters at 1.5 GeV.

| | |
|---|---|
| Number of magnets (16 QF + 16 QD) | 32 |
| Cycle rate, nominal (Hz) | 1 |
| Magnetic length (m) | 0.3 |
| Magnet aperture radius (mm/in.) | 32.5 / 1.280 |
| Good-field radius (mm) | 30.0 |
| Gradient, maximum (T/m) | 15.0 |
| Flux density at pole apex (T) | 0.4875 |
| Steel weight per magnet (lb) | 805 |
| Conductor copper weight per magnet (lb) | 81 |
| Total weight per magnet (lb) | 950 |
| Number of turns per pole | 18 |
| Current (A) | 357 |
| Conductor area ($mm^2$) | 57 |
| DC resistance per magnet (mΩ) | 23.2 |
| Resistive voltage per magnet, at 357 A (V) | 8.3 |
| 16 magnets, excl. leads (V) | 132 |
| Resistive power per magnet, at 357 A (kW) | 2.96 |
| 16 magnets, excl. leads (kW) | 47 |
| Inductance per magnet (mH) | 4.5 |

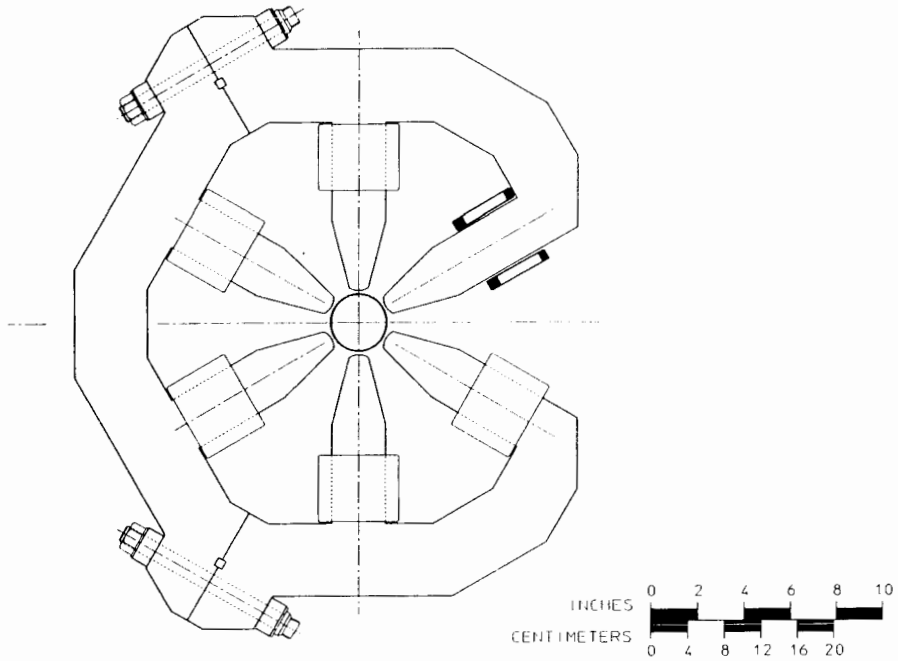


**Fig. 4-15.** Booster sextupole magnet cross section.

**Table 4-10.** Booster sextupole magnet parameters at 1.5 GeV.

| | |
|---|---|
| Number of magnets (8 SF + 16 SD) | 24 |
| Magnetic length (m) | 0.10 |
| Magnet aperture radius (mm) | 35.0 |
| Good-field radius (mm) | 30.0 |
| Sextupole parameter $S = B/r^2$ (T/m$^2$) | 50 |
| Flux density at pole apex (T) | 0.061 |
| Steel weight per magnet (lb) | 650 |
| Copper weight per magnet, all coils (lb) | 30 |
| Total magnet weight (lb) | 750 |
| Number of turns per pole | 120 |
| Current (A) | 4.9 |
| Conductor area (mm$^2$) | 5.2 |
| Voltage drop, per magnet (V) | 5.0 |
| 8 SF magnets, excl. leads (V) | 40 |
| 16 SD magnets, excl. leads (V) | 80 |
| Power per magnet (kW) | 0.025 |
| 8 SF magnets, excl. leads (kW) | 0.20 |
| 16 SD magnets, excl. leads (kW) | 0.40 |
| Inductance per magnet (mH) | 0.14 |

**4.4.3.4 Steering Magnets.** The booster steering magnet design is based upon that for the LBL SuperHILAC correction magnets. Major parameters are given in Table 4-11.

**4.4.3.5 Injection Hardware.** Injection into the booster is described in Section 4.4. The linac beam is directed into the booster by a small, dc septum magnet and is deflected onto the booster orbit by a full-aperture kicker magnet. Major parameters for these magnets are given in Tables 4-12 and 4-13. The modest field strength of the septum (83.5 mT) is obtained by an eight-turn dc magnet shown in Fig. 4-16; this magnet is located inside the booster vacuum system. The full-aperture kicker magnet, shown in Fig. 4-17, has a ferrite

**Table 4-11.** Booster steering magnet parameters at 1.5 GeV.

| | |
|---|---|
| Number of horizontal/vertical steering elements | 28 |
| Magnetic flux density (T) | 0.068 |
| Magnetic length (m) | 0.15 |
| Magnetic aperture radius (mm) | 32 |
| Current (A) | 6 |
| Voltage, excl. leads (V) | 18 |
| Power, excl. leads (kW) | 0.11 |

**Table 4-12.** Booster injection septum magnet parameters.

| | |
|---|---|
| Core material | Steel |
| Length (m) | 0.35 |
| Septum thickness (mm) | 20 |
| Bend angle (deg) | 10.0 |
| Beam aperture (mm) | |
| Vertical | 40 |
| Horizontal | 40 |
| Physical aperture (mm) | |
| Vertical | 40 |
| Horizontal | 71 |
| Magnetic field (T) | 0.0835 |
| Number of turns | 8 |
| Magnet current, dc (A) | 332 |
| Magnet voltage, dc (V) | 1.56 |
| Magnet inductance ($\mu$H) | 66.1 |
| Magnet resistance (m$\Omega$) | 4.7 |

**Table 4-13.** Booster injection kicker parameters.

| | |
|---|---|
| Core material | nickel-zinc ferrite, CMD 5005 |
| Length (m) | 0.5 |
| Bend angle (deg) | 4.5 |
| Beam aperture (mm) | |
| Vertical | 28 |
| Horizontal | 50 |
| Physical aperture (mm) | |
| Vertical | 40 |
| Horizontal | 64 |
| Magnetic field (T) | 0.0262 |
| No. of turns (2 half-turns) | 1 |
| Magnet current (A) | 834 |
| Magnet current, rms (A) | 0.32 |
| Repetition rate, nominal (Hz) | 1 |
| Current flat-top (ns) | 150 |
| Current fall-time (ns) | 100 |
| Magnet inductance, per half ($\mu$H) | 0.61 |
| Magnet resistance, per half (m$\Omega$) | 7 |
| Total inductance ($\mu$H) | 0.30 |
| Total resistance (m$\Omega$) | 3.5 |
| Total current, peak (A) | 1668 |
| Total current, rms (A) | 0.64 |
| Total voltage, peak (kV) | 23.35 |

yoke with a window-frame geometry. It is located around a ceramic vacuum vessel, which allows the rapidly varying fields to penetrate to the beam orbit. The ceramic chamber has a thin conductive coating on the vacuum side to prevent buildup of charge and to present a conducting surface to the circulating beam. The single-turn conductors of the kicker magnet operate as separate half-turn circuit elements, each being fed (at opposite ends of the magnet) by the same power supply, as described in Section 4.4.4.3.

**4.4.3.6 Extraction Hardware.** Booster extraction is a mirror image of the injection system. However, in the case of extraction, the magnetic rigidity of the beam is now 30 times higher than at injection. The extraction kicker magnet deflects the beam into the aperture of a thin septum magnet, which in turn bends the beam into a thick septum that produces the final exit trajectory from the booster. The extraction kicker magnet has the same cross section as the injection kicker, but is twice as long. Its major parameters are given in Table 4-14. The thin septum magnet is identical to the storage ring injection septum, described in Section 3.4.6. The thick septum has the same cross section as the thick storage ring injec-

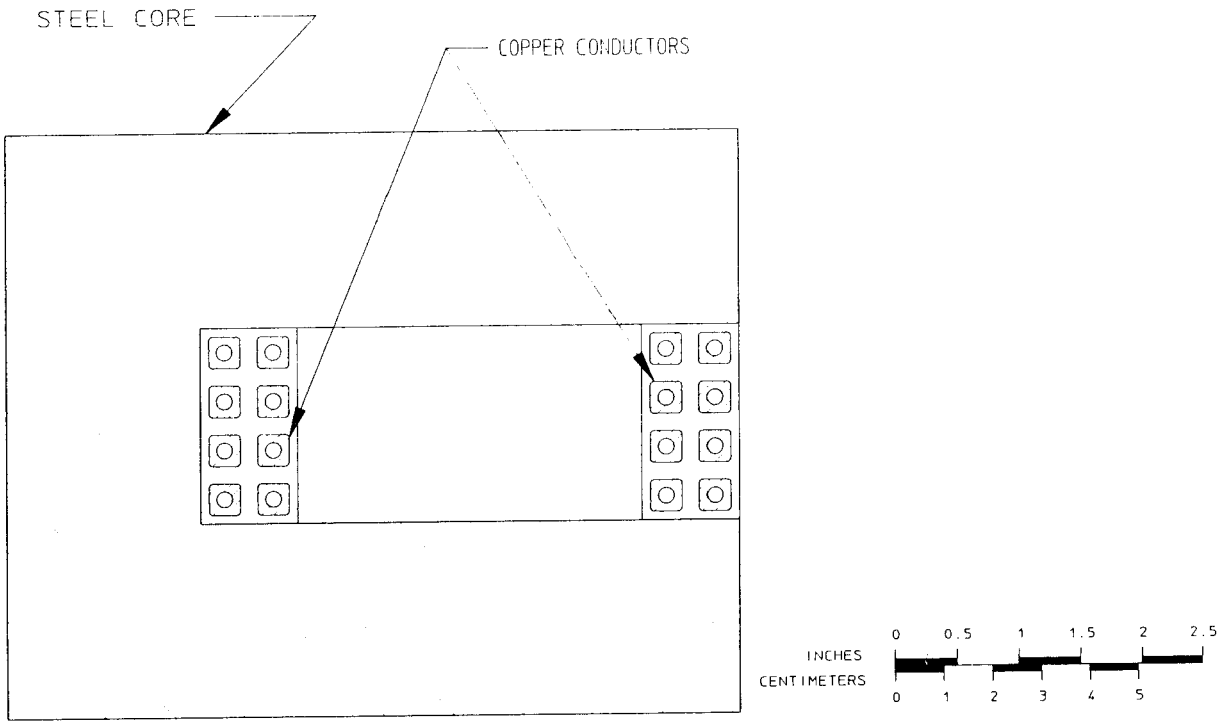


**Fig. 4-16.** Booster injection septum magnet cross section.

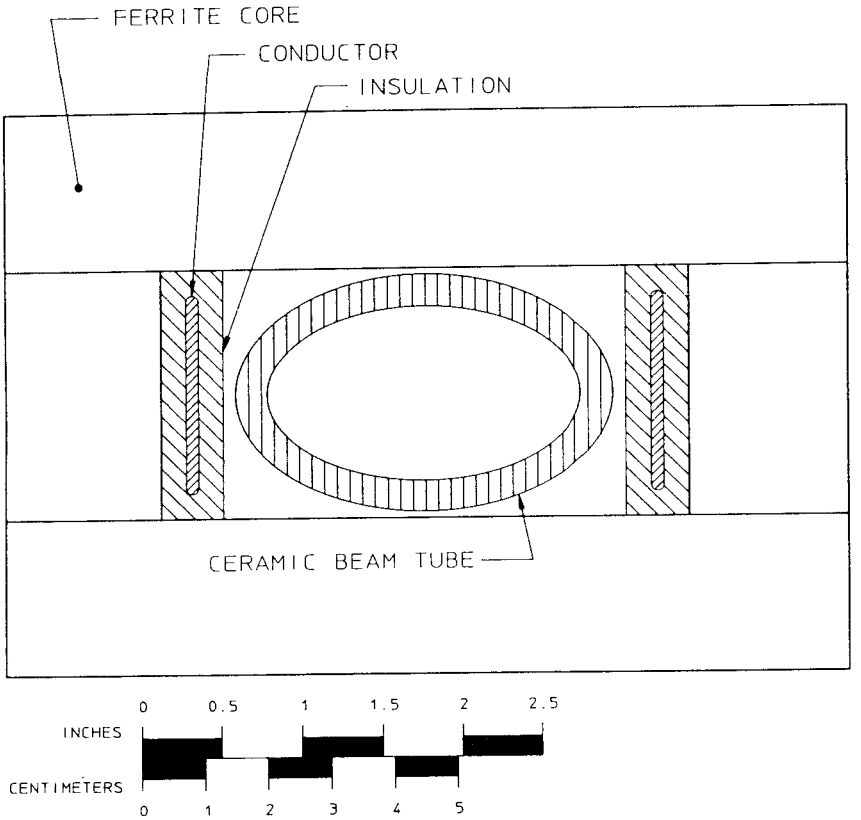


**Fig. 4-17.** Booster injection kicker magnet cross section.

**Table 4-14.** Booster extraction kicker magnet parameters.

| | |
|---|---|
| Core material | nickel-zinc ferrite, CMD 5005 |
| Length, two sections (m) | 1.0 |
| Bend angle (deg/mrad) | 0.57/10 |
| Beam aperture (mm) | |
| Vertical | 28 |
| Horizontal | 50 |
| Physical aperture (mm) | |
| Vertical | 40 |
| Horizontal | 64 |
| Magnetic field (T) | 0.05 |
| No. of turns | 1 |
| Magnet circuit | 4 halves, in parallel |
| Magnet current per half, peak (A) | 1592 |
| Magnet current per half, rms (A) | 0.62 |
| Repetition rate, nominal (Hz) | 1 |
| Current flat-top (ns) | 150 |
| Current rise time (ns) | 100 |
| Total inductance ($\mu$H) | 0.15 |
| Total resistance (m$\Omega$) | 1.75 |
| Total current, peak (A) | 6368 |
| Total current, rms (A) | 2.48 |
| Total voltage, peak (kV) | 22.3 |

tion septum, but it is shorter and has a lower field; its parameters are given in Table 4-15. Both thin and thick extraction septa are located in a common vacuum tank that is integral with the booster vacuum chamber.

**4.4.3.7 Field Measurements.** Magnetic field measurements for the booster magnets will be carried out in a manner similar to that for the storage ring magnets. However, the dipole magnets will be energized with the 1-Hz waveform specified for booster operation. Magnetic line integrals and multipole components will be obtained using integrator circuits in conjunction with sample/hold circuits. Data will be taken at various excitation levels from injection to full energy. The fast pulsed magnets will be measured using search coils and high-frequency oscilloscopes.

**4.4.3.8 Magnet Supports.** The magnets described above are assembled onto 16 girders, similar in design to those in the storage ring, but shorter (only 4.6 meters long). Twelve girders are used for the booster arc sections, each supporting two dipole magnets and the accompanying quadrupoles, sextupoles, and steering magnets. The remaining four girders are for the utility straight sections, which are used for injection, extraction, and the rf cavity. This arrangement permits assembly to proceed in the more favorable environment of

**Table 4-15.** Booster extraction thick-septum magnet parameters.

| | |
|---|---|
| Core material | manganese-zinc ferrite (Ceramic Magnetics MN67) |
| Length (m) | 0.6 |
| Septum thickness (mm) | 6 |
| Bend angle (deg) | 4.0 |
| Beam aperture (mm) | |
| Vertical | 15 |
| Horizontal | 16 |
| Physical aperture (mm) | |
| Vertical | 15 |
| Horizontal | 37 |
| Magnetic field (T) | 0.582 |
| Number of turns | 1 |
| Current, peak (A) | 6950 |
| Current, rms (A) | 49.1 |
| Repetition rate, nominal (Hz) | 1 |
| Current waveform | half sine-wave |
| Current duration ($\mu$s) | 100 |
| Magnet inductance ($\mu$H) | 1.91 |
| Total inductance ($\mu$H) | 2.41 |
| Total resistance, ac (m$\Omega$) | 2.22 |
| Total voltage, peak (V) | 485 |

the Assembly Shop and will allow rapid installation of the booster components after beneficial occupancy of the building.

### 4.4.4 Other Components and Auxiliary Systems

**4.4.4.1 Booster Vacuum System.** The vacuum requirements in the booster synchrotron are relatively modest, about 100 nTorr, and the gas load generated by synchrotron radiation photons is small compared with that in the storage ring. Eight 60-liter/s ion pumps distributed around the ring and two 400-liter/s ion pumps, one each in the large-volume injection and extraction chambers, supply all the required pumping.

The vacuum chamber is constructed from 1-mm-thick stainless steel. At booster repetition rates up to 4 Hz, eddy currents generated in the chamber have a negligible thermal effect. Sextupole fields, which markedly change the chromaticity at low beam energies, are easily compensated by the lattice sextupole magnets. The cross section of the vacuum chamber in the dipoles is elliptical; it is circular elsewhere. There are special chambers to accommodate the injection and extraction septum magnets.

**4.4.4.2 Survey and Alignment.** Survey and alignment techniques used for the booster will be essentially identical to those described for the storage ring (Section 3.6).

**4.4.4.3 Booster Magnet Power Supply Systems.** The booster synchrotron magnet power supply systems are designed to provide a maximum energy of 1.5 GeV. The power supply tracking-accuracy specifications, shown in Table 4-16, are based on the allowable tune shifts that will maintain beam stability. Power supply tracking, including ripple, will be carefully held to these specifications. AC power for the booster ring supplies is provided by a separate transformer bank to minimize interactions with other Light Source operations. The power-supply-controlling inputs and associated monitoring functions are handled by the local microcomputers provided as part of the Light Source control system. Major parameters of the booster magnet power supplies are summarized in Table 4-16.

*Bending Magnet Power Supplies.* The bending magnet array of the booster synchrotron consists of 24 magnets. These magnets are electrically connected in series and require a single SCR power supply that is capable of being operated in both the rectification mode and the inversion mode. The operating repetition rate of the synchrotron is 1 Hz, and 0.45 seconds is allowed for the magnet current to increase from 0 to 851 A. This is accomplished by applying 700 V dc to the magnet windings and letting the current build up with the magnet's 1-second time constant. The voltage and current waveforms are shown in Fig. 4-18. Detectors sense the magnetic field strength of the dipoles and generate a timing signal to trigger the injection of beam into the synchrotron and to trigger the ejection of beam from the synchrotron upon reaching the desired energy. Both injection and ejection of the beam are accomplished "on the fly." As soon as beam ejection has been accomplished, the

**Table 4-16.** Booster magnet power supply parameters.

| | Family total | | | | | | |
|---|---|---|---|---|---|---|---|
| Magnets | $I$ (A) | $V$, dc (V) | $R$ (Ω) | $L$ (H) | Tracking accuracy | $V_{forcing}$ (V) | $V_{ps}$ (V) |
| Bending (24 in series) | 851 | 252 | 0.295 | 0.29 | na | 693 | 700 |
| Quadrupole family QF (16 in series) | 357 | 132 | 0.37 | 0.072 | 0.1% | 57 | 210 |
| Quadrupole family QD (16 in series) | 357 | 132 | 0.37 | 0.072 | 0.1% | 57 | 210 |
| Sextupole family SF (8 in series) | 5 | 40 | 8 | 0.001 | 0.5% | 12.4 | 55 |
| Sextupole family SD (16 in series) | 5 | 80 | 16 | 0.002 | 0.5% | 24.8 | 150 |
| Correction dipoles[a] | 6 | 18 | 3 | 0.15 | 0.5% | 2 | ±20 |

[a]28 horizontal, 28 vertical, each with its own power supply.

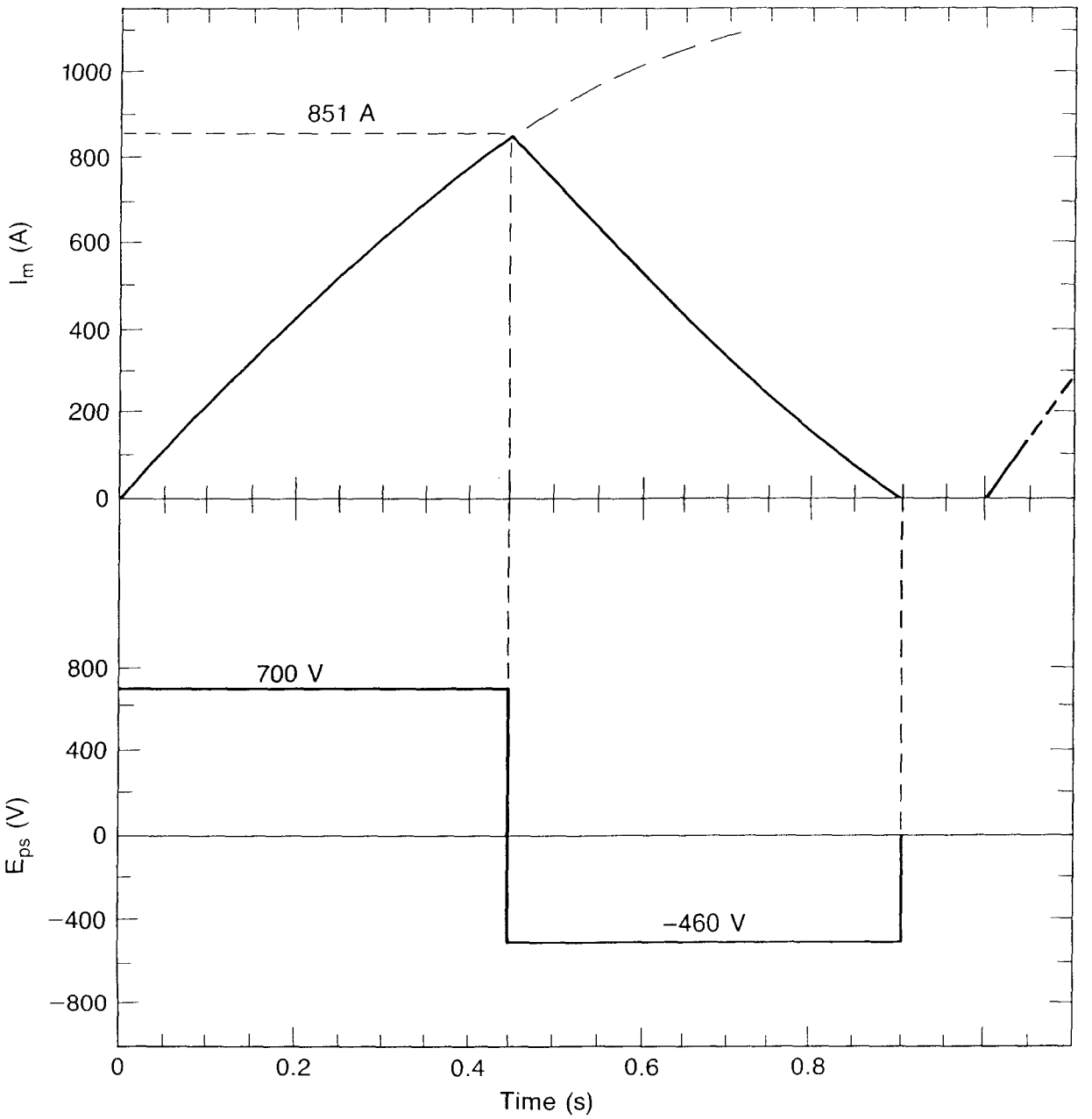


**Fig. 4-18.** Voltage and current waveforms for the booster bending magnets.

SCRs of the power supply are phased to inversion, and the energy stored in the magnets is returned to the ac power line as the magnet current decreases.

A precision current transductor monitors the dipole magnet current; this signal is used as a reference for the transistor regulators of the power supplies for the quadrupole magnets, the sextupole magnets, and the steering magnets, making their respective currents track the current in the bending magnets as it increases from 0 to 851 A. With this technique, the bending magnet current need not be closely regulated.

*Quadrupole Magnet Power Supplies.* The 32 quadrupole magnets in the booster synchrotron are divided into two families (QF and QD) of 16 magnets each, powered by two separate power supply systems consisting of two dc power supplies connected in series, as shown in Fig. 4-19. One is an SCR type, which can be operated in either the rectification

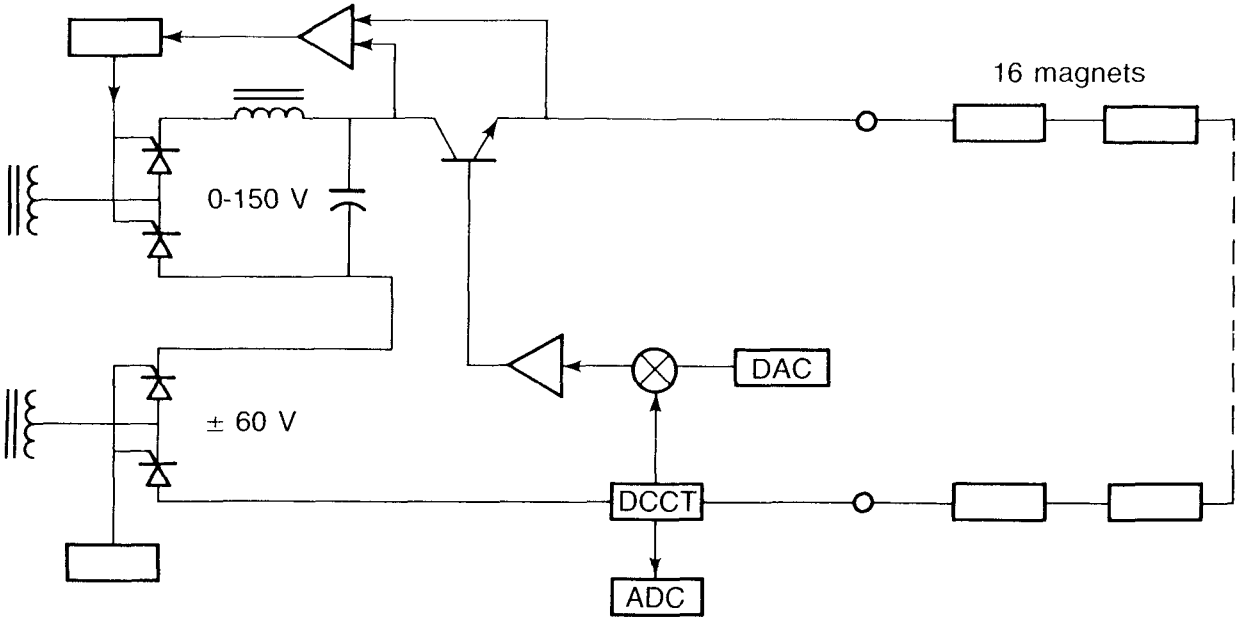


**Fig. 4-19.** Power supplies for the two families of booster quadrupole magnets.

mode or the inversion mode; this supply provides the "forcing" voltage required to obtain the desired current rate-of-rise, as indicated in Fig. 4-20. The second supply is another SCR type whose output voltage can be controlled from 0 to 150 V. This supply also has a series transistor regulator to regulate the output current of both supplies. The transistor regulator is required to obtain the closed-loop frequency response necessary to have the current in the quadrupole magnets track the bending magnet current to within 0.1%.

*Sextupole Magnet Power Supplies.* The 24 sextupole magnets of the booster synchrotron are divided into two families (SF and SD); family SF consists of 8 magnets connected electrically in series, and family SD consists of 16 magnets connected electrically in series. Each of the magnets is rated 5 V, 5 A, and 0.14 H. The SF family of eight magnets requires 40 V dc plus 12.4 V forcing voltage to achieve the desired $dI/dT$. A commercial transistor-regulated power supply (rated 55 V, 10 A) is used for this family. The SD family of 16 magnets in series requires 80 V dc plus 24.8 V forcing voltage, so a larger commercial transistor-regulated power supply (rated 150 V, 7 A) is used. Outputs of these supplies are controlled by analog reference voltages applied to their regulation circuits. Magnet currents are monitored with an ADC connected to a local computer; the computer controls a DAC that furnishes the analog reference voltage necessary to achieve the desired tracking accuracy.

kicker power supply, as shown in Fig. 4-21, is a transmission-line discharge type, with the magnet and associated network carefully compensated to terminate the transmission line and reduce the magnet current to zero after the beam has been injected.

Booster extraction requires three power supplies. A transmission-line discharge power supply provides current to a fast picture-frame kicker magnet system composed of two cells

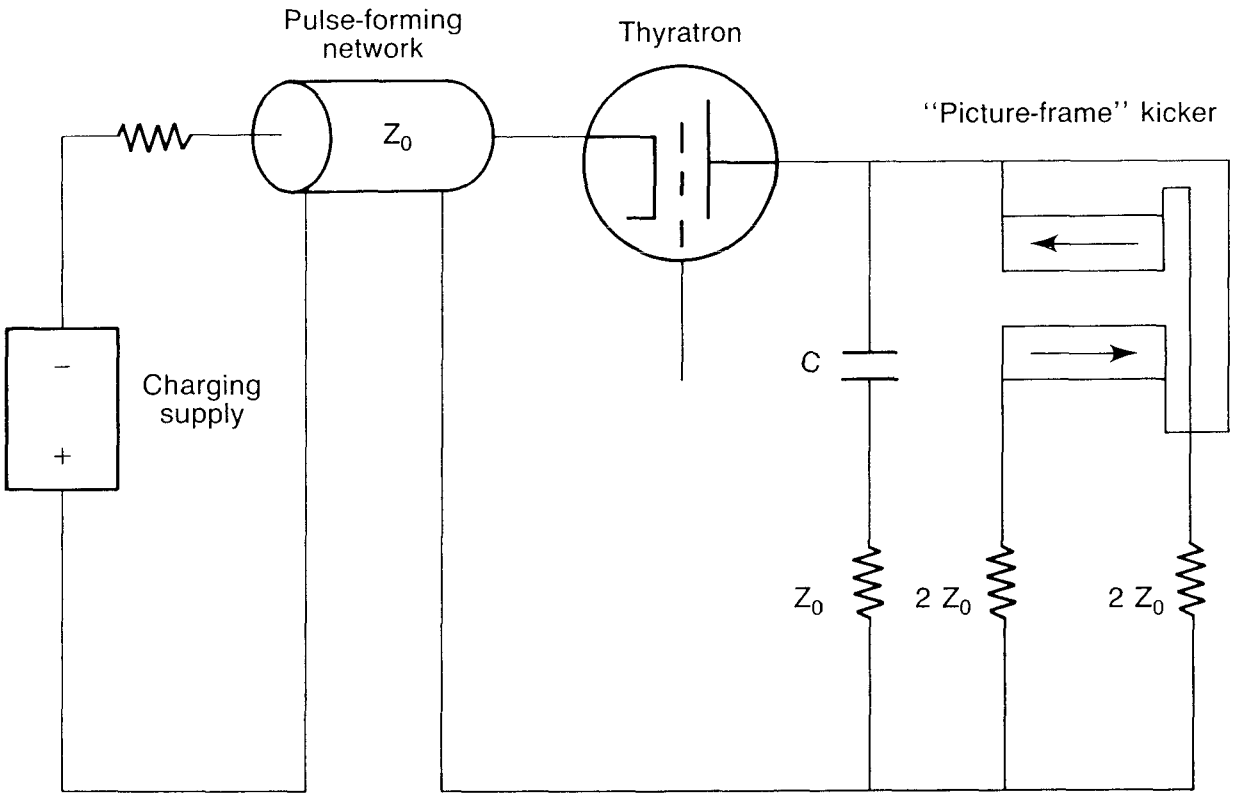


**Fig. 4-21.** Power supply for the booster injection kicker.

(Fig. 4-22); two half-sine-wave, capacitor-discharge-type power supplies, similar to those used for storage-ring injection, supply current to the thin and thick septum magnets, respectively. In addition, existing booster correction magnet power supplies are programmed to move the beam close to the thin septum as part of the extraction process.

Specifications for the booster injection and extraction magnets and power supplies are given in Tables 4-12 through 4-15 in Sections 4.4.3.5 and 4.4.3.6.

**4.4.4.4 Booster rf System.** The rf system for the booster synchrotron uses a single rf cavity identical to those used in the storage ring. The few kilowatts of rf power are easily supplied by a commercial UHF transmitter, modified to our requirements. The phase-and-gradient control system is also identical to that used for the storage ring. The rf signal is fed from the phase-stable reference system to ensure synchronization with the storage-ring rf. Table 4-17 gives the principal parameters of the booster rf system.

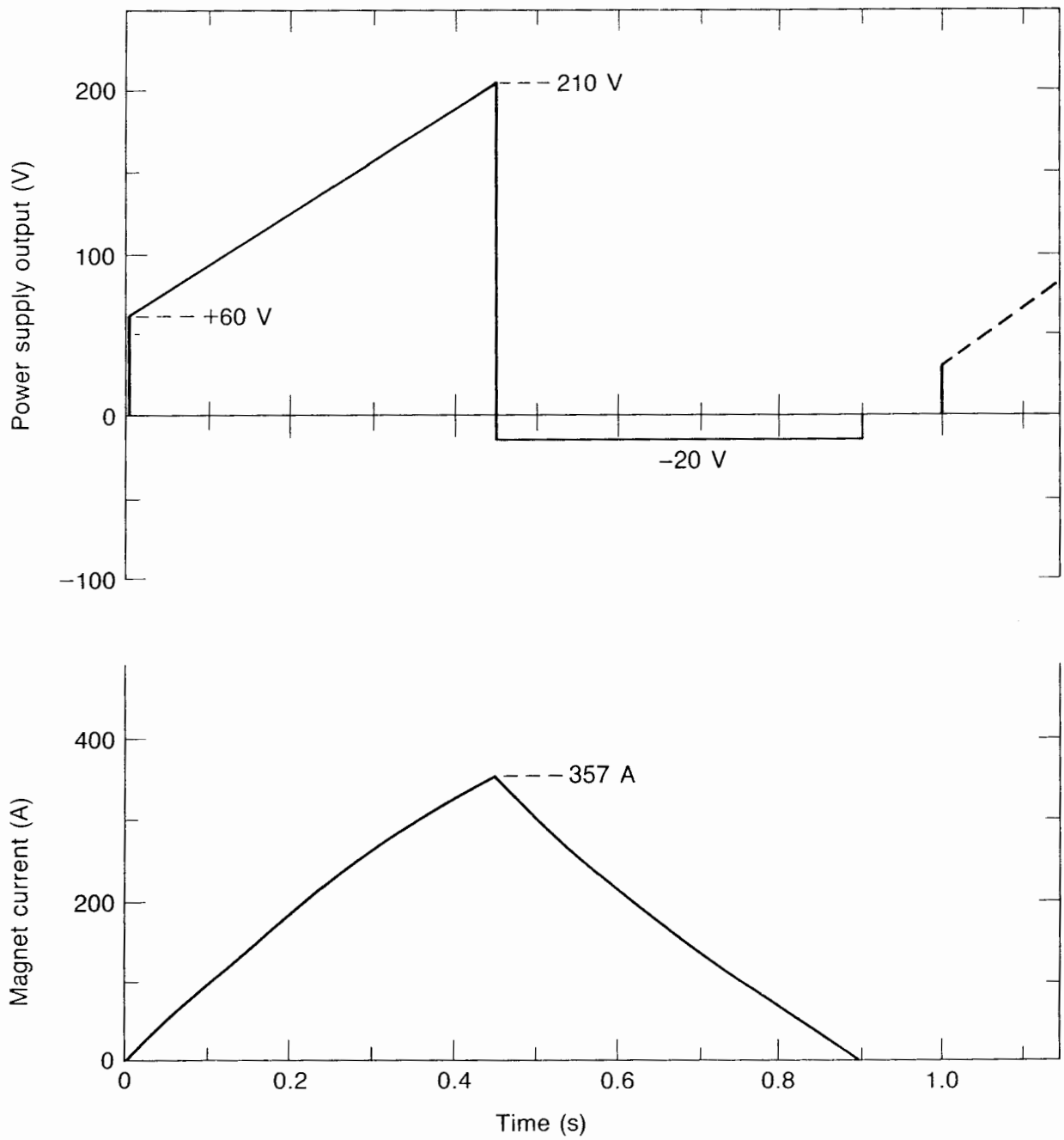


**Fig. 4-20.** Voltage and current waveforms for the booster quadrupole magnets.

*Correction Dipole Power Supplies.* There are 28 correction dipole magnets in the booster synchrotron, each with a horizontal and a vertical correction winding. Each of the 56 windings is powered by a separate, commercially available bipolar power supply.

*Injection and Extraction Magnet Power Supplies.* Injection into the booster ring requires two power supplies, one for a small septum magnet, and the other for a fast picture-frame kicker magnet. The septum magnet power supply is a small commercial dc supply. The

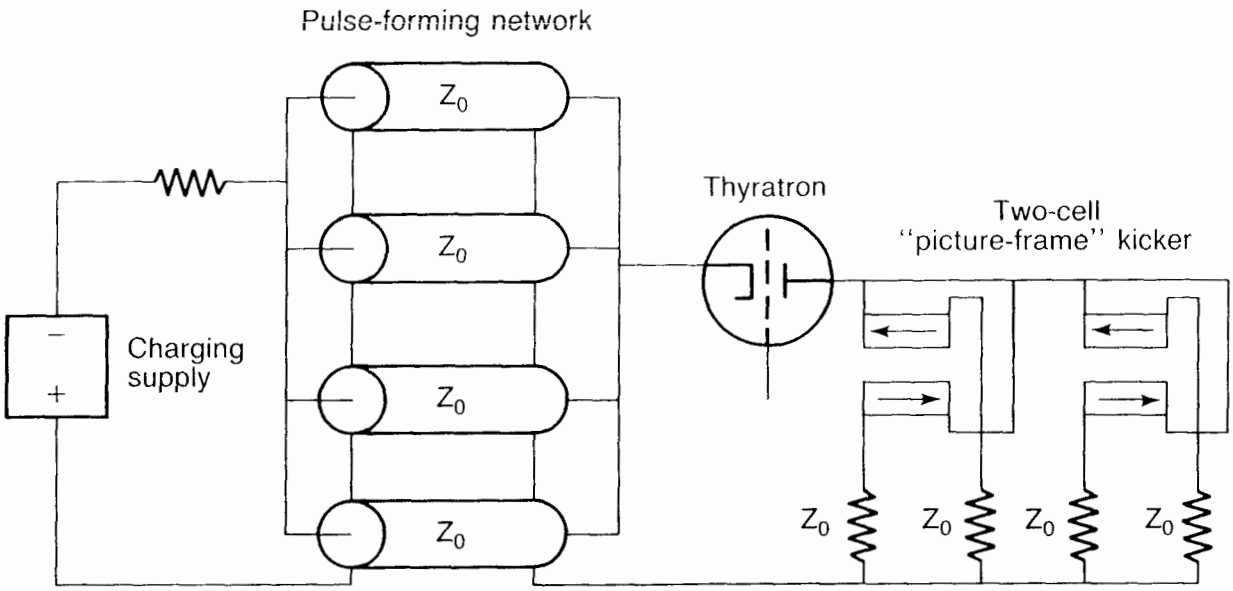


**Fig. 4-22.** Power supply for the booster extraction kicker.

**Table 4-17.** Booster rf system parameters.

| | |
|---|---|
| Frequency (MHz) | 499.65 |
| Harmonic number | 125 |
| Peak effective voltage, $VT$ (kV) | 250 |
| Beam current, multibunch mode (mA) | 20 |
| Synchrotron radiation loss, dipoles (kW) | 2 |
| Total effective shunt impedance, $ZT^2L$ (MΩ) | 8 |
| Fundamental-mode cavity dissipation (kW) | 7.8 |
| Waveguide and other losses[a] (kW) | 1 |
| Total rf power installed (kW) | 30 |

[a]Assumed to be 10%.

**4.4.4.5 Instrumentation.** Beam position in the booster is measured at 32 locations, giving nominally five measurements per horizontal betatron wavelength. The pick-up electrodes are striplines, which offer a greater sensitivity than the buttons used in the storage ring (Sec. 3.9.1). The processing electronics are identical to those used in the storage ring. Wide-band traveling-wave electrodes are installed in two locations for excitation and monitoring of the booster beam. These electrodes are identical to those used in the storage ring (see Section 3.9.2). A dc current transformer is provided for the booster. It is basically the same as the storage-ring device but has higher sensitivity. Optical monitoring of the booster synchrotron light will be possible as the beam is accelerated above a few hundred MeV; a photomultiplier provides the most sensitive optical diagnostic. TV cameras viewing the synchrotron light image give a rough indication of beam size and stability. For

booster commissioning and trouble-shooting, there are four retractable scintillators provided; these are useful for first-turn measurements. Orbit correction is handled by means of 28 correction magnets (16 horizontal and 12 vertical) placed adjacent to quadrupoles in the arcs.

## 4.5 Booster-to-Storage-Ring (BTS) Transfer Line

The function of the BTS transfer line is to deliver the 1.5-GeV beam extracted from the booster to the injection point of the storage ring. For efficient injection, the transfer line must provide a zero-dispersion, focused beam that is matched to the displaced storage ring acceptance. In practice, the general layout of the BTS transfer line is dictated to a large extent by the layout of the storage ring and by the restrictions placed on the position of the booster synchrotron by existing building fixtures (see Section 6). The resulting design is shown in Fig. 4-23.

Momentum matching from booster to storage ring is accomplished by the quadrupole magnets denoted MQ1, MQ2, and MQ3. The remaining six quadrupoles provide

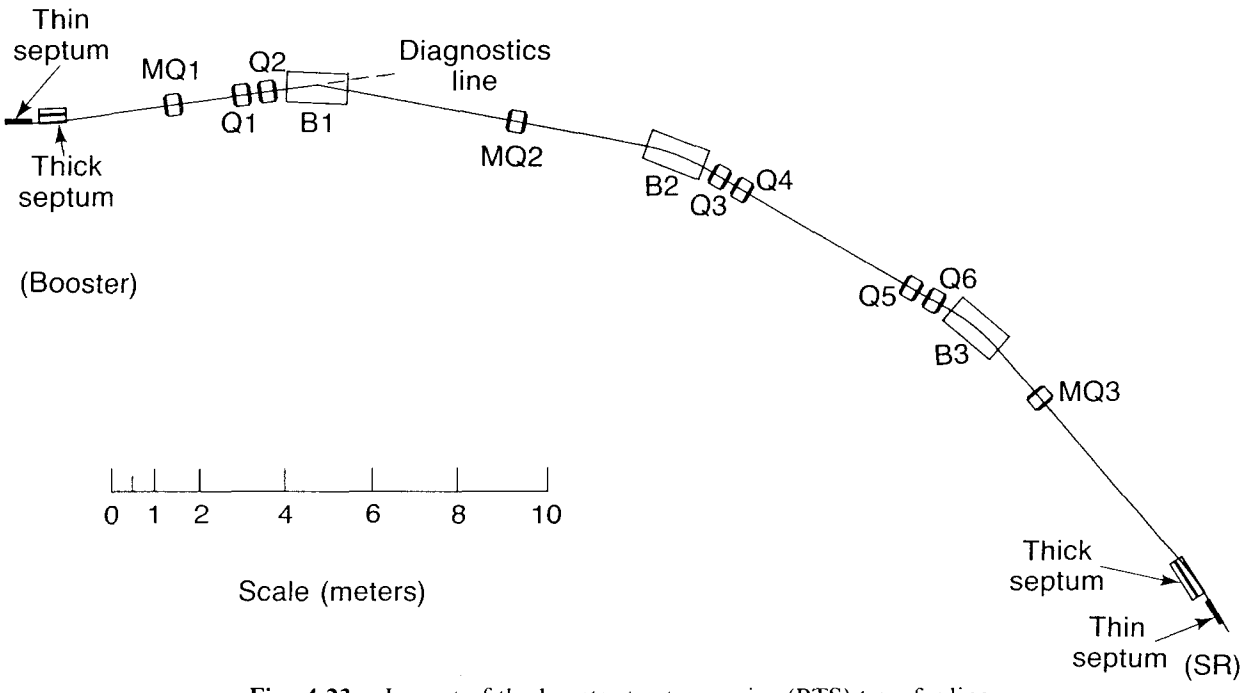


**Fig. 4-23.** Layout of the booster-to-storage-ring (BTS) transfer line.

transverse phase-space matching. Horizontal and vertical beam profiles and the momentum dispersion through the transfer line are shown in Fig. 4-24. It should be noted that the two quadrupole doublets in the dispersion-free section permit final focusing of the electron beam without affecting the momentum matching. To compensate for magnet misalignments, and to permit precise alignment of the beam into the storage ring injection elements, four pairs (horizontal and vertical) of low-field steering magnets are included in the BTS transfer line.

The bending magnets of the BTS transfer line are of the same design and cross section as the booster bending magnets but are longer to provide the increased bending angle required. The quadrupole magnets are also identical to the booster quadrupole magnets. In the assembly shop, these components are mounted onto three separate structural steel girders similar to but longer than those for the booster. This permits rapid installation after beneficial occupancy of the Light Source building.

A booster extraction diagnostics line is also provided. It can be utilized by switching off the first dipole and allowing the beam to enter a well-shielded enclosure containing a viewing screen and a total-current monitor. The diagnostics line permits tune-up of the entire injector complex independently of the operational status of the storage ring. The power supply to the first bending magnet is part of the interlock chain that permits transfer into the storage ring.

Both the LTB and BTS transfer lines utilize commercially available power supplies for all current-regulated dipole, quadrupole, and steering magnet requirements. Each magnet has a separate supply, the specifications of which are given in Table 4-18.

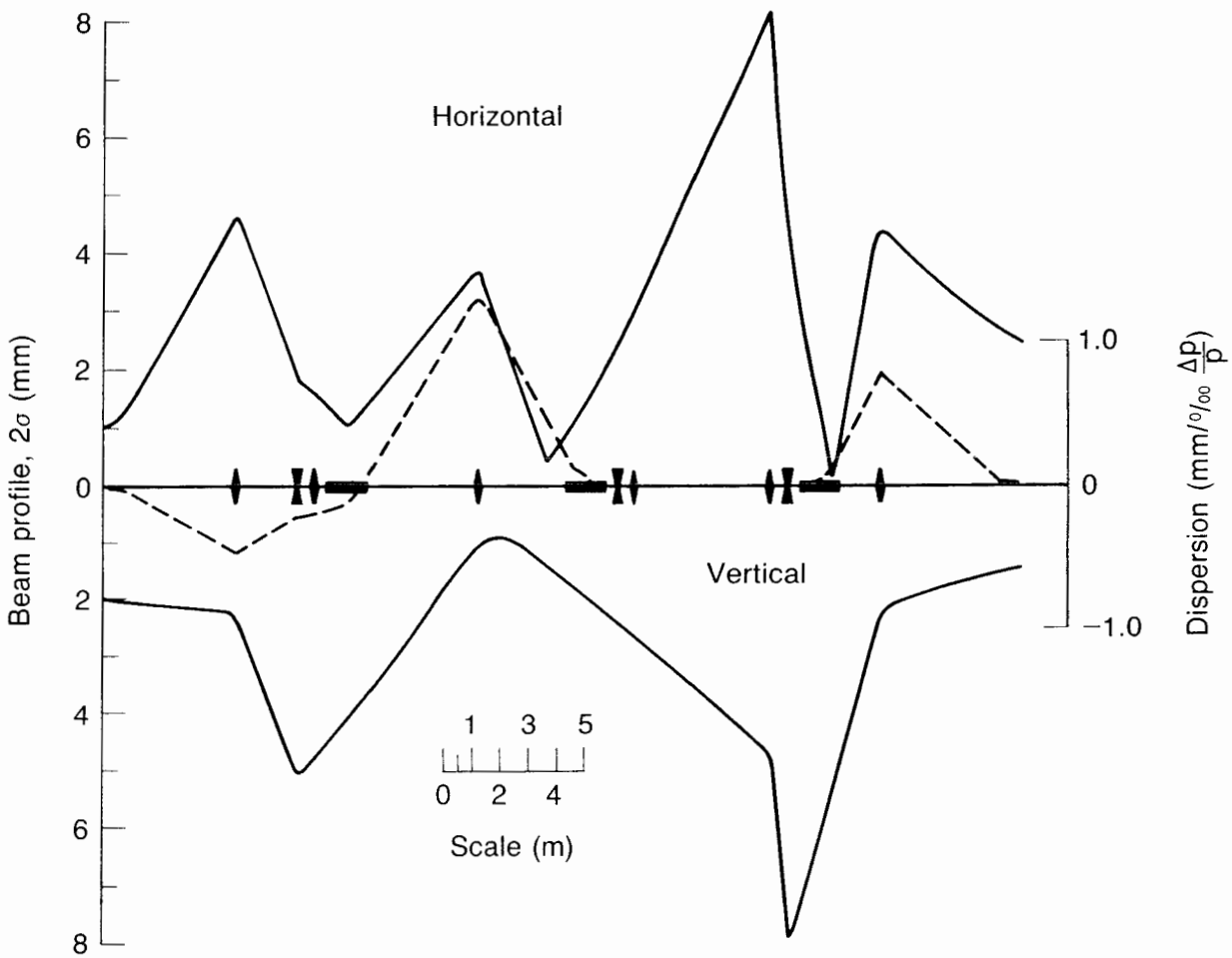


**Fig. 4-24.** Optics of the BTS transfer line.

**Table 4-18.** Transfer line power supply parameters.

| System | Magnet circuit | Number | Current (A) | Voltage (V) | Power (kW) | Stability $\Delta I/I_{max}$ |
|---|---|---|---|---|---|---|
| LTB | Dipole[a] | 2 | 30 | 40 | 1.2 | $\pm 5 \times 10^{-4}$ |
| LTB | Quadrupole | 6 | 10 | 20 | 0.2 | $\pm 5 \times 10^{-4}$ |
| BTS | Dipole | 3 | 851 | 11 | 9.4 | $\pm 5 \times 10^{-4}$ |
| BTS | Quadrupole | 9 | 357 | 9 | 3.2 | $\pm 5 \times 10^{-4}$ |
| LTB, BTS | Dipole, vertical and horizontal correction | 18 | $\pm 10$ | $\pm 20$ | 0.2 | $\pm 5 \times 10^{-4}$ |

[a]Reversing switch on one dipole.

Beam diagnostics for the BTS transfer line are required to provide the same information on intensity and location as the systems in the LTB transfer line. It is not desirable to intercept the high-energy beam and create unnecessary radiation, so only one interceptive diagnostic, a Sabersky probe, is provided. This instrument is a retractable probe that, when hit by the beam, indicates that the beam is in the correct location for storage-ring injection. Beam interception is indicated by measured current in the probe. The five sets of noninterceptive position-monitoring button electrodes are identical to those in the booster. Beam intensity is measured with a gap monitor, as in the linac. Occasionally the scintillators (installed in four locations) are inserted in the beam path as a steering aid. Shielded TV cameras observe the scintillator image, which is viewed in the control room.

# 5. Insertion Devices and Beam Lines

The storage ring and injection system of the Light Source, in proper perspective, are merely tools for producing photon beams—beams that arise from the bending magnets of the ring and, more importantly, from insertion devices in the ring's straight sections. These insertion devices and their beam lines therefore occupy a position of central importance in the design of the 1–2 GeV Synchrotron Radiation Source. This section describes an initial complement of five such insertion devices, together with five insertion device beam lines and two beam lines for synchrotron radiation produced by bending magnets.

## 5.1 Insertion Devices

Undulators and wigglers, collectively referred to as insertion devices, are periodic magnetic structures that operate in the straight sections of storage rings. Compared with bending magnets, such devices are sources of higher photon fluxes in narrower angular cones. Efficient operation of insertion devices requires a small electron beam emittance and long straight sections, both among the design specifications for the storage ring described in this report. A short history of recent developments in insertion device design appears in Section 2.

### 5.1.1 Light Source Insertion Devices and Their Performance

The proposed high-brightness 1–2 GeV Synchrotron Radiation Source, operating at 1.5 GeV, is optimum for insertion device operation in the vacuum ultraviolet (VUV) and soft x-ray spectral regions. On a time-averaged basis, an undulator in such a storage ring is the brightest source available in those photon energy ranges. In addition, for both lower and higher photon energies, undulators and wigglers (respectively) at the Light Source offer very useful capabilities.

Table 5-1 summarizes the parameters for four undulators and a wiggler, selected as an initial complement of Light Source insertion devices. Figures 5-1 and 5-2 summarize the performance of these insertion devices, and Tables 5-2a through 5-2f provide more detailed information. This selection of insertion devices is based on user requirements enunciated at various user workshops, especially the one of November 1985 [*Report of the Workshop*, 1985]. Nonetheless, this selection is open to further adjustment as user preferences evolve.

**Table 5-1.** Parameters for the initial complement of insertion devices chosen for the Light Source.

| Name | Period (cm) | No. of periods | Photon energy range (eV)[a] | Critical energy (keV) |
|---|---|---|---|---|
| **Undulators** | | | | |
| U20.0 | 20.0 | 23 | 0.5–95 [1.5–285] | – |
| U9.0 | 9.0 | 53 | 5–211 [15–633] | – |
| U5.0 | 5.0 | 98 | 50–380 [150–1140] | – |
| U3.65 | 3.65 | 134 | 183–550 [550–1650] | – |
| **Wiggler** | | | | |
| W13.6 | 13.6 | 16 | – | 3.1 |

[a]The photon energy range of the fundamental and the third harmonic (shown in brackets) as $K$ decreases from its maximum value to 0.5.

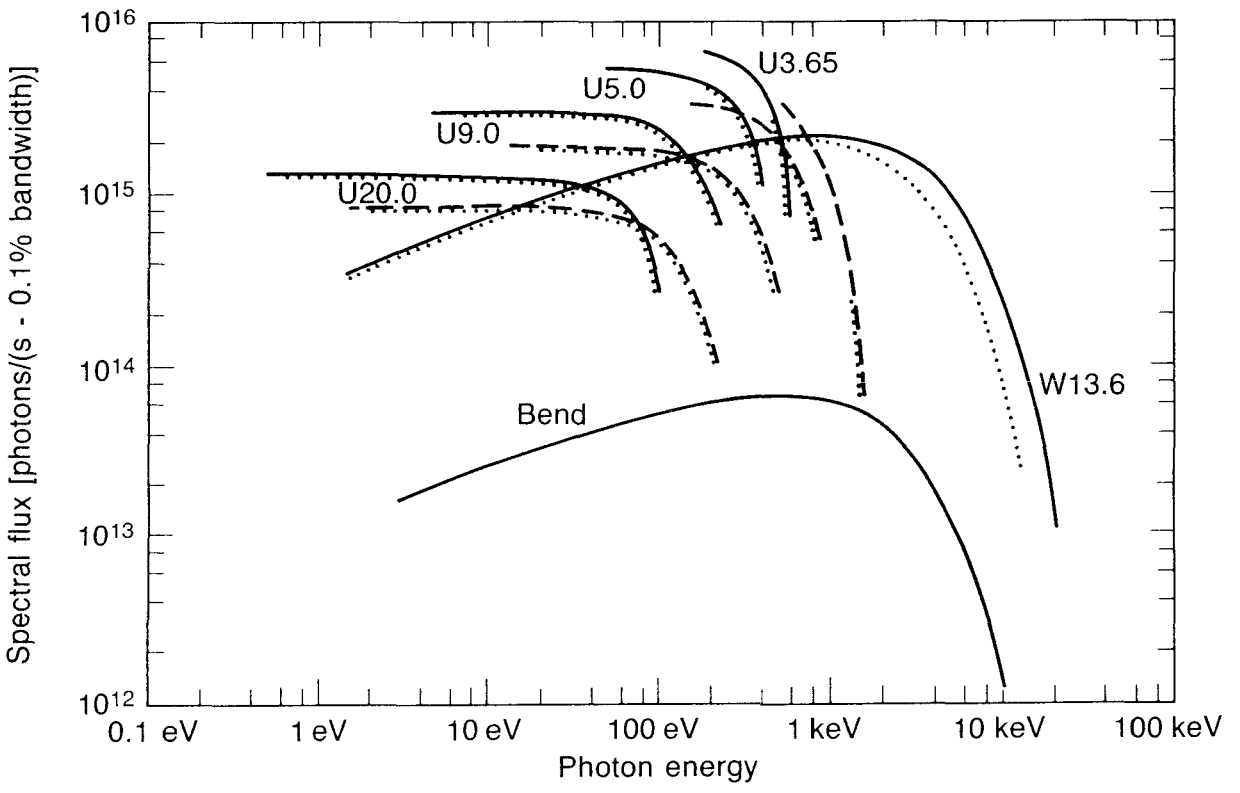


**Fig. 5-1.** Spectral flux as a function of energy for the four undulators and one wiggler described in Table 5-1, together with the bending magnets of the Light Source. For the wiggler and bending magnets, we assume a 5-mrad collection angle. For the undulators, the tuning range is shown for both the fundamental (solid lines) and the third harmonic (dashed lines). The dotted lines show corresponding curves for spectral flux at commissioning, when the minimum magnet gap will be 2.5 cm.

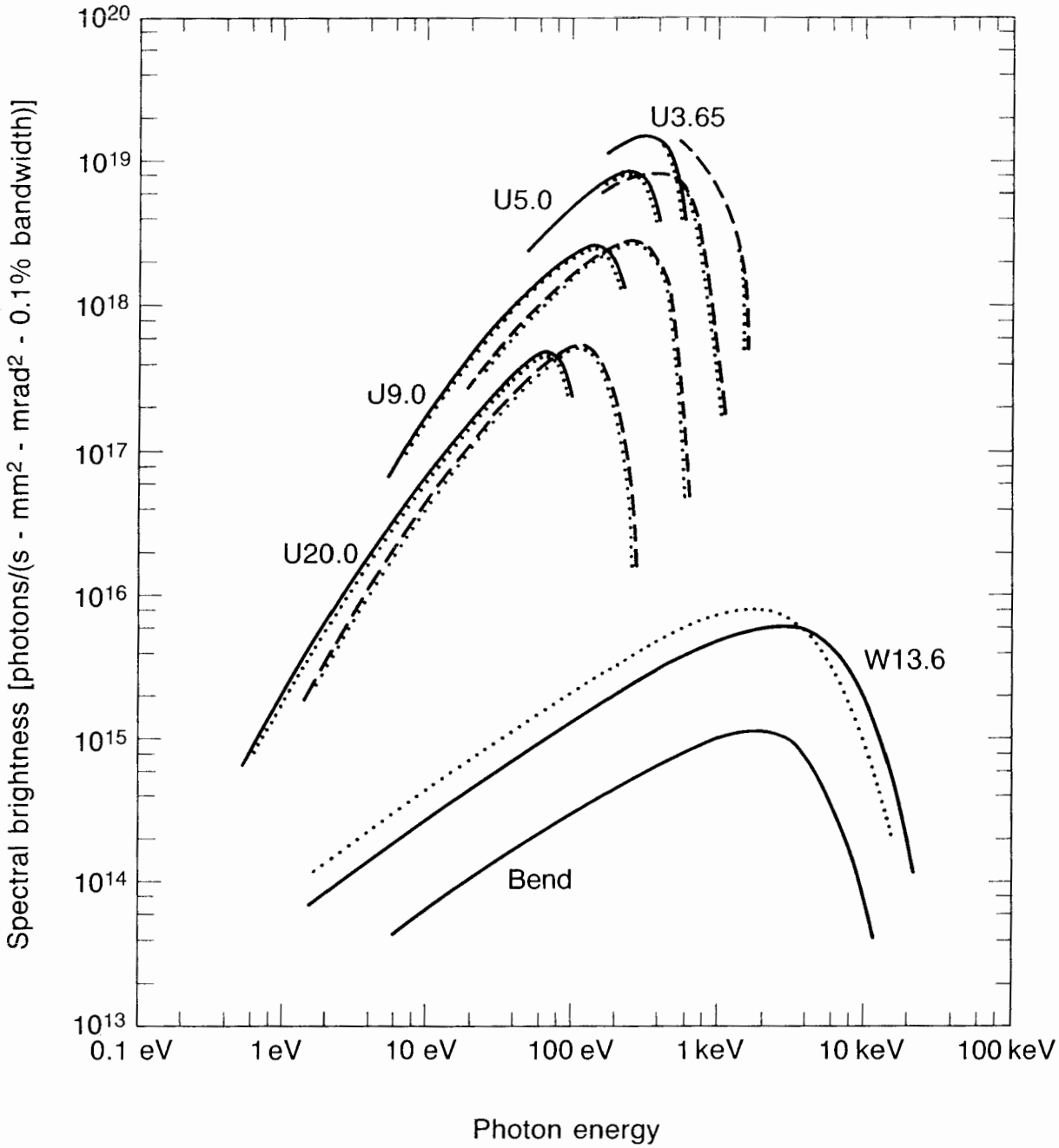


**Fig. 5-2.** Spectral brightness as a function of energy for the four undulators and one wiggler described in Table 5-1, together with the bending magnets of the Light Source. For the undulators, the tuning range is shown for both the fundamental (solid lines) and the third harmonic (dashed lines). The dotted lines show corresponding curves for spectral brightness at commissioning, when the minimum magnet gap will be 2.5 cm.

**Table 5-2 (following pages).** Detailed performance characteristics of the five insertion devices of Table 5-1 and the bending magnets of the Light Source, all at an electron energy of 1.5 GeV: (a) undulator U20.0; (b) undulator U9.0; (c) undulator U5.0; (d) undulator U3.65; (e) wiggler W13.6, with a gap of 1.4 cm; and (f) bending magnets. For the undulators, characteristics are given for the fundamental and for the third and fifth harmonics, for several values of $K$. The symbols used are explained below. The magnetic performance of the insertion devices was calculated by assuming a hybrid structure based on neodymium-iron.

| | |
|---|---|
| BO(T) | Peak magnetic field for undulators and wigglers. |
| BRI | Spectral brightness, i.e., flux per unit phase-space area [photons/(s-mm$^2$-mrad$^2$-0.1% bandwidth)]. |
| E(GeV) | Beam energy. |
| E1(keV) | Photon energy at fundamental frequency. |
| ECR(keV) | Critical energy for wigglers and bending magnets. |
| EP(keV) | Photon energy. |
| F | Spectral flux. For undulators the flux in the central cone; for wigglers and bending magnets, the flux within a 5-mrad horizontal angle and all vertical angles [photons/(s-0.1% bandwidth)]. |
| FDEN1 | Spectral flux per unit horizontal angle [photons/(s-mrad-0.1% bandwidth)]. |
| FDEN2 | Spectral flux per unit solid angle [photons/(s-mrad$^2$-0.1% bandwidth)]. |
| GAP(cm) | Magnet gap (pole to pole) of undulators and wigglers. |
| I(A) | Beam current. |
| K | Peak deflection parameter for undulators. |
| LAMDW(cm) | Period length of undulators and wigglers. |
| N | Number of magnet periods (undulators and wigglers). |
| n | Harmonic number for undulator radiation. |
| NPOLE | Number of wiggler poles. |
| PCEN(W) | Power transmitted through the central angular cone at the fundamental frequency. |
| PCOH(W) | Diffraction-limited power with a 1-$\mu$m coherence length. |
| PDEN1 | Power emitted (all frequencies) per unit horizontal angle [W/mrad]. |
| PDEN2 | Power emitted (all frequencies) per unit solid angle [W/mrad$^2$]. |
| PTOT(kW) | Total power (all angles and all frequencies) emitted by undulators and wigglers. |
| SIGPX(mrad) | Horizontal rms beam divergence in the straight section. |
| SIGPY(mrad) | Vertical rms beam divergence in the straight section. |
| SIGX(mm) | Horizontal rms beam size in the straight section. |
| SIGY(mm) | Vertical rms beam size in the straight section. |
| XLEN(m) | Length of undulators and wigglers. |

**Table 5-2a.** Undulator U20.0.

| E(GeV) | I(Amp) | SIGX(mm) | SIGY(mm) | SIGPX(mr) | SIGPY(mr) | N | LAMBDW(cm) | XLEN(m) |
|---|---|---|---|---|---|---|---|---|
| 1.50 | 0.400 | 0.210 | 0.040 | 0.019 | 0.010 | 23 | 20.00 | 4.6 |

**********

| K | BO(T) | GAP(cm) | E1(keV) | PTOT(kW) | FDEN2(W/(mr**2)) | PCEN(W) |
|---|---|---|---|---|---|---|
| 20.63 | 1.10 | 4.83 | 5.00E-04 | 3.20E+00 | 5.57E+02 | 1.89E+03 |

| n | EP(keV) | F(#/s,0.1%BW) | FDEN2 | BRI | PCOH(W) |
|---|---|---|---|---|---|
| 1 | 5.00E-04 | 1.28E+15 | 3.74E+14 | 6.42E+14 | 1.96E-01 |
| 3 | 1.50E-03 | 8.39E+14 | 7.36E+14 | 2.80E+15 | 9.51E-02 |
| 5 | 2.50E-03 | 6.93E+14 | 1.01E+15 | 5.26E+15 | 6.43E-02 |

| K | BO(T) | GAP(cm) | E1(keV) | PTOT(kW) | FDEN2(W/(mr**2)) | PCEN(W) |
|---|---|---|---|---|---|---|
| 7.17 | 0.38 | 10.22 | 4.00E-03 | 3.86E-01 | 1.94E+02 | 8.22E+01 |

| n | EP(keV) | F(#/s,0.1%BW) | FDEN2 | BRI | PCOH(W) |
|---|---|---|---|---|---|
| 1 | 4.00E-03 | 1.27E+15 | 2.98E+15 | 2.00E+16 | 9.52E-02 |
| 3 | 1.20E-02 | 8.34E+14 | 5.81E+15 | 6.28E+16 | 3.33E-02 |
| 5 | 2.00E-02 | 6.86E+14 | 7.92E+15 | 1.01E+17 | 1.92E-02 |

| K | BO(T) | GAP(cm) | E1(keV) | PTOT(kW) | FDEN2(W/(mr**2)) | PCEN(W) |
|---|---|---|---|---|---|---|
| 2.03 | 0.11 | 19.18 | 3.49E-02 | 3.09E-02 | 5.39E+01 | 2.69E+00 |

| n | EP(keV) | F(#/s,0.1%BW) | FDEN2 | BRI | PCOH(W) |
|---|---|---|---|---|---|
| 1 | 3.49E-02 | 1.15E+15 | 2.29E+16 | 3.34E+17 | 2.09E-02 |
| 3 | 1.05E-01 | 5.66E+14 | 3.19E+16 | 5.47E+17 | 3.80E-03 |
| 5 | 1.75E-01 | 3.36E+14 | 3.00E+16 | 5.33E+17 | 1.34E-03 |

| K | BO(T) | GAP(cm) | E1(keV) | PTOT(kW) | FDEN2(W/(mr**2)) | PCEN(W) |
|---|---|---|---|---|---|---|
| 1.00 | 0.05 | 30.37 | 7.12E-02 | 7.51E-03 | 2.56E+01 | 6.45E-01 |

| n | EP(keV) | F(#/s,0.1%BW) | FDEN2 | BRI | PCOH(W) |
|---|---|---|---|---|---|
| 1 | 7.12E-02 | 7.27E+14 | 2.86E+16 | 4.70E+17 | 7.07E-03 |
| 3 | 2.14E-01 | 1.18E+14 | 1.25E+16 | 2.26E+17 | 3.77E-04 |
| 5 | 3.56E-01 | 2.17E+13 | 3.51E+15 | 6.44E+16 | 3.87E-05 |

| K | BO(T) | GAP(cm) | E1(keV) | PTOT(kW) | FDEN2(W/(mr**2)) | PCEN(W) |
|---|---|---|---|---|---|---|
| 0.50 | 0.03 | 38.7 | 9.50E-02 | 1.88E-03 | 1.09E+01 | 2.10E-01 |

| n | EP(keV) | F(#/s,0.1%BW) | FDEN2 | BRI | PCOH(W) |
|---|---|---|---|---|---|
| 1 | 9.50E-02 | 2.76E+14 | 1.42E+16 | 2.41E+17 | 2.04E-03 |
| 3 | 2.85E-01 | 5.56E+12 | 7.51E+14 | 1.37E+16 | 1.29E-05 |
| 5 | 4.75E-01 | 1.22E+11 | 2.45E+13 | 4.54E+14 | 1.54E-07 |

**Table 5-2b.** Undulator U9.0.

| E(GeV) | I(Amp) | SIGX(mm) | SIGY(mm) | SIGPX(mr) | SIGPY(mr) | N | LAMBDW(cm) | XLEN(m) |
|---|---|---|---|---|---|---|---|---|
| 1.50 | 0.400 | 0.210 | 0.040 | 0.019 | 0.010 | 53 | 9.00 | 4.8 |

**********

| K | B0(T) | GAP(cm) | E1(keV) | PTOT(kW) | PDEN2(W/(mr**2)) | PCEN(W) |
|---|---|---|---|---|---|---|
| 9.64 | 1.15 | 2.09 | 5.00E-03 | 3.57E+00 | 1.33E+03 | 4.37E+02 |

| n | EP(keV) | F(#/s,0.1%BW) | FDEN2 | BRI | PCOH(W) |
|---|---|---|---|---|---|
| 1 | 5.00E-03 | 2.94E+15 | 8.90E+15 | 6.54E+16 | 2.00E-01 |
| 3 | 1.50E-02 | 1.93E+15 | 1.74E+16 | 2.00E+17 | 6.78E-02 |
| 5 | 2.50E-02 | 1.59E+15 | 2.37E+16 | 3.17E+17 | 3.87E-02 |

| K | B0(T) | GAP(cm) | E1(keV) | PTOT(kW) | PDEN2(W/(mr**2)) | PCEN(W) |
|---|---|---|---|---|---|---|
| 6.13 | 0.73 | 3.06 | 1.20E-02 | 1.45E+00 | 8.47E+02 | 1.16E+02 |

| n | EP(keV) | F(#/s,0.1%BW) | FDEN2 | BRI | PCOH(W) |
|---|---|---|---|---|---|
| 1 | 1.20E-02 | 2.93E+15 | 2.12E+16 | 2.26E+17 | 1.20E-01 |
| 3 | 3.60E-02 | 1.91E+15 | 4.06E+16 | 5.92E+17 | 3.49E-02 |
| 5 | 6.00E-02 | 1.57E+15 | 5.43E+16 | 8.67E+17 | 1.84E-02 |

| K | B0(T) | GAP(cm) | E1(keV) | PTOT(kW) | PDEN2(W/(mr**2)) | PCEN(W) |
|---|---|---|---|---|---|---|
| 4.00 | 0.48 | 4.06 | 2.64E-02 | 6.15E-01 | 5.51E+02 | 3.49E+01 |

| n | EP(keV) | F(#/s,0.1%BW) | FDEN2 | BRI | PCOH(W) |
|---|---|---|---|---|---|
| 1 | 2.64E-02 | 2.91E+15 | 4.56E+16 | 6.19E+17 | 6.79E-02 |
| 3 | 7.91E-02 | 1.85E+15 | 8.31E+16 | 1.38E+18 | 1.68E-02 |
| 5 | 1.32E-01 | 1.47E+15 | 1.05E+17 | 1.83E+18 | 8.05E-03 |

| K | B0(T) | GAP(cm) | E1(keV) | PTOT(kW) | PDEN2(W/(mr**2)) | PCEN(W) |
|---|---|---|---|---|---|---|
| 2.00 | 0.24 | 5.91 | 7.91E-02 | 1.54E-01 | 2.72E+02 | 6.00E+00 |

| n | EP(keV) | F(#/s,0.1%BW) | FDEN2 | BRI | PCOH(W) |
|---|---|---|---|---|---|
| 1 | 7.91E-02 | 2.64E+15 | 1.19E+17 | 1.97E+18 | 2.40E-02 |
| 3 | 2.37E-01 | 1.28E+15 | 1.54E+17 | 2.77E+18 | 3.75E-03 |
| 5 | 3.96E-01 | 7.51E+14 | 1.35E+17 | 2.48E+18 | 1.21E-03 |

| K | B0(T) | GAP(cm) | E1(keV) | PTOT(kW) | PDEN2(W/(mr**2)) | PCEN(W) |
|---|---|---|---|---|---|---|
| 1.00 | 0.12 | 8.26 | 1.58E-01 | 3.85E-02 | 1.31E+02 | 1.54E+00 |

| n | EP(keV) | F(#/s,0.1%BW) | FDEN2 | BRI | PCOH(W) |
|---|---|---|---|---|---|
| 1 | 1.58E-01 | 1.67E+15 | 1.42E+17 | 2.50E+18 | 7.61E-03 |
| 3 | 4.75E-01 | 2.72E+14 | 5.59E+16 | 1.03E+18 | 3.50E-04 |
| 5 | 7.91E-01 | 5.00E+13 | 1.45E+16 | 2.71E+17 | 3.30E-05 |

| K | B0(T) | GAP(cm) | E1(keV) | PTOT(kW) | PDEN2(W/(mr**2)) | PCEN(W) |
|---|---|---|---|---|---|---|
| 0.50 | 0.06 | 12.21 | 2.11E-01 | 9.61E-03 | 5.57E+01 | 5.10E-01 |

| n | EP(keV) | F(#/s,0.1%BW) | FDEN2 | BRI | PCOH(W) |
|---|---|---|---|---|---|
| 1 | 2.11E-01 | 6.36E+14 | 6.90E+16 | 1.24E+18 | 2.12E-03 |
| 3 | 6.33E-01 | 1.28E+13 | 3.22E+15 | 5.98E+16 | 1.14E-05 |
| 5 | 1.06E+00 | 2.82E+11 | 9.67E+13 | 1.81E+15 | 1.24E-07 |

**Table 5-2c.** Undulator U5.0.

| E(GeV) | I(Amp) | SIGX(mm) | SIGY(mm) | SIGPX(mr) | SIGPY(mr) | N | LAMBDW(cm) | XLEN(m) |
|---|---|---|---|---|---|---|---|---|
| 1.50 | 0.400 | 0.210 | 0.040 | 0.019 | 0.010 | 98 | 5.00 | 4.9 |

**********

| K | BO(T) | GAP(cm) | E1(keV) | PTOT(kW) | PDEN2(W/(mr**2)) | PCEN(W) |
|---|---|---|---|---|---|---|
| 3.88 | 0.83 | 1.54 | 5.01E-02 | 1.93E+00 | 1.78E+03 | 5.90E+01 |

| n | EP(keV) | F(#/s,0.1%BW) | FDEN2 | BRI | PCOH(W) |
|---|---|---|---|---|---|
| 1 | 5.01E-02 | 5.37E+15 | 1.61E+17 | 2.48E+18 | 7.55E-02 |
| 3 | 1.50E-01 | 3.40E+15 | 2.81E+17 | 4.94E+18 | 1.67E-02 |
| 5 | 2.51E-01 | 2.69E+15 | 3.44E+17 | 6.21E+18 | 7.55E-03 |

| K | BO(T) | GAP(cm) | E1(keV) | PTOT(kW) | PDEN2(W/(mr**2)) | PCEN(W) |
|---|---|---|---|---|---|---|
| 3.00 | 0.64 | 1.86 | 7.77E-02 | 1.15E+00 | 1.37E+03 | 3.00E+01 |

| n | EP(keV) | F(#/s,0.1%BW) | FDEN2 | BRI | PCOH(W) |
|---|---|---|---|---|---|
| 1 | 7.77E-02 | 5.28E+15 | 2.39E+17 | 3.94E+18 | 4.98E-02 |
| 3 | 2.33E-01 | 3.17E+15 | 3.82E+17 | 6.89E+18 | 9.67E-03 |
| 5 | 3.88E-01 | 2.36E+15 | 4.26E+17 | 7.83E+18 | 3.96E-03 |

| K | BO(T) | GAP(cm) | E1(keV) | PTOT(kW) | PDEN2(W/(mr**2)) | PCEN(W) |
|---|---|---|---|---|---|---|
| 2.00 | 0.43 | 2.40 | 1.42E-01 | 5.12E-01 | 9.04E+02 | 1.14E+01 |

| n | EP(keV) | F(#/s,0.1%BW) | FDEN2 | BRI | PCOH(W) |
|---|---|---|---|---|---|
| 1 | 1.42E-01 | 4.88E+15 | 3.85E+17 | 6.73E+18 | 2.53E-02 |
| 3 | 4.27E-01 | 2.37E+15 | 4.61E+17 | 8.49E+18 | 3.55E-03 |
| 5 | 7.12E-01 | 1.39E+15 | 3.83E+17 | 7.14E+18 | 1.07E-03 |

| K | BO(T) | GAP(cm) | E1(keV) | PTOT(kW) | PDEN2(W/(mr**2)) | PCEN(W) |
|---|---|---|---|---|---|---|
| 1.00 | 0.21 | 3.46 | 2.85E-01 | 1.28E-01 | 4.36E+02 | 3.05E+00 |

| n | EP(keV) | F(#/s,0.1%BW) | FDEN2 | BRI | PCOH(W) |
|---|---|---|---|---|---|
| 1 | 2.85E-01 | 3.10E+15 | 4.40E+17 | 7.99E+18 | 7.51E-03 |
| 3 | 8.55E-01 | 5.03E+14 | 1.55E+17 | 2.90E+18 | 3.03E-04 |
| 5 | 1.42E+00 | 9.25E+13 | 3.77E+16 | 7.08E+17 | 2.66E-05 |

| K | BO(T) | GAP(cm) | E1(keV) | PTOT(kW) | PDEN2(W/(mr**2)) | PCEN(W) |
|---|---|---|---|---|---|---|
| 0.50 | 0.11 | 4.83 | 3.80E-01 | 3.20E-02 | 1.85E+02 | 1.04E+00 |

| n | EP(keV) | F(#/s,0.1%BW) | FDEN2 | BRI | PCOH(W) |
|---|---|---|---|---|---|
| 1 | 3.80E-01 | 1.18E+15 | 2.09E+17 | 3.84E+18 | 2.03E-03 |
| 3 | 1.14E+00 | 2.37E+13 | 8.61E+15 | 1.61E+17 | 9.48E-06 |
| 5 | 1.90E+00 | 5.21E+11 | 2.41E+14 | 4.54E+15 | 9.61E-08 |

**Table 5-2d.** Undulator U3.65.

| E(GeV) | I(Amp) | SIGX(mm) | SIGY(mm) | SIGPX(mr) | SIGPY(mr) | N | LAMBDW(cm) | XLEN(m) |
|---|---|---|---|---|---|---|---|---|
| 1.50 | 0.400 | 0.210 | 0.040 | 0.019 | 0.010 | 134 | 3.65 | 4.9 |

**********

| K | B0(T) | GAP(cm) | E1(keV) | PTOT(kW) | PDEN2(W/(mr**2)) | PCEN(W) |
|---|---|---|---|---|---|---|
| 2.10 | 0.61 | 1.40 | 1.83E-01 | 1.05E+00 | 1.78E+03 | 1.80E+01 |

| n | EP(keV) | F(#/s,0.1%BW) | FDEN2 | BRI | PCOH(W) |
|---|---|---|---|---|---|
| 1 | 1.83E-01 | 6.77E+15 | 6.65E+17 | 1.18E+19 | 2.69E-02 |
| 3 | 5.49E-01 | 3.41E+15 | 7.94E+17 | 1.47E+19 | 3.72E-03 |
| 5 | 9.16E-01 | 2.08E+15 | 6.70E+17 | 1.25E+19 | 1.14E-03 |

| K | B0(T) | GAP(cm) | E1(keV) | PTOT(kW) | PDEN2(W/(mr**2)) | PCEN(W) |
|---|---|---|---|---|---|---|
| 1.00 | 0.29 | 2.15 | 3.90E-01 | 2.40E-01 | 8.17E+02 | 4.47E+00 |

| n | EP(keV) | F(#/s,0.1%BW) | FDEN2 | BRI | PCOH(W) |
|---|---|---|---|---|---|
| 1 | 3.90E-01 | 4.23E+15 | 7.69E+17 | 1.41E+19 | 7.08E-03 |
| 3 | 1.17E+00 | 6.87E+14 | 2.54E+17 | 4.76E+18 | 2.65E-04 |
| 5 | 1.95E+00 | 1.27E+14 | 5.95E+16 | 1.12E+18 | 2.25E-05 |

| K | B0(T) | GAP(cm) | E1(keV) | PTOT(kW) | PDEN2(W/(mr**2)) | PCEN(W) |
|---|---|---|---|---|---|---|
| 0.59 | 0.17 | 2.81 | 5.00E-01 | 8.21E-02 | 4.32E+02 | 1.97E+00 |

| n | EP(keV) | F(#/s,0.1%BW) | FDEN2 | BRI | PCOH(W) |
|---|---|---|---|---|---|
| 1 | 5.00E-01 | 2.08E+15 | 4.52E+17 | 8.36E+18 | 2.55E-03 |
| 3 | 1.50E+00 | 7.14E+13 | 2.99E+16 | 5.61E+17 | 1.91E-05 |
| 5 | 2.50E+00 | 2.70E+12 | 1.40E+15 | 2.63E+16 | 3.22E-07 |

| K | B0(T) | GAP(cm) | E1(keV) | PTOT(kW) | PDEN2(W/(mr**2)) | PCEN(W) |
|---|---|---|---|---|---|---|
| 0.36 | 0.11 | 3.55 | 5.50E-01 | 3.11E-02 | 2.09E+02 | 8.92E-01 |

| n | EP(keV) | F(#/s,0.1%BW) | FDEN2 | BRI | PCOH(W) |
|---|---|---|---|---|---|
| 1 | 5.50E-01 | 9.04E+14 | 2.11E+17 | 3.90E+18 | 9.85E-04 |
| 3 | 1.65E+00 | 5.55E+12 | 2.43E+15 | 4.57E+16 | 1.28E-06 |
| 5 | 2.75E+00 | 3.69E+10 | 1.98E+13 | 3.73E+14 | 3.76E-09 |

**Table 5-2e.** Wiggler W13.6.

| E(GeV) | I(Amp) | SIGX(mm) | SIGY(mm) | SIGPX(mr) | SIGPY(mr) |
|---|---|---|---|---|---|
| 1.50 | 0.400 | 0.210 | 0.040 | 0.019 | 0.010 |

| NPOLE | LAMBDW(cm) | XLEN(m) | BO(T) | ECR(keV) | PTOT(kW) | PDEN2(W/(mr**2)) |
|---|---|---|---|---|---|---|
| 32 | 13.60 | 2.18 | 2.07 | 3.10 | 5.31E+00 | 7.27E+02 |

| EP(keV) | F | FDEN1 | FDEN2 | BRI | PCOH(W) |
|---|---|---|---|---|---|
| 5.000E-03 | 5.878E+14 | 1.176E+14 | 1.529E+13 | 1.754E+14 | 5.353E-04 |
| 1.000E-02 | 7.355E+14 | 1.471E+14 | 2.426E+13 | 2.783E+14 | 2.124E-04 |
| 5.000E-02 | 1.212E+15 | 2.425E+14 | 7.070E+13 | 8.112E+14 | 2.476E-05 |
| 1.000E-01 | 1.477E+15 | 2.953E+14 | 1.116E+14 | 1.281E+15 | 9.771E-06 |
| 5.000E-01 | 2.083E+15 | 4.166E+14 | 3.060E+14 | 3.510E+15 | 1.071E-06 |
| 1.000E+00 | 2.161E+15 | 4.321E+14 | 4.384E+14 | 5.029E+15 | 3.837E-07 |
| 5.000E+00 | 9.720E+14 | 1.944E+14 | 4.541E+14 | 5.202E+15 | 1.588E-08 |
| 1.000E+01 | 2.482E+14 | 4.963E+13 | 1.688E+14 | 1.930E+15 | 1.473E-09 |
| 2.000E+01 | 1.298E+13 | 2.597E+12 | 1.282E+13 | 1.460E+14 | 2.785E-11 |
| 5.000E+01 | 1.218E+09 | 2.437E+08 | 1.935E+09 | 2.179E+10 | 6.650E-16 |
| 1.000E+02 | 1.890E+02 | 3.780E+01 | 3.828E+02 | 4.260E+03 | 3.251E-23 |
| 3.098E+00 | 1.537E+15 | 3.073E+14 | 5.551E+14 | 6.363E+15 | 5.060E-08 |

**Table 5-2f.** Bending magnets.

| E(GeV) | I(Amp) | ETAX(m) | SIGE |
|---|---|---|---|
| 1.50 | 0.400 | 0.086 | 1.00E-03 |

| EMTX(mm*mr) | EMTY(mm*mr) | BETAX(m) | ALPHAX | BETAY(m) | ALPHAY |
|---|---|---|---|---|---|
| 4.00E-03 | 4.00E-04 | 7.66E-01 | 0.00E+00 | 1.59E+00 | 0.00E+00 |

| RHO(m) | BO(T) | ECR(keV) | PDEN1(W/mr) | PDEN2(W/(mr**2)) |
|---|---|---|---|---|
| 4.01 | 1.25 | 1.87 | 7.09E+00 | 1.37E+01 |

| EP(keV) | F | FDEN1 | FDEN2 | BRI | PCOH(W) |
|---|---|---|---|---|---|
| 5.000E-04 | 1.017E+13 | 2.033E+12 | 1.387E+11 | 4.875E+12 | 1.488E-03 |
| 1.000E-03 | 1.279E+13 | 2.558E+12 | 2.285E+11 | 1.039E+13 | 7.926E-04 |
| 5.000E-03 | 2.163E+13 | 4.326E+12 | 6.685E+11 | 3.948E+13 | 1.205E-04 |
| 1.000E-02 | 2.699E+13 | 5.398E+12 | 1.061E+12 | 6.438E+13 | 4.912E-05 |
| 5.000E-02 | 4.381E+13 | 8.761E+12 | 3.082E+12 | 1.902E+14 | 5.805E-06 |
| 1.000E-01 | 5.257E+13 | 1.051E+13 | 4.840E+12 | 2.992E+14 | 2.283E-06 |
| 5.000E-01 | 6.762E+13 | 1.352E+13 | 1.253E+13 | 7.750E+14 | 2.365E-07 |
| 1.000E+00 | 6.324E+13 | 1.265E+13 | 1.648E+13 | 1.019E+15 | 7.773E-08 |
| 5.000E+00 | 1.259E+13 | 2.518E+12 | 7.733E+12 | 4.750E+14 | 1.450E-09 |
| 1.000E+01 | 1.139E+12 | 2.278E+11 | 1.017E+12 | 6.195E+13 | 4.727E-11 |
| 2.000E+01 | 7.302E+09 | 1.460E+09 | 9.418E+09 | 5.645E+11 | 1.077E-13 |
| 5.000E+01 | 1.310E+03 | 2.621E+02 | 2.519E+03 | 1.456E+05 | 4.443E-21 |
| 1.000E+02 | 5.994E-09 | 1.199E-09 | 1.479E-08 | 8.218E-07 | 6.270E-33 |
| 1.871E+00 | 4.802E+13 | 9.603E+12 | 1.735E+13 | 1.071E+15 | 2.335E-08 |

The selected insertion devices cover the VUV and the soft x-ray regions in an orderly and overlapping fashion and provide some coverage down to 0.5 eV in the near-infrared region (by means of undulator U20.0) and up to about 10 keV in the hard x-ray region (by means of the wiggler W13.6). The individual devices are not, in general, directed toward any particular scientific application but rather cover a variety of applications. We discuss this point further in Section 5.2.

For undulators we take the view that the first and third harmonics provide useful output (harmonics of higher order are also present, but they are less useful and also more sensitive to construction errors). This point is important, because it is generally possible to design beam line optical systems to handle wider energy ranges than can be covered with the fundamental radiation of an undulator. As a rough guide, the useful operating range of an undulator is considered to lie between the energy of the fundamental at the largest achievable $K$ value and the energy of the third harmonic at $K = 0.5$. It is on this basis that the working ranges of the specified devices are said to overlap.

For a given total length of undulator and for a given desired photon energy, it is usually better to choose a higher value of $K$. This is because the spectral flux in the central cone [see Eq. (9) in Appendix E] is proportional to $Q_n(K)$, which increases with $K$. In addition, the larger $K$ also implies a shorter period length [see Eq. (5) in Appendix E], hence a further increase in flux by virtue of the larger number of periods, $N$. However, the validity of this rule is limited by power considerations: As the value of $K$ becomes large, the undulator effectively becomes a wiggler for large harmonic numbers $n$, and the total power generated, most of which is in unwanted spectral regions, may become unacceptably large. For each insertion device listed in Table 5-1, the total power is limited to a few kilowatts.

Higher photon energies are generally obtained by using a shorter period length; however, there is a lower limit to the practical period length of an undulator, because the magnetic field decreases rapidly as the ratio of the period length to the magnet gap becomes small. As discussed below, the minimum magnet gap during commissioning will be 2.5 cm, decreasing to 1.4 cm later, following the retrofitting of smaller-aperture vacuum chambers.

### 5.1.2 Mechanical Description

A typical 5-meter permanent-magnet insertion device, as proposed here, is shown in Fig. 5-3. Each such device consists of a magnetic structure, a support/drive system, and a vacuum system.

The magnetic structures are of the hybrid configuration, with construction similar to the wigglers for the SSRL Beamlines VI and X. For the Light Source, we use a relatively new permanent-magnet material, neodymium-iron (Nd-Fe), as the current-sheet-equivalent material in the structures. This material has a stronger remanent field, is more durable, and is less expensive than samarium-cobalt. A cross section of a typical magnetic configuration is shown in Fig. 5-4, along with a corresponding quarter-period magnetic flux plot. Shown in the figure is a configuration made up of keeper assemblies, each consisting of a keeper, a pole, and oriented permanent-magnet material, bolted to a backing beam. Also shown in the cross section are tuning studs, variable magnetic shunts that allow fine tuning of the magnetic fields. Based on our fabrication experience, most of the insertion devices will not require the use of these tuning studs, but they will be provided in all devices. A typical magnetic performance curve is given in Fig. 5-5, which shows field versus gap for

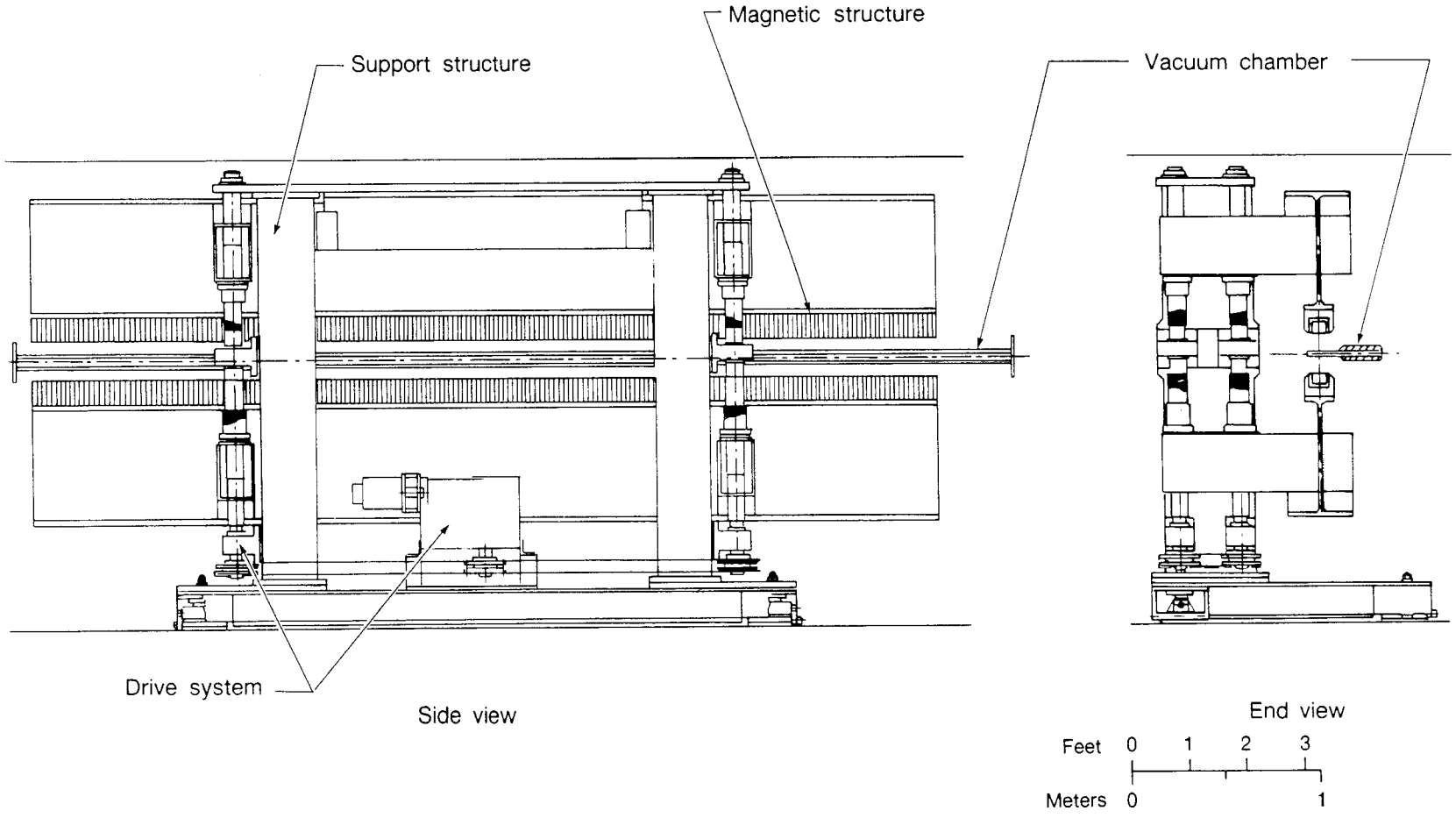


**Fig. 5-3** Side view and end view of a typical Light Source insertion device.

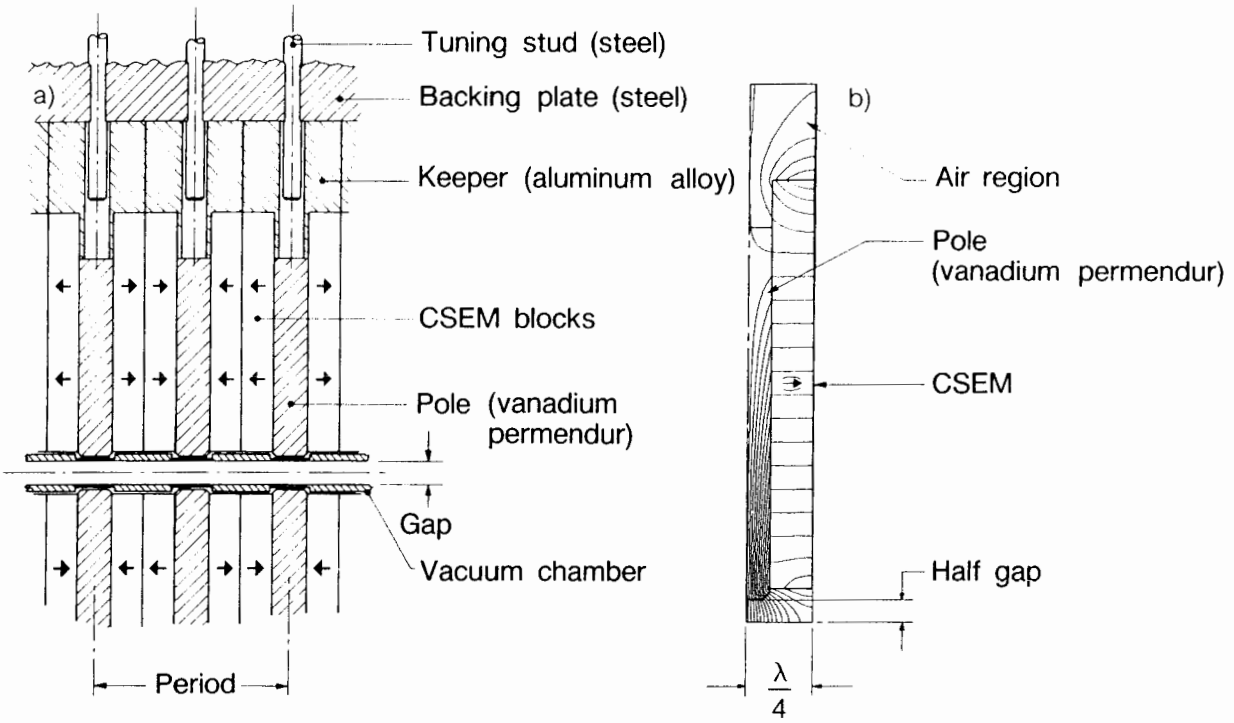


**Fig. 5-4** (a) A cross section and (b) a quarter-period magnetic flux plot for a hybrid insertion device. The current-sheet-equivalent material (CSEM) is neodymium-iron.

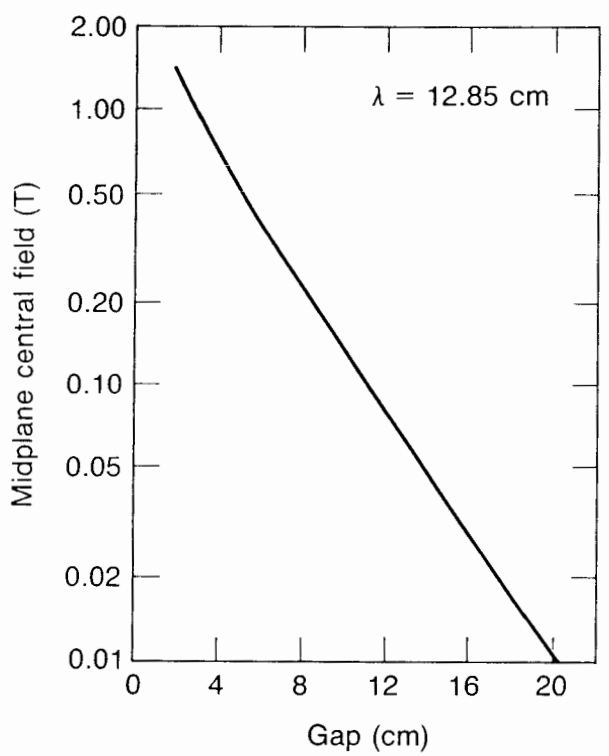


**Fig. 5-5** Magnetic field as a function of gap for the SSRL Beamline X wiggler.

the Beamline X wiggler currently under fabrication at LBL. This 15-period device, shown in Fig. 5-6, also utilizes Nd-Fe and features a rigid vacuum chamber with thin wall pockets into which the wiggler poles fit.

Field end correctors can be either permanent-magnet rotators or small electromagnets. The backing beams, to which the keeper assemblies are attached, are sized so that the maximum gap deflection will be less than 50 $\mu$m under peak field operation.

The support structure and drive system are similar for all insertion devices, with C-type configurations that eliminate interference with the beam lines. The structures extend only 36 inches inward from the electron beam center line, which allows us to maintain a 3-foot aisle within the accelerator tunnel. The maximum structure height is 94 inches, allowing the devices to fit within the 8-foot-high tunnel. Each device has a single drive system for opening and closing the magnetic gap for magnetic field adjustment. The drive mechanism is a ball-screw/chain system similar to those used on the SSRL Beamline VI and X wigglers. This system consists of four right-handed ball-screw/nut assemblies on the upper half and four left-handed ball-screw/nut assemblies on the lower half of the insertion device, coupled together with four drive shafts. These assemblies are driven by a stepper

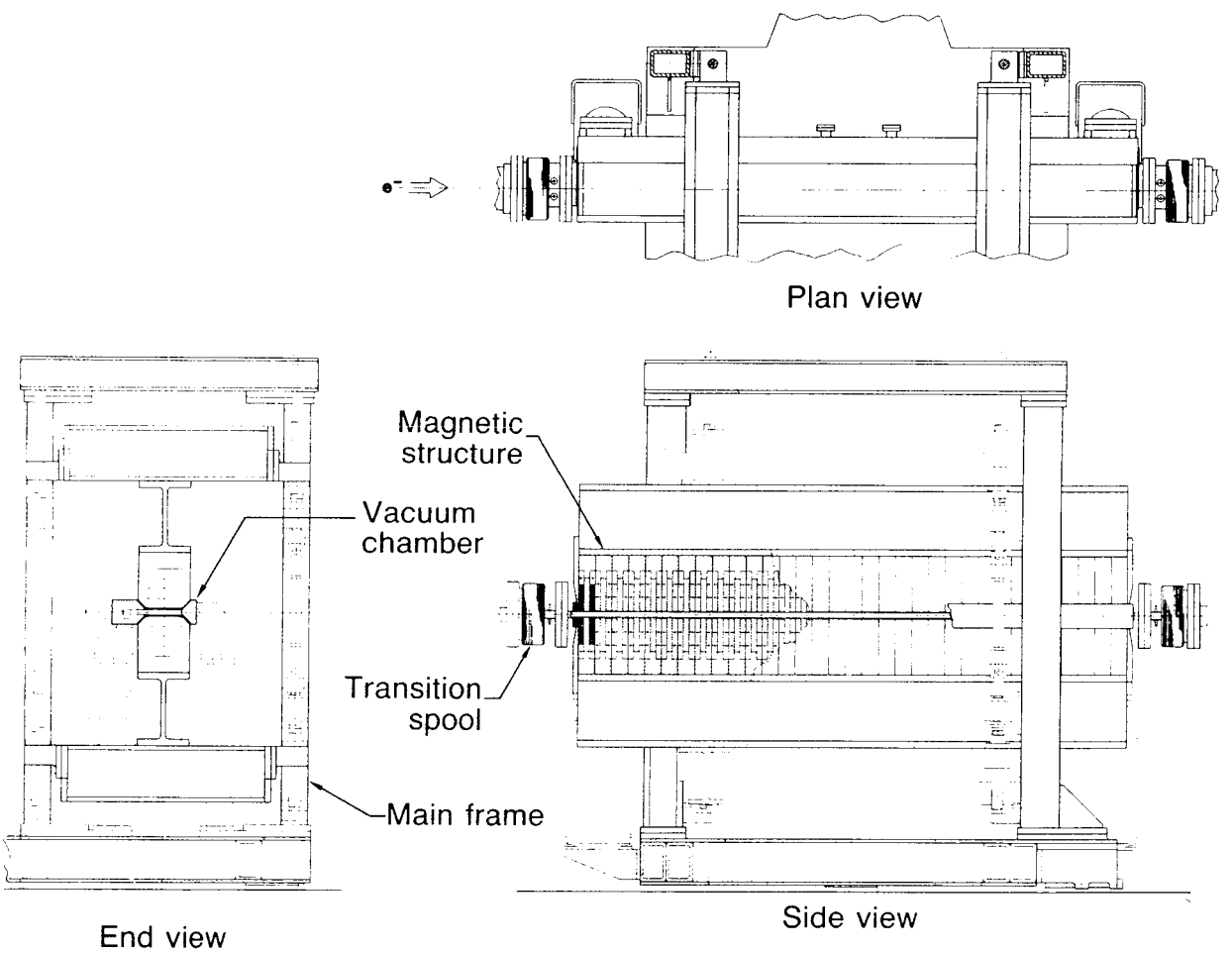


**Fig. 5-6.** Three drawings showing the design of the SSRL Beamline X wiggler currently under construction at LBL.

motor and a reduction unit through a roller chain and sprocket arrangement. Magnet gap position is encoded via a linear encoder. Limit switches and mechanical stops provide system protection.

The vacuum chambers are of the rigid type, similar to that currently being fabricated for the SSRL Beamline X wiggler. For ease of commissioning, the vacuum chambers in the insertion regions will initially have a beam-stay-clear gap of 2 cm. Adding 0.5 cm for fabrication allowances and chamber thicknesses, the minimum magnet gap will be 2.5 cm during commissioning. Figure 5-7 shows a typical transverse cross section of the chamber, together with wiggler W13.6. After commissioning, the insertion devices will be retrofitted with chambers having 1.0-cm minimum vertical apertures, which will allow for operation with magnetic gaps as small as 1.4 cm. The performance characteristics of the insertion devices during the commissioning phase are shown in Figs. 5-1 and 5-2. For undulators, coverage is reduced at low photon energies; for wigglers, the critical energy of the spectrum moves to lower energies.

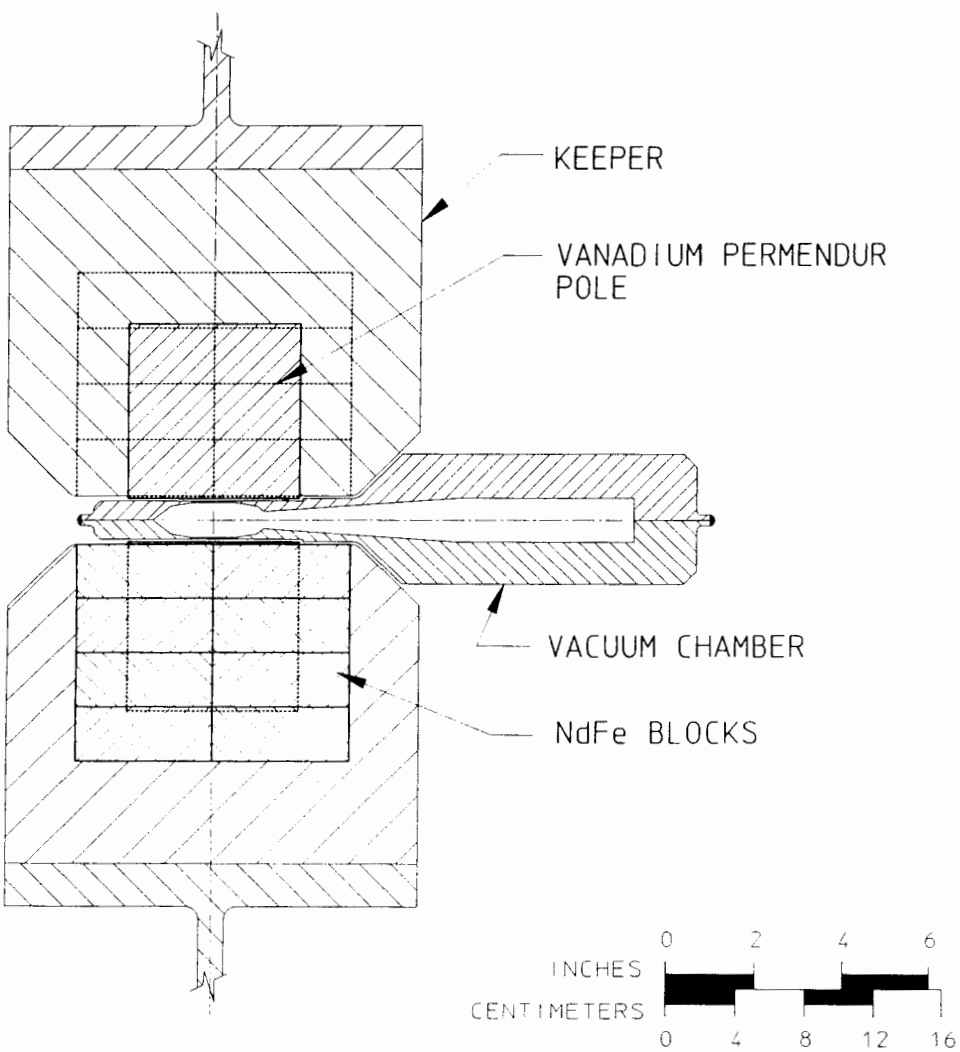


**Fig. 5-7** Cross section of wiggler W13.6 with a 2-cm-vertical-aperture vacuum chamber, designed to fit a 2.5-cm magnet gap.

The effect of initially using the larger stay-clear gap on the energy ranges of the photon beams will be modest; most of the photon energy spectrum will remain covered.

### 5.1.3 Special Undulators for Polarization Control

With the high-brightness electron beam of the Light Source, it is possible to control the polarization of the undulator radiation with the special devices discussed in Appendix F. These devices can be accommodated in the future.

## 5.2 Insertion Device Beam Lines

### 5.2.1 Introduction

**5.2.1.1 Definitions.** Photons from the insertion devices described in Section 5.1 and from the bending magnets emerge from the storage ring vacuum vessel at a 25-cm-diameter flange. We call this a port. After reaching the experimental area the photon beam may be subdivided into branches, each of which services a separate optical system and experimental station. The instrumentation on each port which is common to all the branches is called the front end. The front end, together with the components of a single branch, constitute a beam line. We propose initially to build five insertion device beam lines out as far as the monochromator exit slits. This set comprises four undulator beam lines and one wiggler beam line, although the wiggler port will eventually support more than one beam line.

**5.2.1.2 User Participation.** The user community will be integrated into the operation and use of the new facilities as closely and flexibly as possible. In particular, some users will have resources that they want to contribute to the beam line program to enhance their own research effort. This will be encouraged, but we recognize that many talented members of the user community do not have such resources. To allow participation by these individuals and institutions, LBL proposes to assign a portion of the overall project budget to the creation of insertion devices and beam lines on behalf of the community. This policy has the added benefit of creating a cadre of in-house scientists with expertise in user-related matters. These individuals can provide technical assistance and meaningful liaison with users and can themselves contribute to the overall research effort.

**5.2.1.3 Undulator Beam Lines.** The special properties of undulators are central to the capabilities of the Light Source (see, for example, Attwood et al. [1985], as well as Section 5.1 and Appendix E of this report). Because of the strongly peaked nature of the undulator spectral output, it is necessary for the peak of the undulator spectrum to be tuned by the experimenter to follow the monochromator setting. This requirement means that it is impractical to share an undulator beam between two or more monochromators. For this reason, we assign only one beam line to each of the initial complement of four undulator ports.

For a given harmonic of an undulator, at some particular wavelength that the monochromator has been set to accept, we can make an important statement about the angular distribution of the photon output. All of the photons that are in the monochromator bandpass (presumed narrower than the peak of the undulator spectrum) lie within a narrow

circular cone centered on the undulator axis. The half-angle of the cone is determined by two effects: diffraction and the electron-beam angular spread. At long photon wavelengths, diffraction dominates. At short wavelengths, the electron-beam angular spread dominates. Around 10 angstroms, both effects contribute. In light of these statements, it is obviously advantageous to reject all of the photons that lie outside of the central cone. This is conveniently done using a suitably cooled aperture system that we call the "pinhole," which protects the optical system by absorbing most of the beam power on its front surfaces. These surfaces, unlike those of optical components, are not subject to surface shape tolerances.

### 5.2.2 History

Synchrotron radiation was first used as a light source for scientific research in the 1950s, and its use has increased continuously since then. Initially, researchers made parasitic use of synchrotrons that operated for other programs. Conventional spectrometers designed for discharge and spark sources were used and were generally coupled to light sources by glass optical systems. The photon beam power involved was usually small. In the decades that followed these early experiments, synchrotrons have been superseded by storage rings designed for optimum light output. In recent times, the use of wigglers and undulators has further advanced light source technology. During these years, there have also been corresponding developments in optical systems, and many specialized monochromators have been built.

For the optical designer, all these advances have created new challenges, especially in two areas:

- The source size has become smaller so that relay optics require tighter tolerances to avoid loss of light. The use of smaller slits also becomes practical so that monochromator components also need tighter tolerances to avoid loss of resolution. These tolerances apply to both optical figure and finish.
- The photon beam power has increased to the point that, in addition to satisfying more stringent surface tolerances, optical components must be cooled to control thermal distortions and stresses. This complicates the design and limits the choice of materials.

LBL has played a leading role in the design and use of high-power wigglers, and this has led to its involvement with Exxon and SSRL in the construction of a 54-pole wiggler at the SPEAR storage ring at Stanford, together with the beam line [Bahr et al., 1983] needed to exploit this device. This wiggler is presently the world's most powerful laboratory x-ray source. The chief conclusion following from that exercise was that, when a large heat load is present, it dominates the design and cost of the beam line. The difficulties of dealing with large heat loads have enhanced interest in the properties of undulators, which usually generate lower total power than wigglers. In addition, most of the unwanted power in undulator radiation can be dumped in a nonoptical component (the pinhole described above), which is a great advantage. For the beam lines described here, the power problem is usually quite moderate and, at worst, is similar to that of the 54-pole wiggler beam line. Our strategy for dealing with it is to use pinholes where appropriate, plus active water cooling of the optics.

The most serious problem now faced by the optical designer addressing the design of synchrotron light source beam lines is optical fabrication tolerances. It has been observed that even in present-generation storage rings, such as NSLS and BESSY, the fabrication accuracy of aspheric optical surfaces (paraboloids, ellipsoids, toroids, etc.) is inadequate [Howells and Takacs, 1982] for the full utilization of the source properties. Although manufacturing methods are improving, we take the position that the only sure way to address this problem is to avoid the use of aspheric surfaces altogether and to build beam lines entirely with plane and spherical surfaces. All the important optical technologies—figuring, finishing, and measuring—work best in these cases. Furthermore, one can infer from the demonstrated resolution of certain existing spectrometers [Ito et al., 1986] that fabrication tolerances below one microradian have been achieved for standard spherical gratings.

In what follows, we describe the design of five insertion device beam lines, constructed entirely from flat and spherical optical surfaces.

### 5.2.3 Theory

**5.2.3.1 Diffraction Grating Monochromators.** In Fig. 5-8, we show the notation for the theory of diffraction grating monochromators. To discuss the important question of aberrations, we utilize the analysis of the imaging performance of a grating in terms of the optical

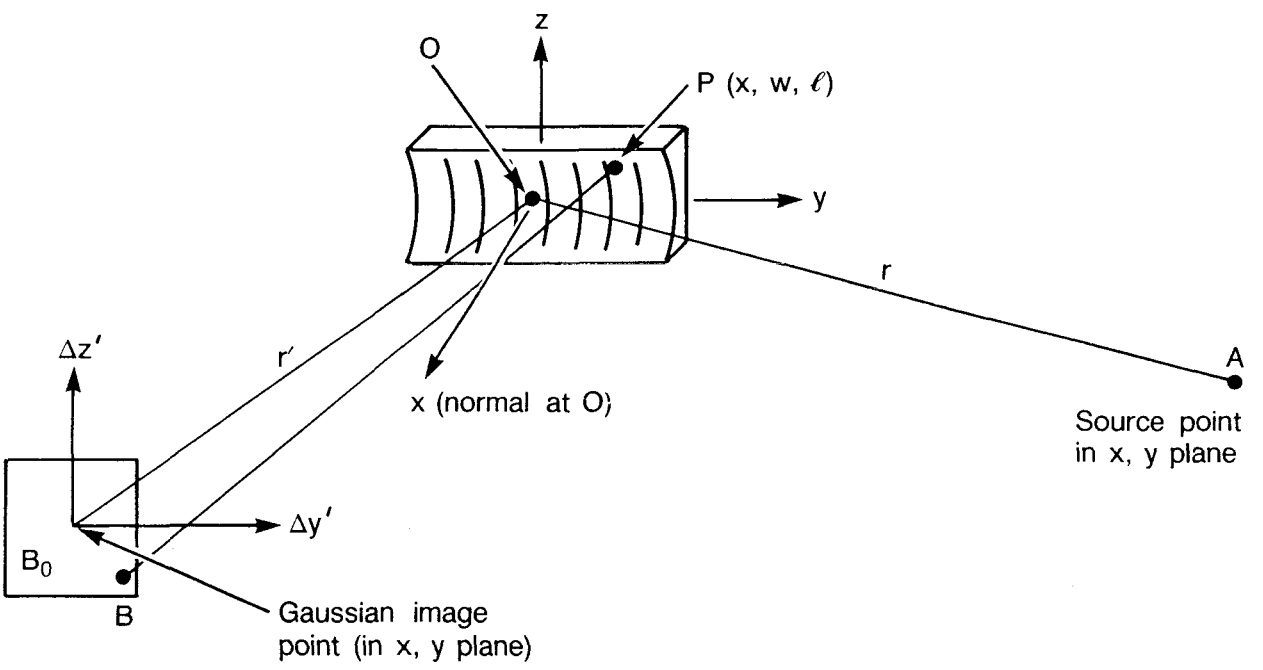


**Fig. 5-8.** Notation for the theoretical treatment of a toroidal (or spherical) Rowland grating illuminated by a point source at $A$. Waves not subject to aberration, such as $AOB_0$ are imaged at the ideal image point $B_0$. Rays farther from the center of the grating aperture suffer aberration and arrive at the receiving plane at points such as $B$, which are displaced from $B_0$.

path function. We consider only the case of a toroidal surface [Haber, 1950; Noda et al., 1974] (of which the spherical is a special case), and we write the optical path function as a power series expansion in the aperture coordinates $w$ and $\ell$ defined in Fig. 5-8:

$$F = F_{000} + wF_{100} + \ell F_{011} + w\ell F_{111} + \frac{1}{2}wF_{102} + \frac{1}{2}w^2F_{200}$$

$$+ \frac{1}{2}\ell^2F_{020} + \frac{1}{2}w\ell^2F_{120} + \frac{1}{2}w^3F_{300} + \frac{1}{8}w^4F_{400} + \cdots + w^i\ell^jF_{ijk} + \cdots \quad (1)$$

where

$$F_{000} = \sum r \qquad \text{Constant term} \qquad (2a)$$

$$F_{100} = \frac{m\lambda}{d} - \sum \sin\alpha \qquad \text{Grating equation} \qquad (2b)$$

$$F_{011} = -\sum \frac{\Delta z}{r} \qquad \text{Magnification} \qquad (2c)$$

$$F_{111} = -\sum \frac{\Delta z \sin\alpha}{r^2} \qquad \text{Line shape} \qquad (2d)$$

$$F_{102} = \sum \frac{\Delta z^2 \sin\alpha}{r^2} \qquad \text{Line shape} \qquad (2e)$$

$$F_{200} = \sum T \qquad \text{Focus} \qquad (2f)$$

$$F_{020} = \sum S \qquad \text{Astigmatism} \qquad (2g)$$

$$F_{120} = \sum \frac{S \sin\alpha}{r} \qquad \text{Astigmatic coma} \qquad (2h)$$

$$F_{300} = \sum \frac{T \sin\alpha}{r} \qquad \text{Primary coma} \qquad (2i)$$

$$F_{400} = \Sigma \left( \frac{4T \sin^2 \alpha}{r^2} - \frac{T^2}{r} + \frac{S}{R^2} \right) \qquad \text{Spherical aberration} \qquad (2j)$$

with

$$T = \frac{\cos^2 \alpha}{r} - \frac{\cos \alpha}{R},$$

$$S = \frac{1}{r} - \frac{\cos \alpha}{\rho}$$

The parameter $\alpha$ is the incidence angle, $\beta$ is the diffraction angle, $m$ is the spectral order, $d$ is the groove spacing, and $R$ and $\rho$ are the major and minor radii of the toroid, respectively. The meaning of the summation sign is that a second term must be added which is identical to the first, apart from the replacements $\alpha \rightarrow \beta$, $r \rightarrow r'$, $\Delta z \rightarrow \Delta z'$.

We see that each term of $F$ represents a type of image imperfection or aberration. It is possible to derive from $F$ the details of the x-ray distribution in the image (exit slit) plane due to a point source in the object (entrance slit) plane. This is the impulse response (or spread function) of the system. The art of optical design is to achieve the smallest possible line spread in the dispersion direction (to get good resolution), while maintaining a high phase-space acceptance for the instrument.

To get a perfect image, all the $F_{ijk}$ would need to be zero, a goal that cannot be achieved for any grating surface. To be in focus, it is necessary that $F_{200} = 0$. One way to achieve this is by setting $r = R \cos \alpha$ and $r' = R \cos \beta$, i.e., the entrance and exit slits lie on the Rowland circle. If this is done, then $F_{300}$ is also identically zero. For all choices of in-focus grazing-incidence configurations, including the Rowland circle, it turns out that astigmatism (where a point is imaged to a line) can be corrected by the grating only if a steeply curved toroid is used. This would be done by choosing $\rho$ so that $F_{020} = 0$. Given our choice of all-spherical surfaces, $\rho = R$ and astigmatism cannot be corrected by the grating.

This does not prevent the achievement of good resolution, however. It can be shown that for a spherical grating the line curvature originating from $F_{111}$, $F_{102}$, and $F_{120}$—which is very troublesome with toroids—is, in cases of interest to us, negligible compared with spherical aberration. In addition, the spherical aberration is itself small compared with diffraction if the grating is fairly small, as would be the case for an undulator beam line. Thus, in principle, our spherical gratings can be diffraction limited. In practice, the goal of the fabricator will be to achieve tolerances consistent with the use of 10-$\mu$m slits in our systems, which means a tolerance of around 1 $\mu$rad. This has been achieved in the past for standard spherical gratings [Ito et al., 1986], although it is far out of reach for aspherics.

To summarize, we conclude that our choice of spherical surfaces as being the safest from a manufacturing viewpoint also has many advantages from an optical viewpoint. The chief disadvantage is a large astigmatism, which we can overcome using the properties of the condensing system. We discuss this in Section 5.2.5.2.

To evaluate the slit-width-limited resolution for a grating monochromator, we note that we must have $F_{100} = 0$ or

$$m\lambda = d\,(\sin\alpha + \sin\beta)\,, \tag{3}$$

which is the grating equation. From this, one can show that the resolution $\Delta\lambda_s$ due to a slit of width $s$ is given by

$$\Delta\lambda_s = \frac{sd\cos\alpha}{r}\,. \tag{4}$$

The one-dimensional phase-space acceptance $A$ is defined as

$$A = W\Delta\theta\cos\alpha\,, \tag{5}$$

where $\Delta\theta$ is the acceptance angle of the spectrometer and $W$ is the width of the diffracting element. One can now derive from Eq. (4) that $A$ is given by

$$A = N\Delta\lambda_s\,, \tag{6}$$

where $N$ is the total number of grooves.

**5.2.3.2 Crystal Monochromators.** Both grating and crystal monochromators are essentially multiple-beam interferometers. A grating produces $N$ beams by dividing the wave front of the incoming light; a crystal or artificial multilayer does it by dividing the amplitude.

The fundamental law governing the operation of a crystal monochromator is the Bragg equation:

$$n\lambda = 2d\sin\theta\,, \tag{7}$$

where $n$ is the order of reflection, $d$ is the crystal period, and $\theta$ is the angle of glancing incidence. In addition, unlike the case of a diffraction grating, the law of reflection must be satisfied, i.e., the angle of incidence must equal the angle of reflection.

For a crystal spectrometer, the angular acceptance $\Delta\theta$ is the angular width of the Bragg diffraction peak. For a given wavelength and crystal, this quantity is essentially fixed. This leads to a much reduced ability to manipulate the resolution/flux trade-off, as compared with gratings.

Differentiating the Bragg equation, we see that

$$\frac{\lambda}{\Delta\lambda} = \frac{\tan\theta}{\Delta\theta}\,, \tag{8}$$

and inserting Eq. (5), we get

$$A = W\sin\theta\tan\theta\,\frac{\Delta\lambda}{\lambda}\,. \tag{9}$$

For a double-crystal spectrometer, the value of $\Delta\theta$ is about $1/\sqrt{2}$ times that for a single crystal. In Fig. 5-17, below, we plot $A$ versus $\lambda$ for two of the higher-resolution crystals that would be used in this region, beryl ($2d$ = 15.94 angstroms) and germanium (111) ($2d$ = 6.532 angstroms). It follows from Eq. (9) that lower-resolution crystals have higher $A$ values. In particular, multilayers, which could cover the 250- to 800-eV region, have $\lambda/\Delta\lambda \simeq 30$ and thus have an even larger phase-space acceptance.

The general conclusion is that, for both wigglers and bending magnets, all of the crystals of practical interest have a phase-space acceptance which is comfortably able to accept the entire beam.

### 5.2.4 User Requirements

Various workshops and consultations with the user community have been held, most recently in November 1985 [*Report of the Workshop*, 1985]. The documents produced by these gatherings form a sound basis for understanding the mixture of user requirements and for identifying areas of particular opportunity. Much more on this matter can be found in Section 2.

With only five beam lines, it is impossible to provide every type of service requested by every possible user; consequently, the only reasonable strategy is to provide general-purpose beam lines. Therefore, we have tried to provide as wide a range of service as possible using LBL-constructed beam lines, while keeping in mind the spectral region to which the Light Source is primarily directed, namely, the VUV and soft x-ray regions. In light of this, it is apparent that one cannot have separate high-flux and high-resolution facilities. Each monochromator must be flexible enough to provide both of these services. For diffraction grating monochromators on undulator beam lines, we know how to do this. The physics of crystal optical systems, however, makes the goal of flexibility harder to achieve, although artificial multilayer devices are beginning to change that.

After studying the wavelength coverage, resolution, flux, and polarization requirements of the various user groups, we adopted the set of insertion devices described in Section 5.1 and the corresponding beam lines described in Table 5-3. We note that to get an undulator to have a wide enough spectral coverage to match that of the monochromators, it is necessary to use a wide range of $K$ values, including large values leading to powerful wiggler beams. These are mainly blocked by the pinhole system. In the next section, we describe the optical systems that provide the capability outlined in Table 5-3.

### 5.2.5 Optical Systems

We propose three types of optical systems:

- A high-resolution normal-incidence monochromator.
- The Rense and Violett spherical grating monochromator system (which we use in three beam lines).
- A soft x-ray crystal monochromator.

These are described in the following sections.

**Table 5-3.** Summary of parameters for the five insertion device beam lines proposed for the Light Source. The scientific applications listed are based on the findings of the November 1985 users' workshop and are examples only; many other applications are possible.

| Radiation source[a] | Max aperture H (mrad) | Max aperture V(mrad) | Spectral range [typical energy] (eV) | Energy resolution at typical energy (eV) | Monochromator type[c] | Examples of scientific applications |
|---|---|---|---|---|---|---|
| A (U20) | 1.8 | 1.8 | 0.5–30 [15] | 0.00015[b] | 5-meter NIM | Chemistry, atomic and molecular spectroscopy |
| B (U9.0) | 0.57 | 0.57 | 5–200 [56] | 0.0012[b] | 10° SGM | Low-energy surface science, atomic and molecular spectroscopy |
| C (U5.0) | 0.185 | 0.18 | 50–800 [280] | 0.024[b] | 3° SGM | High-energy surface science, atomic and molecular spectroscopy |
| D (U3.65) | 0.1 | 0.09 | 200–1500 [540] | 0.076[b] | 2° SGM | Imaging, biology, atomic and molecular spectroscopy |
| E (W13.6) | 18.0 | 0.85 | 800–3500 [1840] | 0.5 | Crystal | Core-level spectroscopy, atomic and molecular spectroscopy |
| | | | 3000–10,000 | | Vacant (suited to development as hard x-ray station) | |

[a]U = undulator, W = wiggler, (xx.xx) = period length in cm.

[b]For undulators, resolution is slit width limited with 10-$\mu$m slit.

[c]NIM = normal-incidence monochromator, SGM = spherical grating monochromator.

**5.2.5.1 A High-Resolution Normal-Incidence Monochromator.** For the spectral region below about 40 eV, it is possible to use normal-incidence reflectors, and for this case, good monochromators with high resolution and good phase-space acceptance can be obtained commercially. We propose to use such a system, having a 5-meter-radius grating, with essentially the same condenser system as for the Rense and Violett scheme, described in detail below. The layout is shown in Fig. 5-9. The mirror and grating parameters are given in Table 5-4, and the operational parameters appear in Table 5-5. Monochromators of this general type have been implemented at most large synchrotron radiation facilities. An example of their potential capability is provided by the recent report from the Photon Factory group [Ito et al., 1986] of a resolving power of $2.5 \times 10^5$ at 790 angstroms. The absence of such an instrument at NSLS adds to the importance of including it here.

**5.2.5.2 The Rense and Violett Spherical Grating Monochromator System.** As discussed in Section 5.2.3, the spherical grating is capable of excellent resolution and meets the needs of beam line applications, provided a way can be found to correct the astigmatism. This is necessary if we are to achieve a final image that is nominally a point rather than a line. Rense and Violett's [1959] approach to this is to use a condensing system that images the source onto the entrance slit in the dispersion (vertical) plane and images the source onto the exit slit in the horizontal plane (see Fig. 5-10). Thus, the astigmatism of the grating is canceled by that of the condenser, and the final image is stigmatic to first order. The effect on the resolution of this method of illuminating the grating can be explored by analytical studies and by exact computer ray tracing. Both methods show that, for the large grating radii of interest to us, the resolution is not compromised.

Three variants on the Rense and Violett optical layout are shown in Figs. 5-11 through 5-13, which show the three beam lines for which we propose to use this system. The optical principles underlying the three beam lines are the same. The application to different wavelength regions is accommodated by different choices of grazing angle. The 3°-grazing-angle instrument (Fig. 5-12) is of the same design as one that is under construction at LBL for use on the LBL/Exxon/SSRL 54-pole wiggler beam line at Stanford. The grating rotation axis and the ingoing and outgoing ray directions are fixed. Wavelength tuning is by simple rotation of the grating. Good focus is preserved throughout the scanning range by sliding the exit slit along the beam direction. The Rowland circle condition can be satisfied exactly over part of the range, and approximately over all of it, by combined motion of both slits. The motion of the slits over a certain range is within the depth of focus of the condenser and the depth of field of the refocusing mirror. Exact accommodation to the slit location can be achieved by very slight elastic deformation of the mirrors.

Our choice of condensing system stems from our all-spherical philosophy. We choose to use two spherical mirrors with their planes of incidence perpendicular to each other, in the configuration originally used by Kirkpatrick and Baez [1948]. The parameters of the mirrors and gratings for the three Rense and Violett systems are included in Table 5-4, and the operational parameters are in Table 5-5.

To evaluate these systems properly, we need to be aware of their phase-space acceptance, as well as their resolution, and this is meaningful only in relation to the emittance of

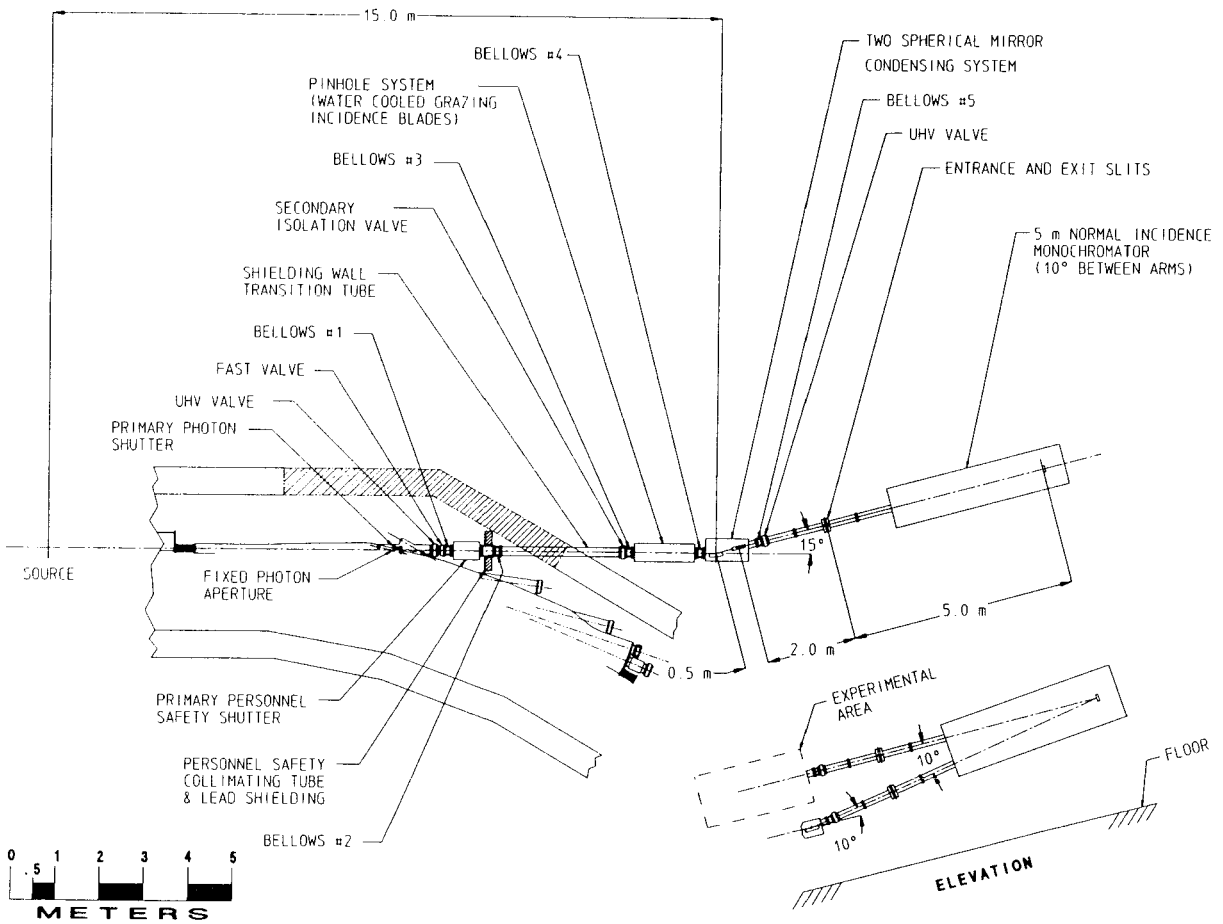


**Fig. 5-9.** Layout of Beam Line A (for undulator U20.0) with a 5-meter normal-incidence monochromator.

**Table 5-4.** Optical component parameters for the five beam lines of Table 5-3.

| | | | Premirror system | | | | | Monochromator | | | | |
|---|---|---|---|---|---|---|---|---|---|---|---|---|
| | | | Mirror | Imaging conjugates | | Central cone power | | | Incidence | | | Nominal |
| | | $\alpha$ | size | r, r′ (m) | | Total | Density | | angle at | Grating | Grating | conjugates r, r′ |
| Beam line | Type | (deg) | (mm) | H | V | (kW) | (W/cm$^2$) | Type | zero order (deg) | size (mm) | radius (m) | (m) |
| A | 2 spherical mirrors in K-B mount | 82.5 | 220×50 | 15, 2.5 | 15.5, 2.0 | 1.9 | 35 | McPherson 5-meter NIM | 5 | 100×100 | 5.0 | 5.0, 5.0 |
| B | ″ | 82.5 | 80×25 | 15, 8.9 | 15.5, 2.0 | 0.44 | 80 | Spherical grating with constant deviation | 80 | 180×50 | 17.3 | 1.7, 4.3 |
| C | ″ | 87.0 | 60×25 | 15, 8.5 | 15.5, 2.0 | 0.06 | 45 | ″ | 87 | 150×50 | 57.3 | 1.8, 4.2 |
| D | ″ | 88.0 | 50×25 | 15, 6.0 | 15.5, 2.0 | 0.02 | 30 | ″ | 88 | 60×50 | 50.2 | 0.8, 2.7 |
| E | ″ | 89.0 | 1000×100<br>500×100 | 10.4, 17.8 | 9.4, 18.8 | 0.5 | 13 | Double crystal | — | 25×25 (crystal) | — | — |

Symbols and abbreviations: $\alpha$ = angle of incidence, K-B = Kirkpatrick-Baez, H = horizontal, V = vertical.

**Table 5-5.** Performance parameters for the five beam lines of Table 5-3.

| Grating [$N$ (lines/mm)] $\lambda_H$ (Å) | $\lambda_1, \lambda_2, \lambda_3$ (Å) | $\alpha_1, \alpha_2, \alpha_3$ or $\theta_1, \theta_2, \theta_3$ (deg) | $\Delta\lambda$(Å) [$\Delta E$(eV)][a] | Vertical phase-space acceptance (m-rad) | Estimated photon flux[b] |
|---|---|---|---|---|---|
| | | **5-meter normal-incidence monochromator** | | | |
| G1 [2400] | 400, 900, 1500 | 7.75, 11.22, 15.41 | 0.008 [0.00013] | $1.9\times10^{-7}$ | $5.5\times10^{13}$ |
| G2 [1200] | 800, 1800, 3000 | 7.75, 11.22, 15.41 | 0.016 [0.00006] | " | $5.5\times10^{13}$ |
| G3 [300] | 2800, 7200, 12000 | 7.42, 11.22, 15.41 | 0.24 [0.00006] | " | $1.3\times10^{14}$ |
| | | **10° spherical grating monochromator** | | | |
| G1 [1200] 502 | 60, 220, 400 | 81.19, 84.36, 87.94 | 0.0048 [0.0012] | $1.0\times10^{-7}$ | $1.5\times10^{14}$ |
| G2 [600] 1005 | 120, 440, 800 | " | 0.0096 [0.0006] | " | $1.5\times10^{14}$ |
| G3 [200] 3012 | 360, 1320, 2400 | " | 0.037 [0.00026] | " | $1.1\times10^{14}$ |
| | | **3° spherical grating monochromator** | | | |
| G1 [1100] 50 | 12, 22, 35 | 87.72, 88.33, 89.11 | 0.0015 [0.038] | $2.4\times10^{-8}$ | $2.7\times10^{13}$ |
| G2 [500] 110 | 26, 48, 80 | 87.71, 88.31, 89.19 | 0.0033 [0.018] | " | $1.1\times10^{14}$ |
| G3 [200] 274 | 65, 120, 200 | " | 0.0082 [0.007] | " | $4.1\times10^{14}$ |
| | | **2° spherical grating monochromator** | | | |
| G1 [1100] 22.1 | 8, 12, 16 | 88.72, 89.08, 89.44 | 0.0018 [0.15] | $1.2\times10^{-8}$ | $2.5\times10^{13}$ |
| G2 [500] 40.5 | 14, 22, 29 | 88.69, 89.08, 89.43 | 0.0033 [0.085] | " | $1.1\times10^{14}$ |
| G3 [200] 81 | 29, 44, 58 | 88.71, 89.08, 89.43 | 0.0067 [0.043] | " | $2.2\times10^{14}$ |
| | | **Double-crystal monochromator** | | | |
| Beryl | 8.3, 9.9, 15.3 | 31.22, 38.45, 73.67 | 0.0054 [0.68] | $6.6\times10^{-6}$ | $1.0\times10^{13}$ |
| Ge(111) | 3.1, 4.1, 6.2 | 28.33, 39.22, 71.67 | 0.0022 [1.6] | $6.9\times10^{-6}$ | $2.6\times10^{12}$ |

Symbols and abbreviations: $\lambda_H$ = horizon wavelength; $\lambda_1, \lambda_2, \lambda_3$ = minimum, center, maximum wavelengths; $\alpha_1, \alpha_2, \alpha_3$ = incidence angles (for gratings); $\theta_1, \theta_2, \theta_3$ = Bragg angles (for crystals).

[a]At $\lambda_2$.

[b]At $\lambda_2$, assuming 10% grating efficiency. Units are photons/(s–400 mA–0.1% bandwidth). For the crystal monochromator, the flux is given for $\Delta\lambda/\lambda$ rather than 0.1% bandwidth.

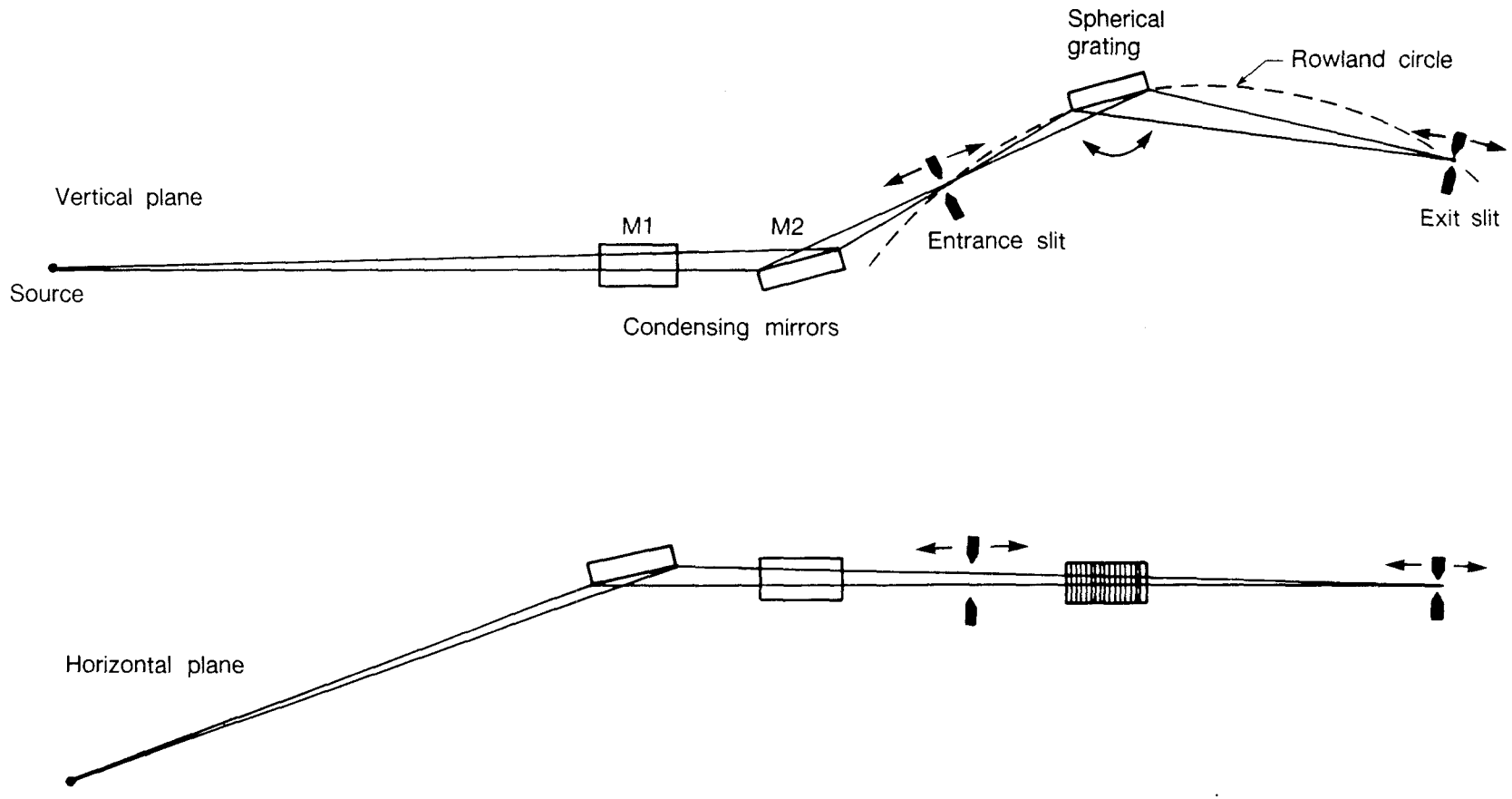


**Fig. 5-10.** Schematic of the Rense and Violett spherical grating monochromator system. The condensing mirrors M1 and M2 are designed so that M1 focuses in the horizontal plane to the exit slit, and M2 focuses in the vertical plane to the entrance slit. Each mirror has essentially zero focusing effect in its sagittal direction.

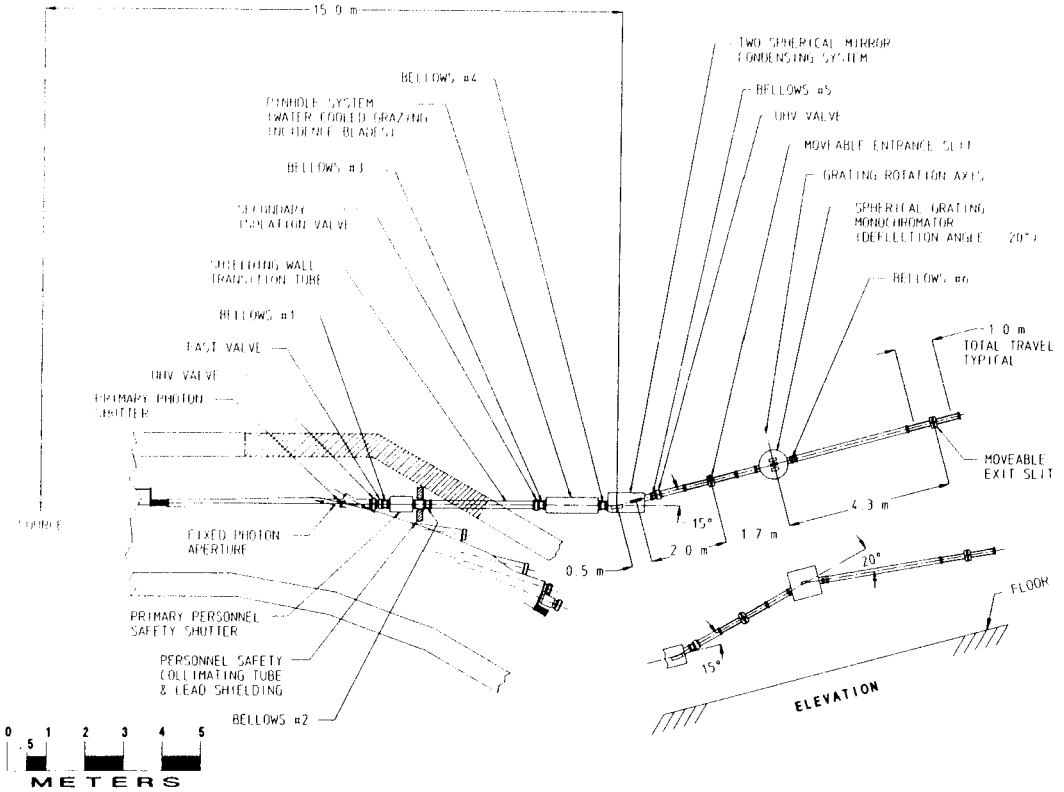


**Fig. 5-11.** Layout of Beam Line B (for undulator U9.0) with a 10° spherical grating monochromator.

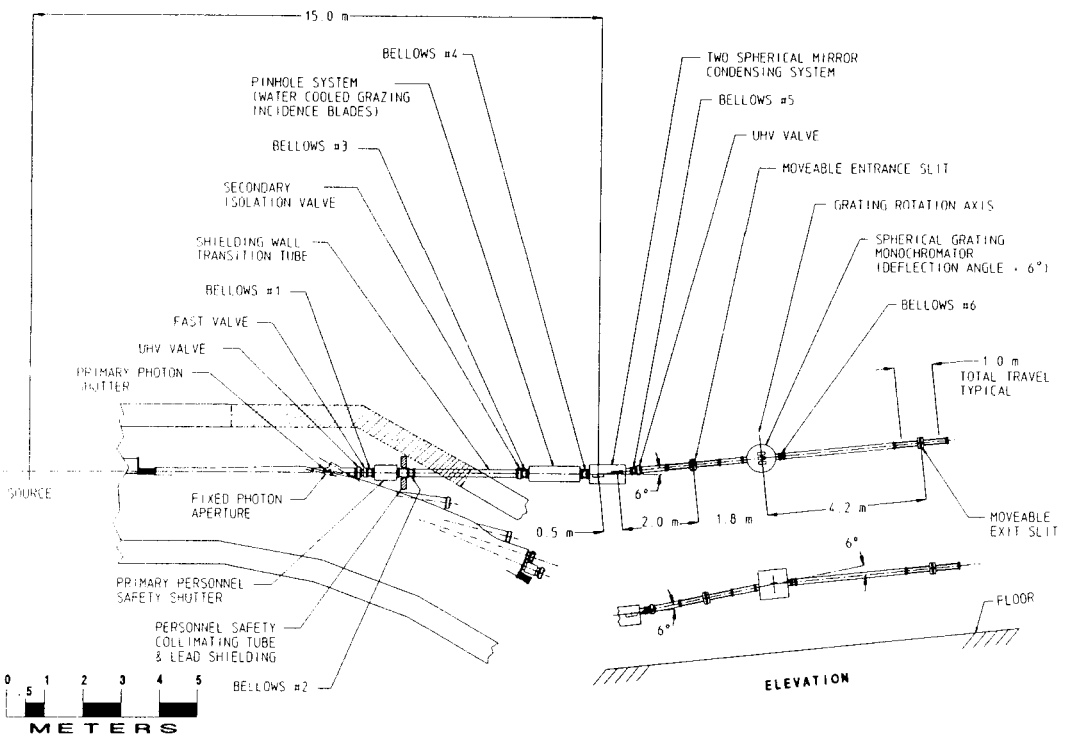


**Fig. 5-12.** Layout of Beam Line C (for undulator U5.0) with a 3° spherical grating monochromator.

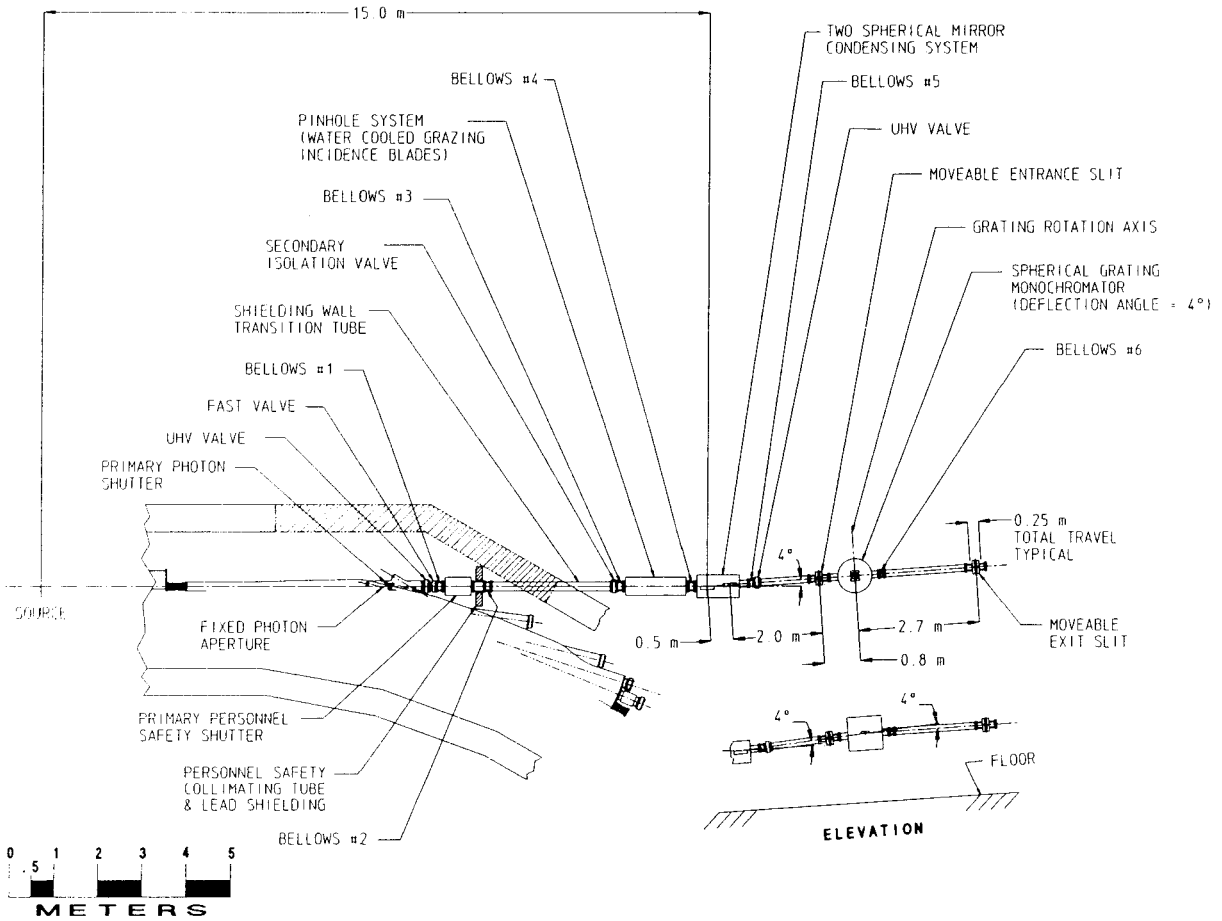


**Fig. 5-13.** Layout of Beam Line D (for undulator U3.65) with a 2° spherical grating monochromator.

the photon beam from the source. In Fig. 5-14, we show the phase-space acceptance of the three monochromators and the corresponding source emittances as a function of wavelength for a 10-$\mu$m slit setting. This is a typical value for a high-resolution experiment, although it is not the ultimate. The slit-width-limited resolution is also indicated at a few wavelengths for 10-$\mu$m slits. To give a more complete picture of the resolution capability of these systems, we show a full plot of the resolution capability of the Beam Line C instrument (3° grazing angle) in Fig. 5-15. This is determined by computer ray traces of rays emerging from a 10-$\mu$m entrance slit. We note that very good values are predicted for the

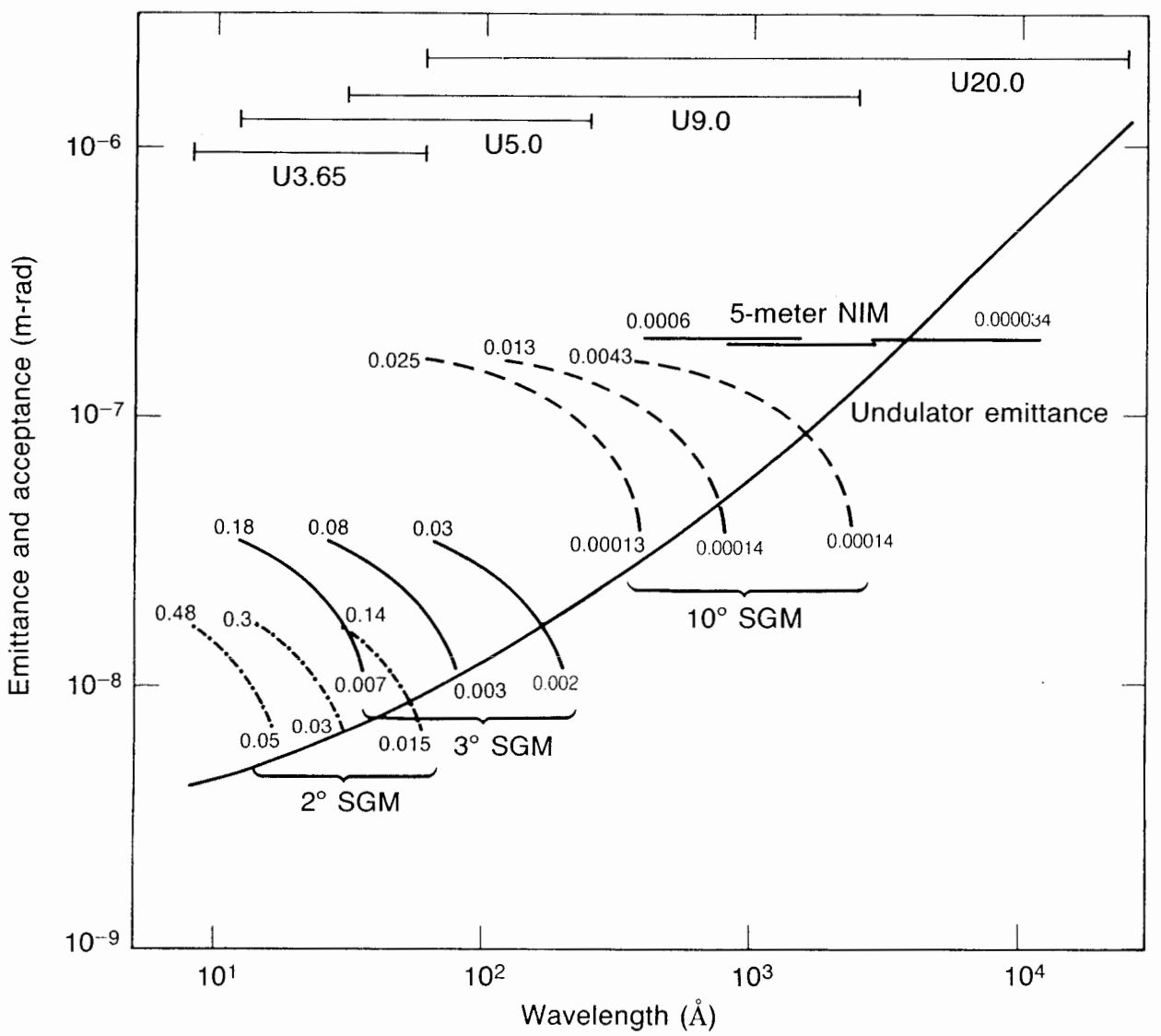


**Fig. 5-14.** Plots of the monochromatic photon-beam emittance in the vertical plane for all four undulators and the phase-space acceptance for the proposed monochromators for these sources, assuming 10-$\mu$m slits. When the acceptance curve lies above the emittance curve, the entire beam can, in principle, be accepted. The numbers associated with the endpoints of the scanning range of each grating are the slit-width-limited energy resolutions (in eV) for a 10-$\mu$m slit at the corresponding wavelengths, except that numbers associated with endpoints below the emittance curve are diffraction-limited resolutions.

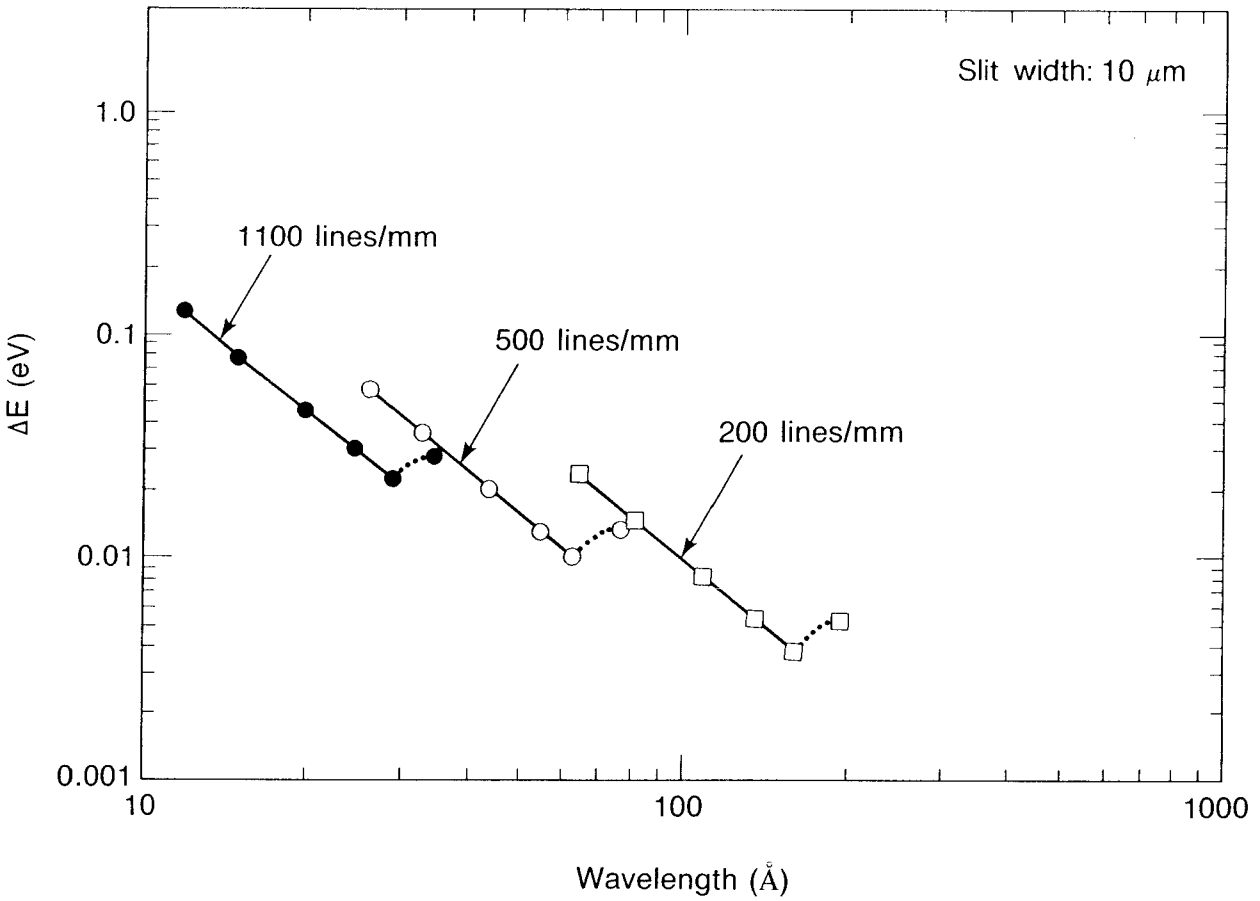


**Fig. 5-15.** Detailed plots of the resolution of the 3° spherical grating monochromator on Beam Line C. The plots are for 10-μm slits and are derived from computer ray traces of the whole beam line. The solid lines correspond to regions where the Rowland condition is exactly satisfied and where resolution is slit width limited. The dotted lines correspond to regions where the Rowland condition is only approximately satisfied and where the resolution is aberration limited.

resolution and that the entire beam can be accepted by the monochromator in most cases, even at the 10-μm slit width (see Fig. 5-14). This is a consequence of the outstanding phase-space properties of the source.

**5.2.5.3 A Soft X-Ray Crystal Monochromator.** There are fewer design options for a crystal monochromator than there are for a grating monochromator operating in the soft x-ray region. If the instrument is required to have constant deviation, then the design is essentially limited to the two-crystal monochromator, with the crystals in the antiparallel position. This type of instrument has been implemented at a number of synchrotron radiation facilities.

The monochromator should ideally operate in parallel light to give the highest resolution. However, since the natural deviation of the x-rays is already small in the vertical direction, we use a vertically deflecting mirror to magnify the source and improve the collimation so that the spectrometer can work in weakly convergent light without impairing its

natural resolution. This mirror is again spherical, so an additional mirror, crossed with the first in the Kirkpatrick-Baez configuration, is required for horizontal collection. Both these mirrors are inside the shield walls. The vertically deflecting mirror is 9.4 meters from the source and focuses at a distance of 18.8 meters for a magnification of 2.0. The horizontally deflecting mirror is at 10.4 meters, yielding a magnification of 1.7.

If the crystals were subjected to the full intensity of the wiggler radiation, even after it had been reflected and filtered by the two mirrors, they would suffer various unwanted changes in their optical properties, particularly in their lattice spacing. The calibration and efficiency of the instrument would consequently change. In addition, some sensitive crystals might be permanently degraded by radiation damage. It is therefore imperative to find some method for reducing the heat and radiation load on the crystals. As shown in Fig. 5-16, we propose to do this by using a pre-monochromator, similar in principle to the main monochromator, except that the two elements will be artificially fabricated multilayer structures, rather than natural crystals. These devices are generally made of refractory elements such as tungsten and carbon or molybdenum and silicon and can be deposited on massive polished metal substrates that can be water cooled. The power density is lower than that on a natural crystal, because the $2d$ spacings are larger and thus the incidence angles are more grazing. Furthermore, the large angular width of the Bragg peak of multilayers implies that the pre-monochromator will not be detuned by small changes in the lattice spacing. Although this is a fairly new concept, experimental results and detailed design studies indicate that the multilayer pre-monochromator approach offers the most satisfactory method of monochromator crystal protection. Both the pre-monochromator and the main monochromator are ultrahigh-vacuum devices.

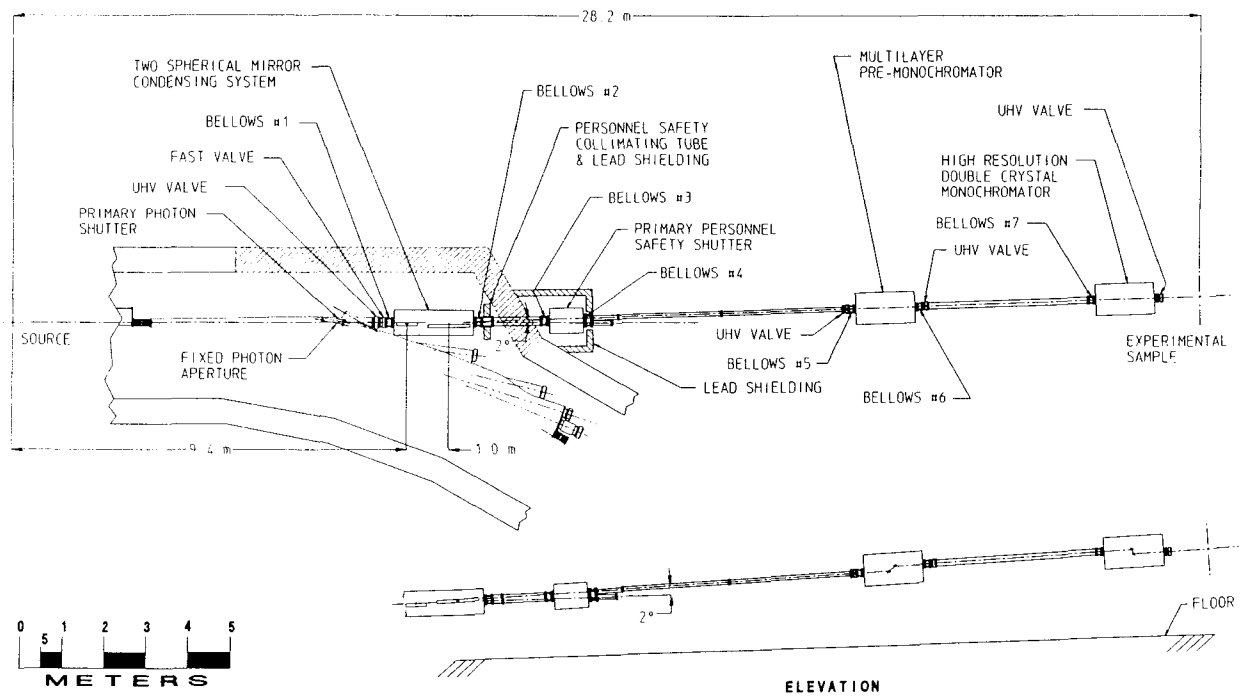


**Fig. 5-16.** Layout of Beam Line E (for wiggler W13.6) with a double-crystal monochromator and special heat-resistant pre-monochromator.

The phase-space acceptance of this system has been calculated and is shown in Fig. 5-17, relative to the emittance of the photon beams emerging from the wiggler and a bending magnet.

### 5.2.6 Beam Line Component Engineering

**5.2.6.1 General Description of Beam Line Components.** Front-end components serve to

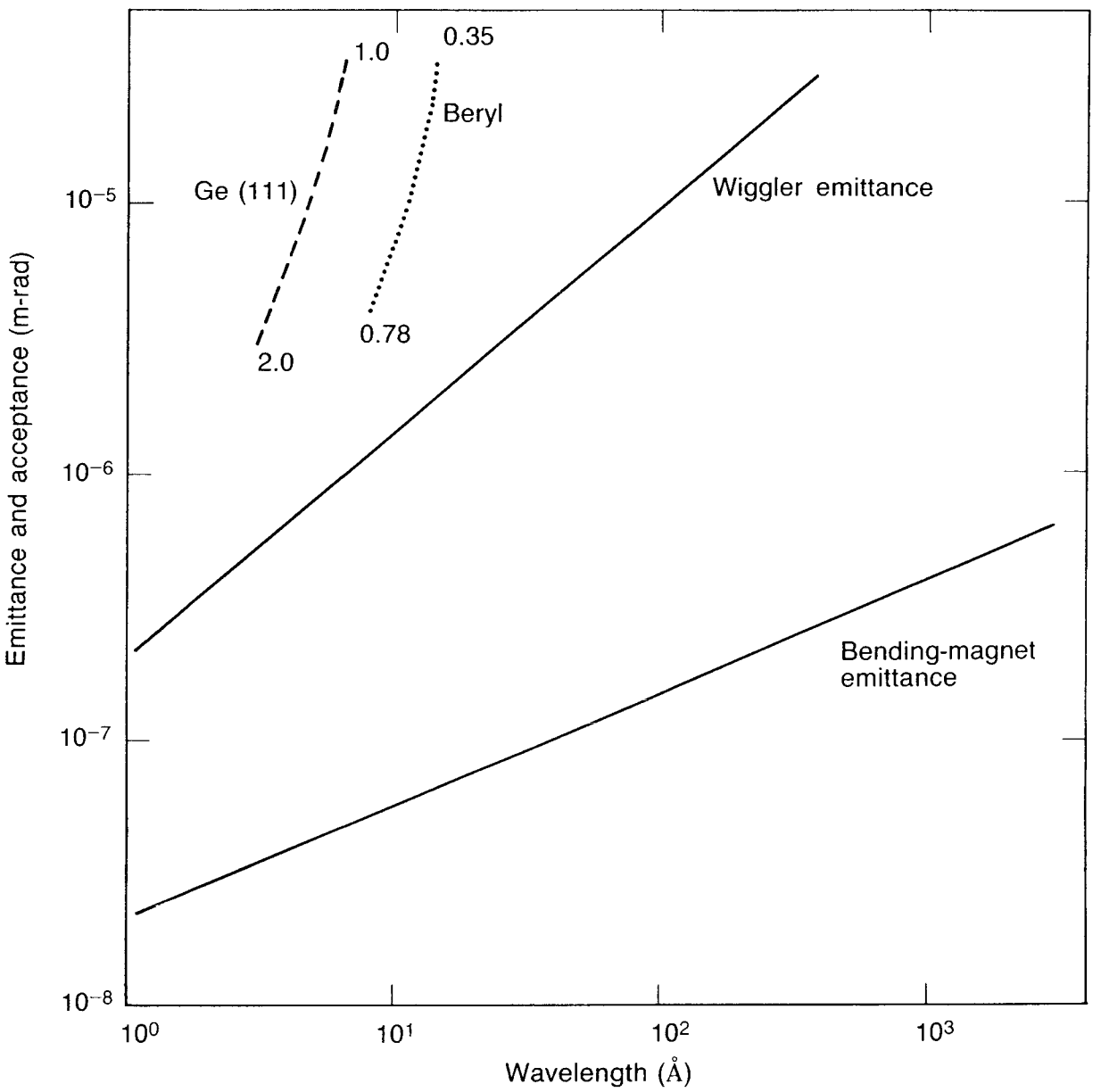


**Fig. 5-17.** Photon-beam emittance in the vertical plane for the wiggler beam line, together with the phase-space acceptance of the crystal monochromator, for two example crystals, beryl and germanium (111), which are assumed to be 25 mm wide. The numbers at the endpoints of the curves are realistic estimates of the resolution (in eV), based on both the rocking curve width and the degree of collimation of the beam. The latter is based on acceptance of everything inside the full width at half maximum.

define a beam aperture for synchrotron radiation and provide necessary beam on/off, radiation-safety, and vacuum-isolation systems for each beam line for both insertion device and bending magnet sources. Front-end components are similar for most beam lines, varying primarily in aperture size and in heat-absorbing capacity, depending on the characteristics of the radiation source. One front end may serve one or more beam lines from a single synchrotron radiation source.

Beam line components include optical system hardware—such as mirrors, monochromators, pinholes, and filters—that relate to the scientific requirements and photon energy ranges for individual beam lines. Significant variations in optical system design are required if we are to meet the needs of specific types of research and the corresponding synchrotron radiation sources; however, the general function of all optical systems is to produce a focused, monochromatic photon beam at an experimental target.

### 5.2.6.2 Front-End Components

*Fixed Photon Aperture.* The fixed photon aperture limits the horizontal and vertical excursion of the synchrotron radiation in a beam line and masks downstream components from the intense radiation. For insertion device beam lines, a water-cooled device with grazing incidence is needed in order to limit peak absorbed power densities to less than approximately 1 $kW/cm^2$. During normal operation, the aperture device absorbs only the low-power tails of the synchrotron radiation beam from the insertion device, together with some adjacent bending magnet radiation; however, it is capable of receiving the full beam intensity, as it might during storage ring injection or as a result of electron beam missteering. The fixed photon aperture is located in the storage ring vacuum chamber itself. During installation, the aperture position is accurately surveyed relative to the locations of the source and the beam exit port.

*Primary Photon Shutter.* Following the fixed photon aperture, an additional thermal absorber is required in order to close the beam line during injection and during any beam line shutdown. This water-cooled, grazing-incidence, movable photon shutter is capable of absorbing the full beam power and protects all downstream components from beam impingement when it is in the closed position. The photon shutter controls are interlocked with vacuum system controls so that the shutter is closed whenever one of the vacuum isolation valves or the fast valve (see below) is closed. It is also interlocked with the personnel-safety shutter system for simultaneous closure. The shutter mechanism has a normally closed control mechanism for fail-safe operation.

*Beam Exit Port and Sector Chamber Extension.* At each exit port, the outside wall of the storage ring vacuum chamber is extended for transition to the pipework of the beam line, starting with the mounting flange for the vacuum isolation valve.

*Primary Vacuum Isolation Valve.* This valve is the primary shutoff for isolating the storage ring sector chamber from a beam line. A standard, commercially available, all-metal, remotely actuated gate valve is used. The valve is pneumatically actuated and is locked in the closed position in case of compressed-air failure. On wiggler beam lines, the 20-cm

clearance diameter of the valve limits the horizontal angular aperture to approximately 18 mrad.

*Fast Valve.* The fast valve closes in accident situations only, namely, in response to a rapid pressure rise in the photon beam line. Although it is not leak-tight, its purpose is to reduce the conductance to the storage ring until the primary isolation valve and the photon shutter close. A commercially available device is used, which can close within 10 ms when triggered by one of the detection units (ion gauges) located at several places on the beam line. The fast valves on high-power insertion device beam lines (where full beam power might damage them) are interlocked so that storage ring rf power is shut off simultaneously with the triggering of the fast valves.

*Personnel-Safety Shutter.* The personnel-safety shutter is an absorber of high-energy bremsstrahlung, whose highest intensities normally occur during storage ring injection. The safety shutter is always closed during injection or whenever personnel require access to locations with a bremsstrahlung line of sight to the electron beam.

The safety shutter itself is a stainless-steel–encased lead block, which can be moved into the beam path. Redundant sensors must simultaneously indicate closure before personnel are allowed access to the affected parts of the beam line.

*Personnel-Safety Collimating Tube and Lead Shielding.* The personnel-safety collimating tube is a rectangular spool piece surrounded by lead shielding. Its purpose is to block all bremsstrahlung paths except those through the beam line itself, which are blocked by the safety shutter when it is closed.

*Secondary Vacuum Isolation Valve.* A second vacuum valve at the exit from the storage ring shielding wall allows vacuum isolation of all beam line components outside the shielding wall. This valve is a standard vacuum valve similar to the primary isolation valve.

#### 5.2.6.3 Beam Line Optical System Components

*Pinhole and Beam-Position Monitor.* The pinhole is a variable-aperture system for undulator beam lines that limits the horizontal and vertical opening size around the desired central cone of the photon beam (see Section 5.2.1.3). Aperture opening size is roughly in the range 1–30 mm, depending on the undulator source characteristics and the desired photon energy.

The pinhole system comprises four independently controlled blades, each of which defines one edge of the beam aperture. Since each blade must be capable of receiving the full, central-beam power in case of missteering or mispositioning, the blades are water cooled and have grazing-incidence surfaces that distribute the heat load. Maximum possible heat loads are similar to those on the LBL/Exxon/SSRL 54-pole wiggler beam line at Stanford, for which a variety of heat absorber systems are used [Avery, 1984]. Photoelectron current due to the radiation absorbed on the electrically isolated pinhole blades is used to monitor the synchrotron-radiation beam position. The photocurrents also provide signals that can be used to control electron-beam steering through the insertion device.

*Mirror Systems.* As discussed in Section 5.2.5, the mirror systems selected for all insertion device beam lines use spherical reflecting surfaces in the Kirkpatrick-Baez configuration. Although the pinhole systems used in undulator beam lines absorb much of the unwanted beam power, thermal distortion of optical surfaces is still a design issue in some cases, owing to the power densities in the central cone of the photon beam.

The first mirror may absorb a significant portion of the beam power, since it usually acts as a low-bandpass filter, absorbing most of the highest-energy photons. LBL's solution to this problem on the VUV branch of the LBL/Exxon/SSRL beam line uses a water-cooled copper-alloy mirror system [DiGennaro et al., 1985]. Material selection and the water-cooling configuration were based on thermal distortion calculations, which determined appropriate water flow rates, cooling channel shape, minimum wall thickness, etc. These methods make it possible to limit thermal distortion of the mirror surface to an acceptable level, with an appropriate margin of safety for thermal stresses. The final design of the above mirror (see Fig. 5-18), which is also being used at NSLS, uses an aluminum-oxide dispersion-strengthened copper alloy which has thermal properties similar to OFHC copper, but a yield strength at least six times greater. Furthermore, it retains its strength after high-temperature brazing and vacuum bake-out cycles. In addition, the mirror is fabricated using traditional machining, brazing, plating, and polishing methods, similar to those applicable to copper and other metal-optics materials.

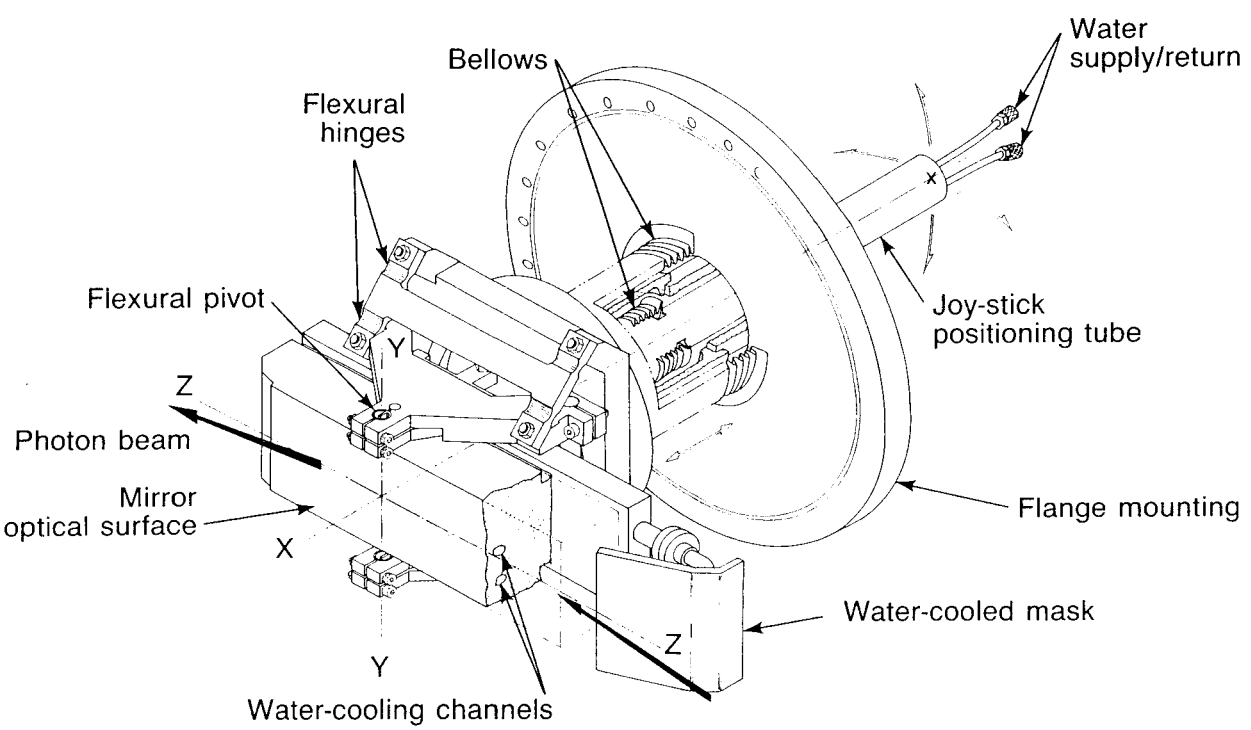


**Fig. 5-18.** The water-cooled metal mirror that is under construction at LBL for use on the LBL/Exxon/SSRL 54-pole wiggler beam line at Stanford. The mirror has remotely controllable motions for yaw, roll, and translation in and out of the beam. The optical surface is gold-coated electroless nickel, plated onto a Glidcop substrate. Glidcop is a dispersion-strengthened copper with 0.15% aluminum oxide particles. It has thermal properties similar to those of copper but a yield stress about six times greater.

We propose to use the same basic mirror design for cases where either the high power loading or close tolerances for allowable surface distortion require substrate cooling. The existing system lends itself well to a variety of mirror sizes and may be mounted in any orientation with respect to the vertical. Figure 5-18 shows the mirror and mounting, with water-cooling pipes passing through a "joy-stick" positioning tube. In the drawing, flexural pivots above and below the mirror define the $Y-Y$ rotation axis (yaw), and two pairs of flexural hinges define the $Z-Z$ rotation axis (roll), both axes being coincident with the mirror surface. An internal bellows accommodates the yaw and roll rotations, while the larger bellows allows the entire assembly to be translated along the $X-X$ axis in order to withdraw the mirror from the photon beam. Water-cooling channels are directly below the mirror optical surface for cooling by convection. The water-cooled mask protects the upstream end of the mirror from normal-incidence impingement of the beam.

*Monochromators.* The monochromator to be used on undulator Beam Line A is a high-resolution, normal-incidence spherical grating monochromator. This type of instrument is commercially available from several suppliers and is well-proven at other synchrotron radiation facilities and elsewhere (see Section 5.2.5.1). To accommodate the relatively high heat loads for this application, several manufacturers have expressed interest in customizing their instruments to accommodate water-cooled gratings.

On undulator Beam Lines B, C, and D, the monochromators all share the same basic design, differing primarily in the ranges of grazing incidence angles, nominally, 10°, 3°, and 2°, respectively. The basic monochromator system is described in Section 5.2.5.2. The device consists of three main components: entrance slit, grating mounting and positioning mechanism, and exit slit. The entrance and exit slits have variable-spacing jaws, held parallel within micrometer tolerances. They utilize a flexural hinge mechanism developed and proven at NSLS and are mounted on linear slides with bellows which allow up to about 1 meter of travel. The grating mounting holds three spherical gratings which can be interchanged without breaking vacuum in the grating chamber (see Fig. 5-19). The gratings are similar to those being developed for the VUV branch of the LBL/Exxon/SSRL beam line at Stanford. They are water-cooled, brazed-copper-alloy assemblies with ion-etched rulings. Despite grazing-incidence angles that distribute the heat load on the grating surface, the close tolerances for the spherical surface figure require direct water cooling.

The operating conditions on the proposed beam lines are considerably different from those at Stanford, and we can predict the grating cooling requirements properly only by a full finite-element analysis similar to our calculations for the VUV branch installation [DiGennaro, 1986]. We have not yet analyzed the actual thermal distortions and cooling requirements for the proposed gratings, but our judgment is that direct water cooling will be needed in all cases. If there are cases where traditional, uncooled fused-silica gratings can be used, our present monochromator system is engineered to accommodate them.

For the wiggler Beam Line E, we are interested in an energy range (0.5–4 keV) for which a crystal monochromator is indicated. However, it is important to be able to use wide-$d$-spacing crystals, some of which are sufficiently fragile to require special protection from high heat and radiation loading. Such protection is also desirable on other grounds. Therefore, we propose to use essentially two double-crystal monochromators (see Section 5.2.5.3). The first is based on multilayer reflectors deposited on water-cooled metal sub-

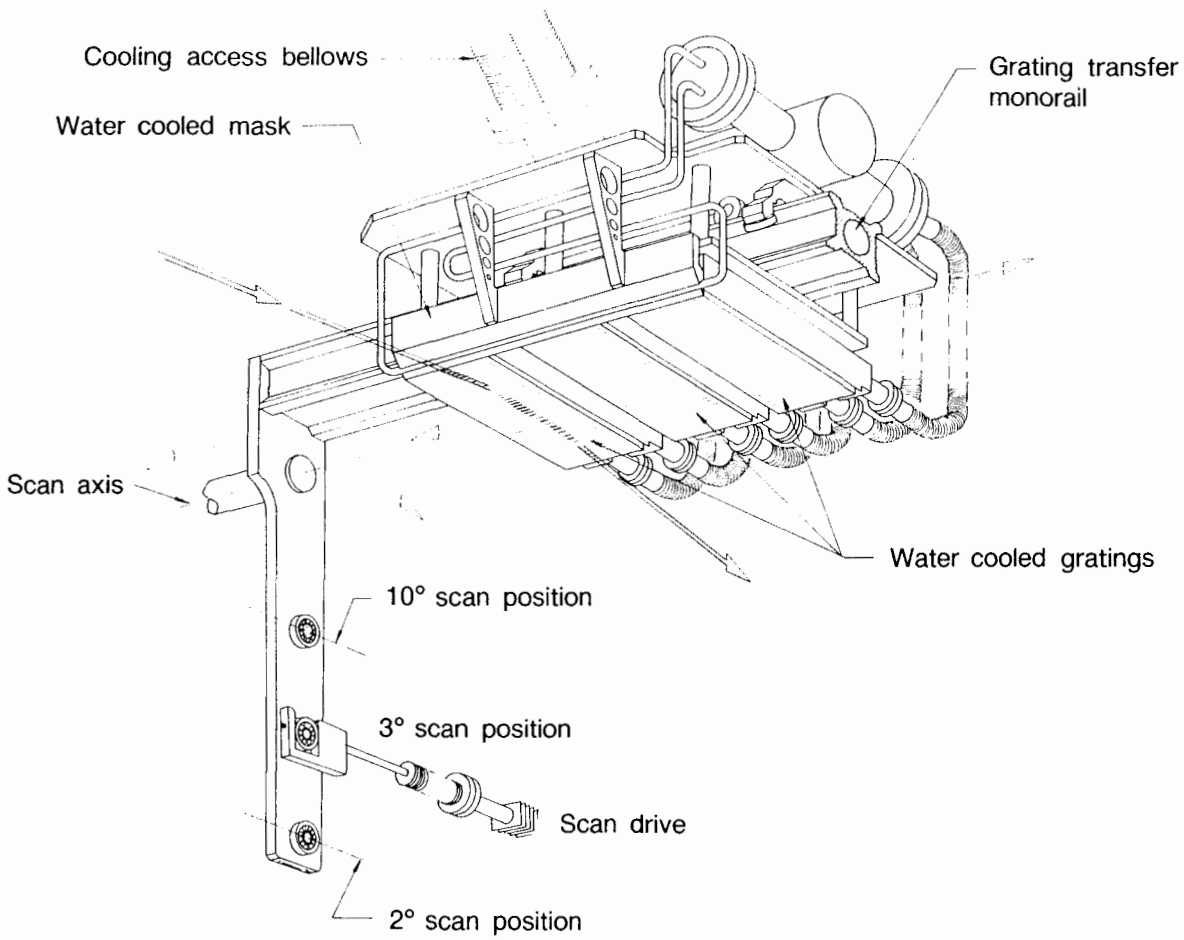


**Fig. 5-19.** Spherical grating monochromator being fabricated for the VUV branch on the LBL/Exxon/SSRL 54-pole wiggler beam line. The mounting holds three water-cooled gratings which can be interchanged without breaking vacuum in the grating chamber. Alternate mounting positions for the scan drive mechanism allow three different scanning ranges.

strates. The substrates will be electroless nickel plated, optically flat, and subjected to a special finishing process that leads to low scattered-light levels. This pre-monochromator is a kind of prefilter of moderate bandpass that protects the high-resolution monochromator. The pre-monochromator design is based on a grazing-incidence, rigidly coupled pair of multilayers similar to a monolithic crystal device. The beam shift caused in this arrangement can be kept below 0.3 mm easily and still smaller with some effort. We believe that the overall system can be made insensitive to beam motions of this size.

The main monochromator is now a relatively straightforward system, and any of the various existing approaches to building it could be adopted. A good example of this is the so-called Hastings-Cowan device used at NSLS. This device is operational and is demon-

strating good performance. It also has the advantage of being part of a continuing program of upgrades based on experience. We use this system for our high-resolution device.

*Vacuum Systems.* Throughout all beam lines, an ultrahigh-vacuum environment must be maintained. A pressure on the order of $1 \times 10^{-9}$ Torr is desired in order to maintain clean optical surfaces and match the vacuum requirements of the storage ring and experiments. The dominant gas loads are expected to be caused by photon-stimulated desorption. Vacuum pumping in the beam lines will be achieved with a combination of standard, commercially available ion pumps and titanium sublimation pumps, supported by a suitable oil-free roughing pump system.

## 5.3 Bending Magnet Beam Lines

The Light Source design includes installation of front-end components and controls for two bending magnet beam lines. Synchrotron radiation from two of the bending magnet sources will thus be made available for future development of beam line optical systems and experimental facilities. In addition, the vacuum chamber on the storage ring includes extensions and beam exit ports for four bending magnet beam lines per sector. Depending on the distance from the source location to the exit port, the horizontal angular aperture for the bending magnet beam lines ranges from about 33 to 40 mrad, with the maximum aperture width being limited by the internal size of the primary vacuum isolation valve located at the exit port.

Front-end components for bending magnet beam lines are nearly identical to those required for insertion device sources (discussed in detail in Section 5.2.6.2), differing primarily in the lower photon intensities, and consequently smaller thermal loads, that must be anticipated at heat absorbers. The fixed apertures and photon shutters are similar, but do not require the grazing incidence angles needed for adequate heat distribution on insertion device beam lines.

The fixed photon apertures for bending magnet beam lines are similar to the water-cooled photon stops that are used with the storage ring vacuum pumping system (see Section 3.5); however, they include a hole or slot which defines the limiting horizontal and vertical radiation fan that is allowed to pass through the beam exit port. Installation of fixed photon apertures for new bending magnet beam lines involves replacement of existing photon stops with slotted aperture devices.

As is the case with insertion device beam lines, the primary isolation valve and other downstream components require protection from beam impingement when a beam line is shut down. A photon shutter system is located immediately upstream of each exit port. The device is a water-cooled copper block which can be moved to the closed position to intercept the full beam power whenever any downstream component is closed.

# 6. Conventional Facilities

In this section, we briefly describe the conceptual design of the conventional facilities that will be modified or constructed to house the Light Source, its beam lines, and experimental areas. The scope of this activity includes site preparation, equipment removals and relocations, and construction. Summary cost and schedule data are included in Section 7.

The Light Source will be located in the Building 6 area of the LBL site and will use many of the services and facilities available there. This is highly cost effective and represents an optimal utilization of this valuable Laboratory resource. The area covers a sizable, flat hilltop site with good foundation conditions, centrally located within the Laboratory. It is in close proximity to electro-mechanical and mechanical technology machine shops and technician facilities, as well as being near the main Laboratory mechanical shops and adjacent to the new Advanced Materials Laboratory.

A plan view of the existing site is shown in Fig. 6-1, where the outer perimeter wall of the new addition is shown as a dotted line and where buildings affected by the construction are shaded. Figure 6-2 shows the new site plan, where the addition connecting Buildings 6, 10, and 80 is shown as a shaded area. The layout of the linac, booster synchrotron, electron storage ring, shielding, and photon beam lines within the expanded Building 6 is shown in Fig. 6-3. Figure 6-4. shows cross-sectional elevations of the facility and the concrete shielding tunnels for the booster and storage ring. All power supplies will be located within the expanded building, and a new electrical transformer and switching substation will be constructed outside the east perimeter wall. The Light Source control room will be located in Building 80.

Building 6 presently houses the 184-Inch Cyclotron, which will be removed (except for the magnet yoke) prior to construction of the Light Source. The existing structure has approximately 37,000 square feet of floor space, and the new addition will provide an additional 44,000 square feet at grade level, giving a total of 81,000 square feet available for the Light Source, its beam lines, and experimental equipment. The addition is designed to be structurally adequate to support a future second story, which would provide an additional 40,000 square feet of office and laboratory space. The structural steel support columns of the new addition are located so that the present 30-ton bridge crane in the Building 6 annex can be extended to serve the full circumference of the Light Source storage ring. The linac and booster will be serviced by the existing 30-ton polar crane operating in the dome area of Building 6. The height of the addition is approximately 29 feet; it thus offers the

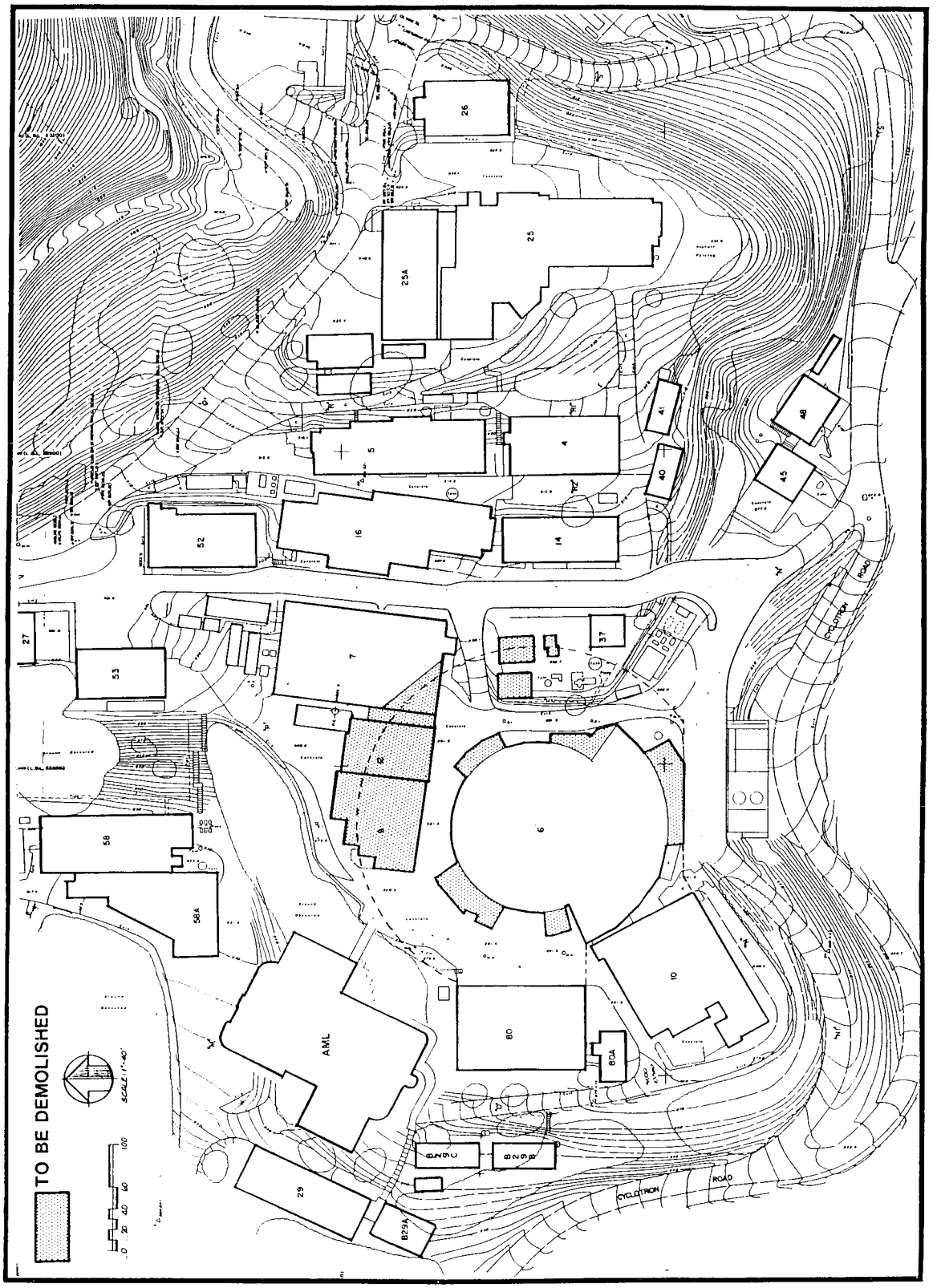


**Fig. 6-1.** Existing site and demolition plan.

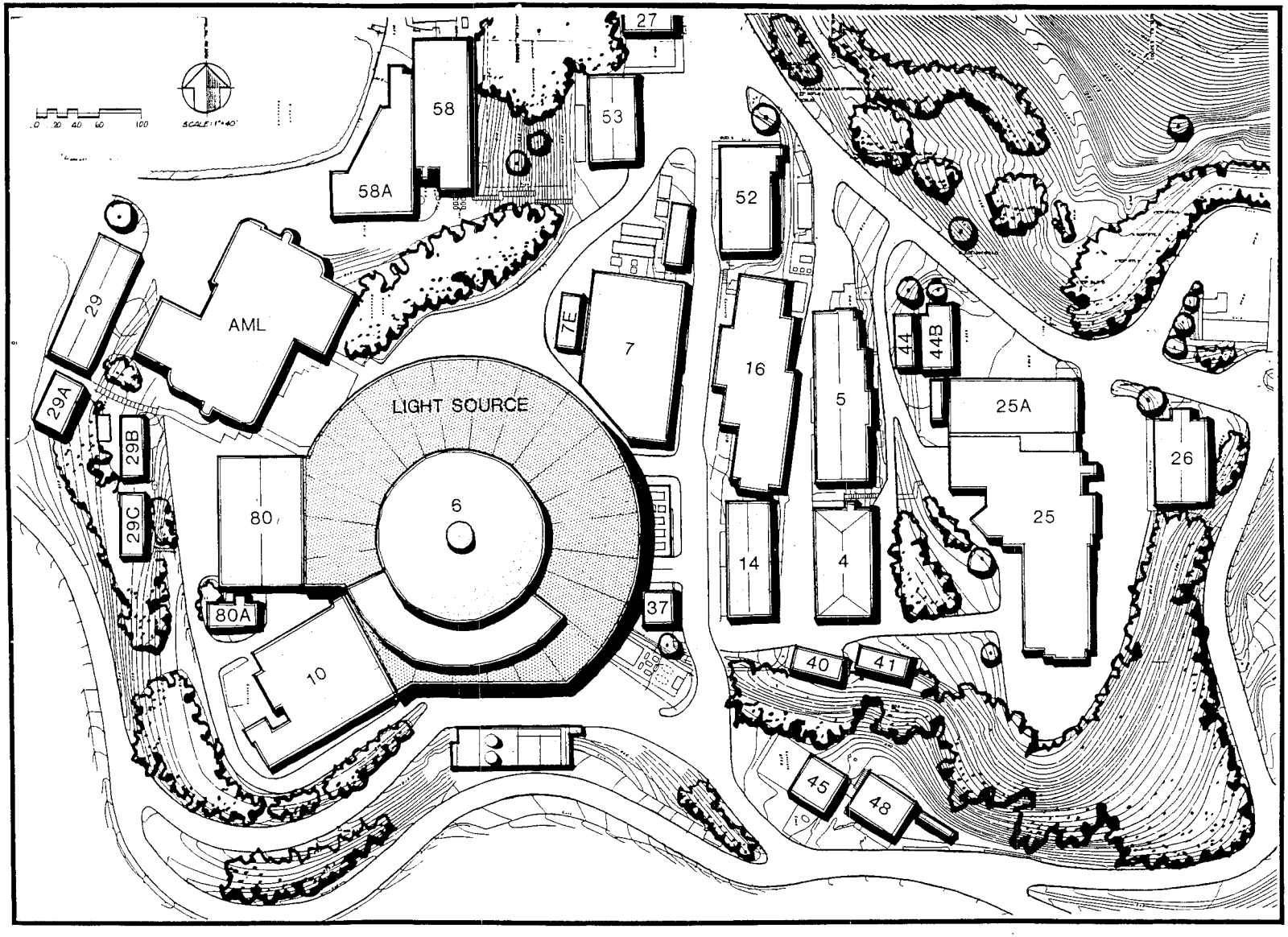


**Fig. 6-2.** Projected site plan.

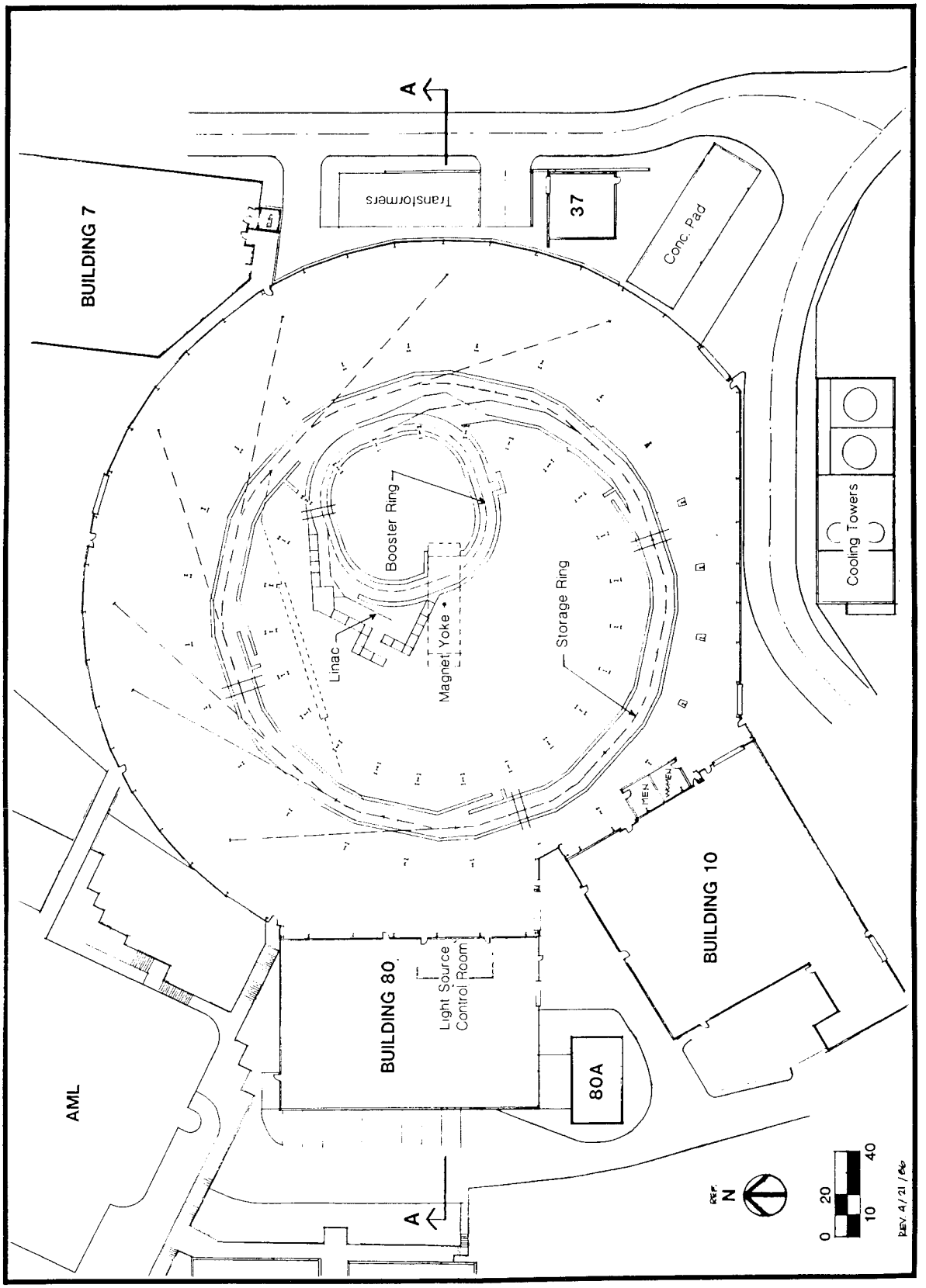


**Fig. 6-3.** Floor plan.

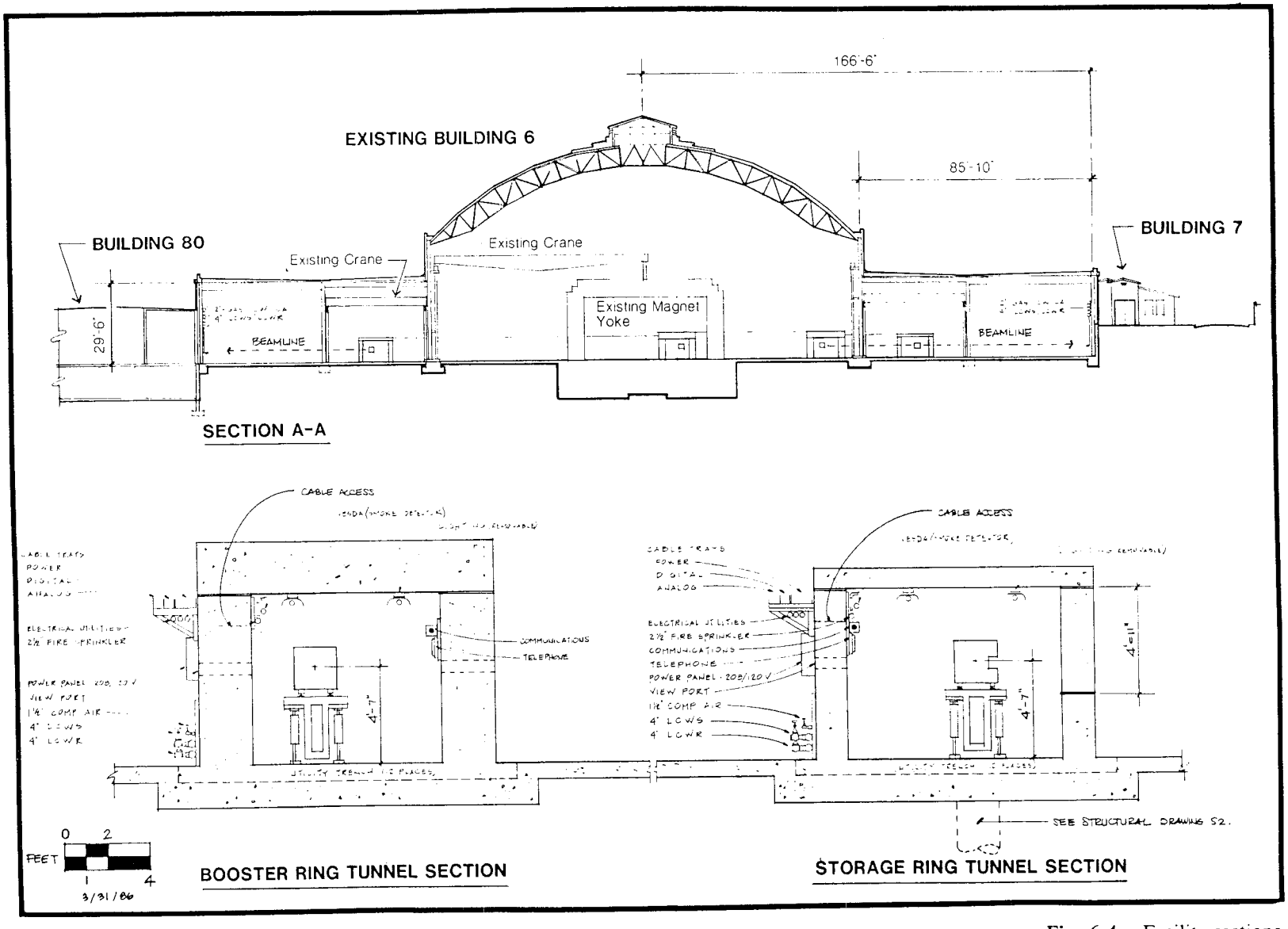


**Fig. 6-4.** Facility sections.

possibility of increased experimental floor space by providing the potential for a future open mezzanine structure in the beam lines hall.

The ground vibration environment at Building 6 has been carefully measured because of the importance of providing a quiet environment for the Light Source. The measurements were made at Building 6, at several nearby sites, and at the SPEAR ring at SLAC (for comparison). The results of the study show that Building 6 is a suitable site for the Light Source. Equipment installed at the 1–2 GeV Synchrotron Radiation Source will exhibit motion amplitudes of less than 0.1 $\mu$m because of ground vibrations, and in fact, most existing sources of ground motion will be removed during construction of the Light Source.

As a summary of the conventional facilities design, we list the design criteria in Table 6-1. The following sections then expand on this summary, the topics following the order of the detailed work breakdown structure.

## 6.1 Site Preparation

### 6.1.1 Demolitions and Shielding Block Removals

The new addition to Building 6 requires the demolition of Buildings 9 and 12, along with the old cooling tower facility. The latter is near the end of its useful life and is presently being replaced by a modern upgraded facility scheduled for completion in December 1986. This new facility is shown to the south of the Light Source building in Fig. 6-3. The shielding blocks of the 184-Inch Cyclotron will be removed from Building 6, and those that have no detectable residual radiation will be disposed of locally. Blocks that show activation will be shipped to Hanford, Washington, for approved burial. The 184-Inch Cyclotron itself will be dismantled and disposed of, leaving only the large magnet yoke in place. This yoke provides the structural support for the polar crane.

### 6.1.2 Utilities Removals and Relocations

Underground site utilities that now occupy the area of the new addition will be removed and relocated after temporary connections are made to maintain service. A new 12-kV switching station and 12-kV transformer will be installed in the new substation area located outside the east perimeter wall of the Light Source building. Modern vacuum circuit breakers will be used throughout, and the transformer will be an energy-efficient, low-loss, fan-cooled unit. This new electrical equipment will provide power to Building 6 and other, outlying Laboratory buildings presently served by a substation adjacent to Building 6. This existing substation will be demolished in concert with the removal of an outmoded 12-kV switching station.

## 6.2 Equipment Removals

Equipment to be removed from Building 6 includes the ISAH patient-positioning chair of the medical facility and a small Van de Graaff machine. Other equipment to be removed includes the coil-winding equipment from Building 9 and stores from Building 12.

**Table 6-1.** Design criteria for the Light Source conventional facilities.

1. General
   (a) In compliance with the LBL Long Range Development Plan as amended, April 1986
   (b) Environmental safety: In compliance with DOE, OSHA, State of California, and LBL standards.
2. Architectural
   (a) Occupancy: 250 people, B4 classification
   (b) Construction type: Type II — one hour
   (c) Fire resistivity: One hour at exterior walls, two hours at adjacent buildings
   (d) Number of man doors: 7
   (e) Number of overhead doors: 4
   (f) Number of cranes: 2 (30-ton capacity each)
   (g) Concrete shielding
      (i) Booster ring: walls, 2′6″ thick; roof, 2′6″ thick; tunnel inside dimensions, 8′0″ high, 9′0″ wide
      (ii) Storage ring: walls, 1′6″ thick; roof, 1′0″ thick; tunnel inside dimensions, 8′0″ high, 10′0″ wide
      (iii) Linac: walls, 4′0″ thick; roof, 4′0″ thick
      (iv) Number of mazes: Linac, 1; booster ring, 2; storage ring, 4
3. Civil/Structural
   (a) Roof to be designed for second floor
   (b) Floor: Cast-in-place reinforced-concrete slab on grade
   (c) Shielding: Cast-in-place tunnel walls, removable roof blocks; storage ring to have removable 4′11″-high outer wall section
   (d) Lateral loads: Wind, 20 psf; seismic, base shear 0.20 of the building weight
4. Mechanical
   (a) Air-handling system: Constant volume, 100% outside air
   (b) Lighting level: 2.0 $W/ft^2$
   (c) Interior design temperature: 67°F
   (d) Fire protection: Sprinkler system; Halon system in control room only
   (e) Utilities: Low-conductivity water, compressed air, natural gas, industrial cold water, sanitary sewer, fire sprinkler system
   (f) Utility distribution: Full circumference of addition outside wall; linac, booster, and storage ring to have low-conductivity water and compressed air only, access through floor trenches
5. Electrical
   (a) Substation: 12 kV
   (b) Large process loads: 480 V
   (c) Stand-by generator: 300 kVA
   (d) Lighting level: 10 foot candles minimum
   (e) Communications: Centrex telephone system, local paging, intercom (tunnel areas only)
   (f) Fire alarm: Very Early Smoke Detection Apparatus, fire call boxes
   (g) Cable access to tunnels: Through distributed cut-outs at wall tops

## 6.3 Construction

### 6.3.1 Site Improvements

Major electrical site improvements will include the installation of a new 12-kV transformer yard. The transformers will be low-loss, fan-cooled, oil-filled units, and the underground feeders will be double ended to allow nondisruptive equipment maintenance. The total power requirement for the Light Source and experimental apparatus is estimated at 6.1 MVA and some 2.1 MVA is required for other Laboratory facilities sharing the same substation. The system is designed for 10 MVA, thus giving a 22% margin for future capacity.

### 6.3.2 Building 6 Addition

**6.3.2.1 Architectural.** The new 44,000-square-foot Building 6 addition is concentric with Building 6, is approximately 30 feet high, and forms an annular shape with an outer radius of some 166 feet. The existing steel frame columns, beams, and truss members will be fireproofed with a sprayed-on cementitious material, and all combustible structural materials in the building will be replaced, with the exception of the heavy-timber dome roof. The addition will have an insulated metal roof deck, and steel roll-up doors will be provided for vehicular access, along with man doors for pedestrians. Adjacent buildings will be modified only to the extent of window and door removals and their replacement with matching wall materials where they are common with the new addition walls. The addition exterior walls occurring at the existing walls of Buildings 10 and 80 will be constructed of 2-hour fire-resistant assemblies.

**6.3.2.2 Civil Structural.** The addition will be a steel frame building that is not structurally attached to any of the existing buildings. The roof will be designed for future expansion that will provide second-floor office space. Cast-in-place concrete caissons will support the building columns, and a new 8-inch concrete slab on grade will be cast in the addition.

The radiation shielding design is based upon the dual design goals of limiting the radiation exposure to the general public to 10 mrem per year and limiting occupational exposure to laboratory workers to 250 mrem per 2000-hour worker year. Pessimistic assumptions are made concerning the number of electrons which will be lost from the beam during routine operation. Shielding thicknesses are then found such that the general-public and laboratory-worker dose-equivalents are acceptable. These calculations take into account both photon and neutron radiation; both point losses and distributed losses are considered. In all cases, the radiation shielding has been designed to be at least as thick as the minimum requirements which were calculated.

The booster and storage ring shielding tunnels will be constructed of cast-in-place concrete walls and precast removable roof panels. The storage ring will have a 4′11″-high removable outer wall section around its entire circumference to facilitate beam line egress from the tunnel. One foot of additional shielding, constructed of precast removable blocks, will be provided for some 20 feet downstream of the injection region. This section will be used for access to the booster during the construction phase. Precast blocks will be used as

shielding for the linac.

**6.3.2.3 Electrical.** Electrical power at 480 V will be distributed to switchboards inside the new addition and then to 480-V process loads and 277-V area-lighting loads. Local step-down transformers will be used for loads requiring lower voltage. Cranes, heating and ventilating equipment, pumps, and miscellaneous motor loads will be supplied by motor control centers. The radio-frequency amplifier plate power will be supplied by a 12,470- to 4160-V transformer, a vacuum contactor, a variable-voltage transformer, and a dc power supply. High-pressure sodium lighting will be provided and enhanced by task lighting where appropriate. A 300-kVA stand-by generator will be installed to provide emergency power to critical Light Source and safety systems. Communications will be provided by a Centrex telephone system, a closed-circuit intercom in the tunnels, and a local building paging system. The fire alarm system design will take account of the limited accessibility of the Light Source major components, and where required, it will be compatible with a radiation environment. A Halon system will be provided for the control room in Building 80.

**6.3.2.4 Mechanical.** The heating and ventilation system will be designed to maintain a minimum 67°F temperature in the beam lines area and to provide forced-air circulation during the summer. Exhaust fans will be used to ventilate the tunnel areas. Utilities to be provided within the facility include low-conductivity water, compressed air, natural gas, industrial cold water, a sanitary sewer, and high-pressure fire-protection water mains. The linac, booster, and storage ring tunnels will be provided with low-conductivity water and compressed air. Access to the tunnels is provided by utility trenches located at intervals around each ring.

## 6.4 Building Modifications

### 6.4.1 Building 7

Building 7 will be modified to allow unobstructed continuity of the Light Source perimeter. This requires the removal and replacement of exterior lateral bracing to accommodate modifications to the southwest corner of the two-story building.

### 6.4.2 Building 80

Building 80 will house the Light Source control room. Doors fire-rated for two hours will be added between the building and the Light Source addition. Modifications will be made to the windows and the present stair and exit area.

### 6.4.3 Building 10

The new addition to Building 6 will require minor modifications to the roll-up door area of Building 10 to maintain access to that building.

# 7. Schedule and Cost Estimate

The work breakdown structure (WBS) is a complete compilation of all the work elements in this construction project. It defines the scope of the project in terms of the work to be done, and it provides a structure for collecting costs in an organized fashion. The costs for both the special research facilities and the conventional facilities have been estimated by LBL personnel.

The complete WBS for the Light Source is given in Table 7-1. Level 1, the item with a one-digit code, is the entire project. Level 2 gives the breakdown into the major categories of project management and administration (1.1), special research facilities (1.2), conventional facilities (1.3), and contingencies (1.4). Still lower levels of the WBS subdivide the project into ever smaller detail. For example, at Level 3, the special research facilities are subdivided into categories such as storage ring (1.2.1), injector system (1.2.2), and control system (1.2.3). Note that the engineering, design, and inspection (ED&I) costs are collected for each Level 3 item.

This cost estimate includes all construction costs which will be incurred after project approval. The project scope includes the accelerator facility, five insertion devices, seven photon beam lines, conventional facilities, ED&I, project management and administration, and contingencies. This estimate does not include preconstruction R&D or preoperational costs associated with project commissioning.

## 7.1 Schedule

The project schedule has been developed under the following important assumptions:

- In FY 1987, $1.5 million of construction funds will be available.
- There will be an accompanying R&D program for accelerator physics studies, engineering models, and development of unique components.
- Preoperations funding will begin in FY 1990 and will continue through FY 1992.
- Preassembly and testing of components before installation will speed installation and commissioning.

Based upon these assumptions, we have developed a project schedule with the following major features:

**Table 7.1** Complete work breakdown structure for the 1–2 GeV Synchrotron Radiation Source.

```
1       1-2 GeV Synchrotron Radiation Source

1.1     Project Management & Administration
        1.1.1 Project Direction & Management
        1.1.2 Project Office Services
        1.1.3 Procurement & Subcontracting Administration
        1.1.4 Performance Measurement & Reporting
        1.1.5 Incremental Indirects

1.2     Special Research Facilities
        1.2.1 Storage Ring
                1.2.1.1 ED&I - Storage Ring
                        1.2.1.1.1 Magnets & Supports
                        1.2.1.1.2 Vacuum System
                        1.2.1.1.3 Survey & Alignment
                        1.2.1.1.4 Magnet Power System
                        1.2.1.1.5 RF System
                        1.2.1.1.6 Instrumentation & Low Level Electronics
                        1.2.1.1.7 Security & Safety
                1.2.1.2 Magnets & Supports
                        1.2.1.2.1 Gradient Magnets
                                1.2.1.2.1.1 Coils
                                1.2.1.2.1.2 Yokes
                                1.2.1.2.1.3 Assembly & Test
                                1.2.1.2.1.4 Fixtures
                        1.2.1.2.2 Quadrupoles
                                1.2.1.2.2.1 Q1 Quadrupoles
                                        1.2.1.2.2.1.1 Coils
                                        1.2.1.2.2.1.2 Cores
                                        1.2.1.2.2.1.3 Assembly & Testing
                                        1.2.1.2.2.1.4 Fixtures
                                1.2.1.2.2.2 Q2 Quadrupoles
                                        1.2.1.2.2.2.1 Coils
                                        1.2.1.2.2.2.2 Cores
                                        1.2.1.2.2.2.3 Assembly & Testing
                                        1.2.1.2.2.2.4 Fixtures
                                1.2.1.2.2.3 QF1 Quadrupoles
                                        1.2.1.2.2.3.1 Coils
                                        1.2.1.2.2.3.2 Cores
                                        1.2.1.2.2.3.3 Assembly & Testing
                                        1.2.1.2.2.3.4 Fixtures
                        1.2.1.2.3 Sextupoles
                                1.2.1.2.3.1 Coils
                                1.2.1.2.3.2 Yokes
                                1.2.1.2.3.3 Assembly & Test
                                1.2.1.2.3.4 Fixtures
                        1.2.1.2.4 Skew Quadrupoles
                        1.2.1.2.6 Steering Magnets
                                1.2.1.2.6.1 Coils
                                1.2.1.2.6.2 Yokes
```

**Table 7-1** continued.

```
                                1.2.1.2.6.3 Assembly & Test
                                1.2.1.2.6.4 Fixtures
                        1.2.1.2.7 Injection Magnets
                                1.2.1.2.7.1 Thick Septum Magnet
                                1.2.1.2.7.2 Thin Septum Magnet
                                1.2.1.2.7.3 Bump Magnets
                        1.2.1.2.8 Stands & Supports
                        1.2.1.2.9 Girder Assembly
                        1.2.1.2.10 Installation
                1.2.1.3 Vacuum System
                        1.2.1.3.1 Vacuum Chambers
                                1.2.1.3.1.1 Sector Chamber
                                1.2.1.3.1.2 Spool Chamber
                                1.2.1.3.1.3 Injection Chamber
                        1.2.1.3.2 Pumping System
                                1.2.1.3.2.1 Roughing System
                                1.2.1.3.2.2 Titanium Sublimation
                                1.2.1.3.2.3 Ion Pump
                        1.2.1.3.3 Assemble & Misc.
                                1.2.1.3.3.1 Sector Valve
                                1.2.1.3.3.2 Bellow
                                1.2.1.3.3.3 Sector Assembly
                                1.2.1.3.3.4 Spool Assembly
                                1.2.1.3.3.5 Bake-out
                        1.2.1.3.4 Installation
                                1.2.1.3.4.1 Sector Chamber
                                1.2.1.3.4.2 Spool Chamber
                                1.2.1.3.4.3 Injection Chamber
                1.2.1.4 Survey & Alignment
                        1.2.1.4.1 Monuments
                        1.2.1.4.2 Liquid Level
                        1.2.1.4.3 Survey Instruments
                        1.2.1.4.4 Alignment Fixtures
                        1.2.1.4.5 Ring Survey & Align
                1.2.1.5 Magnet Power System
                        1.2.1.5.1 Gradient Magnet Power System
                        1.2.1.5.2 Quadrupole Power System
                                1.2.1.5.2.1 QF1 Quadrupole PS
                                1.2.1.5.2.2 Q1 Quadrupole PS
                                1.2.1.5.2.3 Q2 Quadrupole PS
                        1.2.1.5.3 Sextupole Power System
                        1.2.1.5.4 Skew Quadrupoles
                        1.2.1.5.6 Steering Magnet Power System
                                1.2.1.5.6.1 Horizontal Steering Magnet PS
                                1.2.1.5.6.2 Vertical Steering Magnet PS
                                1.2.1.5.6.3 H-V Windings on Sextupoles PS
                        1.2.1.5.7 Injection Power Systems
                                1.2.1.5.7.1 Thick Septum Magnet Power Supply
                                1.2.1.5.7.2 Thin Septum Magnet Power Supply
                                1.2.1.5.7.3 Bump Magnet Power Supply
                        1.2.1.5.8 DC Distribution
                                1.2.1.5.8.1 Raft Wiring
                                1.2.1.5.8.2 Cable Tray & Misc. Wiring
                                1.2.1.5.8.3 Power Supply Racks
                        1.2.1.5.9 Installation
                                1.2.1.5.9.1 Magnet Power System Installation
```

**Table 7-1** continued.

```
                        1.2.1.5.9.2 Power Supply Installation
                        1.2.1.5.9.7 Injection Power Systems
                                1.2.1.5.9.7.1 Thick Septum Magnet PS
                                1.2.1.5.9.7.2 Thin Septum Magnet PS
                                1.2.1.5.9.7.3 Bump Magnet PS
1.2.1.6 RF System
        1.2.1.6.1 Klystron System
        1.2.1.6.2 Waveguide Equipmemt
        1.2.1.6.3 Low Level RF Components
        1.2.1.6.4 Cavity
        1.2.1.6.5 Klystron Cooling
        1.2.1.6.6 High Voltage Equipment
        1.2.1.6.7 Main Power Supply
        1.2.1.6.8 Auxiliary Equipment
        1.2.1.6.9 Control System
1.2.1.7 Instrumentation & Low Level Electronics
        1.2.1.7.1 Beam Diagnostics
                1.2.1.7.1.1 Beam Position Monitors
                        1.2.1.7.1.1.1 BPM Electronics
                1.2.1.7.1.2 Traveling Wave Electrodes
                1.2.1.7.1.3 Beam Transformer
                1.2.1.7.1.4 Optical Monitoring
                1.2.1.7.1.5 Screens
                1.2.1.7.1.6 Racks & Wiring
                1.2.1.7.1.7 Installation
        1.2.1.7.2 Beam Damping
                1.2.1.7.2.1 Local Oscillator
                1.2.1.7.2.2 Heterodyne Receiver
                1.2.1.7.2.3 Feedback Amplifiers
                1.2.1.7.2.4 Filter
                1.2.1.7.2.5 Electrodes
                1.2.1.7.2.6 Installation
        1.2.1.7.3 Control Room Electronics
                1.2.1.7.3.1 Instruments
                1.2.1.7.3.2 Racks & Wiring
                1.2.1.7.3.3 Installation
        1.2.1.7.4 Communications
                1.2.1.7.4.1 Headsets
                1.2.1.7.4.2 Experimenter Intercom
                1.2.1.7.4.3 Public Address
                1.2.1.7.4.4 Installation
        1.2.1.7.5 Vacuum Monitoring & Pump Electronics
                1.2.1.7.5.1 Vacuum Mon & Pump
                1.2.1.7.5.2 Residual Gas Analysis
                1.2.1.7.5.3 Vacuum Bakeout
                1.2.1.7.5.4 Installation
        1.2.1.7.6 Timing
                1.2.1.7.6.1 Synchronization
                1.2.1.7.6.2 Installation
        1.2.1.7.7 Beamline Steering Control
                1.2.1.7.7.1 Processing Electronics
1.2.1.8 Security & Safety
        1.2.1.8.2 Controlled Access Zone
        1.2.1.8.3 Area Monitoring
        1.2.1.8.4 Safety Shutters
        1.2.1.8.5 Misc. Interlocks
```

**Table 7-1** continued.

```
                                1.2.1.8.5.1 Misc. Interlocks #1
                                1.2.1.8.5.2 Misc. Interlocks #2
                                1.2.1.8.5.3 Misc. Interlocks #3
                        1.2.1.8.6 Installation
                                1.2.1.8.6.2 Controlled Access
                                1.2.1.8.6.3 Area Monitoring
                                1.2.1.8.6.4 Safety Shutters
                                1.2.1.8.6.5 Misc. Interlocks

1.2.2 Injection System
        1.2.2.1 ED&I - Injection System
                1.2.2.1.1 Linac
                1.2.2.1.2 Linac to Booster Transfer Line
                1.2.2.1.3 Booster
                1.2.2.1.4 Booster to Storage Ring Transfer Line
        1.2.2.2 Linac
                1.2.2.2.1 Accelerating Structure
                1.2.2.2.2 Support Equipment & Girder
                1.2.2.2.3 Vacuum System
                1.2.2.2.4 Temperature Control
                1.2.2.2.5 Waveguide RF Equipment
                1.2.2.2.6 Klystron Amplifier
                1.2.2.2.7 Modulator & HV Power Supply
                1.2.2.2.8 Driver & Low Level RF
                1.2.2.2.9 Control & Interlock
                1.2.2.2.10 Electron Gun
                1.2.2.2.11 Focusing System
                1.2.2.2.12 Buncher-Chopper
                1.2.2.2.13 Control System
                1.2.2.2.14 Instrumentation & Low Level Electronics
                        1.2.2.2.14.1 Beam Diagnostics
                                1.2.2.2.14.1.1 Beam Position Monitors
                                        1.2.2.2.14.1.1.1 BPM Elect.
                                1.2.2.2.14.1.2 Current Monitor
                                1.2.2.2.14.1.3 Screens
                                1.2.2.2.14.1.4 Racks & Wiring
                        1.2.2.2.14.2 Installation
                1.2.2.2.15 Security & Safety
                        1.2.2.2.15.1 Controlled Access Zone
                        1.2.2.2.15.2 Area Monitoring
                        1.2.2.2.15.3 Misc. Interlocks
                                1.2.2.2.15.3.1 Misc. Interlocks #1
                                1.2.2.2.15.3.2 Misc. Interlocks #2
                                1.2.2.2.15.3.3 Misc. Interlocks #3
                        1.2.2.2.15.4 Installation
                                1.2.2.2.15.4.1 Controlled Access
                                1.2.2.2.15.4.2 Area Monitor
                                1.2.2.2.15.4.3 Misc. Interlocks

        1.2.2.3 Linac to Booster Transfer Line
                1.2.2.3.1 Magnets & Supports
                        1.2.2.3.1.1 Magnets
                        1.2.2.3.1.2 Supports
                1.2.2.3.2 Vacuum
                1.2.2.3.3 Survey & Alignment
                1.2.2.3.4 Magnet Power System
```

**Table 7-1** continued.

```
                        1.2.2.3.4.1 Magnet Power Supplies
                        1.2.2.3.4.2 DC Distribution
                        1.2.2.3.4.3 Magnet & Interlock Wiring
                1.2.2.3.5 Instrumentation & Low Level Electronics
                        1.2.2.3.5.1 Beam Position Monitor
                                1.2.2.3.5.1.1 BPM Electronics
                        1.2.2.3.5.2 Beam Profile Monitor
                        1.2.2.3.5.3 Screens
                        1.2.2.3.5.4 Beam Intensity Monitor
                        1.2.2.3.5.5 X-Y Collimator
                        1.2.2.3.5.6 Racks & Wiring
                        1.2.2.3.5.7 Vacuum Monitoring
                        1.2.2.3.5.8 Installation
                1.2.2.3.6 Installation
                        1.2.2.3.6.1 Magnets
                        1.2.2.3.6.2 Vacuum
                        1.2.2.3.6.4 Magnet Power Supplies
        1.2.2.4 Booster
                1.2.2.4.1 Magnets & Supports
                        1.2.2.4.1.1 Dipoles
                                1.2.2.4.1.1.1 Coils
                                1.2.2.4.1.1.2 Yokes
                                1.2.2.4.1.1.3 Assembly & Test
                                1.2.2.4.1.1.4 Fixtures
                        1.2.2.4.1.2 Quadrupoles
                                1.2.2.4.1.2.1 Coils
                                1.2.2.4.1.2.2 Yokes
                                1.2.2.4.1.2.3 Assembly & Test
                                1.2.2.4.1.2.4 Fixtures
                        1.2.2.4.1.3 Sextupoles
                                1.2.2.4.1.3.1 Coils
                                1.2.2.4.1.3.2 Yokes
                                1.2.2.4.1.3.3 Assembly & Test
                                1.2.2.4.1.3.4 Fixtures
                        1.2.2.4.1.4 Steering Magnets
                        1.2.2.4.1.5 Injection Magnets
                                1.2.2.4.1.5.1 Septum Magnet
                                1.2.2.4.1.5.2 Kicker Magnet
                        1.2.2.4.1.6 Extraction Magnets
                                1.2.2.4.1.6.2 Kicker Magnet
                                1.2.2.4.1.6.3 Thin Septum Magnet
                                1.2.2.4.1.6.4 Thick Septum Magnet
                        1.2.2.4.1.7 Stands & Supports
                        1.2.2.4.1.8 Girder Assembly
                        1.2.2.4.1.9 Installation
                1.2.2.4.2 Vacuum System
                        1.2.2.4.2.1 Booster Vacuum Chamber
                        1.2.2.4.2.2 Extraction & Injection Chamber
                        1.2.2.4.2.3 Appendage Pumps
                        1.2.2.4.2.4 Roughing System
                        1.2.2.4.2.5 Installation
                1.2.2.4.3 Survey & Alignment
                        1.2.2.4.3.1 Magnets to Girder
                        1.2.2.4.3.2 Girder Survey & Adjust
                        1.2.2.4.3.3 Position Monitor Survey
                1.2.2.4.4 Magnet Power System
```

**Table 7-1** continued.

```
                1.2.2.4.4.1 Dipole Power System
                1.2.2.4.4.2 Quadrupole Power System
                1.2.2.4.4.3 Sextupole Power System
                        1.2.2.4.4.3.1 SF Sextupole PS
                        1.2.2.4.4.3.2 SD Sextupole PS
                1.2.2.4.4.4 Steering Magnet Power System
                1.2.2.4.4.5 Injection Power Systems
                        1.2.2.4.4.5.1 Septum Mag. Power Suppy
                        1.2.2.4.4.5.2 Kicker Mag. Power Suppy
                1.2.2.4.4.6 Extraction Power Systems
                        1.2.2.4.4.6.2 Kicker Mag. Pwr. Supply
                        1.2.2.4.4.6.3 Thin Septum Mag. PS
                        1.2.2.4.4.6.4 Thick Septum Mag. PS
                1.2.2.4.4.7 DC Distribution
                        1.2.2.4.4.7.1 DC Distribution
                        1.2.2.4.4.7.2 Straight Section Wiring
                        1.2.2.4.4.7.3 Curved Section Wiring
                1.2.2.4.4.8 Installation
                        1.2.2.4.4.8.1 Power Supply Install.
                        1.2.2.4.4.8.2 Magnet Wiring
                        1.2.2.4.4.8.3 PS Rack Installation
                        1.2.2.4.4.8.5 Injection Power Systems
                                1.2.2.4.4.8.5.2 Kicker Mag. PS
                        1.2.2.4.4.8.6 Extraction Power Systems
                                1.2.2.4.4.8.6.2 Kicker Mag. PS
                                1.2.2.4.4.8.6.3 Thin Sept. PS
                                1.2.2.4.4.8.6.4 Thick Sept. PS
        1.2.2.4.5 RF System
                1.2.2.4.5.1 RF Transmitter
                1.2.2.4.5.2 Transmission Line
                1.2.2.4.5.3 Low Level RF
                1.2.2.4.5.4 Cavity
                1.2.2.4.5.5 Auxiliary Equipment & Installation
                1.2.2.4.5.6 Control System
        1.2.2.4.6 Instrumentation & Low Level Electronics
                1.2.2.4.6.1 Beam Diagnostics
                        1.2.2.4.6.1.1 Beam Position Monitors
                                1.2.2.4.6.1.1.1 BPM Elect.
                        1.2.2.4.6.1.2 Traveling Wave Electrodes
                        1.2.2.4.6.1.3 Beam Transformer
                        1.2.2.4.6.1.4 Optical Monitoring
                        1.2.2.4.6.1.5 Screens
                1.2.2.4.6.2 Vacuum Monitoring
                1.2.2.4.6.3 Booster Field Timing
                1.2.2.4.6.4 Racks & Wiring
                1.2.2.4.6.5 Installation
        1.2.2.4.7 Security & Safety
                1.2.2.4.7.2 Controlled Access Zone
                1.2.2.4.7.3 Area Monitoring
                1.2.2.4.7.5 Misc. Interlocks
                        1.2.2.4.7.5.1 Misc Interlocks #1
                        1.2.2.4.7.5.2 Misc Interlocks #2
                        1.2.2.4.7.5.3 Misc Interlocks #3
                1.2.2.4.7.6 Installation
                        1.2.2.4.7.6.2 Controlled Access Zone
                        1.2.2.4.7.6.3 Area Monitor
```

**Table 7-1** continued.

```
                                        1.2.2.4.7.6.4 Misc. Interlocks

            1.2.2.5 Booster to Storage Ring Transfer Line
                    1.2.2.5.1 Magnets & Supports
                            1.2.2.5.1.1 Dipoles
                            1.2.2.5.1.2 Quadrupoles
                            1.2.2.5.1.3 Steering
                            1.2.2.5.1.4 Stands & Supports
                    1.2.2.5.2 Vacuum
                    1.2.2.5.3 Survey & Alignment
                    1.2.2.5.4 Magnet Power System
                            1.2.2.5.4.1 Magnet Power Supplies
                            1.2.2.5.4.2 DC Distribution
                    1.2.2.5.5 Instrumentation & Low Level Electronics
                            1.2.2.5.5.1 Beam Position Monitors
                                    1.2.2.5.5.1.1 BPM Electronics
                            1.2.2.5.5.2 Screens
                            1.2.2.5.5.3 Beam Profile Monitor
                            1.2.2.5.5.4 Sabersky Finger Beam Probe
                            1.2.2.5.5.5 Beam Charge Monitor
                            1.2.2.5.5.6 Vacuum Monitoring
                            1.2.2.5.5.7 Rack & Wiring
                            1.2.2.5.5.8 Installation
                    1.2.2.5.6 Installation
                            1.2.2.5.6.2 Vacuum
                            1.2.2.5.6.4 Magnet Power System

    1.2.3 Control System
            1.2.3.1 ED&I - Control System
                    1.2.3.1.1 Network & Work Stations
                    1.2.3.1.2 Consoles
                    1.2.3.1.3 Display & Collector Micro Modules
                    1.2.3.1.4 Input/Output Controller Modules
                    1.2.3.1.5 Computer Timing & Synchronization
            1.2.3.2 Network & Work Stations
                    1.2.3.2.1 Network Resource Manager
                    1.2.3.2.2 Work Stations
                    1.2.3.2.3 Network Software & Documentation
                    1.2.3.2.4 Installation
            1.2.3.3 Consoles
                    1.2.3.3.1 Color Monitors & Touch Panels
                    1.2.3.3.2 Video Copier & Mux
                    1.2.3.3.3 Portable Consoles
                    1.2.3.3.4 Operator Interface
                    1.2.3.3.5 Installation
            1.2.3.4 Display & Collector Micro Modules
                    1.2.3.4.1 Display Micro Modules
                    1.2.3.4.2 Operating System
                    1.2.3.4.3 Network Access Software
                    1.2.3.4.4 Parameter Access & Modeling Software Interface
                    1.2.3.4.5 Error Monitoring Software
                    1.2.3.4.6 Display Generation Software
                    1.2.3.4.7 Display Micro Module Documentation
                    1.2.3.4.8 Collector Micro Module
                    1.2.3.4.9 Collector Micro Module Software
                    1.2.3.4.10 Installation
```

**Table 7-1** continued.

```
            1.2.3.5 Input/Output Controller Modules
                    1.2.3.5.1 Intelligent Local Controller(ILC)
                    1.2.3.5.2 ILC Software & Documentation
                    1.2.3.5.3 I/O Micro Modules(IOMM's)
                    1.2.3.5.4 IOMM Software & Documentation
                    1.2.3.5.5 Data Base Generation for I/O Controllers
                    1.2.3.5.6 Installation
                            1.2.3.5.6.1 ILC Installation
                            1.2.3.5.6.2 IOMM Installation
            1.2.3.6 Computer Timing & Synchronization
                    1.2.3.6.1 Manchester Encoder & Timing Module
                    1.2.3.6.2 Manchester Decoder & Fiber Optics
                    1.2.3.6.3 Installation
    1.2.4 Insertion Devices
            1.2.4.1 ED&I - Insertion Devices
                    1.2.4.1.1 Preliminary & General Engineering
                    1.2.4.1.2 Magnetic Structure Engineering
                    1.2.4.1.3 Support & Drive System Engineering
                    1.2.4.1.4 Vacuum System Engineering
                    1.2.4.1.5 Engineering During Fabrication
              1.2.4.2 Insertion Device A
                      1.2.4.2.1 Magnetic Structure
                              1.2.4.2.1.1 Magnetic Material
                              1.2.4.2.1.2 Model Pole
                              1.2.4.2.1.3 Pole Assemblies
                              1.2.4.2.1.4 End Pole Assemblies
                              1.2.4.2.1.5 Backing Beams
                              1.2.4.2.1.6 Magnet Structure Assembly
                              1.2.4.2.1.7 Magnetic Measurements
                      1.2.4.2.2 Support & Drive Systems
                              1.2.4.2.2.1 Support Structure
                              1.2.4.2.2.2 Drive Components
                              1.2.4.2.2.3 Drive System Fabrication
                              1.2.4.2.2.4 Support-Drive Assembly
                      1.2.4.2.3 Vacuum System
                      1.2.4.2.4 Electrical
                      1.2.4.2.5 Installation
                              1.2.4.2.5.1 Mechanical Installation
                              1.2.4.2.5.2 Electrical Installation
              1.2.4.3 Insertion Device B
                      1.2.4.3.1 Magnetic Structure
                              1.2.4.3.1.1 Magnetic Material
                              1.2.4.3.1.2 Model Pole
                              1.2.4.3.1.3 Pole Assemblies
                              1.2.4.3.1.4 End Pole Assemblies
                              1.2.4.3.1.5 Backing Beams
                              1.2.4.3.1.6 Magnet Structure Assembly
                              1.2.4.3.1.7 Magnetic Measurements
                      1.2.4.3.2 Support & Drive Systems
                              1.2.4.3.2.1 Support Structure
                              1.2.4.3.2.2 Drive Components
                              1.2.4.3.2.3 Drive System Fabrication
                              1.2.4.3.2.4 Support-Drive Assembly
                      1.2.4.3.3 Vacuum System
                      1.2.4.3.4 Electrical
```

**Table 7-1** continued.

```
                1.2.4.3.5 Installation
                        1.2.4.3.5.1 Mechanical Installation
                        1.2.4.3.5.2 Electrical Installation
        1.2.4.4 Insertion Device C
                1.2.4.4.1 Magnetic Structure
                        1.2.4.4.1.1 Magnetic Material
                        1.2.4.4.1.2 Model Pole
                        1.2.4.4.1.3 Pole Assemblies
                        1.2.4.4.1.4 End Pole Assemblies
                        1.2.4.4.1.5 Backing Beams
                        1.2.4.4.1.6 Magnet Structure Assembly
                        1.2.4.4.1.7 Magnetic Measurements
                1.2.4.4.2 Support & Drive Systems
                        1.2.4.4.2.1 Support Structure
                        1.2.4.4.2.2 Drive Components
                        1.2.4.4.2.3 Drive System Fabrication
                        1.2.4.4.2.4 Support-Drive Assembly
                1.2.4.4.3 Vacuum System
                1.2.4.4.4 Electrical
                1.2.4.4.5 Installation
                        1.2.4.4.5.1 Mechanical Installation
                        1.2.4.4.5.2 Electrical Installation
        1.2.4.5 Insertion Device D
                1.2.4.5.1 Magnetic Structure
                        1.2.4.5.1.1 Magnetic Material
                        1.2.4.5.1.2 Model Pole
                        1.2.4.5.1.3 Pole Assemblies
                        1.2.4.5.1.4 End Pole Assemblies
                        1.2.4.5.1.5 Backing Beams
                        1.2.4.5.1.6 Magnet Structure Assembly
                        1.2.4.5.1.7 Magnetic Measurements
                1.2.4.5.2 Support & Drive Systems
                        1.2.4.5.2.1 Support Structure
                        1.2.4.5.2.2 Drive Components
                        1.2.4.5.2.3 Drive System Fabrication
                        1.2.4.5.2.4 Support-Drive Assembly
                1.2.4.5.3 Vacuum System
                1.2.4.5.4 Electrical
                1.2.4.5.5 Installation
                        1.2.4.5.5.1 Mechanical Installation
                        1.2.4.5.5.2 Electrical Installation
        1.2.4.6 Insertion Device E
                1.2.4.6.1 Magnetic Structure
                        1.2.4.6.1.1 Magnetic Material
                        1.2.4.6.1.2 Model Pole
                        1.2.4.6.1.3 Pole Assemblies
                        1.2.4.6.1.4 End Pole Assemblies
                        1.2.4.6.1.5 Backing Beams
                        1.2.4.6.1.6 Magnet Structure Assembly
                        1.2.4.6.1.7 Magnetic Measurements
                1.2.4.6.2 Support & Drive Systems
                        1.2.4.6.2.1 Support Structure
                        1.2.4.6.2.2 Drive Components
                        1.2.4.6.2.3 Drive System Fabrication
                        1.2.4.6.2.4 Support-Drive Assembly
                1.2.4.6.3 Vacuum System
```

**Table 7-1** continued.

```
                1.2.4.6.4 Electrical
                1.2.4.6.5 Installation
                        1.2.4.6.5.1 Mechanical Installation
                        1.2.4.6.5.2 Electrical Installation

1.2.5 Insertion Device Beamlines
        1.2.5.1 ED&I - Insertion Device Beamlines
                1.2.5.1.1 Insertion Device Beamline A
                1.2.5.1.2 Insertion Device Beamline B
                1.2.5.1.3 Insertion Device Beamline C
                1.2.5.1.4 Insertion Device Beamline D
                1.2.5.1.5 Insertion Device Beamline E
        1.2.5.2 Insertion Device Beamline A
                1.2.5.2.1 Beamline Front End
                        1.2.5.2.1.1 Front End Components
                                1.2.5.2.1.1.1 Fixed Aperture
                                1.2.5.2.1.1.2 Fast Valve
                                1.2.5.2.1.1.3 Front End Vacuum Sys
                                1.2.5.2.1.1.4 Vacuum Pumping Station
                                1.2.5.2.1.1.5 Personnel Safety Shut.
                                1.2.5.2.1.1.6 Front End Photon Shut.
                        1.2.5.2.1.2 Mechanical Installation
                        1.2.5.2.1.3 Front End Controls
                        1.2.5.2.1.4 Electrical Installation
                1.2.5.2.2 Branchline A1
                        1.2.5.2.2.1 Photon Transport Components
                                1.2.5.2.2.1.1 Undulator Pinhole & BPM
                                1.2.5.2.2.1.2 Undulator Spher. Mirror
                                1.2.5.2.2.1.3 Branchline Vac Sys
                                1.2.5.2.2.1.4 Vacuum Pump Stations
                        1.2.5.2.2.2 Monochromator
                        1.2.5.2.2.3 Mechanical Installation
                        1.2.5.2.2.4 Photon Transport Controls
                        1.2.5.2.2.5 Monochromator Controls
                        1.2.5.2.2.6 Electrical Installation
                1.2.5.2.4 Mechanical & Electrical System Integration
        1.2.5.3 Insertion Device Beamline B
                1.2.5.3.1 Beamline Front End
                        1.2.5.3.1.1 Front End Components
                                1.2.5.3.1.1.1 Fixed Aperture
                                1.2.5.3.1.1.2 Fast Valve
                                1.2.5.3.1.1.3 Front End Vacuum Sys
                                1.2.5.3.1.1.4 Vacuum Pumping Station
                                1.2.5.3.1.1.5 Personnel Safety Shut.
                                1.2.5.3.1.1.6 Front End Photon Shut.
                        1.2.5.3.1.2 Mechanical Installation
                        1.2.5.3.1.3 Front End Controls
                        1.2.5.3.1.4 Electrical Installation
                1.2.5.3.2 Branchline B1
                        1.2.5.3.2.1 Photon Transport Components
                                1.2.5.3.2.1.1 Undulator Pinhole & BPM
                                1.2.5.3.2.1.2 Undulator Spher. Mirror
                                1.2.5.3.2.1.3 Branchline Vac Sys
                                1.2.5.3.2.1.4 Vacuum Pump Stations
                        1.2.5.3.2.2 Monochromator
                                1.2.5.3.2.2.1 Entrance Slit
```

**Table 7-1** continued.

```
                                1.2.5.3.2.2.2 Adjustable Mask
                                1.2.5.3.2.2.3 Grating Chamber
                                1.2.5.3.2.2.4 Exit Slit
                                1.2.5.3.2.2.5 Vacuum Pump Stations
                        1.2.5.3.2.3 Mechanical Installation
                        1.2.5.3.2.4 Photon Transport Controls
                        1.2.5.3.2.5 Monochromator Controls
                        1.2.5.3.2.6 Electrical Installation
                1.2.5.3.4 Mechanical & Electrical System Integration
        1.2.5.4 Insertion Device Beamline C
                1.2.5.4.1 Beamline Front End
                        1.2.5.4.1.1 Front End Components
                                1.2.5.4.1.1.1 Fixed Aperture
                                1.2.5.4.1.1.2 Fast Valve
                                1.2.5.4.1.1.3 Front End Vacuum Sys
                                1.2.5.4.1.1.4 Vacuum Pumping Station
                                1.2.5.4.1.1.5 Personnel Safety Shut.
                                1.2.5.4.1.1.6 Front End Photon Shut.
                        1.2.5.4.1.2 Mechanical Installation
                        1.2.5.4.1.3 Front End Controls
                        1.2.5.4.1.4 Electrical Installation
                1.2.5.4.2 Branchline C1
                        1.2.5.4.2.1 Photon Transport Components
                                1.2.5.4.2.1.1 Undulator Pinhole & BPM
                                1.2.5.4.2.1.2 Undulator Spher. Mirror
                                1.2.5.4.2.1.3 Branchline Vac Sys
                                1.2.5.4.2.1.4 Vacuum Pump Stations
                        1.2.5.4.2.2 Monochromator
                                1.2.5.4.2.2.1 Entrance Slit
                                1.2.5.4.2.2.2 Adjustable Mask
                                1.2.5.4.2.2.3 Grating Chamber
                                1.2.5.4.2.2.4 Exit Slit
                                1.2.5.4.2.2.5 Vacuum Pump Stations
                        1.2.5.4.2.3 Mechanical Installation
                        1.2.5.4.2.4 Photon Transport Controls
                        1.2.5.4.2.5 Monochromator Controls
                        1.2.5.4.2.6 Electrical Installation
                1.2.5.4.4 Mechanical & Electrical System Integration
        1.2.5.5 Insertion Device Beamline D
                1.2.5.5.1 Beamline Front End
                        1.2.5.5.1.1 Front End Components
                                1.2.5.5.1.1.1 Fixed Aperture
                                1.2.5.5.1.1.2 Fast Valve
                                1.2.5.5.1.1.3 Front End Vacuum Sys
                                1.2.5.5.1.1.4 Vacuum Pumping Station
                                1.2.5.5.1.1.5 Personnel Safety Shut.
                                1.2.5.5.1.1.6 Front End Photon Shut.
                        1.2.5.5.1.2 Mechanical Installation
                        1.2.5.5.1.3 Front End Controls
                        1.2.5.5.1.4 Electrical Installation
                1.2.5.5.2 Branchline D1
                        1.2.5.5.2.1 Photon Transport Components
                                1.2.5.5.2.1.1 Undulator Pinhole & BPM
                                1.2.5.5.2.1.2 Undulator Spher. Mirror
                                1.2.5.5.2.1.3 Branchline Vac Sys
                                1.2.5.5.2.1.4 Vacuum Pump Stations
```

**Table 7-1** continued.

```
                                1.2.5.5.2.2 Monochromator
                                        1.2.5.5.2.2.1 Entrance Slit
                                        1.2.5.5.2.2.2 Adjustable Mask
                                        1.2.5.5.2.2.3 Grating Chamber
                                        1.2.5.5.2.2.4 Exit Slit
                                        1.2.5.5.2.2.5 Vacuum Pump Stations
                                1.2.5.5.2.3 Mechanical Installation
                                1.2.5.5.2.4 Photon Transport Controls
                                1.2.5.5.2.5 Monochromator Controls
                                1.2.5.5.2.6 Electrical Installation
                        1.2.5.5.4 Mechanical & Electrical System Integration
                1.2.5.6 Insertion Device Beamline E
                        1.2.5.6.1 Beamline Front End
                                1.2.5.6.1.1 Front End Components
                                        1.2.5.6.1.1.1 Fixed Aperture
                                        1.2.5.6.1.1.2 Fast Valve
                                        1.2.5.6.1.1.3 Front End Vacuum Sys
                                        1.2.5.6.1.1.4 Vacuum Pumping Station
                                        1.2.5.6.1.1.5 Personnel Safety Shut.
                                        1.2.5.6.1.1.6 Front End Photon Shut.
                                1.2.5.6.1.2 Mechanical Installation
                                1.2.5.6.1.3 Front End Controls
                                1.2.5.6.1.4 Electrical Installation
                        1.2.5.6.2 Branchline E1
                                1.2.5.6.2.1 Photon Transport Components
                                        1.2.5.6.2.1.1 Photon BPM
                                        1.2.5.6.2.1.2 Spherical Mirrors
                                        1.2.5.6.2.1.3 Branchline Vac Sys
                                        1.2.5.6.2.1.4 Vacuum Pump Stations
                                1.2.5.6.2.2 Monochromator
                                        1.2.5.6.2.2.1 Double Crystal Monochr.
                                        1.2.5.6.2.2.2 SXR Monochromator Sys
                                1.2.5.6.2.3 Mechanical Installation
                                1.2.5.6.2.4 Photon Transport Controls
                                1.2.5.6.2.5 Monochromator Controls
                                1.2.5.6.2.6 Electrical Installation
                        1.2.5.6.4 Mechanical & Electrical System Integration

        1.2.6 Bend Magnet Beamlines
                1.2.6.1 ED&I - Bend Magnet Beamlines
                        1.2.6.1.1 Bend Magnet Beamline A
                        1.2.6.1.2 Bend Magnet Beamline B
                1.2.6.2 Bend Magnet Beamline A
                        1.2.6.2.1 Beamline Front End
                                1.2.6.2.1.1 Front End Components
                                        1.2.6.2.1.1.1 Fixed Aperture
                                        1.2.6.2.1.1.2 Fast Valve
                                        1.2.6.2.1.1.3 Front End Vacuum Sys
                                        1.2.6.2.1.1.4 Vacuum Pumping Station
                                        1.2.6.2.1.1.5 Personnel Safety Shut.
                                        1.2.6.2.1.1.6 Front End Photon Shut.
                                1.2.6.2.1.2 Mechanical Installation
                                1.2.6.2.1.3 Front End Controls
                                1.2.6.2.1.4 Electrical Installation
                        1.2.6.2.3 Mechanical & Electrical System Integration
                1.2.6.3 Bend Magnet Beamline B
```

**Table 7-1** continued.

```
                        1.2.6.3.1 Beamline Front End
                                1.2.6.3.1.1 Front End Components
                                        1.2.6.3.1.1.1 Fixed Aperture
                                        1.2.6.3.1.1.2 Fast Valve
                                        1.2.6.3.1.1.3 Front End Vacuum Sys
                                        1.2.6.3.1.1.4 Vacuum Pumping Station
                                        1.2.6.3.1.1.5 Personnel Safety Shut.
                                        1.2.6.3.1.1.6 Front End Photon Shut.
                                1.2.6.3.1.2 Mechanical Installation
                                1.2.6.3.1.3 Front End Controls
                                1.2.6.3.1.4 Electrical Installation
                        1.2.6.3.3 Mechanical & Electrical System Integration

1.3     Conventional Facilities
        1.3.1 EDI&A - Conventional Facilities
                1.3.1.1 LBL Activities
                        1.3.1.1.1 Title I
                                1.3.1.1.1.1 Engineering & Design
                                1.3.1.1.1.2 Consultants
                                1.3.1.1.1.3 Subcontract Administration
                        1.3.1.1.2 Title II
                                1.3.1.1.2.1 Engineering & Design
                                1.3.1.1.2.2 Consultants
                                1.3.1.1.2.3 Subcontract Administration
                        1.3.1.1.3 Title III
                                1.3.1.1.3.1 Engineering & Design
                                1.3.1.1.3.2 Consultants
                                1.3.1.1.3.3 Subcontract Administration
                                1.3.1.1.3.4 Inspection
                1.3.1.2 Architect-Engineer Activities
                        1.3.1.2.1 Title I
                        1.3.1.2.2 Title II
                        1.3.1.2.3 Title III

        1.3.2 Site Preparation
                1.3.2.1 Demolition & Shielding Block Removal
                        1.3.2.1.1 Walls, floor, roof
                        1.3.2.1.2 Concrete slab removal
                        1.3.2.1.3 Building foundations
                        1.3.2.1.4 Equipment foundations
                        1.3.2.1.5 Cooling Towers & site work
                        1.3.2.1.6 Remove existing shielding blocks
                        1.3.2.1.7 Miscellaneous
                        1.3.2.1.8 Remove 184" Cyclotron
                1.3.2.2 Utilities Removals & Relocations
                        1.3.2.2.1 Remove fire sprinklers
                        1.3.2.2.2 Remove piping
                        1.3.2.2.3 Remove electrical equipment
                        1.3.2.2.4 Relocate buried mechanical utilities
                1.3.2.3 Electrical Substation
                        1.3.2.3.1 Civil & Structural
                        1.3.2.3.2 Ductbanks (Loc P1)
                        1.3.2.3.3 Underground Feeders (15 & 5KV, 480V)
                        1.3.2.3.4 Major Elec Equip (Loc P1)
                        1.3.2.3.5 Splices & Terminations
                        1.3.2.3.6 Temporary feeders
```

**Table 7-1** continued.

```
                1.3.2.3.7 Fire Sprinklers

1.3.3 Equipment Removals
        1.3.3.1 Remove ISAH
        1.3.3.2 Remove Van de Graaf
        1.3.3.3 Misc (Bldgs 9 & 12)
        1.3.3.4 Remove Cobalt Source

1.3.4 Construction
        1.3.4.1 Site Improvements
                1.3.4.1.1 Architectural (none)
                1.3.4.1.2 Civil (none)
                1.3.4.1.3 Electrical
                        1.3.4.1.3.1 Ductbanks (Loc P2)
                        1.3.4.1.3.2 Underground Feeders
                                1.3.4.1.3.2.1 45 Kvolt
                                1.3.4.1.3.2.2 15 Kvolt
                                1.3.4.1.3.2.5 208 Volt
                                1.3.4.1.3.2.6 Spl & Terms
                        1.3.4.1.3.3 Major Elec Equip (Loc P2)
                1.3.4.1.4 Mechanical
        1.3.4.2 Building 6 Addition
                1.3.4.2.1 Architectural
                1.3.4.2.2 Civil/Structural
                        1.3.4.2.2.1 Building
                        1.3.4.2.2.2 Shielding
                1.3.4.2.3 Electrical
                        1.3.4.2.3.1 Electrical power
                                1.3.4.2.3.1.1 Distribution
                                1.3.4.2.3.1.2 Motor Ctrl Cntr
                                1.3.4.2.3.1.3 Standby Gen
                                1.3.4.2.3.1.4 Transformers
                                1.3.4.2.3.1.5 Dist. Pnl Bds
                                1.3.4.2.3.1.6 Circuit Bkrs
                                1.3.4.2.3.1.7 Equip Conns
                                1.3.4.2.3.1.8 480 V Pwr Fdrs
                                1.3.4.2.3.1.9 Cable Trays
                        1.3.4.2.3.2 Lighting & Receptacles
                        1.3.4.2.3.3 Communications
                                1.3.4.2.3.3.1 Telephone
                                1.3.4.2.3.3.2 Public Address
                                1.3.4.2.3.3.3 Comp/Data
                                1.3.4.2.3.3.4 EMCS
                        1.3.4.2.3.4 Fire Alarm
                                1.3.4.2.3.4.1 System & Ckts
                                1.3.4.2.3.4.2 HALON System
                                1.3.4.2.3.4.3 Smoke Detection
                                1.3.4.2.3.4.4 Bldg 7 & 7E
                1.3.4.2.4 Mechanical
                        1.3.4.2.4.1 HVAC
                        1.3.4.2.4.2 Cooling water
                        1.3.4.2.4.3 Fire sprinklers
                        1.3.4.2.4.4 Utilities
                1.3.4.2.5 Environmental Monitoring Station
        1.3.4.3 Building 7 Modifications
                1.3.4.3.1 Architectural (none)
```

**Table 7-1** continued.

```
                    1.3.4.3.2 Civil/Structural
                    1.3.4.3.3 Electrical (none)
                    1.3.4.3.4 Mechanical
          1.3.4.4 Building 80 Alterations
                    1.3.4.4.1 Architectural
                    1.3.4.4.2 Civil/Structural (none)
                    1.3.4.4.3 Electrical
                    1.3.4.4.4 Mechanical

1.4     Contingencies
        1.4.1 Project Management & Administration
        1.4.2 Storage Ring
        1.4.3 Injector System
        1.4.4 Control System
        1.4.5 Insertion Devices
        1.4.6 Insertion Device Beamlines
        1.4.7 Bend Magnet Beamlines
        1.4.8 Conventional Facilities
```

- The building construction will have first priority in order to achieve beneficial occupancy by July 1, 1989.
- The injection system will be completed approximately at the end of FY 1990, so that its commissioning can take place during FY 1991.
- The storage ring will be completed approximately at the end of FY 1991, at which time its commissioning will begin.
- The project will be completed at the end of FY 1992, with the completion of the insertion devices and photon beam lines.

Figure 7-1 shows the project schedule in a bar-chart form. The milestones and critical path are also indicated. Briefly, the critical path requires the completion of the building construction to the point where installation of the injector system can begin. Then, the installation of the storage ring and other systems can follow in sequence. The schedules for the special research facilities and the conventional facilities are also shown in greater detail.

## 7.2 Cost Estimate

The cost estimate for the 1–2 GeV Synchrotron Radiation Source was developed in terms of FY 1986 dollars, then escalated to obtain the total estimated cost (TEC). The estimate includes project management and administration, ED&I, and deliverables. ED&I includes engineering costs up to the group leader level (such as the leader of the magnet group). Project management and administration include the staff above the group leader level (project director, assistant director, project manager, mechanical systems chief, electrical systems chief, etc.)

Table 7-2 gives a craft code and rate table. LBL labor rates are used for the job categories for which LBL employees will be used. Rates for installation (Davis-Bacon labor) were developed with the help of 1986 data from R. S. Means, Lee Saylor, and other published sources.

A bottom-up cost estimate for the Light Source in FY 1986 dollars is given in Table 7-3. Here the costs have been rolled up no higher than Level 3; in some cases, detail is given down to Level 5. The collection of all cost contingencies for the Light Source is summarized in WBS item 1.4. The contingencies were separately considered for Level 3 items during the estimation stage, and the final contingencies reflect this analysis of budget risk.

Table 7-4 is a project cost summary, where the costs are given in FY 1986 dollars, just as they were originally estimated. Including $19.54 million for escalation during the life of the construction project (see below), we arrive at a TEC of $98.70 million in then-year dollars.

To determine the cost in then-year dollars, a funding profile consistent with the schedules shown in the previous section was developed, and escalation was applied to calculate the cost profile in then-year dollars. The escalation rates, given in Table 7-5, come from the Department of Energy guidelines for construction projects, listed in "Departmental Price Change Index," dated August 1985. This table shows how the $79.16 million cost estimate, in FY 1986 dollars, escalates to $98.70 million of then-year dollars over the life of the project.

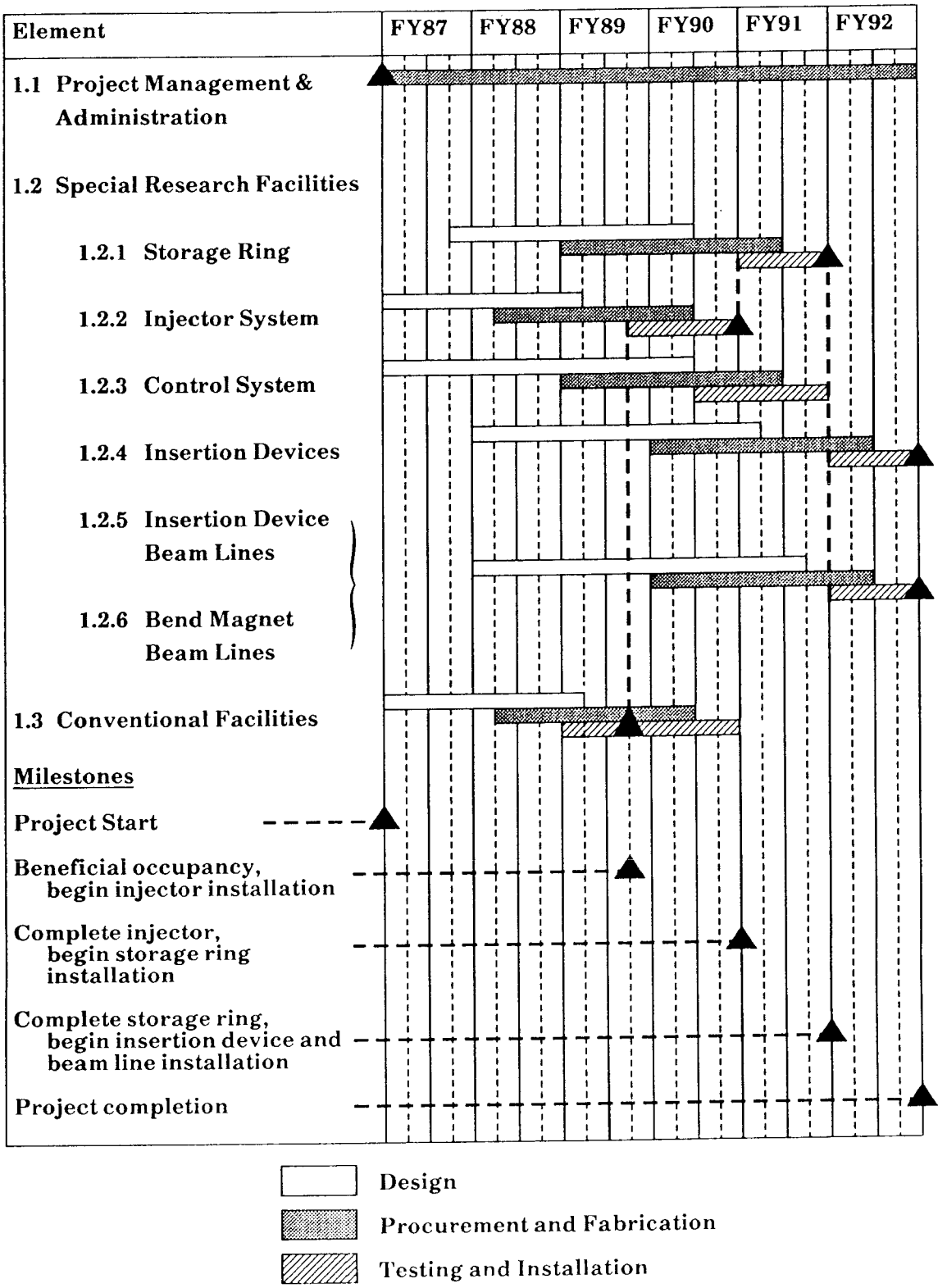


**Fig. 7-1a.** Overall project schedule. The critical path is shown as a dashed line in the upper part of the figure.

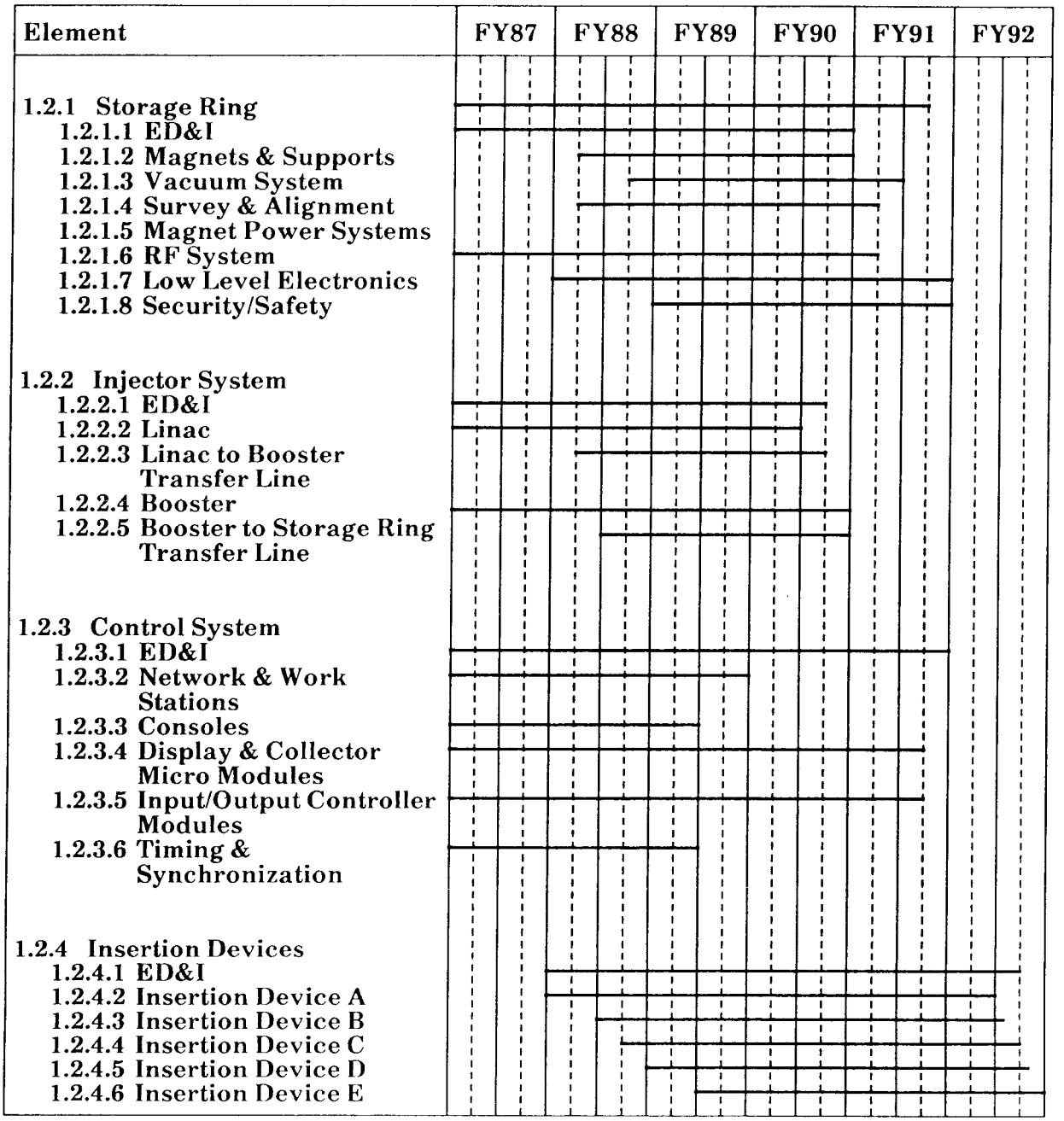


**Fig. 7-1b.** Special research facilities schedule.

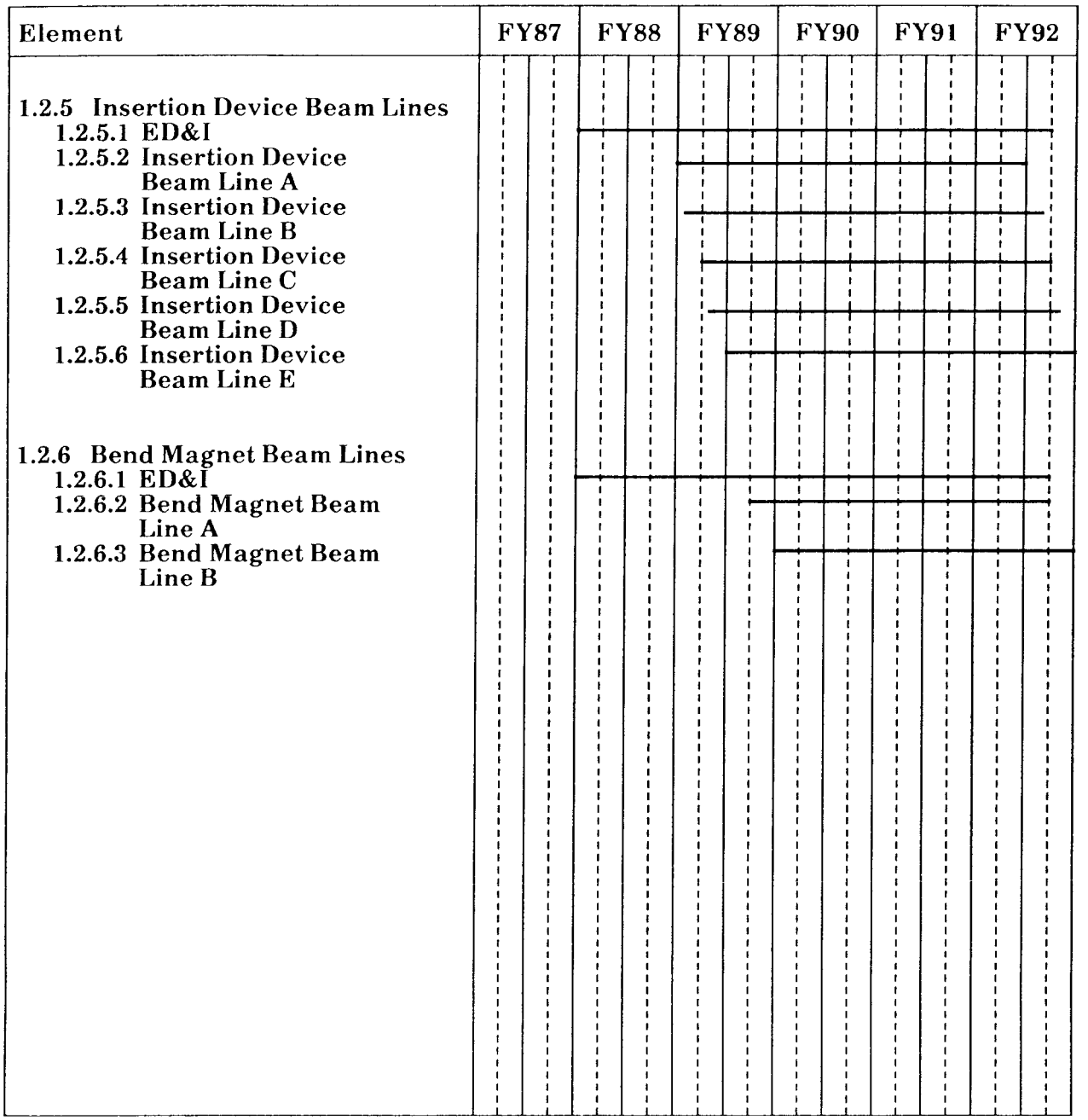


**Fig. 7-1b** continued.

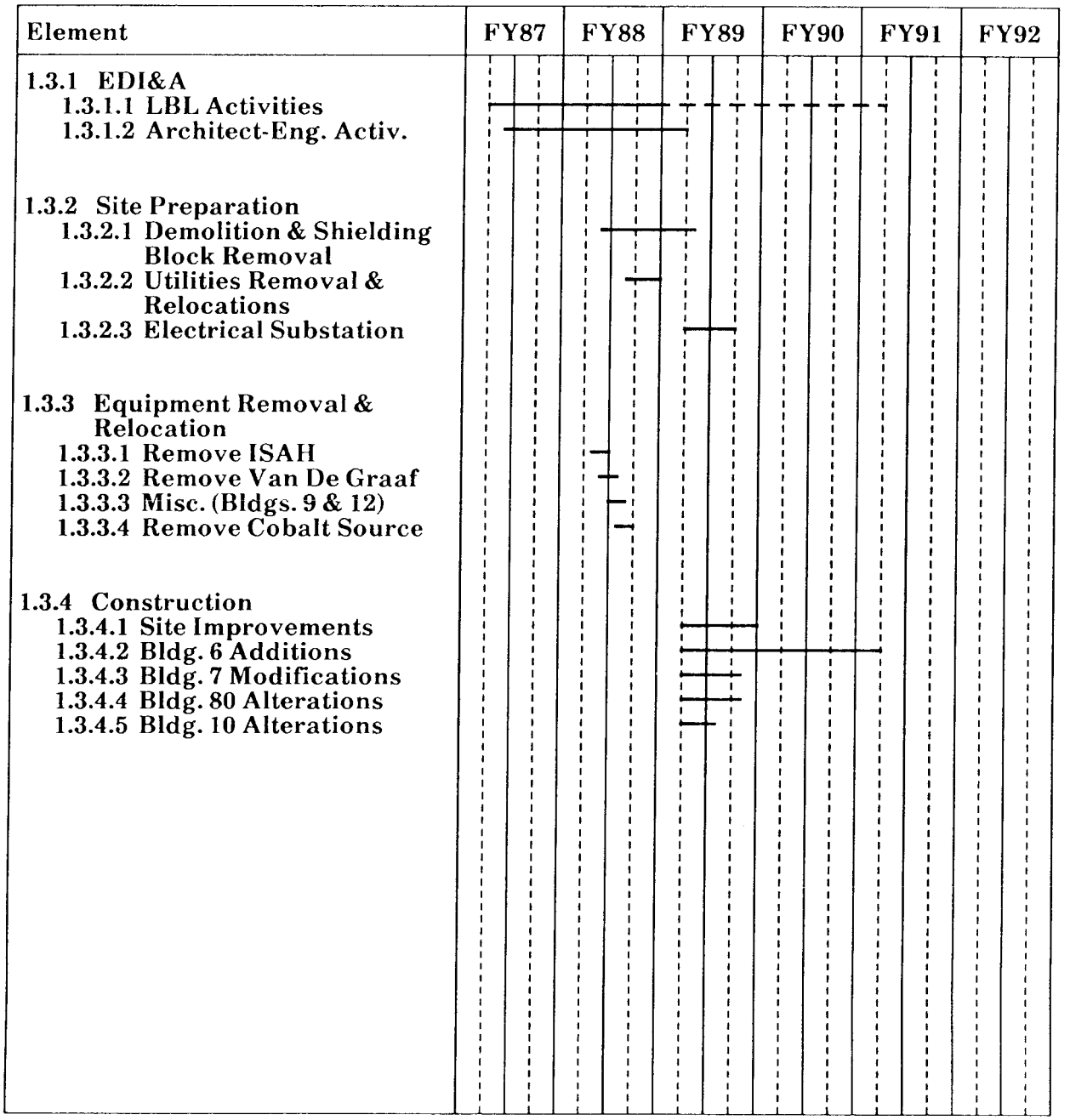


**Fig. 7-1c** Conventional facilities schedule.

**Table 7-2** Craft code and rate table.

| Labor type | Craft code | $/Hr |
|---|---|---|
| **LBL Rates** | | |
| Physicist | PH | 36.25 |
| Administrative Asst. | AA | 36.25 |
| Electronic shops | ES | 26.40 |
| Electronic installation | EI | 26.40 |
| Electronic maintenance | EM | 26.40 |
| Electronic engineering | EE | 40.40 |
| Electronic coordination | EC | 40.40 |
| Electronic drafting | ED | 26.40 |
| Computer programming | CP | 40.40 |
| Instrument Sci Eng | IS | 44.40 |
| Instrument Sci Tech | IT | 28.40 |
| Mechanical shops | MS | 31.60 |
| Mechanical shops nc tool | NC | 47.00 |
| Mechanical technician | MT | 21.20 |
| Mechanical engineer | ME | 42.30 |
| Mechanical designer | MD | 42.30 |
| Mechanical drafting | MF | 42.30 |
| Mechanical technology | MU | 29.80 |
| Plant maint tech | PT | 29.90 |
| Plant laborer | PL | 25.00 |
| Plant carpenter | PC | 32.30 |
| Plant electrician | PE | 32.30 |
| Plant plumber | PPL | 32.30 |
| Plant painter | PP | 32.30 |
| Plant engineering | PEN | 33.70 |
| **Installation** (Davis-Bacon Labor) | | |
| Plumber | IPL | 54.00 |
| Carpenter | ICP | 38.00 |
| Sheet metal worker | ISM | 54.00 |
| Electrician | IEL | 51.00 |
| Painter | IPA | 38.00 |
| Rigger | ICO | 54.00 |
| Laborer | ILB | 30.00 |
| Teamster | ITM | 54.00 |
| Mechanical tech | IMT | 54.00 |
| Electronic tech | IET | 54.00 |
| Supervisor | ISU | 54.00 |

**Table 7-3** Bottom-up cost estimate.

| | | | | | | |
|---|---|---|---|---|---|---|
| 1. | LIGHT SOURCE - TEC (FY 1986 $) | | | | K $ | 79160 |
| 1.1 | PROJECT MANAGEMENT AND ADMINISTRATION | | | | 4033 | |
| 1.1.1 | PROJECT DIRECTION & MANAGEMENT | | | 2313 | | |
| 1.1.2 | PROJECT OFFICE SERVICES | | | 144 | | |
| 1.1.3 | PROCUREMENT & SUBCONTRACTING ADMINISTRATION | | | 288 | | |
| 1.1.4 | PERFORMANCE MEASUREMENT & REPORTING | | | 288 | | |
| 1.1.5 | INCREMENTAL INDIRECTS | | | 1000 | | |
| 1.2 | SPECIAL RESEARCH FACILITIES | | | | 45093 | |
| 1.2.1 | STORAGE RING | | | 18065 | | |
| 1.2.1.1 | ED&I(31%) | | 4276 | | | |
| 1.2.1.2 | MAGNETS & SUPPORTS | | 4993 | | | |
| 1.2.1.2.1 | GRADIENT MAGNETS | 900 | | | | |
| 1.2.1.2.2 | QUADRUPOLES | 2203 | | | | |
| 1.2.1.2.3 | SEXTUPOLES | 716 | | | | |
| 1.2.1.2.4 | SKEW QUADRUPOLES | 0 | | | | |
| 1.2.1.2.5 | OCTUPOLES | 0 | | | | |
| 1.2.1.2.6 | STEERING MAGNETS | 400 | | | | |
| 1.2.1.2.7 | INJECTION MAGNETS | 200 | | | | |
| 1.2.1.2.8 | STANDS & SUPPORTS | 247 | | | | |
| 1.2.1.2.9 | GIRDER ASSEMBLY | 220 | | | | |
| 1.2.1.2.10 | INSTALLATION | 108 | | | | |
| 1.2.1.3 | VACUUM SYSTEM | | 2554 | | | |
| 1.2.1.3.1 | VACUUM CHAMBERS | 754 | | | | |
| 1.2.1.3.2 | PUMPING SYSTEM | 1292 | | | | |
| 1.2.1.3.3 | ASSEMBLY & MISCELLANEOUS | 429 | | | | |
| 1.2.1.3.4 | INSTALLATION | 78 | | | | |
| 1.2.1.4 | SURVEY & ALIGNMENT | | 277 | | | |
| 1.2.1.4.1 | MONUMENTS | 38 | | | | |
| 1.2.1.4.2 | LIQUID LEVEL | 51 | | | | |
| 1.2.1.4.3 | SURVEY INSTRUMENTS | 40 | | | | |
| 1.2.1.4.4 | ALIGNMENT FIXTURES | 24 | | | | |
| 1.2.1.4.5 | RING SURVEY/ALIGN | 124 | | | | |
| 1.2.1.5 | MAGNET POWER SYSTEMS | | 1728 | | | |
| 1.2.1.5.1 | GRADIENT MAGNET POWER SYSTEM | 308 | | | | |
| 1.2.1.5.2 | QUADRUPOLE POWER SYSTEM | 289 | | | | |
| 1.2.1.5.3 | SEXTUPOLE POWER SYSTEM | 38 | | | | |
| 1.2.1.5.4 | SKEW QUADRUPOLES | 9 | | | | |
| 1.2.1.5.5 | OCTUPOLES | 0 | | | | |
| 1.2.1.5.6 | STEERING MAGNET POWER SYSTEM | 583 | | | | |
| 1.2.1.5.7 | INJECTION POWER SYSTEMS | 84 | | | | |
| 1.2.1.5.8 | DC DISTRIBUTION | 251 | | | | |
| 1.2.1.5.9 | INSTALLATION | 166 | | | | |

**Table 7-3** continued.

| | | | | |
|---|---|---|---|---|
| 1.2.1.6 | RF SYSTEM | | 1265 | |
| 1.2.1.6.1 | KLYSTRON SYSTEM | 221 | | |
| 1.2.1.6.2 | WAVEGUIDE EQUIPMENT | 298 | | |
| 1.2.1.6.3 | LOW LEVEL RF COMPONENTS | 24 | | |
| 1.2.1.6.4 | CAVITY | 199 | | |
| 1.2.1.6.5 | KLYSTRON COOLING | 35 | | |
| 1.2.1.6.6 | HIGH VOLTAGE EQUIPMENT | 74 | | |
| 1.2.1.6.7 | MAIN POWER SUPPLY | 234 | | |
| 1.2.1.6.8 | AUXILIARY EQUIPMENT | 100 | | |
| 1.2.1.6.9 | CONTROL SYSTEM | 80 | | |
| 1.2.1.7 | INSTRUMENTATION/LOW LEVEL ELECTRONICS | | 2598 | |
| 1.2.1.7.1 | BEAM DIAGNOSTICS | 1325 | | |
| 1.2.1.7.2 | BEAM DAMPING | 283 | | |
| 1.2.1.7.3 | CONTROL ROOM ELECTRONICS | 308 | | |
| 1.2.1.7.4 | COMMUNICATIONS | 50 | | |
| 1.2.1.7.5 | VACUUM MONITORING & PUMP ELECT. | 499 | | |
| 1.2.1.7.6 | TIMING | 116 | | |
| 1.2.1.7.7 | BEAMLINE STEERING CONTROL | 17 | | |
| 1.2.1.8 | SECURITY/SAFETY | | 374 | |
| 1.2.2 | INJECTOR SYSTEM | | | 8897 |
| 1.2.2.1 | ED&I(28%) | | 1946 | |
| 1.2.2.2 | LINAC | | 1730 | |
| 1.2.2.3 | LINAC TO BOOSTER TRANSFER LINE | | 359 | |
| 1.2.2.4 | BOOSTER | | 4212 | |
| 1.2.2.4.1 | MAGNETS & SUPPORTS | 2128 | | |
| 1.2.2.4.2 | VACUUM SYSTEM | 394 | | |
| 1.2.2.4.3 | SURVEY & ALIGNMENT | 57 | | |
| 1.2.2.4.4 | MAGNET POWER SYSTEM | 561 | | |
| 1.2.2.4.5 | RF SYSTEM | 510 | | |
| 1.2.2.4.6 | INSTRUMENTATION/LOW LEVEL ELECTRONIC | 488 | | |
| 1.2.2.4.7 | SECURITY/SAFETY | 73 | | |
| 1.2.2.5 | BOOSTER/STORAGE RING BEAMLINE | | 649 | |
| 1.2.3 | CONTROL SYSTEM | | | 3500 |
| 1.2.3.1 | ED&I(30%) | | 808 | |
| 1.2.3.2 | NETWORK & WORK STATIONS | | 287 | |
| 1.2.3.3 | CONSOLES | | 347 | |
| 1.2.3.4 | DISPLAY & COLLECTOR MICRO MODULES | | 1213 | |
| 1.2.3.5 | INPUT/OUTPUT CONTROLLER MODULES | | 746 | |
| 1.2.3.6 | COMPUTER TIMING & SYNCHRONIZATION | | 100 | |
| 1.2.4 | INSERTION DEVICES | | | 4506 |

**Table 7-3** continued.

| | | | | |
|---|---|---|---|---|
| 1.2.4.1 | ED&I(33%) | 1118 | | |
| 1.2.4.2 | INSERTION DEVICE A | 558 | | |
| 1.2.4.3 | INSERTION DEVICE B | 644 | | |
| 1.2.4.4 | INSERTION DEVICE C | 777 | | |
| 1.2.4.5 | INSERTION DEVICE D | 825 | | |
| 1.2.4.6 | INSERTION DEVICE E | 584 | | |
| 1.2.5 | INSERTION DEVICE BEAMLINES | | 9110 | |
| 1.2.5.1 | ED&I(33%) | 2260 | | |
| 1.2.5.2 | INSERTION DEVICE BEAMLINE A | 1390 | | |
| 1.2.5.3 | INSERTION DEVICE BEAMLINE B | 1314 | | |
| 1.2.5.4 | INSERTION DEVICE BEAMLINE C | 1314 | | |
| 1.2.5.5 | INSERTION DEVICE BEAMLINE D | 1314 | | |
| 1.2.5.6 | INSERTION DEVICE BEAMLINE E | 1517 | | |
| 1.2.6 | BEND MAGNET BEAMLINES | | 1014 | |
| 1.2.6.1 | ED&I(33%) | 252 | | |
| 1.2.6.2 | BEND MAGNET BEAMLINE A | 381 | | |
| 1.2.6.3 | BEND MAGNET BEAMLINE B | 381 | | |
| 1.3 | CONVENTIONAL FACILITIES | | | 15365 |
| 1.3.1 | ED&I(15%) | | 2004 | |
| 1.3.1.1 | LBL ACTIVITIES | 1022 | | |
| 1.3.1.2 | ARCHITECT-ENGINEERING ACTIVITIES | 982 | | |
| 1.3.2 | SITE PREPARATION | | 4879 | |
| 1.3.2.1 | DEMOLITION & SHIELDING BLOCK REMOVAL | 2524 | | |
| 1.3.2.2 | UTILITIES REMOVALS & RELOCATIONS | 855 | | |
| 1.3.2.3 | ELECTRICAL SUBSTATION | 1500 | | |
| 1.3.3 | EQUIPMENT REMOVALS & RELOCATION | | 323 | |
| 1.3.3.1 | REMOVE ISAH | 187 | | |
| 1.3.3.2 | REMOVE VAN DE GRAAF | 63 | | |
| 1.3.3.3 | MISC (BUILDINGS 9 & 12) | 56 | | |
| 1.3.3.4 | REMOVE COBALT SOURCE | 17 | | |
| 1.3.4 | CONSTRUCTION | | 8159 | |
| 1.3.4.1 | SITE IMPROVEMENTS | 857 | | |
| 1.3.4.2 | BUILDING 6 ADDITION | 6869 | | |
| 1.3.4.3 | BUILDING 7 MODIFICATIONS | 187 | | |
| 1.3.4.4 | BUILDING 80 ALTERATIONS | 230 | | |
| 1.3.4.5 | BUILDING 10 ALTERATIONS | 16 | | |

**Table 7-3** continued.

| | | | |
|---|---|---|---|
| 1.4 | CONTINGENCIES | | 14669 |
| 1.4.1 | PROJECT MANAGEMENT & ADMINISTRATION(8%) | 323 | |
| 1.4.2 | STORAGE RING(25%) | 4516 | |
| 1.4.3 | INJECTOR SYSTEM(24%) | 2113 | |
| 1.4.4 | CONTROL SYSTEM(24%) | 840 | |
| 1.4.5 | INSERTION DEVICES(26%) | 1172 | |
| 1.4.6 | INSERTION DEVICE BEAMLINES(26%) | 2369 | |
| 1.4.7 | BEND MAGNET BEAMLINES(26%) | 264 | |
| 1.4.8 | CONVENTIONAL FACILITIES(20%) | 3073 | |

**Table 7-4** Project cost summary. All figures are in FY 1986 dollars, except for the total estimated cost, which is given in then-year dollars.

| | | | |
|---|---|---|---|
| 1 Light Source Project (TEC, then year $) | | | $98.70 M |
| 1.1 Project Management and Administration | | 4.03 | |
| 1.2 Special Research Facilities | | 45.09 | |
| 1.2.1 Storage Ring | 18.06 | | |
| 1.2.2 Injector System | 8.90 | | |
| 1.2.3 Control System | 3.50 | | |
| 1.2.4 Insertion Devices | 4.51 | | |
| 1.2.5 Ins. Dev. Beamlines | 9.11 | | |
| 1.2.6 Bend Magnet Beamline | 1.01 | | |
| 1.3 Convention Facilities | | 15.37 | |
| 1.3.1 ED&I | 2.01 | | |
| 1.3.2 Site Preparation | 4.88 | | |
| 1.3.3 Equipment Removals and Relocation | .32 | | |
| 1.3.4 Construction | 8.16 | | |
| 1.4 Contingencies | | 14.67 | |
| Escalation | | 19.54 | |

**Table 7-5** Escalation schedule.

| Year | FY86 | FY87 | FY88 | FY89 | FY90 | FY91 | FY92 | Total |
|---|---|---|---|---|---|---|---|---|
| FY86 $ | 0.00 | 1.43 | 9.63 | 20.20 | 22.78 | 17.55 | 7.57 | $79.16 M |
| Inflation (%) | 0.0 | 5.0 | 5.8 | 6.1 | 6.3 | 6.4 | 6.6 | |
| Factor | 1.000 | 1.050 | 1.111 | 1.179 | 1.253 | 1.333 | 1.421 | |
| Then-year $ | 0.00 | 1.50 | 10.70 | 23.81 | 28.54 | 23.39 | 10.76 | $98.70 M |

Table 7-6 is the project cost summary in terms of then-year dollars. Here, escalation does not appear explicitly as a separate line, because escalation has already been absorbed into each of the cost categories.

**Table 7.6** Project cost summary in then-year dollars.

| | | | |
|---|---|---|---|
| 1 Light Source Project (TEC) | | | $98.70 M |
| 1.1 Project Management and Administration | | 4.91 | |
| 1.2 Special Research Facilities | | 56.77 | |
| 1.2.1 Storage Ring | 22.65 | | |
| 1.2.2 Injector System | 10.44 | | |
| 1.2.3 Control System | 4.29 | | |
| 1.2.4 Insertion Devices | 5.89 | | |
| 1.2.5 Ins. Dev. Beamlines | 12.15 | | |
| 1.2.6 Bend Magnet Beamline | 1.35 | | |
| 1.3 Convention Facilities | | 18.24 | |
| 1.3.1 ED&I | 2.26 | | |
| 1.3.2 Site Preparation | 5.69 | | |
| 1.3.3 Equipment Removals and Relocation | .35 | | |
| 1.3.4 Construction | 9.94 | | |
| 1.4 Contingencies | | 18.78 | |

Figure 7-2 shows the integrated obligation and cost profiles for the Light Source project, in graphical form. The obligations and costs are in then-year dollars.

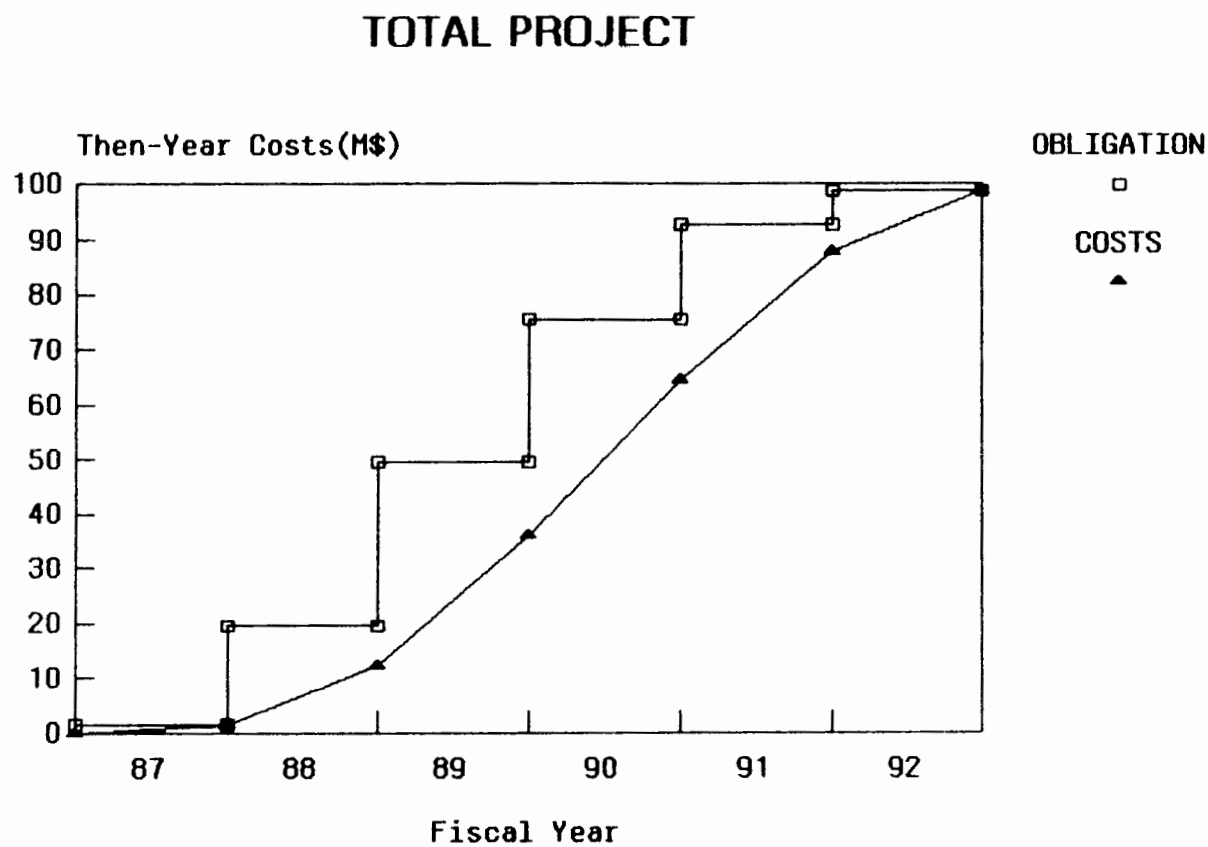


**Fig. 7-2.** Integrated obligation and cost schedule.

Table 7-7 is a cost schedule by major categories. This table breaks down the costs for each fiscal year into major cost categories, showing the profiles of costs for major systems.

**Table 7-7** Cost schedule by major categories, in millions of then-year dollars.

| Year | FY87 | FY88 | FY89 | FY90 | FY91 | FY92 | Totals |
|---|---|---|---|---|---|---|---|
| Project Administration | 0.08 | 1.12 | 1.19 | 1.26 | 0.92 | 0.34 | 4.91 |
| Storage Ring | 0.32 | 1.38 | 3.70 | 9.57 | 7.45 | 0.23 | 22.65 |
| Injector System | 0.40 | 2.65 | 4.88 | 2.33 | 0.18 | | 10.44 |
| Control System | 0.20 | 0.50 | 1.00 | 1.50 | 0.99 | 0.10 | 4.29 |
| Insertion Devices | | 0.20 | 0.51 | 1.59 | 2.10 | 1.49 | 5.89 |
| Beamlines | | 0.21 | 0.69 | 2.04 | 6.01 | 4.55 | 13.50 |
| Conventional Facilities | 0.40 | 3.85 | 8.14 | 4.68 | 1.17 | | 18.24 |
| Contingency | 0.10 | 0.79 | 3.70 | 5.57 | 4.57 | 4.05 | 18.78 |
| Totals by year | 1.50 | 10.70 | 23.81 | 28.54 | 23.39 | 10.76 | 98.70 |

# Appendix A
## Parameter List

Here we present a list of major accelerator physics parameters for the 1–2 GeV Synchrotron Radiation Source.

### 1. Storage Ring Performance Parameters

(All parameters at nominal energy unless otherwise noted)

| | |
|---|---|
| Nominal energy (GeV) | 1.5 |
| Maximum circulating current, multibunch (mA) | 400 |
| Number of stored electrons, multibunch | $1.64 \times 10^{12}$ |
| Maximum circulating current, single bunch (mA) | 7.6 |
| Number of stored electrons, single bunch | $3.12 \times 10^{10}$ |
| Natural emittance (m-rad) | $4.08 \times 10^{-9}$ |
| Natural energy spread, rms | $7.1 \times 10^{-4}$ |
| Energy spread, rms, at max. current | |
| Multibunch | $0.8 \times 10^{-3}$ |
| Single bunch | $1.4 \times 10^{-3}$ |
| Bunch length, rms, natural (mm) | 3.7 |
| Bunch length, 2×rms, natural (ps) | 24 |
| Bunch length, 2×rms, maximum current (ps) | |
| Multibunch | 28 |
| Single bunch | 47 |
| Peak energy (GeV) | 1.9 |
| Beam lifetime, half-life | |
| Gas scattering, 20-mm vertical gap, 1 nTorr $N_2$ (hr) | 30 |
| Touschek, maximum current | |
| Multibunch (hr) | 18.5 |
| Single bunch (hr) | 8.4 |
| Filling time | |
| Multibunch, to 400 mA (min) | 2.1 |
| Single bunch, per 7.6 mA bunch (s) | 16 |

## 2. Storage Ring Lattice and Orbit Parameters

| | |
|---|---|
| Circumference (m) | 196.8 |
| Orbital period (ns) | 656.4 |
| Harmonic number | 328 |
| Radio frequency (MHz) | 499.654 |
| Number of superperiods | 12 |
| Insertion straight length (m) | 6.75 |
| Length available for insertion device (m) | 5.0 |
| Mean radius (m) | 31.32 |
| Bending field (T) | 1.248 |
| Bending radius (m) | 4.0107 |
| Injection energy (GeV) | 1.5 |
| Injection field (T) | 1.248 |
| Number of dipoles per superperiod | 3 |
| Number of quadrupoles per superperiod | 6 |
| Magnetic lengths in 1/2 superperiod (m), | |
| Q = quad, O = drift, B = bend | |
| - OOO (1/2) | 3.375 |
| - Q1 | 0.35 |
| - O1 | 0.425 |
| - Q2 | 0.20 |
| - O1 | 0.425 |
| - B | 0.7 |
| - O2 | 0.3 |
| - SD | 0.2 |
| - O2 | 0.3 |
| - QF1 | 0.5 |
| - O3 | 0.1 |
| - SF | 0.2 |
| - O4 | 0.775 |
| - B (1/2) | 0.35 |
| Betatron tunes | |
| Horizontal | 14.28 |
| Vertical | 8.18 |
| Synchrotron tune | 0.0082 |
| Natural chromaticities | |
| Horizontal | −24.1 |
| Vertical | −28.5 |
| Maximum beta functions (m) | |
| Horizontal | 12.0 |
| Vertical | 22.6 |
| Beta functions at insertion symmetry points (m) | |
| Horizontal | 11.0 |
| Vertical | 4.0 |
| Maximum dispersion (m) | 0.24 |

| | |
|---|---|
| Beam size at insertion symmetry point, rms ($\mu$m) | |
| Horizontal | 201 |
| Vertical, 10% emittance ratio | 38 |
| Momentum compaction | $1.43 \times 10^{-3}$ |
| Damping partition | |
| Horizontal | 1.348 |
| Vertical | 1.000 |
| Longitudinal | 1.652 |
| Damping times (ms) | |
| Horizontal | 13.09 |
| Vertical | 17.64 |
| Longitudinal | 10.68 |
| Radiation loss per turn, dipoles (keV) | 111.7 |
| Radiation loss, 4 undulators, 1 wiggler (keV) | 37.6 |
| Number of sextupole families | 2 |
| Beam elevation above floor (m) | 1.4 |

**3. Storage Ring Tolerances, rms**

| | |
|---|---|
| Quadrupole misalignments (mm) | 0.15 |
| Random dipole field error, $\Delta B/B$ | $1 \times 10^{-3}$ |
| Random dipole roll angle error (mrad) | 0.5 |
| Maximum uncorrected closed orbit, rms (mm) | |
| Horizontal | 5 |
| Vertical | 14 |
| Dipole field stability | $5 \times 10^{-5}$ |
| Quadrupole field stability | $1 \times 10^{-4}$ |
| Random quadrupole strength error, $\Delta k/k$ | $1 \times 10^{-3}$ |
| Sextupole field stability | $1 \times 10^{-3}$ |
| Correction dipole field stability | $5 \times 10^{-4}$ |

**4. Storage Ring Hardware**

| | |
|---|---|
| Magnets and power supplies | |
| Dipoles, combined function | |
| Number | 36 |
| Magnetic length (m) | 0.7 |
| Bending radius (m) | 4.0107 |
| Dipole field (T) | |
| At 1.5 GeV | 1.248 |
| At 1.9 GeV | 1.580 |
| Field gradient ($m^{-2}$) | −1.0 |
| Beam stay clear (mm) | |
| Horizontal | ±12.5 |
| Vertical | ±20.0 |
| Ramp time from 1.5 to 1.9 GeV (min) | 2.0 |
| Type A quads | |

| | |
|---|---|
| Number | 24 |
| No. of families, QF1 | 1 |
| Magnetic length (m) | 0.5 |
| Max. gradient (T/m) | 17.0 |
| Beam stay clear, radius (mm) | 30 |
| Type B quads | |
| Number | 24 |
| No. of families, Q1 | 24 |
| Magnetic length (m) | 0.35 |
| Max. gradient (T/m) | 17.0 |
| Beam stay clear, radius (mm) | 30.0 |
| Type C quads | |
| Number | 24 |
| No. of families, Q2 | 24 |
| Magnetic length (m) | 0.2 |
| Max. gradient (T/m) | 17.0 |
| Beam stay clear, radius (mm) | 30.0 |
| Sextupoles | |
| Number | 48 |
| No. of families, SF, SD | 2 |
| No. in family SF | 24 |
| No. in family SD | 24 |
| Magnetic length (m) | 0.20 |
| Max. gradient ($T/m^2$) | 500.0 |
| Beam stay clear, radius (mm) | 30.0 |
| Dipole correcting field (T) | |
| Horizontal | 0.07 |
| Vertical | 0.07 |
| Skew quadrupoles | |
| Number of circuits | 4 |
| Magnetic length (m) | 0.2 |
| Max. gradient (T/m) | 3.0 |
| Beam stay clear, radius (mm) | 30.0 |
| Correction dipoles | |
| Number of discrete correctors, combined vertical and horizontal | 48 |
| Number of independent power supplies, 96 horizontal, 72 vertical | 168 |
| Magnetic length (m) | 0.2 |
| Field (T) | 0.07 |
| RF system | |
| Number of cavities | 2 |
| Frequency (MHz) | 499.654 |
| Harmonic number | 328 |
| Peak effective voltage, $VT$ (MV) | 1.5 |
| Transit time factor, $T$ | 0.683 |

| | |
|---|---|
| Quality factor, loaded $Q$ | 22,000 |
| Effective shunt impedance, $ZT^2L$ (MΩ) | 16 |
| Fundamental-mode cavity dissipation (kW) | 140 |
| Synchrotron radiation power, dipoles (kW) | 45.0 |
| Synchrotron radiation power, 4 und., 1 wig. (kW) | 20.0 |
| Parasitic mode losses (kW) | 2.0 |
| Waveguide and other losses, 10% (kW) | 20 |
| Total transmitter power available (kW) | 300 |
| Injection hardware | |
| Injection septa | |
| Thin septum | |
| Number | 1 |
| Length (m) | 0.6 |
| Bending angle (deg) | 2.5 |
| Field (T) | 0.364 |
| Thick septum | |
| Number | 1 |
| Length (m) | 1.0 |
| Bending angle (deg) | 8.0 |
| Field (T) | 0.698 |
| Bump magnets | |
| Number | 4 |
| Length (m) | 0.7 |
| Deflection angle (mrad) | 15.0 |
| Field (T) | 0.104 |
| Half-sine-wave pulse width ($\mu$s) | 4.0 |
| Beam Diagnostics | |
| Beam-position monitors | |
| Number | 96 |
| Accuracy (mm) | 0.03 |
| Sensitivity (mm) | 0.02 |
| No. of traveling-wave electrodes | 2 |
| No. of beam-current transformer | 1 |
| Optical monitoring | |
| Number in vacuum (for commissioning) | 6 |
| Station outside vacuum | 1 |
| Beam damping systems | 3 |
| (2 transverse and 1 longitudinal) | |

## 5. Booster Performance Parameters

| | |
|---|---|
| Nominal and peak energy (GeV) | 1.5 |
| Injection energy (MeV) | 50 |
| Cycle rate (Hz) | 1 |
| Maximum circulating current, multibunch (mA) | 20 |
| Number of stored electrons, multibunch | $3.2 \times 10^{10}$ |

| | |
|---|---|
| Extracted current, multibunch (mA) | 16 |
| Injected beam emittance (m-rad) | $1.1 \times 10^{-6}$ |
| Longitudinal bunch area, 50 MeV, $6\pi\sigma_E\sigma_\tau$ (eV-s) | $3.9 \times 10^{-4}$ |
| Natural emittance at 1.5 GeV (m-rad) | $1.45 \times 10^{-7}$ |
| Energy spread, rms, at 1.5 GeV | $6.3 \times 10^{-4}$ |
| Bunch length, rms, natural, at 1.5 GeV (mm) | 30.5 |

**6. Booster Lattice and Orbit Parameters**

| | |
|---|---|
| Circumference (m) | 75.0 |
| Orbital period (ns) | 250.2 |
| Harmonic number | 125 |
| Radio frequency (MHz) | 499.654 |
| Lattice structure: FODO with missing dipole cells | |
| Number of superperiods | 4 |
| Complete FODO cells per superperiod | 3 |
| Missing magnet cells per superperiod | 1 |
| Mean radius (m) | 11.94 |
| Bending field (T) | 1.198 |
| Bending radius (m) | 4.178 |
| Magnetic lengths in complete FODO cell (m), | |
| Q = quad, O = drift, B = bend | |
| - QD (1/2) | 0.15 |
| - OD | 0.475 |
| - BB | 1.094 |
| - OF | 0.475 |
| - QF | 0.3 |
| - OF | 0.475 |
| - BB | 1.094 |
| - OD | 0.475 |
| - QD (1/2) | 0.15 |
| Betatron tunes | |
| Horizontal | 6.26 |
| Vertical | 2.79 |
| Synchrotron tune | |
| At injection | $6.4 \times 10^{-2}$ |
| At extraction | $1.1 \times 10^{-2}$ |
| Natural chromaticities | |
| Horizontal | −10.51 |
| Vertical | −4.81 |
| Beta functions (m) | |
| Maximum horizontal | 11.6 |
| Minimum horizontal | 0.51 |
| Maximum vertical | 11.6 |
| Minimum vertical | 1.76 |
| Maximum dispersion (m) | 1.16 |

| | |
|---|---|
| Momentum compaction | 0.041 |
| Damping partition | |
| Horizontal | 1.006 |
| Vertical | 1.000 |
| Longitudinal | 1.994 |
| Number of sextupole families | 2 |
| Beam elevation above floor (m) | 1.4 |

**7. Booster Tolerances, rms**

| | |
|---|---|
| Quadrupole misalignments (mm) | 0.15 |
| Quadrupole tracking accuracy | $1 \times 10^{-3}$ |
| Sextupole tracking accuracy | $5 \times 10^{-3}$ |

**8. Booster Details**

| | |
|---|---|
| Magnets and power supplies | |
| Dipoles | |
| Number | 24 |
| Magnetic length (m) | 1.094 |
| Bending radius (m) | 4.1778 |
| Dipole field, 1.5 GeV (T) | 1.198 |
| Beam stay clear (mm) | |
| Horizontal | ±30.0 |
| Vertical | ±17.6 |
| Quadrupoles | |
| Number | 32 |
| No. of families, QF, QD | 2 |
| No. in family QF | 16 |
| No. in family QD | 16 |
| Magnetic length (m) | 0.3 |
| Max. gradient (T/m) | 15.0 |
| Beam stay clear, radius (mm) | 30.0 |
| Sextupoles | |
| Number | 24 |
| No. of families, SF, SD | 2 |
| No. in family SF | 8 |
| No. in family SD | 16 |
| Magnetic length (m) | 0.10 |
| Max. gradient ($T/m^2$) | 50.0 |
| Beam stay clear, radius (mm) | 30.0 |
| Correction dipoles, combined horizontal/vertical | |
| Number | 28 |
| No. of independent power supplies | 56 |
| Magnetic length (m) | 0.15 |
| Field (T) | 0.068 |
| RF system | |

| | |
|---|---|
| Number of cavities | 1 |
| Frequency (MHz) | 499.654 |
| Harmonic number | 125 |
| Peak effective voltage, $VT$ (MV) | 0.250 |
| Transit time factor, $T$ | 0.683 |
| Quality factor, loaded $Q$ | 22,000 |
| Effective shunt impedance, $ZT^2L$ (MΩ) | 8.0 |
| Fundamental-mode cavity dissipation (kW) | 7.8 |
| Synchrotron radiation power (kW) | 2.14 |
| Waveguide losses (kW) | 1.0 |
| Total transmitter power available (kW) | 30.0 |
| Injection equipment | |
| Septum magnet | |
| Number | 1 |
| Length (m) | 0.35 |
| Bending angle (deg) | 10.0 |
| Field (T) | 0.0835 |
| Gap (mm) | 40.0 |
| Full-aperture kicker | |
| Number | 1 |
| Length (m) | 0.5 |
| Deflection angle (deg) | 4.5 |
| Field (T) | 0.0262 |
| Gap (mm) | 28 |
| Fall time (ns) | 100 |
| Extraction equipment | |
| Thin septum | |
| Number | 1 |
| Length (m) | 0.6 |
| Bend angle (deg) | 2.5 |
| Field (T) | 0.364 |
| Gap (mm) | 15.0 |
| Thick septum | |
| Number | 1 |
| Length (m) | 0.6 |
| Bend angle (deg) | 4.0 |
| Field (T) | 0.582 |
| Gap (mm) | 15.0 |
| Kicker magnet | |
| Number | 1 |
| Length (m) | 1.0 |
| Deflection angle (mrad) | 10.0 |
| Field (T) | 0.05 |
| Gap (mm) | 28 |
| Beam Diagnostics | |
| Beam-position monitors | |

| | |
|---|---|
| Number | 32 |
| Accuracy (mm) | 0.2 |
| Sensitivity (mm) | 0.2 |
| No. of traveling-wave electrodes | 2 |
| No. of beam-current transformer | 1 |
| Optical monitoring | |
| Number in vacuum (for commissioning) | 4 |

**9. Linac**

| | |
|---|---|
| Gun voltage (kV) | 120 |
| Gun current (A) | |
| Multibunch | 1 |
| Few bunch | 8 |
| Chopper frequency (MHz) | 499.654 |
| Buncher frequency (MHz) | 2997.9 |
| Linac beam energy, nominal (MeV) | 50 |
| Power sources | |
| Number of klystrons | 2 |
| Power per klystron (MW) | 35 |
| Traveling-wave linac structure | $2\pi/3$ |
| Linac frequency (MHz) | 2997.9 |
| Cycle rate (Hz) | |
| Maximum | 10 |
| Nominal | 1 |
| Length of linac beam pulse (ns) | |
| Single bunch | 0.5 |
| Multibunch | 100 |
| Emittance, 50 MeV, rms (m-rad) | $1.1 \times 10^{-6}$ |
| Energy spread, 50 MeV, rms | $3.0 \times 10^{-3}$ |
| Linac length, total, two sections (m) | 4 |
| Power required | |
| Peak (MW) | 49 |
| Average, 10 Hz (kW) | 1 |
| Beam diagnostics (includes LTB transfer line) | |
| Beam-position monitors | 3 |
| Intensity monitors | 2 |
| Viewing screens | 3 |
| Fully adjustable collimator | 1 |

**10. Linac-to-Booster (LTB) Transfer Line**

| | |
|---|---|
| Magnets | |
| Dipoles (one has a current reversing switch) | |
| Number | 2 |
| Magnetic length (m) | 0.5 |
| Field (T) | 0.19 |

| | |
|---|---|
| Bend angle (deg) | 30.0 |
| Gap (mm) | 60.0 |
| Quadrupoles | |
| Number | 6 |
| No. of families | 6 |
| Magnetic length (m) | 0.15 |
| Pole tip inscribed radius (mm) | 35.0 |
| Max. gradient (T/m) | 1.7 |
| Correction dipoles, combined horizontal/vertical | |
| Number | 3 |
| Magnetic length (m) | 0.10 |

**11. Booster-to-Storage-Ring (BTS) Transfer line**

| | |
|---|---|
| Magnets | |
| Dipoles, parallel ended | |
| Number | 3 |
| No. of families | 3 |
| Magnetic length (m) | 1.4 |
| Bend angle (deg) | 20.0 |
| Quadrupoles | |
| Number | 9 |
| No. of families | 9 |
| Magnetic length (m) | 0.30 |
| Pole tip inscribed radius (mm) | 32.5 |
| Max. gradient (T/m) | 15.0 |
| Correction dipoles, combined horizontal/vertical | |
| Number | 4 |
| Magnetic length (m) | 0.15 |
| Field (T) | 0.05 |
| Beam diagnostics | |
| Beam-position monitors | 5 |
| Sabersky finger | 1 |
| Viewing screens in vacuum | 4 |
| Nondestructive profile monitor | 1 |
| Total charge quantometer | 1 |

**12. Insertion devices**

| | |
|---|---|
| Number of undulators | 4 |
| Number of wigglers | 1 |
| Vacuum chamber full vertical aperture (cm) | |
| Light source turn-on | 2.0 |
| After commissioning | 1.0 |
| Magnet gap, minimum (cm) | |
| Light source turn-on | 2.5 |
| After commissioning | 1.4 |

# Appendix B

## Accelerator Theory

Here we present a basic introduction to charged-particle dynamics in circular electron accelerators. This section may serve to clarify some passages in the main text, and several important concepts are defined.

The periodic arrangement of bending and focusing magnets, separated by field-free drift regions, is called the *lattice* of a circular accelerator. From the viewpoint of particle dynamics, this lattice and the radio-frequency (rf) accelerating structure are the fundamental components of an accelerator ring. In many older accelerators, the beam focusing is provided by a constant transverse gradient in the magnetic field that is used to produce a roughly circular orbit of the stored beam. These are known as constant-gradient or *weak-focusing* machines. In contrast, most modern accelerators rely on repeated alternations of the magnetic gradient to focus the beam. These are known as alternating-gradient or *strong-focusing* machines; they are generally characterized by small transverse dimensions of the beam.

The *transverse motion* of particles can best be described in terms of deviations from the *equilibrium orbit.* This orbit is the unique periodic solution of the equations of motion for a particle with the nominal momentum $p_0$. It has the property of being closed on itself and is characterized by a local curvature $\Omega(s) = 1/\rho(s)$, where $s$ is the distance measured along the orbit. A general particle trajectory can be described by $x(s)$ and $y(s)$, the horizontal and vertical distances, respectively, from the equilibrium orbit. For a particle with momentum $p = p_0 + \Delta p$, the equations of motion, to first order, are as follows:

$$\frac{d^2x}{ds^2} + K_x(s)x = \frac{1}{\rho(s)}\frac{\Delta p}{p_0} \text{ and } \frac{d^2y}{ds^2} + K_y(s)y = 0 .$$

The right-hand side of the second equation is zero for accelerator designs in which the beam-bending magnets deflect the beam only in the horizontal plane. The functions $K_x$ and $K_y$ are determined by the lattice elements, and they are usually piecewise constant.

The "pseudo-harmonic" solutions to these equations of motion are given in terms of the *betatron oscillations* of the particle trajectories. For a particle with nominal momentum $p_0$, a trajectory in either plane can be described in terms of oscillations whose amplitude depends on the initial conditions and is proportional to $\beta^{1/2}$, where $\beta(s)$, the Courant-Snyder *beta function*, is a positive function that depends on the lattice configuration and

has the same periodicity as the lattice. This beta function has units of length and is readily calculated using computer codes. The phase of the betatron oscillations is given by

$$\psi(s) = \int_0^s \frac{ds}{\beta(s)} .$$

The trajectories of off-momentum particles exhibit an additional deviation from the equilibrium orbit in the horizontal plane; this offset is given by

$$x_p = D(s)\frac{\Delta p}{p_0} ,$$

where the dispersion function $D(s)$ depends on the lattice configuration and is periodic in $s$.

The *tune* of an accelerator, i.e., the number of betatron periods corresponding to the accelerator circumference $C$, is given by

$$\nu = \frac{1}{2\pi} \int_0^C \frac{ds}{\beta(s)} .$$

The stored beam in an accelerator is often characterized by a Gaussian density distribution in both transverse directions, so the density distribution may be conveniently described by a standard-deviation width $\sigma$. In terms of the lattice functions $\beta_x$ and $\beta_y$, the beam *emittances* are defined as

$$\epsilon_x = \frac{\sigma_x^2(s)}{\beta_x(s)} \text{ and } \epsilon_y = \frac{\sigma_y^2(s)}{\beta_y(s)} .$$

The *longitudinal motion* of an electron is dominated by a balance between the energy loss to synchrotron radiation and the compensating energy gain from the radio-frequency accelerating system. The time-averaged synchrotron-radiation power loss per electron is given by

$$P_\gamma = \frac{2}{3} \frac{r_0 c}{(m_0 c^2)^3} \frac{E^4}{\rho^2} ,$$

where $E$ is the electron energy and $r_0$ is the classical electron radius. The energy loss in one turn is then

$$U_0 = P_\gamma T ,$$

where $T$ is the transit time for one turn. This energy loss is compensated by the rf acceleration voltage

$$V(t) = V_0 \sin(h\omega_0 t) ,$$

where $h$ is an integer (the "harmonic number") and $\omega_0$ is the revolution frequency in radians per second of a particle with $p = p_0$. If $eV_0 > U_0$, the electron can be captured in $h$ stable bunches around the circumference of the storage ring.

Synchrotron radiation is emitted in a forward cone centered about the electron direction of motion, so the electrons lose both longitudinal and transverse momentum. Since the rf system restores only the longitudinal component of momentum, the transverse electron motion is *damped.* Energy damping also occurs, because particles with different momenta follow different trajectories and experience different energy losses.

The above results are obtained by assuming a continuous energy loss to radiation. However, synchrotron radiation is actually a statistical process involving the loss of energy in discrete quanta, and there is a *quantum excitation* of the beam in the horizontal plane in regions with nonzero dispersion. This excitation leads to a random-walk diffusion superimposed on the damping process. The competition between damping and quantum excitation leads to equilibrium values for the energy spread and horizontal emittance of the electron beam. Emittances are larger at higher electron energies.

In a perfectly constructed and perfectly aligned electron storage ring having no coupling between the horizontal and vertical planes, the vertical emittance of the electron beam would become negligibly small. However, in any actual machine, the unavoidable construction and alignment errors produce closed-orbit errors, horizontal-vertical coupling, and vertical dispersion. In turn, these effects can produce a vertical emittance with a magnitude approaching that of the horizontal emittance.

# Appendix C

## Multipole Components in the Lattice Magnets

Multipole components in the iron-dominated bending magnets and quadrupole magnets of the lattice arise because the poles have finite dimensions and because of finite construction tolerances. The former constraint leads to systematic components (the same in each magnet of the same type) which have the same symmetry and orientation as the magnet in which they are found. Such field components are known as "normal" components. Field errors which arise from construction tolerances are random in nature (different from magnet to magnet ) and can be either normal or "skew," i.e., of an orientation about the beam axis which is different from the normal component. An example of a random normal component is that which arises as a result of differences in the magnets' lengths. A random skew component would come from variations in the registration of magnet laminations prior to assembly.

To estimate the magnitude of systematic and random multipole components in our design, we have looked at the results achieved in existing magnets. Our survey of magnet data is far from being comprehensive. Rather, we have taken data from the magnets that members of the LBL team are familiar with, namely, from PEP (SLAC), SPS (CERN), and Daresbury (U.K.).

The purpose of the study was to define field tolerances in the Light Source magnets that lead to an acceptable degradation of the dynamic aperture of the machine. Tracking codes, which are used to find the dynamic aperture, require field components in a particular form. For our studies, we used the computer code DIMAT, which accepts multipole data in the form

$$B(x) = B\rho \sum_{n=0}^{\infty} \frac{k_n x^n}{n!} ,$$

with a rotation about the normal orientation called TILT. We show for the main lattice magnets how the multipole components $k_n$ have been derived.

In studying the data for the PEP quadrupole magnets, we find that the systematic components are those which are expected from symmetry considerations, i.e., 12-pole, 20-pole, etc. We have followed this principle in assigning systematic errors to the lattice magnets.

By contrast, the random components are all present, and, with the definitions given in PEP insertion quadrupole data sheets [Avery, 1986], have a relatively uniform distribution. Figure C-1, taken from Avery et al. [1979], illustrates this point.

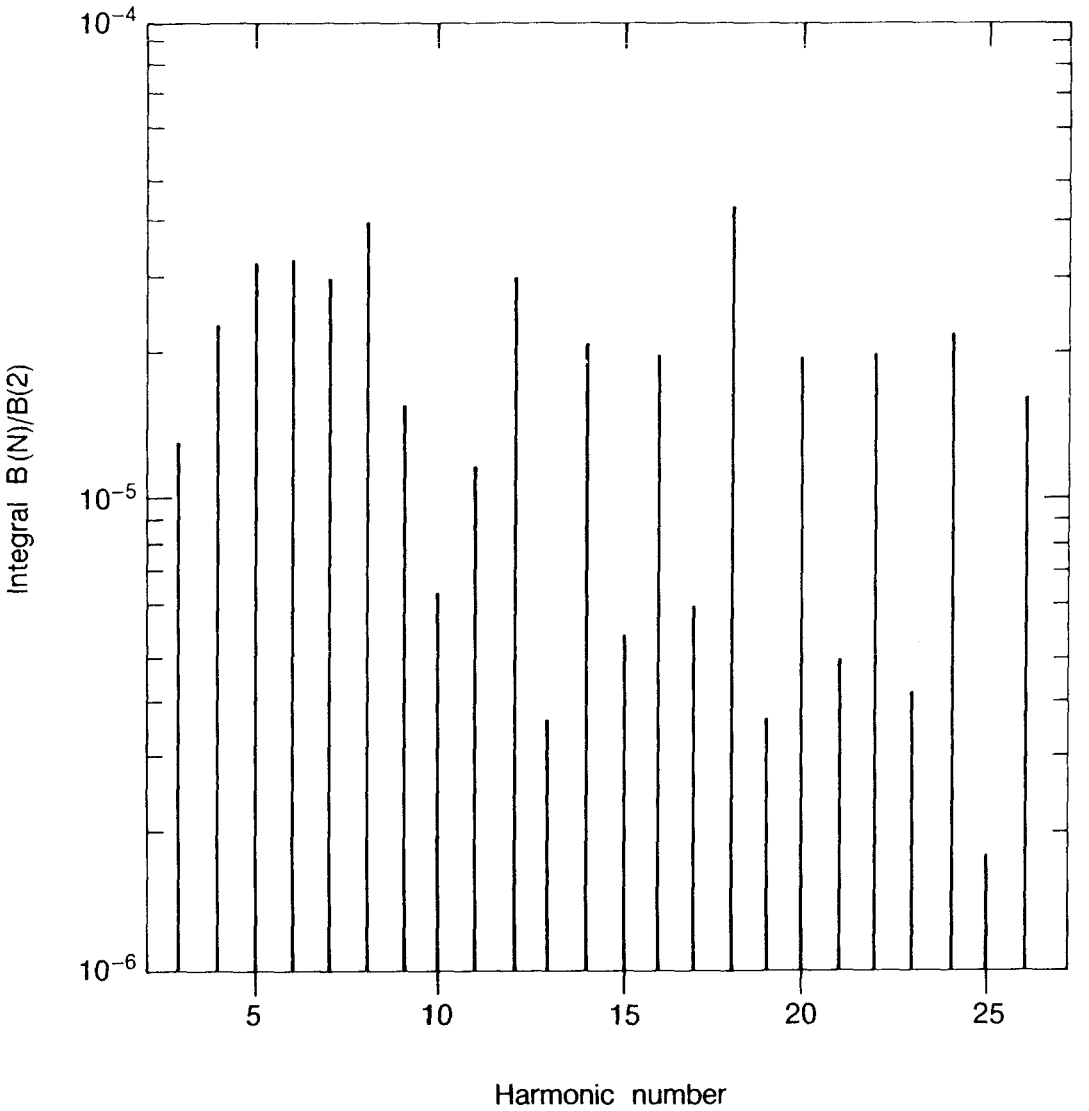


**Fig. C-1.** Harmonic multipole coefficients for a PEP insertion quadrupole, normalized at 8 cm to the quadrupole component for that magnet.

## C.1 Dipole Magnets

The most comprehensive set of data on dipole magnets is published in notes from the SPS (CERN) [Hatton et al., 1975] and PEP (SLAC) [Spencer, 1979]. In both cases, the field is given in terms of a field error, $B(x) - B_0$, at a certain displacement from the magnetic axis. In our analysis, we have assumed that these errors are due entirely to a normal sextupole field. The magnet systems at the Daresbury SRS are described by Marks and Poole [1981], where the sextupole term is extracted explicitly from the measured field data. Figure C-2, taken from this reference, shows the field measured across the aperture of an SRS dipole magnet.

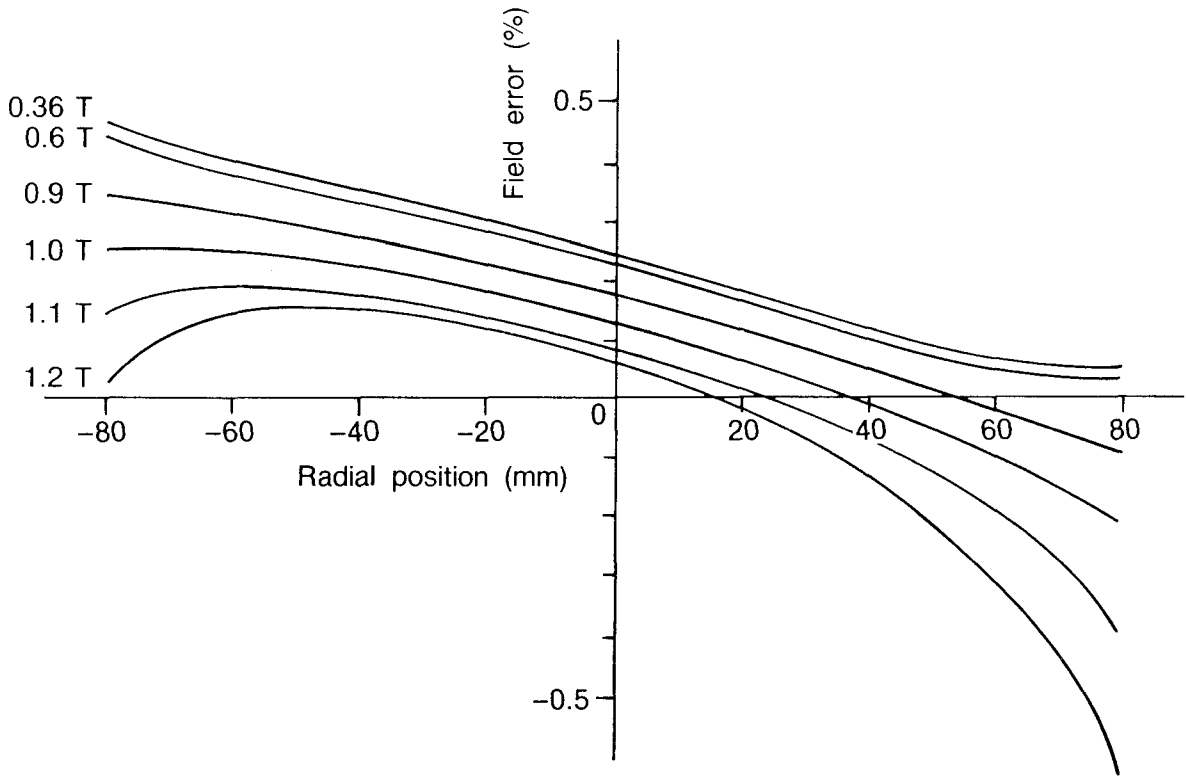


**Fig. C-2.** Typical integrated field errors, compared with an ideal SRS sector magnet.

In Table C-1, we show the expansion of the dipole field used in the tracking code DIMAT and expand the sextupole terms into units which are often quoted or which can be compared directly with the measured data.

The values of both the systematic and random sextupole fields used in the simulation led to no particular pathological behavior of the lattice, and, as can be seen from Table C-1, the random components (which were found to have the greater effect on dynamic aperture) can be regarded as conservative when compared with existing magnets.

## C.2 Quadrupoles

Estimates of the multipole components in the quadrupole magnets were extrapolated from the analysis of the PEP insertion quadrupoles [Avery et al., 1979; Main et al., 1979]. The relative multipole orientation found in these data shows explicitly that the components expected from symmetry are normal components. The symmetry-forbidden components are randomly oriented. Since all the data are normalized to the quadrupole component in each magnet, we must assign the random quadrupole term from other data. In assessing the effects of the random errors, we have taken the four components (higher than quadrupole) with the largest amplitudes, which for the quadrupole magnets are $n = 2$ (sextupole), $n = 3$ (octupole), $n = 5$ (12-pole), and $n = 9$ (20-pole).

The data from the PEP insertion quadrupole data sheets are in the form

$$\frac{\Delta B(x,\phi)}{B_1} = \sum_{n=2}^{\infty} \frac{|b_n|}{|b_1|} \cos\left[(n+1)\phi + \delta_n\right] \left(\frac{x}{r_0}\right)^{n-1},$$

**Table C-1.** Comparison of sextupole components in several dipole magnets.

| | $k_2$ ($m^{-3}$) | $\Delta B/B$ at 10 mm | $\Delta B/B$ at 100 mm | $\Delta B/B$ at 57 mm |
|---|---|---|---|---|
| **Light Source** (assumed) | | | | |
| systematic | 0.05 | $10^{-5}$ | $10^{-3}$ | $3.2 \times 10^{-4}$ |
| random | 0.1 rms | $2 \times 10^{-5}$ | $2 \times 10^{-3}$ | $6.4 \times 10^{-4}$ |
| **SPS** | | | | |
| systematic | | | | $2.8 \times 10^{-4}$ |
| random | | | | $0.6 \times 10^{-4}$ rms |
| **PEP** | | | | |
| systematic | $0.6 \times 10^{-2}$ | | | |
| random | 0.02 rms | | | |
| **SRS** | | | | |
| systematic | 0.01–0.1[a] | | | |
| random | $<<0.1$ rms | | | |

[a]Depends on excitation.

where $b_n/b_1$ is the relative amplitude of the $n$th component, $\delta_n$ is the skew orientation, $r_0$ is the radius at which $b_n/b_1$ is measured (0.08 meter for the PEP data), and $B_1$ is the field derived from the quadrupole component. This is converted to the DIMAT form through

$$\frac{k_n}{k_1} = \frac{n!}{r_0^{n-1}} \frac{b_n}{b_1} .$$

The resulting systematic and random multipole components are given in Table C-2.

**Table C-2.** Multipole components in the PEP insertion quadrupoles.

| | |
|---|---|
| Systematic | |
| $k_5/k_1$ ($m^{-4}$) | $1.8 \times 10^2$ |
| $k_9/k_1$ ($m^{-8}$) | $-6.4 \times 10^9$ |
| Random, rms | |
| $k_2/k_1$ ($m^{-1}$) | $5.0 \times 10^{-4}$ |
| $k_3/k_1$ ($m^{-2}$) | $8.0 \times 10^{-2}$ |
| $k_5/k_1$ ($m^{-4}$) | $1.2 \times 10^2$ |
| $k_9/k_1$ ($m^{-8}$) | $3.2 \times 10^9$ |

It should be pointed out that the PEP insertion quadrupoles were built to extremely tight tolerances and probably represent the best quadrupoles that can be economically built. A more realistic model for the Light Source quadrupoles might be the standard PEP quadrupoles. The multipole components in these magnets are typically 10 to 30 times larger than those of the insertion quadrupoles.

In estimating the multipole components in the Light Source quadrupoles, we must also take into account the smaller inscribed radius of these magnets (32.5 mm), compared with the PEP quadrupoles (50.0 mm). Since we will probably hold the same construction tolerances, we expect the multipole components to increase by about the inverse ratio of the inscribed radii.

For these reasons, we have assigned multipole components in the Light Source quadrupoles that are 50 times greater than those shown in Table C-2.

Typical magnet construction tolerances give a main field repeatability of $1{:}10^3$ rms, and standard survey techniques permit rotational accuracies of better than 0.5 mrad. These values have been attributed both to the bending magnets (dipole field and gradient) and to the quadrupole magnets in estimating the performance of the Light Source. In the case of the sextupole magnets, the more relaxed rotational tolerance of 1.0 mrad rms was used.

## C.3 Conclusions

It has been found (see Section 3.3.1.1) that the field errors described above lead to a significant, but acceptable, effect on the dynamic aperture. The errors are derived from existing magnets and scaled to levels which are consistent with Light Source magnet dimensions and standard engineering tolerances. We feel confident that the problems arising from these errors are understood and that they will not compromise the ultimate performance of the Light Source.

# Appendix D
## Positron Injection

As discussed in Section 3.3.3 of this report, the problems associated with the phenomenon of ion trapping can be avoided in a cost-effective manner by appropriately tailoring the bunch spacing in the Light Source storage ring. However, we cannot exclude the possibility that at some future date it may be desirable to replace the electron beam in the storage ring with a positron beam, since there could be second-order benefits (e.g., a better beam lifetime) from such a change. For this reason, we describe here a facility upgrade for producing positron beams, and we give a cost estimate for this option. With the proposed design, the storage ring could be filled with 400 mA of positrons (in the multibunch mode) in 7 minutes. In the few-bunch mode, the filling time with positrons would be 34 seconds per 7.6-mA bunch.

To ensure at the outset that a positron upgrade could be carried out with minimum impact on the facility, we intend to reserve sufficient floor space within the storage ring to accommodate a positron injector. This is illustrated in Fig. D-1, which shows the facility layout, along with the location of the possible positron injector. The positron layout shown in Fig. D-1 assumes that the original 50-MeV electron linac facility is reutilized for the positrons.

The goals we wish to achieve with the positron injection system are as follows:

- The system must provide a positron beam to the storage ring at its nominal operating energy of 1.5 GeV.
- The filling time should be short—not more than 10 minutes to reach the full current of 400 mA (in the multibunch operating mode).
- The system should be compatible with the use of a higher-intensity electron beam for commissioning, scrubbing, etc.
- The design should allow essentially unrestricted access to user beam lines during the filling procedure.

## D.1 Description of System

The system we propose to satisfy these goals is shown schematically in Fig. D-2. We assume that the original 50-MeV linac is upgraded to 75 MeV by increasing the klystron peak power via the SLED technique. In addition, we add a 175-MeV linac section and a special 50-MeV capture section, located just downstream from the positron conversion tar-

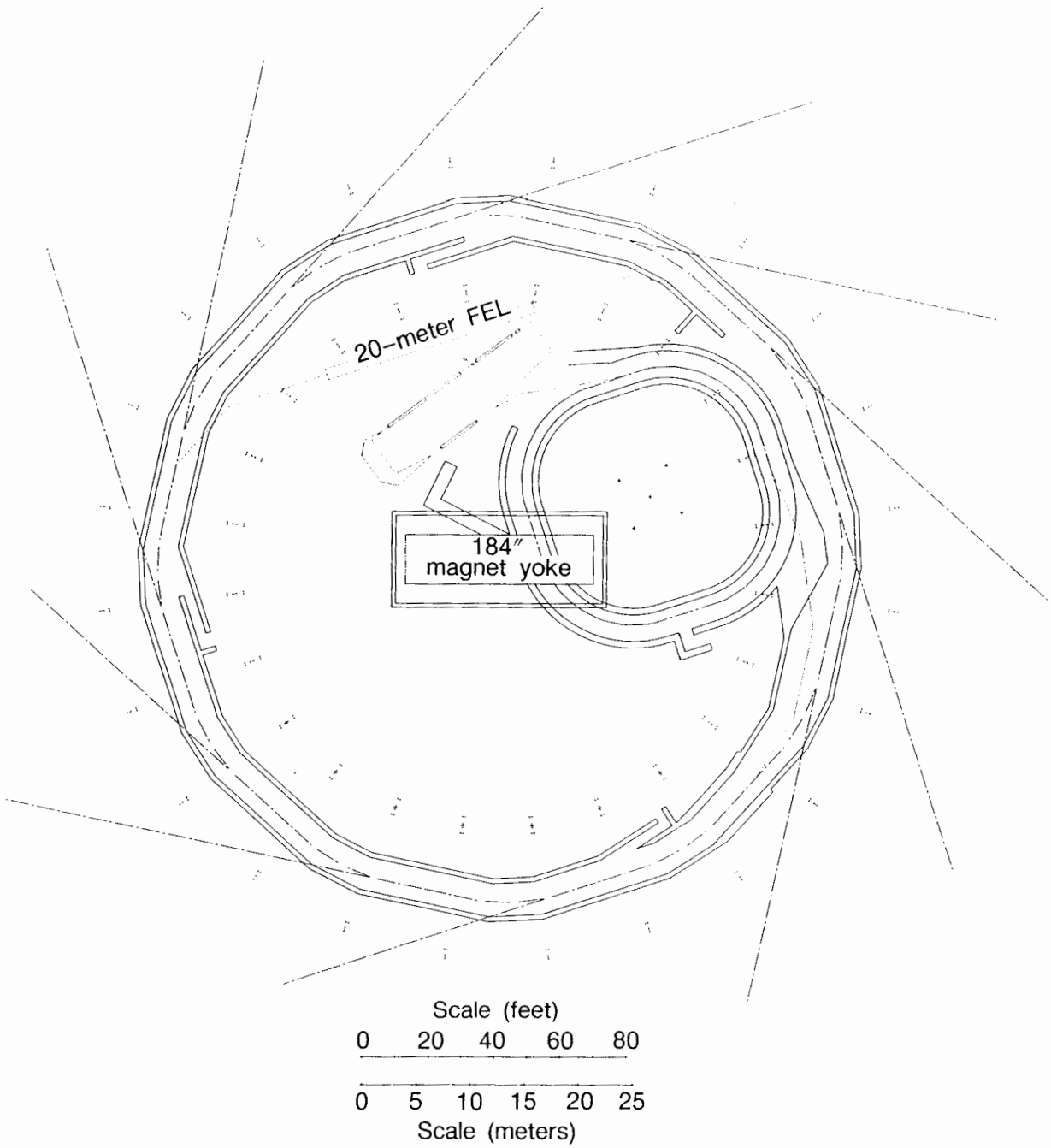


**Fig. D-1.** Layout of the 1–2 Synchrotron Radiation Source (including a foreseeable 20-meter free-electron laser), showing a possible location of a positron injection system.

get. To minimize both the additional hardware requirements and the spatial extent of the positron injection system, we have chosen a "folded" design, which allows the use of most of the linac structure for both electrons and positrons. Finally, to achieve the specified filling times for the storage ring, we assume that the booster would be upgraded to 10-Hz operation. It should be recognized, of course, that the beam energies shown in Fig. D-2 are nominal values. Because of beam-loading effects, we expect the various linac sections to give different energy increments to the electron and positron beams.

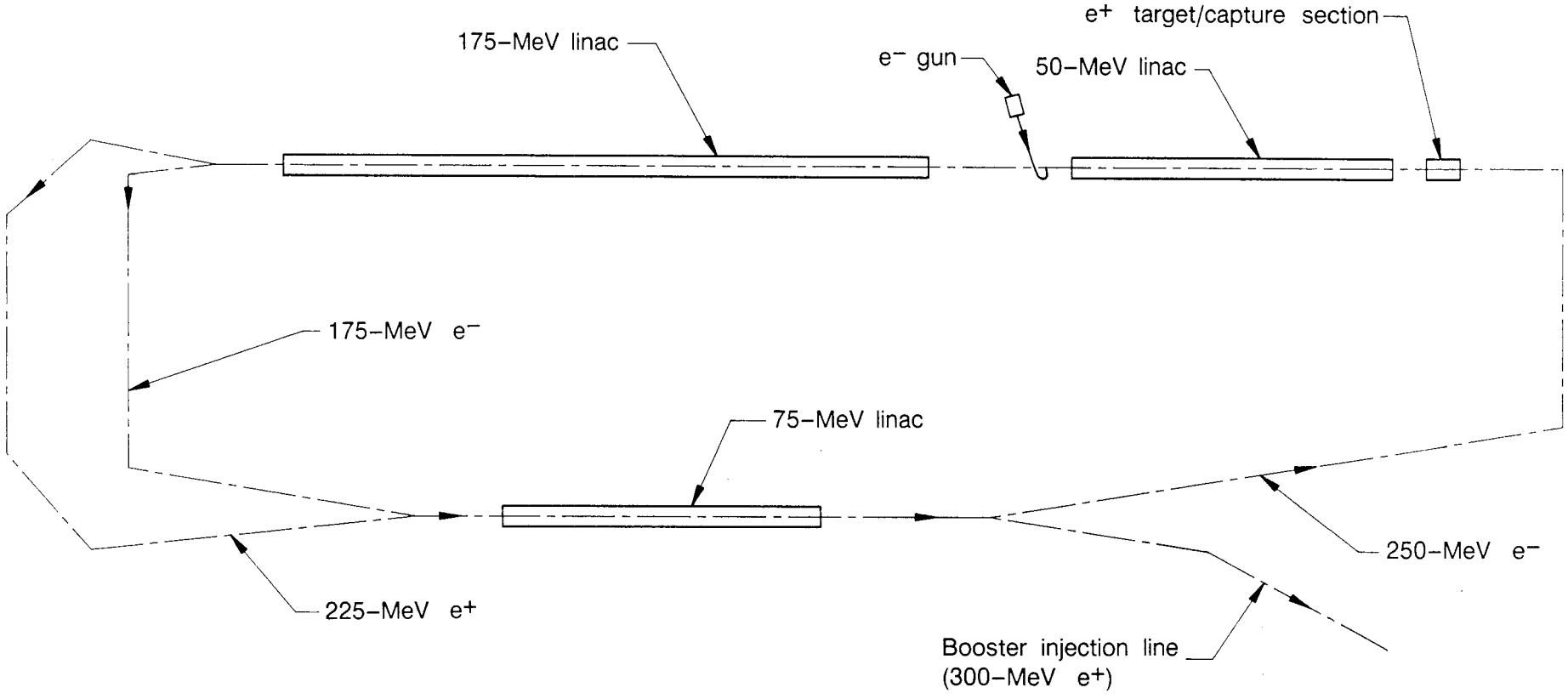


**Fig. D-2.** Schematic of the positron injector.

The injection path of the particles can be seen in Fig. D-2. Electrons are injected from a large-area gun (the same as that used initially for electron injection). To preserve a straight path for the positrons subsequently generated, the electron gun is located off-axis, and the beam is injected into the 175-MeV linac section through a 255° "alpha" magnet [Koontz et al., 1985]. The 175-MeV electrons are then directed through a 180° bend into the original (but now upgraded) linac. At the exit of this section of linac, the 250-MeV electron beam is directed again through 180° onto the positron converter target.

The converter is a tungsten target that is two radiation lengths (about 7 mm) thick. The positrons produced have a mean energy of about 8 MeV and an angular divergence of about 20° [LEP Design Report, 1983]. To achieve a good yield of positrons, it is necessary to maintain a small beam spot size at the converter target. The limit on the spot size due to chromatic effects of the quadrupoles ultimately determines the allowable beam energy spread. Because of beam loading, this, in turn, determines the maximum current in the electron linac.

Positrons emerging from the converter target are then concentrated with a tapered solenoid. The capture section, based on the SLAC design [Aune and Miller, 1979] is made to accept as much as possible of the energy spectrum of positrons from the target and to accelerate them to 50 MeV. Based on the SLAC Blue Book [SLC Conceptual Design Report, 1980], we assume an overall conversion efficiency of 0.31% at an electron beam energy of 250 MeV. Having reached 50 MeV, the positron beam is accelerated in the 175-MeV linac and then the 75-MeV linac. At this point, there is a beam of 300-MeV positrons available for injection into the booster synchrotron.

The beam lines in Fig. D-2 are arranged so that dc magnets can be used. Such an arrangement, which takes advantage of the opposite charge of the two species to separate them in a single "switching" magnet, is quite straightforward. Alignment and steering corrections are made by small dipoles located in beam line segments that are not shared. Note that the first dipole downstream of the 75-MeV linac in Fig. D-2 can be utilized—if so desired—to direct a 250-MeV electron beam into the booster. This mode, which would involve mainly reversing the polarity of the dipoles in that section of the transfer line, should be useful during the commissioning and/or scrubbing phase of the new system. The original LTB transfer line must be upgraded to handle a 300-MeV positron beam; this would require, among other things, a modification of the injection septum and kicker for the booster, since the deflection angles would need to be reduced as a consequence of the higher beam rigidity.

Modifications to the booster to achieve 10-Hz operation would involve replacing the original vacuum chamber with a thin-walled (0.3 mm) design similar to that proposed for the European Synchrotron Radiation Project [Buras and Tazzari, 1985]. This replacement would require the disassembling of the (split-yoke) booster magnets. To deal with the higher power in the magnets, water circuits would be reconfigured from series to parallel flow. In addition, the ramped power supplies would be replaced by biased-sine-wave "White circuit" supplies that are resonant at 10 Hz. Eddy-current heating of the thin stainless-steel vacuum chamber has been estimated to be about 20 W/m, based on published formulas [Hemmie and Rossbach, 1984]; this heating will not be a problem. Similarly, the maximum predicted [Hemmie and Rossbach, 1984] eddy-current contribution to the chromaticity (which occurs near injection energy) is of the order of the natural chromaticity and is easily correctable.

## D.2 Injection Process

As with electron injection, there are two operating modes of the storage ring, requiring different injection scenarios. We assume the same specifications here as for electrons, i.e., 400 mA for the multibunch mode and 7.6 mA per bunch in the few-bunch mode. When using positrons, it is no longer necessary to leave a gap in the bunch train, so the 400 mA multibunch current is distributed in all 328 storage-ring rf buckets; this change with respect to the original electron injection scheme has no operational consequences. Beam transfers into or out of the booster are done in a single turn, using a full-aperture kicker, following the scheme specified for electron injection (but taking account of the higher injection beam energy).

### D.2.1 Multibunch Mode

In the multibunch mode, the electron gun is run with a 150-ns pulse. To achieve the best possible intensity, a subharmonic buncher is used following the gun. Such a device is already in use in the SLC injector [SLC Design Handbook, 1984] and has produced up to $7.5 \times 10^{10}$ electrons in a single S-band linac bunch. In the multibunch case, a subharmonic-buncher frequency of 500 MHz is utilized. It is assumed that the subharmonic buncher compresses 50% of the beam from the gun into 90° of phase angle. A 500-MHz chopper is still employed to ensure that the beam entering the linac is within the acceptance window of the 500-MHz booster rf system.

The linac beam fills 75 (out of 125) contiguous rf buckets in the booster; a gap of 100 ns is left to allow the kicker pulse to decay. This kicker fall-time allowance is consistent with what can presently be achieved. The 75 booster bunches are then accelerated to 1.5 GeV and extracted, in a single turn, via a slow beam bump, a fast kicker, and a pair of septum magnets. Transfer to the storage ring rf system (also 500 MHz) is boxcar fashion.

In Table D-1, we show the beam intensity at various locations in the injection chain, along with the efficiency assumed at each point. Our starting point is a gun pulse of 5 A for 150 ns, i.e., a pulse of $4.7 \times 10^{12}$ electrons. Based on these assumptions, it would take 4211 booster cycles, or 7 minutes, to fill the storage ring to 400 mA.

### D.2.2 Few-Bunch Mode

In the few-bunch mode, the electron gun produces a single pulse. To achieve a suitable filling time, the booster captures the beam with an rf system having a lower frequency than the "standard" 500 MHz. This choice allows a longer gun pulse to be injected, with a concomitant increase in intensity. For the sake of design estimates, we assume that the frequency of the booster rf system used for beam capture (and hence that of the subharmonic buncher) is 40 MHz, i.e., an $h = 10$ system.

The single pulse of electrons is accelerated to 250 MeV and converted to positrons. The positrons are subsequently accelerated to 300 MeV, transferred to the 40-MHz booster bucket, accelerated to about 800 MeV, transferred adiabatically to the 500-MHz booster rf system, and then further accelerated to 1.5 GeV. Extraction from the booster and subsequent injection into the storage ring proceed as for the electron case.

**Table D-1.** Intensities and transmission for positrons in the multibunch mode.

| | $I^a$ (mA) | No. of electrons (or $e^+$) ($10^{10}$) | Efficiency | $e^-$ transmission | $e^+$ transmission |
|---|---|---|---|---|---|
| Gun current[b] | 5000 | 468 | | 1.0 | |
| | | | 0.50 | | |
| Chopper exit[c] | 2500 | 234 | | 0.50 | |
| | | | 0.50 | | |
| Electron linac exit | 1250 | 117 | | 0.25 | |
| | | | 0.0031 | | |
| Positron production/capture | 3.9 | 0.36 | | (0.00078) | 1.0 |
| | | | 0.67 | | |
| Positron linac exit | 2.6 | 0.24 | | | 0.67 |
| | | | 0.40 | | |
| Accepted into booster[d] | 0.62 | 0.097 | | | 0.27 |
| | | | 0.80 | | |
| Extracted from booster[d] | 0.50 | 0.078 | | | 0.21 |
| | | | 0.50 | | |
| Accepted into storage ring[e] | 0.095 | 0.039 | | | 0.11 |

[a]Peak current for gun, chopper, and linacs; average current for booster and storage ring.

[b]Gun pulse length is 150 ns.

[c]500-MHz subharmonic buncher and chopper transmit 50% of beam into 90° of phase, i.e., a 0.5-ns pulse every 2 ns.

[d]In 75 (out of 125) contiguous rf buckets.

[e]In 75 (out of 328) contiguous rf buckets.

Expected beam intensities at various locations for this filling mode are summarized in Table D-2. In general, we assume the same efficiencies as for the multibunch mode described above. Because of the rf gymnastics required in the booster, however, we have reduced the efficiency there accordingly. To fill a single bunch in the storage ring to 7.6 mA would take 343 booster cycles, or 34 seconds.

## D.3 System Parameters

The principal parameters for the buncher and linacs are summarized in Table D-3. In this section, we comment briefly on a few of the tentative parameter choices. These concern the energy at which positron conversion is performed, the energy of the positron beam at injection into the booster synchrotron, and the frequency of the capture rf system in the booster.

The choice of 250 MeV for the conversion energy is a compromise between the desire for a high conversion efficiency (which scales linearly with energy) and the desire to limit the power density at the converter target. To go higher in energy would increase the cost of the linac and recirculation beam lines, as well as increasing the power density (and hence

**Table D-2.** Intensities and transmission for positrons in the few-bunch mode.

| | $I^a$ (mA) | No. of electrons (or $e^+$) ($10^{10}$) | Efficiency | $e^-$ transmission | $e^+$ transmission |
|---|---|---|---|---|---|
| Gun current[b] | 8000 | 125 | | 1.0 | |
| | | | 0.50 | | |
| Chopper exit[c] | 4000 | 62 | | 0.50 | |
| | | | 0.50 | | |
| Electron linac exit | 2000 | 31 | | 0.25 | |
| | | | 0.0031 | | |
| Positron production/capture | 6.2 | 0.097 | | (0.00078) | 1.0 |
| | | | 0.67 | | |
| Positron linac exit | 4.2 | 0.065 | | | 0.67 |
| | | | 0.40 | | |
| Accepted into booster[d] | 0.17 | 0.026 | | | 0.27 |
| | | | 0.70 | | |
| Extracted from booster[e] | 0.12 | 0.018 | | | 0.19 |
| | | | 0.50 | | |
| Accepted into storage ring[e] | 0.022 | 0.009 | | | 0.09 |

[a]Peak current for gun, chopper, and linacs; average current for booster and storage ring.

[b]Gun pulse length is 25 ns.

[c]40-MHz subharmonic buncher and chopper transmit 50% of beam into 90° of phase, i.e., a 6.25-ns pulse for every 25-ns gun pulse.

[d]In a single 40-MHz rf bucket.

[e]In a single 500-MHz rf bucket.

radiation levels) at the converter, with a relatively modest gain in overall efficiency. Because we have adopted a recirculation scheme, we would still need the linac sections to provide the selected positron beam energy. Thus, there is no significant benefit to reducing the electron beam energy unless we reduce the positron energy correspondingly.

The choice of booster injection energy for the positron beam is based on the possible need for a damping/accumulator ring between the linac and the booster. Our present view is that this will not be necessary and that the "accumulation" can be handled simply by utilizing a lower-frequency rf system to capture a long linac pulse, which is subsequently transferred to the 500-MHz booster rf system. On the other hand, the beam energy of 300 MeV would be suitable for injection into a modest-sized damping/accumulator ring. To maintain a 10-Hz rate, the damping time in such a ring must be not more than about 40–50 ms. This requirement gets more difficult to fulfill as the positron energy drops below about 300 MeV. Indeed, the PIA ring at DESY [Febel and Hemmie, 1979] runs at 450 MeV, and the LEP EPA [LEP Design Report, 1983] is designed for 600 MeV. A design [Buras and Tazzari, 1985] exists for a damping ring at an energy as low as 250 MeV, which should satisfy our needs, but we have chosen to specify a somewhat higher energy to ease the specifications for such a ring, should it be needed.

**Table D-3.** Parameters for the positron injector option.

| | |
|---|---|
| **Electron Gun** | |
| Voltage (kV) | 120 |
| Few-bunch mode | |
| Peak current (A) | 8 |
| Pulse length (ns) | 25 |
| Multibunch mode | |
| Peak current (A) | 5 |
| Pulse length (ns) | 150 |
| **Linac** | |
| $e^-$ energy on target (MeV) | 250 |
| $e^-$ spot radius on target (mm) | 2 |
| $e^+/e^-$ conversion efficiency (%) | 0.31 |
| $e^+$ accepted energies (MeV) | 2–10 |
| $e^+$ transverse momentum (MeV/$c$) | 0.6 |
| First section | |
| Energy gain, nominal (MeV) | 175 |
| Length (m) | 8 |
| Second section | |
| Energy gain, nominal (MeV) | 75 |
| Length (m) | 4 |
| $e^+$ linac | |
| Energy gain (MeV) | 50 |
| Length (m) | 4 |
| $e^+$ capture section length (m) | 0.5 |
| S-band buncher length (m) | 0.105 |
| Repetition rate (Hz) | 10 |
| Total rf peak power (MW) | 200 |
| $e^+$ flux at linac exit, per pulse | |
| Multibunch mode | $2.4 \times 10^9$ |
| Few-bunch mode | $6.5 \times 10^8$ |
| $e^+$ beam properties at 300 MeV | |
| Emittance (m-rad) | $5 \times 10^{-6}$ |
| Momentum spread (%) | $\pm 0.5$ |

The choice of the frequency of the capture rf system in the booster is dictated by the desire to make use of a long pulse from the electron gun. A 40-MHz rf system, coupled with a 40-MHz subharmonic buncher and 40-MHz chopper, should allow the capture and compression of a 25-ns gun pulse into a single booster rf bucket. This allows a filling time in the few-bunch mode of about 35 seconds per bunch, i.e., only a factor of two slower than the electron filling time.

## D.4 Cost Estimate

A cost estimate for the positron injector system described here is given in Table D-4. Relatively large contingencies have been assigned, because neither the design nor the cost estimate has been carried out at the same level of detail as that for the 1–2 GeV Synchrotron Light Source described in the main text of this report. The estimated cost of the positron injector, in FY 1986 dollars, is $18.0 million.

**Table D-4.** Positron injection system cost summary in millions of FY 1986 dollars.

| | | | |
|---|---|---|---|
| Positron Injection System | | | 18.0 |
| Project Management and Administration | | 0.9 | |
| Special Research Facilities | | 12.3 | |
| Electron Source Enhancements | 0.5 | | |
| Linear Accelerators | 5.5 | | |
| Transport Lines | 1.4 | | |
| Positron Production System | 0.4 | | |
| Booster Upgrade | 1.8 | | |
| Control and Safety Systems | 0.2 | | |
| ED&I (25%) | 2.5 | | |
| Conventional Facilities | | 0.9 | |
| Shielding/Structural | 0.7 | | |
| Electrical (300 kVA) | 0.05 | | |
| Mechanical | 0.05 | | |
| ED&I (15%) | 0.1 | | |
| Contingencies | | 3.9 | |
| Special Research Facilities (30%) | 3.7 | | |
| Conventional Facilities (25%) | 0.2 | | |

# Appendix E

## Source Characteristics of Synchrotron Radiation

## E.1 Source Characterization

In discussing the propagation properties of radiation, the density of the photon flux in phase space plays a fundamental role and is generally referred to in optics as the brightness. A rigorous treatment of the phase-space concept in synchrotron radiation optics requires a generalization [Kim, 1985] of the textbook discussion of the radiation process in terms of the Wigner distribution function. In this report, we reserve the term *brightness* for the phase-space density of the photon flux, evaluated in the forward direction and at the center of the source, i.e., at the origin of the phase space, as follows:

$$\mathscr{B} = \left. \frac{d^4\mathscr{F}}{d\theta d\psi dx dy} \right|_0 . \tag{1}$$

Here $\theta$ and $\psi$ are the horizontal and vertical angles, and $x$ and $y$ are the horizontal and vertical coordinates, respectively. (It should be noted that this quantity is sometimes called the brilliance.) The brightness uniquely characterizes the strength of a radiation source, as it is invariant under propagation through linear optical elements, such as lenses or free space.

Integrating the phase-space density over the angles or the position coordinates, we obtain the spatial or angular density of flux:

$$\frac{d^2\mathscr{F}}{dxdy} = \int \frac{d^4\mathscr{F}}{d\theta d\psi dx dy} \, d\theta d\psi , \tag{2}$$

$$\frac{d^2\mathscr{F}}{d\theta d\psi} = \int \frac{d^4\mathscr{F}}{d\theta d\psi dx dy} \, dx dy . \tag{3}$$

For synchrotron radiation, the angular density of flux [Eq. (3)] has traditionally been the most familiar quantity, as it can be calculated from standard textbook formulas, and it is sometimes mistakenly called brightness. However, it is not an invariant measure of the

source strength, because its magnitude depends on the nature of the beam line focusing element. Finally, one obtains the flux by integration, as follows:

$$\mathcal{F} = \int \frac{d^2\mathcal{F}}{d\theta d\psi}\, d\theta d\psi = \int \frac{d^2\mathcal{F}}{dxdy}\, dxdy \,. \tag{4}$$

The flux is another invariant that characterizes the source strength.

It would clearly be convenient to consider the various differential fluxes introduced above in a small bandwidth around a given energy. In this case, we use the adjective *spectral.* Thus, we speak of the spectral brightness, spectral flux, the angular density of spectral flux, and so on.

## E.2 Radiation Characteristics of Undulators

The pattern of undulator radiation is illustrated in Fig. E-1. The spectrum is sharply peaked around odd harmonics of the fundamental photon energy given by

$$\epsilon_1\,[\mathrm{keV}] = 0.95\,\frac{E^2[\mathrm{GeV}]}{\lambda_u\,[\mathrm{cm}]\,(1 + K^2/2)} \,. \tag{5}$$

Here, $E$ is the electron energy, $\lambda_u$ is the undulator magnet period, and $K$ is the dimensionless deflection parameter given by

$$K = 0.934\, B_0\,[\mathrm{T}]\lambda_u\,[\mathrm{cm}]\,, \tag{6}$$

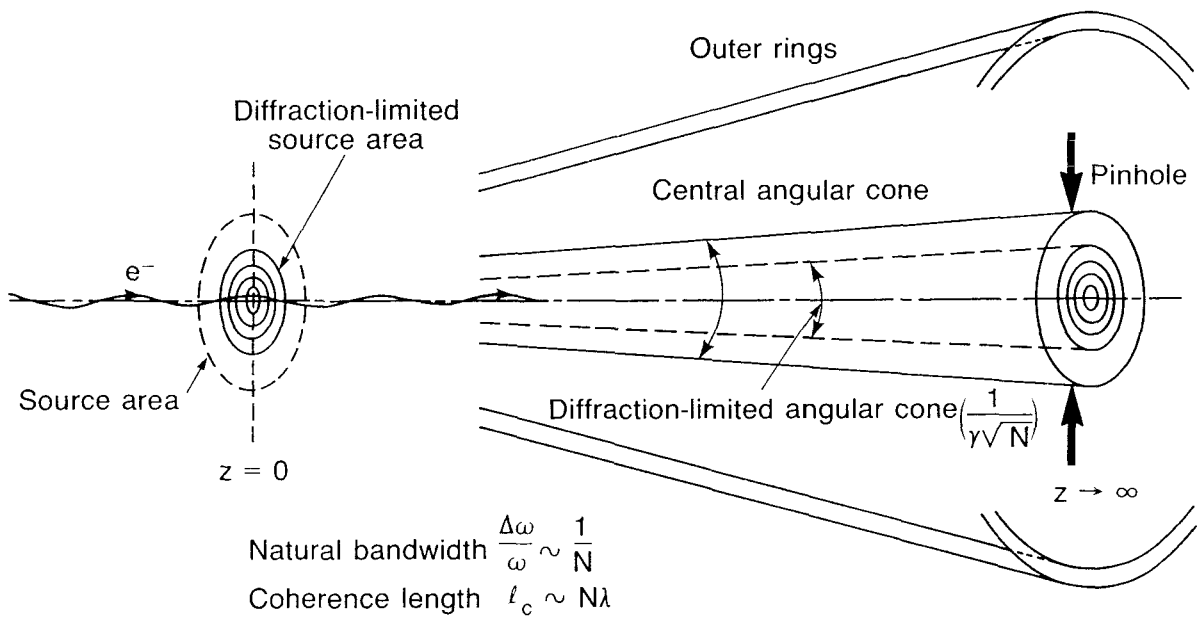


**Fig. E-1.** Schematic illustration of the radiation pattern from an undulator. The spectrum is sharply peaked around $\omega = n\omega_1$; the extent of transverse coherence depends on the ratio of the radiation phase-space area to the electron beam phase-space area.

where $B_0$ is the peak magnetic field.

At each harmonic, the angular distribution has a sharp central cone, which contains most of the useful flux, together with outer rings. The rms angular size of the central cone $\sigma_{Tx'}$ (or $\sigma_{Ty'}$) in the $x$ (or $y$) direction is given by a Gaussian sum of the diffraction-limited angular cone $\sigma_{r'} = (\lambda/L)^{1/2}$ (where $\lambda$ is the radiation wavelength and $L$ is the undulator length) and the electron beam angular divergence $\sigma_{x'}$ (or $\sigma_{y'}$):

$$\sigma_{Tx'} = \sqrt{\sigma_{x'}^2 + \sigma_{r'}^2}\,,$$
$$\sigma_{Ty'} = \sqrt{\sigma_{y'}^2 + \sigma_{r'}^2}\,. \tag{7}$$

If the undulator radiation in the central cone is focused through one-to-one optics, the image has a blur. The size of the blur is called the effective source size and is given in each direction by the diffraction-limited source size $\sigma_r = (1/4\pi)(\lambda L)^{1/2}$ and the electron beam size as follows:

$$\sigma_{Tx} = \sqrt{\sigma_x^2 + \sigma_r^2}\,,$$
$$\sigma_{Ty} = \sqrt{\sigma_y^2 + \sigma_r^2}\,, \tag{8}$$

where $\sigma_x$ and $\sigma_y$ are the rms electron beam sizes in the $x$ and $y$ directions, respectively.

The spectral flux contained in the central cone at the $n$th harmonic, within a 0.1% bandwidth, is given approximately by

$$\mathscr{F}_n = 1.43 \times 10^{14}\, N Q_n(K) I[A]\,, \tag{9}$$

where $N$ is the number of undulator periods, $I$ is the beam current, and $Q_n$ is given as

$$Q_n(K) = \frac{nK^2}{(1 + K^2/2)} \left\{ J_{\frac{n-1}{2}}\left[\frac{nK^2}{4(1 + K^2/2)}\right] - J_{\frac{n+1}{2}}\left[\frac{nK^2}{4(1 + K^2/2)}\right] \right\}^2, \tag{10}$$

where the $J$'s are Bessel functions. The flux densities can now be obtained by dividing Eq. (9) by an appropriate source or angular area. In particular, the spectral brightness is given by

$$\mathscr{B}_n = \frac{\mathscr{F}_n}{(2\pi)^2\, \sigma_{Tx}\, \sigma_{Ty}\, \sigma_{Tx'}\, \sigma_{Ty'}}\,. \tag{11}$$

Owing to the stochastic nature of the electron beam distribution, the phase-space area defined by the central cone and the effective source size is larger than the diffraction-limited phase-space area ($\lambda/2$). This latter portion of the diffraction-limited flux, i.e., the transversely coherent flux, is given by

$$\mathscr{F}_{n,\mathrm{coh}} = \left(\frac{\lambda}{2}\right)^2 \mathscr{B}_n\,. \tag{12}$$

For a low-emittance electron beam, such as that of the Light Source, a substantial fraction of the undulator flux is transversely coherent.

## E.3 Radiation Characteristics of Wigglers and Bending Magnets

Wigglers are distinguished from undulators both by a large value of $K$ and by a high harmonic number $n$. The spectral peaks of wiggler radiation from neighboring harmonics smear out because of electron-beam emittance effects, and the spectral and angular distributions of the radiation become similar to those of bending magnets, except for a $2N$-fold increase in intensity. The spectrum peaks around the critical energy, which is given by $\epsilon_c[\text{keV}] = 0.665E^2[\text{GeV}]B[\text{T}]$, beyond which it decreases exponentially.

The pattern of wiggler or bending-magnet radiation is illustrated in Fig. E-2. The angular density (per milliradian) of spectral flux from a bending magnet in the forward direction, within a 0.1% bandwidth, is given by

$$\left.\frac{d^2\mathcal{F}}{d\theta d\psi}\right|_{\psi=0} = 1.327 \times 10^{13} E^2[\text{GeV}]I[A]y^2K_{2/3}^2(y/2)\,, \tag{13}$$

where $K$ is a modified Bessel function of the second kind and $y$ is the photon energy in units of the critical energy. For wigglers the fluxes should be multiplied by an additional factor $2N$. The distribution, integrated over the vertical angle $\psi$, is

$$\frac{d\mathcal{F}}{d\theta} = 2.46 \times 10^{13}\, E[\text{GeV}]I[A]y\int_y^\infty K_{5/3}(y')dy'\,. \tag{14}$$

For bending magnets, the angular distribution is independent of the horizontal angle $\theta$, whereas it extends to an angle $\delta$ for wigglers, where $\delta = K/\lambda$. Here, $\gamma = E[\text{GeV}] \times 10^3/0.511$. The rms width of the vertical angle, $\sigma_\psi$, can be defined as

$$\sigma_\psi = \frac{1}{\sqrt{2\pi}}\,\frac{d\mathcal{F}}{d\theta} \Big/ \left.\frac{d^2\mathcal{F}}{d\theta d\psi}\right|_{\psi=0}\,. \tag{15}$$

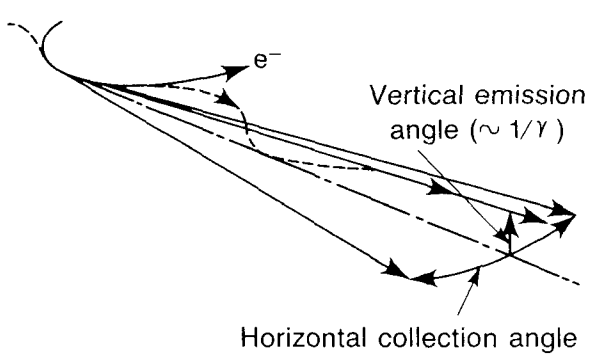


**Fig. E-2.** Schematic illustration of the radiation pattern from wigglers and bending magnets. The spectrum is smooth, with a peak around the critical energy. For wigglers the depth-of-field effect gives the source size.

At the critical energy, this becomes $0.32/\gamma$.

Strictly speaking, the above formula for the angular distribution is applicable only to the cases where the effects of the electron beam divergences can be neglected. Such is, indeed, the case here.

To compute the brightness, we first evaluate the diffraction-limited source size corresponding to the angle $\sigma_\psi$ with the following recipe, which is obtained by approximating the synchrotron radiation by the shape of the Gaussian mode of an optical resonator:

$$\sigma_r = \lambda/(4\pi\sigma_\psi) . \tag{16}$$

To simplify the calculation, we neglect the effect of the curvature of the electron trajectory on the effective source size. The expression for the bending-magnet brightness then becomes

$$\mathscr{B} = \left.\frac{d^2\mathscr{F}}{d\theta d\psi}\right|_0 \Bigg/ 2\pi \left[ (\sigma_x^2 + D^2\sigma_\epsilon^2 + \sigma_r^2)\left(\sigma_y^2 + \sigma_r^2 + \frac{\epsilon_y^2 + \gamma_y\sigma_r^2}{\sigma_\psi^2}\right)\right]^{1/2} \tag{17}$$

In the above, $\gamma_y$ is the third betatron function in the $y$ direction, $\epsilon_y$ is the beam emittance, $D$ is the dispersion function in the $x$ direction, and $\sigma_\epsilon$ is the rms value of the relative energy spread. Notice that the nonvanishing dispersion function in the bending magnet contributes to an additional term in the effective source size, proportional to the energy spread.

The brightness expression for wigglers is

$$\mathscr{B} = \frac{d^2\mathscr{F}}{d\theta d\psi} \sum_{\pm n, |-\frac{N}{2}|}^{|\frac{N}{2}|} \frac{1}{2\pi} \frac{\exp\left[-\frac{1}{2}\left(\frac{x_0^2}{\sigma_x^2 + z_{n\pm}^2\sigma_{x'}^2}\right)\right]}{\left[(\sigma_x^2 + z_{n\pm}^2\sigma_{x'}^2)\left(\frac{\epsilon_y^2}{\sigma_\psi^2} + \sigma_y^2 + z_{n\pm}^2\sigma_{y'}^2\right)\right]^{1/2}} ,$$

$$z_{n\pm} = \lambda_w \left(n \pm \frac{1}{4}\right) \tag{18}$$

Here $\lambda_w$ is the wiggler period. The effects of the depth of field — a result of the contributions from different poles — are apparent in the above expression. The exponential factor in Eq. (18) arises from the fact that wigglers have two source points, separated by $2x_0$, where

$$x_0 = \frac{K}{\gamma}\frac{\lambda_w}{2\pi} . \tag{19}$$

# Appendix F

## Special Undulators for Polarization Control

Planar undulators, in which all the pole faces are parallel, produce radiation with a high degree of linear polarization. Other kinds of polarized radiation can be obtained by using different magnet arrangements.

## F.1 Helical Undulator

Helical undulators produce circularly polarized radiation. A permanent-magnet helical undulator consists of short segments of dipole magnets, each of which is rotated by a fixed angle $\Theta$ relative to the previous one [Halbach, 1981]. Although rather elaborate, it should be possible to design a permanent-magnet helical undulator of variable $\Theta$, hence of variable period. Such an undulator would be a promising source of circularly polarized radiation, tunable over a wide range of photon energies.

## F.2 Crossed Undulator

The sense of the polarization from the helical undulator described above cannot be reversed. For a variable-polarization capability, however, one can use a pair of planar undulators oriented at right angles to each other [Kim, 1984], as shown in Fig. F-1. The amplitude of the radiation from these so-called crossed undulators is a linear superposition of two parts, one linearly polarized along the $x$ direction and another linearly polarized along the $y$ direction. By varying the relative phase of the two amplitudes by means of a variable-field magnet between the undulators, it is possible to modulate the polarization in an arbitrary way: The polarization can be linear and switched between two mutually perpendicular directions, or it can be switched between left circular and right circular. For this device to work, it is necessary to use a monochromator with a sufficiently small bandpass, so that the wave trains from the two undulators are stretched and overlapped. Also, the angular divergence of the electron beam should be sufficiently small; otherwise, the fluctuation in the relative phase limits the achievable degree of polarization.

## F.3 Other Devices

A planar undulator whose pole boundaries are tilted away from a right angle with respect to the axial direction can be used as a helical undulator if the electron trajectory lies a certain distance above or below the horizontal mid-plane of the undulator [Halbach, 1985]. Also, Onuki [1984] has proposed a variant of the crossed undulators in which the two orthogonal undulators overlap in the axial direction. Further study is required to predict the performance of this and other devices.

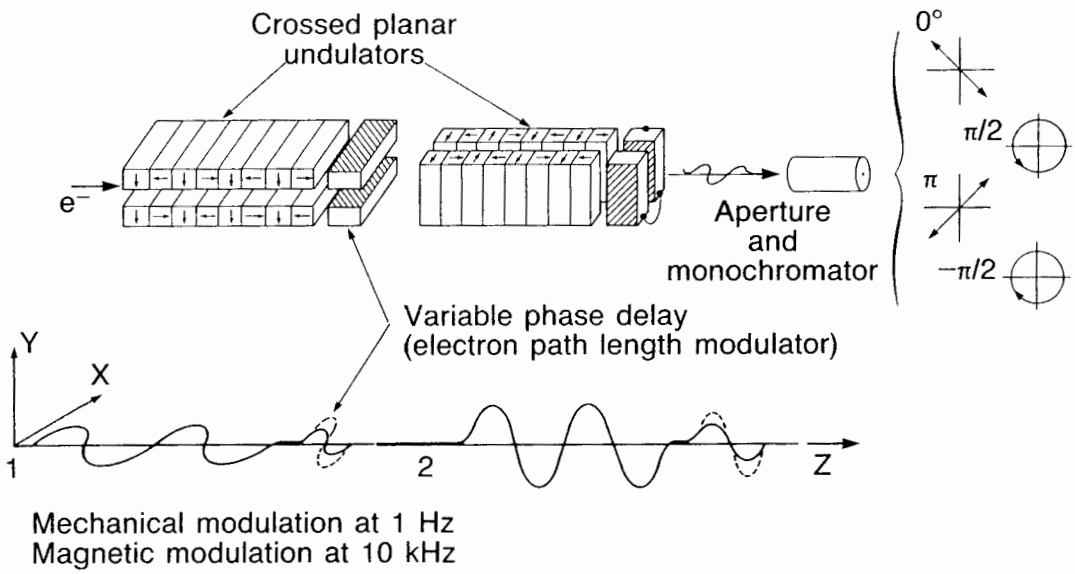


**Fig. F-1.** Schematic of a pair of crossed undulators, which could be used to produce variably polarized radiation.

# References


Attwood, D., K. Halbach, and K.-J. Kim, 1985. *Science,* **228**, 1265.

Aune, B., and R. Miller, 1979. In *Proc. of the 1979 Linear Accel. Conf.*, Montauk, NY, Brookhaven National Laboratory report BNL 51134, p. 440.

Avery, R.T., 1984. *Nucl. Instrum. Methods* **222**, 146.

Avery, R.T., 1986. PEP insertion quadrupole data sheets (private communication).

Avery, R., T. Chan, K. Halbach, R. Main, and J. Tanabe, 1979. "PEP Insertion Quadrupole Design Features," *IEEE Trans. Nucl. Sci.* **NS-26**, 4033.

Baconnier, Y., and G. Brianti, 1980. *The Stability of Ions in Bunched Beam Machines,* CERN report CERN/SPS/80-2(D1).

Bahr, C., *et al.*, 1983. *Nucl. Instrum. Methods* **208**, 117.

Barton, M.Q., 1986. "Ion Trapping with a Symmetric Bunch Filling of the NSLS VUV Ring," to be published in *Nucl. Instrum. Methods Phys. Res.*

Batchelor, K., 1979. *Note on the Proposed RF Parameters for the Photon Factory,* KEK note KEK-79-26.

Batchelor, K., and Y. Kamiya, 1979. KEK report KEK-79-25.

Bisognano, J., *et al.*, 1985. *Feasibility Study of a Storage Ring for a High Power XUV Free Electron Laser,* Lawrence Berkeley Laboratory report LBL-19771.

Bjorken, J.D., and S. Mtingwa, 1983. *Particle Accelerators* **13**, 115.

Bloembergen, N., 1984. *IEEE J. Quant. Electron.* **QE-20**, 556.

Borghi, R.P., *et al.*, 1968. In R.B. Neal, Ed., *The Stanford Two-Mile Accelerator* (Benjamin, New York), p. 116.

Brinkman, W., chairman, Physics Survey Committee (NRC), 1986. *Physics through the 1990s: An Overview* (National Academy Press, Washington, DC).

Brown, G.S., and A. Jackson, 1983. "Measurement of Single Bunch Purity in the SRS," *IEEE Trans. Nucl. Sci.* **NS-30**, 2346.

Buras, B., and S. Tazzari, 1985. *Report of the ESRP*, 3rd ed.

Chao, A.W., 1983. "Coherent Instabilities of a Relativistic Bunched Beam," in *Physics of High Energy Particle Accelerators, AIP Conf. Proc.* **105**, 353.

Chao, A., and J. Gareyte, 1976. *Scaling Law for Bunch Lengthening in SPEAR II*, PEP report PEP-224.

Chattopadhyay, S., 1985. *Coherent Instabilities and Ion Trapping Considerations for Aladdin*, Lawrence Berkeley Laboratory report LBL-19281.

Chattopadhyay, S., 1986. *Head-Tail Growth Rates in the ALS Booster,* Lawrence Berkeley Laboratory ESG Tech. Note 50.

Chattopadhyay, S., 1986. *Coupled Bunch Instabilities and Coherent Feedback System Requirements for the ALS*, Lawrence Berkeley Laboratory internal note.

Chattopadhyay, S., M. Cornacchia, A. Jackson, and M.S. Zisman, 1985. *Accelerator Physics Experiments at Aladdin,* Lawrence Berkeley Laboratory report LBL-19905.

Cornacchia, M., *et al.*, 1986. *Comparison of Lattice Options for a 1–2 GeV Synchrotron Light Source*, Lawrence Berkeley Laboratory report (to be published).

DiGennaro, R., 1986. *Estimated Thermal Distortion of the Grating Surfaces*, Lawrence Berkeley Laboratory note 1161.

DiGennaro, R., W.R. Edwards, and E. Hoyer, 1985. *Proc. SPIE* **582**, 273.

Einfeld, D., and G. Mulhaupt, 1980. "Choice of the Principal Parameters and Lattice of BESSY," *Nucl. Instrum. Methods* **172**, 55.

Eisenberger, P., and M. Knotek, co-chairmen, National Synchrotron Radiation Planning Committee, 1984. *Planning Study for Advanced National Synchrotron Radiation Facilities*, Sandia National Laboratory report.

Eriksson, M., 1986. Private communication.

Febel, A., and G. Hemmie, 1979. *IEEE Trans. Nucl. Sci.* **NS-26**, 3244.

Fugitt, J., *et al.*, 1981. "A Simplified RF Power System for Wideroe-Type Linacs," *IEEE Trans. Nucl. Sci.* **NS-28**, 2955.

Galayda, J., 1985. "Performance of a Correlator Filter in Betatron Tune Measurements and Damping on the NSLS Booster," *IEEE Trans. Nucl. Sci.* **NS-32**, 2132.

Haber, H., 1950. *J. Opt. Soc. Am.* **40**, 153.

Halbach, K., 1981. *Nucl. Instrum. Methods* **187**, 109.

Halbach, K., 1983. *J. Phys. (Paris)* **44**, C1-211.

Halbach, K., 1985. In *Proc. of the SPIE Intern. Conf. on Insertion Devices for Synchrotron Sources*, Stanford, CA.

Hatton, V., A. Riche, and A. Swift, 1975. *Measured Magnetic Properties of the SPS Magnets*, CERN report LabII/MA-Int.75-2.

Helm, R.H., and R. Miller, 1970. In P.M. Lapostolle and A.L. Septier, Eds., *Linear Accelerators* (North-Holland, Amsterdam), p. 115.

Hemmie, G., and J. Rossbach, 1984. DESY report DESY M-84-05.

Hettel, R.O., 1983. "Beam Steering at the Stanford Synchrotron Radiation Laboratory," *IEEE Trans, Nucl. Sci.* **NS-30**, 2228.

Howells, M.R., and P.Z. Takacs, 1982. *Nucl. Instrum. Methods* **195**, 251.

Ishimaru, H., 1984. *J. Vac. Sci. Technol.* **2**, 1170.

Ito, K., *et al.*, 1986. *Appl. Opt.* **25**, 837.

Jackson, A., 1986. *A Comparison of the Chasman-Green and Triple Bend Achromat Lattices*, Lawrence Berkeley Laboratory report LBL-21279.

James, M.B., and R.H. Miller, 1981. *IEEE Trans. Nucl. Sci.* **NS-28**, 3461.

James, M.B., *et al.*, 1983. *IEEE Trans. Nucl. Sci.* **NS-30**, 2992.

Kim, K.-J., 1984. *Nucl. Instrum. Methods* **219**, 425.

Kim, K.-J., 1985. *Brightness, Coherence, and Propagation Characteristics of Synchrotron Radiation*, Lawrence Berkeley Laboratory report LBL-20181.

Kirkpatrick, P., and A. Baez, 1948. *J. Opt. Soc. Am.* **38**, 766.

Koontz, R.F., 1976. *Single-Bunch Beam Loading of the SLAC Two-Mile Accelerator*, SLAC report 195, pp. 34-38.

Koontz, R.F., 1981. In *Proc. of the 1981 Linear Accelerator Conf.*, Santa Fe, p. 62.

Koontz, R.F., *et al.*, 1984. In *Proc. of the 1984 Linear Accelerator Conf.*, Seeheim, p. 430.

Koontz, R.F., *et al.*, 1985. *IEEE Trans. Nucl. Sci.* **NS-32**, 3036

Krinsky, S., S. Tazzari, G. Vignola, and H. Wiedemann, 1986. *Summary: Workshop on 1–2 GeV Light Source Lattices*, Lawrence Berkeley Laboratory report.

Lamb, W.E., 1984. *IEEE J. Quant. Electron.* **QE-20**, 551.

Lancaster, H.D., *et al.*, 1979. "A Microcomputer Control System for the SuperHILAC Third Injector," In *Proc. of the 1979 Linear Accelerator Conf.*, Brookhaven National Laboratory report BNL-51134.

Lancaster, H.D., *et al.*, 1983. "A High Performance Control System for a Heavy Ion Medical Accelerator," *IEEE Trans. Nucl. Sci.* **NS-30**, 2311.

Le Duff, J., 1985. "Current and Density Limitations in Existing Electron Storage Rings," *Nucl. Instrum. Methods* **A239**, 83.

Leiss, J., 1970. In P.M. Lapostolle and A.L. Septier, Eds., *Linear Accelerators* (North-Holland, Amsterdam), p. 157.

*LEP Design Report, Vol. I: The LEP Injector Chain*, 1983. CERN Report CERN-LEP/TH/83-29.

*LEP Design Report, Vol. II*, 1985.

Loew, G.A., and R.B. Neal, 1970. In P.M. Lapostolle and A.L. Septier, Eds., *Linear Accelerators* (North-Holland, Amsterdam), p. 53.

Magyary, S., *et al.*, 1981. "A High Performance/Low Cost Accelerator Control System," *IEEE Trans. Nucl. Sci.* **NS-28**, 1461.

Main, R., J. Tanabe, and K. Halbach, 1979. "Measurements and Corrections of the PEP Interaction Region Quadrupole Magnets," *IEEE Trans. Nucl. Sci.* **NS-26**, 4030.

Marks, N., and M.W. Poole, 1981. "Magnet Systems for the Daresbury Synchrotron Radiation Source," *IEEE Trans. Magn.* **MAG-17**, 1579.

McCarthy, J., and D. Wolff, 1985. "Very High Precision Current Regulated Power Supplies for the Fermilab Antiproton Source," paper presented at the Particle Accelerator Conf., Vancouver, BC, Canada, May 13–16.

Middleton, F., 1981. *IEEE Trans. Nucl. Sci.* **NS-28**, 3298.

Miller, R.H., *et al.*, 1965. *IEEE Trans. Nucl. Sci.* **NS-12**, 804.

Nakamura, M., and J. Hinkson, 1985. "Beam Position Monitor for Storage Rings," *IEEE Trans. Nucl. Sci.* **NS-32**, 1985.

Noda, H., T. Namioka, and M. Seya, 1974. *J. Opt. Soc. Am.* **64**, 1031; this paper is applicable to the treatment given here with $a_{ij}$ values as follows: $a_{20} = 1/(2R)$, $a_{02} = 1/(2\rho)$, $a_{40} = 1/(8R^2)$, $a_{22} = 1/(4R^2\rho)$, $a_{04} = 1/(8\rho^3)$, all other $a_{ij} = 0$ for $i + j \leqslant 4$.

Onuki, H., 1984. Paper presented at the Physics Society of Japan.

Patel, C.N.K., 1984. *IEEE J. Quant. Electron.* **QE-20**, 561.

Pellegrin, J.F., 1980. "A Review of Accelerator Instrumentation," in *Proc. 11th Intern. Conf. on High-Energy Accelerators*, p. 459.

Pines, H., 1983. "Automatic Tuning of the LBL SuperHILAC Third Injector Transport Line," *IEEE Trans. Nucl. Sci.* **NS-30**, 2314.

Rense, W.A., and T. Violett, 1959. *J. Opt. Soc. Am.* **49**, 139.

*Report of the Workshop on an Advanced Soft X-Ray and Ultraviolet Synchrotron Source: Applications to Science and Technology*, 1985. Lawrence Berkeley Laboratory report PUB-5154.

Rice, D., *et al.*, 1983. "Beam Diagnostics Instrumentation at CESR," *IEEE Trans. Nucl. Sci.* **NS-30**, 2190.

Rowe, E., *et al.*, 1981. "Status of the Aladdin Project," *IEEE Trans. Nucl. Sci.* **NS-28**, 3145.

Sabersky, A., 1983. *ALS Diagnostics Outlines*, report submitted by SAB Partners.

Sacherer, F., and F. Pedersen, 1981. "Theory and Performance of the Longitudinal Active

Damping System for the CERN PS Booster," *IEEE Trans. Nucl. Sci.* **NS-28**, 2344.

Schawlow, A.L., 1984. *IEEE J. Quant. Electron.* **QE-20**, 558.

Seitz, F., and D. Eastman, co-chairmen, Major Materials Facilities Committee (NRC), 1984. *Major Facilities for Materials Research and Related Disciplines* (National Academy Press, Washington, DC).

Selph, F.B., 1986. Lawrence Berkeley Laboratory ESG Note 13 (to be published).

Sheehan, J., *et al.*, 1983. "A Single Bunch Transfer System for the National Synchrotron Light Source," *IEEE Trans. Nucl. Sci.* **NS-30**, 2225.

*SLC Design Handbook*, 1984. Stanford Linear Accelerator Center.

Smith, L., 1986. *Effects of Wigglers and Undulators on Beam Dynamics*, Lawrence Berkeley Laboratory ESG Tech. Note 24.

Spencer, J.E., 1979. *Harmonic Strengths of PEP Dipoles*, PEP note 367.

*SRS Design Study*, 1975. Synchrotron Radiation Source (Daresbury) report DL/SRS/R2.

*Stanford Linear Collider Conceptual Design Report*, 1980. Stanford Linear Accelerator Center report SLAC-229.

Stehli, F., chairman, Energy Research Advisory Board Subcommittee (DOE), 1985. *Review of the National Research Council Report "Major Facilities for Materials Research and Related Disciplines"* (Department of Energy).

Timossi, C., *et al.*, 1985. *Error Monitoring for the SuperHILAC Third Injector Control System*, Lawrence Berkeley Laboratory report LBL-20331.

Townes, C.H., 1984. *IEEE J. Quant. Electron.* **QE-20**, 547.

Unser, K., 1981. "A Toroidal DC Beam Current Transformer with High Resolution," *IEEE Trans. Nucl. Sci.* **NS-28**, 2344.

Vignola, G., 1985. "Preliminary Design of a Dedicated 6 GeV Synchrotron Radiation Storage Ring," *Nucl. Instrum. Methods Phys. Res.* **A236**, 414.

Wrulich, A., 1986. *Study of FODO Structures for a Synchrotron Light Source*, Lawrence Berkeley Laboratory report LBL-21215.

Yamazaki, Y., K. Takata, and S. Tokumoto, 1981. "Damping Test of the Higher-Order Modes of the Re-entrant Accelerating Cavity," *IEEE Trans. Nucl. Sci.* **NS-28**, 2915.

Zisman, M.S., 1985. *Parametric Studies of Aladdin Lattices*, Lawrence Berkeley Laboratory report LBL-19191.

Zisman, M.S., S. Chattopadhyay, and J. Bisognano, 1986. *LBL Accelerator Physics Code ZAP*, Lawrence Berkeley Laboratory report LBL-21270 (to be published).

Zisman, M.S., 1986. *Parameter Studies of Candidate ALS Lattices*, Lawrence Berkeley Laboratory report LBL-21760.